LATE CENOZOIC POST-SUBDUCTION TECTONIC, MAGMATIC AND METALLOGENIC EVOLUTION OF THE ANATOLIDE – TAURIDE OROGENIC BELT, TURKEY

by

Fabien Rabayrol

Master's degree, UniLaSalle, 2011

A THESIS SUBMITTED IN PARTIAL FULFILLMENT OF
THE REQUIREMENTS FOR THE DEGREE OF

DOCTOR OF PHILOSOPHY
in
THE FACULTY OF GRADUATE AND POSTDOCTORAL STUDIES
(Geological Sciences)

THE UNIVERSITY OF BRITISH COLUMBIA
(Vancouver)

August 2018

© Fabien Rabayrol, 2018

The following individuals certify that they have read, and recommend to the Faculty of Graduate and Postdoctoral Studies for acceptance, the dissertation entitled:

Late Cenozoic Post-Subduction Tectonic, Magmatic and Metallogenic Evolution of the Anatolide-Tauride Orogenic Belt, Turkey

submitted by Fabien Rabayrol in partial fulfillment of the requirements for the degree of Doctor of Philosophy in Geological Sciences

Examining Committee:

Craig J.R. Hart, Geological Sciences
Supervisor

James K. Mortensen, Geological Sciences
Supervisory Committee Member

Derek J. Thorkelson, Simon Fraser University
Supervisory Committee Member

Dominique Weis, Geological Sciences
University Examiner

Scott W. Dunbar, Mining Engineering
University Examiner

Jeremy P. Richards, Laurentian University
External Examiner

Abstract

The termination of the northward subduction of the Southern Neotethyan oceanic slab beneath the Anatolide-Tauride Block in Turkey led to the onset of the Arabia-Eurasia continental collision in the Oligocene. The subducting Southern Neotethyan slab was affected by post-subduction segmentation manifested by slab break-off (central-eastern Anatolia) and tearing (western Anatolia) during the late Cenozoic. Many igneous complexes formed in the late Cenozoic and some of them host gold-rich porphyry and epithermal prospects and deposits. New temporal (U-Pb, $^{40}Ar/^{39}Ar$ and Re-Os dates), spatial (field observations and GIS) and geochemical data (elemental and Sr-Nd-Pb isotopic analyses) provide robust constraints on the genetic relationship between late Cenozoic slab segmentation tectonic events, Anatolian magmatism and associated gold mineralization.

The newly-defined Eastern Anatolian Magmatic Belt formed in response to the slab break-off initiation at ca. 25 Ma, window opening, westward break-off propagation to central Anatolia and induced asthenospheric flow. The slab break-off-related igneous units were subsequently covered by widespread volcanic products in eastern Anatolia (12 Ma-Present) that resulted from the long-lived asthenospheric heating, destabilization of the thickened Anatolian lithosphere root and its partial removal by convective dripping. Magmatic sources include the shallow melting of the previously-metasomatized Anatolian subcontinental lithospheric mantle and asthenosphere by decompression due to impingement of the Arabian and African sub-slab asthenospheric mantles.

Late Cenozoic Anatolian magmatism produced porphyry and epithermal prospects and deposits that cluster in nine isolated mineral districts controlled by graben, transtensional corridors and pull-apart basins. The bulk of gold mineralization (33 Moz Au) peaked at the beginning of the slab break-off event at 25 Ma in central and eastern Anatolia, and slab tear at 15 Ma in western Anatolia.

The late Cenozoic trench-parallel and -perpendicular migrations of slab rupture and window opening in Anatolia 1) allowed toroidal and poloidal flow of asthenosphere beneath Anatolia, 2) caused the migration of melting source and associated igneous complexes and mineral deposits in the overriding crust, 3) destabilized the Anatolian lithospheric mantle, which reduced the amount of available volatiles and metals, and therefore 4) increased the production of barren, drier and mantle-dominant volcanism through time that partially covers fertile igneous units.

Lay Summary

The increasing demand for metals requires efficient mineral exploration processes and thus well-constrained tectonic, magmatic and metallogenic models for a particular metal-endowed region. The Anatolian region in Turkey has been known for its gold resources for millenniums. However, factors controlling the formation and distribution of Anatolian gold mineralization and associated magmatic rocks have not been determined. New temporal, spatial and geochemical constraints on mineralized magmatic rocks reveal that most of Anatolian gold mineralization occurred for the last 25 million years as a result of mantle flow beneath Anatolia after the onset of the continental collision between the Arabia and Eurasia tectonic plates. The outcomes of this research work provide new empirical criteria and a comprehensive model for gold exploration in Anatolia as well as insights into the geodynamic evolution of the Eastern Mediterranean region and metallogenic processes in collisional domains.

Preface

This thesis is the result of my own work that was carried out at the MDRU – Mineral Deposit Research Unit at The University of British Columbia (UBC) and in the field throughout the Anatolia in Turkey between 2013 and 2018. Craig J.R. Hart (UBC), supervisor, Derek J. Thorkelson (SFU), James K. Mortensen (UBC) and Aleksandar Mišković (UBC), co-supervisors, provided me with advice, comments, suggestions, supervision and editorial co-authorship during our many informal discussions and formal committee meetings. This research work was part of the MDRU's Western Tethyan Metallogeny project (WTM; 2012-2016) sponsored by 16 Canadian and international mining companies including Alamos Gold Inc., AngloGold Ashanti Ltd., Avala Resources Ltd., Centerra Gold Inc., Dunav Resources Ltd., Dundee Precious Metals Inc., Esan, Eldorado Gold Corp./Tüprag Metal Madencilik, First Quantum Minerals Ltd., Kinross Gold Corp., National Iranian Copper Industries Company, Newcrest Mining Ltd., Pilot Gold Inc., Silver Standard Resources Inc., and Teck Resources Ltd. This WTM project was initiated and managed by Aleksandar Mišković and Craig Hart, who also designed the initial research objectives and scope of this PhD. I readjusted those objectives during my research work in collaboration with my supervisory committee to accommodate my own science questions, early findings and new ideas. Many technical reports were prepared by myself and edited by Aleksandar Mišković and Craig Hart, and oral presentations were given to the WTM project's sponsors. Although some components and data presented in those reports were used to develop argumentations and interpretations in this dissertation, none of the sections were literally reproduced. The report and presentation references are listed below.

The research herein is paper-based and built on four main chapters, which each forms a manuscript, bracketed by an introduction (Chapter 1) and conclusion (Chapter 6). Each manuscript aims to be published in reputable journals and is accompanied by supplementary data presented in the thesis appendices (A, B, C and D). Also, each manuscript deals with a specific component of the project that all together contribute to achieve the research objectives. The core ideas of each manuscript are a piece of original work but the redundancy of some background information was inevitable to produce stand-alone manuscripts. I provided the original ideas, wrote the entire content of each manuscript, acquired the data, unless specified below, designed all of the figures and tables, and conducted research work and leadership. Contributions from co-authors are defined below.

During my five-month field work between 2013 and 2015, I was guided by Aleksandar Miskovic (three weeks), Matias Sanchez (six days) and İlkay Kuşcu (Muğla University; four days). Sara Jenkins (MDRU-UBC) assisted me with data compilation, GIS work and design of database templates.

Chapter 2, entitled ***"Migration of Late Cenozoic Magmatism as a Proxy for Slab Break-Off and Mantle Flow Initiation and Propagation, Central and Eastern Anatolia, Turkey"*** is intended for submission to an international peer-reviewed journal. Craig Hart is the only co-author and provided technical and editorial advice, and suggestions to the developed ideas and manuscript. Additional discussions and reviews were brought by Derek Thorkelson, James Mortensen, Thomas Bissig (Goldcorp Inc.) and Armel Menant (Institut du Globe de Paris). Supplementary data to this manuscript are in the Appendix A.

Chapter 3, entitled ***"Geochemical Evolution of Late Cenozoic Post-Subduction Magmatism in Central and Eastern Anatolia, Turkey"***, is intended for submission to an international peer-reviewed journal. Derek Thorkelson provided me with his expertise in igneous petrology and helped me develop ideas and interpretations. He also provided advice and editorial suggestions throughout the preparation of this manuscript. Lithogeochemical data were acquired by Bureau Veritas Labs in Vancouver and the radiogenic Sr-Nd-Pb isotope analyses were conducted by Bruno Kieffer and Kathy Gordon from the Pacific Centre for Isotopic and Geochemical Research (PCIGR) at UBC. During that analytical process, I sampled the rocks, hand-picked the feldspar crystals for Pb isotope analyses and performed the Pb analyses. I also beneficiated from additional discussions about isotopic data quality and interpretation with Dominique Weis and Anaïs Fourny (PCIGR-UBC). Supplementary data to this manuscript are in the Appendix B.

Chapter 4, entitled ***"Tectonic Triggers for Post-Subduction Magmatic-Hydrothermal Gold Metallogeny in the Late Cenozoic Anatolian Metallogenic Trend, Turkey"*** is intended for submission to an international peer-reviewed journal. Craig Hart provided technical and editorial expertise to the developed ideas and manuscript. Robert Creaser (University of Alberta) and Richard Spikings (Université de Genève) were responsible for the Re-Os and $^{40}Ar/^{39}Ar$ dating analyses, respectively. Additional discussions and reviews were brought by Kaleb Boucher (Teck Resources Ltd.), Derek Thorkelson and James Mortensen. Supplementary data to this manuscript are in the Appendix C.

Chapter 5, entitled ***"Petrogenetic Controls on Post-Subduction Magma Fertility in the Late Cenozoic Anatolian Metallogenic Trend, Turkey"***, will also be submitted to an international peer-reviewed journal. Craig Hart, co-author, contributed through feedback, advice and editorial suggestions throughout the preparation of the manuscript. Additional discussion and technical advice were provided by Thomas Bissig, Farhad Bouzari (MDRU-UBC) and Derek Thorkelson. The acquisition protocol of geochemical data presented in this manuscript is the same as stated in Chapter 3 above. Supplementary data to this manuscript are in the Appendix D.

Below is the list of papers, technical reports, oral presentations and posters made or given during this PhD research project:

Papers

Baker, T., Bickford, D., Juras, S., Lewis, P., Öztaş, Y., Ross, K., Tukaç, A., **Rabayrol, F.**, Mišković, A., Friedman, R. and Creaser, R.A., 2016, The geology of the Kışladağ porphyry gold deposit, Turkey: Society of Economic Geologists Special Publication, v.19, p 57-83.

Technical reports

Rabayrol, F., 2013, Metallogeny and Tectonic Associations of the Anatolian Epithermal and Porphyry-Style Deposits: A Synthesis of the 2013 Field Season: *In* Mišković, A. and Hart, C.J.R (eds), Western Tethyan Metallogeny Project, 1st Technical Report to Companies, MDRU, The University of British Columbia, p 69-96.

Rabayrol, F. and Mišković, A., 2013, The Karapınar Cu-Mo porphyry and Demirtepe Cu-rich skarn deposits, Bursa district, NW Anatolia, Turkey: Western Tethyan Metallogeny Project, Technical Memorandum, MDRU, The University of British Columbia, 14 p.

Rabayrol, F., 2014, The Cenozoic Cu-Au metallogeny of Western Anatolia, Turkey: Western Tethyan Metallogeny Project, 2nd Technical Meeting, MDRU, The University of British Columbia, 26 p.

Rabayrol, F., 2014, The Öksüt High-Sulphidation Epithermal Au Deposit, Kayseri District, Central Anatolia, Turkey: *In* Mišković, A. (ed), Western Tethyan Metallogeny Project, Technical Report, MDRU, The University of British Columbia, 20 p.

Rabayrol, F., 2015, Temporal and Spatial Distribution of Porphyry and Epithermal Systems in the Anatolian-Tauride Metallogenic Belt, Turkey: *In* Mišković, A., (ed). Western Tethyan Metallogeny Project, Final Technical Report to Companies, MDRU, The University of British Columbia, p 71-75.

Rabayrol, F. and Hart, C.J.R., 2016, New geochronological ages from the Anatolian porphyry-epithermal systems and associated magmatic units, Turkey: Western Tethyan Metallogeny Project, Technical Memorandum, MDRU, The University of British Columbia, 15 p.

Rabayrol, F., Wainwright, A.J. and Hart, C.J.R., 2017, 2017 New geochronology of Anatolian magmatic units, Turkey: Western Tethyan Metallogeny Project-Phase 2, Technical Memorandum, MDRU, The University of British Columbia, 5 p.

Oral presentations (and associated abstracts)

Rabayrol, F., 2013, Metallogeny and Tectonic Associations of the Anatolian Epithermal and Porphyry-Style Deposits: A Synthesis of the 2013 Field Season. Western Tethyan Metallogeny Project, 1st Technical Meeting, İzmir, Turkey. Oral Presentation (invited).

Rabayrol, F., 2014, The Cenozoic Cu-Au metallogeny of Western Anatolia, Turkey:

Western Tethyan Metallogeny Project, 2nd Technical Meeting, Sofia, Bulgaria. Oral Presentation (invited).

Rabayrol, F., 2015, Temporal and Spatial Distribution of Porphyry and Epithermal Systems in the Anatolian-Tauride Metallogenic Belt, Turkey: *In* Mišković, A., (ed), Western Tethyan Metallogeny Project, Final Technical Meeting, Istanbul, Turkey. Oral Presentation (invited).

Rabayrol, F., Mišković, A., and Hart, C.J.R., 2016, Post-Subduction Porphyry and Epithermal Gold Systems and Associated Magmatism in the Miocene Anatolian Metallogenic Belt, Turkey. SEG 2016 Conference: Tethyan Tectonics and Metallogeny, Çeşme, Turkey, September 25-28. Oral Presentation.

Rabayrol, F., Hart, C.J.R. and Mišković, A., 2016, Temporal, Spatial and Geochemical Constraints on the Post-Subduction Porphyry and Epithermal Gold Systems of the Miocene Anatolian Metallogenic Belt, Turkey: Western Tethyan Metallogeny Project, Tethyan Day, Vancouver, BC, Canada, November 28. Oral Presentation (invited).

Rabayrol, F. and Hart, C.J.R., 2017, Late Cretaceous to Cenozoic subduction-, post-subduction- and post-collision-related porphyry and epithermal Au-Cu systems of the Anatolide-Tauride metallogenic belt, Turkey: Proceedings of the 14th SGA Biennial Meeting, Quebec City, Canada, August 20-23. Oral Presentation.

Rabayrol, F. and Hart, C.J.R., 2018, Petrogenetic Controls on Post-Subduction Magma Fertility in the Late Cenozoic Anatolian Metallogenic Trend, Turkey: Gordon Research Seminar, Mineralizing Processes Across All Scale, Waterville Valley, New Hampshire, USA, August 4-5, Oral Presentation (invited).

Posters (and associated abstracts)

Rabayrol, F., Mišković, A., Hart, C.J.R., Kuşcu, İ., Sanchez, M., 2014, The Cenozoic metallogeny of Western Anatolia, Turkey: SEG 2014 Meeting: Building Exploration Capability for the twenty-first Century, Keystone, Colorado, USA, September 27–30, Poster.

Rabayrol, F., Mišković, A., and Hart, C.J.R., 2016, Porphyry and epithermal metallogeny of the Anatolide-Tauride Belt, Turkey: AME BC Roundup, Vancouver, BC, Canada, January 26, Poster.

Rabayrol, F., Mišković, A., and Hart, C.J.R., 2016, Porphyry and epithermal metallogeny of the Anatolide-Tauride Belt, Turkey: PDAC-SEG Student Minerals Colloquium, Toronto, Ontario, Canada, March 7, Poster.

Rabayrol, F. and Hart, C.J.R., 2018, Petrogenetic Controls on Post-Subduction Magma Fertility in the Late Cenozoic Anatolian Metallogenic Trend, Turkey: Gordon Research Conference, Mineralizing Processes Across All Scale, Waterville Valley, New Hampshire, USA, August 5-10, Poster.

Table of Contents

Abstract iii

Lay Summary iv

Preface v

Table of Contents ix

List of Tables xv

List of Figures xvii

List of Abbreviations xxxiii

Glossary xxxvi

Acknowledgements xxxviii

Dedication xl

Chapter 1: Introduction 1

1.1 Subduction and post-subduction metallogeny 1

1.1.1 Subduction magmatism and porphyry-epithermal systems 1

1.1.2 Post-subduction metallogeny 4

1.1.3 Temporal and spatial distribution of porphyry deposits 5

1.2 Slab break-off and tearing models 6

1.3 Tectono-magmatic framework of the Anatolide-Tauride Block 8

1.4 Late Cenozoic segmentation of the Southern Neotethyan oceanic slab 12

1.5 Metallogeny of the Western Tethyan Orogenic Belt 13

1.6 Overview of the Turkish metallogeny 15

1.6.1 Birthplace of mining 15

1.6.2 Mineral diversity of Turkey 16

1.6.3 Tectono-magmatic context of Anatolian porphyry and epithermal mineralization 17

1.7 Thesis research questions and objectives 19

1.7.1 Part 1: Temporal, spatial and geochemical evolution of late Cenozoic magmatism in central and eastern Anatolia 19

1.7.2 Part 2: Late Cenozoic Anatolian Gold Metallogeny 20

1.8 Thesis approach 21

Part 1: Temporal, spatial and geochemical evolution of late Cenozoic magmatism in central and eastern Anatolia, Turkey 22

Chapter 2: Migration of late Cenozoic magmatism as a proxy for slab break-off and mantle flow initiation and propagation, central and eastern Anatolia, Turkey 23
2.1 Introduction 23
2.2 Geodynamic setting of the Anatolide-Tauride Block 25
2.3 Late Cenozoic magmatism of the central and eastern Anatolide-Tauride Block 29
2.4 Methodology 30
2.4.1 Age data compilation 30
2.4.2 Sample selection 31
2.4.3 LA-ICP-MS U-Pb dating analytical technique 31
2.5 Results 32
2.5.1 U-Pb zircon dating 32
2.5.2 Timing of late Cenozoic magmatism 36
2.6 Discussion 41
2.6.1 Initiation and propagation of the lithospheric slab break-off 41
2.6.2 Spatial extent of the sub-horizontal slab rupture 45
2.6.3 Slab break-off-related sub-slab asthenospheric infiltration 47
2.6.4 Propagation rates of magmatism and crustal uplift 48
2.6.5 Post-late Miocene partial removal of the subcontinental lithospheric mantle in central and eastern Anatolia 51
2.7 Conclusion 53

Chapter 3: Geochemical evolution of late Cenozoic post-subduction magmatism in central and eastern Anatolia, Turkey 55
3.1 Introduction 55
3.2 Geological and tectonic setting of central and eastern Anatolia 57
3.2.1 Tectonic assembly 57
3.2.2 Geological framework 60
3.2.3 Geodynamic history 61
3.3 Late Cenozoic magmatism in central and eastern Anatolia 64
3.3.1 Central Anatolia 64
3.3.2 Eastern Anatolia 69
3.3.3 Other late Cenozoic magmatic domains in central and eastern Turkey 72
3.4 Methodology 72
3.4.1 Geochemical data compilation 72
3.4.2 Sample selection 73
3.4.3 Analytical techniques 74
3.4.3.1 Whole-rock lithogeochemistry 74

3.4.3.2 Sr-Nd-Pb isotopic geochemistry 75
3.5 Results 76
3.5.1 Central Anatolia 76
3.5.1.1 Middle-Late Miocene 76
3.5.1.2 Pliocene 77
3.5.1.3 Quaternary 82
3.5.2 Magmatic transition between central and eastern Anatolia 93
3.5.3 Eastern Anatolia 93
3.5.3.1 Oligocene-early Miocene 93
3.5.3.2 Middle Miocene 94
3.5.3.3 Late Miocene-Pliocene 94
3.5.3.4 Pliocene-Quaternary 95
3.6 Discussion 96
3.6.1 Subduction component 96
3.6.2 Post-subduction magmatism: inheritance from past subduction events 98
3.6.3 Crustal contamination 98
3.6.4 Magma alkalinity 101
3.6.5 Composition and depth of magmatic sources 102
3.6.6 The role of upwelling subslab asthenosphere 108
3.6.7 Geochemical and tectonic evolution of the Eastern Anatolian Magmatic Belt 110
3.6.7.1 Two-stage, post-subduction, syn-collisional magmatism 110
3.6.7.2 Mantle dynamics and regional partial removal of the SCLM 114
3.7 Conclusion 116

Part 2: Late Cenozoic Anatolian Gold Metallogeny, Turkey 118

Chapter 4: Tectonic triggers for post-subduction magmatic-hydrothermal gold metallogeny in the late Cenozoic Anatolian Metallogenic Trend, Turkey 119

4.1 Introduction 119
4.2 Geological and tectonic setting of the Anatolide-Tauride Block 122
4.2.1 Anatolide-Tauride Block 122
4.2.2 Geodynamic evolution 126
4.2.3 Late Cenozoic Anatolian magmatism 128
4.3 Field-based definition of late Cenozoic Anatolian precious and base metal districts 129
4.3.1 Economic features of the Anatolian porphyry and epithermal systems 130
4.3.2 Simav low-sulfidation epithermal Au-Ag, porphyry Mo-Cu and skarn Pb-Zn-Fe district 133

4.3.3 İzmir low- to intermediate-sulfidation epithermal Au district 138
4.3.4 Uşak porphyry Au district 139
4.3.5 Afyon-Sandıklı porphyry Au-Cu prospect 141
4.3.6 Bodrum high-sulfidation epithermal and skarn district 141
4.3.7 Konya high-sulfidation epithermal Au-Ag-(Cu) district 142
4.3.8 Niğde high-sulfidation epithermal district 144
4.3.9 Kayseri high-sulfidation epithermal Au district 144
4.3.10 Hasançelebi high-sulfidation epithermal Au-Ag prospect 148
4.3.11 Tunceli porphyry Cu-Au-Mo district 148
4.3.12 Ağrı porphyry, high-sulfidation epithermal and Carlin-style Au-(Cu-Ag?) district 148
4.4 Methodology of gold mineralization dating 150
4.5 Age dating results 151
4.6 Discussion 155
4.6.1 Style and distribution of gold-bearing ore systems 155
4.6.1.1 Spatial distribution of precious and base metal mineralization in western Anatolia 155
4.6.1.2 Boron-rich hydrothermal alteration in western Anatolia 155
4.6.1.3 Orogenic and epithermal gold mineralization in western Anatolia 156
4.6.1.4 High-sulfidation epithermal mineralization in central Anatolia 157
4.6.1.5 Potential for epithermal- and porphyry-style mineralization in eastern Anatolia 157
4.6.2 Regional structural control on gold mineralization 158
4.6.2.1 Western Anatolia 158
4.6.2.2 Central Anatolia 159
4.6.2.3 Eastern Anatolia 161
4.6.3 Paleodepth of porphyry ore emplacement 162
4.6.4 Timing and duration of gold mineralization events 165
4.6.4.1 Western Anatolia 165
4.6.4.2 Central Anatolia 167
4.6.4.3 Eastern Anatolia 167
4.6.5 Temporal and spatial migration of gold mineralization and mantle dynamics 168
4.6.5.1 Slab roll-back-, back-arc- and slab tear-related gold mineralization in western Anatolia 170
4.6.5.2 Slab steepening- and break-off-related gold mineralization in central and eastern Anatolia 173

4.6.6 Comparison with the neighboring late Cenozoic gold provinces along the Western Tethyan Orogenic Belt....174
4.6.6.1 Greece and northwest Turkey....175
4.6.6.2 Lesser Caucasus and Iran....176
4.7 Conclusion....177

Chapter 5: Petrogenetic controls on post-subduction magma fertility in the late Cenozoic Anatolian Metallogenic Trend, Turkey....179
5.1 Introduction....179
5.2 Late Cenozoic tectonic, magmatic and metallogenic framework of the Anatolide-Tauride Block....181
5.2.1 Tectonic and geodynamic evolution....181
5.2.2 Late Cenozoic Anatolian magmatism....185
5.2.3 Late Cenozoic Anatolian precious and base metal metallogeny....188
5.2.3.1 Western Anatolia....189
5.2.3.2 Central Anatolia....190
5.2.3.3 Eastern Anatolia....190
5.3 Data acquisition and assessment....191
5.4 Results....196
5.5 Discussion....203
5.5.1 Fertility of late Cenozoic Anatolian magmatism....203
5.5.1.1 Magma volatile content and oxidation state....203
5.5.1.2 Early hornblende ± clinopyroxene fractionation....208
5.5.1.3 Magma alkalinity....211
5.5.2 Slab segmentation, mantle dynamics and magma petrogenesis....212
5.5.2.1 Temporal evolution of magma fertility....212
5.5.2.2 Metal and magma source(s)....214
5.5.2.3 Progressive loss of the SCLM and migration of melting loci....217
5.6 Conclusion....219

Chapter 6: Conclusions....222
6.1 Part 1: Temporal, spatial and geochemical evolution of late Cenozoic magmatism along the Eastern Anatolian Magmatic Belt....222
6.1.1 Definition of the Eastern Anatolian Magmatic Belt....222
6.1.2 Slab break-off-related magmatism....223
6.1.3 SCLM removal-related magmatism....224
6.1.4 Implications for the geodynamic evolution of the Eastern Mediterranean region....225

6.2 Part 2: Late Cenozoic Anatolian gold metallogeny 225
6.2.1 Characterization of late Cenozoic Anatolian mineral districts 226
6.2.2 Timing of late Cenozoic Anatolian gold mineralization and tectonic implications 227
6.2.3 Post-subduction magma fertility in Anatolia 228
6.2.4 Implications for post-subduction gold metallogeny 229
6.3 Final remarks 229

References 232

Appendix A 279
A.1 Age data compilation 279
A.2 LA-ICP-MS U-Pb dating analyses 281

Appendix B 290
B.1 Geochemical data compilation, sorting and interpretation 290
B.2 Lithogeochemical analysis QA-QC 293
B.3 Geochemical features of the late Cenozoic igneous complexes in central and eastern Anatolia 308
B.4 Primary melt calculation 310

Appendix C 312

Appendix D 317

Appendix E 318
E.1 Geochronology of the Kışladağ porphyry gold deposit 318
E.2 Age of the Kışladağ magmatic-hydrothermal system 319
E.3 CA-ID-TIMS U-Pb dating analytical procedure 324
E.4 $^{40}Ar/^{39}Ar$ dating analytical procedure 325
E.5 Re-Os dating analytical procedure 326

List of Tables

Table 2.1 U-Pb geochronological results from central and eastern Anatolia. 33

Table 3.1 Major, trace and rare earth element compositions of rock samples from central and eastern Anatolian igneous complexes. 78

Table 3.2 Radiogenic Sr and Nd isotope data from selected late Cenozoic igneous units in central and eastern Anatolia 82

Table 3.3 Radiogenic Pb isotope data from selected late Cenozoic igneous units in central and eastern Anatolia 82

Table 3.4 Primary melt isotopic compositions calculated at Mg # = 70 (if $r^2 \geq 0.5$) or by average of primitive samples ($62 \leq$ Mg # ≤ 70) if available ($n \geq 2$). 105

Table 4.1 Characteristics of the Late Cenozoic Anatolian mineral gold districts and isolated porphyry- and epithermal-style prospects. 131

Table 4.2 Resources, reserves and ore grades of the late Cenozoic Anatolian gold deposits. 134

Table 4.3 Summary of LA-ICP-MS U-Pb, $^{40}Ar/^{39}Ar$ and Re-Os dating results from selected gold deposits and prospects along the late Cenozoic Anatolian Trend. 152

Table 5.1 Major and trace element analyses of igneous rocks hosting precious or base metals along the late Cenozoic Anatolian Metallogenic Trend. 193

Table 5.2 Radiogenic Sr and Nd isotope data from late Cenozoic igneous units in western Anatolia. 195

Table 5.3 Radiogenic Pb isotope data from late Cenozoic igneous units in western Anatolia. 196

Table A.1 Geochronological data compilation, central and eastern Anatolia. 279

Table A.2 LA-ICP-MS U-Pb isotopic analyses. 285

Table B.1 Late Cenozoic igneous complexes of central and eastern Anatolia. 291

Table B.2 Petrographic descriptions of rock samples analyzed for major and trace element and/or Sr-Nd-Pb isotope geochemistry (central and eastern Anatolia) 294

Table B.3 Reference values for BAS-1 standard. 296

Table B.4 Reference values for P-1 standard. 297

Table B.5 Reference values for WP-1 standard. 298

Table B.6 Summary of analyzed reference material and comparison with reference values. 299

Table B.7 Comparison between original and duplicate samples (see text for explanation about MPD (mean percentile difference) and precision calculation. 302

Table B.8 Rb-Sr and Sm-Nd elemental concentration QA-QC. 306

Table B.9 Radiogenic Pb isotope analyses QA-QC. 307

Table C.1 LA-ICP-MS U-Pb isotopic analyses. 313

Table C.2 $^{40}Ar/^{39}Ar$ isotopic analyses. 316

Table D.1 Descriptions of rock samples analyzed for major and trace element and/or Sr-Nd-Pb isotope geochemistry (western Anatolia - Chapter 5). 317

Table E.1 Summary of the new geochronological data obtained from the Kışladağ deposit. 321

Table E.2 U-Th-Pb isotopic data - CA-ID-TIMS 327

Table E.3 $^{40}Ar/^{39}Ar$ dating data – Hypogene alunite (FR-13-65) from the Kışladağ gold mine. 328

List of Figures

Figure 1.1 Subduction zone setting illustrating the melting processes and the formation of porphyry deposits (redrafted from Winter, 2001; Richards, 2011a). 2

Figure 1.2 A) Slab break-off model (modified from Wortel and Spakman, 2000); B) Vertical slab tear model. 6

Figure 1.3 Western Tethyan Orogenic Belt (in light pink) showing the location of the study area, namely the Anatolide-Tauride Block (ATB; pink dotted area) sandwiched between Eurasia and the northward converging Africa and Arabia plates (green arrows), major tectonic boundaries (black lines) and the major porphyry and epithermal deposits, districts and belts. ASF = Aegean subduction front; BSZ = Bitlis suture zone; CSF = Cyprus subduction front; DSF = Dead Sea fault. Background image from ESRI. 9

Figure 1.4 Tectonic map of Turkey (1:6,000,000; Lambert Conic projection; European Datum 1950) showing the location of major tectonic terranes and boundaries (modified from Okay and Tüysüz, 1999; Şengör et al., 2008; Pourteau et al., 2013) and the distribution of ophiolitic units (modified from MTA, 2002). The labels are the tectonic zones within the Anatolide-Tauride Block (light green; study area). BSZ = Bitlis Suture Zone; IAESZ = İzmir-Ankara-Erzincan Suture Zone; ITSZ = Inner Tauride Suture Zone; SASZ = Sevan-Akera Suture Zone. 10

Figure 1.5 Paleogeographic reconstructions of the Middle East showing the Mesozoic northward migration of the Anatolide-Tauride Block (ATB) opening and closing the Northern and Southern Neotethys Oceans: A. Toarcian; B. Aptian; C. Maastrichtian; D. Burdigalian (modified from Barrier and Vrielynck, 2008). 11

Figure 1.6 3D diagram of the subducted Southern Neotethyan oceanic slab beneath Anatolia interpreted from seismic tomographic model and illustrating the segmented geometry of the slab and the projection to the surface of the major tectonic features (modified from Biryol et al., 2011). 13

Figure 1.7 Map of Turkey showing the distribution of metal occurrences, prospects and deposits with an emphasis on magmatic-hydrothermal ore systems, namely porphyry, epithermal, skarn and VMS. Basement boundaries were modified from Okay and Tüysüz, 1999; Şengör et al., 2008; Pourteau et al., 2013; the igneous units were modified from MTA, 2002. 18

Figure 2.1 Tectono-magmatic map of central and eastern Anatolia (1:4,000,000 scale; Lambert Conic projection; European Datum 1950) showing the basement boundaries, late Cenozoic igneous rocks (modified from MTA (2002)), complexes and provinces, and regional structures. The location of dated rock samples and compiled geochronological data is also displayed.

Base map: SRTM 90 m digital elevation models (Jarvis et al., 2008). Background of the location map is from Google Earth. AF = Akşehir Fault; ASF = Aegean Subduction Front; ATB = Anatolide-Tauride Block; Bitlis Sutures Zone; CSF = Cyprus Subduction Front; DSF = Dead Sea Fault; EAFZ = Eastern Anatolian Fault Zone; EF = Ecemiş Fault; ES = Eratosthenes Seamount; IAESZ = İzmir-Ankara-Erzincan Suture Zone; ITSZ = Inner Tauride Suture Zone; MF = Malatya Fault; NAFZ = North Anatolian Fault Zone; SASZ = Sevan-Akera Suture Zone; TGF = Tuz Gölü Fault. 26

Figure 2.2 Concordia diagrams of selected late Cenozoic volcanic rocks from Konya (FR-13-181 and FR-14-73), Melendiz (FR-15-36), Develidağ (FR-13-254) and Tekkedağ volcanic complexes (FR-15-40). Dashed black ellipses are discordant data not included in weighted mean $^{206}Pb/^{238}U$ age calculation. MSWD: mean square of weighted deviates. The cathodoluminescence images for each sample display the internal structure of representative igneous zircon grains. 34

Figure 2.3 Concordia diagrams of selected late Cenozoic magmatic rocks from Yamadağ (FR-14-82), and Ağrı magmatic complexes (FR-14-129, FR-14-142 and FR-14-124). Dashed black ellipses are discordant data not included in weighted mean $^{206}Pb/^{238}U$ age calculation. MSWD: mean square of weighted deviates. The images under optical microscope (left) and cathodoluminescence (right) for each sample display the internal structure of representative igneous zircon grains. 35

Figure 2.4 Age histogram of late Cenozoic magmatism in central (grey) and eastern Anatolia (black) counting the number (n) of available age data for each 1 m.y. bin since 30 Ma. The horizontal segments represent the succession of tectonic events that occurred a few million years prior to the crustal emplacement of dated magmatic units. The Ağrı magmatism is continuous from 21 to 17 Ma. Age data from the Galatian magmatism (22-17 Ma) are not on this histogram as out of Anatolia. Stars are the new U-Pb data reported in this Chapter 2 (refer to Table 2.1). Reference: [1]İmer et al. (2014); references of compiled data are in Table A.1…37

Figure 2.5 Time-sliced tectono-magmatic maps of central and eastern Anatolia (1:4,000,000 scale; Lambert Conic projection; European Datum 1950) showing the westward migration of magmatism in the Oligocene, early Miocene and middle Miocene. The black lines outline the magmatic complexes whereas the dashed lines and grey areas are the interpreted connections between contiguous magmatic complexes, and the older magmatic belts, respectively. ATB = Anatolide-Tauride Block. References: [0]this Chapter; [1]İmer et al. (2014); [2]Leo et al. (1974); [3]Kürüm et al. (2008); [4]Ekici et al. (2009); [5]Varol et al. (2014); [6]Wilson et al. (1997); [7]Kurt et al. (2008); [8]Platzman et al. (1998); [9]Ekici (2016); [10]Asan and Ertürk (2013); [11]Koç et al. (2012); [12]Korkmaz et al. (2017); [13]Lebedev et al. (2010). 39

Figure 2.6 Time-sliced tectono-magmatic maps of central and eastern Anatolia (1:4,000,000 scale; Lambert Conic projection; European Datum 1950) showing the westward migration of magmatism in the late Miocene, Pliocene and Quaternary. The black lines outline the magmatic complexes whereas the dashed lines and grey areas are the interpreted connections between contiguous magmatic complexes, and the older magmatic belts, respectively. References: [0]this Chapter; [1]Leo et al. (1974); [2]Platzman et al. (1998); [3]Pearce et al. (1990); [4]Keskin et al. (1998); [5]Notsu et al. (1995); [6]Dogan (2016); [7]Aydar et al. (2012); [8]Lepetit et al. (2014); [9]Lustrino et al. (2010); [10]Tatar et al. (2007); [11]Aydin et al. (2014); [12]Kuzucuoglu et al. (1998); [13]Schmitt et al. (2011);[14]Arger et al. (2000). 41

Figure 2.7 A. Schematic map of Turkey (1:6,000,000 scale; Lambert Conic Projection, European Datum 1950) displaying the distribution of major late Cenozoic magmatic domains, including the Eastern Anatolian Magmatic Belt (in blue), the area affected by the late Miocene partial removal of the subcontinental lithospheric mantle (SCLM; blue dashed area in eastern Anatolia), and regional faults (NAFZ = North Anatolian Fault Zone; EAFZ = Eastern Anatolian Fault Zone; BSZ = Bitlis Suture Zone; DSF = Dead Sea Fault). The vertical projection of slab margins and contours (in km) from tomography (Biryol et al., 2011) shows the spatial relationship between slab tear/break-off and surface magmatism. References: [1]Jolivet et al. (2015). B. Schematic 3D block (adapted from Wortel and Spakman (2000) and Ferrari (2004)) illustrating the westward migration of magmatism and sub-horizontal slab rupture propagation along the Arabian segment of the Southern Neotethyan slab during the Arabia-ATB collision in the middle Miocene. On this cartoon, the Bitlis-Pütürge Massifs, Central Anatolian Crystalline Complex, ATB and South Armenian Block are part of the same rigid overriding slab that undergoes the Arabian. 42

Figure 3.1 Tectono-magmatic map of central and eastern Anatolia (1:4,000,000 scale; Lambert Conic projection; European Datum 1950) showing the location of late Cenozoic igneous units (modified from MTA, 2002), complexes, belts and provinces (Chapter 2), basement boundaries (modified from Görür and Tüysüz, 2001; Şengör et al., 2008; Pourteau et al., 2010). Base map: SRTM 90 m digital elevation models (Jarvis et al., 2008). Background of the location map is from Google Earth. ASF = Aegean Subduction Front; ATB = Anatolide -Tauride Block; BSZ = Bitlis Suture Zone; CSF = Cyprus Subduction Front. 59

Figure 3.2 Magmatic map of central Anatolia (1:1,500,000 scale; Lambert Conic projection; European Datum 1950) showing the distribution of late Cenozoic igneous units (unit age modified from MTA, 2002), magmatic complexes and regional structures. The location of analyzed igneous rock samples and compiled geochemical data is also displayed. Base map: SRTM 90 m digital elevation models (Jarvis et al., 2008)..... 65

Figure 3.3 Field photographs illustrating representative magmatic complexes and rock samples from central Anatolia: the succession of lava flows at the Melendiz stratovolcano (A) including an andesitic rock sample from the village of Altunhişar (B – FR-14-34), the Develidağ stratovolcano from the Öksüt gold mine (C), and an andesitic lava flow from the Tekkedağ volcano near the village of Başdere (D – FR-15-40), and the ignimbrite (E) and andesitic units (F – FR-13-181) of the Konya volcanic complex in the area of İnlice. 67

Figure 3.4 Optical microphotographs showing selected rock textures and minerals from central and eastern Anatolia. Detailed sample descriptions are in the appendix B (Table B.2); A. clinopyroxene-bearing andesite from Başdere at the Tekkedağ volcano (FR-15-40; plane-polarized light); B. two-pyroxene-bearing andesite from Öksüt at the Develidağ stratovolcano (FR-13-237; cross-polarized light); C. biotite-bearing andesite from Mihaliç tepe at the Konya volcanic complex (FR-14-59; plane-polarized light); D. clinopyroxene-bearing andesite from Hasançelebi at the Yamadağ volcanic complex (FR-14-82; cross-polarized light); E. two-pyroxene-bearing andesite from Idrisli in the Erzurum volcanic plateau (FR-14-117; cross-polarized light); F. monzonite from Diyadin in the Ağrı magmatic complex (FR-14-132; cross-polarized light). 68

Figure 3.5 Magmatic map of eastern Anatolia (1:2,500,000 scale; Lambert Conic projection; European Datum 1950) showing the distribution of late Cenozoic igneous units (unit age modified from MTA, 2002), complexes and provinces, and regional structures. The locations of analyzed igneous rock samples and compiled geochemical data are indicated. Base map: SRTM 90 m digital elevation models (Jarvis et al., 2008) 70

Figure 3.6 Photographs of representative magmatic complexes and rock samples from eastern Anatolia including: an andesitic lava flow at the Yamadağ volcanic complex, north of the town of Hasançelebi (A – B; FR-14-80), the basaltic plateau near the city of Erzurum as part of the Erzurum volcanic suite (C – D; FR-14-112), and the Taşlıçay (E) and Taşkapı granitic intrusions (F – FR-14-143) that belong to the Ağrı magmatic complex. 71

Figure 3.7 Total alkali versus silica diagram (Le Maitre et al., 2002) showing the composition of volcanic rocks from central Anatolia (A. Late Miocene; B. Pliocene; C. Quaternary), transition central/eastern Anatolia (D. Middle to late Miocene; E. Pliocene) and eastern Anatolia (F. Oligocene-early Miocene; G. Middle Miocene; H. Late Miocene-Pliocene; I. Pliocene-Quaternary). The references of compiled and previously published geochemical data are detailed in the appendix B (Table B.1). 83

Figure 3.8 K_2O versus SiO_2 diagram (Peccerillo and Taylor, 1976) showing the composition of volcanic rocks from central Anatolia (A. Late Miocene; B. Pliocene; C. Quaternary), transition central/eastern Anatolia (D. Middle to late Miocene; E. Pliocene) and eastern Anatolia

(F. Oligocene-early Miocene; G. Middle Miocene; H. Late Miocene-Pliocene; I. Pliocene -Quaternary). The references of compiled and previously published geochemical data are detailed in appendix B (Table B.1). 85

Figure 3.9 Extended N-MORB-normalized trace element diagram (SiO_2 < 56 wt %) displaying the composition of volcanic rocks from central Anatolia (A. Late Miocene; B. Pliocene; C. Quaternary), transition central/eastern Anatolia (D. Middle to late Miocene; E. Pliocene) and eastern Anatolia (F. Early-middle Miocene; G. Late Miocene-Pliocene; H. Pliocene-Quaternary). N-MORB normalization and E-MORB, and OIB values from Sun and McDonough (1989); Depleted MORB Mantle (DMM) reference values from Workman and Hart (2005); Upper and Lower Crust reference values from Rudnick and Gao (2014); Continental and Oceanic Arc reference values from Kelemen et al. (2014). The references of compiled geochemical data are detailed in the appendix B (Table B.1). 87

Figure 3.10 Chondrite-normalized trace element diagram (SiO_2 < 56 wt %) displaying the composition of volcanic rocks from central (A. Late Miocene; B. Pliocene; C. Quaternary), transition central/eastern (D. Middle to late Miocene; E. Pliocene) and eastern Anatolia (F. Early-middle Miocene; G. Late Miocene-Pliocene; H. Pliocene-Quaternary). Chondrite normalization, E-MORB, N-MORB and OIB reference values from Sun and McDonough (1989); Depleted MORB Mantle (DMM) reference values from Workman and Hart (2005); Upper and Lower Crust reference values from Rudnick and Gao (2014); Continental and Oceanic Arc reference values from Kelemen et al. (2014). The references of compiled geochemical data are detailed in the appendix B (Table B.1).....89

Figure 3.11 $(^{87}Sr/^{86}Sr)_i$ versus $(^{143}Nd/^{144}Nd)_i$ (A. New data; B. Central Anatolia; C. Eastern Anatolia) and $(^{207}Pb/^{204}Pb)_i$ (C. New and E. All data) and $(^{208}Pb/^{204}Pb)_i$ (D. New and F. All data) versus $(^{206}Pb/^{204}Pb)_i$ diagrams. BSE = bulk silicate Earth (Bouvier et al., 2008). The different reservoirs plotted include: Mediterranean sediments (Klaver et al., 2015); Kula lavas, western Anatolia (Alıcı et al., 2002; Chakrabarti et al., 2012; Aldanmaz et al., 2015); Karacadağ volcanic shield, northern Arabian platform, Turkey (Lustrino et al., 2010; Keskin et al., 2012; Ekici et al., 2014); Aegean arc and Red Sea MORB reservoirs from GeoRoc database (Sarbas and Nohl, 2008, consulted on 2017/05/30); Afar plume and Red Sea MORB reservoirs (Pik et al., 1999; Bertrand et al., 2003). GLOSS = global subducting sediment composition (Plank and Langmuir, 1998); NHRL = Northern Hemisphere reference line (Hart, 1984); EMI, EMII, HIMU, PREMA, DMM reservoirs from Zindler and Hart (1986); AFC = assimilation and/or crystal fractionation (DePaolo, 1981). The Sr and Nd isotopic composition of primary melts was calculated for each igneous suite at Mg # = 70 based on the protocol and statistical analysis provided in the appendix B (Figure B.4). The grey arrow is the magmatic trend related to the

SCLM partial removal event in eastern Anatolia from the middle Miocene to Present. 91

Figure 3.12 Trace element diagrams used to investigate the petrogenesis of mafic magmatic rocks (SiO_2 < 56 wt %) from central and eastern Anatolia. A. Ta/Yb versus Th/Yb diagram (Pearce, 1983); B. Ba/Nb versus Th/Nb diagram (Kepezhinskas et al., 1996; Temizel et al., 2016). Primitive mantle (PM), OIB, E-MORB and N-MORB reference values from Sun and McDonough (1989) and upper (UC) and lower crust (LC) reference values from Rudnick and Gao (2014). Symbol legend is provided Figure 7. Kula volcanism is used as proxy for Anatolian OIB-like reservoir and African mantle reservoir (Aldanmaz, 2002; Alıcı et al., 2002; Chakrabarti et al., 2012; Grützner et al., 2013; Aldanmaz et al., 2015). Karacadağ volcanism is a proxy for Arabian mantle reservoir (Pearce et al., 1990; Şen et al., 2004; Alpaslan, 2007; Lustrino et al., 2010; Keskin et al., 2012; Ekici et al., 2014). 97

Figure 3.13 $(^{87}Sr/^{86}Sr)_i$ versus SiO_2 diagram. Symbol legend is provided in Figure 3.7.....100

Figure 3.14 A. K_2O versus Na_2O (Le Maitre et al., 2002); B. $K_2O + Na_2O$ versus longitude illustrating the eastward increasing alkalinity trend; C. $K_2O + Na_2O$ versus age in central Anatolia; D. $K_2O + Na_2O$ versus age in eastern Anatolia showing the alkalinity increase through time during the SCLM removal event (grey arrow). Only the mafic rocks are displayed (SiO_2 < 56 wt %). The horizontal alkalinity reference line at ca. 6.8 wt % on Figures C and D represents the position of TAS diagram's alkalinity line (Le Maitre et al., 2002) at 56 wt % SiO_2. This means that rocks plotted above this line are alkaline whereas the ones below are either subalkaline or alkaline. Symbol legend is provided on Figure 3.7. All the data plotted have a SiO_2 content lower than 56 wt %. The grey arrow is the magmatic trend related to the SCLM removal event in eastern Anatolia from the middle Miocene to Present. 103

Figure 3.15 A. Primitive mantle-normalized $(La/Yb)_N$ versus Zr/Nb diagram (Münker, 2000); B. Nb/Yb versus Nb/Th diagram (Münker, 2000); C. Primitive mantle-normalized $(Tb/Yb)_N$ versus Nb/La diagram with horizontal reference lines from Gill (1981); the spinel and garnet stability field boundary at $(Tb/Yb)_N = 1.8$ was empirically determined by Wang et al. (2002). Primitive mantle (PM), OIB, E-MORB and N-MORB reference values from Sun and McDonough (1989), and upper (UC) and lower crust (LC) reference values from Rudnick and Gao (2014). Kula volcanism is used as proxy for the Anatolian OIB-like and African mantle reservoirs (Aldanmaz, 2002; Alıcı et al., 2002; Chakrabarti et al., 2012; Grützner et al., 2013; Aldanmaz et al., 2015). Karacadağ volcanism is a proxy for the Arabian mantle reservoir (Pearce et al., 1990; Şen et al., 2004; Alpaslan, 2007; Lustrino et al., 2010; Keskin et al., 2012; Ekici et al., 2014). All the data plotted have a SiO_2 content lower than 56 wt %. The white arrow represents slab break-off-related magmatic trend in eastern Anatolia (early-middle Miocene to Pliocene). 107

Figure 3.16 Schematic 3D cartoons illustrating the geometry of the Southern Neotethyan oceanic slab fragmented into the Arabian and Cyprus segments (inspired from Biryol et al., 2011; Schildgen et al., 2014; Menant et al., 2016) and westward migration of magmatism during the early to middle Miocene slab break-off propagation (A) and subsequent gap opening and SCLM partial removal since the middle Miocene (Chapter 2). The Galatian magmatic province (A), Sulutas (B) and Konya (C) volcanic complexes represent the southward migration of volcanism as result of the Cyprus slab roll-back since the early Miocene. The slab rupture allowed subslab asthenosphere infiltration and heat accumulation at the base of ATB, considered a unique continent fragment during Cenozoic. On this cartoon, the Bitlis-Pütürge Massifs, Central Anatolian Crystalline Complex, ATB and South Armenian Block are part of the same rigid overriding slab that undergoes the Arabian collision and resulting slab break-off tectono-magmatic effects. The detached slab segment sinks into the asthenosphere and is linked to the attached Cyprus slab and also the westerly Aegean slab, which is not represented here. The small insert in the cartoon B illustrates the SCLM destabilization and partial removal by convective dripping (after Gazel et al., 2012; Reid et al., 2017). Sinking subduction-modified SCLM drips release volatiles and favor melting of the upwelling asthenosphere by decompression (see text for explanations). 111

Figure 3.17 $(\varepsilon_{Nd})_i$ (A), Ba/Ta (B), $(Tb/Yb)_N$ (C) and Nb/Zr (D) variation through longitude (°). Only mafic rocks are plotted (SiO_2 < 56 wt %); A. variation of mantle input ($(\varepsilon_{Nd})_i$ > 0). The stars are the primitive melt compositions calculated at Mg # = 70, as in Figure 11, and following the methodology provided in the appendix B (Figure B.4). The white and grey arrows are the slab break-off- and SCLM-related magmatism. Spatial extend of each tectono-magmatic event constrained in Chapter 2 is also provided; B. Ba/Ta ratio used as a proxy for magma metasomatism. Lower ratio indicates drier magma melting conditions. Arc andesites have a Ba/Ta ratio > 428 (Gill, 1981); C. Primitive mantle-normalized $(Tb/Yb)_N$ ratio shows the variation in the magma source depth. The spinel and garnet stability field boundary at $(Tb/Yb)_N$ = 1.8 was empirically determined by Wang et al. (2002); D. Nb/Zr ratio used as a proxy for mantle source enrichment. OIB, E-MORB and N-MORB reference values from Sun and McDonough (1989). The references for composition range of the OIB-like Kula and Karacadağ volcanic suites are provided in Figure 3.15. Symbol legend is on Figure 3.7. 113

Figure 4.1 Tectono – magmatic map of Turkey (1:6,000,000 scale; Lambert Conic projection; European Datum 1950) showing the basement boundaries (modified from Görür and Tüysüz, 2001; Şengör et al., 2008; Pourteau et al., 2010), late Cenozoic magmatic rocks (modified from MTA, 2002), major precious and base metal occurrences and districts, and the late Cenozoic Anatolian Metallogenic Trend. The Eastern Anatolian Magmatic Belt is from Chapter 2. HS/

IS/LS stand for high/intermediate/low-sulfidation epithermal. Background of the location map is from Google Earth. ASF = Aegean Subduction Front; ATB = Anatolide-Tauride Block; BSZ = Bitlis Suture Zone; CSF = Cyprus Subduction Front; DSF = Dead Sea Fault; IAESZ = İzmir-Ankara-Erzincan Suture Zone; IBTZ = İzmir-Balıkesir Transfer Zone; ITSZ = Inner Tauride Suture Zone; RPB = Rhodope-Pontide Block; SASZ = Sevan-Akera suture zone; UMTZ = Uşak-Muğla Transfer Zone. 123

Figure 4.2 Tonnage versus Au grade (g/t) for Turkish and worldwide porphyry (top) and epithermal deposits (bottom). World deposit data from Singer et al. (2008). HS/IS/LS = high-/intermediate-/low-sulfidation. 133

Figure 4.3 Geological maps (modified from MTA, 2002) of the Simav district (A – 1:400,000 scale), Simav and Uşak districts (B – 1:400,000 scale), İzmir district (C – 1:250,000), Afyon area (D – 1:400,000 scale) and Bodrum district (E – 1:150,000 scale) showing the distribution of porphyry, epithermal and skarn occurrences, prospects and deposits, and analyzed samples in western Anatolia. Lambert Conic projection, European Datum 1950. Base map: SRTM 90 m digital elevation models (Jarvis et al., 2008). 135

Figure 4.4 Macro-photographs of mineralized porphyry and epithermal occurrences in western Anatolia. A. Silica replacement after bladed calcite at the Kepez low-sulfidation epithermal Au-Ag deposit, Simav district; B. Quartz-rhodochrosite ± rhodonite-pyroxmangite-pyrite-galena crustiform-colloform textured vein (vein stage 4) cutting Mn-oxidized quartz- rhodochrosite -rhodonite-calcite vein (vein stage 3) and rhyolite dike from the Efemçukuru low- to intermediate-sulfidation epithermal Au deposit, İzmir district; C. Northeast-looking panoramic view of the Pınarbaşı porphyry Mo-Cu prospect, Simav district; D. North-looking panoramic view of the Afyon-Sandıklı porphyry Au-Cu prospect illustrating the short distance between the high-temperature potassic alteration zone and the overlying advanced argillic lithocap; E. Close-up photograph of the argillic- and phyllic-altered monzonitic stock at the Pınarbaşı porphyry Mo-Cu prospect, Simav district; F. Close-up photograph of the dense quartz -sulfide vein stockwork and potassic alteration within the monzonitic stock at the Afyon-Sandıklı porphyry Au-Cu prospect; G. Core photograph of the mineralized potassic alteration (Intrusive phase 1) at the Kışladağ porphyry Au deposit, Uşak district; H. Silica cap overlying an argillic-altered andesitic unit at the Karatoprak high-sulfidation epithermal occurrence, Bodrum district. 138

Figure 4.5 Optical micro-photographs of mineralized porphyry and epithermal occurrences in western Anatolia. A. Cross polarized light (x 5): post-mineralization monzonite at the Pınarbaşı porphyry Mo-Cu prospect; B. Cross polarized light (x 10): potassic and tourmaline-white mica (sericite) alteration assemblages at the Kışladağ porphyry Au deposit, Uşak district; C. Plane

polarized and reflected light (x 20): sulfide mineralization within the monzonitic stock at the Kışladağ porphyry Au deposit, Uşak district; D. Cross polarized light (x 2): monzonite host rock at the Afyon-Sandıklı porphyry Au-Cu prospect; E. Cross polarized light (x 10): lithocap at the Afyon-Sandıklı porphyry Au-Cu prospect; F. Cross polarized light (x 10): skarn alteration of the Kadıkalesi monzonite, Bodrum district. Al = alunite; Au = gold; Bt = biotite; Cal = calcite; Chl = chlorite; Ep = epidote; Hb = hornblende; Hm = hematite; Ksp = K-feldspar; Mo = molybdenite; Pl = plagioclase; Py = pyrite; Qz = quartz; Ser = sericite (white mica); Tur = tourmaline. 140

Figure 4.6 Geological maps (modified from MTA, 2002) of the Konya district (A – 1:300,000 scale), Niğde and Kayseri districts (B – 1:500,000 scale), Hasançelebi area (C – 1:300,000) and Ağrı district (D – 1:250,000 scale) showing the distribution of porphyry, epithermal, Carlin-style and skarn occurrences, prospects and deposits, and analyzed samples in central and eastern Anatolia. Lambert Conic projection, European Datum 1950. Base map: SRTM 90 m digital elevation models (Jarvis et al., 2008). 143

Figure 4.7 Macro-photographs of mineralized porphyry occurrences in central Anatolia. A. East-looking panoramic view of the Inlice high-sulfidation epithermal Au deposit, Konya district; B. West-looking panoramic view of the Keltepe ore body at the Öksüt high-sulfidation epithermal Au deposit, Kayseri district; C. Polymict, Au-bearing, silica-pyrite, phreatic breccia, İnlice high sulfidation epithermal Au deposit, Konya district; D. Silica-altered clasts, Fe-oxide diatreme breccia, Öksüt high-sulfidation epithermal Au deposit, Kayseri district; E. Northeast-looking panoramic view of the argillic-altered Altunhişar high-sulfidation epithermal occurrence, Niğde district; F. Argillic-altered andesitic unit from the Boz Tepe high-sulfidation epithermal occurrence, Niğde district; G. Silica-alunite advanced argillic alteration affecting a volcanic breccia at the Doğanbey high-sulfidation epithermal Au prospect, Konya district; H. Northeast-looking photograph of the Başdere high-sulfidation epithermal occurrence, Kayseri district. 146

Figure 4.8 Optical micro-photographs of mineralized porphyry and epithermal occurrences in central and eastern Anatolia. A. Cross polarized light (x 10): vuggy silica alteration from the İnlice high-sulfidation epithermal Au deposit, Konya district; B. Cross polarized light (x 5): advanced argillic alteration assemblage from the Doğanbey high sulfidation epithermal Au prospect, Konya district; C. Plan polarized and reflected light (x 20): mineralized, Fe-oxide diatreme breccia with silica-altered clasts, Öksüt high-sulfidation epithermal Au deposit, Kayseri district; D. Cross polarized light (x 5): vuggy silica alteration at the Hasançelebi high-sulfidation epithermal Au-Ag prospect; E. Cross polarized light (x 10): decalcification and silica replacement alteration at the Carlin-style Mollakara Au-Ag deposit, Ağrı district; F.

Cross polarized light (x 10): phyllic-altered granodiorite in the porphyry zone of the Taşkapı porphyry-epithermal prospect, Ağrı district. Al = alunite; Hm = hematite; Py = pyrite; Qz = quartz; Ser = sericite (white mica). 147

Figure 4.9 Macro-photographs of mineralized hydrothermal occurrences in eastern Anatolia. A. East-looking view of the Hasançelebi high-sulfidation epithermal Au-Ag prospect; B. Southwest-looking view of the high-sulfidation epithermal zone of the Taşkapı porphyry-epithermal prospect, Ağrı district; C. Close-up photograph of massive silica alteration in a silica ledge at the Hasançelebi high-sulfidation epithermal Au-Ag prospect; D. East-looking view of phyllic-altered porphyry zone of the Taşkapı porphyry-epithermal prospect, Ağrı district; E. Mineralized vuggy silica alteration at the Hasançelebi high-sulfidation epithermal Au-Ag prospect; F. Close-up photograph of the phyllic alteration zone within the Taşkapı granodiorite, Ağrı district; G. Decalcification alteration at the Carlin-style Mollakara Au-Ag deposit, Ağrı district; H. Propylitic-altered granite at the Taşlıçay porphyry prospect, Ağrı district. 149

Figure 4.10 Concordia and weighted average $^{206}U/^{238}U$ age plots for igneous zircons from the late Cenozoic post-mineralization monzonite at the Pınarbaşı porphyry Mo-Cu prospect (A-B), monzonitic host rock at the Afyon-Sandıklı porphyry Au-Cu (C-D) and Kadıkalesi skarn prospects (E-F). Discordant and outlier analyses are in blue; analyses used for calculation of the weighted average $^{206}Pb/^{238}U$ age for each sample are in black. All errors are reported at 2σ level. MSWD: mean square of weighted deviates. The images (right) under optical microscope and cathodoluminescence for each sample display the internal structure of representative igneous zircon grains. 153

Figure 4.11 $^{40}Ar/^{39}Ar$ age plateaus and inverse isochron for analyzed hypogene alunite from the İnlice (A), Hasançelebi (B) and Doğanbey (C-D) high-sulfidation epithermal Au (-Ag) prospects and deposits. Excluded analyses are in black. All errors are reported at 2σ level. MSWD: mean square of weighted deviates. 154

Figure 4.12 Top: simplified tectono-magmatic map of Turkey illustrating the distribution of the late Cenozoic magmatic domains, key mineral deposits and prospects, mineral districts and the late Cenozoic Anatolian Metallogenic Trend defined in this Chapter. The slab contours (in km; Biryol et al., 2011) show the segmentation of the Southern Neotethyan slab and the resulting mantle flow directions (grey arrows). Bottom: simplified tectono-magmatic map of western Anatolia displaying the distribution of mineral deposits, prospects and districts, late Cenozoic magmatic complexes, magmatic front migration (white arrow), major structures, deformation zones and extent of the tear-related slab window defined by Biryol et al. (2011). 160

Figure 4.13 Schematic geometry and relative metal endowment of Anatolia porphyry and

epithermal environments (upper part) and simplified relationship between emplacement depth of the causative intrusion and mineralization style in a volcanic environment (lower part; after Bissig et al., 2015; inspired from Murakami et al., 2010). Left: shallow-emplaced porphyry stock (< 3 km) leading to the Cu and Au co-precipitation in the porphyry zone only (western Anatolia and at Cevizlidere in the eastern part of eastern Anatolia); Right: deeply-emplaced intrusion controlling the high-temperature co-precipitation of Cu and Mo in the porphyry zone and transportation of Au-bearing bisulfide complexes to the shallower epithermal zone (central Anatolia and Hasançelebi in the western part of eastern Anatolia). 164

Figure 4.14 Time scale illustrating the timing of gold mineralization in western (red), central (blue) and eastern Anatolia (grey), with the exception of the Baklan skarn Pb-Zn occurrence. Error bars are reported at 2σ level. Gold mineralization is inferred to occur during the deposition of sulfides, dated by Re-Os technique, and hypogene alunite, dated by $^{40}Ar/^{39}Ar$ technique, in porphyry and high-sulfidation epithermal systems, respectively. The dating of pre- or post-mineralization igneous units by U-Pb and K-Ar methods also provides constraints on the timing of gold mineralization illustrated by horizontal full (high confidence) and dashed bars (low confidence). The early Miocene skarn Fe-Pb-Zn occurrences at the Eğrigöz and Alaçam plutons (ca. 21-20 Ma) are not displayed because of the high number of available dates in the literature, as opposed to the Baklan pluton. References: [1]İmer et al., 2014; [2]Chapter 2; [3]this Chapter; [4]Delibaş et al., 2017; [5]Yılmaz et al., 2013; [6]Aydoğan et al., 2008; [7]Baker et al., 2016; [8]Bickford et al., 2016; [9]Boucher, 2016.....166

Figure 4.15 Geological time scale illustrating the succession and association of post-subduction tectonic, magmatic and metallogenic events in western (red), central (blue) and eastern Anatolia (grey) since the Oligocene. The timing of tectonic events are from Jolivet et al. (2015) and Chapter 2. Timing and references of porphyry (star), high-sulfidation (diamond) and low- and intermediate-sulfidation epithermal (triangle) and skarn (circle) mineralization events are provided in Figure 4.14. The age histogram of plutonic and volcanic units results from the compilation of U-Pb, $^{40}Ar/^{39}Ar$ and K-Ar isotopic dates from the literature in western Anatolia (n = 312; this Chapter) and central and eastern Anatolia (n = 428; Chapter 2). 171

Figure 5.1 Simplified tectono-magmatic map of Turkey showing the location of the basement boundaries, late Cenozoic magmatic belts, provinces and other domain, and the Anatolian Metallogenic Trend. The map also displays the succession of major tectonic events since the Oligocene that includes the Arabian continental collision (1), Arabian slab break-off and westward propagation to central Anatolia (2), and the Aegean slab tear (3) as the result of the differential roll-back rates between the Aegean and Cyprus slabs (see Chapter 2 for more details). Background on the location map is from Google Earth. BSZ = Bitlis Suture Zone;

IAESZ = İzmir-Ankara-Erzincan Suture Zone; ITSZ = Inner Tauride Suture Zone; SASZ = Sevan-Akera Suture Zone. References: [1]Chapter 2; [2]Jolivet et al., 2015; [3]Biryol et al., 2011; [4]Chapter 3.....182

Figure 5.2 Maps of western (A) and central and eastern Anatolia (B) displaying the basement boundaries, late Cenozoic igneous units (modified from MTA, 2002), belts and provinces, and major intrusion-related occurrences, prospects, deposits and districts (Chapter 4). The fertile igneous units hosting and causing hydrothermal mineralization are in pink whereas representative barren igneous suites are in grey. Some fertile plutons are too small and not visible on those maps such as at the Afyon-Sandıklı, Pınarbaşı, Baklan and Cevizlidere prospects and deposits. The green stars show the location of samples for element and isotopic analyses in western Anatolia. IBTZ = İzmir-Balıkesir Transfer Zone; UMTZ = Uşak-Muğla Transfer Zone.....187

Figure 5.3 Alteration index (Al_2O_3-CaO+Na_2O-K_2O) ternary diagram to quantify the degree of weathering of analyzed rock samples (Nesbitt and Young, 1982); References: [1]Aydoğan et al., 2008; [2]Delibaş et al., 2017; [3]Baker et al., 2016; [4]Chapter 3; [5]İmer et al., 2014.....192

Figure 5.4 Total alkali versus silica (TAS) diagram for fertile volcanic (A; Le Maitre et al., 2002) and plutonic rocks (B; Middlemost, 1994); K_2O versus SiO_2 (C; Peccerillo and Taylor, 1976); K_2O versus Na_2O diagrams (D; Le Maitre et al., 2002); References: [1]Aydoğan et al., 2008; [2]Delibaş et al., 2017; [3]Baker et al., 2016; [4]Chapter 3; [5]İmer et al., 2014.....197

Figure 5.5 Macro-photographs of the Alaçam granodiorite (A), Simav granite (B), Pınarbaşı monzonite (C), Kışladağ monzonite (INT-3; D), Afyon-Sandıklı monzonite (E) and Bodrum monzonite (F) from western Anatolia.....198

Figure 5.6 Primitive mantle-normalized trace element (McDonough et al., 1992) and chondrite-normalized rare earth element diagrams (Sun and McDonough, 1989) of fertile rock samples from western (A-B), central (C-D) and eastern Anatolia (E-F). References: [1]Chapter 3; [2]İmer et al., 2014.....199

Figure 5.7 Initial $^{87}Sr/^{86}Sr$ versus $^{143}Nd/^{144}Nd$ diagram displaying the isotopic signature of fertile (large symbols) and barren (small open circles) late Cenozoic igneous units in Anatolia. BSE = bulk silicate Earth (Bouvier et al., 2008); EMI, EMII, HIMU, PREMA, DMM reservoirs from Zindler and Hart (1986). Data source for barren igneous rocks: western Anatolia (Alıcı et al., 2002; Innocenti et al., 2005; Dilek and Altunkaynak, 2009; Agostini et al., 2010; Dilek and Altunkaynak, 2010; Hasözbek et al., 2011; Altunkaynak et al., 2012; Chakrabarti et al., 2012; Çoban et al., 2012; Erkül and Erkül, 2012; Ersoy et al., 2012a; Ersoy et al., 2012b; Erkül et al., 2013; Aldanmaz et al., 2015; Yücel-Öztürk, 2016), central Anatolia (Notsu et al., 1995; Deniel

et al., 1998; Kürkçüoğlu et al., 1998; Şen et al., 2004; Siebel et al., 2011; Reid et al., 2017) and eastern Anatolia (Pearce et al., 1990; Notsu et al., 1995; Buket and Temel, 1998; Keskin et al., 1998; Keskin et al., 2006; Özdemir, 2011; Çubukçu et al., 2012; Özdemir and Güleç, 2013; Lebedev et al., 2016; Oyan et al., 2016; Kaygusuz et al., 2018). Reference: [1]Chapter 3. 201

Figure 5.8 A. $(^{206}Pb/^{204}Pb)_i$ versus $(^{207}Pb/^{204}Pb)_i$; B. $(^{206}Pb/^{204}Pb)_i$ versus $(^{208}Pb/^{204}Pb)_i$ diagrams displaying the isotopic signature of fertile (large symbols) and barren (small open circles) late Cenozoic igneous units in Anatolia. GLOSS = global subducting sediment composition (Plank and Langmuir, 1998); NHRL = Northern Hemisphere reference line (Hart, 1984); EMI, EMII, HIMU, DMM reservoirs from Zindler and Hart (1986). Orogene, upper and lower crust evolution curves are from Zartman and Doe (1981). Data source for barren igneous rocks: western Anatolia (Notsu et al., 1995; Alıcı et al., 2002; Innocenti et al., 2005; Dilek and Altunkaynak, 2010; Chakrabarti et al., 2012; Aldanmaz et al., 2015), central Anatolia (Notsu et al., 1995; Deniel et al., 1998; Kürkçüoğlu et al., 1998; Şen et al., 2004; Siebel et al., 2011; Reid et al., 2017) and eastern Anatolia (Pearce et al., 1990; Notsu et al., 1995; Keskin et al., 1998; Keskin et al., 2006; Özdemir, 2011; Özdemir and Güleç, 2013; Lebedev et al., 2016; Oyan et al., 2016). Refence: [1]Chapter 3.....202

Figure 5.9 Optical microphotographs of representative rock texture and mineralogy from Anatolian fertile igneous rocks and highlighting the distribution of mafic phenocrysts (see Table D.1 for sample descriptions): A. Megacrystic monzonite, Afyon-Sandıklı porphyry Au-Cu prospect (FR-14-47; cross polarized light); B. Monzonite, Bodrum district (FR-15-32; plane polarized light); C. Biotite andesite, Konya district (FR-13-181; cross polarized light); D. Clinopyroxene andesite with Fe-oxide rims around hornblende crystals, Hasançelebi high-sulfidation epithermal Au-Ag prospect (FR-14-82; plane polarized light); E. Granite, Ağrı district (FR-14-143; plane polarized light); F. Monzodiorite, Ağrı district (FR-14-132; plane polarized light). Bt = biotite; Cpx = clinopyroxene; Fd = feldspar; Feox = iron oxide (magnetite and/or hematite); Hb = hornblende; Ksp = alkali feldspar; Pl = plagioclase; Qz = quartz; Ti = titanite. 204

Figure 5.10 A. Ba/Ta versus age (Ma); the dashed line represents the composition of an arc-type andesite defined by Gill (1981) at Ba/Ta = 428; arrows represent temporal increase/decrease; only the mafic and intermediate igneous rocks are plotted (SiO_2 < 64 wt %) to minimize the effect of crustal contamination and fractionation; B. $(Dy/Yb)_N$ versus SiO_2 (Davidson et al., 2007). Data source for barren igneous rocks (small open circles): Pearce et al., 1990; Aydar et al., 1995; Notsu et al., 1995; Aydar and Gourgaud, 1998; Deniel et al., 1998; Kürkçüoğlu et al., 1998; Aydar and Gourgaud, 2002; Aydin, 2008 Keskin et al., 1998; Alıcı et al., 2002; Şen et al., 2003; Şen et al., 2004; Tokçaer et al., 2005; Keskin et al., 2006; Dogan et al., 2008; Güçtekin

and Köprübaşı, 2009; Dilek and Altunkaynak, 2010; Ustunisik and Kilinc, 2011; Çubukçu et al., 2012; Dogan et al., 2013; Grützner et al., 2013; Aydin et al., 2014; Dogan, 2016; Lebedev et al., 2016 Aldanmaz, 2002; Özdemir et al., 2006; Özdemir, 2011; Aldanmaz et al., 2015; Peretyazhko et al., 2015; Oyan et al., 2016; Reid et al., 2017. References: [1]Aydoğan et al., 2008; [2]Delibaş et al., 2017; [3]Baker et al., 2016; [4]Chapter 3; [5]İmer et al., 2014. 205

Figure 5.11 A. Total FeO content (FeO_t) versus log (Fe_2O_3/FeO) diagram (modified from Blevin, 2004) illustrating the redox affinity of fertile and barren Anatolian magmatism. Blevin (2004) recommends to use petrographic and magnetic criteria for rocks yielding a FeO_t content lower than 2 wt %; B. FeO + MnO-Fe_2O_3 + TiO_2-MgO ternary diagram (modified from Chappell and White, 1992); C. Fe^{3+}/Fe^{2+} versus longitude; D. Fe^{3+}/Fe^{2+} versus age. References: [1]Aydoğan et al., 2008; [2]Delibaş et al., 2017; [3]Baker et al., 2016; [4]Chapter 3; [5]İmer et al., 2014. 207

Figure 5.12 Sr/Y versus Y diagrams for western (A) and central and eastern Anatolia (B; fields and trends from Defant and Drummond (1990) and Richards and Kerrich (2007)); mafic igneous rocks are excluded ($SiO_2 \leq 56$ wt %); Sr/Y versus SiO_2 diagrams for western (C) and central and eastern Anatolia (D; Richards and Kerrich, 2007). Average andesite composition by Gill (1981); References: [1]Aydoğan et al., 2008; [2]Delibaş et al., 2017; [3]Baker et al., 2016; [4]Chapter 3; [5]İmer et al., 2014. 209

Figure 5.13 La/Yb versus Yb diagrams for western (A) and central and eastern Anatolia (B; fields and trends from Castillo et al. (1999) and Richards and Kerrich (2007); mafic igneous rocks are excluded ($SiO_2 \leq 56$ wt %); La/Yb versus SiO_2 diagrams for western (C) and central and eastern Anatolia (D; Richards and Kerrich, 2007). Average andesite composition by Gill (1981); References: [1]Aydoğan et al., 2008; [2]Delibaş et al., 2017; [3]Baker et al., 2016; [4]Chapter 3; [5]İmer et al., 2014. 210

Figure 5.14 A. Alkalinity ($K_2O + Na_2O$) versus age; B. Na_2O versus age. The horizontal dashed line is the approximate maximum threshold for fertility ($Na_2O \leq 5$ wt %). Refer to Figures 5.3 and 5.10 for the references and symbols; only the mafic and intermediate igneous rocks are plotted ($SiO_2 < 64$ wt %) to minimize the effect of crustal contamination and fractionation; References: [1]Aydoğan et al., 2008; [2]Delibaş et al., 2017; [3]Baker et al., 2016; [4]Chapter 3; [5]İmer et al., 2014. 212

Figure 5.15 Age versus Sr/Y (A), La/Yb (B), $(\varepsilon_{Nd})_i$ (C) and $(Sm/Yb)_N$ (D; base diagram from Kay and Mpodozis (2001); Px = pyroxene; Amp = amphibole; Gar = garnet); timing of tectonic episodes are from Chapter 2 and Jolivet et al. (2015); Refer to Figures 5.3 and 5.10 for the references and symbols; only the mafic and intermediate igneous rocks are plotted ($SiO_2 < 64$ wt %) in the diagram 5.15D to minimize the effect of crustal contamination and fractionation;

References: [1]Aydoğan et al., 2008; [2]Delibaş et al., 2017; [3]Baker et al., 2016; [4]Chapter 3; [5]İmer et al., 2014.....215

Figure 5.16 3D cartoon of the segmentation of the Southern Neotethyan oceanic slab in the late Miocene due to the easterly slab break-off and westerly slab tear events (inspired from Menant et al., 2018 and Chapter 2, and based on tomographic interpretations (Biryol et al., 2011) in Figure 5.1). The opening of slab windows induced toroidal (west) and poloidal (east) asthenospheric flow fields that gradually eroded the metasomatized subcontinental lithospheric mantle (SCLM) beneath the Anatolide-Tauride Block. 218

Figure A.1 Concordia plots and $^{206}Pb/^{238}U$ weighted mean histograms of Plešovice zircon standards. 282

Figure A.2 Concordia plots and $^{206}Pb/^{238}U$ weighted mean histograms of Temora2 zircon standards. 284

Figure B.1 Examples of iterative error calculation for duplicate samples (left: K_2O; right: La). The samples are included within the error envelope (y = mx + b) obtained from the addition of the absolute (b) and relative (m) errors.....305

Figure B.2 AFM (A; Irvine and Baragar, 1971) and Th/Yb versus Zr/Y diagrams (B; Ross and Bedard, 2009) showing the calc-alkaline affinity of the late Cenozoic igneous suites in central and eastern Anatolia. The Total Alkali versus Silica diagram (C) for plutonic rocks (Middlemost, 1994) provides rock names for the Oligocene to early Miocene plutonic rocks in eastern Anatolia; these rock samples were plotted in the Total Alkali versus Silica diagram for volcanic rocks in Chapter 3 (Figure 3.7). 308

Figure B.3 Nd model age histogram from late Cenozoic igneous rocks along the Eastern Anatolian Magmatic Belt; single-stage model age calculation.....309

Figure B.4 $(\varepsilon_{Nd})_i$, $(^{143}Nd/^{144}Nd)_i$ and $(^{87}Sr/^{86}Sr)_i$ versus Mg# (assuming $Fe^{3+}/Fe^{2+} = 0.2$) showing the regression lines of isotopic data from the late Cenozoic igneous suites in central and eastern Anatolia. Primary melt calculation were made at Mg # = 70 (see text above for explanation). 311

Figure E.1 A. and B. U-Pb Concordia plots for FR-13-66 (Intrusion 2, n = 3) and FR-13-68 (Intrusion 3, n = 2) also showing the two anticrystic grains analyzed. C. D. E. and F. $^{40}Ar/^{39}Ar$ plateau age diagrams for GC-115-465 (hydrothermal biotite, potassic alteration, Intrusion 1), GC-52-216.4 (hydrothermal biotite, potassic alteration, Intrusion 2), GC-40-415 (hydrothermal biotite, potassic alteration, Intrusion 1) and FR-13-65 (hypogene alunite, advanced argillic alteration, latite lava flows).....322

Figure E.2 Timescale diagram illustrating the succession of the magmatic (M) and hydrothermal (H) events in the Uşak - Güre basin (left side) and at the Kışladağ deposit (right side). Magmatism in the Uşak - Güre basin took place in three distinct episodes: (M1) Elmadağ volcano (17.29 ± 0.13-16.28 ± 0.09 Ma); (M2) İtecektepe volcano (15.04 ± 0.10 Ma); and (M3) Beydağı volcano (~15-12.15 ± 0.15 Ma). The latter magmatic phase can be divided into three local magmatic episodes: (M3.1) preporphyry latitic lava flows (> 14.76 ± 0.01 Ma); (M3.2) porphyry intrusive phases including Intrusion 1 (> 14.76 ± 0.01 Ma; M3.2a), Intrusion 2 (14.76 ± 0.01 Ma; M3.2b) and Intrusion 3 (14.36 ± 0.02 Ma; M3.2c). Hydrothermal events likely occurred in at least three distinct pulses at Kışladağ including: (H1) potassic alteration, sulfide precipitation, and gold deposition (14.49 ± 0.06-14.42 ± 0.12 Ma); (H2) weak potassic alteration post-Intrusion 3 (< 14.36 ± 0.02-14.15 ± 0.15 Ma); and (H3) late advanced argillic alteration (< 14.36 ± 0.02-12.15 ± 0.15 Ma). 323

List of Abbreviations

Geochemistry

Ag: Silver
Al: Aluminium
Al_2O_3: Aluminium oxide
Ar: Argon
Au: Gold
Ba: Barium
Ca: Calcium
Cl: Chlorine
Ce: Cerium
Co: Cobalt
Cr: Chromium
Cu: Copper
Dy: Dysprosium
Eu: Europium
Eu_N/Eu*: Europium anomaly
Fe: Iron
FeO: Iron (II) oxide
Fe_2O_3: Iron (III) oxide
He: Helium
Hf: Hafnium
Hg: Mercury
H_2O: Water
K: Potassium
K_2O: Potassium oxide
La: Lanthanum
LOI: Loss On Ignition
Lu: Lutetium
Mg: Magnesium
Mg #: Magnesium number (= 100 x Mg/(Mg + Fe^{2+}))
MgO: Magnesium oxide
MnO: Manganese oxide
Mo: Molybdenum
Na_2O: Sodium oxide
Nb: Niobium
Nd: Neodymium
Os: Osmium
Pb: Lead
PGE: Platinum-group elements
Rb: Rubidium
Re: Rhenium
S: Sulfur
Sb: Antimony
Sm: Samarium
SiO_2: Silicon dioxide or silica
Sr: Strontium
Ta: Tantalum
Tb: Terbium
Te: Tellurium
Ti: Titanium
TiO_2: Titanium oxide
Th: Thorium
U: Uranium
V: Vanadium
W: Tungsten
Y: Yttrium
Yb: Ytterbium
Zn: Zinc
Zr: Zirconium

ε_{Nd}: Deviation of $^{143}Nd/^{144}Nd$ from the bulk earth silicate value
τ_{DM}: Neodymium model age

fO_2: Oxygen fugacity or oxidation state
fS_2: Sulfur fugacity

AFC: Assimilation and/or crystal fractionation
CIA: Chemical Index Alteration

HFSE: High Field Strength Elements
LILE: Large Ion Lithophile Elements
REE: Rare Earth Elements
HREE: Heavy Rare Earth Elements
LREE: Light Rare Earth Elements
MREE: Medium Rare Earth Elements
TAS: Total Alkali versus Silica

Geochemical reservoirs

BSE: Bulk Silicate Earth
DMM: Depleted (MORB) Mantle
EM: Enriched Mantle
E-MORB: Enriched Mid-Oceanic Ridge Basalt
GLOSS: Global Subducting Sediment
HIMU: High U/Pb Mantle
LC: Lower Crust
MASH: Melting, Assimilation, Storage and Homogenization
MORB: Mid-Oceanic Ridge Basalt
NHRL: Northern Hemisphere reference line
N-MORB: Normal Mid-Oceanic Ridge Basalt
OIB: Oceanic Island Basalt
PREMA: Prevalent Mantle
UC: Upper Crust

Tectonics

AF: Akşehir Fault
ASF: Aegean Subduction Front
ATB: Anatolide-Tauride Block
BSZ: Bitlis Suture Zone
CSF: Cyprus Subduction Front
DSF: Dead Sea Fault
EAFZ: Eastern Anatolian Fault Zone
EF: Ecemiş Fault
ES: Eratosthenes Seamount
Hs: Hasandağ
IAESZ: İzmir-Ankara-Erzincan Suture Zone
ITSZ: Inner Tauride Suture Zone
Kp: Karapınar
MF: Malatya Fault
NAFZ: North Anatolian Fault Zone
SASZ: Sevan-Akera Suture Zone
SCLM: Subcontinental Lithospheric Mantle
TGF: Tuz Gölü Fault

Geochronology

MSWD: Mean Square Weighted Deviation
Wtg. Mean: Weighted Mean
Ma: mega-annum (absolute date)
m.y.: million years (duration)
k.y.: thousand years (duration)

Mineralogy

Al: Alunite
Bt: Biotite
Cal: Calcite
Chl: Chlorite
Cpx: Clinopyroxene
Ep: Epidote
Fd: Feldspar
FeOH: iron oxihydroxide
Feox: Iron oxide
FMQ: Fayalite-magnetite-quartz buffer
Hb: Hornblende
Hm: Hematite
Ksp: Alkali feldspar
Mo: Molybdenite
Pl: Plagioclase
Py: Pyrite
Qz: Quartz

Ser: Sericite (white mica)
Ti: Titanite
Tur: Tourmaline

Analytical methods

CA-TIMS: Chemical Abrasion Thermal Ionization Mass Spectrometry
LA-ICP-MS: Laser Ablation Inductively Coupled Plasma Mass Spectrometry
MC-ICP-MS: Multi-Collector ICP-MS
XRF: X-ray Fluorescence
INAA: Instrumental neutron activation analysis

Metallogeny

HS: High-sulfidation
IS: Intermediate-sulfidation
IOCG: Iron Oxide Copper Gold
LS: Low-sulfidation
MVT: Mississippi Valley Type
SEDEX: Sedimentary Exhalative
VMS: Volcanogenic Massive Sulfide

Units of measurement

Bt: Billion tonnes
Mt: Million tonnes
Mlbs: Million pounds
Moz: Million ounces
ppm: part per million
ppb: part per billion
g/t: gram per tonne
wt %: weight percent

Geography

N: North
S: South
W: West
E: East
NW: Northwest
NE: Northeast
SE: Southeast
ENE: East-northeast
ESE: East-southeast
WNW: West-northwest
WSW: West-southwest
NNE: north-northeast
NNW: North-northwest
Lat: Latitude
Long: Longitude
GIS: Geographic Information System
SRTM: Shuttle Radar Topography Mission

Miscellaneous

MDRU: Mineral Deposit Research Unit
MTA: Mineral Research and Exploration of Turkey
PCIGR: The Pacific Centre for Isotopic and Geochemical Research
UBC: The University of British Columbia

Glossary

Tectonics

Asthenosphere: highly viscous and convecting part of the upper mantle below the rigid lithosphere (Houseman, 1996). Seismic asthenosphere is a layer of low velocity and high attenuation of the seismic waves.

Continental collision: the moment of time when two opposite converging continental plates first come into contact at a point where intervening oceanic lithosphere, or slab, has been completely subducted (Hu et al., 2016).

Lithosphere: rigid outer layer of the Earth composed of the oceanic or continental crust and the cold uppermost mantle, named oceanic or subcontinental lithospheric mantle (SCLM), which are separated by the Moho discontinuity (Houseman, 1996).

Ophiolites: portion of the oceanic lithosphere exposed above sea level and often emplaced onto continental crust.

Orogeny: large structural deformation along converging plates, or lithospheres, responsible for the formation of mountain ranges, or **orogenic belt**.

Post-collision: tectonic, magmatic or metallogenic events that take place once the collision and converging forces have ceased, and are driven by gravitational instability and possibly by earlier subduction-related features.

Post-subduction: tectonic, magmatic or metallogenic events that take place once the subduction has ceased or migrated, and are driven by earlier subduction-related features (Menant et al., 2018).

Slab: portion of a tectonic lithosphere that is being subducted.

Subduction: geological process that takes place at convergent boundaries of tectonic plates where one plate, usually oceanic lithosphere, moves under an oceanic or continental lithosphere, and is forced or sinks due to gravity into the mantle.

Metallogeny

Belt: elongate area, or domain, that links similar mineral districts (**metallogenic belt**) or magmatic complexes (**magmatic belt**) as a result of a same tectonic event (**orogenic belt**).

Mineral deposit: mineral prospect that has been tested and is known to be of sufficient size, grade, and accessibility to be producible to yield a profit.

Mineral district: restricted area gathering mineral occurrences, prospects and/or deposits that share similar geological, structural, metallogenic, age and tectonic features.

Mineral occurrence: concentration of a mineral that is considered valuable by someone somewhere, or that is of scientific or technical interest (USGS).

Prospect: mineral occurrence of sufficient size (**tonnage**) and concentration (**grade**) that might be considered to have economic potential under favorable circumstances.

Province: large-scale area, or domain, characterized a concentration of mineral occurrences, prospects and/or deposits (**mineral province**) or magmatic complexes (**magmatic province**), regardless of their compoistion, age and tectonic affinity.

Trend: elongate area that links similar mineral districts (**metallogenic trend**) or magmatic complexes (**magmatic trend**) from different tectonic domains.

Acknowledgements

I would like to spotlight and thank all the people who helped and supported me, and collaborated on this research work. During all this time, I felt lucky to be part of MDRU and UBC, and get access to state-of-the-art facilities, high-level scientific expertise, academic and professional opportunities, and more importantly, fascinating people. That is why I am truly thankful to my main supervisor, Craig Hart, for giving me this opportunity. The quality of this research work results from my many interactions with the members of my supervisory committee: Craig Hart, Derek Thorkelson, Jim Mortensen and Aleksandar Mišković. I strongly appreciated their guidance, patience, constructive criticisms, wisdom and expertise in tectonics, igneous petrology, geochronology and regional metallogeny (> 100 years of experience all together!!).

This PhD program was part of the Western Tethyan Metallogeny project designed and led by Aleksandar Mišković and Craig Hart, and financially supported by Alamos Gold Inc., AngloGold Ashanti Ltd., Avala Resources Ltd., Centerra Gold Inc., Dunav Resources Ltd., Dundee Precious Metals Inc., Esan, Eldorado Gold Corp./Tüprag Metal Madencilik, First Quantum Minerals Ltd., Kinross Gold Corp., National Iranian Copper Industries Company, Newcrest Mining Ltd., Pilot Gold Inc., Silver Standard Resources Inc., and Teck Resources Ltd. Additional research grants and scholarships were provided by SEG Canada Foundation, SRK Canada and Mitacs (Globalink and Accelerate Programs) that allowed me to test new ideas and collect more data.

Special thanks to the companies (and people) who supported my field work in Turkey: Alamos Gold Inc. (Mehtap Özcan), Centerra Gold Inc. (Malcolm Stallman, Mustafa Cihan, Tolga Tosun, Aliser Erdoğan, Deniz Serçe), Esan (Ali Can Akpınar, Tuna Kaskati, Serçan Bozan), Eldorado Gold Corp./Tüprag Metal Madencilik (Tim Baker, Dave Bickford, Keith Patterson, Yücel Öztaş, Ahmet Tukaç, Ali Riza Çolakoğlu, Ahmet Özer, Şafak Sönmez), First Quantum Minerals Ltd. (Nikolay Petrov, Chris Van Wijk), Pilot Gold Inc. (Moira Smith, Hakan Boran), Teck Resources Ltd. (Adrian King, Andrew Davies, Claire Chamberlain, Uğur Kızıltepe, Bayram Artun, Nuri Ceyhan, Nihal Yavuz). I also thank the non-sponsor companies, which generously offered the free access to their projects, rock samples and sometimes hospitality: Alacer Gold Corp., Ariana Resources Plc., Polimetal, Aksu Madencilik, Lodos Madencilik, Stratex International Plc. and Columbus Copper. Thanks to Bryan Wilson and Centerra Gold Inc. for their welcome to their Toronto head office for my MITACS internships.

I am grateful to the following researchers and colleagues for their fruitful discussions and feedback on scientific issues: İlkay Kuşcu, Armel Menant, Peter Grieve, Matías Sánchez, Thomas Bissig, Farhad Bouzari, Erdin Bozkurt, Hervé Rezeau, Ali Aluç and all people met at conferences and UBC. During my fieldwork, I had the chance to get the expertise of Aleksandar

Mišković, İlkay Kuşcu and Matías Sánchez. I was assisted by Demirhan Uzunal, Hami Keserci, Onur Bozdemir and Haydar Terzi, who all showed me the beauty and delights of Turkey from İzmir to Van, made my life much easier and safer throughout my journeys. Special thanks to Hami, who courageously negotiated field authorizations for me in eastern Turkey, despite the difficulty of the local political context.

At UBC, guidance, training, help and advice during my phase of data collection were provided by Sara Jenkins, Mana Rahimi, Lynn Connally, Denyse Yong, Xavier Semmelink (GIS and data compilation), Richard Friedman, Rob Creaser, Richard Spikings, Vivian Lai, Joel Angen, Rob Lee, Murray Allan, Albert Ding, Bahram Najafian, Hai Lin (geochronology), Dominique Weis, Bruno Kiefer, Kathy Gordon, Anais Fourny (isotope geochemistry) and Guillaume Lesage (feldspar staining). Thanks to all the MDRU researchers, staff, student peers, office mates and alumni for their support, collaboration and encouragement.

During this unforgettable adventure, I was accompanied by my fellow colleagues and friends in the Western Tethyan Metallogeny project: Kaleb Boucher, Paula Brunetti, Graham Leroux, Raja Yarra, Jelena Zivanovic, Dragan Dragic and Erde Bilir. We banded together to face the numerous challenges, learn from each other and enjoy wonderful moments. Also, special wink at the world-famous Data Miners, who took me up to the 2nd place at the Integra Gold Rush Challenge.

I would like to thank my parents and sister for their patience, understanding and unwavering support throughout my life and studies, despite the distance and my short visits.

Last but not least, I dedicate this thesis to my mentor and friend, Anna Fonseca, who has unconditionally supported and inspired me for so many years. I would not have made it this far, or not at all, without her.

"Productive stupidity means being ignorant by choice. Focusing on important questions puts us in the awkward position of being ignorant. One of the beautiful things about science is that it allows us to bumble along, getting it wrong time after time, and feel perfectly fine as long as we learn something each time."

Schwartz, 2008 - Journal of Cell Science

Chapter 1: Introduction

The increasing demand for precious (Au-Ag) and base (Cu-Pb-Zn) metals implies the need for an increasing rate of mineral discoveries. However, the efficiency of mineral exploration processes requires well-constrained tectonic, magmatic and metallogenic models. Subduction zones along convergent margins host a significant amount of metals, mainly hosted within porphyry deposits that supply about three-quarters of the world's Cu, half the Mo and about one-fifth of the Au (Sillitoe, 2010). The formation of those porphyry and associated epithermal deposits above active subduction zones is well understood compared to those that form in post-subduction tectonic settings. The 1500 x 200 km Anatolian segment of the Western Tethyan Orogenic Belt in Turkey was affected by various tectonic events including back-arc and post-subduction slab roll-back, slab tearing and break-off, and partial lithospheric mantle removal during the late Cenozoic (e.g., Keskin, 2007; Jolivet et al., 2013). Geochronology of new mineral deposit discoveries in Anatolia indicates that some porphyry and epithermal systems formed contemporaneously with post-subduction tectonic events in the late Cenozoic.

This PhD research study investigates the metallogenic, tectonic and magmatic processes active during the late Cenozoic post-subduction slab tearing and break-off events in Anatolia by establishing the genetic links between the time-space distribution of mineral deposits and the complex geodynamic processes. Background information about slab break-off and tearing theories, the tectono-magmatic framework of Anatolia, post-subduction metallogeny exemplified by the Western Tethyan Orogenic Belt with a focus on the Turkish metallogeny, are presented in this Chapter, which further states the research objectives that will be investigated and achieved in this thesis.

1.1 Subduction and post-subduction metallogeny

1.1.1 Subduction magmatism and porphyry-epithermal systems

The genetic relationship between porphyry systems and arc magmatism along orogenic belts has been recognized for decades and emphasized by the use of geochronology (Livingston

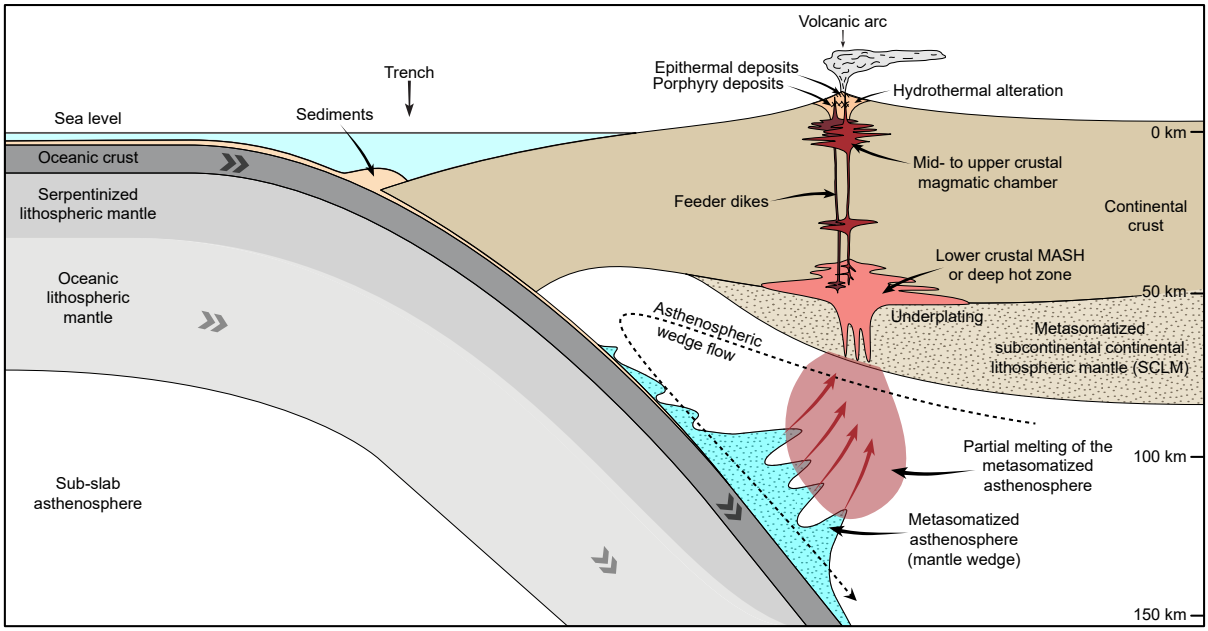

Figure 1.1 Subduction zone setting illustrating the melting processes and the formation of porphyry deposits (redrafted from Winter, 2001; Richards, 2011a).

et al., 1968; Moore et al., 1968; Sillitoe, 1972; Kesler, 1973; Titley, 1975; Gustafson, 1978; Mortensen et al., 1995). Arc magmas result from the complex interaction between fluids released from the subducting oceanic slab and the overlying asthenospheric mantle wedge between the subducting oceanic and overriding oceanic or continental lithospheres (Figure 1.1; Ringwood, 1977; Gill, 1981; Tatsumi et al., 1983; Arculus, 1994). Partial melting of the metasomatized mantle wedge generates high-alumina, hot, hydrous, relatively oxidized, depending on sulfate-oxide-sulfide assemblages in the subducting slab, and volatile-rich (H_2O, Cl, S) basalt (Tatsumi et al., 1983; Tatsumi et al., 1986; Parkinson and Arculus, 1999). Mafic magma ascending from the mantle wedge is denser than crustal rocks (Herzberg et al., 1983) and thus accumulates near the base of the crust (Fyfe, 1992). The build-up of heat caused by the ponding of mafic magma results in partial melting and assimilation of lower crustal rocks as envisaged in the MASH (melting, assimilation, storage and homogenization) or deep hot zone models of Hildreth and Moorbath (1988) and Annen et al. (2005), respectively. The homogenization of mafic magmas with evolved crustal rocks generates a layer of lower density hybrid calc-alkaline andesitic magma that is stored at the base of the crust and continually evolves to become enriched in

volatiles, sulfur and incompatible elements (Hildreth and Moorbath, 1988; Annen et al., 2005). At some point, the evolving magma will have sufficient buoyancy to rise into the upper crust (Walker, 1989) along large-scale lithospheric structural pathways (Clemens and Mawer, 1992; Benn et al., 1998; Vigneresse, 2004). Certain structural geometries such as jogs, step-overs and fault intersections, preferentially along trench-parallel lithospheric structures, represent low-stress extensional volumes developed during transpressional or transtensional strain (Tosdal and Richards, 2001). Such sites provide highly permeable vertical conduits where magma is most likely to ascend. Structural focusing of volatile-rich and evolved magma in the upper crust, followed by further magmatic fractionation, volatile enrichment and exsolution are what ultimately lead to the development of ore-forming magmatic-hydrothermal systems (Richards, 2003). After emplacement in the upper crust, crystallizing plutons release fluids during their cooling which can generate proximal porphyry Cu ± Au ± Mo (Lowell and Guilbert, 1970; Sillitoe, 2010) and Cu-Fe-W-Zn-Pb-Sn-Au skarn deposits (Einaudi et al., 1981; Meinert, 2005), and distal high-sulfidation Au-Ag ± Cu (Hedenquist and Lowenstern, 1994; Simmons et al., 2005) and carbonate replacement Au deposits (Sillitoe and Bonham, 1990).

The bulk of precious and base metals in arc settings is provided by the metasomatized asthenospheric mantle and to lesser extent by the oceanic crust and sediments through dehydration of volatiles or melting (McInnes et al., 1999; Richards, 2011b), although the mantle itself is not anomalously enriched in Cu (Lee et al., 2012). Oxidation state (fO_2) and sulfur fugacity (fS_2) control the behaviour of chalcophile (Cu) and siderophile metals (Au) during partial melting; partial melting at high fS_2 and fO_2 conditions results in the saturation of sulfide phases that will preferentially trap Au relative to Cu giving way to a high Cu:Au ratio magma and ultimately Cu-rich porphyry deposits and potentially Au-rich residual cumulates in the lower crust (Peach et al., 1990; Hattori and Keith, 2001; Richards, 2009, 2011a). Ideal magmatic conditions for the formation of porphyry systems require high oxidation states (> FMQ+1.3-2; e.g., Mungall, 2002; Richards and Kerrich, 2007; Lee et al., 2012), and high water (> 4 wt %; Richards, 2011a) and sulfur contents (> 1000 ppm; Chambefort et al., 2008).

Such conditions favor hornblende fractionation and suppress the early plagioclase fractionation giving way to adakitic magma signature (i.e., $SiO_2 \geq 56$ wt %; $Al_2O_3 \geq 15$ wt %; $Na_2O \geq 3$ wt %; $Sr/Y \geq 20$; $La/Yb \geq 20$; $Y \leq 10$ ppm; $Yb \leq 1$ppm; Richards and Kerrich, 2007; Castillo, 2012). Worldwide porphyry systems are commonly associated with high Sr/Y and La/Yb magmas that accumulated and matured at the base of the crust in the MASH zone in arc settings (Richards and Kerrich, 2007; Chiaradia et al., 2012). However, similar fertile magmas and associated porphyry systems can be produced in post-subduction and post-collisional tectonic settings (Richards, 2009) that yield similar elemental and isotopic geochemical signatures (Richards, 2015).

1.1.2 Post-subduction metallogeny

Although the formation of arc magmas and their genetic relationship with porphyry deposits in subduction zones have been well-established, new mineral discoveries, improvement in geodynamic models and geochronological techniques revealed that porphyry and epithermal deposits can also form in the back-arc, post-subduction settings including slab roll-back, tearing, break-off, and during and/or after a collision in response to crustal thickening, lithospheric mantle delamination and orogenic collapse (e.g., Richards et al., 1990; De Boorder et al., 1998; Blundell, 2002; Lips, 2002; Cloos et al., 2005; Richards et al., 2006; Wang et al., 2006; Vos et al., 2007; Hou et al., 2009; Richards, 2009). The geological and geochemical similarities between arc-related and post-subduction to collisional porphyry systems suggest identical second- and third-order controls during their emplacement in the crust; alternatively, different tectonic settings imply contrasting first-order controls on magma fertility involving contributions of crustal, lithospheric and asthenospheric components to the magmatic sources and processes. In the absence of subduction-modified asthenospheric mantle wedge, the metal source(s) in post-subduction settings are matter of debate and include: 1) previously-fertilized subcontinental lithospheric mantle (SCLM; Pettke et al., 2010; Mair et al., 2011) by asthenosphere-derived low-degree partial melts (Hronsky et al., 2012; Griffin et al., 2013); 2) subduction-modified cumulates in the lower crust as remnants of previous cycles of arc magmatism (Chiaradia et al.,

2009; Richards, 2009); 3) juvenile lower crust after arc magma underplating (Hou et al., 2009; Shafiei et al., 2009). The infiltration of hot asthenosphere as a response to post-subduction slab ruptures or windows, or lithospheric delamination or dripping can play a critical role to remobilize fertile material in the lithospheric mantle and/or lower crust which can lead to the formation of porphyry deposits (Lips, 2002; Wang et al., 2006; Vos et al., 2007; Hou et al., 2009; Richards, 2009, 2011b; Logan and Mihalynuk, 2014). However, remobilization processes may cause the dilution of hydrous, fertile magmas by barren and drier, asthenosphere-derived melts (Hronsky et al., 2012) leading to the drastic reduction of magma fertility for precious and base metal mineralization through time. Those remelting mechanisms are not well understood and deserve further investigations.

1.1.3 Temporal and spatial distribution of porphyry deposits

Porphyry and epithermal deposits commonly form during specific epochs and in clusters that may be lined up along magmatic belts (Sillitoe, 2010). Mineralized porphyry intrusions are typically the final episode of a given magmatic cycle in the Andes (Richards, 2003; Chiaradia et al., 2009). In contrast, post-subduction porphyry deposits may form at the early stages of tectonic perturbations (e.g., Pettke et al., 2010). Trench advancement and retreat in response to variations in convergence rate result in arc migrations, change in crustal regime and thus magmatic peaks and gaps (Bertrand et al., 2014). The transpressional regime favors the development of large magma chambers in the crust; stress relaxation facilitates the release of metal-rich fluids (Tosdal and Richards, 2001). The reversal of subduction polarity (Solomon, 1990), flat subduction (Kay and Mpodozis, 2001; Hronsky et al., 2012) caused by ridge subduction (Hollings et al., 2005), subduction of major transform structures (Richards and Holm, 2013), cessation of subduction (Sillitoe, 1997), crustal thickening associated with compressive tectonism (Sillitoe, 1998), and oblique convergence (Tosdal and Richards, 2001) are favorable tectonic scenarios for the production of fertile magma and associated porphyry deposits. In addition, slab segmentation and rupture propagation in the mantle also affect the spatial distribution of magmatism and associated mineralization that across- or along-strike

migration. Recent numerical and seismic tomographic models can image the 3D complexity of subduction and collisional zones. Thus, the temporal, spatial and geochemical evolution of fertile magmatism and associated porphyry-style mineralization interpreted with well-constrained 3D slab dynamics allow to determine first-order factors controlling the formation of those Cu-Au deposits in a particular metallogenic province.

1.2 Slab break-off and tearing models

Initially proposed by analogue modeling (e.g., Isacks et al., 1968) and subsequently supported by seismic tomography (Spakman et al., 1988), slab break-off is defined as the buoyancy-driven detachment of the subducting oceanic lithosphere from the continental lithosphere during the continental collision by the lateral propagation of a sub-horizontal rupture (Figure 1.2A; Davies and von Blanckenburg, 1995; Wortel and Spakman, 2000). A slab rupture can also be sub-vertical within the subducting slab, known as slab tear (Figure 1.2B), to accommodate different roll-back velocities along the length of the subduction system (Govers and Wortel, 2005; Rosenbaum et al., 2008). The term slab detachment is frequently used as a synonym to slab break-off (Gerya et al., 2004) but refers to tectonic events that might take place before or independently from continental collision and subduction processes (van der Voo et al., 1999; Levin et al., 2002). The term slab detachment also includes the delamination of a cooler, denser and over-thickened lithospheric mantle, which is peeled away from the overlying continental crust and founders into the underlying asthenosphere (Bird, 1978, 1979;

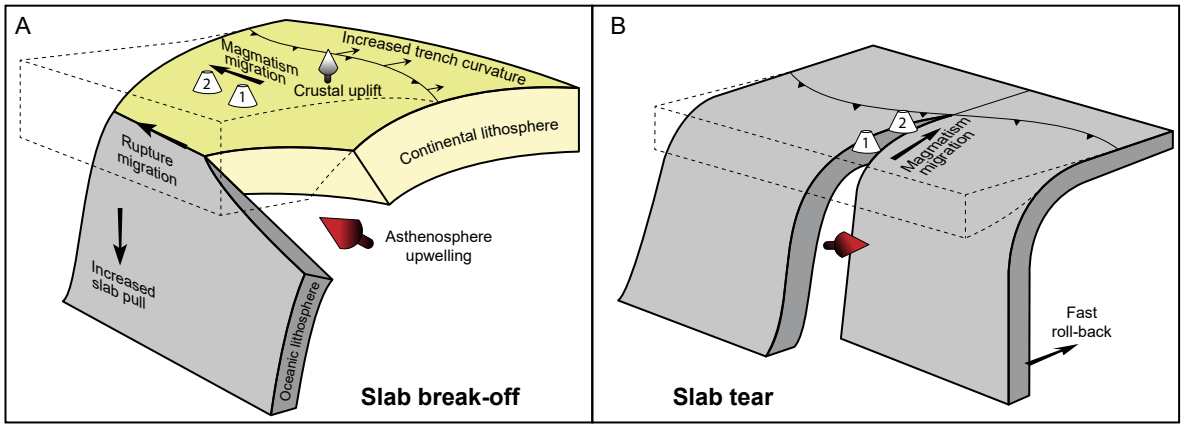

Figure 1.2 A) Slab break-off model (modified from Wortel and Spakman, 2000); B) Vertical slab tear model.

Houseman et al., 1981; Platt and England, 1994). The opening of a sub-horizontal or sub-vertical window within the subducting slab allows the upwelling of hot and dry asthenosphere, and the significant heat influx into the hydrated mantle wedge, which facilitates the production of magma (Davies and von Blanckenburg, 1995; van de Zedde and Wortel, 2001). As the asthenospheric heat flux increases during sub-horizontal slab rupture propagation and expansion of the slab window, the resultant magmatism is expected to form a narrow belt (< ca. 200 km) and migrate laterally (Davies and von Blanckenburg, 1995; Ferrari, 2004).

The slab break-off concept has been widely applied, in particular along the Western Tethyan Orogenic Belt, to account for a variety of phenomena including magmatism above the slab rupture (Zhu et al., 2015; Ekici, 2016). In the overriding plate, slab break-off tends to be manifested by an increase in oceanic island basalt (OIB)-like deep mantle signature, and a decrease in arc signature. (Keskin et al., 1998; Ferrari, 2004; Prelević et al., 2015). This shift has been rationalized by decreasing involvement of subduction-hydrated mantle and increasing contribution from the dry asthenosphere rising from depth, particularly from beneath the slab (e.g., Maury et al., 2000; Coulon et al., 2002; Keskin, 2003; Ferrari, 2004; Prelević et al., 2015), a pattern also established at sites of ridge subduction (Thorkelson et al., 2011). Additionally, a slab break-off episode can account for rapid crustal uplift (Huang et al., 2010; Schildgen et al., 2014) and exhumation of metamorphic massifs (Davies and von Blanckenburg, 1995; O'Brien, 2001), increasing sediment supply (Sinclair, 1997), changes in crustal stress regime from compression to extension (Sue et al., 1999; Kaymakçı et al., 2010), anomalous distribution of seismicity (Sperner et al., 2001), inversion of subduction polarity (Teng et al., 2000) and ore-forming processes (Cloos et al., 2005; Neubauer et al., 2005; Vos et al., 2007; Logan and Mihalynuk, 2014). However, a broad range of contemporaneous post-subduction geological phenomena such as magmatic episodes, rapid crustal uplift, changes in crustal stress regime and ore-forming processes can be explained by either slab break-off, tearing, roll-back, or lithospheric mantle removal by either delamination or dripping. In addition, the interpretation of geochemical data in post-subduction settings is often ambiguous

(Garzanti et al., 2017) and cannot be used unequivocally as a direct evidence for slab break-off or tearing models. Thus, the combination of 3D numerical modeling, seismic tomography and surface studies on the geochronological and spatial constraints on magmatism provide robust evidence for slab rupture initiation, propagation and orientation.

1.3 Tectono-magmatic framework of the Anatolide-Tauride Block

The Western Tethyan Orogenic Belt is > 6,000 km from the Alps to Pakistan via Eastern Europe, Turkey, Lesser Caucasus and Iran. This Belt was generated through the accretion of many Gondwana-derived, ribbon-like, continental fragments to the southern margin of Laurasia closing the various branches of the Paleotethys and Neotethys Oceans during the Paleozoic to Mesozoic accretionary and the Cenozoic collisional orogenesis (Figure 1.3; Le Pichon and Angelier, 1979; Şengör and Kidd, 1979; Şengör and Yılmaz, 1981; Şengör et al., 1984; Sengör and Natal'In, 1996; Jolivet and Faccenna, 2000; Stampfli, 2000; Stampfli and Borel, 2004; Barrier and Vrielynck, 2008; Faccenna et al., 2014). The Anatolide-Tauride Block (ATB), which is one of those continental fragments, is the central segment of the Western Tethyan Orogenic Belt and defined by the 1500 x 200 km area centered along the 39th parallel in Turkey. It is bordered to the north by the Rhodope-Pontide Block, the Aegean Sea and volcanic archipelago to the west, the Mediterranean Sea to the south-west, the Arabia plate to the south-east and the Iran plateau, or Sanandaj-Sirjan terrane, to the east (Figures 1.3 and 1.4; e.g., Okay and Tüysüz, 1999).

The ATB consists of Neoproterozoic to Mesozoic metamorphosed and exhumed massifs (e.g., Menderes, Tavşanlı Zone and Afyon-Ören Zone), non-metamorphosed Paleozoic to Mesozoic sedimentary platforms (e.g., Taurus and Eastern Anatolian Accretionary Complex) and Mesozoic ophiolitic complexes (Figure 1.4; e.g., Şengör and Yılmaz, 1981; Okay and Tüysüz, 1999; Moix et al., 2008; Robertson et al., 2013). The ATB docked to the southern active margin of Laurasia, now called Eurasia, along the İzmir-Ankara-Erzincan suture zone after the closure of the Northern Neotethys Ocean in the Late Cretaceous-Paleocene (Figure 1.5; Şengör and Yılmaz, 1981; Okay and Tüysüz, 1999; Barrier and Vrielynck, 2008; Meijers

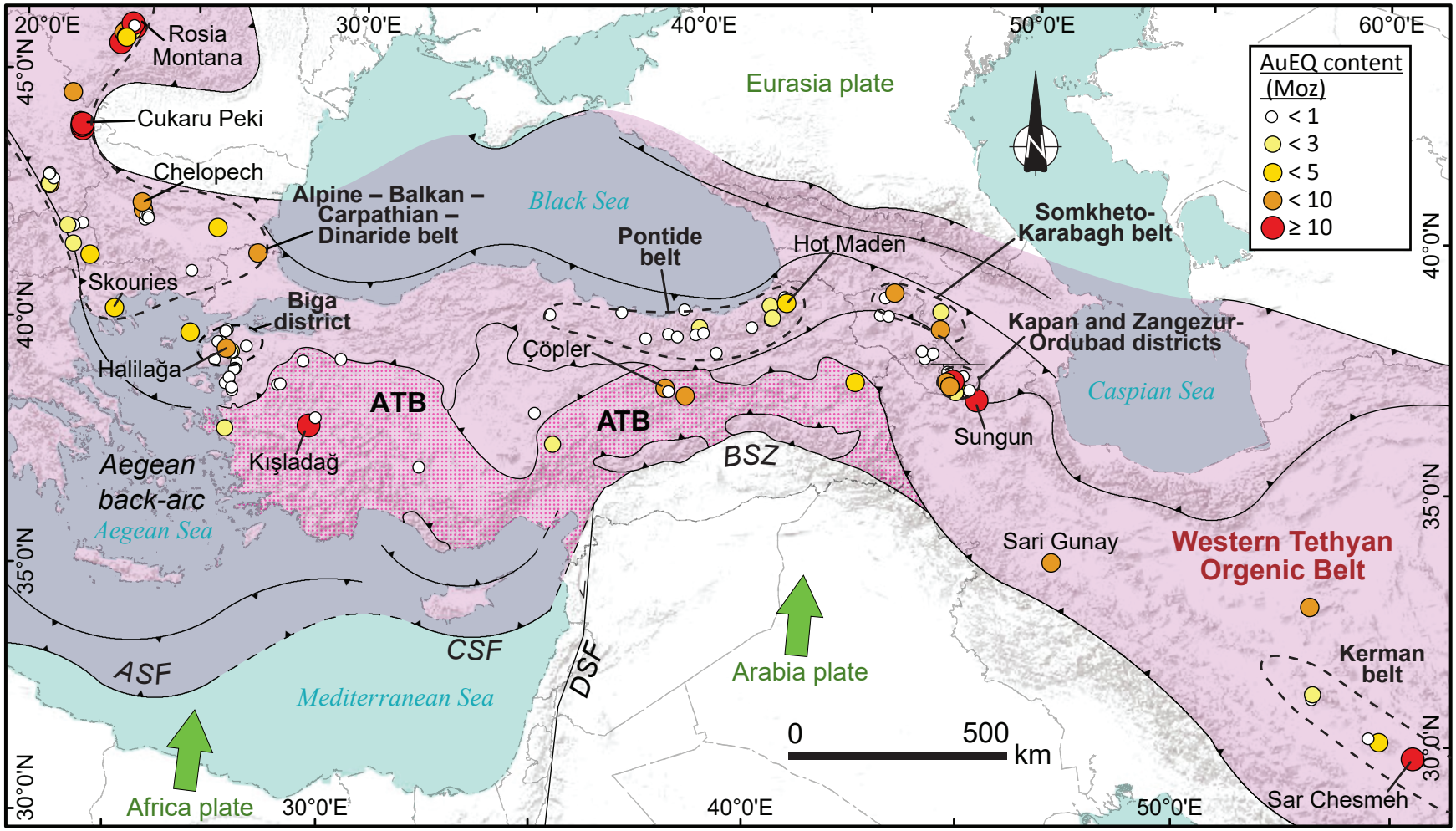

Figure 1.3 Western Tethyan Orogenic Belt (in light pink) showing the location of the study area, namely the Anatolide-Tauride Block (ATB; pink dotted area) sandwiched between Eurasia and the northward converging Africa and Arabia plates (green arrows), major tectonic boundaries (black lines) and the major porphyry and epithermal deposits, districts and belts. ASF = Aegean subduction front; BSZ = Bitlis suture zone; CSF = Cyprus subduction front; DSF = Dead Sea fault. Background image from ESRI.

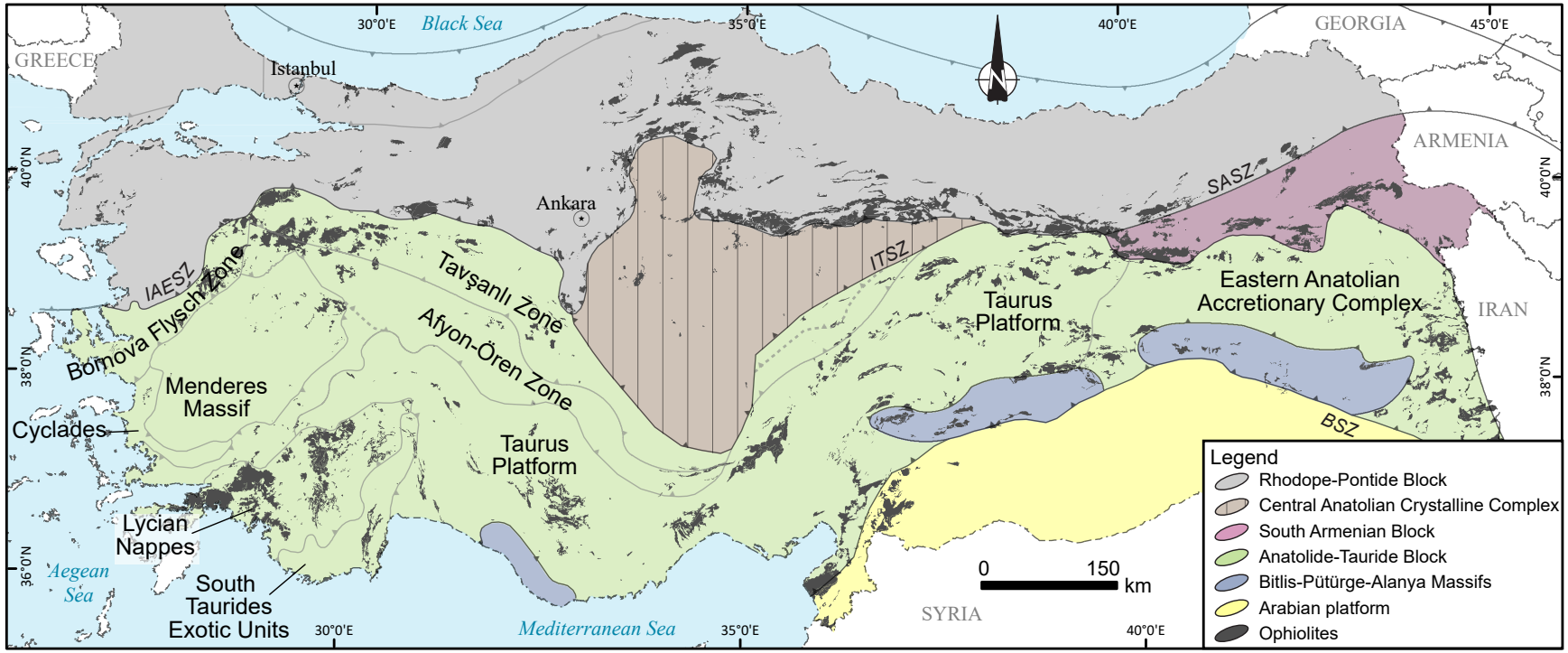

Figure 1.4 Tectonic map of Turkey (1:6,000,000; Lambert Conic projection; European Datum 1950) showing the location of major tectonic terranes and boundaries (modified from Okay and Tüysüz, 1999; Şengör et al., 2008; Pourteau et al., 2013) and the distribution of ophiolitic units (modified from MTA, 2002). The labels are the tectonic zones within the Anatolide-Tauride Block (light green; study area). BSZ = Bitlis Suture Zone; IAESZ = İzmir-Ankara-Erzincan Suture Zone; ITSZ = Inner Tauride Suture Zone; SASZ = Sevan-Akera Suture Zone.

et al., 2010; van Hinsbergen et al., 2016). Numerous continental fragments (i.e., Central Anatolian Crystalline Complex, Bitlis-Pütürge Massifs, South Armenian and Rhodope-Pontide Blocks, and Arabian platform), and remnants of oceanic basins (i.e., İzmir-Ankara-Erzincan or Northern Neotethys, Berit, Inner Tauride and Southern Neotethys) surround the ATB but their number, nature, age and timing of closure are matter of debate (Robertson et al., 2013; van Hinsbergen et al., 2016). Only the northward subduction of the Southern Neotethys Ocean,

Figure 1.5 Paleogeographic reconstructions of the Middle East showing the Mesozoic northward migration of the Anatolide-Tauride Block (ATB) opening and closing the Northern and Southern Neotethys Oceans: A. Toarcian; B. Aptian; C. Maastrichtian; D. Burdigalian (modified from Barrier and Vrielynck, 2008).

initiated in the Late Cretaceous, remained active beneath ATB during the Paleogene (e.g., Robertson et al., 2013) until the indentation of Arabia into eastern Anatolia along the Bitlis suture zone (Dewey et al., 1986; McClusky et al., 2000; Robertson, 2000; Reilinger et al., 2006). The Arabia-Eurasia (ATB) continental collision likely initiated in the Oligocene (Jolivet and Faccenna, 2000; Agard et al., 2005; Allen and Armstrong, 2008; Barrier and Vrielynck, 2008; McQuarrie and van Hinsbergen, 2013; Karaoğlan et al., 2016) rather than in the Eocene (Rolland et al., 2012) and the Miocene (Şengör and Yılmaz, 1981; Dewey et al., 1986; Yılmaz, 1993; Yiğitbaş and Yilmaz, 1996; Robertson et al., 2007; Hüsing et al., 2009; Okay et al., 2010; Robertson et al., 2016).

1.4 Late Cenozoic segmentation of the Southern Neotethyan oceanic slab

The resulting continental collision between Arabia and Eurasia terminated subduction and led to the steepening and break-off of the Southern Neotethyan oceanic slab and/or delamination of the lithospheric mantle beneath central and/or eastern Anatolia (Keskin, 2003; Faccenna et al., 2006; Keskin, 2007; Şengör et al., 2008; Kaymakçı et al., 2010; Bartol and Govers, 2014; Neill et al., 2015; Delph et al., 2017; Oruç et al., 2017; Topuz et al., 2017). Although many researchers have indicated that late Cenozoic magmatism in central and eastern Anatolia is the major magmatic response to Southern Neotethyan oceanic slab steepening, break-off and/or delamination, there is considerable debate about the spatial constraints and timing of those post-subduction tectonic events, most specifically whether they initiated in the Oligocene (Agard et al., 2005; Hafkenscheid et al., 2006; Kaymakçı et al., 2010; İmer et al., 2014), middle Miocene (Çolakoğlu and Arehart, 2010; Ekici, 2016), middle-late Miocene (Karaoğlan et al., 2016), or late Miocene (Keskin, 2003, 2007; Şengör et al., 2008). According to Faccenna et al. (2006), the sub-horizontal slab rupture propagation in eastern Anatolia increased and focused the load on the neighboring, and still attached, western and central segments, namely the Aegean and Cyprus slabs since 11 Ma (Keskin, 2003; Figure 1.6). The additional slab pull force accelerated the Aegean slab roll-back, Hellenic trench retreat and curvature, westward extrusion of the Anatolian microplate along the North Anatolian fault

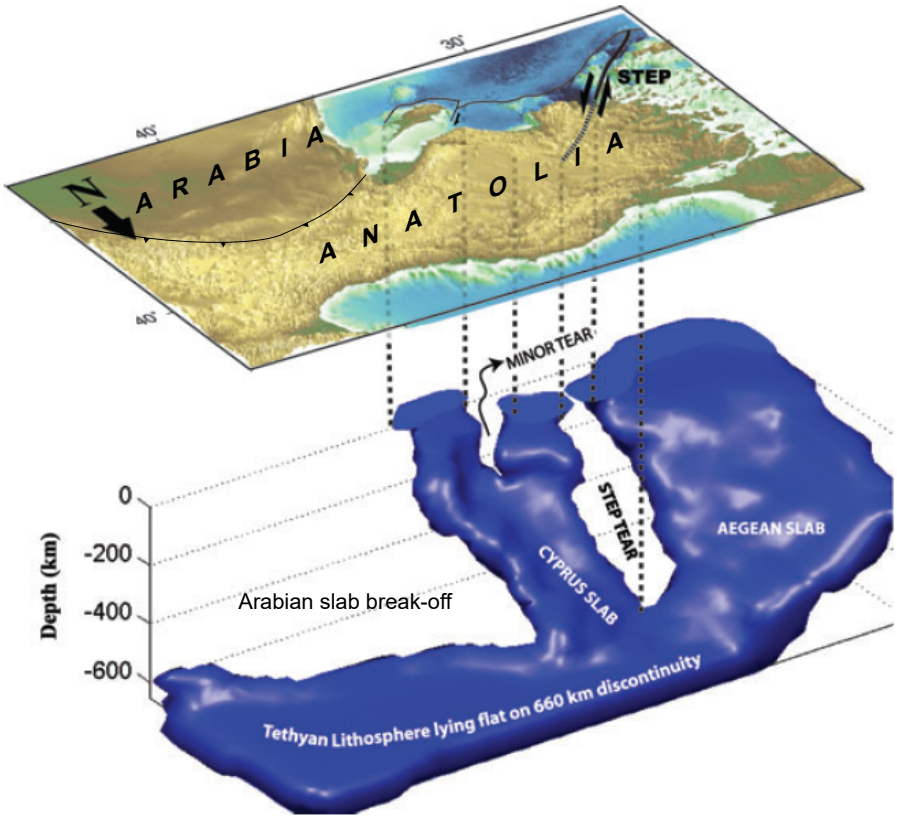

Figure 1.6 3D diagram of the subducted Southern Neotethyan oceanic slab beneath Anatolia interpreted from seismic tomographic model and illustrating the segmented geometry of the slab and the projection to the surface of the major tectonic features (modified from Biryol et al., 2011).

zone (Wortel and Spakman, 2000; Faccenna et al., 2006). The acceleration of the Aegean slab roll-back velocity relative to the Cyprus slab segment beneath central Anatolia initiated a south-trending sub-vertical tear between both slabs from 15 to 8 Ma (Jolivet et al., 2015). Thus, the slab tear in western Anatolia developed before the slab break-off in eastern Anatolia, according to those previous studies cited above.

1.5 Metallogeny of the Western Tethyan Orogenic Belt

The complex tectono-magmatic framework of this Western Tethyan Orogenic Belt was favorable for the generation of fertile magmatism and ore-forming processes in arc, back-arc, post-subduction (e.g., slab tearing, roll-back and break-off), and post-collisional lithospheric mantle delamination tectonic settings (Dixon and Pereira, 1974; Janković, 1977, 1997;

Lips, 2002; Cassard et al., 2004; Neubauer et al., 2005; Richards et al., 2006; Yiğit, 2006; Zimmerman et al., 2008; Shafiei et al., 2009; Yiğit, 2009; Richards et al., 2012; Yiğit, 2012; Kuşcu et al., 2013; Bertrand et al., 2014; Richards, 2015; Moritz et al., 2016a; Moritz et al., 2016b; Richards and Sholeh, 2016; Menant et al., 2018). The ore deposits within the Tethyan domain include porphyry Cu-Mo-Au, podiform chromite, sediment-hosted Pb-Zn (SEDEX and MVT), Kuroko- and Cyprus-type volcanogenic massive sulfide (VMS), skarn Fe-Pb-Zn-Cu, Carlin-style Au-Ag, iron oxide copper-gold (IOCG), high-, intermediate and low-sulfidation epithermal Au-Ag and orogenic Au deposits (Janković, 1977, 1997; Yiğit, 2009; Bertrand et al., 2014; Richards, 2015; Moritz et al., 2016a; Baker, 2017; Melfos and Voudouris, 2017; Menant et al., 2018). This emerging Belt hosts numerous world-class porphyry and epithermal Cu-Au deposits such as Rosia Montana, Kışladağ, Sar Cheshmeh and Reko Diq (Janković, 1977; Hezarkhani, 2006; Manske et al., 2006; Razique et al., 2014; Baker et al., 2016) and remains a focus of on-going exploration efforts (Figure 1.3). However, the distribution of porphyry and epithermal systems along the Western Tethyan Orogenic Belt is neither uniform in time nor space (Zimmerman et al., 2008; Bertrand et al., 2014; Richards, 2015). Major clustering resulted in specific metallogenic periods and along distinct Belt segments such as the Oligocene to Miocene Urumieh-Doktar Belt in southeast Iran (Richards and Sholeh, 2016), the Jurassic to Cretaceous Somkheto-Karabagh Belt and the Eocene to Pliocene ore deposits of the Zangezur-Ordubad region in the Lesser Caucasus (Moritz et al., 2016a; 2016b), the Cretaceous and Oligo-Miocene deposits of the Alpine-Balkan-Carpathian-Dinaride Belt (Heinrich and Neubauer, 2002), the Biga district of northwest Turkey (Yiğit, 2012; Smith et al., 2014; Brunetti, 2016; Leroux, 2016; Sánchez et al., 2016; Smith et al., 2016) and the Pontide Belt on the Rhodope-Pontide Block of northern Turkey (Bilir, 2015; Delibaş et al., 2016). The Anatolian segment of the Western Tethyan Orogenic Belt in Turkey seems to be characterized by isolated porphyry and epithermal deposits rather than mineral clusters (Yiğit, 2006, 2009; Bertrand et al., 2014; Richards, 2015).

1.6 Overview of the Turkish metallogeny

1.6.1 Birthplace of mining

Situated at the cross-roads between the European, Asian and African continents and surrounded by the Mediterranean, Aegean and Black Seas, Anatolia, in the current Turkey, occupied the heart of a vast trading network and provided access to the rich cities of lower Mesopotamia and westward into the Aegean for centuries. Since the Neolithic, Anatolia has been the birthplace of many civilizations and the prominent centre of commerce. The civilization growth and trading was accompanied by the development of currencies, and ultimately by the use of metals. The earliest traces of worked copper ore were reported in Çayönü Tepesi near Diyarbakir-Ergani in 9000 BC (Cambel and Braidwood, 1970), and more significant metallurgical workings in the Çatalhöyük and Ergani regions in southeastern Turkey in 6000 BC (Bucha and Mellaart, 1967; Wagner and Öztunalı, 2000). Anatolian metallurgy peaked during the Phrygian period (700-550 BC) where bronze materials were exported to Greece and Italy (Akurgal, 1962). The domination of the Lycian kingdom (700-550 BC) in western Anatolia relied on the exploitation of placer gold deposits in the Menderes region, notably along the famous Pactolus (Gediz) River, or "river that flowed with golden waves" (Young, 1972). Croesus (560-546 BC), King of Lydia, was so wealthy that the popular reference "as rich as Croesus" originated in reference to him. According to the legend, his wealth came from the sands of the Pactolus River in which the legendary King Midas washed his hands to rid himself of the "Midas Touch", which turned everything he laid hands on into gold, and made the sands of the river rich in gold. Prior to Croesus, King Gyges (687-652 BC) was credited for the invention of the first coins of gold and silver (Akcil, 2006).

The Anatolian mineral endowment contributed to the hegemony of the successive Persian, Hellenistic, Roman, Byzantine, Seljuk and Ottoman Empires through the long accumulation of metallurgical skills and technique improvements. The old Anatolian tradition of metal production thrived through centuries and revealed the outstanding potential for precious and base metals, still considered as underexploited based on the modern standards.

Modern exploration techniques and metal endowment assessment have only been conducted for the last four decades due to recent amendments of the mining law in 1985 and 2004, and economic stability that boosted the exploration licenses attribution by the mining bureau (Yiğit, 2006). Modern mineral exploration in Turkey is mainly driven by the distribution and reinterpretation of old prospects and deposits that sometimes leads to the life extension of old mines (e.g., Ergani and Gümüşköy), or the discovery of modern-sized deposits such as Ovacık and Çöpler around the Greek workings in Pergamon (Bergama) and Roman workings near Erzincan, respectively (Akcil, 2006; İmer et al., 2016). Nevertheless, Turkey still largely remains an unexplored country with a base of diverse mineral resources as well as being one of the least studied segment of the Western Tethyan Orogenic Belt.

1.6.2 Mineral diversity of Turkey

The tectonic and magmatic activity in Turkey has been a favorable environment for the formation of metal-endowed magmas and hot fluids since the Cretaceous. The majority of precious metal resources and reserves are hosted within porphyry and high-, intermediate-, and low-sulfidation deposits such as at Kışladağ (21.5 Moz Au), Çöpler (12.8 Moz Au) and Efemçukuru (3.4 Moz Au). These metal-rich, hydrothermal systems will be extensively reviewed the Chapter 4.

Volcanogenic massive sulfide (VMS) deposits contain most of the economic base metal endowment in Turkey. The Kuroko-type VMS systems that formed in back-arc basins (Franklin et al., 2005) are Cretaceous in age and cluster in the Pontides (Figure 1.7) such as Cayeli, Cerratepe and Murğlu, and are rich in Cu (± Pb ± Zn) and less commonly in Au, except for Hot Maden (2.6 Moz Au and 0.3 Mlbs Cu; Sandstorm Gold Royalties, 2018). In contrast, the Cu-rich Cyprus-type VMS deposits, such as Ergani and Siirt, are hosted within ophiolitic rocks along the Bitlis suture zone, and in the Kure district in northern Turkey. Recent discoveries of stratabound massive sulfide bodies within the Anatolian metamorphic units have been made at Yenıpazar in Central Anatolia (0.91 Moz Au, 30 Moz Ag, 0.21 Mlbs Cu, 660 Mlbs Pb and 961 Mlbs Zn; Armstrong et al., 2012) and Gediktepe (0.4 Moz Au, 8 Moz Ag, 315 Mlbs Cu and 780

Mlbs Zn; Alacer Gold, 2016) in western Anatolia. The minor Fe-Cu, Pb-Zn, W and Mo skarn (e.g., Çelebi, Keskin, Höröz, Ayazmant and Karamadazı), IOCG deposits (e.g., Şamlı, Divriği and Hasançelebi) and metamorphic- and ophiolite-hosted orogenic Au-bearing quartz veins (e.g., Kaymaz; 0.6 Moz Au; Koza Gold, 2015) do not significantly contribute to the precious and base metal endowment of Turkey.

The widespread Tauride carbonate platform hosts several small (< 0.5 Mt ore), Paleozoic to Cenozoic, MVT-, SEDEX- and carbonate replacement-type Pb-Zn deposits such as in the Bolkardağ, Yahyali, Tufanbeyli, Malatya, Keban and Hakkari districts (Ceyhan, 2003). Turkey is an emergent precious and base metal producer but also plays an important role in the world production of podiform chromite ore. Those deposits, rarely greater than 1 Mt, are hosted within ultramafic cumulates of the Mesozoic ophiolitic assemblages such as in the Pozanti-Karsanti and Harmancik districts (Yiğit, 2009). Other minor types of deposits such as placer gold, mainly in the Menderes Massif with the famous Pactolus and Sardis Rivers, sediment-hosted copper in Cenozoic basins in Central Anatolia and lateritic bauxite ore in the Tauride platform have also been reported by Yiğit (2009).

Metallogenic studies in Turkey are restricted to mineral inventories (Yiğit, 2006, 2009) or to some specific areas (Kuşcu and Erler, 1998; Delibaş and Genç, 2012; Yiğit, 2012; Kuşcu et al., 2013; Eyuboğlu et al., 2014; Delibaş et al., 2016). In the last few years, numerous deposit-scale metallogenic studies focused on porphyry and epithermal deposits and prospects have emerged (e.g., Çolakoğlu et al., 2011; İmer et al., 2013; Yılmaz et al., 2013; İmer et al., 2014; Yılmazer et al., 2014; Baker et al., 2016; Boucher, 2016; Brunetti, 2016; İmer et al., 2016; Leroux, 2016; Sönmez and Kuşcu, 2016; Delibaş et al., 2017) and provide an improved basic knowledge to this regional study for the implementation of a comprehensive metallogenic model that encompasses all of those Oligocene to Miocene deposits and prospects.

1.6.3 Tectono-magmatic context of Anatolian porphyry and epithermal mineralization

Formation of Anatolian porphyry- and epithermal-style mineralization peaked in the Late Cretaceous, Eocene and since the late Cenozoic (Yiğit, 2006, 2009; Kuşcu et al., 2013).

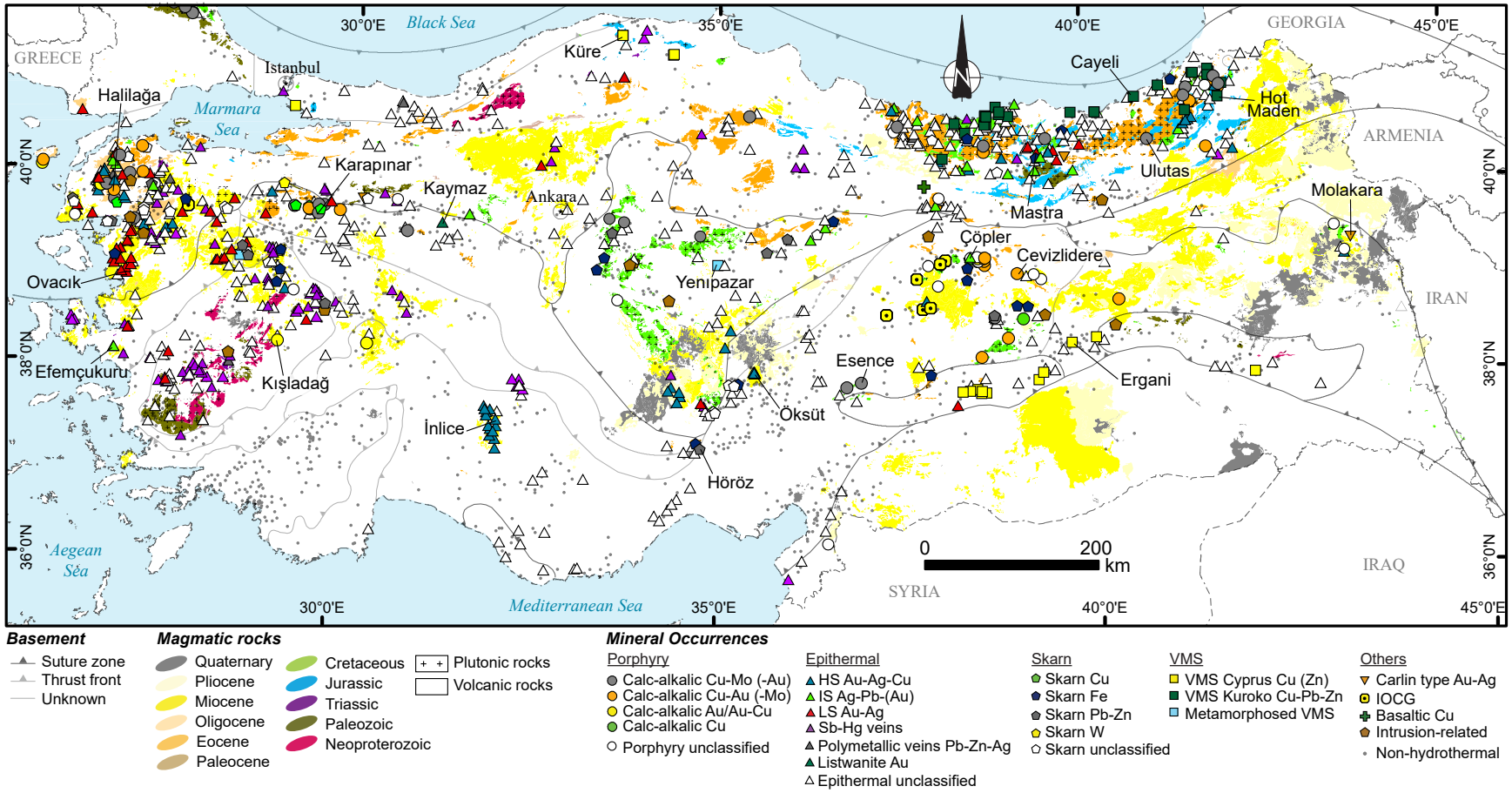

Figure 1.7 Map of Turkey showing the distribution of metal occurrences, prospects and deposits with an emphasis on magmatic-hydrothermal ore systems, namely porphyry, epithermal, skarn and VMS. Basement boundaries were modified from Okay and Tüysüz, 1999; Şengör et al., 2008; Pourteau et al., 2013; the igneous units were modified from MTA, 2002.

Late Cretaceous and Eocene porphyry, epithermal, skarn and IOCG prospects and deposits formed during arc, back-arc and post-collisional magmatic episodes as a result of the evolution towards closure of the Northern Neotethys and the subduction of the Southern Neotethys (İmer et al., 2013; Kuşcu et al., 2013).

Recent geochronological studies indicate that numerous major gold-rich porphyry and epithermal systems such as Kışladağ (Baker et al., 2016), Pınarbaşı (Delibaş et al., 2017) and Cevizlidere (İmer et al., 2014) are hosted within late Cenozoic igneous units. Those deposits are lined up along the Anatolian Metallogenic Trend that links the westerly Aegean back-arc to the easterly Arabian continental collision domains (Chapter 4). The Anatolian Trend therefore provides an excellent natural laboratory to investigate mechanisms of back-arc, post-subduction and syn-collisional metallogeny.

1.7 Thesis research questions and objectives

The genetic relationship between tectonics, magmatism and metallogeny in Anatolia since the late Cenozoic is a fundamental unresolved question, despite recent efforts in western Anatolia (Baker et al., 2016; Gessner et al., 2017; Menant et al., 2018). However, the determination of first-order controls on gold metallogeny in Anatolia requires a well-constrained tectono-magmatic framework in which mineral deposits will be placed and their genesis interpreted. Therefore, this thesis is divided into two parts that are dedicated to the definition of 1) a robust tectono-magmatic framework in Anatolia (Chapters 2 and 3), and 2) lithospheric-scale factors controlling the formation of late Cenozoic Anatolian gold mineralization (Chapters 4 and 5). New results and interpretations will provide new insights into the geodynamic evolution of the Eastern Mediterranean region and the role of asthenosphere upwelling on post-subduction magmatism and metallogeny.

1.7.1 Part 1: Temporal, spatial and geochemical evolution of late Cenozoic magmatism in central and eastern Anatolia

As summarized above, the timing of slab tear in western Anatolia is well-constrained

by paleomagnetic rotations, and metamorphic and magmatic events (van Hinsbergen, 2010; Jolivet et al., 2015); whereas many uncertainties about the tectono-magmatic evolution of central and eastern Anatolia remain and include: 1) the timing of slab break-off initiation in eastern Anatolia; 2) the spatial propagation of the sub-horizontal slab rupture to central Anatolia; and 3) melting sources and processes involved in the production of post-subduction late Cenozoic magmatism. Those approximations thereby add some uncertainty to the geodynamic relationships between slab break-off at the onset of the Arabia-Eurasia continental collision in eastern Anatolia and the Aegean slab roll-back in western Anatolia. Thus, the main objective of Part 1 is to define the temporal, spatial and geochemical evolution of late Cenozoic magmatism in the least-studied central and eastern Anatolian regions to constrain the slab break-off event. Chapter 2 provides temporal and spatial constraints on the evolution of the Southern Neotethyan slab break-off and window opening events in central and eastern Anatolia at the onset of the Arabian continental collision. Chapter 3 determines the magmatic processes and sources involved during the late Cenozoic slab break-off and partial lithospheric mantle removal events in central and eastern Anatolia.

1.7.2 Part 2: Late Cenozoic Anatolian Gold Metallogeny

The lack of temporal, spatial and chemical constraints on mineralized igneous rocks hinders to place the late Cenozoic Anatolian porphyry and epithermal deposits into the regional tectono-magmatic framework and identify the first-order factors controlling their formation. Therefore, Part 2 aims to build up a comprehensive genetic model for late Cenozoic Anatolian gold metallogeny. More precisely, Chapter 4 characterizes the late Cenozoic porphyry and epithermal districts, constrains the timing of gold mineralization and determines the regional structural control on mineralized igneous units along the late Cenozoic Anatolian Metallogenic Trend. Chapter 5 focuses on the determination of petrogenetic controls on magma fertility in the late Cenozoic Anatolian Metallogenic Trend.

1.8 Thesis approach

The new data acquired for this study include 1) outcrop and petrographic observations, and rock sampling, among the numerous mineralization-bearing igneous units throughout Anatolia; 2) multi-technique geochronological data (U-Pb, $^{40}Ar/^{39}Ar$ and Re-Os methods); and 3) elemental and isotopic geochemical analyses (Sr-Nd-Pb). However, Part 1 primarily relies on the extensive compilation, critical evaluation, integration and interpretation of previously-published geochronological, geochemical and geological data, and tectono-magmatic models from the literature focused on the central and eastern Anatolian regions. In contrast, interpretations in Part 2 are mainly supported by those new mineralization-focused geochronological and geochemical data. The newly-acquired U-Pb age data and geochemical analyses from mineralization-bearing igneous units can provide constraints on both local magmatic episodes in central and eastern Anatolia (Part 1) and mineralization events (Part 2), and thus are used in both Parts.

Part 1: Temporal, spatial and geochemical evolution of late Cenozoic magmatism in central and eastern Anatolia, Turkey

Chapter 2: Migration of late Cenozoic magmatism as a proxy for slab break-off and mantle flow initiation and propagation, central and eastern Anatolia, Turkey

2.1 Introduction

Slab break-off is a major tectonic process that commonly develops during the waning stages of subduction and occurs by the lateral propagation of a sub-horizontal rupture and subsequent detachment of the leading edge of the hanging, sinking lithospheric slab (Wortel and Spakman, 2000). This opposes slab tear which is a sub-vertical rupture within the subducting slab that accommodates different roll-back velocities along the length of the subduction system (Govers and Wortel, 2005; Rosenbaum et al., 2008). The opening of a sub-horizontal or sub-vertical window within the subducting slab allows the upwelling of hot and dry asthenosphere, and the significant heat influx into the hydrated mantle wedge, which facilitates the production of magma (Davies and von Blanckenburg, 1995; van de Zedde and Wortel, 2001). Magma ascent and emplacement in the crust are controlled by regional stress fields. Those magmas are preferentially focused along active trans-crustal structures (Vigneresse, 2004). As the asthenospheric heat flux increases during sub-horizontal slab rupture propagation and expansion of the slab gap, the resultant magmatism is expected to form a narrow belt (< ca. 200 km) and migrate laterally (Davies and von Blanckenburg, 1995; Ferrari, 2004). Although seismic tomography can image the present-day geometry of a subducting slab in the asthenosphere (e.g., Hafkenscheid et al., 2006; Lei and Zhao, 2007; Biryol et al., 2011), temporal constraints on past slab rupture initiation and propagation have been poorly documented because of the lack of appropriate sampling and precise geochronological constraints on the resultant magmatism.

The late Cenozoic tectonic complexity of the Eastern Mediterranean region is due to the indentation of the Arabian platform into the Turkish Anatolide-Tauride Block (ATB), which closed the Southern Neotethyan oceanic basin along the Bitlis suture zone (Figure 2.1; Şengör and Yılmaz, 1981; Yılmaz et al., 1993; Westaway, 2003). The resulting collision terminated

subduction and led to the steepening and break-off of the Southern Neotethyan oceanic slab and/or delamination of the lithospheric mantle beneath central and/or eastern Anatolia (Keskin, 2003; Faccenna et al., 2006; Keskin, 2007; Şengör et al., 2008; Kaymakçı et al., 2010; Bartol and Govers, 2014; Neill et al., 2015; Delph et al., 2017; Oruç et al., 2017; Topuz et al., 2017). Although many researchers have indicated that late Cenozoic magmatism in central and eastern Anatolia is the major magmatic response to Southern Neotethyan oceanic slab steepening, break-off and/or delamination, there is considerable debate about the spatial constraints and timing of those post-subduction tectonic events, most specifically whether they initiated in the Oligocene (Agard et al., 2005; Hafkenscheid et al., 2006; Kaymakçı et al., 2010; İmer et al., 2014), middle Miocene (Çolakoğlu and Arehart, 2010; Ekici, 2016), middle-late Miocene (Karaoğlan et al., 2016), or late Miocene (Keskin et al., 1998; Keskin, 2003, 2007; Şengör et al., 2008). The sub-horizontal slab rupture propagation in eastern Anatolia transferred the slab pull force to the western segment of the Southern Neotethyan or Aegean slab since 11 Ma, resulting in the acceleration of Aegean slab roll-back velocity and the westward extrusion of the Anatolian microplate along the North Anatolian fault zone (Faccenna et al., 2006). The acceleration of the Aegean slab roll-back velocity relative to the Cyprus slab segment beneath central Anatolia initiated a south-trending sub-vertical tear between both slabs from 15 to 8 Ma (Jolivet et al., 2015). Thus, the time constraints on slab rupture events suggest that the slab tear in western Anatolia developed before the slab break-off in eastern Anatolia. Overall, the timing of slab tear in western Anatolia is well-constrained by paleomagnetic rotations, and metamorphic and magmatic events (van Hinsbergen et al., 2010; Jolivet et al., 2015); whereas the timing of slab break-off initiation in eastern Anatolia is only approximate, thereby adding to the uncertainty about the geodynamic relationships between slab break-off at the onset of the Arabia-ATB continental collision in eastern Anatolia and the Aegean slab roll-back in western Anatolia.

The temporal and spatial variations of late Cenozoic magmatism in central and eastern Anatolia resulted from the progressive westward sub-horizontal rupture and break-off of the

Southern Neotethyan oceanic slab and that the resulting mantle flow propagation was followed by the partial lithospheric mantle removal during the collision of the Arabian platform with the Eurasian continental active margin (ATB). Supporting evidence includes the compilation, integration and interpretation of previously-published age determinations, mantle tomography and numerical models from this region. The regional geochronological data compilation was completed by additional, new U-Pb age data from the least-constrained late Cenozoic magmatic complexes in central and eastern Anatolia, namely Konya, Melendiz, Tekkedağ, Develidağ, Yamadağ and Ağrı. Taken all together, the interpretation of compiled and newly-acquired data in this Chapter aims to constrain the timing of slab break-off initiation and its westward propagation in central and eastern Anatolia.

2.2 Geodynamic setting of the Anatolide-Tauride Block

The Western Tethyan Orogenic Belt in the Eastern Mediterranean region formed through the accretion of many Gondwana-derived, ribbon-like, continental fragments to the southern margin of Laurasia since the Paleozoic (e.g., Şengör and Yılmaz, 1981; Şengör et al., 1984; Stampfli and Borel, 2004; Barrier and Vrielynck, 2008). The Anatolide-Tauride Block (ATB), which is one of those continental fragments, consists of the Paleozoic-Mesozoic Taurus platform, Malatya-Keban metamorphic massif, Eastern Anatolian Accretionary Complex and Mesozoic ophiolitic complexes in central and eastern Turkey (Şengör et al., 2008; Yılmaz et al., 2010; Robertson et al., 2013). The ATB has been part of the Anatolian microplate along southern active margin of Laurasia-now called Eurasia, since the Late Cretaceous-Paleocene (Şengör and Yılmaz, 1981; Okay and Tüysüz, 1999; Barrier and Vrielynck, 2008; Meijers et al., 2010; van Hinsbergen et al., 2016). Numerous continental fragments (i.e., Central Anatolian Crystalline Complex, Bitlis-Pütürge Massifs, South Armenian and Rhodope-Pontide Blocks, and Arabian platform; Figure 2.1), and remnants of oceanic basins (i.e., İzmir-Ankara-Erzincan or Northern Neotethys, Berit, Inner Tauride and Southern Neotethys) surround the ATB but their number, nature, age and timing of closure are matter of debate (Robertson et al., 2013; van Hinsbergen et al., 2016).

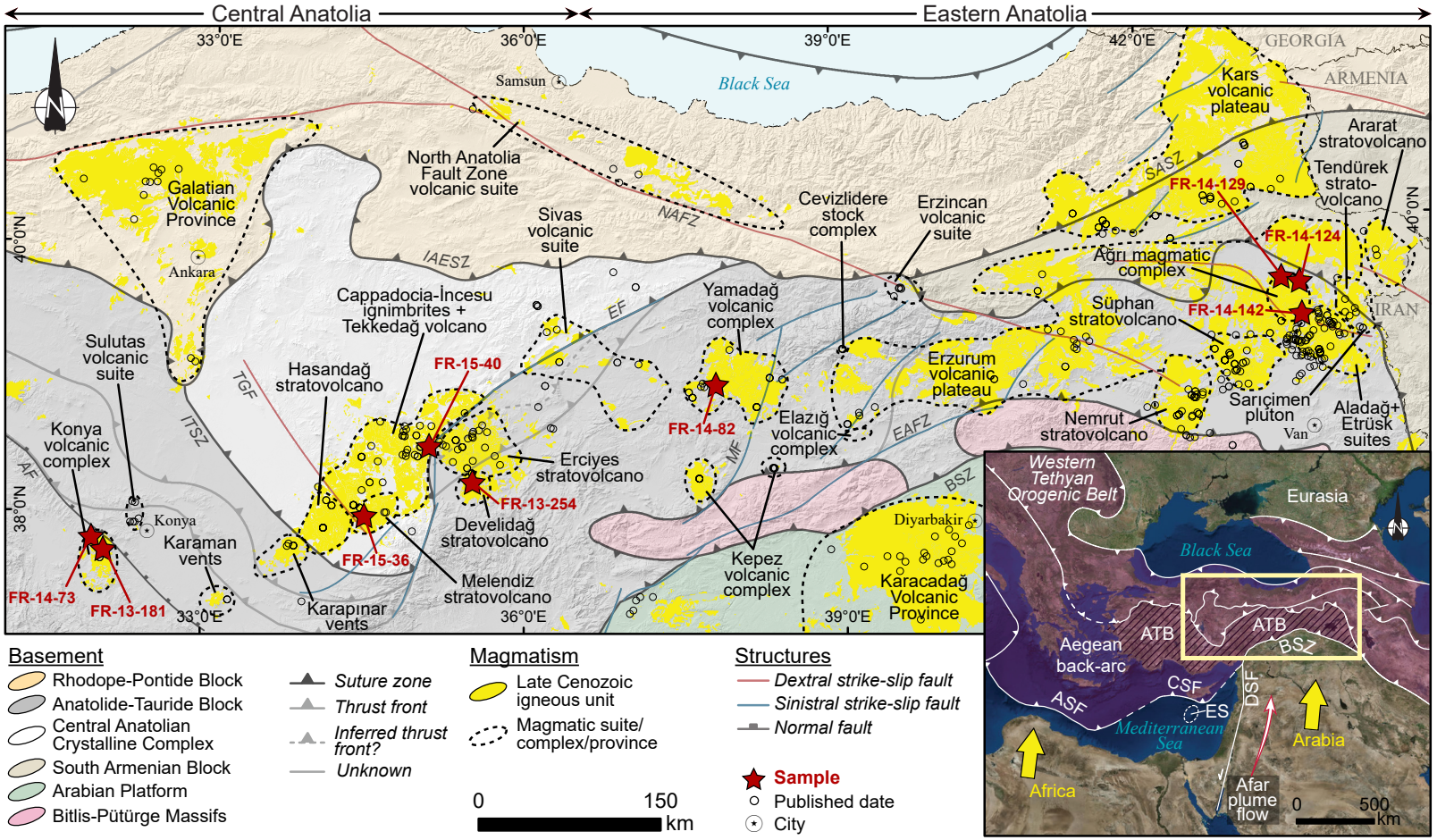

Figure 2.1 Tectono-magmatic map of central and eastern Anatolia (1:4,000,000 scale; Lambert Conic projection; European Datum 1950) showing the basement boundaries, late Cenozoic igneous rocks (modified from MTA (2002)), complexes and provinces, and regional structures. The location of dated rock samples and compiled geochronological data is also displayed. Base map: SRTM 90 m digital elevation models (Jarvis et al., 2008). Background of the location map is from Google Earth. AF = Akşehir Fault; ASF = Aegean Subduction Front; ATB = Anatolide-Tauride Block; Bitlis Sutures Zone; CSF = Cyprus Subduction Front; DSF = Dead Sea Fault; EAFZ = Eastern Anatolian Fault Zone; EF = Ecemiş Fault; ES = Eratosthenes Seamount; IAESZ = İzmir-Ankara-Erzincan Suture Zone; ITSZ = Inner Tauride Suture Zone; MF = Malatya Fault; NAFZ = North Anatolian Fault Zone; SASZ = Sevan-Akera Suture Zone; TGF = Tuz Gölü Fault.

In Turkey, slab break-off tectonic events systematically occurred after subduction terminated due to the closure of the Northern Neotethys (Altunkaynak, 2007; Keskin et al., 2008; Dilek and Altunkaynak, 2009; Sosson et al., 2010), Inner Tauride (Kadıoğlu et al., 2006) and Southern Neotethys oceans (e.g., Keskin, 2003; Şengör et al., 2008). The break-off of the Northern Neotethyan and Inner Tauride oceanic slabs occurred in the Eocene (Altunkaynak, 2007; Keskin et al., 2008; Dilek and Altunkaynak, 2009; Sosson et al., 2010) and Late Cretaceous (Kadıoğlu et al., 2006), respectively, and thus did not play any role in the production of the late Cenozoic magmatism (Neill et al., 2015). Only the northward subduction of the Southern Neotethys remained active beneath Anatolia during the Paleogene (Robertson et al., 2013) until the indentation of Arabia into eastern Anatolia (Dewey et al., 1986; McClusky et al., 2000; Reilinger et al., 2006) along the Bitlis suture zone (Robertson, 2000; Westaway, 2003; Figure 2.1). The Arabian collision and indenture caused westward escape of the Anatolian microplate along the North and East Anatolian fault zones (e.g., McKenzie, 1972; Dewey et al., 1986; McClusky et al., 2000; Faccenna et al., 2006), and delamination-, slab break-off-, tear- and roll-back-related tectonism and magmatism since the late Cenozoic (e.g., Keskin, 2003; Jolivet et al., 2013).

The timing of the initial Arabian collision in eastern Anatolia is controversial and variably includes the Eocene (Rolland et al., 2012), the most accepted Oligocene (Jolivet and Faccenna, 2000; Agard et al., 2005; Allen and Armstrong, 2008; Barrier and Vrielynck, 2008; McQuarrie and van Hinsbergen, 2013; Karaoğlan et al., 2016), and the Miocene on the basis of stratigraphy, deformation history, climate transition and thermochronological interpretations (Şengör and Yılmaz, 1981; Dewey et al., 1986; Yılmaz, 1993; Yiğitbaş and Yilmaz, 1996; Robertson et al., 2007; Şengör et al., 2008; Hüsing et al., 2009; Okay et al., 2010; Robertson et al., 2016). Subduction of the Southern Neotethyan oceanic slab beneath eastern Anatolia terminated with collision and initiation of steepening and rupture of the subducting Arabian oceanic slab segment. The timing of the slab rupture is similarly controversial, with suggestions of the Oligocene (Hafkenscheid et al., 2006; İmer et al., 2014), middle Miocene (Faccenna et

al., 2006; Schildgen et al., 2014; Ekici, 2016), middle-late Miocene (Karaoğlan et al., 2016), or late Miocene (Keskin et al., 1998; Keskin, 2003, 2007; Şengör et al., 2008). The initiation age of the slab rupture has been interpreted from either magmatic events (Keskin et al., 1998; Keskin, 2003, 2007; Şengör et al., 2008; Çolakoğlu and Arehart, 2010; İmer et al., 2014; Ekici, 2016), crustal uplift initiation estimates from thermochronology (Karaoğlan, 2016; Karaoğlan et al., 2016), crustal deformation (Kaymakçı et al., 2010), biostratigraphy (Cosentino et al., 2012), semi-quantitative paleotopographic results (Schildgen et al., 2014), seismic tomography with analogue modeling (Faccenna et al., 2006), and seismic tomography with tectonic reconstructions (Hafkenscheid et al., 2006; Lei and Zhao, 2007; Li et al., 2013). The resultant sub-horizontal rupture is interpreted to propagate westwards all the way to the Cyprus segment of the Southern Neotethyan slab beneath central Anatolia (Piromallo and Morelli, 2003; Faccenna et al., 2006; Gans et al., 2009; Schildgen et al., 2014). This hypothesis is ruled out by numerical modeling (Menant et al., 2016), which supports recent tomography (Biryol et al., 2011) that postulates slab rupture propagation only along the strong lateral rheological contrast between the buoyant Arabian continental and the Southern Neotethyan oceanic lithospheres, leaving the Cyprus oceanic slab steep and unbroken.

The roll-back of the western segment of the Southern Neotethyan, or Aegean slab, was initiated at 35 Ma (Jolivet et al., 2013). Then, the acceleration of the Hellenic trench retreat velocity (ca. 30 mm/year) relative to the Cyprus trench (ca. 10 mm/year; McClusky et al., 2003; Wdowinski et al., 2006; Jolivet et al., 2015) progressively tore the slab from 25 to 16 Ma (Jolivet et al., 2015). The active slab tearing and slab window opening occurred between 15 and 8 Ma and consequently induced fast clockwise rotation of the Hellenides (van Hinsbergen et al., 2010; Jolivet et al., 2015; Govers and Fichtner, 2016). The roll-back and subsequent tearing of the Aegean slab also caused magmatism that migrated southwestward in western Anatolia since the Eocene (Ersoy and Palmer, 2013, and references therein). The Isparta angle at the intersection of the southward-convex Hellenic and Cyprus trenches is an artifact of the slab tear between the downgoing Aegean and Cyprus slabs (Koç et al., 2016, and references

therein).

The steepening and break-off and/or delamination of the Southern Neotethyan oceanic slab is responsible for the formation of the central and eastern Anatolian magmatism since the middle to late Miocene (Pearce et al., 1990; Keskin, 2003, 2007; Şengör et al., 2008; Bartol and Govers, 2014; Abgarmi et al., 2017; Delph et al., 2017; Reid et al., 2017). This model is based on the southward age progression of magmatism from middle to late Miocene (ca. 13-11 Ma) to Present in eastern Anatolia, the apparent absence of, or thin, lithospheric mantle beneath eastern Anatolia, and systematic changes in magma geochemistry from subduction- to OIB-like affinity through time (Keskin, 2003). Recent age and geochemical data on Oligocene to middle Miocene magmatic units in eastern Anatolia (e.g., Çolakoğlu and Arehart, 2010; Lebedev et al., 2010; İmer et al., 2014) support neither the southward magmatic migration nor the previously proposed slab steepening and delamination models.

2.3 Late Cenozoic magmatism of the central and eastern Anatolide-Tauride Block

Late Miocene to Quaternary volcanic rocks of central Anatolia overlie Permian metamorphic basement, Triassic limestone and Jurassic-Cretaceous ophiolitic complexes and Late Cretaceous batholiths of the Central Anatolian Crystalline Complex and the Mesozoic carbonates of the Taurus platform (Toprak and Göncüoğlu, 1993; Aydar et al., 1995). Those volcanic rocks were emplaced at intersections between the regional, conjugate, NW-trending, dextral Tuz Gölü and NE-trending, sinistral Ecemiş faults, and ENE-trending structures (Pasquare et al., 1988), or along the Akşehir normal fault. Those structures result from transtensional and transpressional kinematics related to the regional N-S compression (Toprak, 1998; Figure 2.1). The central Anatolian volcanic edifices form NW- to NE-trending elongate stratovolcanoes (e.g., Hasandağ, Melendiz, Erciyes, Tekkedağ and Develidağ), ENE-trending linear clusters of monogenetic, bimodal vents and volcanoes (e.g., Acigöl, Karaman and Karapınar), volcanic ridges and widespread ignimbrite provinces (e.g., Cappadocia and İncesu; Pasquare et al., 1988; Toprak and Göncüoğlu, 1993; Aydar et al., 1995).

Late Cenozoic magmatism of eastern Anatolia consists of the westerly Yamadağ, Elazığ

and Kepez volcanic complexes, Cevizlidere intrusive stock, Erzurum-Kars volcanic plateau overlain by a NE-oriented trend of stratovolcanoes (e.g., Nemrut, Süphan, Etrüsk, Tendürek and Ararat), and easterly Ağrı and Sarıçimen magmatic complexes. Those magmatic complexes were emplaced on the Paleozoic to Mesozoic imbricated sedimentary and ophiolitic nappes of the Taurus platform, and the Paleozoic metamorphic basement, Mesozoic ophiolites, and Cretaceous to Oligocene flysch of the Eastern Anatolian Accretionary Complex (Robertson et al., 2007; Şengör et al., 2008; Yılmaz et al., 2010; Topuz et al., 2017).

Other late Cenozoic volcanic provinces formed in central and eastern Turkey such as the post-subduction Galatian (Varol et al., 2014, and references therein) and the collisional foreland Karacadağ volcanic provinces (Ekici et al., 2014, and references therein) in the central Rhodope-Pontide Block and on the Arabian platform, respectively (Figure 2.1). Post-subduction Quaternary volcanism also occurred within pull-apart basins (e.g., Niksar and Erzincan) along the North Anatolian fault zone, mainly in the Rhodope-Pontide Block (Tatar et al., 2007; Karsli et al., 2008).

2.4 Methodology

2.4.1 Age data compilation

This study primarily relies on the compilation and interpretation of 428 isotopic dates from late Cenozoic igneous rocks in central and eastern Anatolia. Most dates were obtained by K-Ar and $^{40}Ar/^{39}Ar$ dating techniques on igneous biotite, hornblende, feldspar, groundmass, and whole-rock material from volcanic rock samples. Those dates can be interpreted as crystallization ages, but are susceptible to alteration and partial to whole resetting, which may conspire to yield dates that may be too young. Ages for undated magmatic rock units were estimated from the 1:500,000-scale geological map of Turkey (MTA, 2002). Rock unit age information on the MTA geological maps was updated from the compiled age data in this study, but many uncertainties remain, especially in eastern Turkey. The time ranges of the 27 late Cenozoic magmatic complexes and the Galatian volcanic province defined in this study

from the age data compilation (Table A.1) are in the appendix A.

2.4.2 Sample selection

In order to complete the existing age database, nine rock samples were collected with a focus on the oldest and less-constrained late Cenozoic igneous complexes in central and eastern Anatolia (Figure 2.1). Those complexes include the early to middle Miocene Yamadağ complex (FR-14-82), and the undated Ağrı plutons (FR-14-124, FR-14-129 and FR-14-142) in the east that were previously inferred to be Late Cretaceous (MTA, 2002) or early Miocene in age (Topuz et al., 2017), or coeval with the middle Miocene Sarıçimen pluton, which was the oldest igneous unit dated in the Eastern Anatolian Accretionary Complex before this study (Çolakoğlu and Arehart, 2010). In central Anatolia, the undated Tekkedağ (FR-15-40) and Develidağ volcanoes (FR-13-254), inferred to be late Miocene in age (MTA, 2002), and the poorly constrained late Miocene to Pliocene Melendiz stratovolcano (FR-15-36) were dated in this study. In contrast, the timing of the Hasandağ, Erciyes and Cappadocia-İncesu volcanic units in central Anatolia was well constrained by previous studies (e.g., Notsu et al., 1995; Platzman et al., 1998; Aydar et al., 2012; Dogan, 2016; Reid et al., 2017). The oldest lavas in the Konya volcanic complex were also dated herein (FR-13-181 and FR-14-73) because of the limited published geochronological data (Keller et al., 1977; Platzman et al., 1998).

2.4.3 LA-ICP-MS U-Pb dating analytical technique

Those nine U-Pb zircon dates were obtained by laser ablation-inductively coupled plasma-mass spectrometry (LA-ICP-MS) method at the Pacific Center for Isotopic and Geochemical Research (PCIGR), The University of British Columbia, Canada. Results are presented in Table 2.1; the Th-U-Pb isotopic analyses and quality control results are in the Appendix A (Figures A.1 and A.2; Table A.2). Zircon grains from igneous rocks were extracted from 1- to 3-kg samples following the conventional mineral separation procedures, namely crushing, grinding Wilfley table, heavy-liquid separation (diiodomethane; $\rho > 3.32$ g/cm3), and hand magnet and Frantz magnetic separation. Non-magnetic, euhedral and inclusion-free

grains were handpicked, and a representative set of 20 to 40 grains per sample was mounted in thermal-setting epoxy pucks together with several grains of Plešovice (337.13 ± 0.37 Ma; Sláma et al., 2008) and Temora2 (416.78 ± 0.33 Ma; Black et al., 2004). These zircons were ground and polished to reveal internal surfaces. After carbon coating, the zircon grains were imaged at the University of British Columbia Electron Microbeam and X-Ray Diffraction facility using the Philips XL-30 scanning electron microscope (SEM) in the cathode-luminescence mode under the under the operating conditions of 15.0 kV of accelerating potential and 15-20 nA beam current. The zircon grains were subsequently rinsed by 5 vol% HNO_3 solution.

U-Pb dating on zircons was conducted using the New Wave UP-213 laser ablation system and a Thermo Finnigan Element2 single collector, double-focusing, magnetic sector ICP-MS with a 25 μm laser beam and 42 % laser energy; employing line scans instead of spot analyses to minimize within-run elemental fractionation. ^{238}U and ^{232}Th data were acquired in analog mode, whereas ^{208}Pb, ^{207}Pb, ^{206}Pb, ^{204}Pb, and ^{202}Hg were acquired using ion-counting mode1. Analyses of zircon reference material (Plešovice and Temora2) systematically bracketed every five zircon unknowns (Figures A.1 and A.2). Data reduction was carried out using IOLITE software (Hellstrom et al., 2008) and carefully avoided portions of signal reflecting Pb loss, older inherited cores and/or altered zones in the zircon analyzed. Concordia diagrams were generated by the ISOPLOT version 4.15 software (Ludwig, 2012). Published ages are based on a weighted average of overlapping, concordant $^{206}Pb/^{238}U$ ages of individual analyses for each sample as $^{206}Pb/^{238}U$ age is the most precisely determined age for relatively young (Phanerozoic) zircons yielding the best estimate for the crystallization age of the samples (Tafti et al., 2009). Reported ages include both internal and propagated errors.

2.5 Results

2.5.1 U-Pb zircon dating

The Konya volcanic complex, 200 km west of Hasandağ (Figure 2.1), is spatially isolated and composed of porphyritic andesitic lavas and domes yield data that indicate

formation at 8.67 ± 0.13 (FR-13-181) and 10.21 ± 0.13 Ma (FR-14-73) based on 16 concordant zircon analyses each (Table 2.1; Figure 2.2). Those samples are older than the previously-dated rocks (6.9 ± 0.3 Ma by K-Ar) from the Konya volcanic complex by Platzman et al. (1998). Nonetheless, the Konya volcanic rocks are younger than the more northerly Galatia (23-17 Ma) and Sulutas (16-11.5 Ma) volcanic units. The Melendiz volcanic edifice is represented by a clinopyroxene-bearing andesite (FR-15-36) that yields an age of 3.62 ± 0.06 Ma (Table 2.1; Figure 2.2), determined from the analysis of 20 zircon grains and is within the range of previous K-Ar dates from 4.43 ± 0.16 to 2.40 ± 0.15 Ma (Platzman et al., 1998). The Develidağ volcanic complex pre-dates the Melendiz complex according to concordant data obtained from 14 zircon grains from a two-pyroxene-bearing andesitic flow (FR-13-254) that yields a $^{206}Pb/^{238}U$ weighted mean age of 5.34 ± 0.21 Ma (Table 2.1; Figure 2.2). The porphyritic clinopyroxene-bearing andesite (FR-14-40) from the Tekkedağ volcano yields a crystallization age of 7.92 ± 0.14 Ma based on 19 concordant zircon analyses (Table 2.1; Figure 2.2). Many zircon grains from this sample contain inherited cores; four zircon xenocrysts yield $^{206}Pb/^{238}U$ ages of 80.3 ± 2.2, 81.7 ± 5.6, 351 ± 13 (discordant) and 2502 ± 50 Ma (discordant), consistent with the crystalline basement age (Whitney et al., 2007; Toksoy-Köksal et al., 2009; Paquette and Le Pennec, 2012).

Table 2.1 U-Pb geochronological results from central and eastern Anatolia.

Sample number	Locality	Lat (°N)	Long (°E)	Igneous complex	Lithology	Age[a] (Ma)	Error (2σ)	MSWD[b]	n[c]
Central Anatolia									
FR-13-181	İnlice	37.751	32.075	Konya volcanic complex	Biotite andesite	8.67	0.13	1.7	16
FR-14-73	Doğanbey	37.823	31.946	Konya volcanic complex	Two-pyroxene andesite	10.21	0.13	0.62	16
FR-15-36	Boz Tepe	38.221	27.063	Melendiz volcanic complex	Clinopyroxene andesite	3.62	0.06	1.2	20
FR-15-40	Başdere	38.590	28.576	Tekkedağ volcanic complex	Clinopyroxene andesite	7.92	0.14	0.9	19
FR-13-254	Öksüt	38.289	35.512	Develidağ volcanic complex	Two-pyroxene andesite	5.36	0.20	0.88	16
Eastern Anatolia									
FR-14-82	Hasançelebi	39.008	37.823	Yamadağ volcanic complex	Clinopyroxene andesite	21.23	0.33	0.63	22
FR-14-129	Taşlıçay	39.599	43.264	Ağrı magmatic complex	Monzonite	21.32	0.29	1.6	15
FR-14-142	Taşkapı	39.280	43.469	Ağrı magmatic complex	Monzonite	17.38	0.36	0.49	15
FR-14-124	Diyadin	39.569	43.435	Ağrı magmatic complex	Granite	19.84	0.19	0.98	19

[a] $^{206}Pb/^{238}U$ weighted mean ages

[b] Mean square of weighted deviates

[c] Excluding discordant and outlier analyses, and xenocrystic zircons.

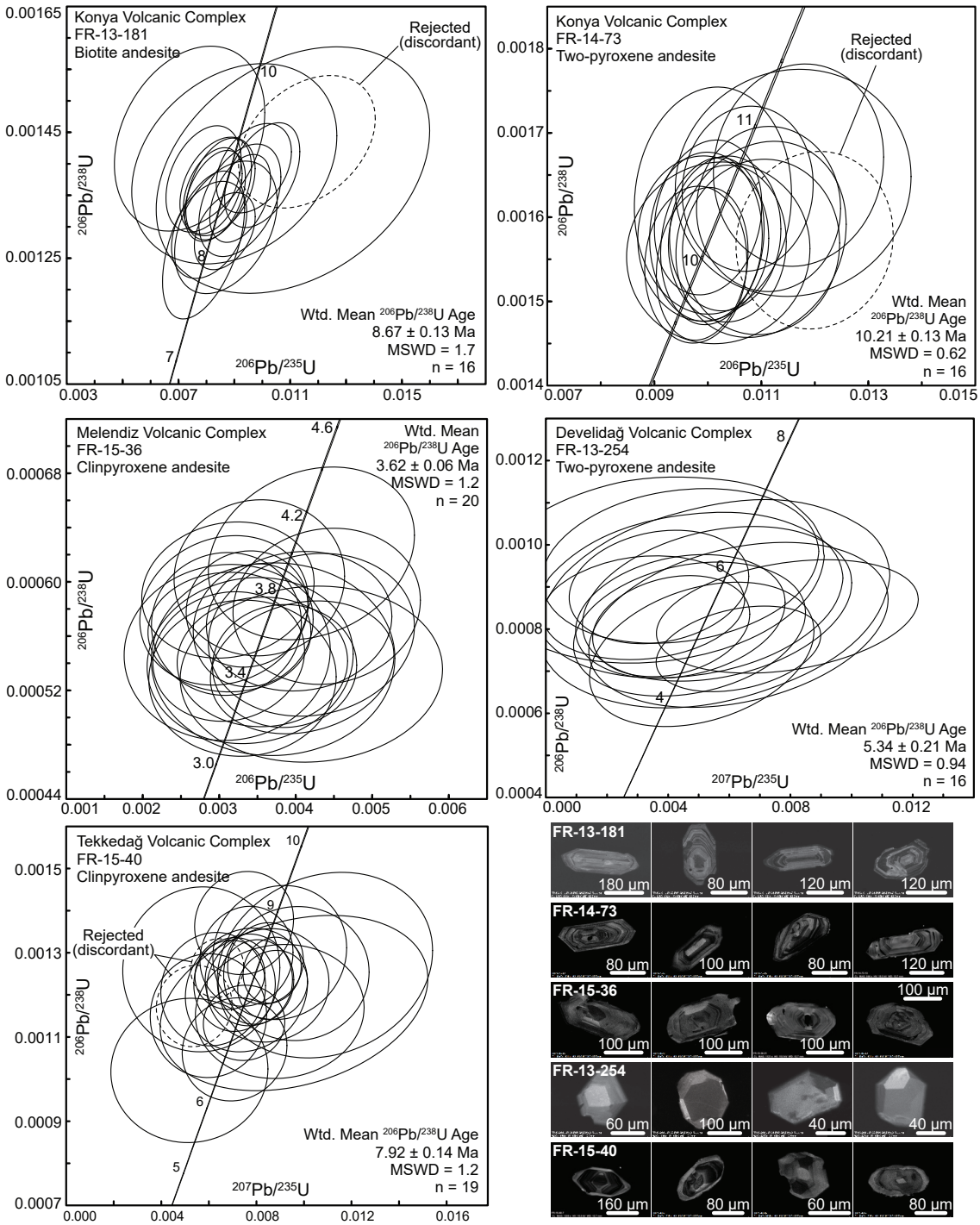

Figure 2.2 Concordia diagrams of selected late Cenozoic volcanic rocks from Konya (FR-13-181 and FR-14-73), Melendiz (FR-15-36), Develidağ (FR-13-254) and Tekkedağ volcanic complexes (FR-15-40). Dashed black ellipses are discordant data not included in weighted mean $^{206}Pb/^{238}U$ age calculation. MSWD: mean square of weighted deviates. The cathodoluminescence images for each sample display the internal structure of representative igneous zircon grains.

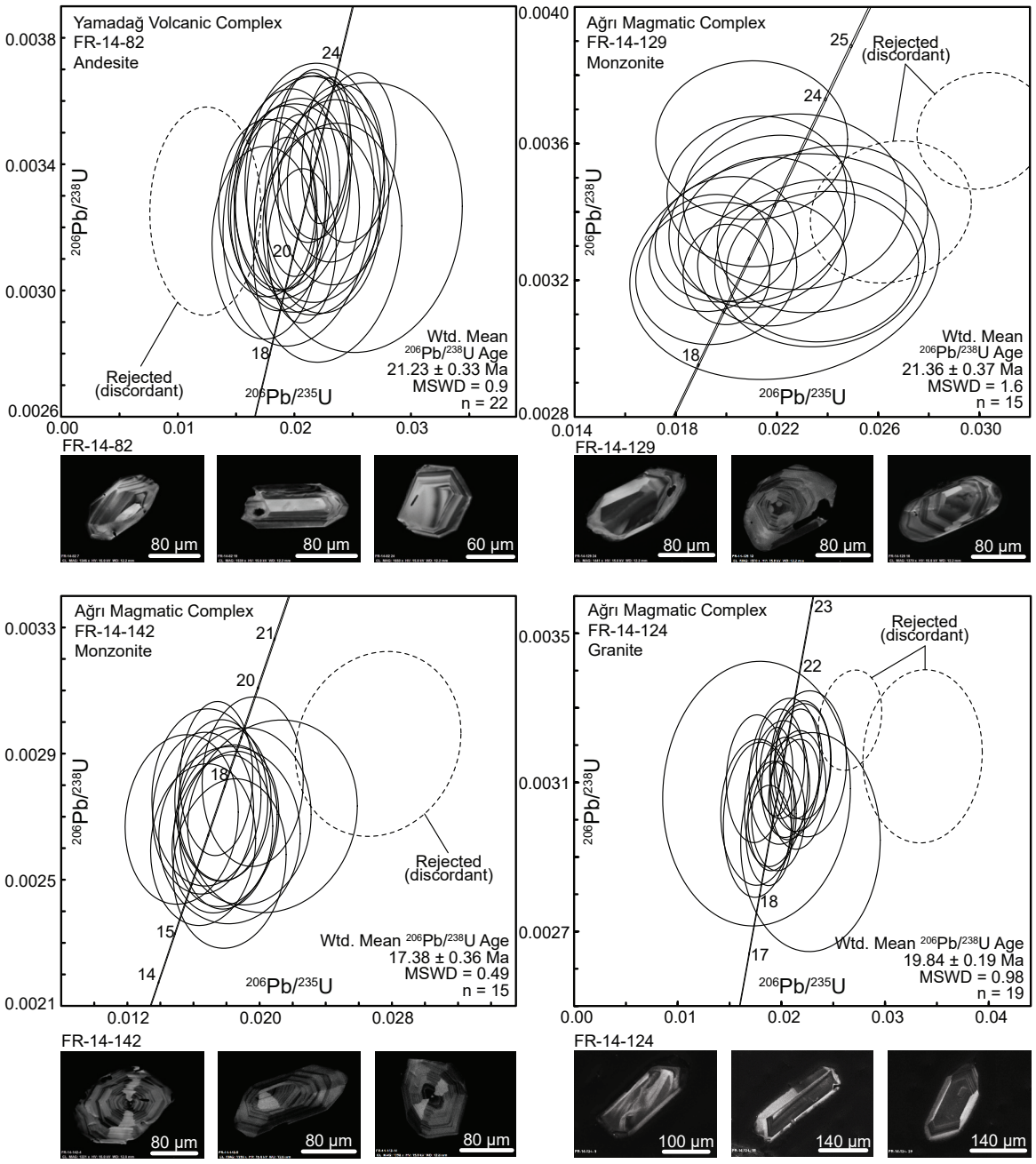

Figure 2.3 Concordia diagrams of selected late Cenozoic magmatic rocks from Yamadağ (FR-14-82), and Ağrı magmatic complexes (FR-14-129, FR-14-142 and FR-14-124). Dashed black ellipses are discordant data not included in weighted mean $^{206}Pb/^{238}U$ age calculation. MSWD: mean square of weighted deviates. The images under optical microscope (left) and cathodoluminescence (right) for each sample display the internal structure of representative igneous zircon grains.

In eastern Anatolia, the Yamadağ volcanic complex is composed of porphyritic clinopyroxene-bearing andesite (FR-14-82) where zircon grains crystallized at 21.23 ± 0.33 Ma (Table 2.1; Figure 2.3). This age is older than published K-Ar and $^{40}Ar/^{39}Ar$ age data from Yamadağ (18.7 ± 0.5 to 8.90 ± 0.70 Ma; Leo et al., 1974; Kürüm et al., 2008; Ekici et al., 2009). Monzonitic to granitic rocks (FR-14-129, FR-14-124 and FR-14-142) from the Ağrı magmatic complex give dates of 21.32 ± 0.29, 19.84 ± 0.19 and 17.38 ± 0.36 Ma, respectively (Table 2.1; Figure 2.3). Those three ages are notably older than K-Ar cooling age data from the Sarıçimen monzonitic pluton (12.6 ± 0.3 to 11.9 ± 0.4 Ma; Çolakoğlu and Arehart, 2010), 50 km southeast of sample FR-14-142. Samples FR-14-129 and FR-14-124 contained zircon xenocrysts that yielded ancient $^{206}Pb/^{238}U$ dates of 428.3 ± 28 and 328.4 ± 11 Ma (concordant analyses), respectively, consistent with protolith age of the Paleozoic crystalline basement in eastern Anatolia (Topuz et al., 2017).

2.5.2 Timing of late Cenozoic magmatism

Magmatic activity was initiated in the late Oligocene in central and eastern Anatolia at the onset of the Arabian continental collision (Figure 2.4). The E-trending alignment of late Cenozoic magmatic complexes formed the Eastern Anatolian Magmatic Belt (Figure 2.5). The earliest magmatic phase of this Belt consisted of the rare exposures of late Oligocene igneous rocks such as at Cevizlidere (26-25 Ma; İmer et al., 2014). This brief magmatic event was followed by a 4 million-year (m.y.) magmatic hiatus from 25 to 21 Ma (Figure 2.4). Magmatism continued into the early Miocene (21-17 Ma) with the formation of the localized Yamadağ (21-9 Ma) and Ağrı magmatic complexes (21-17 Ma), thereby extending the east-trending Eastern Anatolia Magmatic Belt westward (Figure 2.5). This period is also marked by the formation of the Galatian magmatic province (23-17 Ma) in the region of Ankara.

The magmatic activity increased in the middle Miocene (16-11.6 Ma), notably in the Aladağ (15-13 Ma), Kepez (16-13 Ma), and Yamadağ volcanic complexes, and the Sarıçimen pluton (13-11.5 Ma; Çolakoğlu and Arehart, 2010). Magmatism continued to evolve westerly to the Ecemiş fault in central Anatolia, and broadened the Eastern Anatolia Magmatic Belt

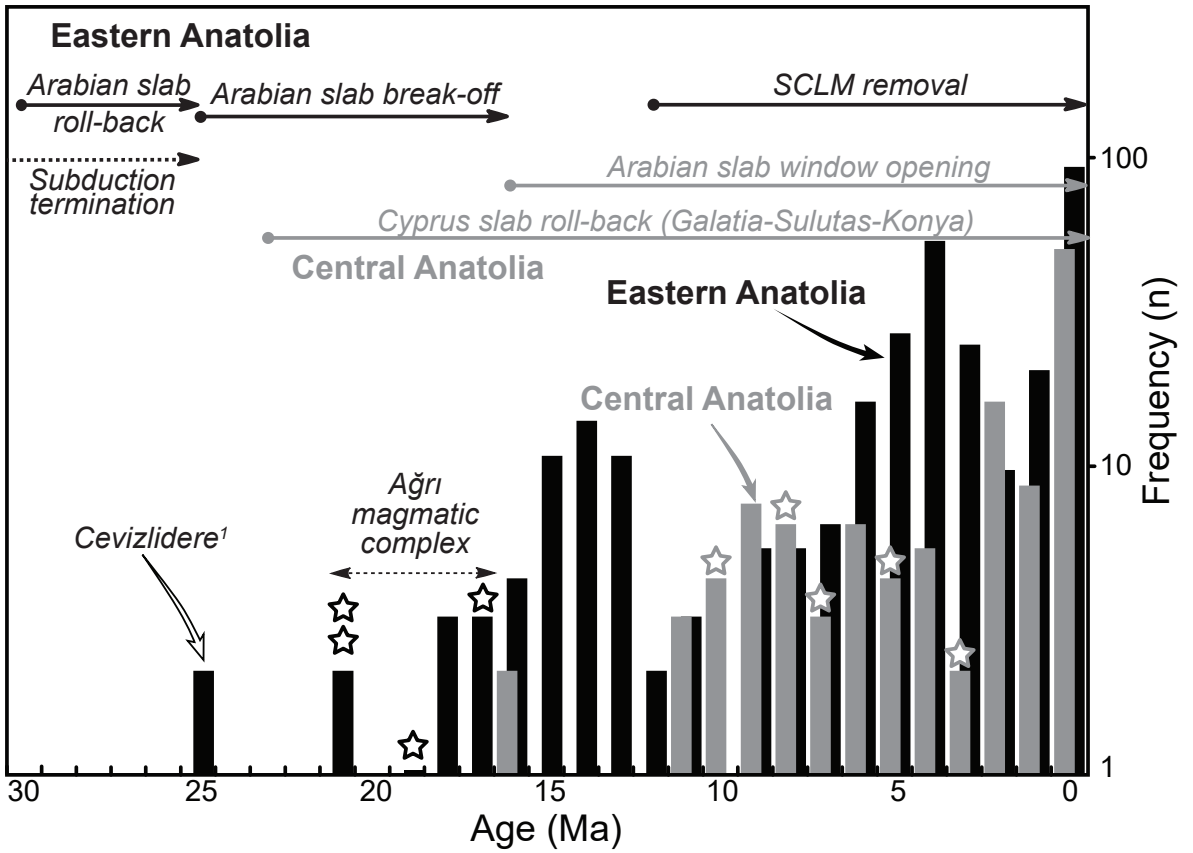

Figure 2.4 Age histogram of late Cenozoic magmatism in central (grey) and eastern Anatolia (black) counting the number (n) of available age data for each 1 m.y. bin since 30 Ma. The horizontal segments represent the succession of tectonic events that occurred a few million years prior to the crustal emplacement of dated magmatic units. The Ağrı magmatism is continuous from 21 to 17 Ma. Age data from the Galatian magmatism (22-17 Ma) are not on this histogram as out of Anatolia. Stars are the new U-Pb data reported in this Chapter 2 (refer to Table 2.1). Reference: [1]İmer et al. (2014); references of compiled data are in Table A.1.

in eastern Anatolia (Figure 2.5). This Belt reached central Anatolia at ca. 15 Ma as recorded in the formation of the Sivas volcanic suite (15-1 Ma). In central Anatolia, middle Miocene magmatism migrated southwards from Galatia (23-17 Ma) to Sulutas (17-11.5 Ma), northwest of Konya.

Magmatic activity produced its highest volume in the late Miocene (11.6-5.3 Ma), dominantly in eastern Anatolia where it formed the first stage of the triangular-shaped Erzurum-Kars volcanic plateau (ca. 13-11 Ma-Present) on the Rhodope-Pontide Block, South Armenian Block and ATB (Figure 2.6). The westward extension of the Eastern Anatolia Magmatic Belt reached central Anatolia in the late Miocene and overlies the tectonic boundaries. In the late

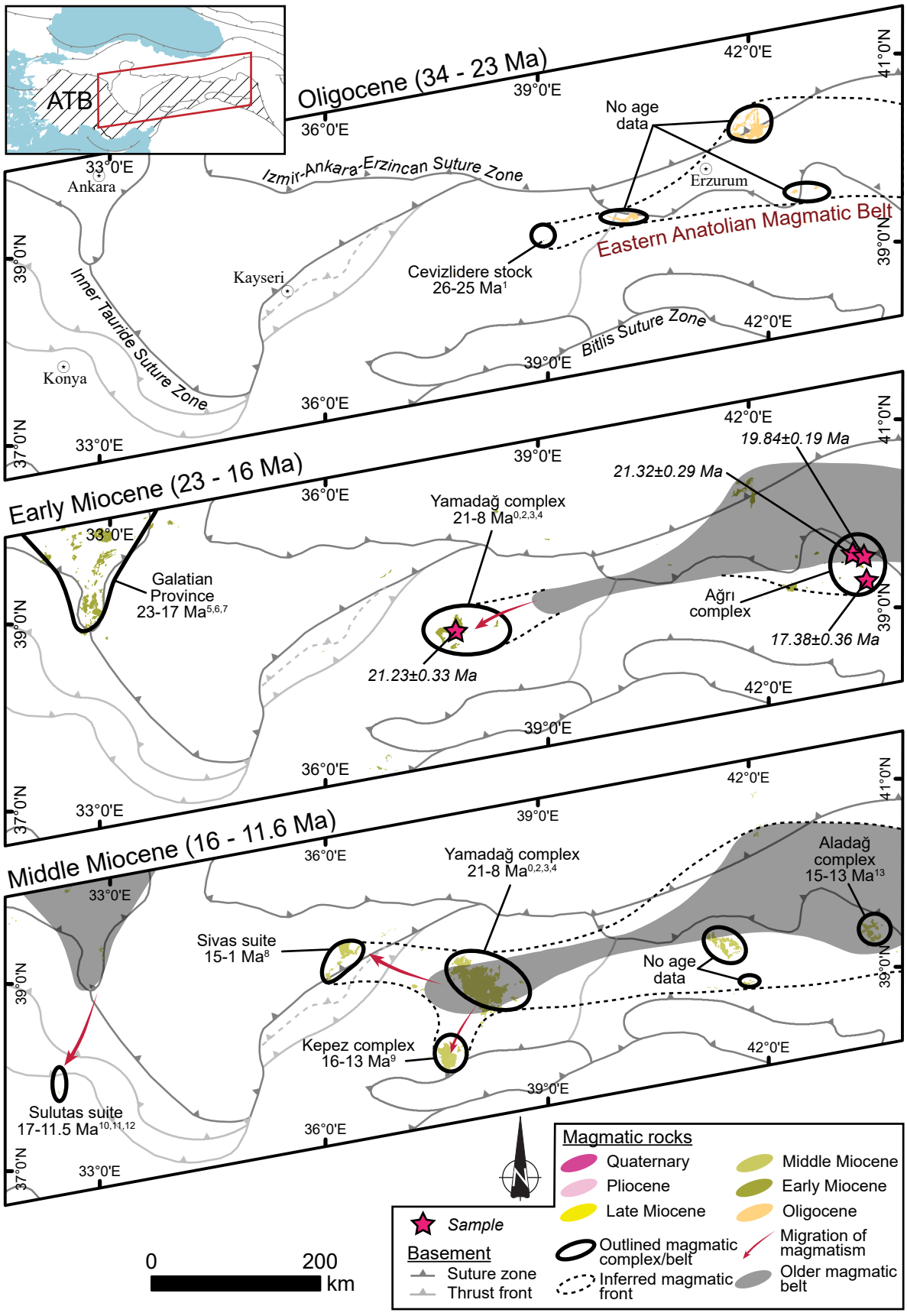
ATB
Oligocene (34 - 23 Ma)
Izmir-Ankara-Erzincan Suture Zone
Ankara
Erzurum
No age data
Eastern Anatolian Magmatic Belt
Cevizlidere stock
26-25 Ma[1]
Kayseri
Inner Tauride Suture Zone
Konya
Bitlis Suture Zone
Early Miocene (23 - 16 Ma)
Yamadağ complex
21-8 Ma[0,2,3,4]
19.84±0.19 Ma
21.32±0.29 Ma
Galatian Province
23-17 Ma[5,6,7]
Ağrı complex
17.38±0.36 Ma
21.23±0.33 Ma
Middle Miocene (16 - 11.6 Ma)
Aladağ complex
15-13 Ma[13]
Sivas suite
15-1 Ma[8]
Kepez complex
16-13 Ma[9]
Sulutas suite
17-11.5 Ma[10,11,12]
0
200
km
Magmatic rocks
Quaternary
Pliocene
Late Miocene
Middle Miocene
Early Miocene
Oligocene
Sample
Basement
Suture zone
Thrust front
Outlined magmatic complex/belt
Inferred magmatic front
Migration of magmatism
Older magmatic belt

Figure 2.5 Time-sliced tectono-magmatic maps of central and eastern Anatolia (1:4,000,000 scale; Lambert Conic projection; European Datum 1950) showing the westward migration of magmatism in the Oligocene, early Miocene and middle Miocene. The black lines outline the magmatic complexes whereas the dashed lines and grey areas are the interpreted connections between contiguous magmatic complexes, and the older magmatic belts, respectively. ATB = Anatolide-Tauride Block. References: [0]this Chapter; [1]İmer et al. (2014); [2]Leo et al. (1974); [3]Kürüm et al. (2008); [4]Ekici et al. (2009); [5]Varol et al. (2014); [6]Wilson et al. (1997); [7]Kurt et al. (2008); [8]Platzman et al. (1998); [9]Ekici (2016); [10]Asan and Ertürk (2013); [11]Koç et al. (2012); [12]Korkmaz et al. (2017); [13]Lebedev et al. (2010).

Miocene, central Anatolian magmatism consisted of the Cappadocia and İncesu ignimbrites (ca. 11 Ma-Present), the Tekkedağ volcanic center (8-7 Ma) and the Develidağ stratovolcano (6-5 Ma). This period was also characterized by the formation of the Konya volcanic complex (10-6 Ma), southeast of Sulutas, in the western part of central Anatolia.

Although Konya volcanism stopped in the late Miocene, the construction of volcanic edifices in central Anatolia continued in the Pliocene and Quaternary dominated by the emergence of the Acigöl volcano (1 Ma-Present), and Melendiz (5-2 Ma), Erciyes (4 Ma-Present) and Hasandağ stratovolcanoes (2 Ma-Present; Figure 2.6). Those stratovolcanoes were accompanied by the formation of numerous monogenetic vents such as the Karaman (3 Ma-Present) and Karapınar (5 Ma-Present) volcanoes at the southwesternmost Eastern Anatolia Magmatic Belt in central Anatolia.

In eastern Anatolia, the Erzincan-Kars volcanic plateau built up and experienced a southward shrinking of the active magmatic domain along the NE-oriented Nemrut-Ararat axis. This volcanic trend includes the Nemrut (2 Ma-Present), Süphan (6 Ma-Present), Etrüsk (5-3 Ma), Tendürek (1 Ma-Present) and Ararat stratovolcanoes (2 Ma-Present). Volcanism was also emplaced along the North Anatolian fault zone in the Quaternary (1 Ma-Present), north of the Eastern Anatolia Magmatic Belt.

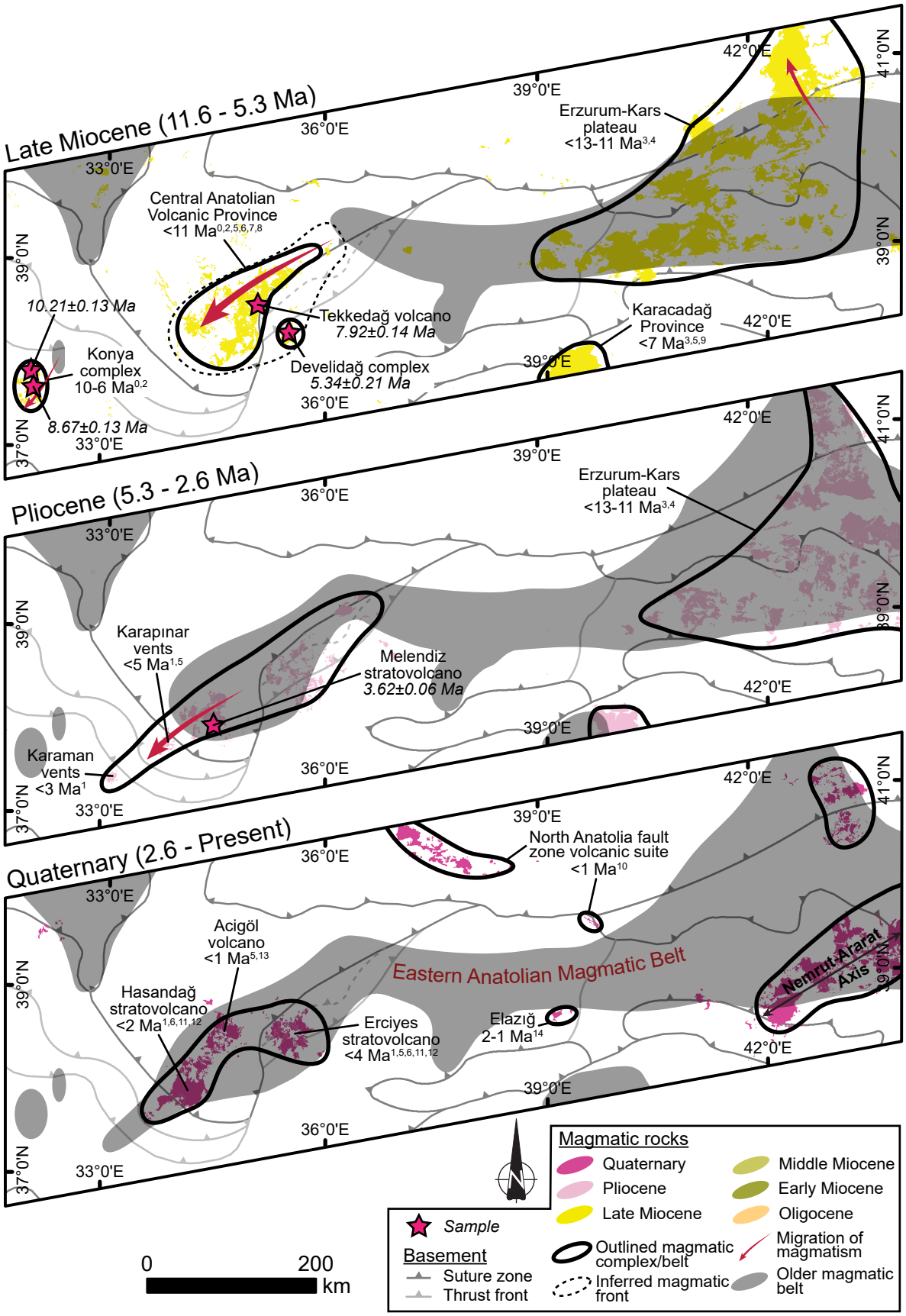
Late Miocene (11.6 - 5.3 Ma)
Pliocene (5.3 - 2.6 Ma)
Quaternary (2.6 - Present)
Erzurum-Kars plateau <13-11 Ma3,4
Central Anatolian Volcanic Province <11 Ma0,2,5,6,7,8
10.21±0.13 Ma
Konya complex 10-6 Ma0,2
8.67±0.13 Ma
Tekkedağ volcano 7.92±0.14 Ma
Develidağ complex 5.34±0.21 Ma
Karacadağ Province <7 Ma3,5,9
Karapınar vents <5 Ma1,5
Melendiz stratovolcano 3.62±0.06 Ma
Karaman vents <3 Ma1
North Anatolia fault zone volcanic suite <1 Ma10
Acigöl volcano <1 Ma5,13
Hasandağ stratovolcano <2 Ma1,6,11,12
Erciyes stratovolcano <4 Ma1,5,6,11,12
Elazığ 2-1 Ma14
Eastern Anatolian Magmatic Belt
Nemrut-Ararat Axis
33°0'E
36°0'E
39°0'E
42°0'E
37°0'N
39°0'N
41°0'N
0
200
km
Magmatic rocks
Quaternary
Pliocene
Late Miocene
Middle Miocene
Early Miocene
Oligocene
Sample
Basement
Suture zone
Thrust front
Outlined magmatic complex/belt
Inferred magmatic front
Migration of magmatism
Older magmatic belt

Figure 2.6 Time-sliced tectono-magmatic maps of central and eastern Anatolia (1:4,000,000 scale; Lambert Conic projection; European Datum 1950) showing the westward migration of magmatism in the late Miocene, Pliocene and Quaternary. The black lines outline the magmatic complexes whereas the dashed lines and grey areas are the interpreted connections between contiguous magmatic complexes, and the older magmatic belts, respectively. References: [0]this Chapter; [1]Leo et al. (1974); [2]Platzman et al. (1998); [3]Pearce et al. (1990); [4]Keskin et al. (1998); [5]Notsu et al. (1995); [6]Dogan (2016); [7]Aydar et al. (2012); [8]Lepetit et al. (2014); [9]Lustrino et al. (2010); [10]Tatar et al. (2007); [11]Aydin et al. (2014); [12]Kuzucuoglu et al. (1998); [13]Schmitt et al. (2011);[14]Arger et al. (2000).

2.6 Discussion

2.6.1 Initiation and propagation of the lithospheric slab break-off

Late Cenozoic magmatism initiated first in eastern Anatolia at the beginning of the Arabian collision in the late Oligocene, and subsequently migrated westwards to form the narrow E- to NE-trending Eastern Anatolia Magmatic Belt that links magmatic complexes in both eastern and central Anatolia (Figure 2.7). This westward migration of magmatism through time was accompanied by localized NW-SE extension (Kaymakçı et al., 2010) and the propagation of crustal uplift that started at ca. 23-20 and 15-10 Ma in eastern and central Anatolia, respectively (Okay et al., 2010; Cosentino et al., 2012; Schildgen et al., 2012; Schildgen et al., 2014; Karaoğlan, 2016; Karaoğlan et al., 2016; McNab et al., 2017). Both magmatic migration and crustal uplift propagation reflect the slab rupture trend that is imaged by seismic tomography (Piromallo and Morelli, 2003; Zor et al., 2003; Hafkenscheid et al., 2006; Lei and Zhao, 2007; Biryol et al., 2011; Bakırcı et al., 2012) and modeled by analogue and numerical studies (Faccenna et al., 2006; Menant et al., 2016). This suggests that there is a genetic and spatial relationship between slab break-off propagation, slab break-off-induced asthenospheric upwelling, crustal uplift and deformation, and late Cenozoic magmatism in central and eastern Anatolia.

The northward mantle flow in the Middle East was driven by the Afar plume in eastern Africa and played a crucial role in the Eastern Mediterranean geodynamics (Faccenna et al., 2013). This plume may have generated a mantle convection cell that entrained the Arabia plate northward, facilitated the slab break-off in eastern Anatolia and thereby accelerated

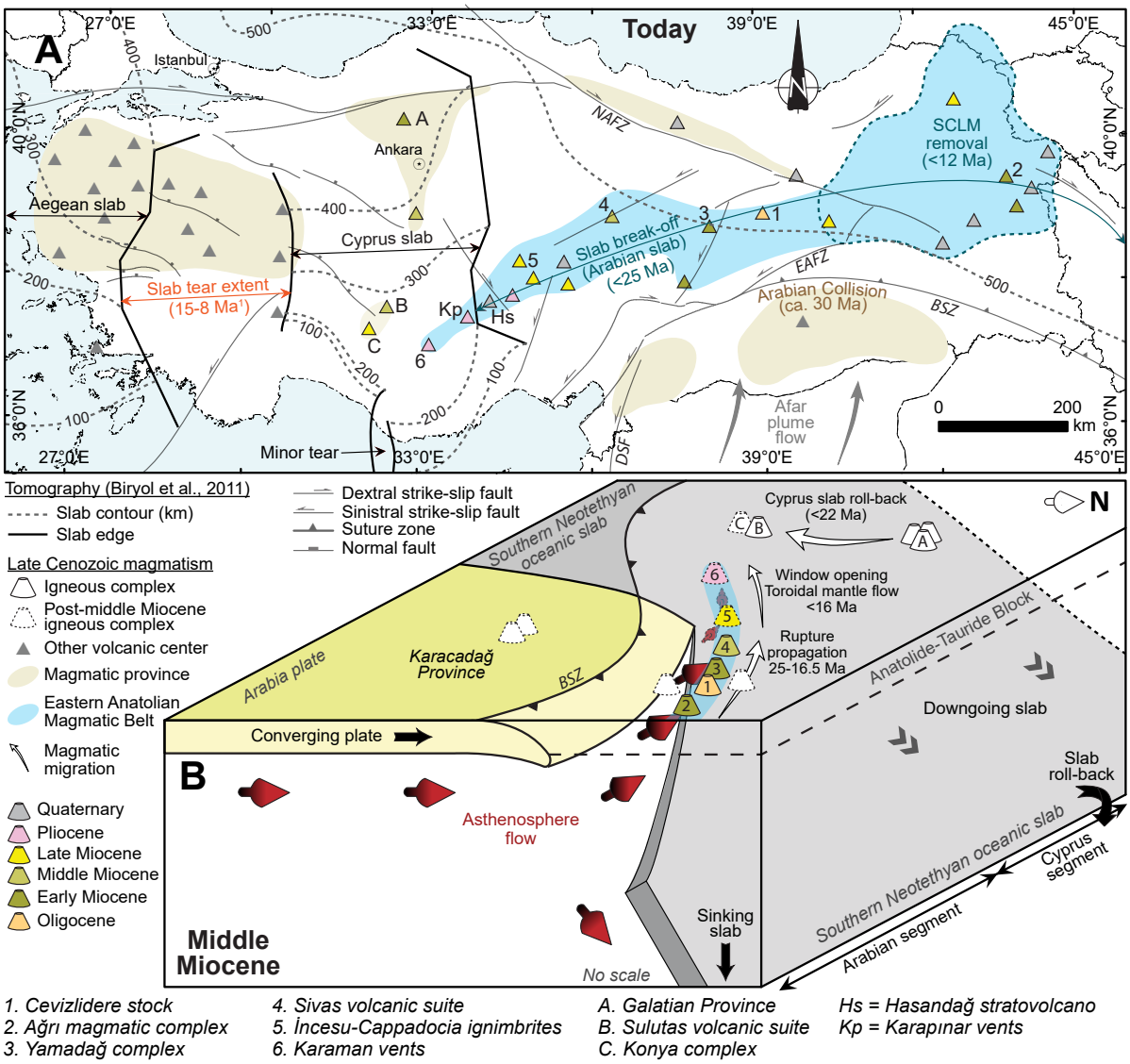

1. Cevizlidere stock
2. Ağrı magmatic complex
3. Yamadağ complex
4. Sivas volcanic suite
5. İncesu-Cappadocia ignimbrites
6. Karaman vents
A. Galatian Province
B. Sulutas volcanic suite
C. Konya complex
Hs = Hasandağ stratovolcano
Kp = Karapınar vents

Figure 2.7 A. Schematic map of Turkey (1:6,000,000 scale; Lambert Conic Projection, European Datum 1950) displaying the distribution of major late Cenozoic magmatic domains, including the Eastern Anatolian Magmatic Belt (in blue), the area affected by the late Miocene partial removal of the subcontinental lithospheric mantle (SCLM; blue dashed area in eastern Anatolia), and regional faults (NAFZ = North Anatolian Fault Zone; EAFZ = Eastern Anatolian Fault Zone; BSZ = Bitlis Suture Zone; DSF = Dead Sea Fault). The vertical projection of slab margins and contours (in km) from tomography (Biryol et al., 2011) shows the spatial relationship between slab tear/break-off and surface magmatism. References: [1]Jolivet et al. (2015). B. Schematic 3D block (adapted from Wortel and Spakman (2000) and Ferrari (2004)) illustrating the westward migration of magmatism and sub-horizontal slab rupture propagation along the Arabian segment of the Southern Neotethyan slab during the Arabia-ATB collision in the middle Miocene. On this cartoon, the Bitlis-Pütürge Massifs, Central Anatolian Crystalline Complex, ATB and South Armenian Block are part of the same rigid overriding slab that undergoes the Arabian.

the retreat of the Hellenic trench in the Aegean domain and the westward extrusion of the Anatolian microplate along the North Anatolian fault zone (Faccenna et al., 2013). The drop in convergence rate at the beginning of the Arabian collision in the Oligocene (Bertrand et al., 2014; Menant et al., 2016) accelerated the roll-back of the Southern Neotethyan slab beneath Anatolia; the resulting suction of the asthenosphere into the mantle wedge and subsequent upward flux of hydrous mantle wedge (Freeburn et al., 2017) produced melts that generated the first peak of magmatism in the late Oligocene in eastern Anatolia (Figure 2.4). This brief magmatic event (1 m.y.) was followed by a 4 m.y. magmatic hiatus during which time slab heating, weakening, and rupture initiated. Tomographic models and kinematic reconstructions support slab break-off initiation at 30 Ma or older in northeast Zagros in Iran (Hafkenscheid et al., 2006; Mouthereau et al., 2012), certainly at the maximum contortion of the Southern Neotethyan oceanic slab. Slab rupture subsequently propagated westwards to eastern Anatolia and perhaps southeastwards along the Sanandaj-Sirjan zone (Hafkenscheid et al., 2006) where it also produced magmatism (Ghasemi and Talbot, 2006; Omrani et al., 2008). The first break-off-derived magmas in eastern Anatolia were likely emplaced into the crust in the early Miocene at Ağrı and Yamadağ (ca. 21 Ma), and igneous activity then migrated westwards to form the narrow E- to NE-trending Eastern Anatolia Magmatic Belt.

This Belt has an average width of ca. 150 km and a maximum width of 250 km in the middle Miocene (Figure 2.5), similar to slab break-off magmatic belts in northern Maghreb (< 200 km; Maury et al., 2000), central Mexico (ca. 150 km; Ferrari, 2004) and the Eocene magmatic belt related to the break-off of the northern Neotethyan oceanic slab along the İzmir-Ankara-Erzincan suture zone (ca. 100-150 km; Altunkaynak, 2007; Keskin et al., 2008; Sosson et al., 2010). Break-off likely occurred at ca. 300 km north of the Bitlis suture zone, now ca. 200 km, because of the continental collision and resulting crustal shortening (Şengör et al., 2008). By analogy, the Eastern Anatolian Magmatic Belt is currently located 150 to 200 km north of the Bitlis suture zone, thus likely formed at ca. 300 km in the early to middle Miocene.

The timing of the early Miocene magmatic event provides a minimum age on slab

rupture initiation in Anatolia because of the time delay of a few million years required between slab rupture, asthenospheric upwelling, melting, and magma ascent and emplacement in the crust (McKenzie, 1972; Paterson and Tobisch, 1992; Ferrari, 2004; Cesare et al., 2009). Thus, slab rupture initiation in eastern Anatolia occurred between ca. 30 (collision onset) and 21 Ma, approximated at ca. 25 Ma. This contrasts with previous models that proposed the onset of slab break-off at ca. 13-10 Ma, mainly based on previous geochronological studies of middle Miocene to Present volcanic cover in eastern Anatolia (Keskin, 2003; Şengör et al., 2008; van Hunen and Allen, 2011; Cosentino et al., 2012; Schildgen et al., 2014). In addition, recent seismic tomographic studies show that the upper edge of the detached slab is imaged at a depth of ca. 660 km below eastern Anatolia whereas the rest of the Southern Neotethyan slab continues beyond the mantle discontinuity into the lower mantle (e.g., Hafkenscheid et al., 2006; Biryol et al., 2011). This suggests sinking times between 13 and 28 m.y. considering free sinking rates of 2-4 cm/year in the upper mantle and break-off depth between 100 and 150 km (Zor, 2008; Schildgen et al., 2014; Menant et al., 2016). Hence, the slab break-off must have occurred well before 13 Ma in eastern Anatolia.

A slab rupture at relatively great depth (i.e., > 100 km deep) is common but would not be expected to generate a large volume of magma (Davies and von Blanckenburg, 1995; Freeburn et al., 2017). However, numerical models showed that previous subduction-related partial melts were already present at the base of the overriding crust during the slab break-off event, and sustained toroidal asthenospheric flow dragged those melts northwards away from the collisional front (Menant et al., 2016). Another evidence for pre-Oligocene, subduction-related melting processes in the region is the presence of Cretaceous- and Eocene-aged intrusions (e.g., Kuşcu et al., 2010). Despite the deep slab rupture, those tectono-magmatic conditions were sufficient to produce some hydrous magma during the slab break-off event which formed small and isolated magmatic complexes as observed in eastern Anatolia (Figure 2.5) and did not prevent asthenospheric flow from reaching shallow depths (< 50 km; Şengör et al., 2003; Delph et al., 2017; Reid et al., 2017).

2.6.2 Spatial extent of the sub-horizontal slab rupture

The geometry and extent of the sub-horizontal slab rupture beneath central Anatolia is matter of debate. Some tomography and crustal uplift studies infer the partial rupture of the Cyprus slab to be the result of the westward slab break-off propagation from eastern Anatolia (Piromallo and Morelli, 2003; Faccenna et al., 2006; Gans et al., 2009; Schildgen et al., 2014). In contrast, numerical modeling with recent tomography (Biryol et al., 2011) demonstrates that the slab rupture propagation, caused by buoyancy variations between the Arabian continental and the Southern Neotethyan oceanic lithospheres, ceased at the northwesternmost edge of the Arabia plate (Menant et al., 2016), and ultimately did not reach the Cyprus slab. The current eastern margin of the Cyprus slab in the mantle is sharp since the Arabian segment is now completely detached, and can be vertically projected along a north-south axis through central Anatolia (Biryol et al., 2011; Figure 2.7a), approximately between the Karapınar vents and Hasandağ stratovolcano (Reid et al., 2017). The discontinuous lithosphere-asthenosphere boundary in this area, and significantly west of the Dead Sea fault, separates the African and Arabian plates (Kind et al., 2015). Although the western part of the Cyprus slab is coherent, the eastern part has a blocky appearance on tomographic images that, in association with the stagnation of subduction and subvertical slab geometry, implies that the slab is tearing (Biryol et al., 2011). Thus, the slab break-off trend extends to the Quaternary Hasandağ stratovolcano, excluding the Pliocene to Quaternary Karapınar and Karaman volcanoes that are apparently located above the Cyprus slab. The validity of this interpretation relies on the approximate projection of the Cyprus slab margin on the surface from tomographic images. Regardless of the exact location of Karaman and Karapınar volcanoes with respect to the underlying slab rupture, the Cyprus slab is too deep (ca. 250 km) to produce magma in this region in the Pliocene-Quaternary (Biryol et al., 2011).

Slab rupture and window opening drastically modified mantle flow such that resulting magmatism may not have been emplaced immediately above the underlying rupture. This could explain the southwestward extension of the Eastern Anatolian Magmatic Belt above the

Cyprus slab. In addition, the SW-trending, slow, upper mantle wave velocities beneath central Anatolia indicate the presence of melts at shallow depth (Delph et al., 2017); the high Bouguer gravity anomalies below eastern Anatolia and narrowing westward to central Anatolia support the presence of buoyant asthenospheric material beneath the Moho (Ates et al., 1999) and mimic the shape of the Eastern Anatolian Magmatic Belt.

Notably, the westernmost evidence of slab break-off-related magma is the Karaman volcano in central Anatolia. The formation of the isolated, middle to late Miocene, Sulutas and Konya volcanic complexes lack spatial relationships with the other coeval central Anatolian volcanic edifices at ca. 200 km east since they are not lined up with the late Miocene to Present, SW-trending axis of Sivas-Cappadocia-Hasandağ-Karaman volcanic complexes (Figure 2.7a). Instead, the age progression from the northerly Galatian province (23-17 Ma) to the Sulutas volcanic suite (17-11.5 Ma) to the southerly Konya volcanic complex (10-6 Ma) suggests a southward migration of the magmatic front resulting from the roll-back of the Cyprus slab, which has not detached (Biryol et al., 2011), since the early (this Chapter) or middle Miocene (Koç et al., 2012; Abgarmi et al., 2017; Figures 2.5 and 2.6). This tectonic event also resulted in the formation of basins in central Taurides, north of Cyprus subduction (e.g., Altınapa basin; Koç et al., 2012). Alternative scenarios involve crustal decoupling, subduction of the Cyprus lithospheric mantle and its subsequent delamination (Bartol and Govers, 2014; Delph et al., 2017) or gravitational instability of the thickened arc root by drip tectonics to account for the today-presence of thin lithospheric mantle and regional > 1 km crustal uplift (Göğüş et al., 2017). However, the arguments against those models include: 1) the presence of melts and volatiles significantly reduce shear wave velocities in the upper mantle which leads to uncertainties about lithosphere thickness (e.g., Kaviani et al., 2007; Foulger et al., 2015); 2) thin SCLM and regional crustal uplift can be explained by small-scale convection in a post-subduction setting (Kaislaniemi et al., 2014); 3) central Anatolian magmatism involves a significant component of subduction-modified lithospheric mantle (Deniel et al., 1998; Şen et al., 2004).

In addition, Quaternary alkaline volcanism emplaced in extensional pull-apart basins

(e.g., Niksar and Erzincan) along the North Anatolian fault zone, north of the Eastern Anatolian Magmatic Belt (Figure 2.6), was also produced in response to asthenospheric upwelling (Tatar et al., 2007; Karsli et al., 2008). Despite the distance (max. 150 km) from the Eastern Anatolian Magmatic Belt, it might be considered that the sub-slab asthenosphere, remotely driven by the Afar plume (Faccenna et al., 2013; McNab et al., 2017), flowed far enough to the north to heat and produce magma that conveyed through and along the lithospheric North Anatolian fault zone that extends to the upper mantle (Fichtner et al., 2013). Lastly, the late Miocene to Quaternary Karacadağ volcanism on the Arabia platform in southeast Turkey is located on the collisional foreland (Ekici et al., 2014 and references therein; Figure 2.1). The mantle source of Karacadağ magmatism has not been affected by the Southern Neotethyan subduction and the fate of the oceanic slab contrary to Anatolian magmatism (e.g., Keskin et al., 2012; Ekici et al., 2014).

2.6.3 Slab break-off-related sub-slab asthenospheric infiltration

Late Cenozoic post-subduction magmatism in central and eastern Anatolia was emplaced during the short period of localized W- to NW-trending extension, manifested as transtensional pull-apart basins along regional strike-slip faults, from the late Oligocene to middle Miocene, and since the late Miocene in eastern and central Anatolia, respectively (Şengör, 1985; Dhont et al., 1998; Toprak, 1998; Kaymakçı et al., 2010; İmer et al., 2014). Magmatism is characterized by a temporal transition from calc-alkaline to alkaline affinity (Yılmaz, 1990; Keskin, 2003; Aydin, 2008), coexistence of both calc-alkaline and alkaline melts (Kürüm et al., 2008; Dogan-Kulahci et al., 2018), or interactions between lithospheric and asthenospheric melts (e.g., Kürkçüoğlu et al., 2004; Özdemir and Güleç, 2013; Reid et al., 2017). Those patterns reflect the heat input caused by sustained asthenospheric flow through the slab rupture to the hydrated mantle wedge (Davies and von Blanckenburg, 1995), which is in accordance with geophysical and modeling studies cited above. Alkaline magmas are sparsely present in the middle Miocene such as at the Yamadağ volcanic complex (Kürüm et al., 2008), and dominantly in the Pliocene to Quaternary including at the Sivas volcanic suite

at the transition between central and eastern Anatolia (Kürkçüoğlu et al., 2015), Tendürek and Nemrut stratovolcanoes in eastern Anatolia (Pearce et al., 1990; Özdemir et al., 2006) and at lesser extent at the Hasandağ stratovolcano in central Anatolia (Aydar and Gourgaud, 1998; Dogan-Kulahci et al., 2018). The increasing magma alkalinity and asthenospheric component through time caused by asthenospheric infiltration into the base of the overriding lithosphere is typical of all post-subduction and post-collisional tectonic scenarios including those with a slab tear (e.g., Gasparon et al., 2009; Prelević et al., 2015), slab break-off (e.g., Maury et al., 2000; Coulon et al., 2002; Keskin et al., 2008) and lithospheric mantle delamination (e.g., Pearce et al., 1990; Kay et al., 1994). The time-space distribution of post-subduction or post-collisional magmatism presented herein, coupled with seismic tomography, modeling and crustal uplift studies provide more robust constraints on slab geometry and evolution than magmatic petrogenesis alone. Thus, the data presented herein suggest that the temporal, spatial and also geochemical evolution of the Eastern Anatolian Magmatic Belt is a direct, upper crustal magmatic proxy of the westward propagation of the slab break-off and resulting asthenospheric mantle flow beneath central and eastern Anatolia since the early Miocene as a response to the indentation of the Arabian platform in the Oligocene.

2.6.4 Propagation rates of magmatism and crustal uplift

Slab rupture likely occurs episodically, and in segments, rather than at a continuous rate (Wortel and Spakman, 2000), and starts on an existing tear or contortion in the slab, or where the continental crust is subducted deepest (Davies and von Blanckenburg, 1995) about 2 to 25 m.y. after the onset of continental subduction (van de Zedde and Wortel, 2001; van Hunen and Allen, 2011). Temperature and thus rheological contrasts control the initiation of slab rupture that might occur at a distance between 110 and 610 km from the collisional front, 26 and 330 km depth and over a period between 1.7 and 39 m.y., based on numerical modeling (Ton and Wortel, 1997). The impingement of the sub-slab asthenosphere during the slab break-off causes magmatism and crustal uplift (2 to 6 km; Davies and von Blanckenburg, 1995; Buiter, 2000). The underplating and rebound of the subducted thinned continental crust after the oceanic slab

rupture also contributes to the confined uplift of the overriding plate and the migration of the melts in the mantle wedge away from the suture zone (Menant et al., 2016; Magni et al., 2017).

Migration of the magmatic front was accompanied by the westward propagation of crustal uplift from eastern to central Anatolia (Schildgen et al., 2014; McNab et al., 2017). In eastern Anatolia, thermochronological data suggests that the timing of uplift ranged between 30 and 10 Ma (Karaoğlan et al., 2016), or 18 and 13 Ma (Okay et al., 2010) whereas regional magmatic studies suggest that crustal uplift was initiated almost at the same time as magmatism at ca. 13-11 Ma (Keskin, 2007). The 30-10 Ma time range coincides with the onset of the Arabia-ATB continental collision and subsequent slab break-off in the east (Karaoğlan et al., 2016). This range includes data reported by Okay et al. (2010) that represent the timing when the samples analyzed by apatite fission-track reached a depth range between 4 and 2 km (Karaoğlan et al., 2016). Thus, it is argued that: 1) this first Oligocene-Miocene uplift episode exhumed the Ağrı plutons and particularly the Cevizlidere stock to near the surface, given the absence of outcropping coeval volcanic rocks in the region and presence of post-middle Miocene volcanic cover; 2) the inferred second uplift phase started at ca. 13-11 Ma was due crustal rebound during the partial removal of the lithospheric mantle and formation of the Erzurum-Kars volcanic plateau as suggested by Keskin (2003). Madanipour et al. (2017) also measured these two uplift phases (ca. 27-23 and 13 Ma) by U-Th/He thermochronology in northwest Iran which they attributed to two exhumation stages during the Arabian collision.

In central Anatolia, crustal uplift was initiated in the late Miocene (ca. 10-5.45 Ma; 0.24 to 0.37 mm/year) and accelerated in the Pleistocene (0.72 to > 1 mm/year; Cosentino et al., 2012; Schildgen et al., 2012; Karaoğlan, 2016; Abgarmi et al., 2017). The first slow uplift phase is attributed to either the thickening of the accretionary wedge above the subduction zone (Schildgen et al., 2014), or slab break-off (Karaoğlan, 2016; Abgarmi et al., 2017; Delph et al., 2017). The accretion and entrance of the Eratosthenes Seamount (Figure 2.1), south of the Cyprus island, and the thinned continental margin of the Africa plate in the Cyprus subduction zone (Schildgen et al., 2012), post-break-off rebound (Abgarmi et al., 2017) or

asthenospheric upwelling (Cosentino et al., 2012) may have contributed to uplift acceleration in central-southern Anatolia since Pleistocene and the slowing of trench retreat (Netzeband et al., 2006). Although the contribution of the Eratosthenes Seamount to slab break-off in central Anatolia has also been invoked (Schildgen et al., 2014), tomography (e.g., Biryol et al., 2011) and geochronological data on slab break-off-related magmatism, presented here, do not support this hypothesis.

Numerical modeling suggests a slab rupture propagation rate at 100-150 mm/year in the Arabian domain, which is consistent with the rupture of an old, strong oceanic slab (van Hunen and Allen, 2011). Similarly, a crustal uplift propagated from eastern to central Anatolia at a rate of ca. 100-175 mm/year in the late Cenozoic (Schildgen et al., 2014) which contrasts with break-off-induced toroidal asthenospheric flow velocity at ca. 50-100 mm/year (Menant et al., 2016). However, the front of magmatism that migrated along the 1000 km-long Eastern Anatolian Magmatic Belt between Ağrı and Karaman propagated at an average rate of 48 mm/year since 21 Ma. This rate is slower than those of slab rupture, crustal uplift, and asthenospheric flows. In central Mexico, slab break-off-related magmatic front propagated at a rate of ca. 100-250 mm/year (Ferrari, 2004). The fast slab rupture propagation rates in central Mexico compared to those in Anatolia are explained by the age of the subducted oceanic crust. Young oceanic slabs such as the late Cenozoic-aged oceanic crust in central Mexico experience faster rupture propagation rates than old oceanic slabs such as the Mesozoic-aged Southern Neotethyan slab according to numerical modeling results (van Hunen and Allen, 2011).

The lateral extent of the buoyant Arabia plate constrained the rupture propagation in space and thus in time. Once the sub-horizontal rupture reached its maximum lateral length, it was followed by slab window opening and westward toroidal flow of asthenosphere (Figure 2.7b). The geometry of the slab window, i.e., the sharp eastern edge of the Cyprus slab and the current depth of westernmost tip of the slab rupture (Figure 2.7a), results from the subduction of the Cyprus slab beneath central Anatolia that sunk the hanging Arabian slab into the mantle during the late Cenozoic and southward retreat of the Cyprus trench (Menant et al., 2016).

Magma production was continuous during the entire process of slab rupture and window opening since 21 Ma (Figure 2.4). However, there is a rate discrepancy between the magmatic migration and slab rupture propagation in central and eastern Anatolia. Considering a slab rupture propagation rate of 100-150 mm/year (van Hunen and Allen, 2011) along the 850 km-long Arabian slab segment between the current surface projection of the eastern Cyprus slab margin in central Anatolia and the Ağrı magmatic complex in eastern Anatolia (Figure 2.7a), sub-horizontal slab rupture propagation is expected to be terminated in 5.5 to 8.5 m.y., i.e., at ca. 19.5-16.5 Ma, assuming slab rupture initiated at ca. 25 Ma in eastern Anatolia, as discussed above. Thus, early to middle Miocene magmatism in eastern Anatolia (21-15 Ma) is the response to slab rupture propagation and poloidal flow of asthenosphere whereas late Miocene to Present magmatism (12 Ma-Present) in central Anatolia is related to the slab window opening and toroidal flow of asthenosphere. The cessation of slab break-off propagation coincides with 1) the onset of volcanic activity in central Anatolia at ca. 12 Ma, still considering a delay of a few million years for magmatism to emplace in the crust (Ferrari, 2004; Cesare et al., 2009), 2) slab tearing in western Anatolia at 15 Ma (van Hinsbergen et al., 2010; Jolivet et al., 2015), and 3) the formation of the Erzurum-Kars volcanic plateau in eastern Anatolia (ca. 13-11 Ma; Keskin, 2003, 2007).

2.6.5 Post-late Miocene partial removal of the subcontinental lithospheric mantle in central and eastern Anatolia

The current accepted model for the formation of the late Miocene to Quaternary Erzurum-Kars volcanic plateau in eastern Turkey invokes the delamination of subcontinental lithospheric mantle (SCLM) below the Rhodope-Pontide Block in the north, and the steepening and break-off of the Neotethyan oceanic slab beneath eastern Anatolia in the south (Keskin, 2003; Şengör et al., 2003; Keskin, 2007; Şengör et al., 2008). This model is based on the geologic and tectonic interpretation of the eastern ATB termination which is defined as the Eastern Anatolia Accretionary Complex by Şengör et al. (2003). This Accretionary Complex deposited on the subducting Neotethyan oceanic crust and is devoid of lithospheric root (Şengör

et al., 2003; Keskin, 2007), as confirmed by the current attenuated or absent SCLM beneath eastern Anatolia (Al-Lazki et al., 2003; Gök et al., 2003; Zor et al., 2003; Angus et al., 2006). However, evidence for a Paleozoic metamorphic basement in eastern Anatolia suggests the existence of a rigid continental crust beneath the accretionary complex sequence and thus a SCLM accordingly (Yılmaz et al., 2010; Topuz et al., 2017). The discovery of ancient pristine igneous zircon xenocrysts from the early Miocene Ağrı plutons with Paleozoic $^{206}Pb/^{238}U$ ages (328.40 ± 11 and 428.3 ± 28 Ma; concordant analyses) in this study confirms this interpretation. Thus, the long-lived asthenospheric heating below eastern Anatolia since the late Oligocene contributed to the partial removal of the Anatolian SCLM by either delamination (Pearce et al., 1990; Oruç et al., 2017; Topuz et al., 2017) or small-scale sublithospheric convection (Kaislaniemi et al., 2014; Neill et al., 2015). This tectonic event increased magma production and caused the formation of the widespread late Miocene to Quaternary, Erzurum-Kars volcanic plateau (Figure 2.6).

The southward steepening of the Neotethyan slab proposed by Keskin (2003) in eastern Anatolia was also invoked in central Anatolia by Bartol and Govers (2014) to suggest a unique Neotethyan slab that horizontally subducted below both central and eastern Anatolia, and then retreated southwards since the early Miocene causing the wholesale lithospheric delamination beneath central and eastern Anatolia. However, the belt-like geometry of central Anatolian magmatism, and the southward (Galatia-Sulutas-Konya trend) and westward (Sivas-Cappadocia-Hasandağ-Karaman axis) magmatic migrations determined in this study do not support the wholesale lithospheric delamination model (Schildgen et al., 2014; this Chapter). Nonetheless, slab window opening may have triggered lithospheric instability and subsequent ‘dripping’ to account for the thin lithospheric mantle beneath the central Anatolia and the high density of brittle structures (Delph et al., 2017; Göğüş et al., 2017; Reid et al., 2017). The SCLM removal by local catastrophic delamination or small-scale sublithospheric convection processes may account for the triangular-shaped Galatian volcanic province in northern central Anatolia (Figure 2.5). This isolated volcanic province is characterized by widespread post-

subduction or post-collision volcanism, absence of apparent spatial magmatic migration, local temporal increases of magma alkalinity, and extensional tectonic regime (e.g., Varol et al., 2014 and references therein). Thus, the north-south Galatia-Sulutas-Konya trend is the magmatic response to the roll-back of Cyprus slab since the early Miocene which started during the break-off initiation of the Arabian slab further east.

2.7 Conclusion

The interpretation of age data compilation, complemented by new U-Pb geochronology data from less-constrained late Cenozoic magmatic complexes in central and eastern Anatolia, suggests in this study that magmas were produced in response to sub-horizontal rupture propagation of the subducting Southern Neotethyan oceanic slab and resulting asthenospheric flow since ca. 25 Ma after the onset of the Arabia-ATB continental collision at ca. 30 Ma. The brief late Oligocene magmatic pulse (26-25 Ma) resulted in response to slab steepening (30-25 Ma) subsequent to Arabia-ATB collision, and was delayed a few millions years during weakening and breaking off of the slab. This new model suggests that magmatism was active a few million years after the slab rupture initiation and began earlier than previously documented, specifically in the early Miocene (21 Ma) in eastern Anatolia. The westward migration (48 mm/year) of the slab break-off-related magmatic front from eastern (21-15 Ma) to central Anatolia (12 Ma-Present) generated the newly-defined, narrow, E- to NE-trending Eastern Anatolian Magmatic Belt. Although eastern Anatolian magmatism formed in response to the sub-horizontal slab rupture propagation (25-16.5 Ma), the results presented herein indicate that middle Miocene to Present magmatism in central Anatolia, with the exception of the Konya and Sulutas volcanic complexes, resulted from slab window opening and the lateral sub-slab mantle flow from eastern Anatolia that initiated when the sub-horizontal slab rupture reached the northwestern edge of the Arabian continental lithosphere in the middle Miocene. The magmatic response of sub-horizontal slab rupture propagation and window opening was characterized by the production of calc-alkaline magmas that progressively evolved to alkaline magmas through time as a result of increasing inputs of hot asthenospheric flow. The magmatic

activity was accompanied by slab break-off-related crustal uplift that started at ca. 23 Ma in eastern Anatolia (Karaoğlan et al., 2016), and propagated westwards to reach central Anatolia at ca. 15-7 Ma (Cosentino et al., 2012; Schildgen et al., 2014; Karaoğlan, 2016; McNab et al., 2017). Slab break-off-related magmatism was subsequently covered by the volcanic products of the Erzurum-Kars plateau since ca. 13-11 Ma in eastern Anatolia due to the SCLM partial removal by either delamination (Pearce et al., 1990; Topuz et al., 2017) or small-scale sublithospheric convection (Kaislaniemi et al., 2014; Neill et al., 2015).

This study proposes that slab break-off initiated in eastern Anatolia (ca. 25 Ma) before the slab tear in western Anatolia (15 Ma; van Hinsbergen et al., 2010; Jolivet et al., 2015). Thus, the westward propagation of the sub-horizontal slab rupture stopped at the northwesternmost edge of the Arabia plate at ca. 19.5-16.5 Ma. This slab break-off event played a role in the acceleration of the Aegean slab roll-back and North Anatolian fault zone development in the middle-late Miocene due to the slab pull force increase and deep lateral continuity of the Southern Neotethyan slab in the mantle (Faccenna et al., 2006). It is argued herein that slab break-off in eastern and central Anatolia also contributed to the initiation of the slab tear between the Aegean and Cyprus slabs (15-8 Ma; van Hinsbergen et al., 2010; Jolivet et al., 2015), roll-back of the Cyprus slab since the early Miocene (Biryol et al., 2011; Koç et al., 2012), SCLM partial removal in eastern Anatolia in the late Miocene (e.g., Neill et al., 2015; Topuz et al., 2017), and the production of the widespread late Cenozoic magmatism in central and eastern Anatolia.

Chapter 3: Geochemical evolution of late Cenozoic post-subduction magmatism in central and eastern Anatolia, Turkey

3.1 Introduction

A continental collision typically includes processes that affect the subducting and overriding lithospheres. The downgoing slab may undergo bending, roll-back, tearing (vertical rupture) and ultimately break-off. Concomitantly, the subcontinental lithospheric mantle (SCLM) of one or both plates may undergo Rayleigh-Taylor gravitational instability where the cold and dense SCLM is above the hot and light asthenosphere (Houseman and Molnar, 1997). Within a few tens of million years, portions of the lithosphere may detach and sink into the asthenosphere by delamination or dripping (van Hunen and Miller, 2015). Loss of the SCLM may occur more than once, as different regions undergo critical instability at different times (Rosenbaum et al., 2008; Garzanti et al., 2017). The detachment of slab and SCLM generates upward flow of asthenospheric mantle which, in turn, provides advective heat to the base of the remaining lithosphere. During slab and SCLM detachment, the asthenosphere beneath the SCLM may consist of previously slab-metasomatized peridotite, particularly in the former mantle wedge beneath the overriding plate, and newly introduced, drier peridotite which has flowed upwards from depth (e.g., Kay and Kay, 1993; Keskin, 2007). Taken together, these processes yield a mantle environment which consists of three distinct mantle components: the SCLM, the remnant metasomatized asthenospheric mantle wedge, and upwelling sub-slab asthenosphere.

The three mantle components may all be involved in the generation of basaltic magma. The metasomatized mantle has a lower melting point and, a result, melts more readily than the drier mantle. Melts of metasomatized peridotite can be produced by heat input from the upwelling asthenosphere whereas the drier mantle can melt by either input of volatiles from the detached oceanic slab or SCLM (Gazel et al., 2012; Kaislaniemi et al., 2014), or by decompression at shallow depths (< 50 km; Davies and von Blanckenburg, 1995). Melting

of the hydrated component will generate arc-like calc-alkaline magma (e.g., Pearce et al., 1990; Whalen et al., 2006). However, the abundance of hydrated mantle is limited and magma production may shift over time to yield ocean-island (OIB)-like, alkaline compositions, as commonly reported in post-subduction, post-collisional and slab window tectonic settings (e.g., Hole et al., 1991; Coulon et al., 2002; Thorkelson et al., 2011; Mullen and Weis, 2013). The SCLM may also undergo melting in response to advective heat transfer from uprising asthenosphere and passage of basaltic magma. Melting of the SCLM may be focused at sites of previous veining, dyking and other locations where mantle fertility has been enhanced, and the nature of the melts produced may vary significantly over time and space. Consequently, in locations where slab tearing, break-off and SCLM removal are time-transgressive beneath a collision zone, a simple progression from arc-like to OIB-like compositions may not occur. In such environments, the record of magmatism expressed by mafic igneous complexes in the crust may yield a complex geochemical signature, which is difficult to ascribe to specific processes and source components.

The late Cenozoic geodynamic evolution of the Eastern Mediterranean region was controlled by the closure of the Southern Neotethyan Ocean and collision of Arabia with Eurasia (e.g., McKenzie, 1972; Reilinger et al., 2006; Le Pichon and Kreemer, 2010). Collision occurred from northward migration and subsequent indentation of the Arabian platform into the Anatolide-Tauride Block either in the Eocene (Rolland et al., 2012), Oligocene (Jolivet and Faccenna, 2000; Agard et al., 2005; Allen and Armstrong, 2008; Barrier and Vrielynck, 2008; McQuarrie and van Hinsbergen, 2013; Karaoğlan et al., 2016), or Miocene (Şengör and Yılmaz, 1981; Dewey et al., 1986; Yılmaz, 1993; Yiğitbaş and Yilmaz, 1996; Robertson et al., 2007; Şengör et al., 2008; Hüsing et al., 2009; Okay et al., 2010; Robertson et al., 2016). The collision terminated the subduction of the Southern Neotethyan oceanic slab and initiated slab break-off, which resulted in asthenosphere upwelling. The upflow of mantle triggered SCLM partial removal in central and eastern Anatolia (e.g., Keskin, 2003, 2007; Delph et al., 2017; Reid et al., 2017). The magmatic response to the slab break-off and SCLM partial removal

events formed the Eastern Anatolian Magmatic Belt (Chapter 2). Additional processes such as subduction, slab deformation, continental collision, back-arc extension, block rotation and SCLM removal influenced the tectonic history of the region and focused the style and location of magmatism (e.g., Faccenna et al., 2006; Şengör et al., 2008; Jolivet et al., 2013; Faccenna et al., 2014).

Many studies in central and eastern Anatolia have focused on the regional evolution of late Cenozoic magmatism (Pearce et al., 1990; Yılmaz, 1990; Keskin et al., 1998; Keskin, 2003; Şen et al., 2004; Şengör et al., 2008; Chapter 2), or on individual volcanic suites and volcanoes such as Erciyes, Hasandağ, Yamadağ, Kars, Süphan and Nemrut (e.g., Deniel et al., 1998; Keskin et al., 1998; Şen et al., 2003; Özdemir et al., 2006; Özdemir and Güleç, 2013; Reid et al., 2017). Chapter 2 showed that late Cenozoic magmatism along the Eastern Anatolian Magmatic Belt in central and eastern Anatolia could result from similar tectonic events. Thus, aspects of both previously-published regional and local studies are combined herein to constrain the magmatic sources and processes along the Eastern Anatolian Magmatic Belt. To accomplish this goal, numerous whole-rock geochemical and Sr-Nd-Pb isotopic analyses from previously-published studies were compiled, integrated and interpreted in this Chapter 3. This newly-compiled geochemical database was completed by new whole-rock major and trace element, and Sr-Nd (whole-rock) and Pb (feldspar) isotopic analyses from less-constrained magmatic complexes throughout the Eastern Anatolian Magmatic Belt. The data constrain the geochemical evolution of magmatism along the belt through time and space, and provide insights into the role of slab break-off, SCLM removal and asthenospheric upwelling on regional magmatism.

3.2 Geological and tectonic setting of central and eastern Anatolia

3.2.1 Tectonic assembly

The study area lies within the Western Tethyan Orogenic Belt. This belt resulted from the accretion of several Gondwana-derived, ribbon-like continental fragments, including

the Anatolide-Tauride Block (ATB), Central Anatolian Crystalline Complex, Bitlis-Pütürge Massifs, and Rhodope-Pontide Block in Turkey (Figure 3.1) to southern Laurasia (now called Eurasia), from the Paleozoic to Cenozoic (Şengör and Yılmaz, 1981; Robertson and Dixon, 1984; Şengör et al., 1984; Sengör and Natal'In, 1996; Okay and Tüysüz, 1999; Stampfli, 2000; Okay et al., 2006; Pourteau et al., 2013; Robertson et al., 2013; van Hinsbergen et al., 2016). The ATB was a continental lithosphere-derived platform when it drifted away from Gondwana in the Triassic (Şengör and Yılmaz, 1981; Frizon de Lamotte et al., 2011). The Anatolide units (e.g., Tavşanlı and Afyon Zones) of the ATB were affected by the Late Cretaceous collisional deformation with the Rhodope-Pontide Block of the southern active margin of Laurasia, along the present İzmir-Ankara-Erzincan suture zone. In contrast, the Tauride units are the non-metamorphosed, thrusted and folded external platform of southern Turkey (Pourteau et al., 2013). The Central Anatolian Crystalline Complex is considered as either unroofed crystalline complexes within the ATB (Şengör and Yılmaz, 1981; Göncüoğlu, 1986; Floyd et al., 2000; Moix et al., 2008; Boztuğ et al., 2009; van Hinsbergen et al., 2016) or a single crystalline fragment that drifted between the Rhodope-Pontide and Anatolide-Tauride Blocks in the late Mesozoic and surrounded by the Northern Neotethys and Inner Tauride oceans (Okay, 1984; Robertson and Dixon, 1984; Whitney and Dilek, 1997; Okay and Tüysüz, 1999; Fayon et al., 2001; Clark and Robertson, 2002; Kadıoğlu et al., 2006). The Bitlis and Pütürge Massifs in southeast Turkey formed a single ribbon-shaped allochthonous crustal fragment between ATB and Arabia. Both Massifs were emplaced on the Taurus platform in the Late Cretaceous closing the Berit Ocean (e.g., Robertson et al., 2013). In the Anatolides, the Tavşanlı and Afyon Zones are high pressure and low temperature metamorphic zones diachronously exhumed in the Late Cretaceous (Pourteau et al., 2013). Both zones warp around the Central Anatolian Crystalline Complex along the Inner Tauride suture zone, and are tectonically over the Taurus carbonate platform to the south (Pourteau et al., 2013). The eastward termination of ATB is composed of the Taurus platform and the Eastern Anatolian Accretionary Complex between the Arabian platform, Rhodope-Pontide and South Armenian Blocks (Figure 3.1). The tectonic

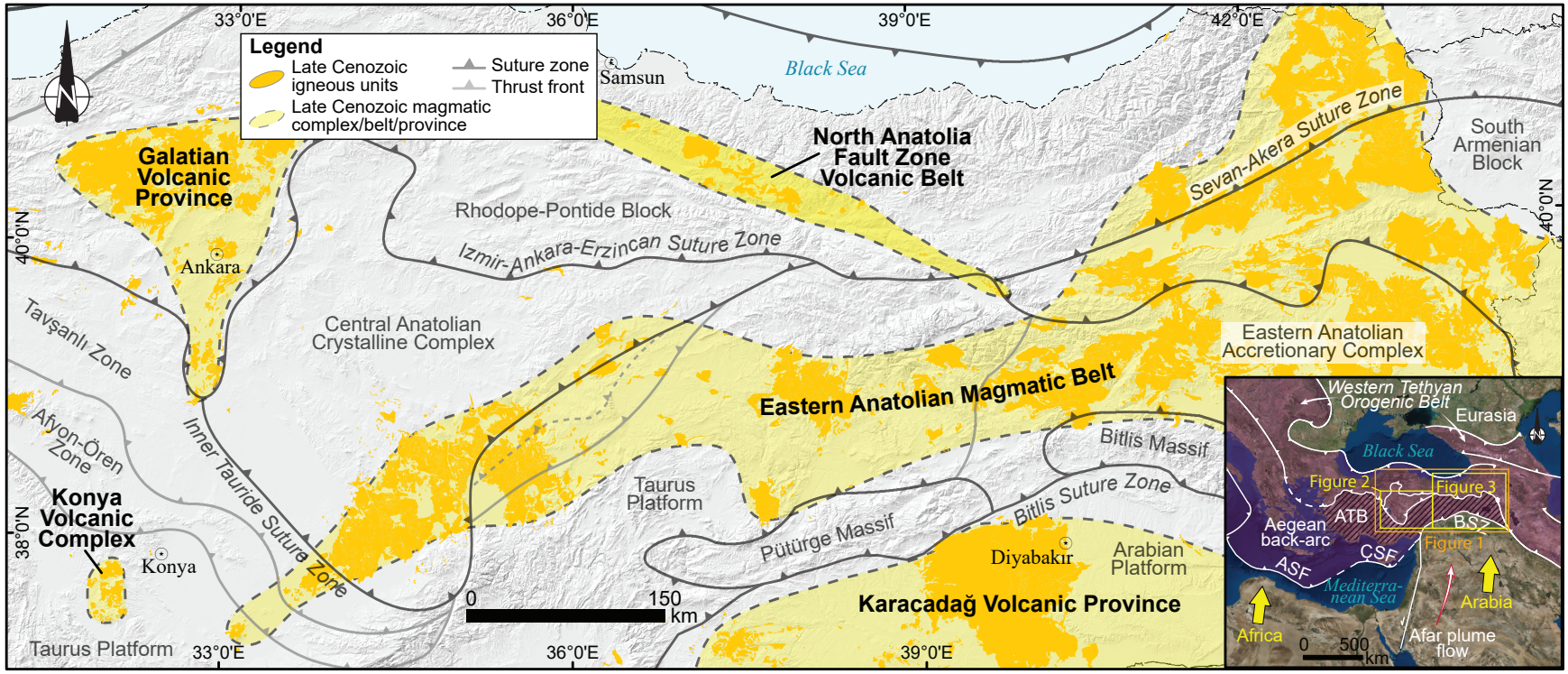

Figure 3.1 Tectono-magmatic map of central and eastern Anatolia (1:4,000,000 scale; Lambert Conic projection; European Datum 1950) showing the location of late Cenozoic igneous units (modified from MTA, 2002), complexes, belts and provinces (Chapter 2), basement boundaries (modified from Görür and Tüysüz, 2001; Şengör et al., 2008; Pourteau et al., 2010). Base map: SRTM 90 m digital elevation models (Jarvis et al., 2008). Background of the location map is from Google Earth. ASF = Aegean Subduction Front; ATB = Anatolide -Tauride Block; BSZ = Bitlis Suture Zone; CSF = Cyprus Subduction Front.

mosaic in Turkey is highlighted by the fragmented distribution of Mesozoic ophiolitic units that surround the various Gondwana-derived continental fragments. Those ophiolitic units are the relic of ancient oceanic basins (e.g., Northern and Southern Neotethys, Inner Tauride and Berit) that all closed in the Late Cretaceous-Paleocene, except for the Southern Neotethys, which remained open until the continental collision between ATB-Bitlis-Pütürge Massifs and the Arabian platform during the Cenozoic (e.g., Robertson et al., 2013).

3.2.2 Geological framework

The ATB is dominated by the Taurus platform that is a large nappe stack composed of the late Paleozoic to Mesozoic carbonate platform, known as the Malatya-Keban platform in eastern Anatolia, thrusted over Late Cretaceous ophiolites (Robertson et al., 2007; Parlak et al., 2009). This assemblage is intruded by Late Cretaceous to Eocene calc-alkaline to alkaline igneous complexes, and overlain by Cenozoic pelagic and continental sedimentary and volcanic units (Aktaş and Robertson, 1984; Yılmaz, 1993; Robertson et al., 2007; Rızaoğlu et al., 2009; Kuşcu et al., 2010; İmer et al., 2013; Nurlu et al., 2016).

The eastward termination of ATB consists of a Late Ordovician to early Silurian metamorphic basement overthrusted by Mesozoic ophiolites, unconformably overlain by Cretaceous to Oligocene southward-imbricated slices of flysch, intruded by early Miocene plutons and covered by the middle Miocene to Present volcanic rocks of the Erzurum and Kars plateaus (Sengör and Natal'In, 1996; Şengör et al., 2003; Yılmaz et al., 2010; Topuz et al., 2017).

The southeast part of ATB is separated from the Bitlis-Pütürge Massifs to the south by late Mesozoic ophiolitic complexes (Robertson et al., 2007; Parlak et al., 2009). The Bitlis-Pütürge Massifs are made of a Neoproterozoic Pan-African basement of gneiss and schist, and a Paleozoic-Mesozoic sedimentary cover (Ustaömer et al., 2009; Oberhänsli et al., 2010; Ustaömer et al., 2012). This complex is separated from the Arabian platform by the Killan imbrication zone, which is composed of Late Cretaceous to Miocene mélange and olistostrome (Aktaş and Robertson, 1984; Yılmaz, 1993; Robertson et al., 2007).

The ATB is separated from the northerly Central Anatolian Crystalline Complex by the inferred Inner Tauride suture zone (Figure 3.2). The basement of the Central Anatolian Crystalline Complex consists of Paleozoic to Mesozoic, high temperature and low pressure metamorphic massifs exhumed during Cenozoic (Dilek and Whitney, 2000; Fayon et al., 2001; Whitney et al., 2001). Those massifs are unconformably overlain by dismembered Late Cretaceous ophiolites, intruded by Late Cretaceous calc-alkaline to alkaline plutons and batholiths, and covered by Cenozoic to Quaternary volcanic rocks and sediments (Görür et al., 1984; Yaliniz and Göncüoglu, 1998; Whitney et al., 2003; Kadıoğlu et al., 2006; Boztuğ et al., 2009; Lefebvre et al., 2011; Lefebvre et al., 2013).

3.2.3 Geodynamic history

The number of oceanic basins and thus active subduction zones in the Late Cretaceous, represented now by suture zones (Figure 3.1), are matter of debate; however, it is widely accepted that only the northward subduction of the Southern Neotethys remained active beneath ATB during the Paleogene (e.g., Barrier and Vrielynck, 2008; Robertson et al., 2013). The northward subduction of the Southern Neotethyan oceanic slab started in the Late Cretaceous and produced arc and back-arc magmatism that peaked from 88 and 69 Ma, and from 54 to 43 Ma (Rızaoğlu et al., 2009; Kuşcu et al., 2010; Robertson et al., 2013; Karaoğlan et al., 2016).

The ATB is now part of the Anatolian microplate that has been deformed by the indentation of Arabia into the eastern ATB and Bitlis-Pütürge Massifs along the Bitlis suture zone (Dewey et al., 1986; McClusky et al., 2000; Robertson, 2000; Reilinger et al., 2006). This collision began in either the Eocene (Rolland et al., 2012), the Oligocene, as commonly accepted (Jolivet and Faccenna, 2000; Agard et al., 2005; Allen and Armstrong, 2008; Barrier and Vrielynck, 2008; McQuarrie and van Hinsbergen, 2013; Karaoğlan et al., 2016), or Miocene, on the basis of stratigraphy, tectonic reconstructions, deformation history, climate transition and thermochronological interpretations (Şengör and Yılmaz, 1981; Dewey et al., 1986; Yılmaz, 1993; Yiğitbaş and Yilmaz, 1996; Şengör et al., 2008; Hüsing et al., 2009; Okay et al., 2010; Robertson et al., 2016).

The Arabia-Eurasia continental collision interrupted the subduction of the Southern Neotethyan oceanic slab, and initiated post-subduction, syn-collisional tectonism and magmatism in central and eastern Anatolia during the late Cenozoic (e.g., Pearce et al., 1990; Keskin et al., 1998; Keskin, 2003, 2007; Şengör et al., 2008; Bartol and Govers, 2014). Previous hypotheses involved the delamination, and slab steepening and break-off of the horizontal subducted Southern Neotethys slab beneath eastern (Keskin, 2003; Şengör et al., 2003; Keskin, 2007; Şengör et al., 2008) and central Anatolia (Bartol and Govers, 2014; Delph et al., 2017). Recent tectonic models based on new geochronological data, existing tomography and numerical modelling proposed that the drop in convergence rate at the onset of the Arabia-Eurasia continental collision caused the steepening of the Arabian segment of the Southern Neotethyan slab beneath eastern ATB between 30 and 25 Ma (Chapter 2). Steepening was followed by initiation of slab break-off in eastern Anatolia and westward propagation to the northwestern edge of the Arabian continental crust beneath central Anatolia (25-16 Ma), and opening of a slab-free area beneath eastern and central Anatolia since 16 Ma (Chapter 2). Consequential asthenospheric upwelling and lithospheric heating triggered the regional removal of the lithospheric mantle by slab steeping (Keskin, 2003, 2007; Şengör et al., 2008), delamination (Pearce et al., 1990; Bartol and Govers, 2014; Delph et al., 2017; Topuz et al., 2017), or large- or small-scale sublithospheric convection in central and eastern Anatolia and the Lesser Caucasus (Kaislaniemi et al., 2014; Neill et al., 2015; Göğüş et al., 2017). This model describes the history of central and eastern Anatolian magmatism in three discrete episodes related to 1) Arabian slab steepening in eastern Anatolia (26-25 Ma), 2) break-off initiation and propagation from eastern to central Anatolia (21-15 Ma), 3) descent of the disconnected slab and consequent asthenospheric upwelling and SCLM partial removal in both central and eastern Anatolia (12 Ma to Present; Chapter 2).

Regional seismic tomography studies show lateral continuity of the Southern Neotethyan slab at ca. 500-660 km beneath ATB (e.g., Piromallo and Morelli, 2003; Biryol et al., 2011). Thus, the break-off of the Arabian segment of the Southern Neotethyan slab in eastern Anatolia

increased and focused the load on the neighboring, and still attached, western and central segments, namely the Aegean and Cyprus slabs (Faccenna et al., 2006). The additional slab pull force contributed to accelerate the Aegean slab roll-back, Hellenic trench retreat and curvature, westward extrusion of the Anatolian microplate along the North and East Anatolian fault zones (McKenzie, 1972; Dewey et al., 1986; Armijo et al., 1999; McClusky et al., 2000; Wortel and Spakman, 2000; Faccenna et al., 2006), and initiate of the Cyprus slab roll-back since the early Miocene (Biryol et al., 2011; Chapter 2). The acceleration of the Aegean trench retreat (ca. 30 mm/year) relative to the Cyprus trench (ca. 10 mm/year; McClusky et al., 2003; Wdowinski et al., 2006; Jolivet et al., 2015) progressively tore the slab between 25 and 16 Ma (Jolivet et al., 2015). These processes resulted in the fast clockwise rotation of the Hellenides, southwestward migration of magmatism and exhumation of metamorphic complexes (Dilek and Altunkaynak, 2009; van Hinsbergen, 2010; Jolivet et al., 2015; Prelević et al., 2015). The southward age progression of early to late Miocene volcanism along the Galatia-Sulutas-Konya trend above the Cyprus slab in central Anatolia reflects slab roll-back (Biryol et al., 2011; Koç et al., 2012; Chapter 2).

In the overriding plate, slab break-off-related magmatism tends to be manifested by an increase in OIB-like signature, and a decrease in arc signature (Ferrari, 2004). This shift has been identified by decreasing involvement of subduction-hydrated mantle and increasing contribution from the dry asthenosphere rising from depth, particularly from beneath the slab (e.g., Yılmaz, 1990; Maury et al., 2000; Coulon et al., 2002; Keskin, 2003; Ferrari, 2004), a pattern also established at sites of ridge subduction (Thorkelson et al., 2011). The late Cenozoic igneous history of the ATB was strongly affected by segmentation of the Southern Neotethyan oceanic slab (Keskin, 2003, 2007; Şengör et al., 2008; Dilek and Altunkaynak, 2009, 2010; Ersoy and Palmer, 2013; Chapter 2), and previous studies have related changes in slab and mantle configurations to magmatism (Keskin, 2003; Şengör et al., 2003; Keskin, 2007; Şengör et al., 2008; Dilek and Altunkaynak, 2009, 2010; Prelević et al., 2012; Ersoy and Palmer, 2013; Prelević et al., 2015). However, a complete synthesis of tectonics and magma genesis for the

ATB, particularly in both central and eastern Anatolia regions, has not yet been established. Following a brief review of igneous complexes in central and eastern Anatolia, such a synthesis is provided herein through a comprehensive review of igneous compositions in the context of recent geochronology and current models of lithosphere-asthenosphere interaction.

3.3 Late Cenozoic magmatism in central and eastern Anatolia

The late Cenozoic igneous complexes of central and eastern Anatolia occur within the 1000 km-long, E- to NE-trending Eastern Anatolian Magmatic Belt (Figure 3.1). This belt extends further east and southeast to Armenia and Iran.

3.3.1 Central Anatolia

The late Miocene to Quaternary volcanic products of central Anatolia overlie the Permian metamorphic basement, Mesozoic Tauride carbonate platform and ophiolitic complexes, and Late Cretaceous batholiths of the Central Anatolian Crystalline Complex (Karakaya, 1991; Toprak and Göncüoğlu, 1993; Aydar et al., 1995; Lefebvre et al., 2011). The simplified stratigraphy of late Cenozoic volcanism in central Anatolia consists of the late Miocene İncesu-Cappadocia felsic ignimbrites and the lavas and domes of the Tekkedağ and Develidağ volcanic edifices (11-5 Ma), followed by the mafic to felsic volcanic and volcaniclastic units of the Pliocene to Quaternary Hasandağ and Erciyes stratovolcanoes and Acigöl, Karapınar and Karaman monogenetic volcanic centers (4 Ma to Present; Figure 3.2). The volcanic edifices of central Anatolia are lined up along a SW-trending axis that includes the Sivas-Cappodocia-Hasandağ-Karaman complexes controlled by the NW-trending dextral Tuz Gölü and NE-trending, sinistral Ecemiş faults, and ENE-trending structures (Pasquare et al., 1988; Toprak, 1998).

The Pliocene to Quaternary Hasandağ and Melendiz stratovolcanoes emplaced along the Tuz Gölü dextral strike-slip fault in the western part of central Anatolia. The Hasandağ stratovolcano consists of a succession of basaltic to dacitic domes and lavas, ignimbrites, block-and-ash flows and rhyodacitic domes emplaced since 7 Ma (Aydar and Gourgaud, 1998;

Deniel et al., 1998). The Melendiz stratovolcano is characterized by a succession of andesitic lava flows and tuff deposits dated between 5 and 3 Ma and overlain by the northwesterly Hasandağ volcanic complex (Figures 3.3A-B and 3.4A; Aydar and Gourgaud, 1998; Chapter 2). In addition, a series of Pliocene to Quaternary monogenic basaltic volcanoes (4 Ma to Present), namely Acigöl, Karapınar and Karaman, are lined up along a NE-trending depression at the northeast and southwest of Hasandağ (Keller, 1974; Pasquare et al., 1988; Notsu et al., 1995; Toprak, 1998; Schmitt et al., 2011; Siebel et al., 2011; Reid et al., 2017).

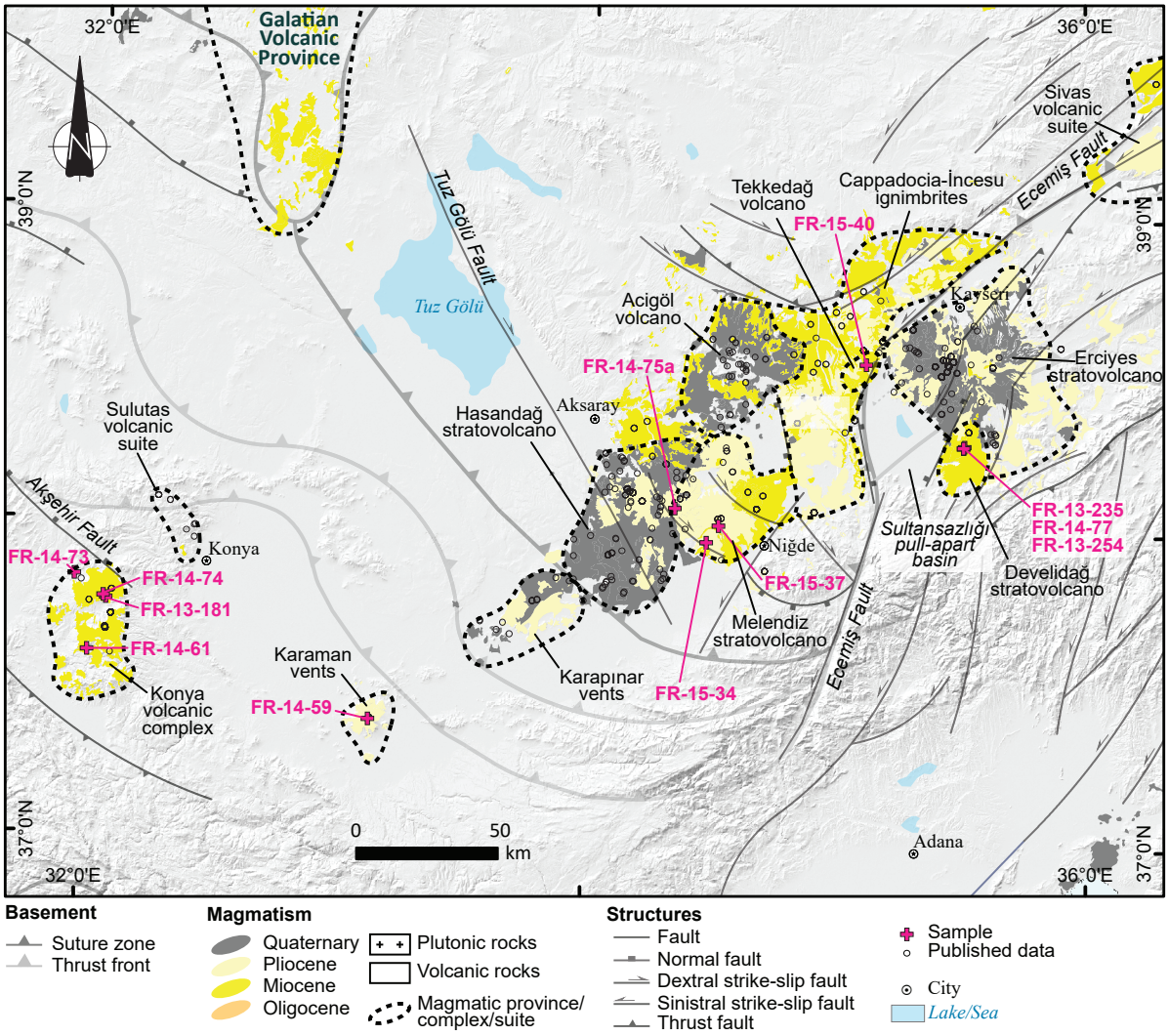

Figure 3.2 Magmatic map of central Anatolia (1:1,500,000 scale; Lambert Conic projection; European Datum 1950) showing the distribution of late Cenozoic igneous units (unit age modified from MTA, 2002), magmatic complexes and regional structures. The location of analyzed igneous rock samples and compiled geochemical data is also displayed. Base map: SRTM 90 m digital elevation models (Jarvis et al., 2008).

The eastern part of central Anatolia is dominated the Erciyes and Develidağ stratovolcanoes, Tekkedağ volcano, and the widespread Cappadocia and İncesu ignimbrite formations. The Erciyes stratovolcano is located on the Sultansazlığı pull apart basin that developed during the Ecemiş fault activity since the Pliocene (Koçyiğit and Beyhan, 1998). The construction of the Erciyes stratovolcano consists basaltic andesite to dacite flows and domes, pyroclastic deposits, followed by block-and-ash flows derived from rhyodacitic domes (Şen et al., 2003; Dogan et al., 2013). The Develidağ stratovolcano and coeval Tekkedağ andesitic volcano emplaced on the east and west flanks, respectively, of the Sultansazlığı pull apart basin and formed at the early stage of the basin extension (Koçyiğit and Beyhan, 1998; Toprak, 1998). The Develidağ stratigraphy consists of late Miocene basaltic and andesitic lavas and post-Miocene pyroclastic deposits (Figures 3.3B-D; Kürkçüoğlu, 2010; Chapter 2). The İncesu and Cappadocia formations are made of a late Miocene felsic ignimbrites deposited on the west side of the Sultansazlığı pull apart basin, north of Tekkedağ (Koralay, 2010), and overlain by the Erciyes volcanic products (Temel et al., 1998b; Le Pennec et al., 2005).

The Konya volcanic complex, ca. 100 km west of the Hasandağ stratovolcano, is an isolated volcanic complex located at the termination of the Akşehir normal fault on the Taurus platform. This complex is composed of three volcanic centers made of andesitic to dacitic ignimbrites, lavas and domes between 12 and 3 Ma (Keller et al., 1977; Temel et al., 1998a; Chapter 2). The Konya volcanic complex postdates the alkaline basalts and calc-alkaline dacites (ca. 16 Ma; Korkmaz et al., 2017), and lamprophyre units (14-12 Ma; Asan and Ertürk, 2013) of the Sulutas volcanic complex, northwest of Konya.

The basaltic lava flows of the middle Miocene to Quaternary Sivas suite (15-1 Ma; Platzman et al., 1998; Jaffey et al., 2004) are sparsely distributed at the transition between the central and eastern Anatolian magmatic provinces (Guezou et al., 1996), and also on both sides of the northeastern segment of the Ecemiş sinistral strike-slip fault (Figure 3.2).

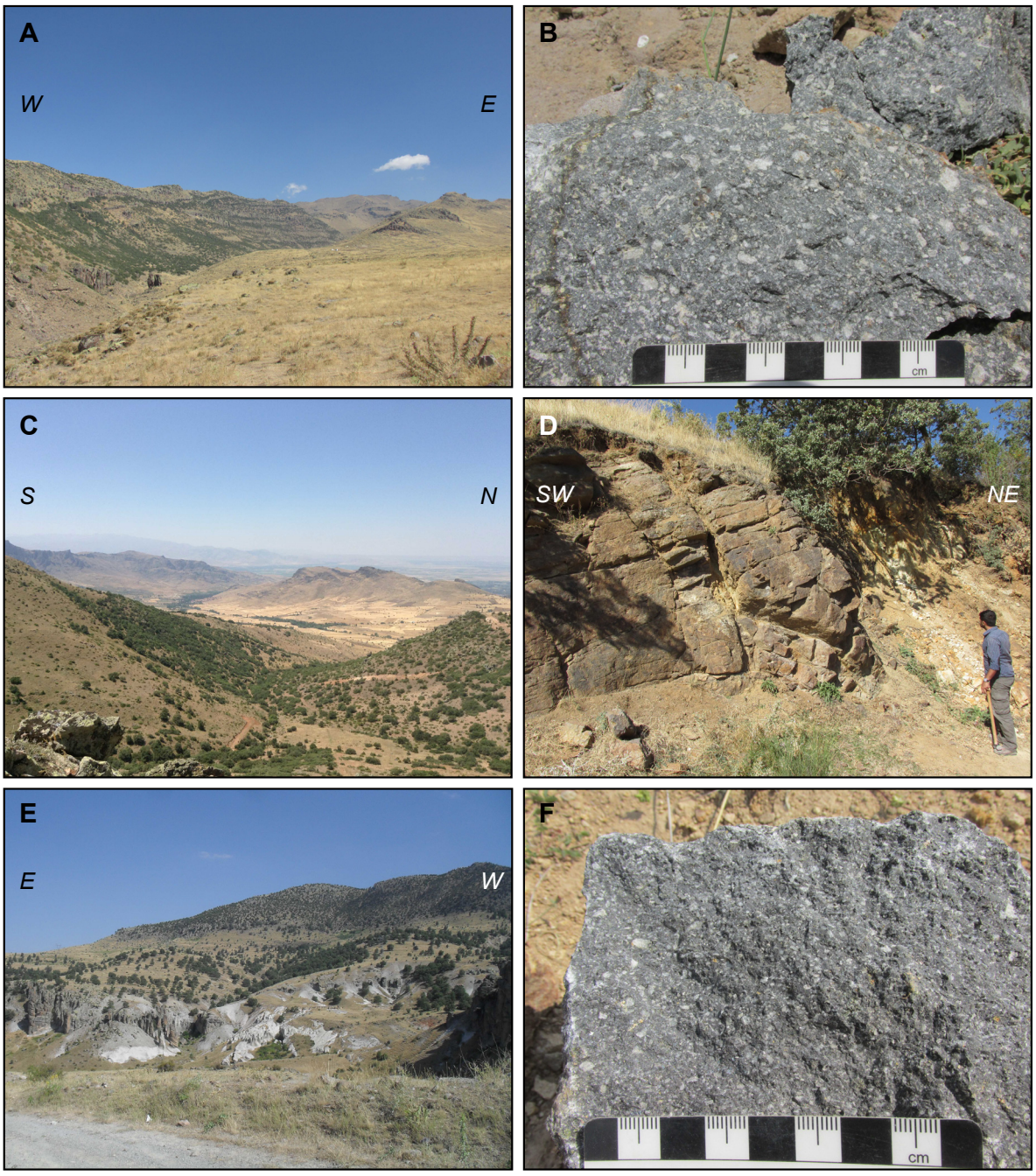

Figure 3.3 Field photographs illustrating representative magmatic complexes and rock samples from central Anatolia: the succession of lava flows at the Melendiz stratovolcano (A) including an andesitic rock sample from the village of Altunhişar (B – FR-14-34), the Develidağ stratovolcano from the Öksüt gold mine (C), and an andesitic lava flow from the Tekkedağ volcano near the village of Başdere (D – FR-15-40), and the ignimbrite (E) and andesitic units (F – FR-13-181) of the Konya volcanic complex in the area of İnlice.

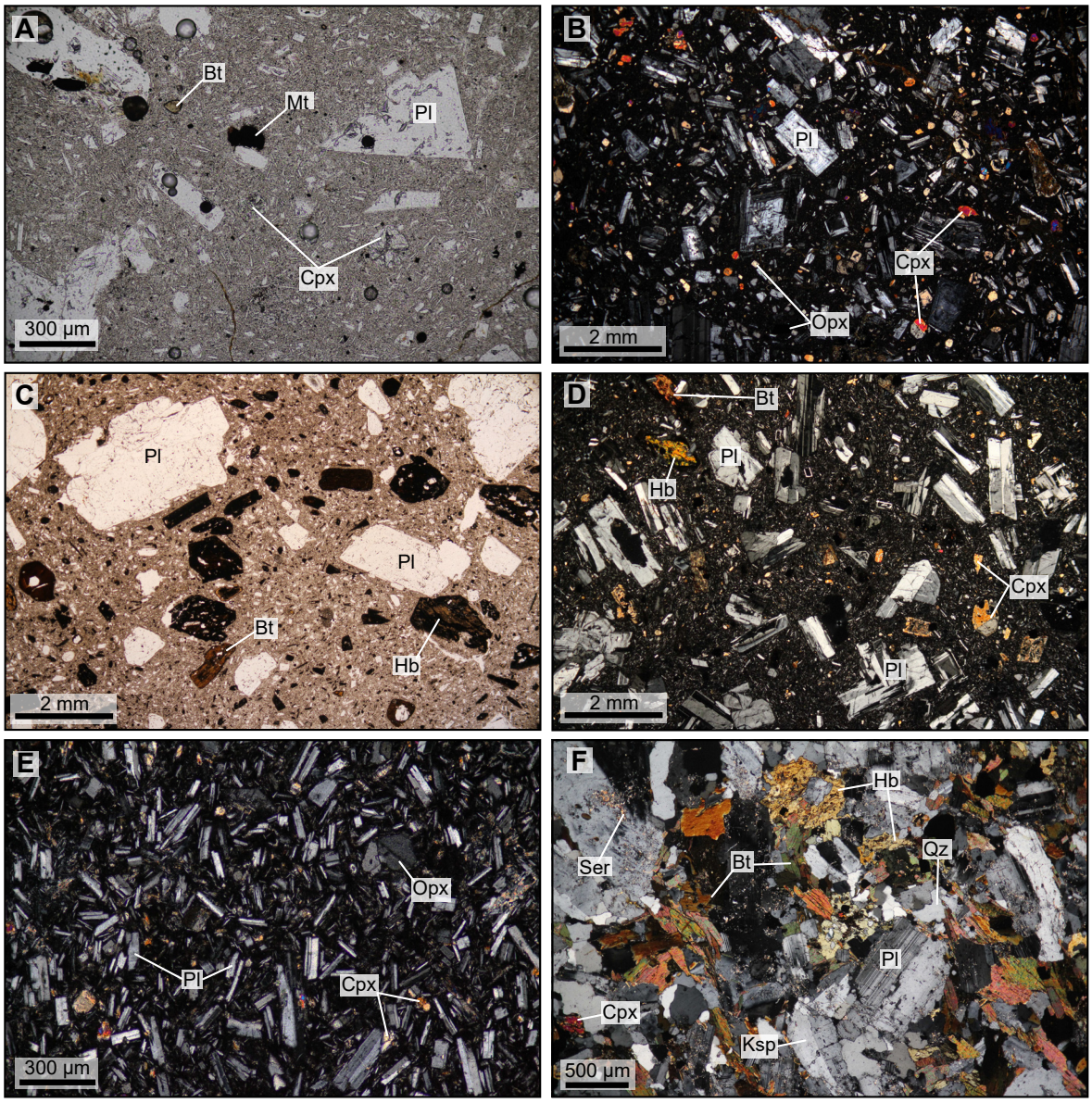

Figure 3.4 Optical microphotographs showing selected rock textures and minerals from central and eastern Anatolia. Detailed sample descriptions are in the appendix B (Table B.2); A. clinopyroxene-bearing andesite from Başdere at the Tekkedağ volcano (FR-15-40; plane-polarized light); B. two-pyroxene-bearing andesite from Öksüt at the Develidağ stratovolcano (FR-13-237; cross-polarized light); C. biotite-bearing andesite from Mihaliç tepe at the Konya volcanic complex (FR-14-59; plane-polarized light); D. clinopyroxene-bearing andesite from Hasançelebi at the Yamadağ volcanic complex (FR-14-82; cross-polarized light); E. two-pyroxene-bearing andesite from Idrisli in the Erzurum volcanic plateau (FR-14-117; cross-polarized light); F. monzonite from Diyadin in the Ağrı magmatic complex (FR-14-132; cross-polarized light).

3.3.2 Eastern Anatolia

Late Cenozoic magmatism in eastern Anatolia includes the westerly Yamadağ, Elazığ and Kepez volcanic complexes, Cevizlidere intrusions, Erzurum-Kars volcanic plateau, and easterly Ağrı and Sarıçimen plutonic complexes (Figure 3.5). The distribution of those magmatic complexes are controlled by the many strike-slip faults such as the Malatya, Ovacık, and Northern and Eastern Anatolian fault zones.

The western area of eastern Anatolia consists of the northerly late Oligocene Cevizlidere intrusions, the early to middle Miocene Yamadağ and southerly middle Miocene Kepez volcanic complexes. The NW-trending, elongated, late Oligocene porphyritic dioritic and granodioritic stocks of Cevizlidere intruded the Paleozoic limestones of the Malatya-Keban platform in the Ovacık pull-apart basin (26-25 Ma; İmer et al., 2014). The Yamadağ volcanic complex is composed of volcanoclastic deposits intercalated by basaltic andesitic to dacitic lava flows emplaced between 21 and 12 Ma along the NNE-trending, Malatya sinistral strike-slip fault (Figures 3.4D, 3.5 and 3.6A-B; Kürüm et al., 2008; Ekici et al., 2009; Chapter 2). The Kepez volcanic complex is dominated by dacitic lava flows and domes, successively overlain by andesitic and then basaltic lavas, south of the Yamadağ volcanic complex along the Malatya fault (ca. 16-13 Ma; Ekici, 2016).

The widespread late Miocene to Present Erzurum-Kars volcanic plateau dominates the eastern part of eastern Anatolia and the Lesser Caucasus region (Yılmaz et al., 1987; Pearce et al., 1990; Keskin et al., 1998; Keskin, 2003; Şengör et al., 2003; Keskin, 2007; Şengör et al., 2008; Neill et al., 2015). The Erzurum volcanic sequence includes andesite and dacite overlain by basaltic andesite pyroclastic deposits and lavas (Figures 3.4E and 3.6C-D; Yılmaz et al., 1987; Pearce et al., 1990; Kaygusuz et al., 2018). The Kars volcanic units are basaltic to rhyolitic lava flows and pyroclastic products (Pearce et al., 1990; Notsu et al., 1995; Keskin et al., 1998; Lebedev et al., 2010). The volcanic units of Erzurum and Kars suites are overlain by the mafic to felsic silicate saturated to undersaturated lavas of the Pliocene to Quaternary Nemrut, Süphan, Etrüsk, Tendürek and Ararat stratovolcanoes and Yiğitdağ volcanic suite (e.g.,

Keskin et al., 1998; Keskin, 2003; Lebedev et al., 2010; Özdemir and Güleç, 2013; Oyan et al., 2016). The stratovolcanoes are lined up along a NE-trending axis defined by the Nemrut-Ararat complexes, north of Lake Van. In addition, minor Quaternary basaltic lavas occur in the area of Elazığ, east of Kepez. The aforementioned late Miocene to Quaternary volcanic sequence covers the early Miocene monzonitic to granitic plutons of the Ağrı magmatic complex (Figures 3.4F and 3.6E-F; 21-17 Ma; Chapter 2) and the middle Miocene Sarıçimen quartz-monzonite that crops out along the Iranian border (13-11.5 Ma; Çolakoğlu and Arehart, 2010).

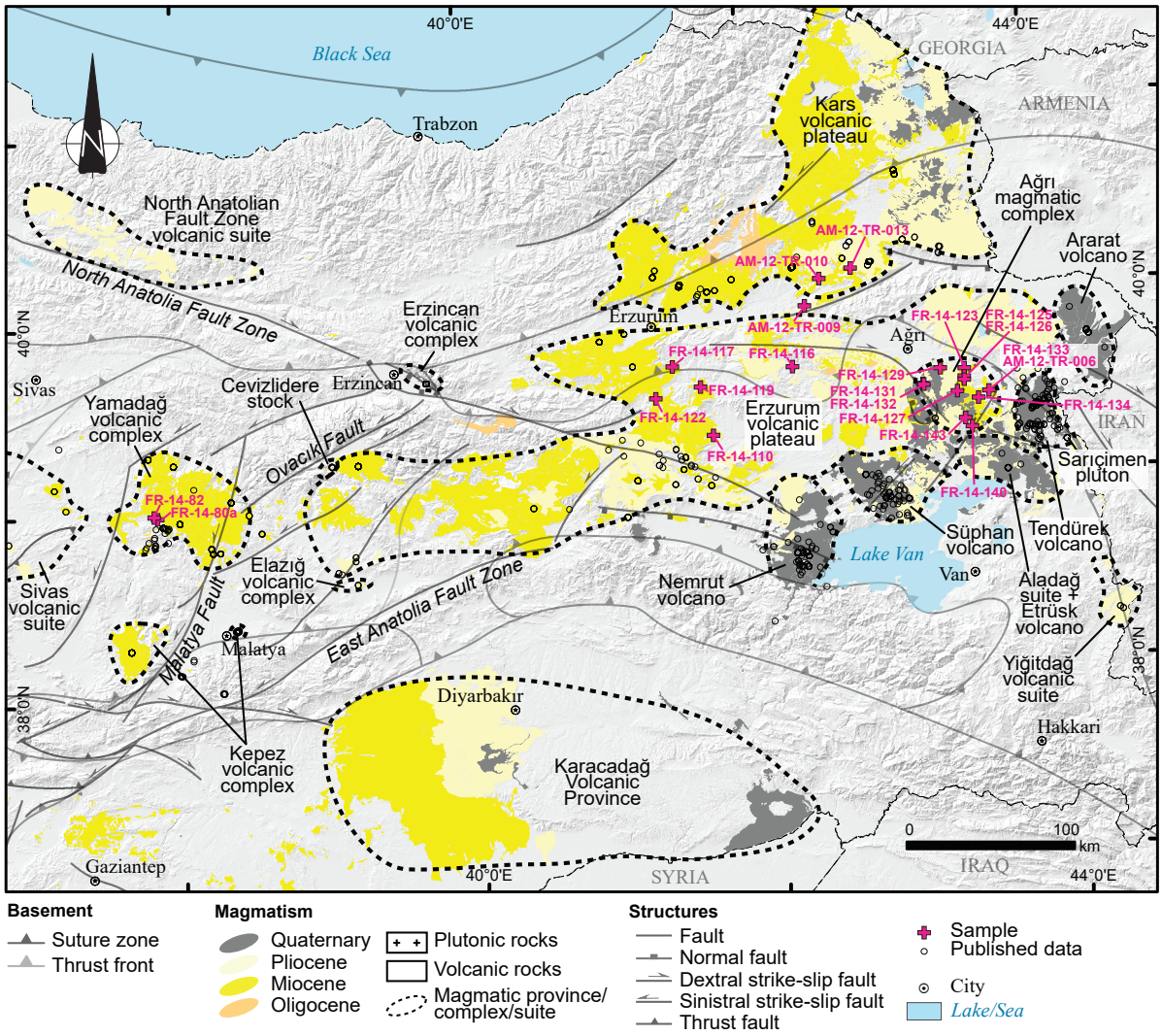

Figure 3.5 Magmatic map of eastern Anatolia (1:2,500,000 scale; Lambert Conic projection; European Datum 1950) showing the distribution of late Cenozoic igneous units (unit age modified from MTA, 2002), complexes and provinces, and regional structures. The locations of analyzed igneous rock samples and compiled geochemical data are indicated. Base map: SRTM 90 m digital elevation models (Jarvis et al., 2008).

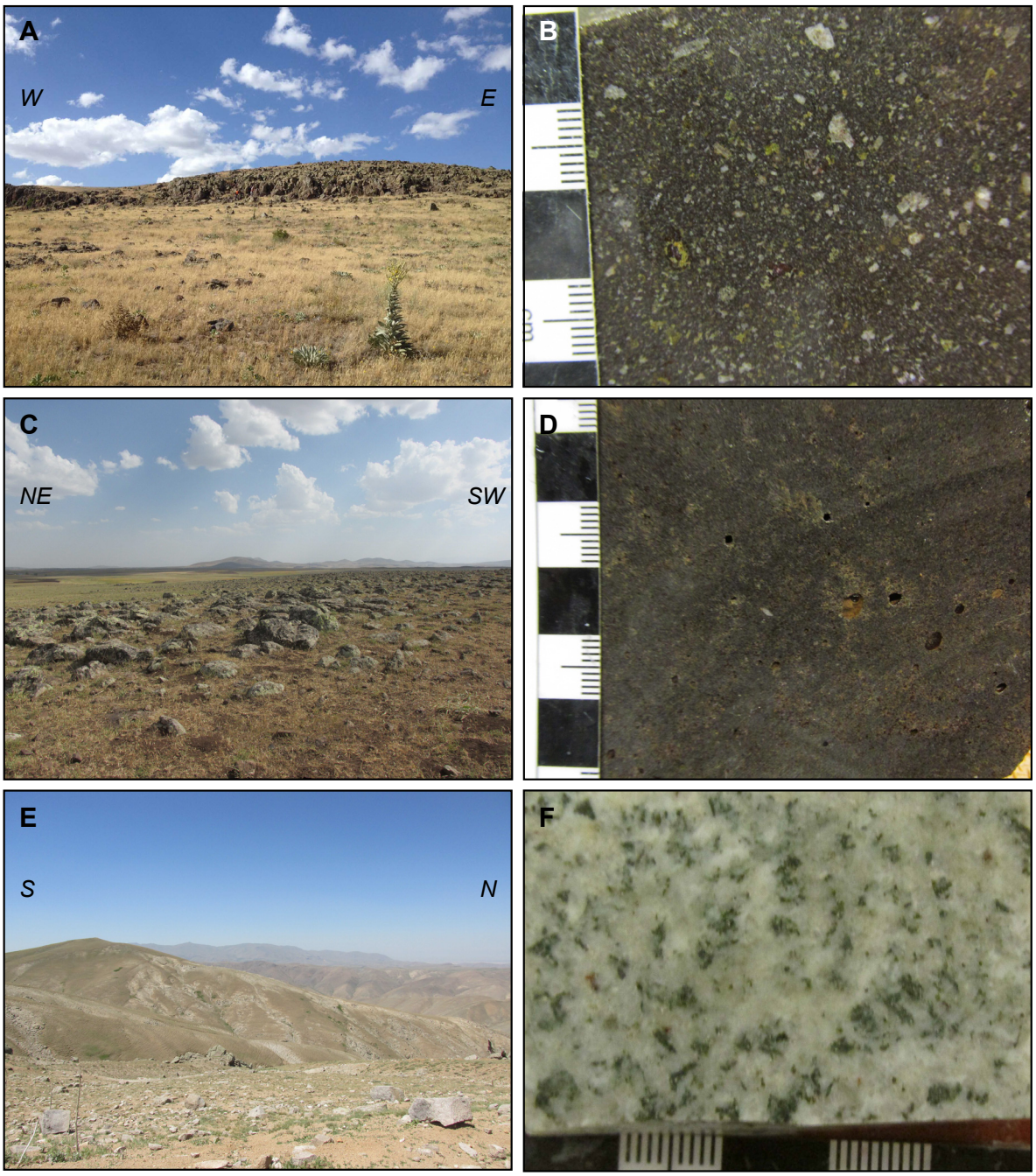

Figure 3.6 Photographs of representative magmatic complexes and rock samples from eastern Anatolia including: an andesitic lava flow at the Yamadağ volcanic complex, north of the town of Hasançelebi (A – B; FR-14-80), the basaltic plateau near the city of Erzurum as part of the Erzurum volcanic suite (C – D; FR-14-112), and the Taşlıçay (E) and Taşkapı granitic intrusions (F – FR-14-143) that belong to the Ağrı magmatic complex.

3.3.3 Other late Cenozoic magmatic domains in central and eastern Turkey

In addition to the late Cenozoic magmatic edifices in central and eastern Anatolia, contemporaneous volcanism occurred in the Galatia and Karacadağ Volcanic Provinces, and along the North Anatolian fault zone on the Rhodope-Pontide Block in northern Turkey and the Arabian platform after the initiation of the Arabia-Eurasia continental collision (Figure 3.1).

The Galatian Volcanic Province in the region of Ankara consists of a 2 km-thick volcano-sedimentary sequence composed of early to middle Miocene continental sediments and andesitic to rhyolitic lava flows, pyroclastic deposits and minor alkali basaltic to tranchyandesitic lavas that dominantly occurred between 20 and 16 Ma (Keller et al., 1992; Wilson et al., 1997; Tankut et al., 1998; Koçyiğit et al., 2003; Kurt et al., 2008).

The Karacadağ Volcanic Province is a shield volcano that produced intraplate-like basaltic lava flows along the lateral flanks of the N-trending fissure in the Arabian collisional foreland domain, south of the Bitlis suture zone (Lustrino et al., 2010; Keskin et al., 2012; Ekici et al., 2014). The volcanic lavas cover the Cretaceous to early Miocene sedimentary sequence of the Arabian platform and show a northward and eastward age migration from 11 Ma to Quaternary (Lustrino et al., 2010; Ekici et al., 2014).

The activation of the dextral North Anatolian Fault Zone in the late Miocene formed pull-apart basins such as the Niksar and Erzincan basins (McKenzie, 1972; Şengör, 1985) in which Quaternary trachyandesite to rhyolite domes and lavas emplaced (e.g., Adiyaman et al., 2001; Tatar et al., 2007; Karsli et al., 2008).

3.4 Methodology

3.4.1 Geochemical data compilation

This regional tectono-magmatic study is based on the compilation of previously-published whole-rock geochemical and Sr-Nd-Pb isotopic analyses from late Cenozoic igneous units in central and eastern Anatolia. Data were carefully filtered to generate a working database of 2270 analyses. All the analyses from altered or weathered samples, yielding a

total volatile content (LOI) greater than 5 wt % and acquired from enclaves, cumulates or xenoliths were eliminated. The published data were plotted in various standard classification diagrams and sorted into magmatic suites based on their age, spatial distribution and major element signatures (Table B.1). During this step, outlying compositions were discarded in order to increase the internal coherence of the database. Despite this screening procedure, the resultant database suffers from a lack of homogeneity, data control (QA-QC) and analytical differences as analyses were obtained through different analytical packages including variable set of elements, instrument (XRF, ICP-MS, INAA, etc.) and dissolution methods (total fusion, aqua regia, etc.) from various laboratories (Bureau Veritas, ActLabs, ALS, Universities, etc.). The report of Fe oxidation state in the literature suffers from some approximation despite a careful data compilation (e.g., Fe_2O_3, FeO, FeO_t and Fe_2O_{3t}).

Approximations also lie in sample age and location as this information is not always provided in the literature. Age data were provided by the regional compilation of radiometric data carried out in Chapter 2 whereas the samples without coordinates were places arbitrarily within their respective igneous complex.

Published Sr-Nd (n = 318) and Pb radiogenic isotope data (n = 124) were compiled from literature. All the published Sr and Nd isotopic data were obtained from whole-rock pulps. Their ratios were corrected to age to get initial isotopic ratios when the element concentration of Sr, Rb, Nd and Sm was available. Most of the published Pb analyses were bracketed by the SRM981 standard. As reference values varies among publications, all the published data were normalized to Galer and Abouchami (1998) like the new data set acquired in this study (see below). In addition, all those published Pb data were obtained from whole-rock pulps yielding various Th, U and Pb concentrations that thereby could have decayed through time. Therefore, age correction was carried out to get the initial Pb isotopic ratios.

3.4.2 Sample selection

To this compiled geochemical data set, new data from 35 rock samples were collected from igneous complexes throughout the Eastern Anatolian Magmatic Belt (Figures 3.4 and

3.5); analytical results and sample coordinates are in Tables 3.1 to 3.3; sample descriptions are in the appendix B (Table B.2). Most of the new data were acquired from the oldest and less-studied igneous complexes in the belt identified in Chapter 2. For example, in central Anatolia, the late Miocene to Pliocene Konya, Melendiz, Karaman, Tekkedağ and Develidağ volcanic edifices were preferentially sampled as opposed to the well-studied Quaternary Hasandağ and Erciyes stratovolcanoes, and Cappadocia-İncesu ignimbrite sequences (Figure 3.2). The early Miocene plutons of the Ağrı magmatic complex in eastern Anatolia were abundantly sampled; two samples from the oldest lavas of the early to middle Miocene Yamadağ volcanic complex were collected in addition to a selection of a few selected lava rocks in the late Miocene to Pliocene Erzurum and Kars volcanic suites (Figure 3.5). Only samples with basaltic to basaltic andesitic compositions (< 56 wt % SiO_2) were used on trace element diagrams in order to minimize the effects of crystal fractionation and crustal assimilation.

Among the rock samples analyzed for lithogeochemistry, seven samples from Konya (FR-14-61; FR-14-73), Melendiz (FR-15-34), Develidağ (FR-14-77), Yamadağ (FR-14-82) and Ağrı (FR-14-125; FR-14-140) were also analyzed for Sr-Nd-Pb radiogenic isotopic systematics where no or little data was available (Tables 3.2 and 3.3). Only the samples from Konya were not analyzed for Sr-Nd isotope systematics as reliable data were already available (Temel et al., 1998a).

3.4.3 Analytical techniques

3.4.3.1 Whole-rock lithogeochemistry

Lithogeochemical analyses were carried out at Bureau Veritas Mineral Laboratories in Vancouver, British Columbia, Canada. The concentration of major and trace elements were determined by X-ray fluorescence and ICP-MS, respectively, after total fusion of the material by lithium borate for all of the elements. Only the following elements: Mo, Cu, Pb, Zn, Ni, As, Cd, Sb, Bi, Ag, Au, Hg, Tl, Sc, Se and Te were analyzed after aqua regia dissolution. FeO concentration was obtained by titration on rock pulps. The degree of alteration and weathering were assessed petrographically prior to the rock selection (Table B.2) to exclude samples that

were affected by iron oxidation and hydrothermal sericite, potassic (biotite, alkali feldspar), chlorite, clay, silica and epidote alteration. Among the least-altered rocks analyzed, the samples, which yielded a total volatile content (LOI) greater than 5 wt %, were rejected. If the LOI content was between 1 and 5 wt %, the oxide content were proportionally recalculated based on the dry oxide total. The Mg # was calculated assuming a Fe^{3+}/Fe^{2+} ratio of 0.2 (McNab et al., 2017). Quality control and assessment is described in the Appendix B (Figure B.1; Table B.3 to B.7).

3.4.3.2 Sr-Nd-Pb isotopic geochemistry

The analyses of radiogenic isotope ratios were performed on whole-rock pulps (Sr and Nd) and hand-picked feldspar separates (Pb). Pb and Nd isotopic ratios were analyzed by the Nu Plasma 214 multi-collector ICP-MS whereas Sr isotopic ratios were obtained by the Triton TIMS instrument at PCIGR, The University of British Columbia in Canada, following the protocol described by Weis et al. (2006) and Fourny et al. (2016). Sample duplicates and replicates as well as certified reference material (USGS AGV-2, G-3) and standard (SRM981, SRM987, JNdi) were used for the quality assurance and control. The analyses of multiple blanks for those three isotopic systems allowed to monitor potential contamination during chemistry. Age correction was applied to all the measured Sr-Nd radiogenic isotopic ratios based on elemental Rb, Sr, Nd and Sm concentrations measured by the Thermo Finnigan Element2 high resolution ICP-MS instrument (Table B.8). The measured Sr reference material AGV-2 is $^{87}Sr/^{86}Sr = 0.703963 \pm 7$ and G-3 is $^{87}Sr/^{86}Sr = 0.709962 \pm 8$ and 0.709975 ± 9. The on-line data correction for mass fractionation was $^{86}Sr/^{88}Sr = 0.1194$. The average of measured SRM standard (n = 8) is $^{87}Sr/^{86}Sr = 0.710234 \pm 30$. The normalizing SRM987 value is 0.710248 (Weis et al., 2006). For Nd, the average (n = 2) of measured G-3 reference material is $^{143}Nd/^{144}Nd = 0.512241 \pm 15$. Data were first on-line corrected for mass fractionation ($^{146}Nd/^{144}Nd = 0.7219$) and then normalized to $^{143}Nd/^{144}Nd = 0.512116$ (JNdi; Tanaka et al., 2000) after sample-standard bracketing correction. In contrast, log-log correction was applied to Pb isotopic results because it yielded more reproducible replicates and showed lower sensitivity to residual matrix effects

on the MC-ICP-MS for those Pb analyses (Fourny et al., 2016). Data were normalized to $^{208}Pb/^{204}Pb = 36.7219$, $^{207}Pb/^{204}Pb = 15.4963$, and $^{206}Pb/^{204}Pb = 16.9405$ (Galer and Abouchami, 1998). Sr-Nd-Pb sample replicate, duplicate, standard analyses are reported in the appendix B (Tables B.8 to B.9). Measured Pb isotope ratios are assumed to be similar to the initial Pb isotope ratios of the sample magmatic source as feldspar are too young (< 25 Ma; Chapter 2) and have high Pb and low Th and U concentrations (Hemming et al., 1994).

3.5 Results

The Eastern Anatolian Magmatic Belt is composed of 25 late Cenozoic igneous complexes including the Sivas volcanic suite at the transition between central and eastern Anatolia. For this regional work, some small volcanic vents and suites were grouped together or to the closest prominent complex or stratovolcano (e.g., Hasandağ and Erciyes stratovolcanoes, İncesu and Cappadocia ignimbrites, and Erzurum and Kars volcanic plateaus). The igneous complexes are divided by Epoch as defined by the International Commission on Stratigraphy (Cohen et al., 2015). The Pleistocene and Holocene epochs are gathered into the Quaternary Period. Figures 3.2 and 3.5 illustrate the spatial distribution of those suites; their time ranges of emplacement are provided in Chapter 2. The following section characterizes the geochemical signature of those complexes using both previously-published and newly-acquired data (Table B.1). It is widely accepted in the literature that late Cenozoic magmatism in central and eastern Anatolia is either calc-alkaline or alkaline (e.g., Yılmaz, 1990; Keskin et al., 1998; Şen et al., 2004; Figure B.2).

3.5.1 Central Anatolia

3.5.1.1 Middle-Late Miocene

The late Miocene rocks from the Develidağ volcanic complex yield compositions ranging from basalt to andesite whereas Tekkedağ volcanic rocks are exclusively andesite (Figure 3.7A). The İncesu-Cappadocia ignimbrites of late Miocene age are more felsic ranging from dacitic to rhyolitic compositions and are associated with minor basaltic andesitic and

andesitic lavas. The volcanic rocks of the Konya complex are dominated by andesite and dacite with minor basaltic andesite, basaltic trachyandesite and trachyandesite. The middle Miocene Sulutas volcanic units, northeast of Konya, consist of trachybasalt, basalt and dacite and are associated with coeval lamprophyres (Asan and Ertürk, 2013). The Develidağ and Tekkedağ volcanic rocks are medium-K calc-alkaline, whereas the late Miocene lavas and pyroclastic deposits of the Konya, Sulutas and Tekkedağ volcanic complexes and İncesu-Cappadocian ignimbrites are medium- to high-K calc-alkaline (Figure 3.8A). The middle Miocene Konya lamprophyres have a shoshonitic affinity that contrasts with the other late Miocene volcanic suites in central Anatolia. On a N-MORB-normalized trace element spider diagram (Figure 3.9A), the late Miocene mafic volcanic rocks of central Anatolia have negative Ta and Nb and positive Ba anomalies relative to large ion lithophile elements (LILE). Those patterns resemble those from average upper crust (Gudnick and Gao, 2014) and continental arcs (Kelemen et al., 2014). On a chondrite-normalized rare earth element (REE) diagram (Figure 3.10A), the middle to late Miocene rocks of central Anatolia share a similar pattern including a moderate light REE (LREE) negative slope, and a flatter medium (MREE) and heavy REE (HREE) pattern. Only the İncesu-Cappadocia ignimbrites and lavas display a weak Eu negative anomaly. Late Miocene volcanic suites of central Anatolia have initial $^{87}Sr/^{86}Sr$ ratios ranging between 0.70379 and 0.70717, and initial $^{143}Nd/^{144}Nd$ ratios between 0.51239 and 0.512620 (Figure 3.11A-B). In addition, their initial $^{206}Pb/^{204}Pb$, $^{207}Pb/^{204}Pb$ and $^{208}Pb/^{204}Pb$ ratios fall between 18.455 and 19.075, 15.690 and 15.735, and 38.718 and 39.257, respectively (Figures 3.11D-G).

3.5.1.2 Pliocene

The Pliocene Karaman volcanic complex consists of andesitic volcanic rocks whereas those from the Melendiz complex display a broader compositional range from basalt and trachybasalt to rhyolite but are dominated by andesite (Figure 3.11B). The rare Pliocene ignimbrites from İncesu-Cappadocia are dacite. The Pliocene Karaman and İncesu-Cappadocia volcanic rocks form a high-K calc-alkaline suite. Those contrast with the Melendiz volcanic rock suite that contains both medium- and high-K calc-alkaline with minor shoshonitic rocks

Table 3.1 Major, trace and rare earth element compositions of rock samples from central and eastern Anatolian igneous complexes.

	Central Anatolia						
Sample #	**FR-13-181**	**FR-14-74**	**FR-14-65[a]**	**FR-14-61**	**FR-14-73**	**FR-14-59**	**FR-14-75a**
Locality	Inlice	Inlice	Inlice	Oğlakçı	Doğanbey	Karaman	Çömlekçı
Lat (°N)	37.751	37.757	37.756	37.584	37.823	37.394	38.085
Long (°E)	32.075	32.066	32.087	32.009	31.946	33.138	34.348
Igneous complex	Konya	Konya	Konya	Konya	Konya	Karaman	Melendiz
Rock type	Andesite	Andesite	Andesite	Andesite	Andesite	Andesite	Andesite
Age (Ma)[c]	8.67 ± 0.13	Late Miocene	Late Miocene	Late Miocene	10.21 ± 0.13	Late Miocene	Pliocene
SiO_2	62.7	61.6	55.4	61.0	59.9	62.3	61.4
TiO_2	0.60	0.61	0.82	0.62	0.73	0.51	0.54
Al_2O_3	16.28	16.18	16.77	16.95	15.79	16.71	17.11
$Fe_2O_{3\,(t)}$	4.81	5.02	6.39	4.51	5.61	4.39	5.26
FeO	1.02				0.58		2.2
CaO	4.68	4.61	4.95	4.06	4.38	5.53	6.07
MgO	1.97	2.00	3.47	1.00	1.41	2.7	3.01
Na_2O	3.56	3.42	2.93	3.05	3.03	3.67	3.58
K_2O	3.12	3.08	2.78	2.72	2.99	2.48	2.06
MnO	0.09	0.08	0.1	0.03	0.06	0.09	0.08
P_2O_5	0.24	0.24	0.37	0.21	0.20	0.28	0.18
Cr_2O_3	<0.001	0.002	<0.001	<0.001	<0.001	0.002	0.005
SO_3	<0.002	<0.002	0.024	0.071	<0.002	<0.002	<0.002
V_2O_5	0.020	0.030	0.026	0.025	0.028	0.02	0.019
LOI	1.37	1.62	5.66	3.04	2.8	0.66	0.86
TOTAL	101.04	100.29	99.87	100.42	99.78	99.54	100.28
Mg#	50.8	50.0		35.8	38.7	60.8	59.0
Ba	1070	1038	1142	915	795	764	472
Be	<1	4	1	3	2	4	<1
Co	11.4	10.8	14.1	24.7	10	12.9	15.7
Cs	5	4.1	0.7	2.1	6.2	3.2	1.9
Ga	15.4	15.1	16.2	16.1	16.4	14.6	13.2
Hf	4.4	4.1	4.7	4.5	4.8	3.3	2.7
Nb	12.2	11.1	10.8	11.1	12.7	16.3	9.2
Rb	100.2	98.7	82.9	100.9	117.8	78.8	60.8
Sn	2	1	1	2	1	<1	<1
Sr	742	702.5	698.2	566.6	597.7	838.6	481.2
Ta	1	0.9	0.7	1	1.2	1.1	0.7
Th	22	21.3	15.8	17.9	19.8	20	10.2
U	7.5	7.6	4.7	5.6	7.4	7.4	3.3
V	91	154	155	147	168	114	104
W	0.7	1.8	1.3	1.3	3	0.7	0.8
Zr	174.6	160.7	178.8	179.3	179.4	137.1	108.2
Y	21.5	21.1	24.2	84.7	24.1	14	14.1
La	48.2	49	45.6	48.8	41.5	47.3	28.3
Ce	88.2	81.4	78.1	97.5	70.3	74.4	46.7
Pr	8.77	8.81	9.08	11.89	7.78	7.61	4.78
Nd	30.5	32.1	33.3	51.4	28.9	25.8	17
Sm	5.45	5.37	5.97	11.63	5.17	3.87	2.94
Eu	1.22	1.29	1.47	4	1.19	1.05	0.82
Gd	4.53	4.61	5.14	14.08	4.79	3.26	2.81
Tb	0.66	0.68	0.77	2.16	0.72	0.43	0.42
Dy	3.67	3.89	4.15	12.89	4.38	2.4	2.4
Ho	0.76	0.76	0.81	2.74	0.9	0.47	0.48
Er	2.15	2.34	2.33	7.46	2.61	1.28	1.39
Tm	0.32	0.33	0.33	1.09	0.38	0.21	0.21
Yb	2.13	2.37	2.42	6.74	2.62	1.31	1.48
Lu	0.33	0.36	0.35	1.05	0.4	0.2	0.24
Mo	0.7	0.4	0.5	0.4	0.7	0.8	0.8
Cu	12.7	9.6	12.7	32.8	5.4	17.2	20.6
Pb	1.6	6.8	3.8	6.7	3.5	2.5	3.8
Zn	32	35	74	87	41	26	25
Ni	8.7	5.3	3.1	5.9	3	11.3	15.2
As	<0.5	0.7	<0.5	2.7	1.3	0.6	0.9
Cd	<0.1	<0.1	<0.1	0.1	<0.1	<0.1	<0.1
Sb	<0.1	0.1	<0.1	<0.1	0.2	<0.1	0.1
Bi	<0.1	<0.1	<0.1	0.4	<0.1	<0.1	<0.1
Ag	<0.1	<0.1	<0.1	<0.1	<0.1	<0.1	<0.1
Au	0.5	<0.5	<0.5	0.8	<0.5	2.1	<0.5
Hg	<0.01	<0.01	<0.01	<0.01	<0.01	<0.01	<0.01
Tl	<0.1	<0.1	<0.1	0.2	<0.1	<0.1	<0.1
Se	<0.5	<0.5	<0.5	<0.5	<0.5	<0.5	<0.5
Sc	3.3	5.8	8.8	6.2	10.9	2.7	2.3
Te	<1	<0.2	<0.2	<0.2	<0.2	<0.2	<0.2

Table 3.1 (Continued) Major, trace and rare earth element compositions of rock samples from central and eastern Anatolian igneous complexes.

	Central Anatolia						
Sample #	**FR-15-34**	**FR-15-37**	**FR-15-40**	**FR-13-234[a]**	**FR-13-235**	**FR-14-77**	**FR-13-254**
Locality	Balcı	Boz tepe	Başdere	Öksüt	Öksüt	Öksüt	Öksüt
Lat (°N)	37.978	38.030	38.548	38.284	38.284	38.285	38.289
Long (°E)	34.476	34.525	35.113	35.508	35.508	35.508	35.512
Igneous complex	Melendiz	Melendiz	Tekkedağ	Develidağ	Develidağ	Develidağ	Develidağ
Rock type	Andesite	Andesite	Andesite	Andesite	Andesite	Andesite	Andesite
Age (Ma)[c]	Pliocene	Pliocene	Late Miocene	Late Miocene	Late Miocene	Late Miocene	5.36 ± 0.20
SiO_2	62.1	62.2	61.5	55.9	59.0	58.8	62.6
TiO_2	0.59	0.52	0.68	0.69	0.68	0.69	0.73
Al_2O_3	16.69	15.31	17.88	16	16.60	16.27	16.54
$Fe_2O_{3\,(t)}$	4.69	3.22	3.96	5.62	4.73	5.24	5.4
FeO	1.88		0.70			1.87	
CaO	5.96	4.01	4.73	5.83	5.48	5.45	4.83
MgO	2.66	2.47	0.59	4.4	2.69	2.91	3.12
Na_2O	3.57	2.94	3.88	3.24	3.77	3.71	3.88
K_2O	2.13	2.82	2.71	1.48	1.85	1.79	2.35
MnO	0.08	0.06	0.04	0.09	0.07	0.09	0.08
P_2O_5	0.19	0.14	0.17	0.13	0.19	0.19	0.17
Cr_2O_3	0.002	0.007	0.002	0.016	0.010	0.009	0.009
SO_3	0.003	0.034	<0.002	1.192	0.108	0.098	<0.002
V_2O_5	0.017	0.016	0.024	0.025	0.019	0.020	0.019
LOI	0.48	2.95	1.7	6.15	2.59	2.46	0.96
TOTAL	99.3	99.72	99.69	100.89	100.53	100.24	100.86
Mg#	58.8	65.9	27.3		58.8	58.3	59.3
Ba	390	469	477	380	539	524	562
Be	3	4	4	<1	<1	3	<1
Co	14.5	11	18.1	20.2	20.3	17.5	15.8
Cs	1.8	5.1	2.7	0.5	1	0.6	1.8
Ga	16.1	16.7	17.3	14.3	15.3	16	14.7
Hf	3.4	4.5	5.1	3	3.8	3.8	4.4
Nb	10.3	13.2	10	5.5	8.2	8.5	9
Rb	69.8	129.2	97.9	32.7	52.7	52.2	68.3
Sn	<1	<1	1	<1	<1	<1	<1
Sr	453.2	476.7	380.6	433.5	467.7	473.4	377.3
Ta	0.8	0.9	0.9	0.5	0.6	0.6	0.6
Th	16.2	23.1	16	7.9	10.1	9	12.2
U	4.7	6.2	4.8	2.6	3.2	2.7	3.9
V	95	91	127	109	87	120	81
W	1.8	3.1	1.5	1.3	0.8	0.7	1.6
Zr	132.7	173.5	189.6	111.9	153	157.3	162.9
Y	14.4	16.5	32	15.7	16.5	15.1	19.5
La	26.8	34.5	33.1	16.7	25.2	24.3	28.1
Ce	46.9	63.7	59.9	32	47	42.9	51.2
Pr	4.96	6.49	6.8	3.41	4.94	4.68	5.61
Nd	18.1	22.6	25.6	13.9	18.7	16.8	21.7
Sm	3.29	3.88	5.51	2.75	3.82	3.21	3.98
Eu	0.9	1.03	1.57	0.86	1.1	0.96	1.02
Gd	2.99	3.51	6.46	2.95	3.67	3.43	3.97
Tb	0.44	0.48	0.97	0.47	0.56	0.49	0.6
Dy	2.59	2.82	5.99	2.78	3.05	2.93	3.43
Ho	0.52	0.57	1.19	0.59	0.63	0.58	0.67
Er	1.56	1.69	3.44	1.7	1.86	1.57	1.85
Tm	0.22	0.26	0.46	0.25	0.26	0.24	0.29
Yb	1.48	1.74	2.94	1.67	1.75	1.59	1.83
Lu	0.24	0.27	0.45	0.25	0.26	0.25	0.29
Mo	0.5	0.2	0.6	1.5	1.2	0.6	2.1
Cu	17	6.7	13.5	44.6	31.6	27.5	23.4
Pb	2.2	2.5	1.5	5.1	5.2	6.2	5.1
Zn	14	5	120	78	45	47	27
Ni	10.5	6	9.7	44.6	29.6	23.5	10
As	1	<0.5	<0.5	5.7	3	3.2	1.4
Cd	<0.1	<0.1	0.5	0.1	<0.1	<0.1	<0.1
Sb	0.3	<0.1	<0.1	<0.1	0.1	<0.1	0.2
Bi	<0.1	<0.1	<0.1	<0.1	<0.1	<0.1	<0.1
Ag	<0.1	<0.1	<0.1	<0.1	<0.1	<0.1	<0.1
Au	<0.5	<0.5	<0.5	8.6	<0.5	<0.5	<0.5
Hg	<0.01	<0.01	<0.01	0.01	0.02	<0.01	<0.01
Tl	<0.1	<0.1	<0.1	<0.1	<0.1	<0.1	<0.1
Se	<0.5	<0.5	<0.5	<0.5	<0.5	<0.5	<0.5
Sc	1.5	2.6	5.9	8.8	4.2	4.5	2.6
Te	<1	<1	<1	<1	<1	<0.2	<1

Table 3.1 (Continued) Major, trace and rare earth element compositions of rock samples from central and eastern Anatolian igneous complexes.

	Eastern Anatolia									
Sample #	**FR-14-80a**	**FR-14-82**	**FR-14-110**	**FR-14-116**	**FR-14-117**	**FR-14-119**	**FR-14-122a**	**FR-14-123**	**FR-14-125**	**FR-14-126**
Locality	Hasançelebi	Hasançelebi	Hınıs	Köyceğiz	Katranlı	Güneşli	Gökoğlan	Taşlıçay	Taşlıçay	Taşlıçay
Lat (°N)	38.999	39.008	39.326	39.664	39.702	39.587	39.537	39.589	39.545	39.528
Long (°E)	37.847	37.823	41.674	42.248	41.421	41.606	41.294	43.427	43.423	43.421
Igneous complex	Yamadağ	Yamadağ	Hınıs-Muş	Hınıs-Muş	Hınıs-Muş	Hınıs-Muş	Hınıs-Muş	Ağrı	Ağrı	Ağrı
Rock type	Basaltic andesite	Andesite	Trachy-andesite	Basalt	Andesite	Andesite	Basaltic trachyandesite	Granite	Granite	Granite
Age[c] (Ma)	Early Miocene	21.23 ± 0.33	Late Miocene - Pliocene	Late Miocene - Pliocene	Late Miocene - Pliocene	Late Miocene - Pliocene	Late Miocene - Pliocene	Early Miocene	Early Miocene	Early Miocene
SiO_2	53.7	59.5	56.5	47.7	59.2	60.0	52.5	77	76.6	71.5
TiO_2	0.68	0.64	1.72	1.42	0.72	0.66	1.92	0.18	0.14	0.27
Al_2O_3	15.63	17.10	16.42	16.54	16.54	16.45	17.76	13.07	12.57	14.74
$Fe_2O_{3\,(t)}$	6.23	5.35	8.65	10.52	5.23	4.83	9.6	0.51	0.67	1.98
FeO		0.51							0.22	
CaO	6.71	5.90	5.49	9.82	6.70	5.82	7.44	0.23	0.49	1.62
MgO	2.44	1.42	2.3	8.34	3.65	1.98	4.4	0.14	0.1	0.54
Na_2O	3.79	3.85	4.91	3.63	3.96	4.14	4.31	3.78	3.74	4.34
K_2O	2.06	1.83	2.31	0.84	1.43	1.87	1.47	4.71	4.79	3.97
MnO	0.14	0.17	0.11	0.17	0.07	0.07	0.15	<0.01	0.03	0.08
P_2O_5	0.17	0.17	0.42	0.36	0.29	0.40	0.44	0.03	0.01	0.07
Cr_2O_3	0.010	<0.001	<0.001	0.031	0.020	0.012	0.004	<0.001	<0.001	<0.001
SO_3	0.005	<0.002	0.004	<0.002	<0.002	<0.002	<0.002	<0.002	<0.002	<0.002
V_2O_5	0.027	0.024	0.03	0.037	0.019	0.015	0.03	<0.002	<0.002	0.006
LOI	3.72	2.06	0.71	0.41	1.11	1.75	0.08	0.74	0.37	0.63
TOTAL	99.03	100.07	99.69	99.89	100.21	99.88	100.19	100.44	99.51	99.95
Mg#	49.7	40.1	40.1	66.6	63.7	50.8	53.6	40.9	27.3	40.7
Ba	332	437	370	291	437	563	285	562	166	944
Be	<1	<1	<1	<1	2	<1	<1	<1	2	<1
Co	16.6	13.6	20.5	41	18.1	14	28.9	0.3	0.6	2.5
Cs	3.2	0.5	1.9	0.6	1	0.9	0.3	1	1.7	1.6
Ga	15.9	14.9	16.7	17.2	16.6	16.6	18.3	11.6	14.4	15.1
Hf	3.2	3.2	6.4	3.2	3.5	4	5.7	3.9	4	5.6
Nb	7.2	10.9	17.7	10.2	15.3	19.2	15.4	32.3	39.9	32
Rb	36	46.8	71.5	18.5	37.2	49	24.6	130.1	110.2	99.3
Sn	<1	<1	2	2	3	<1	2	1	2	2
Sr	477.9	456.2	472.4	461.7	498.2	493.4	455.7	54.2	32.9	197.3
Ta	0.6	0.9	1.1	0.7	0.9	1.4	0.9	2.3	3	2.5
Th	4.5	7.4	10.6	4.3	7	9.8	5	20	27.9	21.7
U	1.1	2.1	3.3	0.9	2.1	2.5	1.3	2.3	5.9	4.1
V	165	141	158	210	111	91	169	9	<8	30
W	<0.5	0.6	1.4	<0.5	0.7	12.1	1.3	2.2	1.3	0.7
Zr	118.4	133.7	297.8	153.4	159.8	181.4	251	124.1	94.2	201.1
Y	17.5	21.9	29.1	27.1	12.2	20	27.6	19.1	11.6	20.9
La	15.4	21	33.6	19.9	29.6	42.8	26.5	42.1	27.6	50.7
Ce	29.3	36	67.1	40.8	46.4	62	50.7	71.7	46.9	87.9
Pr	3.6	4.22	7.51	5.07	5.11	7.25	6.51	7.63	4.38	8.8
Nd	15	17	29.5	20.7	18	24.4	26.7	24.6	11.8	28.4
Sm	3.12	3.32	5.67	4.45	3.04	4.25	5.83	3.97	1.66	4.61
Eu	1.01	0.96	1.61	1.48	0.99	1.29	1.72	0.49	0.29	0.89
Gd	3.52	3.44	5.48	4.81	3.15	4.22	5.95	3.55	1.45	4
Tb	0.55	0.55	0.83	0.79	0.42	0.58	0.84	0.52	0.24	0.57
Dy	3.21	3.5	5.11	5.18	2.32	3.38	5.11	3.22	1.44	3.48
Ho	0.65	0.76	0.92	1.1	0.42	0.61	0.99	0.64	0.35	0.66
Er	2.02	2.15	2.93	2.91	1.25	1.71	2.87	1.83	1.39	2.22
Tm	0.27	0.33	0.4	0.43	0.17	0.25	0.39	0.31	0.25	0.35
Yb	1.9	2.3	2.79	3.03	1.2	1.52	2.72	2.07	1.93	2.55
Lu	0.29	0.37	0.39	0.48	0.17	0.24	0.41	0.33	0.35	0.4
Mo	1.2	0.4	1.6	1	1.3	0.3	0.5	0.2	0.1	0.3
Cu	14.8	14.7	34.2	53.5	34.1	22.2	26.5	2.3	2	1.8
Pb	2	1.6	4.7	1.1	3.9	2.4	1.6	1.1	1.9	3.3
Zn	52	30	76	71	41	44	57	3	8	26
Ni	9.5	5.8	4.7	125.2	27	41.8	28.3	1.2	0.5	0.9
As	1.1	<0.5	2	0.9	1.2	1.5	0.8	<0.5	0.5	0.7
Cd	<0.1	0.1	<0.1	<0.1	<0.1	<0.1	<0.1	<0.1	<0.1	<0.1
Sb	<0.1	<0.1	0.1	<0.1	<0.1	<0.1	<0.1	<0.1	<0.1	<0.1
Bi	<0.1	<0.1	<0.1	<0.1	<0.1	<0.1	<0.1	<0.1	0.2	<0.1
Ag	<0.1	<0.1	<0.1	<0.1	<0.1	<0.1	<0.1	<0.1	<0.1	<0.1
Au	<0.5	<0.5	<0.5	<0.5	1	2.2	<0.5	<0.5	<0.5	<0.5
Hg	<0.01	<0.01	0.01	<0.01	<0.01	<0.01	<0.01	<0.01	<0.01	<0.01
Tl	<0.1	<0.1	<0.1	<0.1	<0.1	<0.1	<0.1	<0.1	<0.1	0.1
Se	<0.5	<0.5	<0.5	0.6	<0.5	<0.5	<0.5	<0.5	<0.5	<0.5
Sc	13.7	7	3.2	1.6	3.6	5.6	2	0.6	0.6	2
Te	<1	<0.2	<0.2	<0.2	<0.2	<0.2	<0.2	<0.2	<0.2	<0.2

Table 3.1 (Continued) Major, trace and rare earth element compositions of rock samples from central and eastern Anatolian igneous complexes.

	Eastern Anatolia										
Sample #	**FR-14-127**	**FR-14-129**	**FR-14-131**	**FR-14-132**	**FR-14-133**	**FR-14-134**	**FR-14-140**	**FR-14-143**	**AM-12-TR-005[b]**	**AM-12-TR-006**	**AM-12-008A**
Locality	Yeltepe	Oğlaklı	Demirkapı	Demirkapı	Ulukent	Kotancı	Taşkapı	Gergili	Taşlıçay	Taşlıçay	Tahir
Lat (°N)	39.471	39.599	39.523	39.519	39.460	39.427	39.276	39.323	43.502	43.569	42.430
Long (°E)	43.368	43.264	43.133	43.142	43.584	43.508	43.451	43.408	39.600	39.396	39.824
Igneous complex	Ağrı	Ağrı	Ağrı	Ağrı	Ağrı	Ağrı	Ağrı	Ağrı	Ağrı	Ağrı	Kars
Rock type	Trachy-andesite	Monzonite	Monzonite	Monzodiorite	Trachyte	Monzonite	Monzonite	Granite	Alkalic gabbro	Monzodiorite	Basaltic trachyandesite
Age (Ma)[c]	Early Miocene	21.32 ± 0.29	Early Miocene	Early Miocene	Early Miocene	Early Miocene	Early Miocene	Early Miocene	Early Miocene	Early Miocene	Late Miocene - Pliocene
SiO_2	59.8	59.7	56.3	53.6	64.5	61.3	61.7	67.3	46.6	56.6	55.6
TiO_2	1.08	0.60	0.87	0.84	1.07	0.32	0.50	0.59	2.66	0.81	0.92
Al_2O_3	16.84	15.61	18.82	17.67	16.71	16.08	15.13	16.35	13.84	17.48	16.98
$Fe_2O_{3\,(t)}$	6.23	4.84	5.11	7.01	4.14	2.49	5.34	1.38	14.30	7.25	5.83
FeO			1.50					0.80	10.04	3.86	1.18
CaO	4.57	1.45	7.04	7.29	2.37	3.16	0.29	4.11	9.45	7.18	6.55
MgO	2.28	3.18	3.59	3.49	0.58	0.64	1.13	2.09	6.59	3.61	2.81
Na_2O	4.65	4.50	6.42	3.43	5.25	7.36	2.13	6.03	3.31	3.93	4.33
K_2O	3.03	3.36	0.50	2.79	4.64	0.90	5.23	0.53	0.21	1.98	2.40
MnO	0.13	0.07	0.03	0.12	0.06	0.14	0.11	0.01	0.22	0.14	0.05
P_2O_5	0.43	0.16	0.49	0.46	0.32	0.12	0.13	0.14	0.26	0.28	0.53
Cr_2O_3	0.006	<0.001	0.002	0.003	<0.001	<0.001	<0.001	<0.001	0.007	0.004	<0.004
SO_3	<0.002	0.014	<0.002	<0.002	<0.002	0.049	<0.002	<0.002	<0.002	<0.002	<0.002
V_2O_5	0.022	0.018	0.048	0.031	0.01	0.007	0.016	0.018	0.045	0.038	0.025
LOI	0.89	3.03	0.95	1.98	0.51	3.74	4.12	1.14	2.27	0.49	1.97
TOTAL	100.17	99.63	100.26	100.88	100.34	100.04	99.91	100.92	99.8	99.92	100.14
Mg#	48.0	62.3	63.9	55.6	26.1	39.4	34.8	79.1	53.7	55.6	54.8
Ba	625	839	265	954	787	668	813	135	16	670	662
Be	2	<1	3	2	<1	1	<1	3	2	2	1
Co	15.9	8.8	7.1	17.9	4.1	3.6	10.5	2.4	29.3	19.2	18.1
Cs	1.9	0.8	0.2	2.2	5.1	0.5	6.1	0.8	<0.1	1.8	0.5
Ga	17.6	15.4	18.1	17.3	17.8	15.4	14.3	14.7	20.6	16.9	17.9
Hf	6.4	4.8	5.7	5.4	11.2	4.5	4.9	4.3	5.4	2.9	5
Nb	22.9	13.9	12.7	15.8	45.1	21.4	10.7	12.8	23.3	8.5	27.8
Rb	85.8	74.1	7.6	87.5	169	27.3	161.8	14	0.7	61.2	53.9
Sn	2	2	3	2	4	2	1	4	1	1	1
Sr	423.5	140.4	651.5	636.8	279.9	504.9	53.9	361.6	267.8	582.8	790.1
Ta	1.3	1	0.8	0.8	2.7	1.8	0.8	1.1	1.6	0.6	1.5
Th	14.7	12.1	12.7	8.6	28.6	11.9	14.4	15.3	3.3	10.6	13.4
U	3.9	4.5	1.9	2.1	8.4	2.1	2.9	4	0.7	3.5	3.3
V	116	102	270	168	52	28	94	98	259	209	128
W	1.3	1.4	<0.5	<0.5	2.8	2.1	2.3	0.7	1.1	0.8	1.1
Zr	291.2	187.9	252.7	228.3	514.3	171.6	190.7	166.8	199.9	116.8	193.8
Y	41.7	20.8	19.2	23.8	42.5	19.7	13.4	23.6	36.7	18.3	16.1
La	68.2	30.4	35.6	40.9	78.2	40.4	21.7	11.9	20.6	33.4	47.2
Ce	95	51.7	73.2	78.9	132.6	68.9	37.7	32.8	46.4	60.7	83
Pr	14.12	6.36	8.97	9.46	16.92	7.85	4.12	5.16	6.18	6.7	9.36
Nd	50	23.1	31.7	35.8	58.6	26.5	14.7	21.7	29.1	25.5	33.2
Sm	8.63	4.36	5.15	6.26	10.29	4.19	2.58	5.11	6.05	4.41	5.21
Eu	2.02	0.99	1.46	1.62	2.12	1	0.83	1	2.03	1.35	1.43
Gd	8.88	3.8	4.78	5.59	9.37	3.96	2.64	4.93	6.89	3.7	4.27
Tb	1.24	0.59	0.65	0.78	1.33	0.58	0.39	0.74	1.09	0.54	0.56
Dy	7.41	3.54	3.66	4.67	7.97	3.55	2.54	4.2	6.57	3.1	3.2
Ho	1.36	0.71	0.69	0.82	1.49	0.71	0.51	0.8	1.36	0.64	0.55
Er	4.1	2.08	1.93	2.48	4.36	2.21	1.59	2.47	3.67	1.82	1.65
Tm	0.59	0.33	0.28	0.36	0.63	0.34	0.25	0.38	0.53	0.27	0.22
Yb	3.8	2.16	1.96	2.2	4.02	2.33	1.72	2.46	3.32	1.72	1.55
Lu	0.57	0.35	0.28	0.33	0.63	0.36	0.29	0.38	0.47	0.28	0.21
Mo	1.7	0.1	<0.1	0.2	2.5	0.6	3.9	<0.1	0.8	0.4	1.3
Cu	15.1	1.4	1.9	22.5	2.4	6.3	64.4	1.2	0.6	14.5	29
Pb	2.8	0.5	3.8	4.6	9.7	5.5	1	2.4	1.5	3.1	5.8
Zn	56	42	9	52	87	37	44	4	27	23	53
Ni	21.6	9	11.3	11	2	0.8	6.7	1.5	5.5	5.6	106.3
As	1.3	1	1.1	0.9	1.5	<0.5	0.8	1.1	<0.5	0.6	0.7
Cd	0.2	<0.1	<0.1	<0.1	<0.1	<0.1	<0.1	<0.1	<0.1	<0.1	<0.1
Sb	<0.1	<0.1	<0.1	<0.1	0.1	<0.1	<0.1	0.2	<0.1	<0.1	0.1
Bi	<0.1	<0.1	<0.1	<0.1	0.1	<0.1	<0.1	<0.1	<0.1	<0.1	0.2
Ag	<0.1	<0.1	<0.1	<0.1	<0.1	<0.1	<0.1	<0.1	<0.1	<0.1	<0.1
Au	<0.5	0.5	<0.5	<0.5	<0.5	0.7	0.7	<0.5	<0.5	<0.5	0.9
Hg	<0.01	<0.01	<0.01	<0.01	<0.01	<0.01	<0.01	0.01	<0.01	<0.01	<0.01
Tl	0.3	<0.1	<0.1	0.4	0.1	<0.1	<0.1	<0.1	<0.1	0.2	<0.1
Se	<0.5	<0.5	<0.5	<0.5	<0.5	<0.5	<0.5	<0.5	<0.5	<0.5	<0.5
Sc	5.6	4.9	4.6	6.3	5.3	1.9	3	2.7	-	-	-
Te	<0.2	<0.2	<0.2	<0.2	<0.2	<0.2	<0.2	<0.2	-	-	-

[a] Altered sample (LOI > 5 wt %) [b] Altered sample (very low LILE: Ba, Sr, Cs, Th, U) [c] U-Pb age data from Chapter 2

Table 3.2 Radiogenic Sr and Nd isotope data from selected late Cenozoic igneous units in central and eastern Anatolia

Samples[a]	Igneous complex	Age[b] (Ma)	Rb (ppm)	Sr (ppm)	$^{87}Sr/^{86}Sr$	±2σ	$(^{87}Sr/^{86}Sr)_i$	Sm (ppm)	Nd (ppm)	$^{143}Nd/^{144}Nd$	±2σ	$(^{143}Nd/^{144}Nd)_i$	ε_{Nd}	$(\varepsilon_{Nd})_i$	τ_{DM}[c]	τ_{DM}[d]
FR-14-77	Develidağ	5.8	45.96	397.83	0.704858	0.000008	0.70476	3.35	16.44	0.512619	0.000006	0.51262	-0.2	-0.3	0.9	0.9
FR-15-34	Melendiz	3	64.18	419.54	0.704979	0.000009	0.70485	3.23	17.22	0.512681	0.000007	0.51268	0.9	0.9	0.7	0.8
FR-14-140	Ağrı	17.4	148.71	51.17	0.708782	0.000008	0.70639	2.52	13.00	0.512582	0.000006	0.51257	-0.7	-0.9	0.9	0.9
FR-14-125	Ağrı	19.8	109.85	32.54	0.708454	0.000007	0.70568	1.77	12.24	0.512554	0.000006	0.51254	-1.1	-1.3	0.7	1.0
FR-14-82	Yamadağ	21.2	45.82	419.56	0.704128	0.000007	0.70404	3.69	17.23	0.512682	0.000007	0.51266	1.4	1.0	0.9	0.8

[a] Sample description, location and trace element concentrations can be found in the appendix B.

[b] LA-ICP-MS U-Pb dates from Chapter 2; 3 and 19.8 Ma are the ages used for the samples FR-15-34 and FR-14-125, respectively

[c] Single-stage DM model age

[d] Two-stage DM model age (Liew and Hofmann, 1988)

Table 3.3 Radiogenic Pb isotope data from selected late Cenozoic igneous units in central and eastern Anatolia

Samples[a]	Igneous Complex	Age[b] (Ma)	$^{206}Pb/^{204}Pb$	±2σ	$^{207}Pb/^{204}Pb$	±2σ	$^{208}Pb/^{204}Pb$	±2σ
FR-14-77	Develidağ	5.8	18.9587	0.0013	15.6904	0.0013	39.0976	0.0035
FR-14-61	Konya	9	19.0750	0.0012	15.7269	0.0011	39.2566	0.0030
FR-14-73	Konya	10.2	18.9871	0.0013	15.7350	0.0012	39.1587	0.0033
FR-15-34	Melendiz	3	18.8431	0.0020	15.6722	0.0016	38.9850	0.0058
FR-14-140	Ağrı	17.4	18.9309	0.0012	15.6813	0.0011	39.0815	0.0031
FR-14-125	Ağrı	19.8	18.8993	0.0013	15.6723	0.0012	39.0521	0.0029
FR-14-82	Yamadağ	21.2	18.8556	0.0011	15.6360	0.0011	38.8844	0.0025

[a] Sample description and location can be found in the appendix B;
Those feldspar samples are too young and contain too little Th and U to change Pb isotope ratios through time; measured ratio = initial ratio

[b] LA-ICP-MS U-Pb dates from Chapter 2; 9, 3 and 19.8 Ma are the ages used for the samples FR-14-61, FR-15-34 and FR-14-125, respectively

(Figure 3.8B). The trace element signature of Pliocene volcanic samples shows weak negative anomalies in Ta, Nb, Hf and Ti relative to LILE (Figure 3.9B). The REE signature of Pliocene volcanic rocks of central Anatolia is similar to their late Miocene counterparts, except the absence of Eu anomaly (Figure 3.10B). Isotopic data reveal that those Pliocene rocks have initial $^{87}Sr/^{86}Sr$ and $^{143}Nd/^{144}Nd$ ranging from 0.70440 to 0.70551 and 0.51253 to 0.51274, respectively (Figure 3.11A-B). In addition, they yield initial $^{206}Pb/^{204}Pb$, $^{207}Pb/^{204}Pb$ and $^{208}Pb/^{204}Pb$ ratios from 18.834 to 18.843, 15.665 to 15.672, and 38.928 to 38.985, respectively (Figures 3.11D-G).

3.5.1.3 Quaternary

The two Quaternary stratovolcanoes of central Anatolia, named Hasandağ and Erciyes, have a broad compositional range from basalt to rhyolite (Figure 3.7C). The Hasandağ geochemical group also includes the geochemical analyses from the surrounding monogenetic basaltic vents, which are spatially distinct from Karapınar (Reid et al., 2017). In terms of alkalinity, the volcanic rocks of the Erciyes stratovolcano are dominantly medium-K calc-alkaline whereas the Hasandağ volcanic rocks show medium- to high-K calc-alkaline affinities

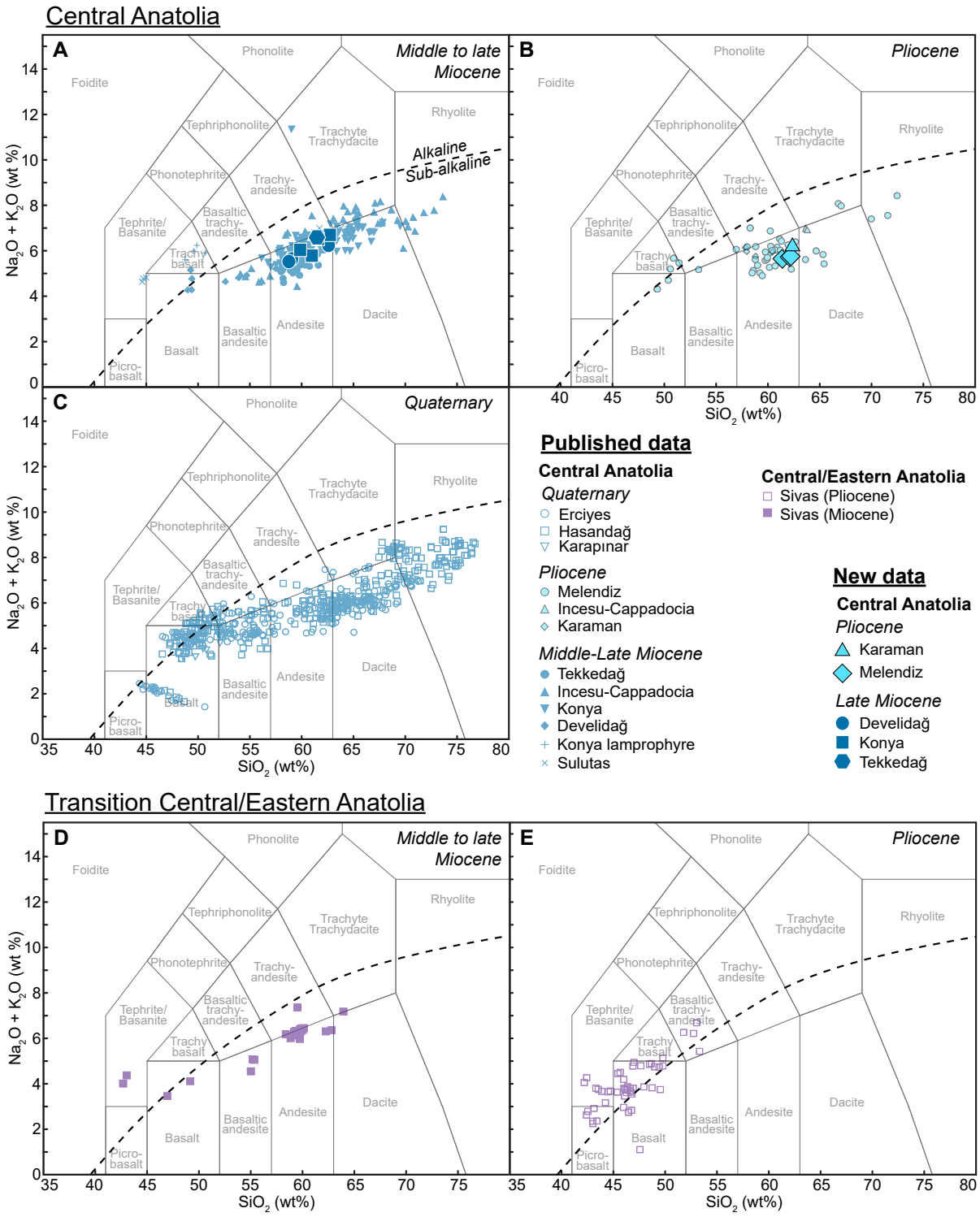

Figure 3.7 Total alkali versus silica diagram (Le Maitre et al., 2002) showing the composition of volcanic rocks from central Anatolia (A. Late Miocene; B. Pliocene; C. Quaternary), transition central/eastern Anatolia (D. Middle to late Miocene; E. Pliocene) and eastern Anatolia (F. Oligocene-early Miocene; G. Middle Miocene; H. Late Miocene-Pliocene; I. Pliocene-Quaternary). The references of compiled and previously published geochemical data are detailed in the appendix B (Table B.1).

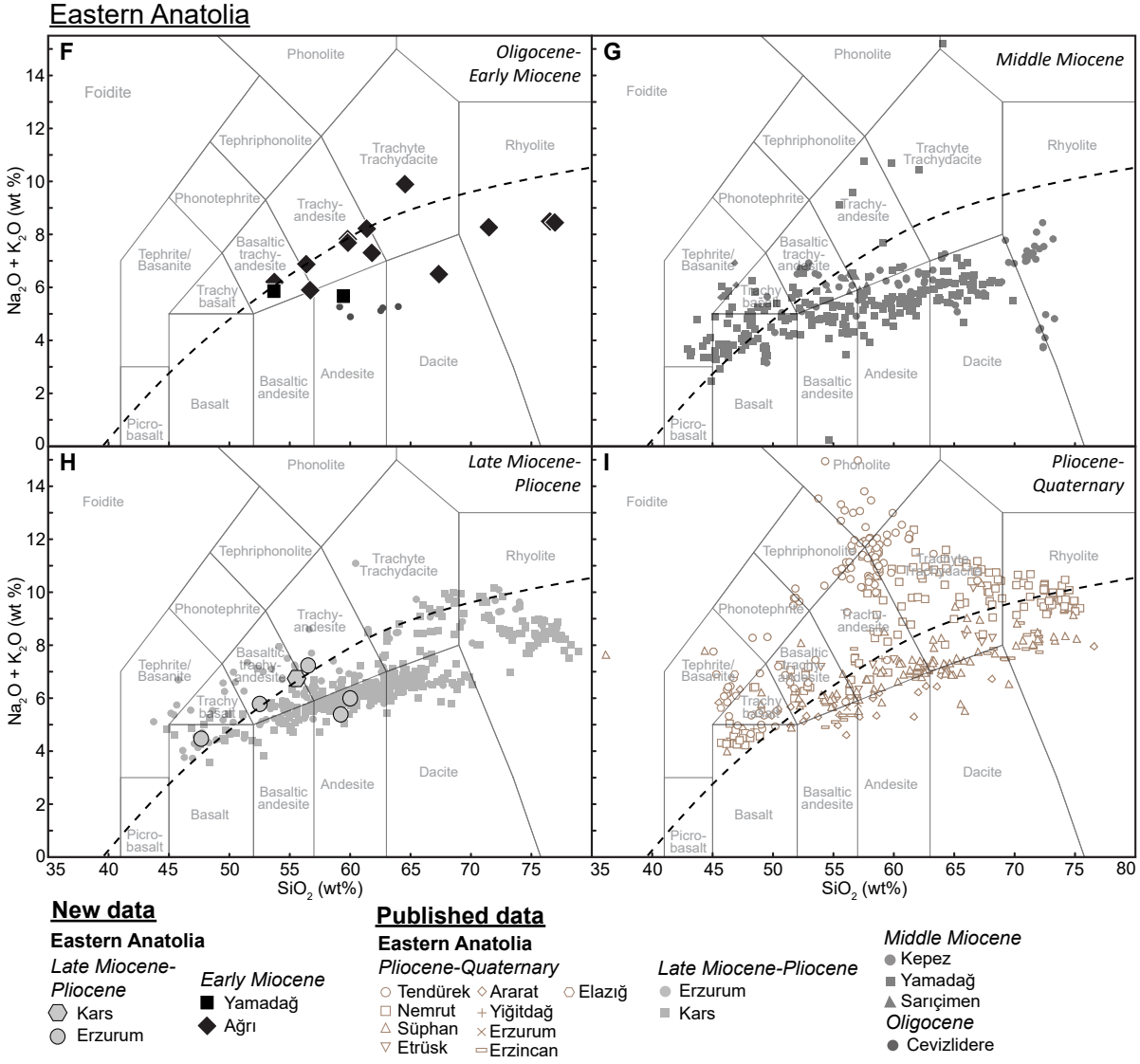

Figure 3.7 (Continued) Total alkali versus silica diagram (Le Maitre et al., 2002) showing the composition of volcanic rocks from central Anatolia (A. Late Miocene; B. Pliocene; C. Quaternary), transition central/eastern Anatolia (D. Middle to late Miocene; E. Pliocene) and eastern Anatolia (F. Oligocene-early Miocene; G. Middle Miocene; H. Late Miocene -Pliocene; I. Pliocene-Quaternary). The references of compiled and previously published geochemical data are detailed in the appendix B (Table B.1).

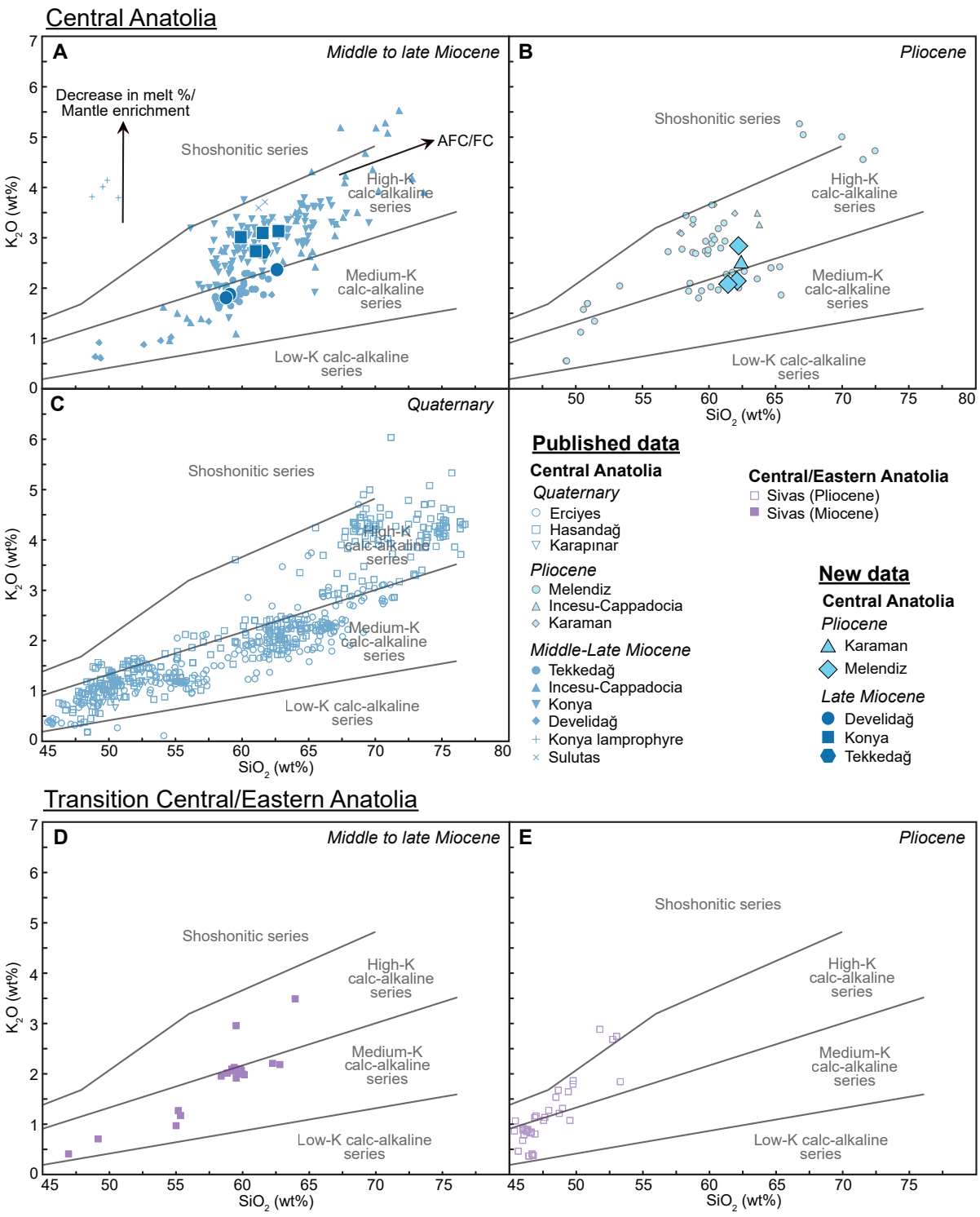

Figure 3.8 K_2O versus SiO_2 diagram (Peccerillo and Taylor, 1976) showing the composition of volcanic rocks from central Anatolia (A. Late Miocene; B. Pliocene; C. Quaternary), transition central/eastern Anatolia (D. Middle to late Miocene; E. Pliocene) and eastern Anatolia (F. Oligocene-early Miocene; G. Middle Miocene; H. Late Miocene-Pliocene; I. Pliocene -Quaternary). The references of compiled and previously published geochemical data are detailed in appendix B (Table B.1).

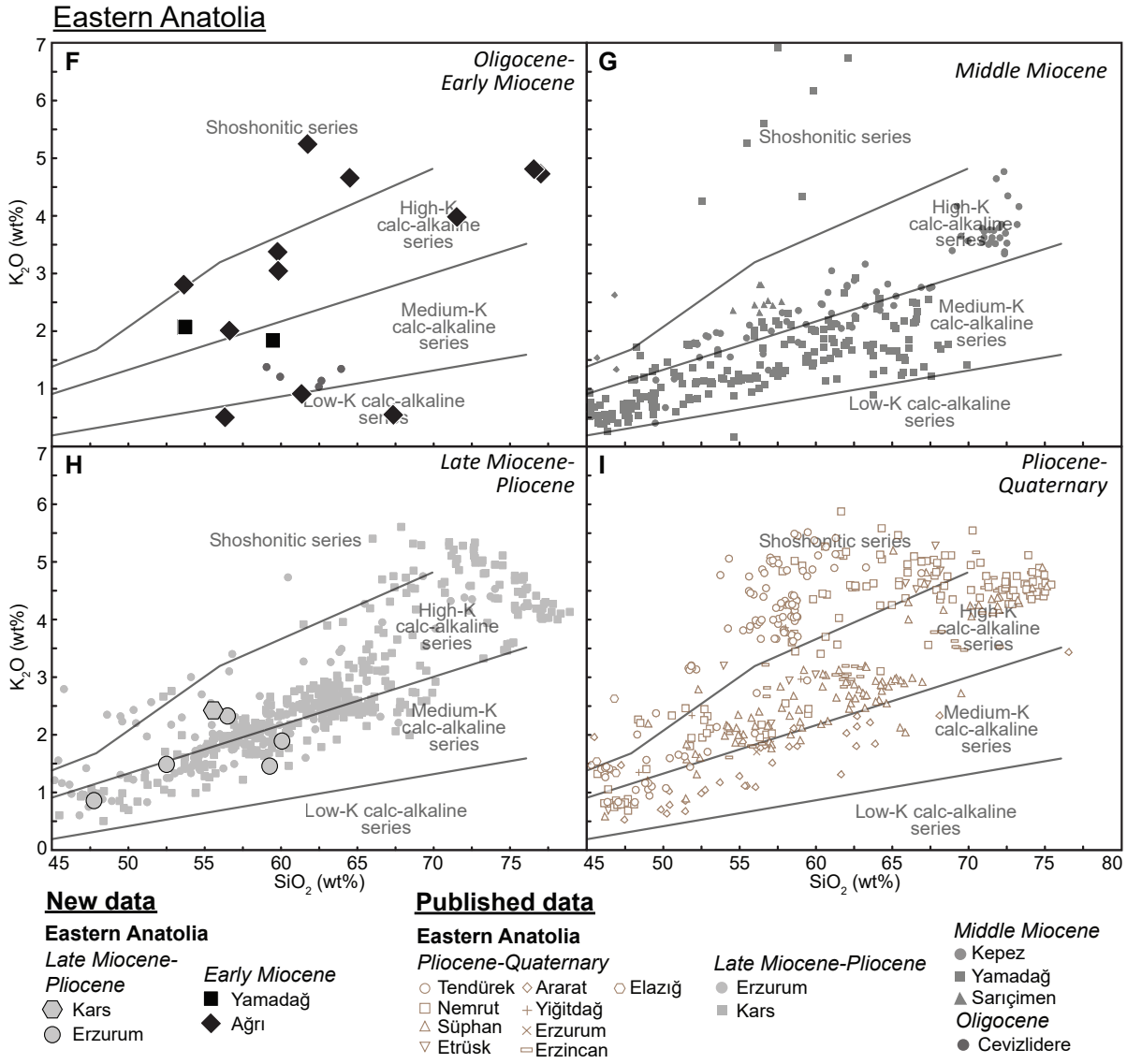

Figure 3.8 (Continued) K_2O versus SiO_2 diagram (Peccerillo and Taylor, 1976) showing the composition of volcanic rocks from central Anatolia (A. Late Miocene; B. Pliocene; C. Quaternary), transition central/eastern Anatolia (D. Middle to late Miocene; E. Pliocene) and eastern Anatolia (F. Oligocene-early Miocene; G. Middle Miocene; H. Late Miocene-Pliocene; I. Pliocene-Quaternary). The references of compiled and previously published geochemical data are detailed in appendix B (Table B.1).

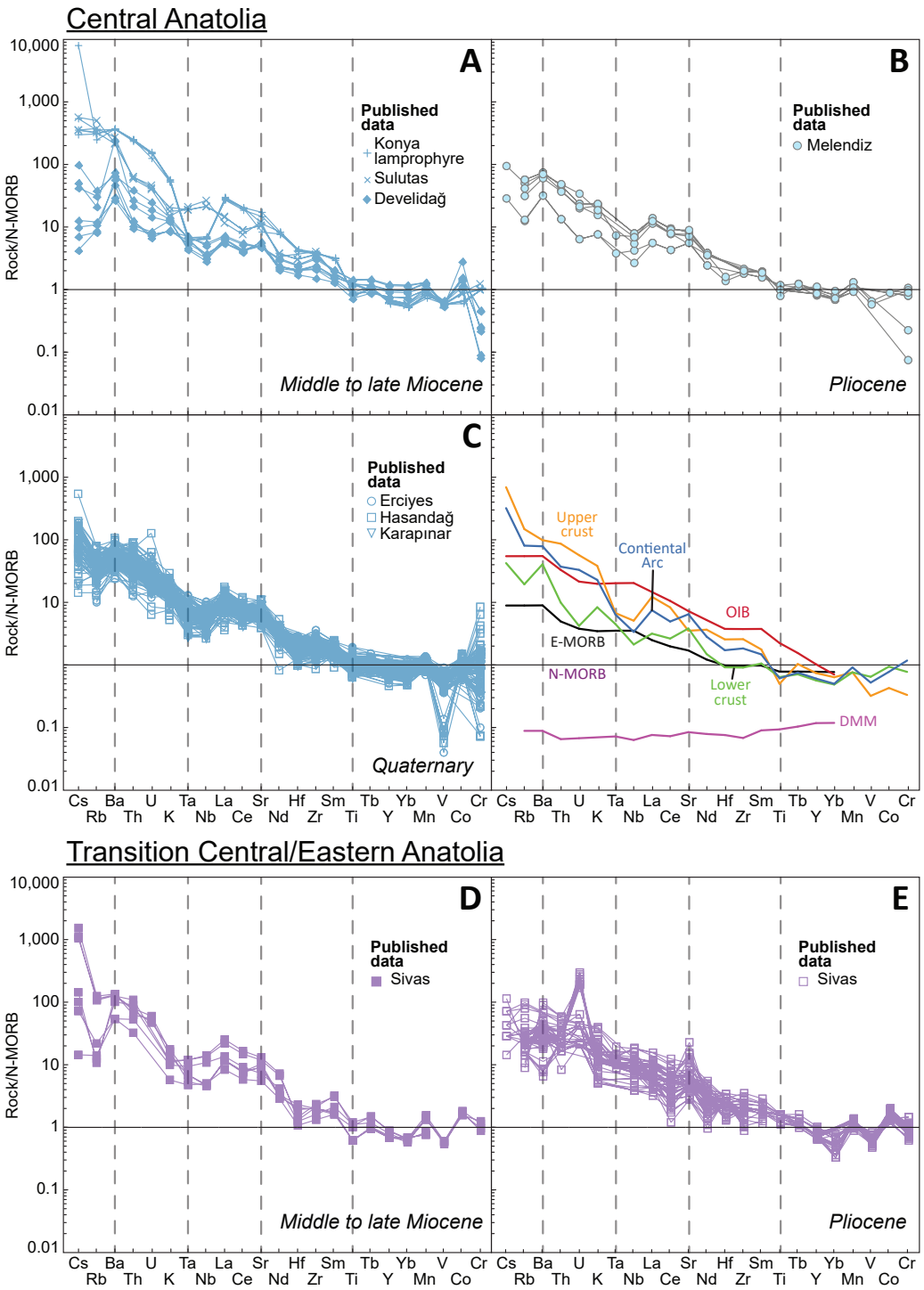

Figure 3.9 Extended N-MORB-normalized trace element diagram (SiO_2 < 56 wt %) displaying the composition of volcanic rocks from central Anatolia (A. Late Miocene; B. Pliocene; C. Quaternary), transition central/eastern Anatolia (D. Middle to late Miocene; E. Pliocene) and eastern Anatolia (F. Early-middle Miocene; G. Late Miocene-Pliocene; H. Pliocene-Quaternary). N-MORB normalization and E-MORB, and OIB values from Sun and McDonough (1989); Depleted MORB Mantle (DMM) reference values from Workman and Hart (2005); Upper and Lower Crust reference values from Rudnick and Gao (2014); Continental and Oceanic Arc reference values from Kelemen et al. (2014). The references of compiled geochemical data are detailed in the appendix B (Table B.1).

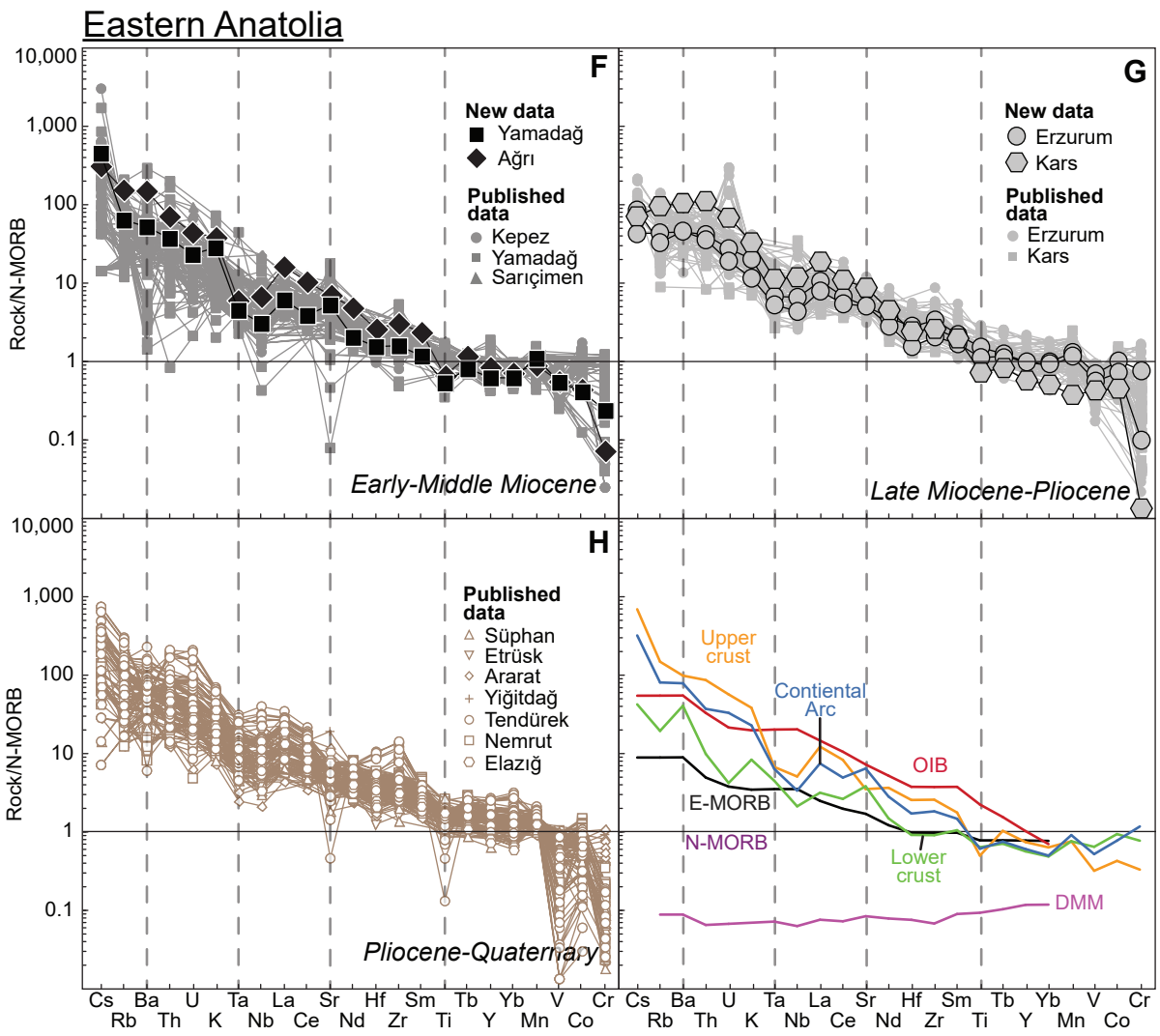

Figure 3.9 (Continued) Extended N-MORB-normalized trace element diagram (SiO_2 < 56 wt %) displaying the composition of volcanic rocks from central Anatolia (A. Late Miocene; B. Pliocene; C. Quaternary), transition central/eastern Anatolia (D. Middle to late Miocene; E. Pliocene) and eastern Anatolia (F. Early-middle Miocene; G. Late Miocene-Pliocene; H. Pliocene-Quaternary). N-MORB normalization and E-MORB, and OIB values from Sun and McDonough (1989); Depleted MORB Mantle (DMM) reference values from Workman and Hart (2005); Upper and Lower Crust reference values from Rudnick and Gao (2014); Continental and Oceanic Arc reference values from Kelemen et al. (2014). The references of compiled geochemical data are detailed in the appendix B (Table B.1).

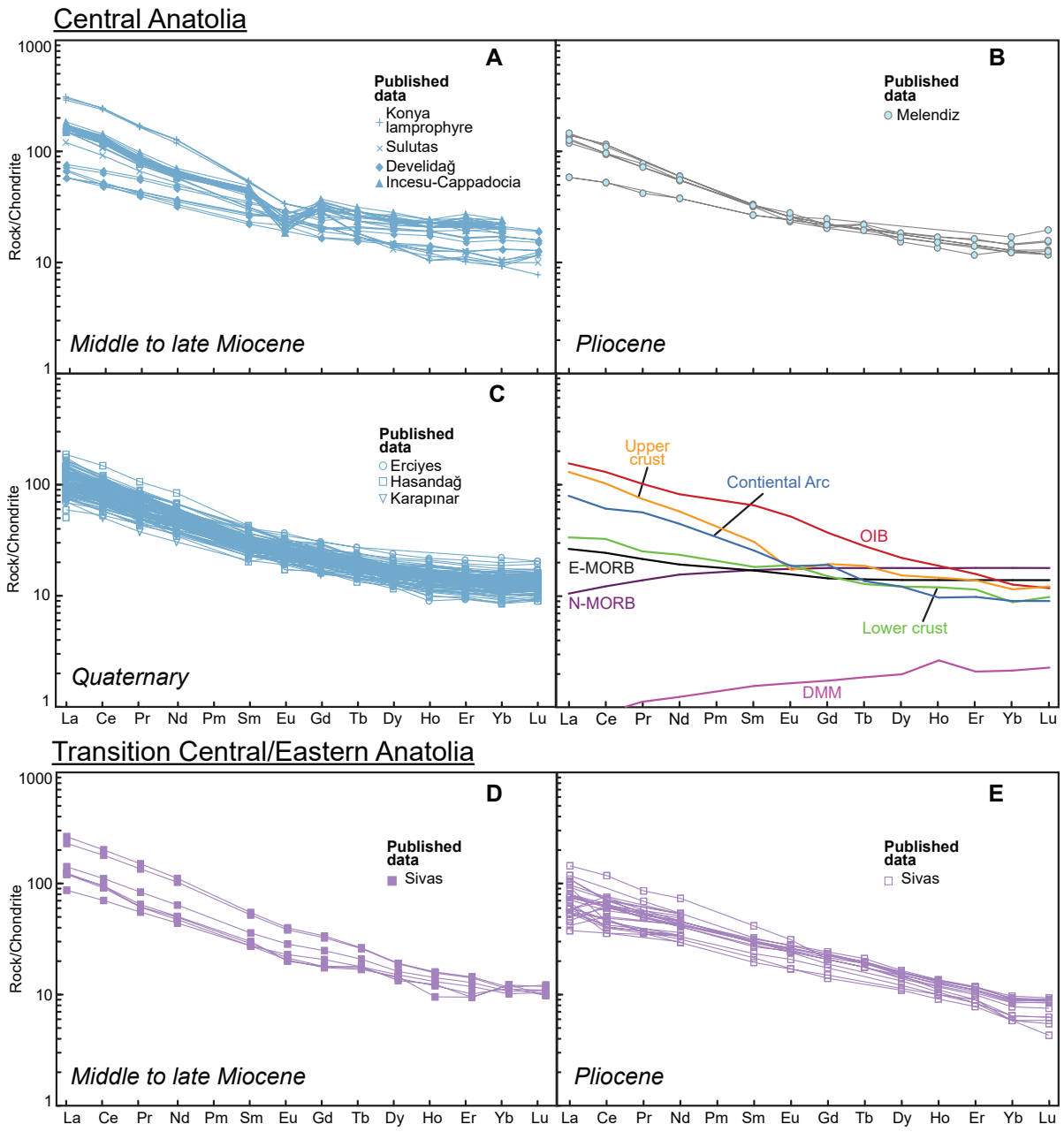

Figure 3.10 Chondrite-normalized trace element diagram (SiO_2 < 56 wt %) displaying the composition of volcanic rocks from central (A. Late Miocene; B. Pliocene; C. Quaternary), transition central/eastern (D. Middle to late Miocene; E. Pliocene) and eastern Anatolia (F. Early-middle Miocene; G. Late Miocene-Pliocene; H. Pliocene-Quaternary). Chondrite normalization, E-MORB, N-MORB and OIB reference values from Sun and McDonough (1989); Depleted MORB Mantle (DMM) reference values from Workman and Hart (2005); Upper and Lower Crust reference values from Rudnick and Gao (2014); Continental and Oceanic Arc reference values from Kelemen et al. (2014). The references of compiled geochemical data are detailed in the appendix B (Table B.1).

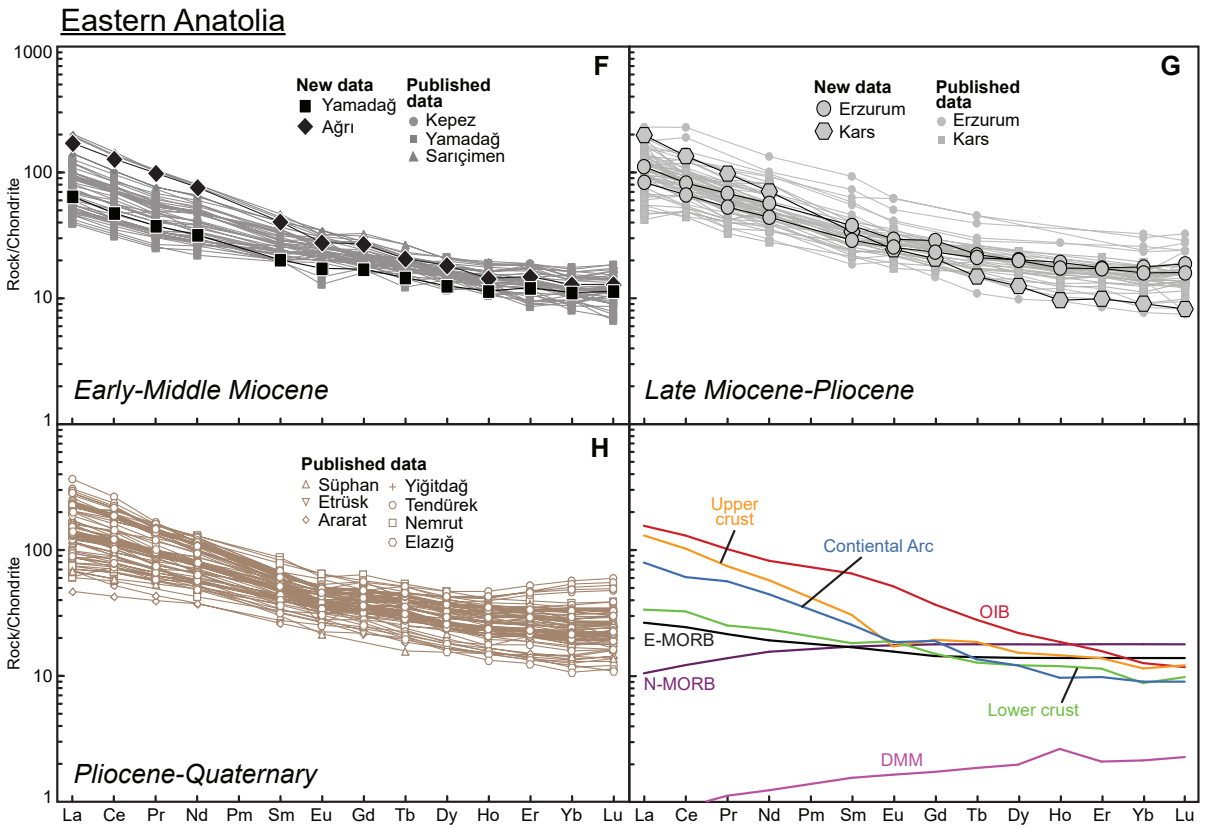

Figure 3.10 (Continued) Chondrite-normalized trace element diagram (SiO_2 < 56 wt %) displaying the composition of volcanic rocks from central (A. Late Miocene; B. Pliocene; C. Quaternary), transition central/eastern (D. Middle to late Miocene; E. Pliocene) and eastern Anatolia (F. Early-middle Miocene; G. Late Miocene-Pliocene; H. Pliocene-Quaternary). Chondrite normalization, E-MORB, N-MORB and OIB reference values from Sun and McDonough (1989); Depleted MORB Mantle (DMM) reference values from Workman and Hart (2005); Upper and Lower Crust reference values from Rudnick and Gao (2014); Continental and Oceanic Arc reference values from Kelemen et al. (2014). The references of compiled geochemical data are detailed in the appendix B (Table B.1).

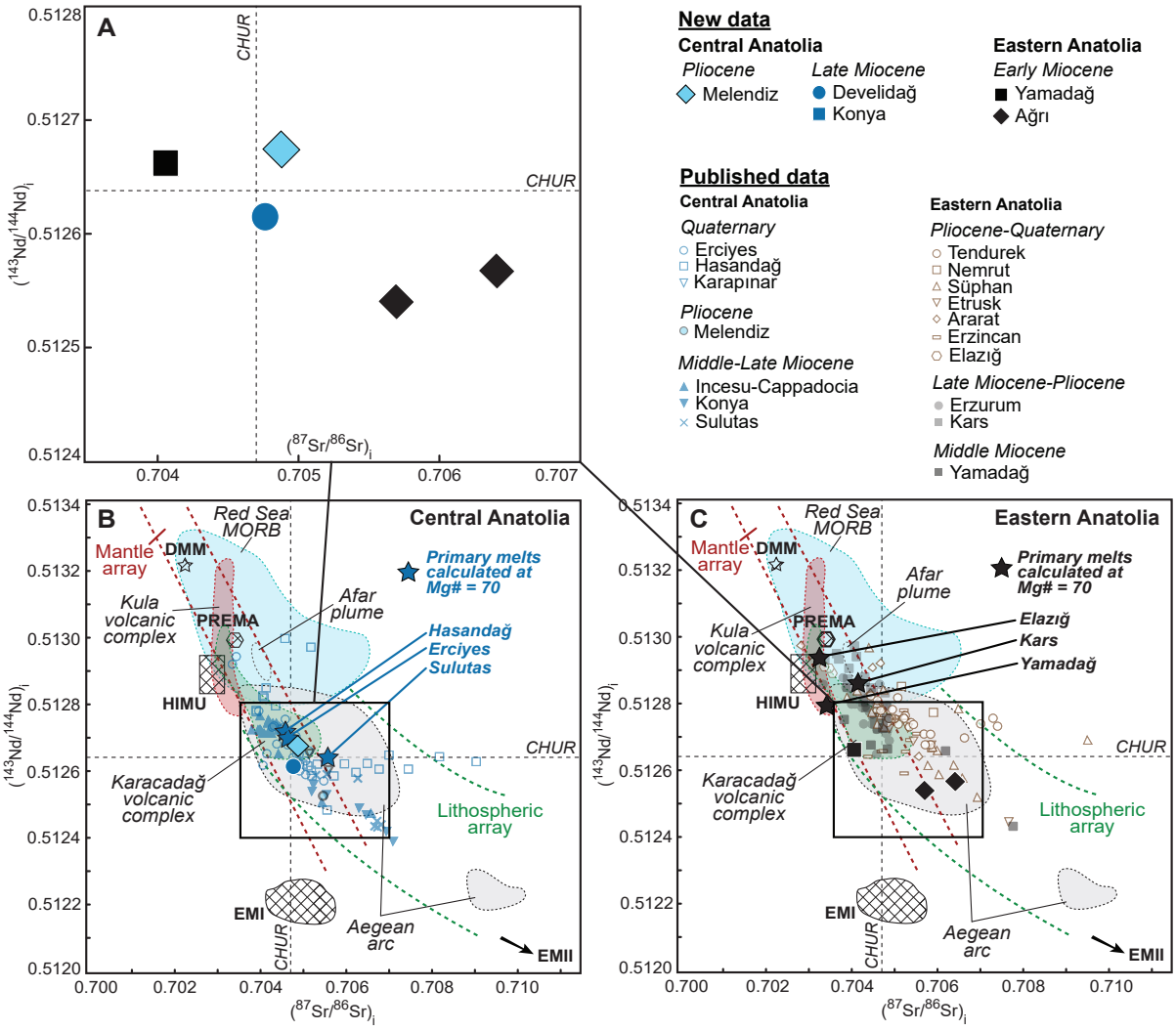

Figure 3.11 $(^{87}Sr/^{86}Sr)_i$ versus $(^{143}Nd/^{144}Nd)_i$ (A. New data; B. Central Anatolia; C. Eastern Anatolia) and $(^{207}Pb/^{204}Pb)_i$ (C. New and E. All data) and $(^{208}Pb/^{204}Pb)_i$ (D. New and F. All data) versus $(^{206}Pb/^{204}Pb)_i$ diagrams. BSE = bulk silicate Earth (Bouvier et al., 2008). The different reservoirs plotted include: Mediterranean sediments (Klaver et al., 2015); Kula lavas, western Anatolia (Alıcı et al., 2002; Chakrabarti et al., 2012; Aldanmaz et al., 2015); Karacadağ volcanic shield, northern Arabian platform, Turkey (Lustrino et al., 2010; Keskin et al., 2012; Ekici et al., 2014); Aegean arc and Red Sea MORB reservoirs from GeoRoc database (Sarbas and Nohl, 2008, consulted on 2017/05/30); Afar plume and Red Sea MORB reservoirs (Pik et al., 1999; Bertrand et al., 2003). GLOSS = global subducting sediment composition (Plank and Langmuir, 1998); NHRL = Northern Hemisphere reference line (Hart, 1984); EMI, EMII, HIMU, PREMA, DMM reservoirs from Zindler and Hart (1986); AFC = assimilation and/or crystal fractionation (DePaolo, 1981). The Sr and Nd isotopic composition of primary melts was calculated for each igneous suite at Mg # = 70 based on the protocol and statistical analysis provided in the appendix B (Figure B.4). The grey arrow is the magmatic trend related to the SCLM partial removal event in eastern Anatolia from the middle Miocene to Present.

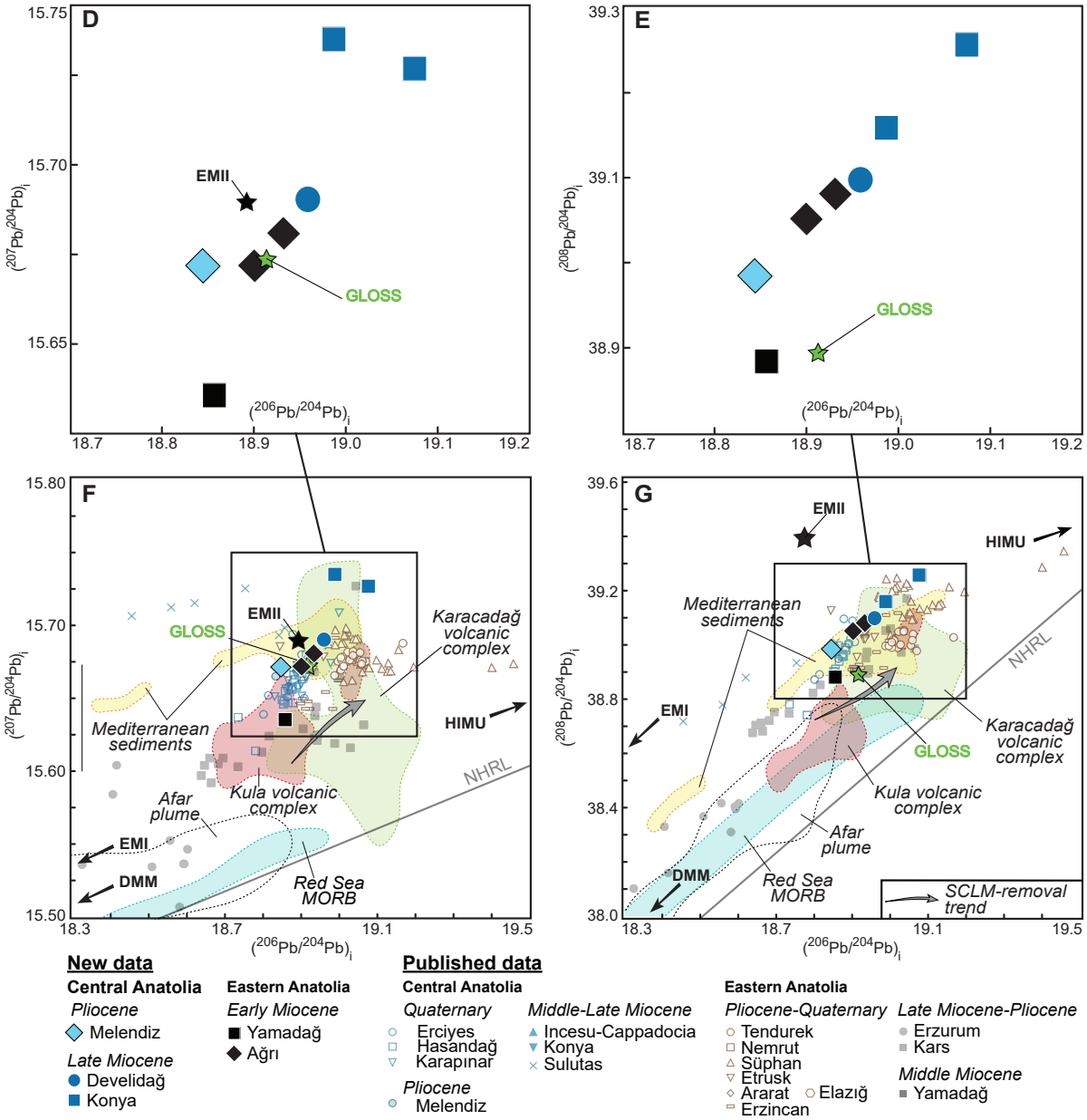

Figure 3.11 (Continued) $(^{87}Sr/^{86}Sr)_i$ versus $(^{143}Nd/^{144}Nd)_i$ (A. New data; B. Central Anatolia; C. Eastern Anatolia) and $(^{207}Pb/^{204}Pb)_i$ (C. New and E. All data) and $(^{208}Pb/^{204}Pb)_i$ (D. New and F. All data) versus $(^{206}Pb/^{204}Pb)_i$ diagrams. BSE = bulk silicate Earth (Bouvier et al., 2008). The different reservoirs plotted include: Mediterranean sediments (Klaver et al., 2015); Kula lavas, western Anatolia (Alıcı et al., 2002; Chakrabarti et al., 2012; Aldanmaz et al., 2015); Karacadağ volcanic shield, northern Arabian platform, Turkey (Lustrino et al., 2010; Keskin et al., 2012; Ekici et al., 2014); Aegean arc and Red Sea MORB reservoirs from GeoRoc database (Sarbas and Nohl, 2008, consulted on 2017/05/30); Afar plume and Red Sea MORB reservoirs (Pik et al., 1999; Bertrand et al., 2003). GLOSS = global subducting sediment composition (Plank and Langmuir, 1998); NHRL = Northern Hemisphere reference line (Hart, 1984); EMI, EMII, HIMU, PREMA, DMM reservoirs from Zindler and Hart (1986); AFC = assimilation and/or crystal fractionation (DePaolo, 1981). The Sr and Nd isotopic composition of primary melts was calculated for each igneous suite at Mg # = 70 based on the protocol and statistical analysis provided in the appendix B (Figure B.4). The grey arrow is the magmatic trend related to the SCLM partial removal event in eastern Anatolia from the middle Miocene to Present.

(Figure 3.8C). The mafic Karapınar volcano vents are composed of medium-K calc-alkaline basalts, basaltic andesites and trachybasalts whereas the Acigöl area is dominated by bimodal volcanic units. The Quaternary volcanic suites of central Anatolia show a relative narrow range of trace element signature on the N-MORB-normalized spider diagram and include troughs in Ta, Nb relative to LILE and variable compatible element compositions (V and Cr; Figure 3.9C). Those volcanic suites share a consistent REE pattern, similar to the Miocene and Pliocene volcanic rocks in the region (Figure 3.10C). Regarding their radiogenic isotopic signature, the Karapınar, Hasandağ and Erciyes volcanic suites have initial $^{87}Sr/^{86}Sr$ and $^{143}Nd/^{144}Nd$ ratios ranging from 0.70336 to 0.70736 and 0.51248 to 0.51230, respectively (Figure 3.11B). Their initial $^{206}Pb/^{204}Pb$, $^{207}Pb/^{204}Pb$ and $^{208}Pb/^{204}Pb$ ratios are comprised between 18.785 and 18.987, 15.626 and 15.709, and 38.807 and 39.160, respectively (Figures 3.11F-G).

3.5.2 Magmatic transition between central and eastern Anatolia

In the region of Sivas, the Miocene volcanic rocks are medium- to high-K calc-alkaline basanites/basalts to trachydacites whereas their Pliocene counterparts are dominantly mafic from picrobasaltic to basaltic trachyandesitic compositions, and medium-K calc-alkaline to shoshonitic (Figures 3.7D-E and 3.8D-E). The Miocene rocks of the Sivas volcanic suite display negative Ba, Nb, Ta, Hf and Ti anomalies on the N-MORB-normalized trace element diagram, and the Pliocene rocks have a flatter trace element pattern that only shows positive anomalies in U and Sr as well as a broader range of LILE enrichment (Figures 3.9D-E). However, all of those rocks have a similar OIB-like steep REE pattern (Figures 3.10D-E).

3.5.3 Eastern Anatolia

3.5.3.1 Oligocene-early Miocene

The Oligocene-early Miocene Period in eastern Anatolia is dominated by low-K calc-alkaline to shoshonitic basalt to trachydacite rock compositions at Yamadağ, Ağrı and Cevizlidere (Figures 3.7F and 3.8F). The Cevizlidere and Ağrı magmatic complexes are dominated by their intrusive equivalents including diorite, monzodiorite, monzonite, granodiorite and granite

(Figure B.2). The trace element signature of the Oligocene to early Miocene mafic magmatic rocks in eastern Anatolia is characterized by negative anomalies in Ta, Nb and Ti relative to LILE and depletion in compatible elements (V, Co, Cr) relative to N-MORB composition (Figure 3.9F). On the chondrite-normalized REE diagram, those rocks display continental arc- and upper crustal-like pattern with no Eu negative anomaly (Figure 3.10F). The Sr and Nd isotopic signature of those Oligocene to early Miocene magmatic complexes is characterized by initial $^{87}Sr/^{86}Sr$ and $^{143}Nd/^{144}Nd$ ratios ranging from 0.70404 to 0.70639, and from 0.51255 to 0.51258, respectively (Figure 3.11A-C). Their initial $^{206}Pb/^{204}Pb$, $^{207}Pb/^{204}Pb$ and $^{208}Pb/^{204}Pb$ ratios are between 18.856 to 18.931, 15.636 to 15.681, and 38.884 to 39.082, respectively (Figures 3.11D-G), similar to the GLOSS composition (global subducting sediment; Plank and Langmuir, 1998).

3.5.3.2 Middle Miocene

The middle Miocene igneous units of the Yamadağ, Kepez and Sarıçimen complexes have compositional range from basalt to rhyolite and also include some alkaline rocks from basanitic to trachytic composition sharing medium- to high-K calc-alkaline and shoshonitic affinities (Figures 3.7G and 3.8G). Those rocks have variable trace element patterns marked by a relative high range of LILE and compatible element compositions and dominant negative anomalies in Ta, Nb and weakly in Ti (Figure 9G). Nonetheless, they share a consistent and narrow REE pattern similar to their counterparts in central Anatolia (Figure 3.10G). The published initial $^{87}Sr/^{86}Sr$ and $^{143}Nd/^{144}Nd$ ratios from the middle Miocene igneous rocks of eastern Anatolia yield isotopic compositions ranging from 0.7033 to 0.7059 and 0.5125 to 0.5129, respectively, consistent with the underlying early Miocene counterparts (Figure 3.11C).

3.5.3.3 Late Miocene-Pliocene

The late Miocene to Pliocene Erzurum-Kars volcanic plateau in the eastern part of eastern Anatolia is composed of medium- to high-K calc-alkaline, basalt to trachyandesite to rhyolite (Figures 3.7H and 3.8H). A few samples from the Erzurum volcanic suite display a shoshonitic affinity. The trace element signature of the Kars and Erzurum volcanic rocks yield

negative anomalies in Ta and Nb relative to LILE and various degree of LILE enrichment (Figure 3.9G). Their REE pattern show flat MREE and HREE slopes (Figure 3.10G). The initial $^{87}Sr/^{86}Sr$ and $^{143}Nd/^{144}Nd$ ratios of those volcanic suites varies from 0.70333 to 0.70497 and 0.51265 to 0.51297, respectively (Figure 3.11A-C); their initial $^{206}Pb/^{204}Pb$, $^{207}Pb/^{204}Pb$ and $^{208}Pb/^{204}Pb$ ratio ranges are 18.325 to 19.064, 15.507 to 15.697, and 18.102 and 39.347, respectively (Figures 3.11D-G).

3.5.3.4 Pliocene-Quaternary

The Pliocene-Quaternary Period is dominated by the formation of stratovolcanoes (Nemrut, Süphan, Ararat, Tendürek and Etrüsk) lying on the Erzurum-Kars volcanic plateau, and the Yiğitdağ, Elazığ and Erzincan volcanic suites. The compositional range of those volcanic suites varies from basalt to rhyolite and from basanite to phonolite to trachydacite (Figure 3.7I). The Ararat volcanic rocks are medium-K calc-alkaline, and the Pliocene to Quaternary volcanic rocks of eastern Anatolia are high-K calc-alkaline to shoshonitic (Figure 3.8I). The mafic components of those volcanic suites are characterized by a broad trace element range showing weak Nb, Ta, Ti, Ba and Sr negative anomalies and depleted compatible element abundances, similar to upper crust (Kelemen, 2014; Figure 3.9H). Their REE signature also displays a broad compositional range and upper crust-like pattern with flat MREE and HREE slopes (Figure 3.10H). Despite the similar REE patterns between the various Pliocene to Quaternary volcanic suites, the range of element concentrations is broader showing an order-of-magnitude variation. This high range of major and trace element compositions is also reflected in the initial $^{87}Sr/^{86}Sr$ and $^{143}Nd/^{144}Nd$ isotope ratios ranging from 0.70311 to 0.70823 and 0.51247 to 0.51298, respectively, for those volcanic suites based on published isotopic data (Figure 3.11C). The Tendürek and Süphan suites lie predominantly in the lithospheric array, the Ararat suite in the mantle array, and the Etrüsk and Nemrut suites are scattered between both domains. The published radiogenic Pb isotope data from the Tendürek, Etrüsk and Süphan stratovolcanoes yield initial $^{206}Pb/^{204}Pb$, $^{207}Pb/^{204}Pb$ and $^{208}Pb/^{204}Pb$ ratio ranges of 18.844 to 19.413, 15.643 to 15.699, and 38.909 to 39.347, respectively, thus dominantly higher than

those from their older counterparts throughout eastern Anatolia (Figures 3.11F-G).

3.6 Discussion

Previous studies, mainly focused on local late Cenozoic volcanic complexes along the Eastern Anatolian Magmatic Belt, emphasized the complex interplay between subduction, lithospheric and asthenospheric components on magma petrogenesis as a result of asthenospheric upwelling and progressive SCLM removal following cessation of subduction. The following section discusses the geochemical signature of magmatism, mantle source regions and magmatic processes along the belt, and investigates the temporal and spatial evolution of magmatism in relation to recent geodynamic models involving the break-off of the Southern Neotethyan oceanic slab and its westward propagation from eastern to central Anatolia, followed by the SCLM partial removal, during the late Cenozoic.

3.6.1 Subduction component

The mantle source of most of the late Cenozoic volcanic complexes in central and eastern Anatolia was affected by subduction-related metasomatism (e.g., Pearce et al., 1990; Deniel et al., 1998; Keskin et al., 1998; Kürkçüoğlu et al., 2004; Şen et al., 2004) that was dominated by sediment melts (Keskin et al., 2006; Asan and Ertürk, 2013; Özdemir and Güleç, 2013; Oyan et al., 2016; McNab et al., 2017; Reid et al., 2017). Evidences for contributions from pelagic sediments to the magma source include: 1) elevated initial $^{87}Sr/^{86}Sr$ ratios (> 0.706), and Pb isotope ratios that are similar to the eastern Mediterranean sediments (Klaver et al., 2015) and GLOSS Pb isotopic composition (global subducting sediments; Plank and Langmuir, 1998; Figure 3.11); 2) the presence of phlogopite-bearing lamprophyres in the region of Sulutas in central Anatolia (Asan and Ertürk, 2013).

Most of the central and eastern Anatolian mafic igneous units (SiO_2 < 56 wt %) share common geochemical features such as moderate depletions in Ta, Nb and variably in Ti relative to the LILE and LREE (Figure 3.9). This trace element signature results from past or current subduction-related metasomatic processes and/or crustal contamination as it was previously

interpreted in central and eastern Anatolia (e.g., Pearce et al., 1990; Deniel et al., 1998; Keskin et al., 1998; Kürkçüoğlu et al., 2004; Şen et al., 2004; Reid et al., 2017). The depletions are less pronounced in the middle Miocene and Pliocene to Quaternary mafic rocks of eastern Anatolia, and in the Pliocene at the transition between central and eastern Anatolia, indicating lower contributions from subduction and/or crustal assimilation. Overall, the data plot above and parallel to the mantle array on the Ta/Yb versus Th/Yb diagram, and are characterized by a Th/Ta ratio of ca. 1 (Figure 3.12A). The higher Th/Yb ratios relative to the mantle array indicate either subduction-related contributions to the mantle source or crustal assimilation for most of the igneous suites, except a few volcanic rocks from the Sivas and Yamadağ complexes. On a Ba/Nb versus Th/Nb diagram (Figure 3.12B), the mafic rocks of central and eastern Anatolia are characterized by increasing Th/Nb with increasing Ba/Nb. This trend reflects the regional metasomatism of the magma source by sediment melts as previously determined at Süphan (Özdemir and Güleç, 2013), Etrüsk (Oyan et al., 2016) and Hasandağ (Reid et al., 2017).

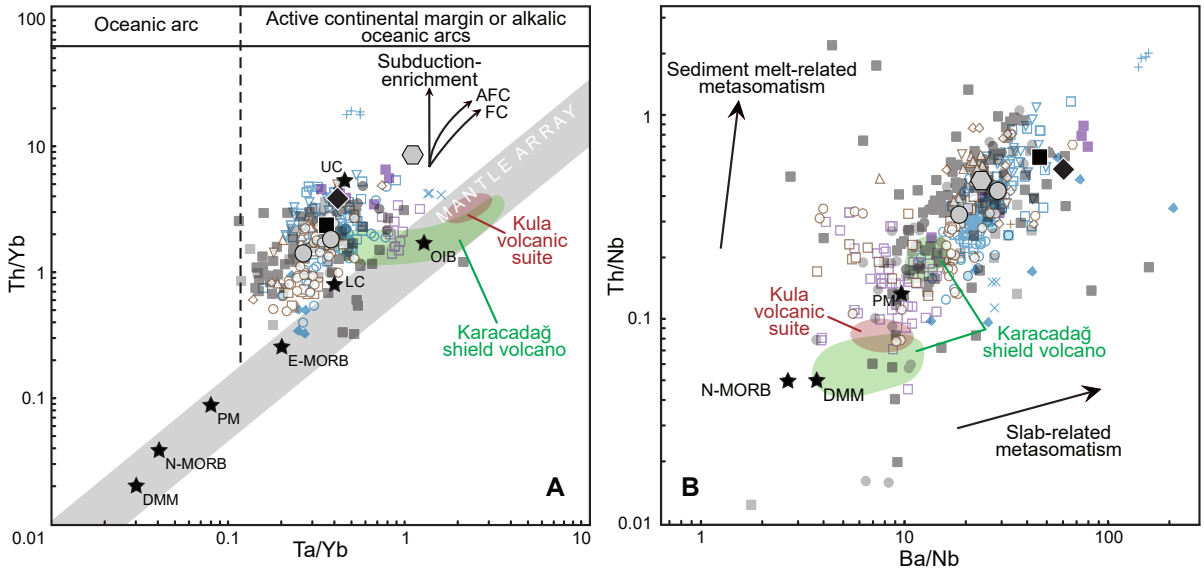

Figure 3.12 Trace element diagrams used to investigate the petrogenesis of mafic magmatic rocks (SiO_2 < 56 wt %) from central and eastern Anatolia. A. Ta/Yb versus Th/Yb diagram (Pearce, 1983); B. Ba/Nb versus Th/Nb diagram (Kepezhinskas et al., 1996; Temizel et al., 2016). Primitive mantle (PM), OIB, E-MORB and N-MORB reference values from Sun and McDonough (1989) and upper (UC) and lower crust (LC) reference values from Rudnick and Gao (2014). Symbol legend is provided Figure 7. Kula volcanism is used as proxy for Anatolian OIB-like reservoir and African mantle reservoir (Aldanmaz, 2002; Alıcı et al., 2002; Chakrabarti et al., 2012; Grützner et al., 2013; Aldanmaz et al., 2015). Karacadağ volcanism is a proxy for Arabian mantle reservoir (Pearce et al., 1990; Şen et al., 2004; Alpaslan, 2007; Lustrino et al., 2010; Keskin et al., 2012; Ekici et al., 2014).

3.6.2 Post-subduction magmatism: inheritance from past subduction events

In central and eastern Anatolia, the subduction signature of late Cenozoic magmatism was inherited from pre-Miocene metasomatism of the Anatolian SCLM (e.g., Pearce et al., 1990; Notsu et al., 1995; Keskin et al., 1998; Şen et al., 2004). Regional seismic tomography, modelling studies and tectonic reconstructions showed the absence of active subduction since the Oligocene in eastern Anatolia, and the deep Cyprus slab (> 200 km) beneath the western part of central Anatolia (e.g., Biryol et al., 2011). Reid et al. (2017) added that the metasomatism beneath central Anatolia likely occurred after 150 Ma based on residence time constraints from Lu/Hf systematics. Taken together, this information indicates that subduction beneath the region has been inactive for several million years, and that modern arc processes are not the cause of late Cenozoic magmatism in central and eastern Anatolia (Schildgen et al., 2014; Delph et al., 2017; Reid et al., 2017; Chapter 2).

The inherited subduction signature may have come from subduction events such as during the closure of the Southern Neotethyan Ocean from the Late Cretaceous to Oligocene, and also the Berit and Inner Tauride oceanic basins in the Late Cretaceous (Robertson et al., 2013). Those subduction events metasomatized the Anatolian SCLM adding LILE and volatiles. Evidences of Late Cretaceous continental arc magmatism are common in central and eastern Anatolia such as the Göksun-Afşin, Baskil, Ağaçören and Behrekdağ batholiths (e.g., Kadıoğlu et al., 2006; Parlak, 2006; Rızaoğlu et al., 2009). However, contributions from the Ediacarian-Cambrian arc magmatism during the Gondwana amalgamation are possible because of the presence of Neoproterozoic arc-type plutons in the Bitlis Massif basement in eastern Anatolia (Ustaömer et al., 2009) and the Neoproterozoic-aged Anatolian lithosphere (τ_{DM} comprised between 0.4 and 0.9 Ga; median of 0.7 ± 0.2 Ga (1σ); see Table B.3).

3.6.3 Crustal contamination

Effects of crustal process such as crustal contamination and crystal fractionation were observed in most of the central and eastern Anatolian igneous suites (Figure 3.12A; e.g., Keskin et al., 1998; Şen et al., 2004). The degree of crustal contamination is a function of

the composition and thickness of the crustal column along which magma will be interacting during its ascent and emplacement (Thorpe and Francis, 1979; Leeman, 1983; Ellam, 1992). The current crustal thickness of the Anatolian microplate varies from ca. 45 km to 35 km in eastern and central Anatolia, respectively (Zor et al., 2003; Barazangi et al., 2006; Şengör et al., 2008; Mutlu and Karabulut, 2011; Tezel et al., 2013). Crustal thickness also varies from north to south in eastern Anatolia from Kars (ca. 50 km) to Van (ca. 38 km; Şengör et al., 2008). The crystalline basement in central and eastern Anatolia is composed of pre-Cenozoic medium- to high-grade metamorphic, plutonic, ophiolitic and carbonate rocks (e.g. Whitney et al., 2003; Şengör et al., 2008; Yılmaz et al., 2010; Aydar et al., 2012; Topuz et al., 2017). Zircon dating in Chapter 2 and Paquette and Le Pennec (2012) reported Cretaceous, Paleozoic and Archean xenocrystic igneous zircons within late Cenozoic igneous units in both central and eastern Anatolia suggesting assimilation from the Anatolian crystalline basement during the magma ascent and emplacement.

Petrological modelling in central Anatolia revealed that the ratios of assimilation rate to the fractional crystallization rate, or r values (DePaolo, 1981), were relatively constant from the late Miocene Tekkedağ (r = 0.2-0.3; Koralay, 2010), Konya (r = 0.1-0.2; Temel et al., 1998a), Develidağ (r = 0.2; Kürkçüoğlu, 2010) and İncesu (r = 0.25) to Quaternary Karapınar (r = 0.05-0.2; Dogan, 2016), Erciyes (r = 0.1-0.3; Kürkçüoğlu et al., 2004; Dogan, 2016) and Hasandağ volcanic complexes (r = 0.05-0.3; Dogan, 2016). However, the crust-like component in Hasandağ lavas likely reflected changes in the mantle source rather than crustal assimilation based on the absence of covariation of crustal-sensitive Zn/Fe, Nb/U and Ce/Pb ratios with basalt Mg#, proxy for magma differentiation (Reid et al., 2017). In eastern Anatolia, degrees of crustal contamination are variable: late Miocene to Pliocene Kars and Erzurum suites (r = 0.1 on average; Keskin et al., 1998); Quaternary Etrüsk (r < 0.35; Oyan et al., 2016); Nemrut (r = 0.2-0.4; Keskin et al., 1998; Çubukçu et al., 2012); Süphan (r = 0.02-0.1; Keskin et al., 1998; Özdemir and Güleç, 2013). Magma-crust interaction via assimilation and fractionated crystallization processes increased from 11 Ma to Present (Keskin et al., 1998); average r values

varied from 0.1 to 0.35. Contributions from the lower crust as contaminant were suggested in eastern Anatolia (Keskin et al., 2006; Oyan, 2018) but excluded in central Anatolia (McNab et al., 2017).

In addition to elevated Th/Yb and Ta/Yb ratios (Figure 3.12A), elevated radiogenic Sr isotopes clearly suggest the incorporation of crustal material, in addition to sediment melts, into the ascending magma in both central and eastern Anatolia (Figure 3.11). Constant initial $^{87}Sr/^{86}Sr$ ratio with variations in SiO_2 content reflects the fractional crystallization in a closed system whereas the variations in initial $^{87}Sr/^{86}Sr$ ratio for a range of SiO_2 content result from crustal assimilation (e.g., Wang et al., 2006; Figure 3.13). The igneous rocks from the Konya, Ağrı and some rocks from the Pliocene to Quaternary Hasandağ, Nemrut, Süphan and Tendürek stratovolcanoes and middle Miocene Yamadağ volcanic suites have initial $^{87}Sr/^{86}Sr$ isotopic ratios greater than 0.706, reflecting significant crustal contamination. Most of the central Anatolian volcanic units have initial $^{87}Sr/^{86}Sr$ ratios between 0.7035 and 0.7055. Also, the lack of initial $^{87}Sr/^{86}Sr$ covariation with time and SiO_2 content goes against a temporal decrease in crustal contamination in central Anatolia and supports compositional variations in the mantle source as suggested by Reid et al. (2017). The igneous units of eastern Anatolia have a broad

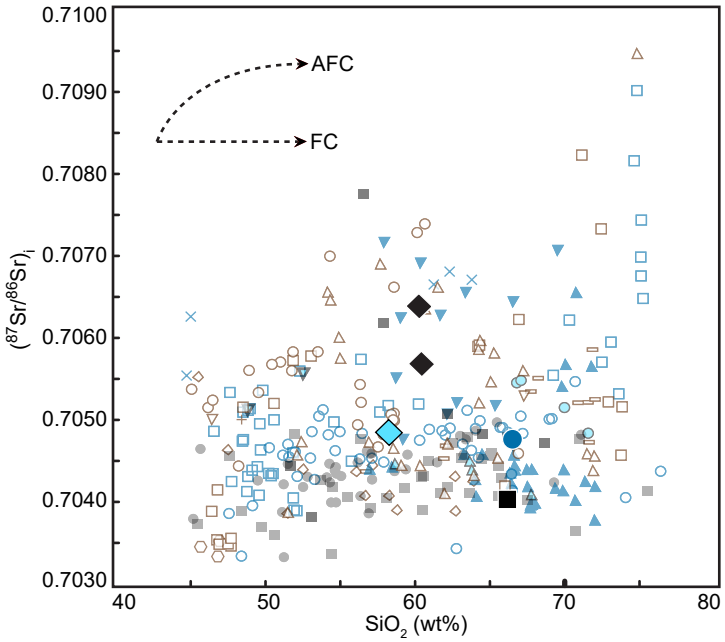

Figure 3.13 $(^{87}Sr/^{86}Sr)_i$ versus SiO_2 diagram. Symbol legend is provided in Figure 3.7.

range of initial $^{87}Sr/^{86}Sr$ ratios between 0.703 and 0.709 emphasizing the role of the lithospheric column on magma petrogenesis.

Radiogenic Pb isotope ratios in eastern Anatolia increase from the late Miocene to the Quaternary (Figures 3.11F-G) as a result of the temporal increase of crustal contamination, as initially proposed by Keskin et al. (1998), and/or subducted sediments input with insignificant contributions from the lower crust. This temporal increase excludes the early to middle Miocene igneous rocks of the Yamadağ and Ağrı complexes. In central Anatolia, the temporal trend from the late Miocene to Quaternary towards less radiogenic Pb isotopes indicates the increasing contribution from the subslab mantle and/or decreasing input of subducted sediments but excludes any significant contributions from the lower crust. However, the Sulutas and Konya igneous complexes in the western part of central Anatolia display a similar Pb isotopic evolution as the late Miocene to the Quaternary volcanic units of eastern Anatolia between 16 and 8 Ma. Both igneous complexes are also characterized by higher initial $^{207}Pb/^{204}Pb$ ratios that reflect a greater crustal and/or subduction component than the other igneous suites in central and eastern Anatolia.

3.6.4 Magma alkalinity

The common trend of increasing alkalinity in active continental margins was explained by higher pressure and greater depth of melting source reflecting the greater distance from the arc trench and thicker crust towards the continent (Miyashiro, 1974; Dickinson, 1975). In post-subduction and post-collisional tectonic settings, magma alkalinity was thought to increase through time due to (Bonin, 1990): 1) readjustment of regional isotherms after a subduction or collision event; 2) the asthenosphere infiltration into the subduction-modified SCLM such as during a slab break-off (e.g., Davis and Hawkesworth, 1993; Liégeois et al., 1998; Coulon et al., 2002; Ferrari, 2004; Oyhantçabal et al., 2007) or delamination event (Pearce et al., 1990; Black and Liegeois, 1993; Tack et al., 1994).

The late Cenozoic igneous complexes of central and eastern Anatolia consist of subalkaline and alkaline suites (Figure 3.7). Early studies in Anatolia proposed a genetic

correlation between increasing degree of alkalinity and temporal change in tectonic regime from compression (orogenic) to extension (anorogenic; Yılmaz, 1990; Deniel et al., 1998). More recently, some researchers argued that this geochemical evolution as well as the shift of tectonic regime both reflected a change in the subducting slab geometry, or slab break-off, and SCLM delamination after the onset of the Arabian continental collision (e.g., Keskin et al., 1998; Keskin, 2003). However, McNab et al. (2017) noted the apparent absence of temporal alkalinity increase in central Anatolia by studying high MgO basalt only. In addition, some field-based studies reported that alkaline lavas did not always occupy the top of the local volcanic stratigraphy and were commonly intercalated with coeval calc-alkaline lavas and pyroclastic deposits such as in Pliocene to Quaternary volcanic suites in central Anatolia (Deniel et al., 1998; Dogan-Kulahci et al., 2018) and middle Miocene Yamadağ volcanic complex (Kürüm et al., 2008).

The data compilation presented herein shows that the mafic volcanic rocks of central Anatolia are dominantly transitional to sodic regardless of rock age, with a Na_2O content ranging between ca. 1 and 3 wt % and K_2O content varying from ca. 0.2 to 2 wt %, with the exception of the Konya lamprophyres (up to 4 wt % K_2O; Figure 3.14A). Similarly, the mafic igneous rocks of eastern Anatolia are transitional to sodic but their Na_2O (ca. 2.5 to 9 wt %) and K_2O content ranges (ca. 0.2 to 4.8 wt %) are much broader than those in central Anatolia. Magma alkalinity ($K_2O + Na_2O$) in central and eastern Anatolia dominantly increases eastwards (Figure 3.14B) where the crust is thicker (see the discussion above). In addition, magma alkalinity only increases from the late Miocene to Quaternary in eastern Anatolia. This temporal increase excludes the early to middle Miocene igneous units in eastern Anatolia; magma alkalinity does not vary significantly in central Anatolia (Figures 3.14C-D).

3.6.5 Composition and depth of magmatic sources

The possible compositions and relative depths of melting sources in eastern Anatolia include the subcontinental lithospheric (SCLM; Pearce et al., 1990; Yılmaz et al., 1998; Kheirkhah et al., 2009), asthenospheric (Keskin, 2003, 2007; Şengör et al., 2008; Lebedev et

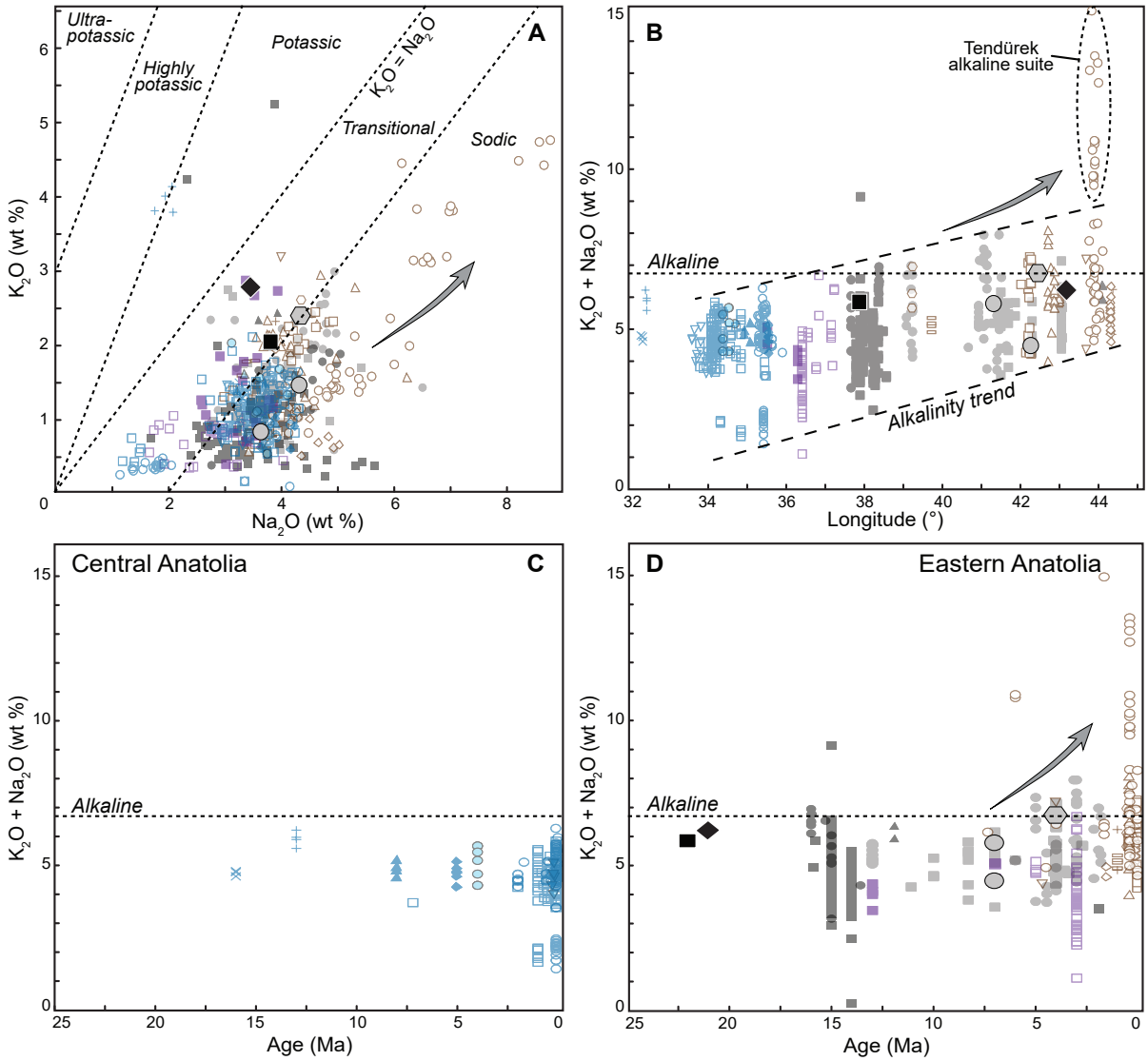

Figure 3.14 A. K_2O versus Na_2O (Le Maitre et al., 2002); B. K_2O + Na_2O versus longitude illustrating the eastward increasing alkalinity trend; C. K_2O + Na_2O versus age in central Anatolia; D. K_2O + Na_2O versus age in eastern Anatolia showing the alkalinity increase through time during the SCLM removal event (grey arrow). Only the mafic rocks are displayed (SiO_2 < 56 wt %). The horizontal alkalinity reference line at ca. 6.8 wt % on Figures C and D represents the position of TAS diagram's alkalinity line (Le Maitre et al., 2002) at 56 wt % SiO_2. This means that rocks plotted above this line are alkaline whereas the ones below are either subalkaline or alkaline. Symbol legend is provided on Figure 3.7. All the data plotted have a SiO_2 content lower than 56 wt %. The grey arrow is the magmatic trend related to the SCLM removal event in eastern Anatolia from the middle Miocene to Present.

al., 2016), or both lithospheric and asthenospheric mantles (Özdemir and Güleç, 2013). The SCLM contribution increased and the depth of melting decreased from garnet-dominant-facies to spinel-dominant-facies peridotite from the late Miocene to Quaternary in eastern Anatolia (Özdemir and Güleç, 2013). The Sivas basalts between central and eastern Anatolia likely

formed at the spinel-garnet transition in the SCLM (Kürkçüoğlu et al., 2015). In central Anatolia, the Hasandağ magmatism was generated by an interplay between shallow, metasomatized MORB-like magma, certainly produced at the lithosphere-asthenosphere boundary based in the presence of thin or absent SCLM, and deeper, asthenosphere-derived, intraplate-like melts (Reid et al., 2017).

All of the magmas resulted from similar degrees of partial melting such as at Develidağ (3-4 %; Kürkçüoğlu, 2010), Hasandağ and Karapınar volcanic edifices (8-9 %; Dogan, 2016) in central Anatolia, and at the Erzurum (mostly 6-10 %; Kaygusuz et al., 2018), Tendürek (1.5 %; Şen et al., 2004) and Etrüsk volcanic complexes in eastern Anatolia (0.8-4 %; Oyan et al., 2016). In general, the relative low degrees of partial melting (< 10 %) in central and eastern Anatolia are consistent with the generation of post-subduction and post-collision-related magmas (Davies and von Blanckenburg, 1995; Jiang et al., 2006) as opposed to volcanic arc magmas (10 to 25 %; Plank and Langmuir, 1988; Hirose and Kawamoto, 1995). These differences may reflect lower fluid abundances and shallower melting in the Anatolian source rocks than in typical suprasubduction-zone mantle.

Ultrapotassic rocks are present throughout western Anatolia related to the roll-back and tearing of the Aegean slab (e.g., Çoban and Flower, 2006; Prelević et al., 2010; Yılmaz, 2010; Prelević et al., 2012; Ersoy et al., 2014) and in Iran in a syn-collisional setting (e.g., Ahmadzadeh et al., 2010; Pang et al., 2013). However, in central and eastern Anatolia, their presence is restricted to the region of Konya where coeval, middle to late Miocene minette-type lamprophyres and high-K calc-alkaline lavas coexist (Asan and Ertürk, 2013; Korkmaz et al., 2017). Both lithologies highlight the heterogeneity of the Anatolian SCLM above the Cyprus slab segment and may be explained by the vein-plus-wall-rock melting model of Foley (1992). This model invokes melting of phlogopite-clinopyroxene- or amphibole-bearing veins and peridotite wall-rock within the SCLM (Foley, 1992; Pilet et al., 2008; Asan and Ertürk, 2013). Increasing melting of surrounding peridotite generates shoshonitic and high-K calc-alkaline magmas by dilution of the alkaline component (Conticelli et al., 2009).

In order to further assess mantle sources, initial ε_{Nd} values for primary magmas in the volcanic fields of central and eastern Anatolia were calculated (see appendix B and Figure B.4 for methodology). As shown in Table 3.4 and Figures 11A-B, the calculated primary magmas in eastern Anatolia have higher initial ε_{Nd} ($\geq$ 4.1, except in the Ararat volcanic suite which has ε_{Nd} = -0.3) than in central Anatolia ($\varepsilon_{Nd} \leq 2.5$). These data indicate that the mantle sources for eastern Anatolian magmas were more depleted in incompatible elements, with higher Sm/Nd and lower ε_{Nd}. Mantle enrichment can also be monitored by decreasing Zr/Nb and increasing $(La/Yb)_N$ ratios in response of interaction between depleted MORB mantle and enriched OIB-like mantle sources, lower degree of partial melting, or addition of slab components to the magma (Münker, 2000; Kirchenbaur et al., 2011). The compiled data have a large range of $(La/Yb)_N$ ratios (Figure 3.15A) that likely reflects heterogeneity of the mantle source rather than variations in the degree of partial melting, which is fairly consistent among the volcanic regions, as noted above. As showed in Figure 3.12B, late Cenozoic Anatolian magmas were metasomatized by sediment melts (high Th/Nb ratios). Figure 3.15B shows a

Table 3.4 Primary melt isotopic compositions calculated at Mg # = 70 (if $r^2 \geq 0.5$) or by average of primitive samples ($62 \leq$ Mg # ≤ 70) if available ($n \geq 2$).

	$(\varepsilon_{Nd})_i$				$(^{143}Nd/^{144}Nd)_i$				$(^{87}Sr/^{86}Sr)_i$			
Igneous complex	**Coefficient**	**Intercept**	**r^2**	**Primary $(\varepsilon_{Nd})_i$ calculated**	**Coefficient**	**Intercept**	**r^2**	**Primary $(^{143}Nd/^{144}Nd)_i$ calculated**	**Coefficient**	**Intercept**	**r^2**	**Primary $(^{87}Sr/^{86}Sr)_i$ calculated**
Central Anatolia												
1. Erciyes	0.06	-2.46	0.2	1.28[b]	3.5E-06	0.5125	0.2	0.5127[b]	-1.7E-06	0.7047	0.0	0.7046[b]
2. Hasandağ	0.06	-1.75	0.5	2.47[a]	3.1E-06	0.5125	0.5	0.5127[a]	-3.9E-05	0.7073	0.6	0.7046[a]
3. Karapınar	0.16	-9.35	0.1	1.92[b]	8.2E-06	0.5122	0.1	0.5127[b]	-	-	-	0.7054[b]
4. Melendiz	0.09	-4.72	0.7	1.86[a]	5.0E-06	0.5124	0.7	0.5128[a]	4.0E-05	0.7036	0.2	-
5. Incesu	0.02	-0.91	0.0	-	1.1E-06	0.5126	0.0	-	-2.9E-05	0.7061	0.1	-
6. Konya	0.09	-7.45	0.1	-	4.8E-06	0.5123	0.1	-	-5.0E-05	0.7088	0.1	-
7. Sulutas	0.18	-12.40	0.9	0.08[a]	9.1E-06	0.5120	0.9	0.5126[a]	-5.9E-05	0.7097	0.9	0.7056[a]
Eastern Anatolia												
8. Tendürek	0.01	1.80	0.0	-	1.1E-07	0.5127	0.0	-	-3.4E-05	0.7066	0.3	-
9. Süphan	-0.02	2.67	0.0	-	-1.1E-06	0.5128	0.0	-	-5.5E-05	0.7073	0.2	-
10. Etrüsk	-0.01	2.56	0.1	-	-2.5E-07	0.5128	0.0	-	5.4E-06	0.7048	0.1	-
11. Ararat	-0.46	31.83	0.9	-0.30[a]	2.4E-05	0.5143	0.9	0.5126[a]	2.2E-05	0.7031	0.2	0.7050[b]
12. Erzincan	0.01	0.37	0.0	-	7.3E-07	0.5127	0.0	-	-1.9E-05	0.7057	0.5	0.7044[a]
13. Elazığ	0.04	3.36	1.0	6.05[a]	2.0E-06	0.5128	1.0	0.5129[a]	-1.7E-05	0.7044	0.8	0.7032[a]
14. Erzurum	0.08	-0.49	0.5	5.45[a]	4.4E-06	0.5126	0.5	0.5129[a]	-1.4E-05	0.7050	0.3	-
15. Kars	-0.02	6.18	0.1	4.56[b]	-8.6E-07	0.5130	0.1	0.5129[b]	1.6E-06	0.7039	0.0	0.7041[b]
16. Yamadağ	0.14	-5.61	0.7	4.09[a]	7.1E-06	0.5123	0.7	0.5128[a]	-8.4E-05	0.7093	0.8	0.7034[a]

[a] value calculated at Mg# = 70 for igneous suites having $r^2 \geq 0.5$

[b] average value for all the primitive samples (Mg# $\geq$ 62; $n \geq 2$)

positive correlation between Nb/Th and Nb/Yb ratios for the Sivas, Yamadağ and Erzurum volcanic rocks towards OIB-like Kula and Karacadağ volcanic suites. This trend suggests that the Sivas, Yamadağ and Erzurum volcanic suites resulted from an interaction between MORB- and OIB-like mantle reservoirs (Münker, 2000) as they are characterized by limited subduction and crustal components (low Th content). Thus, although the enrichment degree of Anatolian magmas was primarily caused by sediment melts (low Nb/Th and Nb/Yb ratios; Figure 3.15B), some volcanic suites (i.e., Sivas, Yamadağ and Erzurum) recorded an OIB-like component (high Nb/Th and Nb/Yb ratios).

The relative depth of magma source can be represented by medium over heavy rare earth element ratios. Wang et al. (2002) empirically set the boundary between spinel and garnet stability fields at $(Tb/Yb)_N = 1.8$, as garnet fractionation preferentially retains Yb in the melting source. Among the compiled rock samples, only those from the Sivas, Yamadağ, Erzurum and Elazig volcanic suites were produced in the garnet stability field ($(Tb/Yb)_N > 1.8$; Figure 3.15C). In addition, the Nb/La ratio on primitive rocks (Figure 3.15C) can distinguish metasomatized lithospheric mantle (Nb/La < 0.5) from dry asthenosphere (Nb/La > 1; Bradshaw and Smith, 1994; Karsli et al., 2014). Thus, it is suggested herein that most of Anatolian magmas resulted from the melting of metasomatized MORB-like mantle material at shallow depth in the spinel stability field (< 80 km; Takahashi and Kushiro, 1983; Klemme and O'Neill, 2000) in the lithospheric mantle.

Those trace element ratios evolve through time. For instance, the $(Tb/Yb)_N$, Nb/Th and Nb/La ratios (Figure 3.15B-C) increase from the early Miocene (Yamadağ and Ağrı suites) to Pliocene (Sivas suite) in eastern Anatolia. The early Miocene Yamadağ and Ağrı igneous rocks result from the melting of spinel-facies peridotite ($(Tb/Yb)_N < 1.7$) in the lithospheric mantle (Nb/La < 0.5) whereas the middle Miocene volcanic units from the Yamadağ complex and the middle Miocene to Pliocene Sivas basalts have higher $(Tb/Yb)_N$ (ca. 2) and Nb/La (> 0.9) ratios suggesting a garnet-(spinel) facies asthenosphere, or asthenosphere-lithosphere transition. In contrast, the late Miocene to Quaternary volcanic rocks of eastern Anatolia are characterized

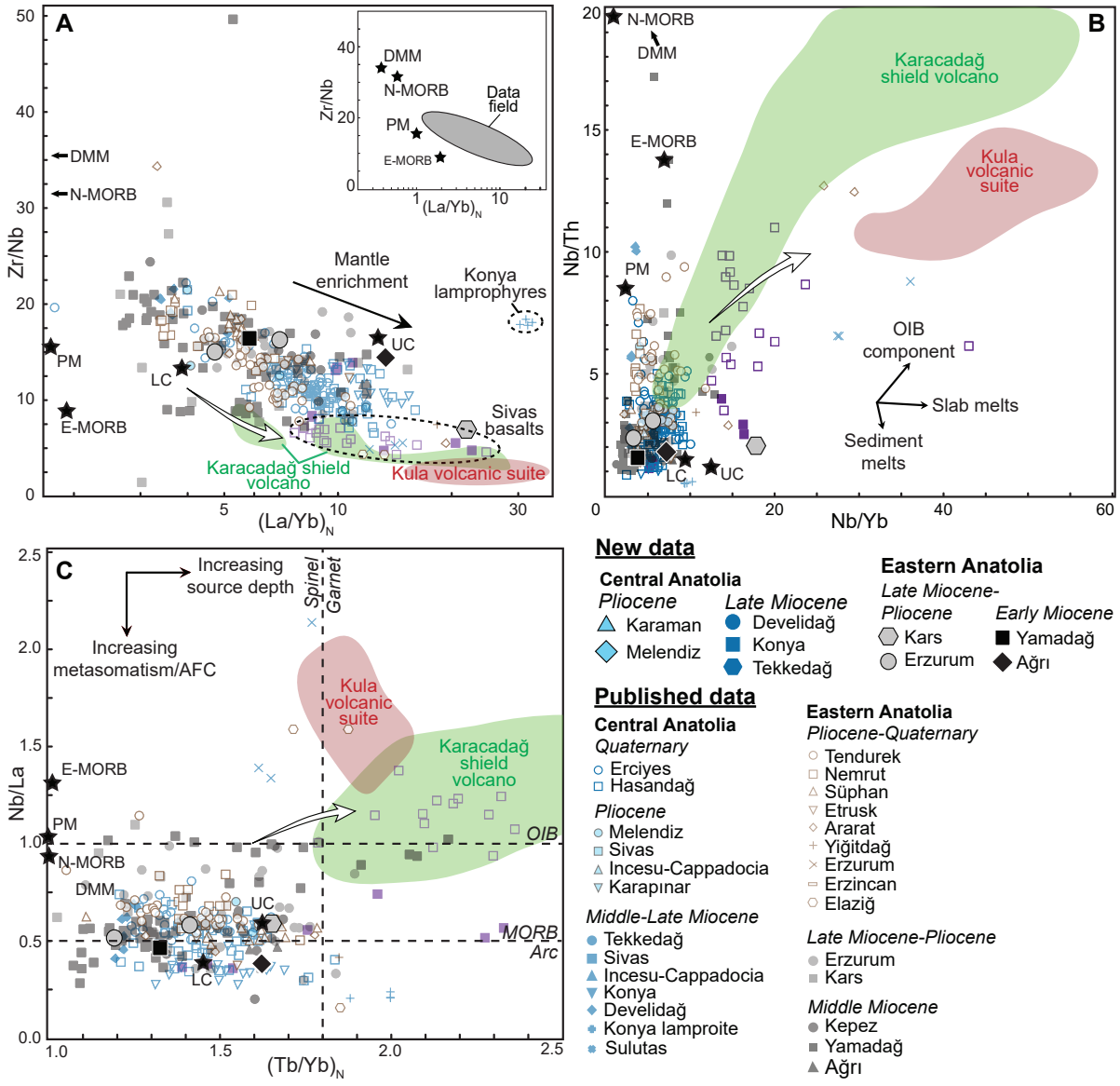

Figure 3.15 A. Primitive mantle-normalized $(La/Yb)_N$ versus Zr/Nb diagram (Münker, 2000); B. Nb/Yb versus Nb/Th diagram (Münker, 2000); C. Primitive mantle-normalized $(Tb/Yb)_N$ versus Nb/La diagram with horizontal reference lines from Gill (1981); the spinel and garnet stability field boundary at $(Tb/Yb)_N = 1.8$ was empirically determined by Wang et al. (2002). Primitive mantle (PM), OIB, E-MORB and N-MORB reference values from Sun and McDonough (1989), and upper (UC) and lower crust (LC) reference values from Rudnick and Gao (2014). Kula volcanism is used as proxy for the Anatolian OIB-like and African mantle reservoirs (Aldanmaz, 2002; Alıcı et al., 2002; Chakrabarti et al., 2012; Grützner et al., 2013; Aldanmaz et al., 2015). Karacadağ volcanism is a proxy for the Arabian mantle reservoir (Pearce et al., 1990; Şen et al., 2004; Alpaslan, 2007; Lustrino et al., 2010; Keskin et al., 2012; Ekici et al., 2014). All the data plotted have a SiO_2 content lower than 56 wt %. The white arrow represents slab break-off-related magmatic trend in eastern Anatolia (early-middle Miocene to Pliocene).

by variable Nb/La (0.5-1.1) but low $(Tb/Yb)_N$ ratios (< 1.8) that indicate shallow melting source (spinel-facies) and variable mixing of lithospheric and asthenospheric components as suggested by Özdemir and Güleç (2013).

In central Anatolia, the Th/Yb, $(La/Yb)_N$, $(Tb/Yb)_N$ and Nb/La ratio ranges of mafic rocks reflect various degrees of mantle metasomatism and enrichment of spinel-facies melting source as identified in the local volcanic edifices (e.g., Kürkçüoğlu, 2010; Dogan et al., 2013; Reid et al., 2017). However, the compiled data presented herein show that late Miocene magmatism in central Anatolia was preferentially generated in the sub-continental lithospheric mantle whereas their Pliocene to Quaternary counterparts dominantly result from asthenosphere and lithosphere melt interactions, as demonstrated by Reid et al. (2017) at Hasandağ, but at lesser degree than the volcanic rocks of the Yamadağ and Sivas suites further east.

3.6.6 The role of upwelling subslab asthenosphere

The late Cenozoic segmentation of the Southern Neotethyan oceanic slab induced toroidal and poloidal asthenospheric flow fields beneath Anatolia (Faccenna et al., 2006; Biryol et al., 2011; Faccenna et al., 2013; Sternai et al., 2014; Menant et al., 2016). Asthenospheric upwelling is consistent with anomalously high mantle potential temperatures (> 1350°C) at shallow depths beneath Anatolia (ca. 60 km; McNab et al., 2017; Reid et al., 2017), and high Bouguer gravity anomalies (Ates et al., 1999) that mimic the shape of the slab break-off-related Eastern Anatolian Magmatic Belt. Upwelling of hot asthenospheric material may have destabilized and displaced Anatolian SCLM (e.g., Prelević et al., 2012; McNab et al., 2017).

Mantle regions associated with the African and Arabian plates are considered enriched asthenospheric reservoirs that invaded the depleted, metasomatized Anatolian asthenospheric mantle and SCLM through breaches in the Southern Neotethyan slab (e.g., Faccenna et al., 2013; Klaver et al., 2016). The Kula volcanoes in western Anatolian were derived solely from geochemically enriched asthenosphere beneath the African lithosphere (e.g., Aldanmaz et al., 2000; Alıcı et al., 2002; Klaver et al., 2016; Reid et al., 2017). The Karacadağ volcanic shield on the northern part of the Arabian platform resulted from melting of the Arabian enriched

lithospheric and asthenospheric mantles (e.g., Keskin et al., 2012; Faccenna et al., 2013; Ekici et al., 2014).

The asthenosphere below the Arabian plate is affected by upwelling of the Afar plume beneath eastern Africa, which initiated ca. 45-40 Ma (McQuarrie et al., 2003; Le Pichon and Kreemer, 2010). Northward, channeled, horizontal mantle flow from the Afar plume may have reached Arabia at ca. 30 Ma and Anatolia at 11 Ma (Ershov and Nikishin, 2004; Faccenna et al., 2013). The contribution of the Afar plume to the Karacadağ volcanic shield on the northern part of the Arabian platform is uncertain and matter of debate based on the interpretation of radiogenic Nd and Pb isotope ratios (Keskin et al., 2012; Ekici et al., 2014).

The negative correlation between $(La/Yb)_N$ and low Zr/Nb ratios and positive correlation between Nb/Th and Nb/Yb ratios for the compiled data from the Sivas, Yamadağ and Erzurum volcanic complexes suggests the interplay between depleted MORB- and OIB-like magma sources as result of subslab mantle input (Figure 3.15A-B). In addition to the radiogenic Pb isotope ratios, initial $^{87}Sr/^{86}Sr$ and $^{143}Nd/^{144}Nd$ ratios of the late Miocene to Quaternary volcanic rocks in eastern Anatolia overlap the Karacadağ field and trend towards the Kula reservoir, similar to the central Anatolian rocks, but differ from the Afar plume Sr-Nd isotopic signature (Figure 3.11). Thus, the interpretation of compiled data suggests that 1) magmatism in both central and eastern Anatolia show evidence for increasing interaction with the subslab mantle through time, namely Sr-Nd-Pb isotopic signature close to Kula; and 2) the Afar plume did not affect the production of magmatism in eastern Anatolia and may have not reached the Anatolian asthenosphere yet as possibly opposed to Karacadağ magmatism in northern Arabia. The Afar-derived mantle flow had not reached the northern edge of the Arabia plate in the Oligocene-early Miocene (Faccenna et al., 2013) when the Southern Neotethyan slab break-off beneath Anatolia began (ca. 25 Ma; Chapter 2). Nonetheless, the Afar plume could be the driver of the so-called Tethyan mantle convection cell (Faccenna et al., 2013) thereby providing sufficient heat to generate and sustain the mantle upwelling throughout the Eastern Mediterranean region, including Anatolia, since the late Miocene (Faccenna et al., 2013; McNab et al., 2017).

3.6.7 Geochemical and tectonic evolution of the Eastern Anatolian Magmatic Belt

3.6.7.1 Two-stage, post-subduction, syn-collisional magmatism

Reconstructing the post-subduction tectonic environment of Anatolia has been accomplished in Chapter 2 using geochronology, seismic tomography, numerical modelling and crustal uplift studies (e.g., Faccenna et al., 2006; Biryol et al., 2011; Schildgen et al., 2014; Menant et al., 2016) supported in this Chapter 3 by igneous petrology (e.g., Pearce et al., 1990; Keskin, 2003, 2007; McNab et al., 2017; Reid et al., 2017). The results have shown that the closure of the Southern Neotethyan Ocean resulted in the westward propagation of a sub-horizontal slab rupture from eastern to central Anatolia (Figure 3.16A), followed by SCLM partial removal by sublithospheric convection along the Eastern Anatolian Magmatic Belt, and concurrent roll-back of the Cyprus slab in central Anatolia (Figure 3.16B ; Biryol et al., 2011; Schildgen et al., 2014; Chapter 2).

The Zr/Nb, $(Tb/Yb)_N$, $(La/Yb)_N$ and Nb/La trace element and Sr-Nd-Pb isotopic patterns of late Cenozoic magmatism in central and eastern Anatolia were caused by melts derived from different mantle sources and modified by assimilation of continental crust. Geochronological and tectonic interpretations in Chapter 2 suggest that the early Miocene to Pliocene igneous rocks of the Yamadağ, Ağrı and Sivas suites are products of slab break-off. Those units are characterized by an increasing melting source depth from spinel- to garnet (-spinel)-facies (Figure 3.17C) and interaction between depleted MORB and enriched OIB-like melts (i.e., broad range of $(La/Yb)_N$ and low Zr/Nb ratios, and Pb isotopes; Figures 11, 15A-B and 17D). The slab break-off-related magmatism was succeeded by the formation of the late Miocene to Pliocene Kars-Erzurum volcanic plateau and the Pliocene to Quaternary Ararat, Nemrut, Etrüsk, Tendürek and Süphan stratovolcanoes and Yiğitdağ, Elazığ and Erzincan volcanic suites in eastern Anatolia. Those volcanic units resulted from shallower melting depths ($(Tb/Yb)_N < 1.8$; Wang et al., 2002) and less, or not, metasomatized (low Ba/Ta ratio), more alkaline and more depleted melts (higher initial ε_{Nd}). This geochemical signature can be caused by the coeval and prolonged exposure to flowing asthenosphere and subsequent SCLM partial removal (Figure

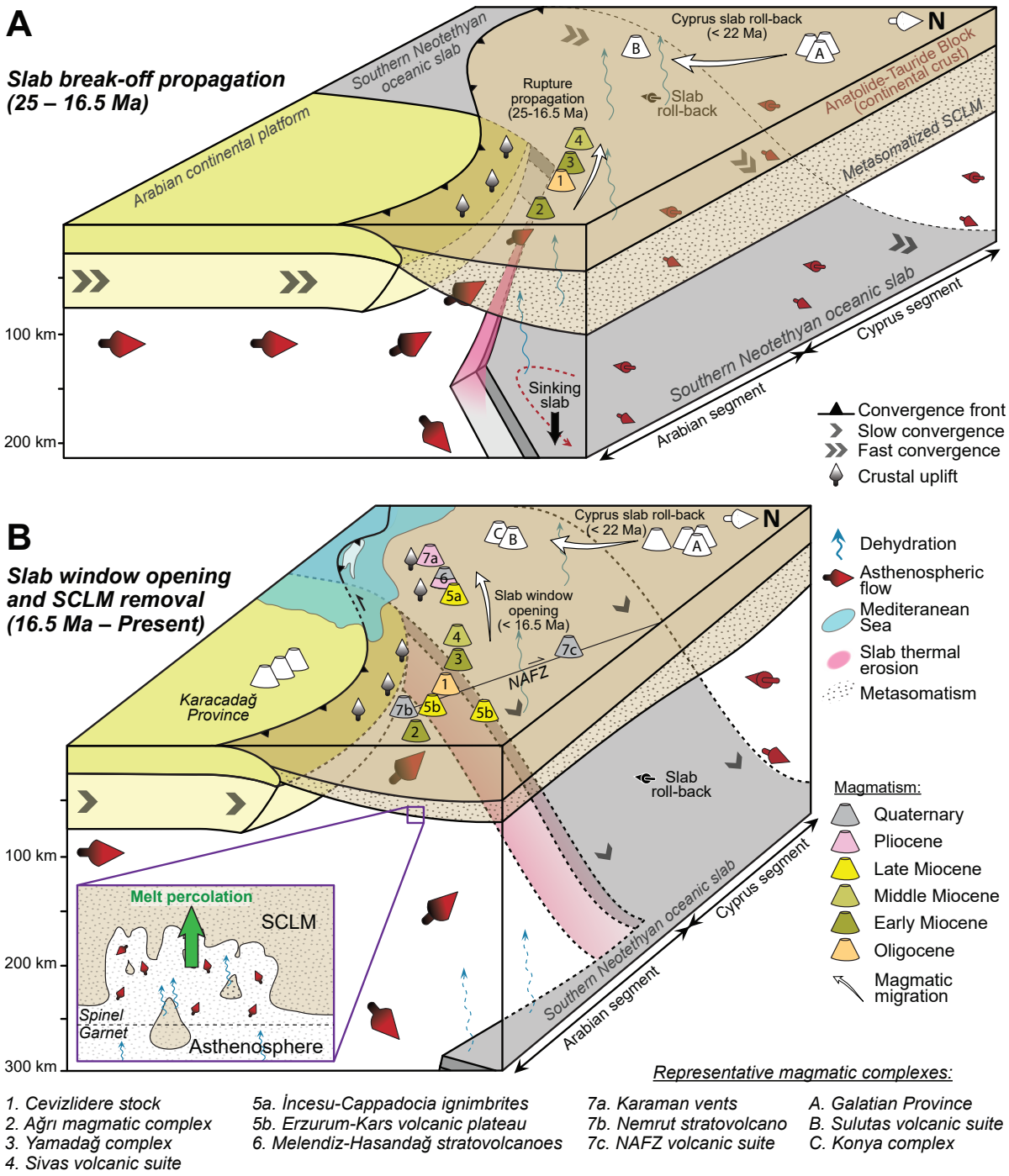

Figure 3.16 Schematic 3D cartoons illustrating the geometry of the Southern Neotethyan oceanic slab fragmented into the Arabian and Cyprus segments (inspired from Biryol et al., 2011; Schildgen et al., 2014; Menant et al., 2016) and westward migration of magmatism during the early to middle Miocene slab break-off propagation (A) and subsequent gap opening and SCLM partial removal since the middle Miocene (Chapter 2). The Galatian magmatic province (A), Sulutas (B) and Konya (C) volcanic complexes represent the southward migration of volcanism as result of the Cyprus slab roll-back since the early Miocene. The slab rupture allowed subslab asthenosphere infiltration and heat accumulation at the base of ATB, considered a unique continent fragment during Cenozoic. On this cartoon, the Bitlis-Pütürge

Massifs, Central Anatolian Crystalline Complex, ATB and South Armenian Block are part of the same rigid overriding slab that undergoes the Arabian collision and resulting slab break-off tectono-magmatic effects. The detached slab segment sinks into the asthenosphere and is linked to the attached Cyprus slab and also the westerly Aegean slab, which is not represented here. The small insert in the cartoon B illustrates the SCLM destabilization and partial removal by convective dripping (after Gazel et al., 2012; Reid et al., 2017). Sinking subduction-modified SCLM drips release volatiles and favor melting of the upwelling asthenosphere by decompression (see text for explanations).

3.17; Chapter 2) that are monitored by seismic tomography images (e.g., Biryol et al., 2011; Delph et al., 2017) and also responsible for the shallow heat anomaly beneath Anatolia (e.g., McNab et al., 2017) and regional crustal uplift (Keskin, 2007; Şengör et al., 2008).

To the west, volcanic products in central Anatolia are a result of more recent and less mature slab break-off magmatism. This magmatism resulted from various degrees of SCLM metasomatism and enrichment of spinel-facies melting source, and possibly recorded an input of asthenospheric melts in the Quaternary as suggested by Reid et al. (2017). Although the SCLM beneath central and eastern Anatolia is thin according to today's seismic tomographic images, the results presented herein show a greater lithosphere-asthenosphere interaction in eastern Anatolia than in central Anatolia. Evidence for asthenospheric melting is recorded by the middle to late Miocene volcanism in eastern Anatolia, i.e., earlier than in central Anatolia, that resulted from drier, deeper and more enriched melts (e.g., Sivas suite; Figure 3.15). This interpretation is in accordance with models suggesting the westward opening of the break-off-related window and resulting toroidal flow of asthenosphere (Biryol et al., 2011; Schildgen et al., 2014; Menant et al., 2016; Chapter 2).

The roll-back of the Cyprus slab beneath the western part of central Anatolia produced the igneous rocks of the Sulutas and Konya complexes (Chapter 2). Those units resulted from the melting of the metasomatized SCLM without any contributions from asthenospheric melts. The geochemical signature of Sulutas and Konya igneous complexes is characterized by more radiogenic Sr and Pb isotope ratios (Figure 3.11) than their contemporaneous volcanic complexes along the SW-trending axis that includes the Sivas-Cappadocia-Hasandağ-Karaman complexes located near the locus of break-off (Figure 3.16).

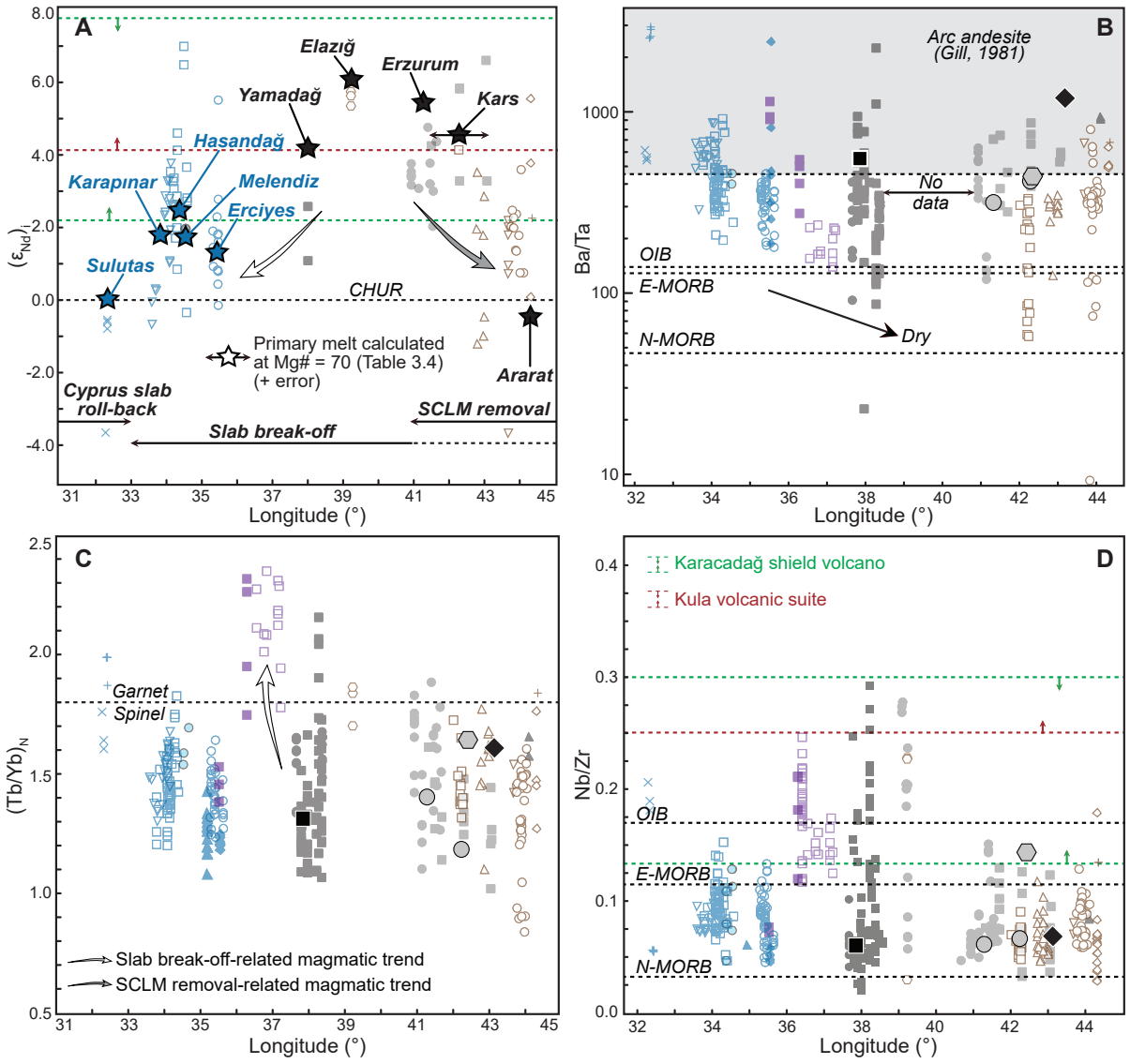

Figure 3.17 $(\varepsilon_{Nd})_i$ (A), Ba/Ta (B), $(Tb/Yb)_N$ (C) and Nb/Zr (D) variation through longitude (°). Only mafic rocks are plotted (SiO_2 < 56 wt %); A. variation of mantle input ($(\varepsilon_{Nd})_i$ > 0). The stars are the primitive melt compositions calculated at Mg # = 70, as in Figure 11, and following the methodology provided in the appendix B (Figure B.4). The white and grey arrows are the slab break-off- and SCLM-related magmatism. Spatial extend of each tectono-magmatic event constrained in Chapter 2 is also provided; B. Ba/Ta ratio used as a proxy for magma metasomatism. Lower ratio indicates drier magma melting conditions. Arc andesites have a Ba/Ta ratio > 428 (Gill, 1981); C. Primitive mantle-normalized $(Tb/Yb)_N$ ratio shows the variation in the magma source depth. The spinel and garnet stability field boundary at $(Tb/Yb)_N$ = 1.8 was empirically determined by Wang et al. (2002); D. Nb/Zr ratio used as a proxy for mantle source enrichment. OIB, E-MORB and N-MORB reference values from Sun and McDonough (1989). The references for composition range of the OIB-like Kula and Karacadağ volcanic suites are provided in Figure 3.15. Symbol legend is on Figure 3.7.

3.6.7.2 Mantle dynamics and regional partial removal of the SCLM

The interpretation of tomographic data suggested that the thickness of the Anatolian lithosphere could range from ca. 60 to 70 km in central Anatolia and 60 to 90 km in eastern Anatolia, without showing apparent local variations, and thus the SCLM is thin in both regions (Al-Lazki et al., 2003; Angus et al., 2006; Gök et al., 2007; Kind et al., 2015; Komut, 2015; Delph et al., 2017; Oruç et al., 2017). The depth of the lithosphere-asthenosphere boundary results from the interpretation of S and Pn wave velocity contrasts between the inferred cold SCLM (fast wave velocities) and hot upwelling asthenosphere (slow wave velocities). However, slow wave velocities can be due to the presence of melts and/or volatiles in the SCLM, and/or high temperatures potentially caused by asthenospheric upwelling (Maggi and Priestley, 2005; Kaviani et al., 2007; Foulger et al., 2015). The area of slow velocity in the upper mantle (Gans et al., 2009; Mutlu and Karabulut, 2011) mimics the shape of the Eastern Anatolian Magmatic Belt and suggests thin SCLM. The thin Anatolian SCLM is likely to have been destabilized and replaced by partially molten asthenosphere (e.g., Houseman and Molnar, 1997; Keskin, 2003, 2007; Levander et al., 2011; Neill et al., 2015; Bao et al., 2016; McNab et al., 2017). Gravitational destabilization and resulting thinning of the SCLM can occur by delamination and sinking of intact lithospheric blocks (e.g., Kay and Kay, 1993; Elkins-Tanton, 2007), small- or large-scale SCLM dripping (e.g., Yuen and Fleitout, 1985; Houseman and Molnar, 1997; Morency et al., 2002; Hernlund et al., 2008), or gradual thermal erosion from upwelling, hot asthenosphere (e.g., Monnereau et al., 1993; Davies and von Blanckenburg, 1995; Lenoir et al., 2001). Beneath Anatolia, large, intact blocks of foundering lithospheric mantle have not been seismically identified, leaving more localized features such as dripping and thermal erosion as the most likely styles of SCLM thinning (Hernlund et al., 2008; Kaislaniemi et al., 2014; Neill et al., 2015; Göğüş et al., 2017).

Late Miocene to Quaternary magmatism along the SCLM-denuded Eastern Anatolian Magmatic Belt post-dates the onset of collision between Arabia and Eurasia (Pearce et al., 1990; Aydar et al., 1995; Keskin et al., 1998; Keskin, 2003; Şengör et al., 2003; Şen et al.,

2004; Keskin et al., 2006; Keskin, 2007; Şengör et al., 2008). However, this magmatism is broadly coincident with break-off and foundering of the Southern Neotethyan slab (Keskin, 2003, 2007; Şengör et al., 2008; Chapter 2). In eastern Anatolia, slab break-off occurred at depths of ca. 50 to 150 km (Şengör et al., 2003; Zor, 2008; Schildgen et al., 2014; Menant et al., 2016), leading to a sub-vertical window between the remnant stub of the Arabian continental plate and its foundering Southern Neotethyan oceanic conjugate. The formation of this window led to upwelling of the subslab asthenosphere, which was previously part of the African and Arabian mantle reservoirs, as commonly observed in regions affected by slab break-off (Davies and von Blanckenburg, 1995; Wortel and Spakman, 2000), slab tear (Rosenbaum et al., 2008; Sternai et al., 2014), and ridge subduction settings (Thorkelson et al., 2011). Inducement of asthenospheric upwelling may therefore have been a key trigger in the removal of parts of the SCLM.

In the slab break-off scenario, melting of the asthenosphere occurred through a combination of decompression and metasomatism, possibly from the sinking slab (Freeburn et al., 2017) and the foundering SCLM fragments (Kaislaniemi et al., 2014). Asthenospheric uprise and melting may have been retarded at the base of the lithosphere (Reid et al., 2017), but the transfer of heat to the lithosphere, in part from uprising asthenospheric melts, resulted in SCLM partial melting. In this way, both mantle domains beneath Anatolia melted simultaneously leading to volcanic compositions with blended, variable geochemical character (Özdemir and Güleç, 2013; Reid et al., 2017; this Chapter). This style of melt generation occurred near at the spinel-garnet boundary through small-scale convective dripping (Kaislaniemi et al., 2014; Neill et al., 2015; Figure 3.16). This process could account for the longevity of syn-collisional magmatism (> 10 m.y.), irregular distribution of late Miocene to Quaternary volcanic complexes in eastern Anatolia, and widespread magmatism in the absence of crustal extension (Kaislaniemi et al., 2014; Neill et al., 2015). The wholesale lithospheric delamination scenario proposed by some studies in central and/or eastern Anatolia (e.g., Pearce et al., 1990; Bartol and Govers, 2014; Delph et al., 2017) would have instead resulted in southward migration of

magmatism with time and, which is not observed in central and eastern Anatolia (Chapter 2). The generation of post-subduction metasomatism and melting is expected to last for several million years depending on the remaining volatile content (Freeburn et al., 2017). As such, the magmatic fields in Anatolia are likely to become less active with time, unless other factors such as mantle upwelling, remotely sustained by the Afar plume, begin to play a larger role.

3.7 Conclusion

The geochemical analyses from igneous rocks in the 26 late Oligocene to Quaternary igneous complexes along the Eastern Anatolian Magmatic Belt were compiled in this study, and complemented by a few new lithogeochemical and Sr-Nd-Pb isotope analyses from the less-studied Konya, Karaman, Tekkedağ, Melendiz, Develidağ, Yamadağ and Ağrı igneous complexes. The interpretation of this geochemical database suggests that late Cenozoic magmatism along that Belt formed in response to (1) asthenospheric upwelling during break-off of the Southern Neotethyan slab and (2) partial removal of the SCLM. Slab break-off-related igneous suites of central Anatolia and the Yamadağ, Ağrı and Sivas areas in eastern Anatolia share similar magmatic features including 1) a temporal increase in the depth of melting, degree of enrichment and asthenospheric component; 2) general consistency in magma alkalinity; 3) a decreasing subduction signature through time. This new magmatic model suggests that magma was generated by the melting of the previously-metasomatized Anatolian SCLM and asthenosphere by decompression, which was largely controlled by the slab rupture propagation and break-off, and ingress of Arabian and African subslab asthenosphere. This geochemical evolution proposed herein fits with models developed for similar tectonic configurations for magmatism in post-subduction tectonic settings (e.g., Ferrari, 2004). The presence of water and the sustained advection of asthenospheric heat destabilized the thickened Anatolian SCLM root, leading to its partial removal by small-scale convection and the second major magmatic event in eastern Anatolia (Kaislaniemi et al., 2014; Neill et al., 2015). This magmatism generated the middle Miocene to Pliocene Kars-Erzurum volcanic plateau and Pliocene to Quaternary stratovolcanoes in eastern Anatolia. The interpretation of compiled geochemical

data suggests that this recent magmatism was characterized by 1) increasing contributions from the crust; 2) drier mantle source conditions, even though subduction signature was still recorded in some Quaternary stratovolcanoes (e.g., Ararat); 3) coexistence of highly alkaline, silica-undersaturated (e.g., the Tendürek stratovolcano) and calc-alkaline, silica-saturated magmatism (e.g., the Ararat stratovolcano); 4) decreasing depth of mantle sources. This new magmatic model emphasizes that the geochemical signature of post-subduction, syn-collisional magmatism, as recorded by primitive basalts, constantly evolves through time and space, and recorded shifting in mantle source domains. Anatolia is thereby a natural laboratory to investigate the complex geochemical evolution of post-subduction magmatism, controlled by the three-dimensional subducted slab dynamics, asthenosphere upwelling and change in lithosphere thickness.

Part 2: Late Cenozoic Anatolian Gold Metallogeny, Turkey

Chapter 4: Tectonic triggers for post-subduction magmatic-hydrothermal gold metallogeny in the late Cenozoic Anatolian Metallogenic Trend, Turkey

4.1 Introduction

Porphyry and associated epithermal deposits dominantly form in subduction arc setting along worldwide accretionary belts (e.g., Sillitoe, 1972; Hedenquist and Lowenstern, 1994; Richards, 2003; Candela and Piccoli, 2005; Simmons et al., 2005; Sillitoe, 2010). The accumulation of abundant fertile, hydrous, oxidized basaltic melts at the base of a thickened crust over a period of a few tens of million years and during focused tectono-magmatic events is required to develop a mature magmatic system favorable for ore-forming processes (e.g., Richards, 2003; Richards et al., 2012; Chiaradia, 2014). The formation of mineral deposits and related magmatic rocks peak at specific times when the tectono-magmatic conditions are optimal, typically at the terminal stage of a long-lived mature arc magmatic episode (e.g., Chiaradia et al., 2009; Chiaradia et al., 2012; Bissig et al., 2015). However, the production of arc magmas may cease due to changes in the convergence rate and thus angle of subduction (e.g., Kay et al., 2005; Bertrand et al., 2014) or at the onset of continental collisional (e.g., Gasquet et al., 2005).

Metallogenic investigations along collisional belts and advances in geochronology reveal that porphyry systems can occur after the cessation of subduction, and during or after a collision, including slab tearing (i.e., trench-perpendicular subvertical slab rupture) and break-off (i.e., trench-parallel subhorizontal slab rupture) tectonic events (e.g., De Boorder et al., 1998; Vos et al., 2007; Hou et al., 2009; Richards, 2009, 2015). The asthenospheric upwelling that results from slab rupture initiation and propagation, and subsequent slab window opening, plays a crucial role in the formation of post-subduction porphyry and epithermal deposits (De Boorder et al., 1998; Vos et al., 2007; Richards, 2009; Logan and Mihalynuk, 2014; Richards, 2015). Hot asthenosphere can remobilize metal-rich sulfide residues left from previous subduction arc magmatism in the lithospheric mantle (Hronsky et al., 2012; Griffin et al., 2013)

and/or lower crust (Richards, 2009; Shafiei et al., 2009). Although the genetic relationship between post-subduction slab ruptures and the production of porphyry and epithermal deposits has been identified (e.g., De Boorder et al., 1998; Vos et al., 2007; Richards, 2015), the temporal and spatial constraints on post-subduction porphyry and epithermal mineralization are generally poorly documented, particularly in light of time-space evolution of crust and mantle interactions such as slab rupture propagation, window opening and resulting asthenosphere invasion.

The Western Tethyan Orogenic Belt that extends from the Alps to Pakistan was generated during the Paleozoic to Mesozoic accretionary and the Cenozoic collisional orogenesis between Laurasian and small Gondwana-derived crustal fragments (e.g., Şengör et al., 1984; Stampfli and Borel, 2004). The successive amalgamation of those crustal fragments, including the Anatolide-Tauride Block in Turkey, produced long- and short-lived subduction episodes and a complex tectonic framework that were favorable for ore-forming processes. This emerging Belt hosts numerous world-class porphyry and epithermal copper and gold deposits such as Rosia Montana, Chelopech, Majdanpek, Kışladağ, Çöpler, Sar Cheshmeh and Reko Diq (Janković, 1977, 1997; Ciobanu et al., 2002; Lips, 2002; von Quadt et al., 2005; Peytcheva et al., 2008; Zimmerman et al., 2008; Shafiei et al., 2009; Yiğit, 2009; Richards et al., 2012; İmer et al., 2013; Kuşcu et al., 2013; Razique et al., 2014; Richards, 2015; Baker et al., 2016), and remains a focus of on-going exploration efforts for precious and base metals. However, the distribution of porphyry and epithermal systems along the Western Tethyan Orogenic Belt is neither uniform in time nor space (Zimmerman et al., 2008; Bertrand et al., 2014; Richards, 2015). Major clustering resulted in specific metallogenic periods and along distinct Belt segments such as the Oligo-Miocene Urumieh-Doktar Belt in southeast Iran (Richards and Sholeh, 2016), the Jurassic to Cretaceous Somkheto-Karabagh Belt and the Eocene to Pliocene ore deposits of the Zangezur-Ordubad region in the Lesser Caucasus (Moritz et al., 2016a; 2016b), the Cretaceous and Oligocene-Miocene deposits of the Alpine-Balkan-Carpathian-Dinaride Belt (Heinrich and Neubauer, 2002), the Biga district of northwest Turkey (Yiğit, 2012; Smith et al., 2014;

Smith et al., 2016) and the Pontide Belt on the Rhodope-Pontide Block of northern Turkey (Bilir, 2015; Delibaş et al., 2016). However, the Anatolide-Tauride, or Anatolian, segment of the Western Tethyan Orogenic Belt in Turkey seems to be characterized by isolated porphyry and epithermal deposits rather than mineral clusters (Yiğit, 2006, 2009; Bertrand et al., 2014; Richards, 2015).

Recent geochronological studies indicate that numerous major gold-rich porphyry and epithermal deposits and prospects throughout Anatolia such as Kışladağ (Baker et al., 2016), Pınarbaşı (Delibaş et al., 2017) and Cevizlidere (İmer et al., 2014) are hosted within late Cenozoic igneous units (Yiğit, 2006, 2009). Thus, mineralization and associated magmatism occurred during the various segmentation episodes of the Southern Neotethyan oceanic slab after the onset of the Arabia-Eurasia continental collision (Gessner et al., 2017; Menant et al., 2018). The E-trending alignment of Oligocene to Miocene porphyry and epithermal deposits and prospects along the Anatolide-Tauride Block is defined herein as the late Cenozoic Anatolian Metallogenic Trend. Although the tectonic complexity in the late Cenozoic along the entire Anatolian Trend is relatively well-documented and understood, the temporal and spatial distribution of those Au (-Cu) deposits and prospects remains undetermined. The Anatolian Trend therefore provides an excellent natural laboratory to investigate mechanisms of post-subduction metallogeny.

This field-based regional study 1) defines the late Cenozoic mineral districts along the late Cenozoic Anatolian Metallogenic Trend on the Anatolide-Tauride Block hosting porphyry and epithermal mineralization, 2) constrains the timing of gold mineralization, and 3) determines the control of regional structures on the spatial distribution of Au (-Cu) mineralization synchronous with the development of trench-parallel and trench-perpendicular slab ruptures and resulting flow of asthenosphere. New field observations and multi-technique geochronological data (LA-ICP-MS U-Pb, Re-Os and $^{40}Ar/^{39}Ar$ dating methods) from the most significant late Cenozoic porphyry and high-sulfidation epithermal occurrences, prospects and deposits from the Anatolian Metallogenic Trend are provided herein and interpreted with

previously-published, deposit-focused geochronological data throughout Anatolia (Yılmaz et al., 2013; İmer et al., 2014; Baker et al., 2016; Delibaş et al., 2017).

4.2 Geological and tectonic setting of the Anatolide-Tauride Block

Many crustal fragments rifted away from the Gondwana continent, migrated northwards, subsequently accreted into the Laurasia continent and closed the numerous branches of the Neotethys Ocean in the Paleozoic and Mesozoic (Şengör and Yılmaz, 1981; Robertson and Dixon, 1984; Sengör and Natal'In, 1996; Okay and Tüysüz, 1999; Stampfli, 2000; Okay et al., 2006; Pourteau et al., 2013; van Hinsbergen et al., 2016). The Anatolide-Tauride Block in Turkey, or 'Anatolia', is one of those Gondwana-derived crustal fragments that accreted to the Rhodope-Pontide Block of southern Laurasia during the Late Cretaceous closing the Northern Neotethys Ocean along the present İzmir-Ankara-Erzincan suture zone (Figure 4.1; Şengör and Yılmaz, 1981; Okay and Tüysüz, 1999). Once docked to Laurasia, the Anatolide-Tauride Block became the southern active margin of Laurasia along which the Southern Neotethys Ocean closed and it collided the Arabia platform in the late Cenozoic (Şengör and Yılmaz, 1981; Jolivet and Faccenna, 2000; Robertson et al., 2013).

4.2.1 Anatolide-Tauride Block

A succession of orogenic events in the Anatolide-Tauride Block is responsible for its complex tectonic framework. Traditionally, the metamorphosed and exhumed units (e.g., Tavşanlı Zone, Afyon-Ören Zone and Menderes Massif) define the Anatolide platform whereas the underthrusted, un-metamorphosed equivalent units (e.g., Taurus platform and Eastern Anatolian Accretionary Complex) refer to the Tauride platform (Ketin, 1966; Şengör and Yılmaz, 1981; Okay, 1984; Pourteau et al., 2010; van Hinsbergen et al., 2016).

The oldest exhumed unit of the Anatolides is the Tavşanlı Zone, which is a Paleozoic to Mesozoic passive margin sedimentary sequence that reached a high-pressure and low-temperature metamorphic peak between 92 and 83 Ma (Okay et al., 1998; Okay and Tüysüz, 1999; Sherlock et al., 1999; Plunder et al., 2015) followed by blueschist-facies retrogression at

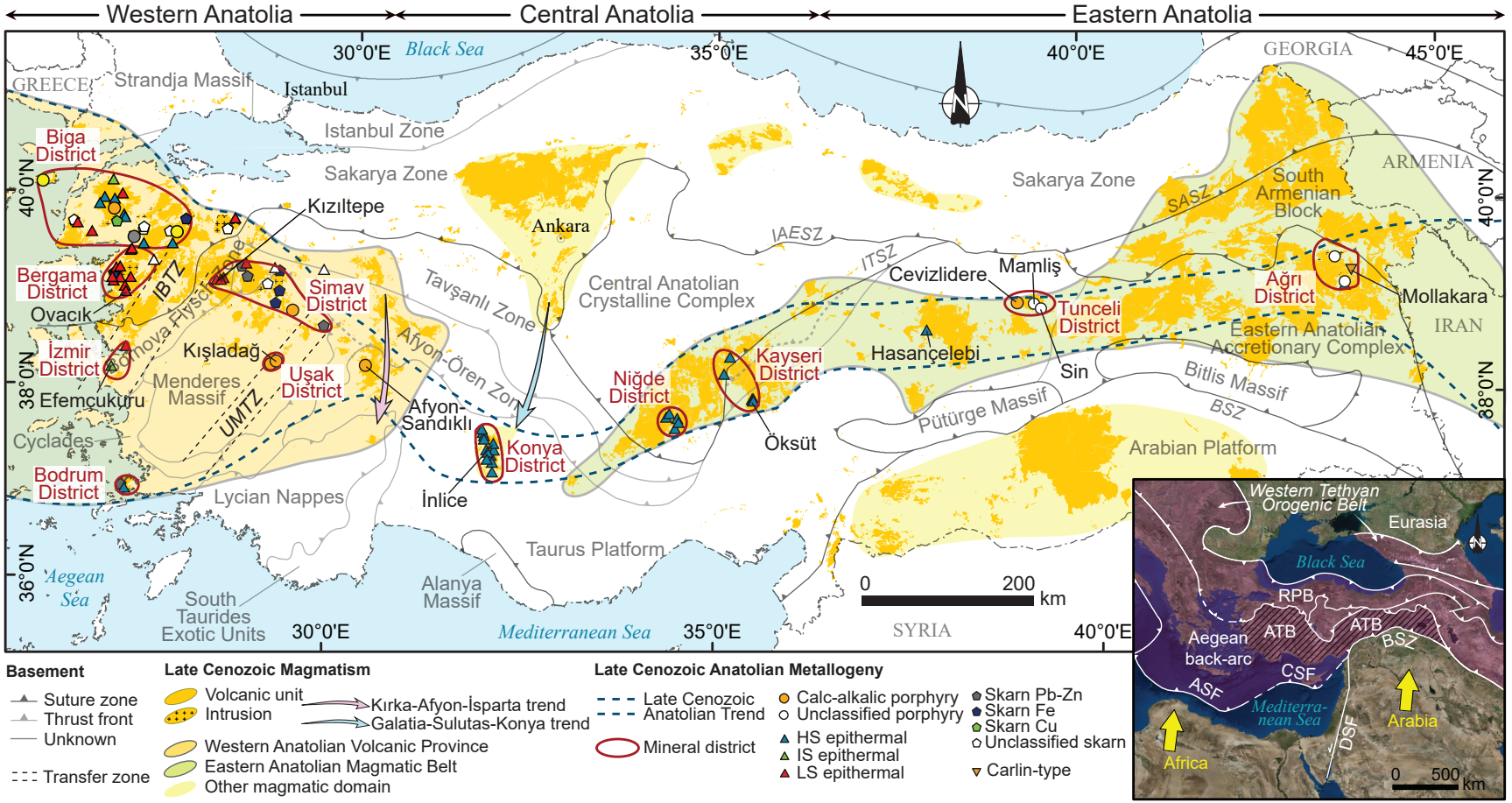

Figure 4.1 Tectono – magmatic map of Turkey (1:6,000,000 scale; Lambert Conic projection; European Datum 1950) showing the basement boundaries (modified from Görür and Tüysüz, 2001; Şengör et al., 2008; Pourteau et al., 2010), late Cenozoic magmatic rocks (modified from MTA, 2002), major precious and base metal occurrences and districts, and the late Cenozoic Anatolian Metallogenic Trend. The Eastern Anatolian Magmatic Belt is from Chapter 2. HS/IS/LS stand for high/intermediate/low-sulfidation epithermal. Background of the location map is from Google Earth. ASF = Aegean Subduction Front; ATB = Anatolide-Tauride Block; BSZ = Bitlis Suture Zone; CSF = Cyprus Subduction Front; DSF = Dead Sea Fault; IAESZ = İzmir-Ankara-Erzincan Suture Zone; IBTZ = İzmir-Balıkesir Transfer Zone; ITSZ = Inner Tauride Suture Zone; RPB = Rhodope-Pontide Block; SASZ = Sevan-Akera suture zone; UMTZ = Uşak-Muğla Transfer Zone.

83-60 Ma (Sherlock et al., 1999). South of and below the Tavşanlı Zone, the Afyon-Ören Zone consists of Precambrian to Mesozoic rift-to-passive margin volcano-sedimentary sequence (Okay et al., 1996; Candan et al., 2005) that experienced high-pressure and low-temperature metamorphism, then crustal exhumation from 67 to 62 and 62 to 59 Ma at Afyon and Ören, respectively (Okay, 1984; Okay et al., 1998; Rimmelé et al., 2003, 2006; Pourteau et al., 2010; 2013). The Afyon-Ören Zone tectonically underlies the Cycladic Blueschist Unit, or Cyclades, in southwest Turkey that underwent a high-pressure and low-temperature metamorphic peak at 50 Ma (Lister et al., 1984; Candan, 1997; Ring et al., 1999; Rimmelé et al., 2003; Pourteau et al., 2013). The Menderes Massif, which tectonically overlies the Cyclades, is exposed in western Anatolia and is a metamorphic core complex composed of a late Precambrian gneissic core and a Paleozoic cover of schist and marble (e.g., Şengör and Yılmaz, 1981; Bozkurt and Oberhänsli, 2001; Lips et al., 2001). This Massif recorded late Neoproterozoic Pan-African and Eocene to Oligocene Alpine metamorphism and deformation (Candan et al., 2001; Lips et al., 2001). The Menderes Massif was exhumed along regional E-trending, shallowly-dipping, N- and S-verging detachment faults (e.g., Simav, Kuzey and Güney) in the Miocene, and subsequently reworked by steeply-dipping normal faults bounding the present grabens (e.g., Gediz and Büyük; Bozkurt and Park, 1994; Lips et al., 2001). The Bornova Flysch Zone is a regional Mesozoic to Paleocene sheared mega-olistostrome and ophiolitic mélange that formed along a sinistral transform zone at the northwestern edge of the Anatolide-Tauride Block. This Flysch Zone was thrust over the northwest edge of the Menderes Massif along the İzmir-Ankara-Erzincan suture zone (Okay et al., 1996).

In the Taurides, the Lycian ophiolitic nappes of southwestern Turkey are an allochthonous Mesozoic passive margin succession remnant of the Northern Neotethys Ocean that was obducted in the Late Cretaceous and thrust over the Menderes Massif during its exhumation from Eocene to late Miocene (Collins and Robertson, 1997; Lips et al., 2001). The Taurus platform, which wraps around the southern margin of the Anatolide-Tauride Block and the Central Anatolian Crystalline Complex, consists of a Precambrian basement and a Paleozoic

to Mesozoic cover that is dominated by carbonate platform sediments, and was thrust over the Late Cretaceous ophiolites (Robertson et al., 2007). This basement sequence was intruded by the Late Cretaceous to Eocene plutons and subsequently covered by Cenozoic pelagic and continental sediments and volcanic units (Aktaş and Robertson, 1984; Yılmaz, 1993; Robertson et al., 2007; Rızaoğlu et al., 2009; Kuşcu et al., 2010; Nurlu et al., 2016). The deformation of the Taurus platform resulted from the continental collision of the Anatolide-Tauride Block and Arabia plate with Eurasia between the Cretaceous and Miocene. The eastern termination of the Anatolide-Tauride Block consists of a Late Ordovician to early Silurian metamorphic basement unconformably overlain by Mesozoic ophiolites, Cretaceous to Oligocene southward-imbricated slices of flysch (Yılmaz et al., 2010; Topuz et al., 2017). This basement sequence was subsequently intruded by early to middle Miocene plutons and finally covered by the middle Miocene to Present volcanic products of the Erzurum-Kars plateau (Şengör et al., 2003; Yılmaz et al., 2010; Topuz et al., 2017).

The triangular-shaped Central Anatolian Crystalline Complex of central Turkey is a crustal fragment that is distinct from the Anatolide-Tauride and Rhodope-Pontide Blocks and separated from those Blocks by the İzmir-Ankara-Erzincan and inferred Inner Tauride suture zones (Figure 4.1). The stratigraphy of the Central Anatolian Crystalline Complex consists of Paleozoic to Mesozoic crystalline massifs (Kırşehir, Akdağ and Niğde) that experienced high-grade metamorphism in the Late Cretaceous and exhumed during the Cenozoic (Dilek and Whitney, 2000; Whitney et al., 2001; Lefebvre et al., 2011, 2013). Those massifs were thrusted by dismembered Late Cretaceous Tethyan ophiolites, intruded by Late Cretaceous calc-alkaline to alkaline plutons and batholiths, and unconformably covered by Cenozoic to Quaternary volcanic rocks and sediments (Görür et al., 1984; Yaliniz and Göncüoglu, 1998; Whitney et al., 2003; Kadıoğlu et al., 2006; Boztuğ et al., 2009; Lefebvre et al., 2011, 2013).

The Bitlis and Pütürge Massifs of southeast Anatolia are composed of a Neoproterozoic Pan-African basement of gneiss and schist, and a Paleozoic to Mesozoic cover of metaclastic and carbonate rocks that underwent a high-pressure and low-temperature metamorphism in the

Late Cretaceous (Ustaömer et al., 2009; Oberhänsli et al., 2010; Ustaömer et al., 2012).

4.2.2 Geodynamic evolution

The late Cenozoic geodynamic evolution of the Anatolide-Tauride Block is dominated by the closure of the Southern Neotethys Ocean, manifested as the Arabian continental collision in eastern Anatolia along the current Bitlis suture zone (Robertson, 2000; Westaway, 2003) and the subduction of the Aegean and Cyprus segments of the Southern Neotethyan oceanic slab in western and central Anatolia, respectively (e.g., Le Pichon and Angelier, 1981; Biryol et al., 2011; Jolivet et al., 2013).

The continental collision between Eurasia (Anatolide-Tauride Block) and Arabia has been interpreted to have started in either the Eocene (Rolland et al., 2012), Oligocene (as commonly accepted; Jolivet and Faccenna, 2000; Agard et al., 2005; Allen and Armstrong, 2008; Barrier and Vrielynck, 2008; McQuarrie and van Hinsbergen, 2013; Karaoğlan et al., 2016), or Miocene (Şengör and Yılmaz, 1981; Dewey et al., 1986; Yılmaz, 1993; Yiğitbaş and Yilmaz, 1996; Robertson et al., 2007; Şengör et al., 2008; Hüsing et al., 2009; Okay et al., 2010; Robertson et al., 2016). The acceleration of the Arabia plate convergence (Jolivet and Faccenna, 2000) and its subsequent indentation into the eastern part of the Anatolide-Tauride Block (Dewey et al., 1986; McClusky et al., 2000; Reilinger et al., 2006) caused the steepening and subsequent break-off of the easterly Arabian segment of the Southern Neotethyan oceanic slab (e.g., Keskin, 2003, 2007). The resulting sub-horizontal slab rupture propagated westwards up to the Cyprus slab since the late Oligocene (Faccenna et al., 2006; Biryol et al., 2011; Schildgen et al., 2014; Chapter 2). The slab break-off event in the Arabian domain was followed by the partial removal of the lithospheric mantle below the Eastern Anatolian Accretionary Complex leading to the crustal doming and formation of the Erzurum-Kars volcanic plateau since ca. 13-11 Ma (Keskin, 2003; Şengör et al., 2003; Keskin, 2007; Şengör et al., 2008).

In central Anatolia, the roll-back (Koç et al., 2012; Chapter 2) or delamination of the Cyprus slab (Bartol and Govers, 2014; Delph et al., 2017) resulted in the southward migration of the magmatic front since the early Miocene, and the uplift of the Taurus platform since the

Oligocene (Karaoğlan, 2016) or late Miocene (Cosentino et al., 2012; Schildgen et al., 2012; Schildgen et al., 2014; McNab et al., 2017).

The Hellenic trench retreat caused the formation of an extensional back-arc basin (i.e., the Aegean Sea) and continental rifting in western Anatolia since the late Oligocene (Le Pichon and Angelier, 1981; Jolivet et al., 2013). The slab break-off event in eastern Anatolia associated with the deep lateral continuity of the Southern Neotethyan slab in the mantle increased the load on the westerly Aegean slab segment leading to the acceleration of the Hellenic trench retreat (Faccenna et al., 2006) since the middle Miocene (Jolivet et al., 2015), the modification of mantle flow patterns (Le Pichon and Kreemer, 2010; Sternai et al., 2014), and the westward extrusion of the Anatolian microplate along the North and East Anatolian fault zones (Faccenna et al., 2006; Özeren and Holt, 2010). Also, the acceleration of the Hellenic trench retreat, relative to the Cyprus trench, dramatically curved and consequently tore the Aegean slab. This slab tear event resulted in the upwelling of the hot asthenosphere beneath the western Anatolia between 15 and 8 Ma (De Boorder et al., 1998; Dilek and Altunkaynak, 2009; Biryol et al., 2011; Karaoğlu and Helvacı, 2014; Jolivet et al., 2015; Prelević et al., 2015; Menant et al., 2016). This S-trending subvertical tear was spatially and temporally accompanied by the production of alkaline magmatism along the S-trending Kırka-Afyon-İsparta trend (Figure 4.1; Dilek et al., 2010; Prelević et al., 2012; 2015). The combination of slab roll-back and tearing, and back-arc development facilitated the exhumation of metamorphic core complexes such as the Menderes Massif and Cyclades (Satır and Friedrichsen, 1986; Rimmele et al., 2005; van Hinsbergen, 2010; Jolivet et al., 2013). Paleomagnetic data and deformation distribution revealed that the eastern edge of the Aegean slab retreated faster than its western part leading to the clockwise rotation of the External Hellenides in northern Greece (Kissel et al., 2003; van Hinsbergen and Schmid, 2012) and the anticlockwise rotation of the Menderes Massif (van Hinsbergen, 2010). The Menderes Massif is bounded by the two NE-trending, İzmir-Balıkesir and Uşak-Muğla Transfer Zones along which volcanic edifices emplaced. Both Transfer Zones are the surface expression of the Menderes Massif rotation and differential exhumation with

Cyclades during the eastern Aegean slab roll-back and tearing in the Neogene (Erkül et al., 2005b; Uzel and Sözbilir, 2008; van Hinsbergen, 2010; Ersoy and Palmer, 2013; Karaoğlu and Helvacı, 2014).

4.2.3 Late Cenozoic Anatolian magmatism

The successive closure of the various Neotethyan oceanic branches around the Anatolide-Tauride Block produced widespread magmatism in subduction, back-arc, post-subduction and post-collisional settings since the Late Cretaceous (Keskin et al., 1998; Boztuğ, 2000; Keskin, 2003; Kadıoğlu et al., 2006; Dilek and Altunkaynak, 2009; Rızaoğlu et al., 2009; Kuşcu et al., 2010; Ersoy and Palmer, 2013; Chapter 2). Late Cenozoic (26 Ma to Present) magmatism covers a significant part of the Anatolide-Tauride Block forming the spatially-distinct Western Anatolian Volcanic Province and Eastern Anatolian Magmatic Belt (Figure 4.1).

The late Cenozoic igneous rocks of the Western Anatolian Volcanic Province are assembled into the following magmatic domains as defined by Ersoy and Palmer (2013): 1) İzmir-Balıkesir Transfer Zone, 2) Menderes Core Complex, and 3) Kırka-Afyon-İsparta trend. The northerly early Miocene and southerly middle Miocene magmatic complexes of the İzmir-Balıkesir Transfer Zone were emplaced along NE-trending strike-slip and normal faults (Erkül et al., 2005b, 2005a; Dilek and Altunkaynak, 2010; Erkül, 2012; Ersoy et al., 2014; Seghedi et al., 2015). The Miocene exhumation of the Menderes metamorphic core complex took place during one (Jolivet et al., 2013) or two extensional phases (e.g., Bozkurt, 2003; Gessner et al., 2013; Uzel et al., 2015). This tectonic event was accompanied by syn-tectonic magmatism that was exposed on the Menderes footwall units in the early Miocene (e.g., Eğrigöz pluton; Ring and Collins, 2005) and middle Miocene (e.g., Salihli and Turgutlu plutons; Glodny and Hetzel, 2007) along NE-trending graben basins (17-12 Ma; Ersoy et al., 2010; Karaoğlu et al., 2010; Ersoy et al., 2012). The igneous units of the S-striking Kırka-Afyon-İsparta trend are spatially and tectonically distinct from the Menderes metamorphic core complex (Figure 4.1). Those units have an age and geochemical evolution that evolve from the northerly, early Miocene, calc-alkaline to alkaline Kırka (21-17 Ma) to middle Miocene, alkaline, Afyon (14-8 Ma) and

southerly, Pliocene to Quaternary, ultrapotassic İsparta-Gölcük igneous rocks (< 4 Ma; Alıcı et al., 1998; Kumral et al., 2006; Dilek and Altunkaynak, 2010; Prelević et al., 2012; Platevoet et al., 2014).

The volcanic products of the western part of the Eastern Anatolian Magmatic Belt in central Anatolia include elongate stratovolcanoes and volcanoes (e.g., Hasandağ, Melendiz, Erciyes, Develidağ and Tekkedağ), linear clusters of monogenetic vents (e.g., Karaman, Karapınar and Acigöl), volcanic ridges and widespread ignimbrite provinces (e.g., Cappadocia; Pasquare et al., 1988; Toprak and Göncüoğlu, 1993; Aydar et al., 1995). Those volcanic edifices were emplaced on Permian metamorphic basement, Triassic limestone and Jurassic-Cretaceous ophiolitic complexes (Karakaya, 1991; Toprak and Göncüoğlu, 1993). West of the Eastern Anatolian Magmatic Belt, the Konya volcanic complex is isolated located at the termination of the Akşehir normal fault in the Central Taurides. Despite having similar volcanic stratigraphy and compositions to central Anatolian volcanic edifices, the Konya complex is not considered as part of the Eastern Anatolian Magmatic Belt. Instead, this volcanic complex is part of the Galatia-Sulutas-Konya trend (Figure 4.1) that results from the southward migration of early Miocene, northerly Galatia volcanism (23-17 Ma) on the Rhodope-Pontide Block to the middle Miocene Sulutas volcanism (16-11.5 Ma) and lamprophyres to the late Miocene, southerly Konya volcanic complex (12-3 Ma; Chapter 2). Magmatism in the eastern part of the Eastern Anatolia Magmatic Belt took place in two stages: 1) sparse Oligocene to middle Miocene volcanic units (Yamadağ complex) and intrusions (Cevizlidere, Ağrı and Sarıçimen), and 2) widespread late Miocene to present time volcanic plateau dominated by Pliocene to Quaternary stratovolcanoes (e.g., Nemrut, Süphan and Ararat; Chapter 2).

4.3 Field-based definition of late Cenozoic Anatolian precious and base metal districts

The 1500 km-long Anatolian Metallogenic Trend is defined in this study by the E-W alignment of late Cenozoic Anatolian mineral deposit clusters (Figure 4.1). The mineral deposits in those clusters, or mineral districts, share similar geological, structural, metallogenic, tectonic, geochemical and geochronological features. Based on new field investigations and

local studies, nine new porphyry and epithermal districts are defined herein in the western, central and eastern segments of the Anatolian Trend that are correlated with the Aegean, Cyprus and Arabian tectonic domains, respectively (Table 4.1). Those districts are prospective areas for gold mineralization. However, some prospects (e.g., Afyon-Sandıklı and Hasançelebi) are apparently spatially isolated and have distinct features that prevent them from being included in a district. These newly-defined district names were chosen based on the nearest major geographical feature, city or town.

Those new field investigations focus on the late Cenozoic porphyry and epithermal Au-Cu systems located on the Anatolide-Tauride Block, thereby excluding the well-endowed and studied Biga and Bergama districts in northwest Turkey (e.g., Yılmaz, 2002; Murakami et al., 2005; Yilmaz et al., 2010; Yiğit, 2012; Smith et al., 2014; Yılmazer et al., 2014; Brunetti, 2016; Çiçek and Oyman, 2016; Leroux, 2016; Sánchez et al., 2016; Smith et al., 2016), and the Eocene porphyry Cu-Mo prospects in the Bursa district in the northern part of western Anatolia (e.g., Yiğit, 2009). Although the Biga and Bergama districts are part of the northwestward extension of the late Cenozoic Anatolian Metallogenic Trend, their mineral deposits and associated igneous units formed on another tectonic terrane, namely the Rhodope-Pontide Block, north of the İzmir-Ankara-Erzincan suture zone (Figure 4.1). Pre-Oligocene, non-precious and non-base metal mineralization are also beyond the scope of this Chapter.

4.3.1 Economic features of the Anatolian porphyry and epithermal systems

Evaluation of current Anatolian precious and base metal resources related to late Cenozoic magmatism in this study indicates that the late Cenozoic Anatolian porphyry and epithermal are dominantly endowed in gold mineralization. The 33 Moz of gold resources and reserves compiled herein are distributed among the Kışladağ, Efemçukuru, Kızıltepe, Tavşan, İnlice, Öksüt, Mollakara and Cevizlidere epithermal and porphyry deposits, whereas the region's copper endowment (3.7 Blbs; inferred resources) is limited and mainly restricted to the Cevizlidere porphyry Cu-Au-Mo deposit (Figure 4.2; Table 4.2). Porphyry and intermediate-sulfidation epithermal deposits provide most of gold resources in Anatolia, similar

Table 4.1 Characteristics of the Late Cenozoic Anatolian mineral gold districts and isolated porphyry- and epithermal-style prospects.

	Western Anatolia				
	Simav District	**İzmir District**	**Uşak District**	**Afyon-Sandıklı porphyry deposit**	**Bodrum District**
Basement	Bornova Flysch Zone, Menderes Massif	Bornova Flysch Zone	Menderes Massif	Taurus platform	Afyon-Ören Zone
Formation	Simav and Sındırğı magmatic complexes, Baklan, Alaçam, Eğrigöz and Pınarbaşı plutons	Cumaovası volcanic suite, Bornova Flysch	Beydağ voclanic complex	Afyon volcanic complex	Bodrum volcanic complex
Age (Ma)	23 - 17	17 - 13	17 - 12	14 - 8	12 - 9
Tectonic setting	Aegean slab roll-back, back-arc	Aegean slab roll-back, back-arc	Aegean slab tear/roll-back, back-arc	Aegean slab tear/roll-back	Aegean slab tear/roll-back, back-arc
Rock type	Granite, monzonite, dacitic to rhyolitic ignimbrites and lavas	Metasediments, rhyolite	Monzonite	Trachyte, monzonite	Andesite, monzonite
Magma association	Calc-alkaline	Calc-alkaline	Calc-alkaline to alkaline	Alkaline	Alkaline
Host rock age (Ma)	ca. 21 - 18	Late Cretaceous to 13.17 ± 0.25	14.76 ± 0.01	11.64 ± 0.20	9.76 ± 0.06
Kinematic association	Extension, transtension	Extension, transtension	Extension	Extension	Extension
Regional structural control	Dextral normal and detachment Simav faults, Erdogmus – Yenigediz graben	Seferihişar horst	NE-trending Uşak-Güre graben	Sandıklı graben	E-trending Gokova
Alteration system	LS epithermal, porphyry, skarn	LS-IS epithermal	Porphyry, HS epithermal	Porphyry, HS epithermal	HS epithermal, skarn
Commodity	Au (-Ag-Pb-Zn-Fe)	Au (-Pb-Zn-Ag)	Au	Au-Cu	Pb-Zn-Au?
Alteration assemblage	Argillic, skarn, potassic, sericitic, adv. argillic, silicification	Argillic, calc-silicate	Potassic, phyllic, tourmaline, argillic, adv. argillic, silicification	Potassic, phyllic, tourmaline, argillic, adv. argillic, silicification	Silicification, argillic, skarn
Mineralization	Py, gn, sp, cpy, mo	Py, gn, electrum, sp	Cpy, py, bn, mo	Cpy, py, bn, mo, cc	Unknown
Gangue	Qz, ad, calc, ep, chl, gar	Qz, rdc, rdn, calc, ax	Qz, tur, ser	Qz, ser, tur	Si, ep, chl, gar
Orebody	Vein, breccia, stockwork	Vein, breccia	Stockwork, dissemination	Stockwork, dissemination	Veins
Alteration age (Ma)	18.3 ± 0.1 to 18.2 ± 0.1	< 13.17 ± 0.25	14.51 ± 0.06 to 13.84 ± 0.29	11.63 ± 0.05	< 9.76 ± 0.06
RSV+RSC (MozAu/MlbsCu)	0.5/-	3.40/-	21.5/-	-	-
Deposits/ Prospects	Kepez, Kızıltepe, Tavşan, Baklan	Efemçukuru, Arapdağ	Kışladağ, Sayacik	-	Kadıkalesi, Karatoprak, Girelbelen
References	1, 2, 3, 4	5	6, 7	8, 9	8

Table 4.1 (Continued) Characteristics of the Late Cenozoic Anatolian mineral gold districts and isolated porphyry- and epithermal-style prospects.

	Central Anatolia			Eastern Anatolia		
	Konya District	**Niğde District**	**Kayseri District**	**Hasançelebi HS deposit**	**Tunceli District**	**Ağrı District**
Basement	Taurus platform	Central Anatolian Crystalline Complex	Taurus platform	Taurus platform	Taurus platform	Eastern Anatolian Accretionary Complex
Formation	Konya volcanic complex	Melendizdağ volcanic complex	Tekkedağ and Develidağ volcanic complex	Yamadağ volcanic complex	Cevizlidere intrusive stock	Ağrı magmatic complex
Age (Ma)	12 - 3	5 - 3	12 - 5	22 - 12	26 - 25	22 - 17
Tectonic setting	Cyprus slab roll-back	Arabian slab break-off	Arabian slab break-off	Arabian slab break-off	Arabian slab break-off	Arabian slab break-off
Rock type	Andesite	Andesite	Andesite	Volcanic sandstone, andesite	Diorite, granodiorite	Granodiorite
Magma association	Calc-alkaline	Calc-alkaline	Calc-alkaline	Calc-alkaline	Calc-alkaline	Calc-alkaline to alkaline
Host rock age (Ma)	10.21 to 8.67 ± 0.17	3.62 ± 0.06	7.92 ± 0.14 to < 5.36 ± 0.20	ca. 22 - 21	25.49 ± 0.10 to 25.10 ± 0.14	21.32 ± 0.29 to 17.38 ± 0.36
Kinematic association	Extension?	Transtension/ transpression?	Transtension	Extension/transtension?	Transtension	Extension/transtension ?
Regional structural control	NW-trending Akşehir normal fault	NW-trending Tuz Gölu dextral fault	Sultansazlığı pull-apart basin	NNE-trending Malatya and NE-trending Yakapınar-Göksun sinistral faults	Ovacık pull-apart basin	Diyadin fault
Alteration system	HS epithermal	HS epithermal	HS epithermal	HS epithermal	Porphyry, skarn	Carlin-style, porphyry, HS epithermal
Commodity	Au	Au?	Au	Au (-Ag)	Cu-Au-Mo (-Pb-Zn)	Au, Cu?
Alteration assemblage	Silicification, advanced argillic, argillic	Argillic	Silicification, advanced argillic, argillic	Silicification, advanced argillic	Potassic, phyllic	Decalcification, phyllic, advanced argillic, argillic, silicification
Mineralization	Py, en, lz	Unknown	Py, electrum, en, lz	Py, en?	Cpy, py, mo, bn	Py
Gangue	Si, al	Si, clay	Si, feox, al	Silica, clay, feox	Qz, mt	Si, jasp
Orebody	Ledge veinlet, breccia	Unknown	Diatreme breccia, ledge	Ledge, breccia	Dissemination, stockwork, sheeted vein	Stockwork, lens, ledge
Alteration age (Ma)	ca. 10 - 8	< 3.62±0.06	7.92 ± 0.14 to 5.36 ± 0.20	21.30 to 21.03	24.90 ± 0.10 to 24.73 ± 0.08	< 21.32 ± 0.29
RSV+RSC (MozAu/MlbsCu)	0.26/-	-	1.32/-	-	1.6/3727	4.5/-
Deposits/ Prospects	İnlice, Doğanbey	Altunhişar, Çömlekçı	Ökşüt, Başdere	-	Cevizlidere, Sin, Mamliş	Mollakara, Taşkapı, Taşlıçay
References	8, 10, 11	8, 10	8, 10, 12	8, 10	13, 14	8, 10, 15

Abbreviations: ad = adularia; al = alunite; ax = axinite; bn = bornite; calc = calcite; cc = chalcocite; chl = chlorite; cpy = chalcopyrite; en = enargite; ep = epidote; feox = Fe-oxide; gar = garnet; gn = galena; jasp = jasperoid; lz = luzonite; mo = molybdenite; mt = magnetite; py = pyrite; qz = quartz; rdc = rhodochrosite; rdn = rhodonite; ser = sericite; sp = sphalerite; tur = tourmaline

References: (1) Sener et al., 2009; (2) Yilmaz et al., 2013; (3) Van Coller et al., 2016; (4) Delibas et al., 2017; (5) Boucher, 2016; (6) Baker et al., 2016; (7) Bickford, 2016; (8) this Chapter; (9) Sonmez and Kuscu, 2016; (10) Chapter 2; (11) Hall et al., 2007; (12) Reid et al., 2015; (13) Imer et al., 2014; (14) Kociumba and Page, 2009; (15) Çolakoğlu et al., 2011.

to their counterparts throughout the broader Cenozoic magmatism within the Western Tethyan Orogenic Belt (Baker, 2017), in particular in the Carpathian to Anatolian regions as opposed to the contemporaneous Lesser Caucasus and Iranian magmatic-hydrothermal systems. However, the limited number of gold deposits and their modest grade and tonnage in Anatolia, except the Kışladağ porphyry gold deposit, can be explained by the non-optimal geological factors, poorly mineral preservation, and/or recent history of modern mineral exploration and changes in the Turkish mining law (Yiğit, 2006). Most of the Anatolian porphyry and epithermal systems are sub-economic, or at the prospect exploration stage, making the assessment of metal endowment, tenor and ratios (Ag:Au and Cu:Au) difficult.

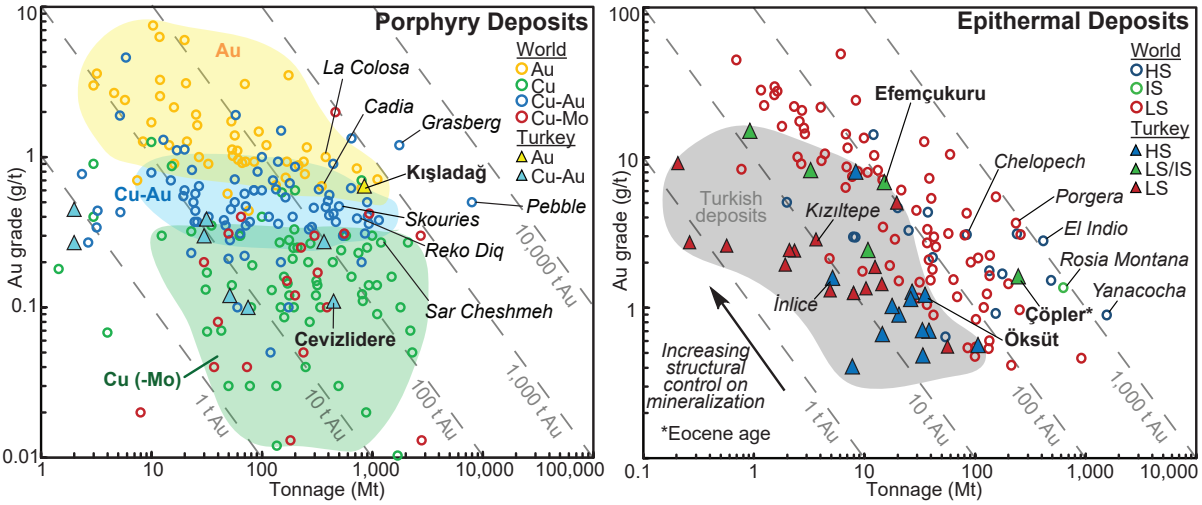

Figure 4.2 Tonnage versus Au grade (g/t) for Turkish and worldwide porphyry (top) and epithermal deposits (bottom). World deposit data from Singer et al. (2008). HS/IS/LS = high-/intermediate-/low-sulfidation.

4.3.2 Simav low-sulfidation epithermal Au-Ag, porphyry Mo-Cu and skarn Pb-Zn-Fe district

The Simav district has the highest density of precious and base metal occurrences in Anatolia and includes a broad range of commodities (Au, Ag, Cu, Mo, Sb, Hg, Pb, Fe and Zn) and styles of mineralization including low-sulfidation epithermal, skarn, porphyry and possibly orogenic. The mineralized systems of the Simav district share some geological and metallogenic features with the contemporaneous low-sulfidation epithermal such as the Ovacık and Çukuralan Au-Ag deposits (1.7 Moz Au; Koza Gold, 2015) and skarn systems in the well-endowed Bergama district on the Rhodope-Pontide Block (Figure 4.1).

Table 4.2 Resources, reserves and ore grades of the late Cenozoic Anatolian gold deposits.

District	Deposit	Resources/Reserves - ore grade	Total Au (t)	Total Au (Moz)	Total Cu (Mt)	Total Cu (Mlbs)	References
Western Anatolia							
Simav	Kızıltepe	3.8 Mt @ 2.1 g/t Au and 39.7 g/t Ag (measured, indicated and inferred resources)	7.98	0.26		-	Ariana Resources, 2017
Simav	Tavşan	4.9 Mt @ 1.3 g/t Au and 3.9 g/t Ag (indicated and inferred resources)	6.37	0.20		-	Ariana Resources, 2017
Simav	Kızılçukur	0.16 Mt @ 2.39 g/t Au and 48.5 g/t Ag (inferred resources)	0.39	0.01		-	Ariana Resources, 2017
İzmir	Efemçukuru	15.55 Mt @ 6.79 g/t Au (all resources, reserves and past production)	106	3.40		-	Eldorado Gold, 2017
Uşak	Kışladağ	843 Mt @ 0.62 g/t Au average (all resources, reserves and past production)	668	21.5		-	Eldorado Gold, 2017
Central Anatolia							
Konya	İnlice	5.2 Mt @ 1.57 g/t Au (inferred resources)	8.09	0.26		-	Oral Communication
Kayseri	Öksüt	32.9 Mt @ 1.25 g/t Au (all resources and reserves)	41.1	1.32		-	Reid et al., 2015
Eastern Anatolia							
Tunceli	Cevizlidere	445 Mt @ 0.38 % Cu, 0.11 g/t Au and 48 ppm Mo (inferred resources)	49	1.6	1.69	3728	Kociumba and Page, 2009
Ağrı	Mollakara	165 Mt @ 0.86 g/t Au (all resources and reserves)	141	4.5		-	Koza Gold, 2015
		Total	**1027**	**33**	**1.69**	**3728**	

The numerous precious metal-rich, low-sulfidation epithermal-style veins are hosted by early Miocene dacitic to rhyolitic volcanic and pyroclastic units in the Bigadiç, Sındırgı and Simav areas near the coeval Alaçam, Eğrigöz and Koyunoba granodioritic to granitic plutons in the northern part of western Anatolia (Figure 4.3A; Table 4.1). Those veins such as Kızıltepe (0.26 Moz Au; Ariana Resources, 2017), Kepez, Karakavak and Kızılçukur formed during the early stage of the Menderes metamorphic core complex exhumation in the late Oligocene to early Miocene (van Coller et al., 2016). Mineralization occurred in dilational jogs that define the ENE-trending Sındırgı Gold Corridor and are controlled by dextral strike-slip structures within the Sındırgı transtensional pull-apart basin (Yılmaz et al., 2013; van Coller et al., 2016). This basin is on the hanging-wall of the ESE-trending, N-dipping Simav dextral normal fault (Oygür and Erler, 2000; Yılmaz et al., 2013; van Coller et al., 2016). Mineralization consists of Au-Ag-rich quartz veins showing colloform/crustiform banding, quartz pseudomorphs after bladed calcite and multiple brecciation events, and surrounded by illite-smectite-dickite-nacrite hydrothermal alteration halo (Yılmaz et al., 2013; van Coller et al., 2016). Yılmaz et al. (2013) report three stages of veining: 1) coarse-grained quartz, illite, pyrite, and minor precious

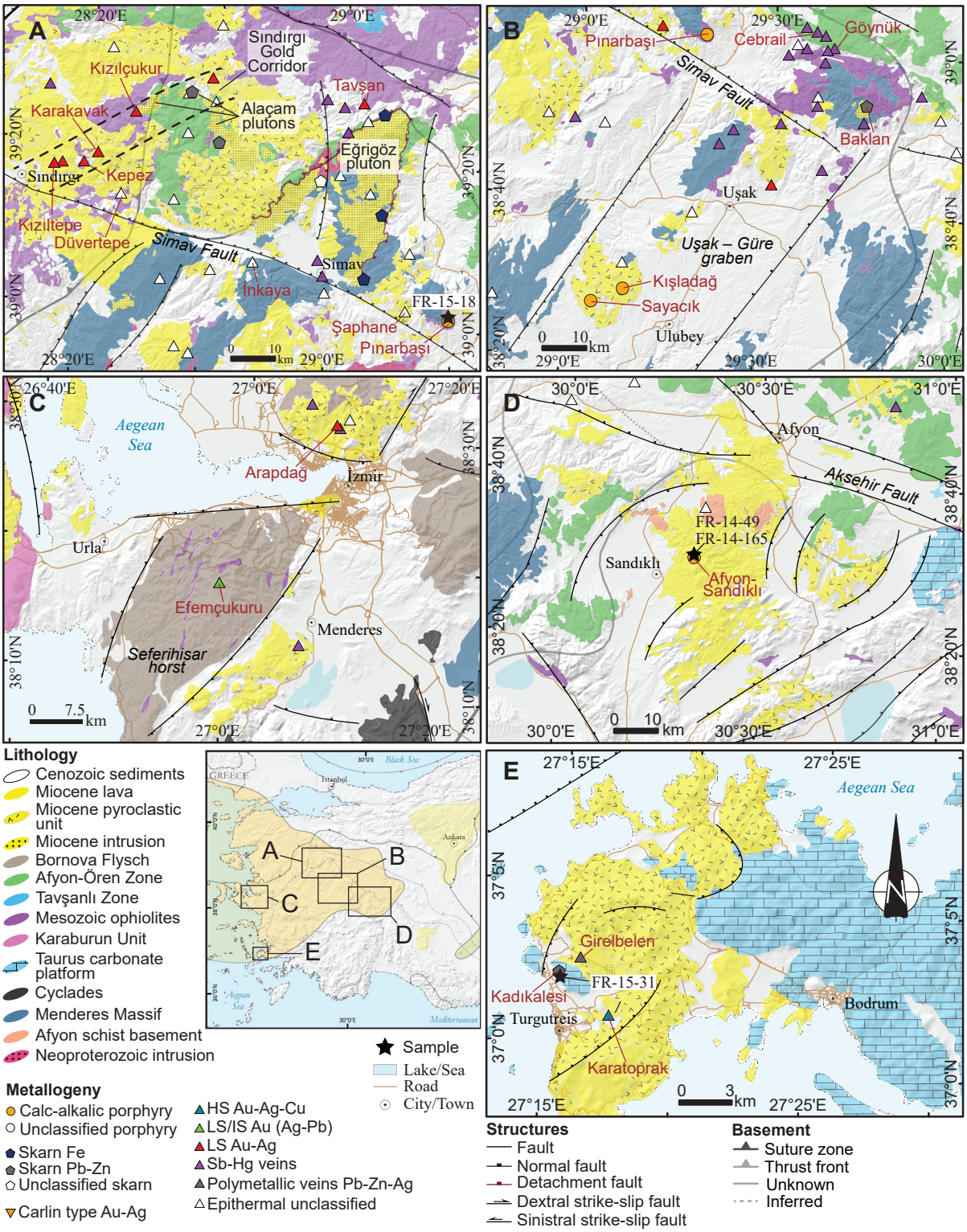

Figure 4.3 Geological maps (modified from MTA, 2002) of the Simav district (A – 1:400,000 scale), Simav and Uşak districts (B – 1:400,000 scale), İzmir district (C – 1:250,000), Afyon area (D – 1:400,000 scale) and Bodrum district (E – 1:150,000 scale) showing the distribution of porphyry, epithermal and skarn occurrences, prospects and deposits, and analyzed samples in western Anatolia. Lambert Conic projection, European Datum 1950. Base map: SRTM 90 m digital elevation models (Jarvis et al., 2008).

metals, followed by 2) the economic Au-Ag-bearing medium-grained crustiform quartz veins accompanied by carbonate replacement and hydrothermal breccia textures (Figures 4.3 and 4.4A), and 3) colloform-crustiform chalcedonic silica.

Widespread steam-heated alunite and kaolinite alteration such as at Düvertepe (Ece et al., 2013) and Şaphane (Mutlu et al., 2005), and active geothermal fields also occur along the Simav fault. Low-sulfidation epithermal veins do not have any genetic relationships with the coeval intrusions in the Simav fault hanging-wall, despite a few deep, base metal targets reported by Van Coller et al. (2016). Rather, those intrusions are surrounded by occurrences of Fe-Pb-Zn skarn-style mineralization at Eğrigöz (Kumral et al., 2016; Uğurcan and Oyman, 2016), Alaçam and Baklan.

The metamorphic basement of the Simav district also hosts numerous metal-rich hydrothermal systems. For instance, the distal Tavşan gold-rich jasperoid mineralization (0.2 Moz Au) occurs along the NW-trending thrust contact between Jurassic limestone and Late Cretaceous ophiolites, and post-dates the early Miocene syn-tectonic Eğrigöz pluton (Şener et al., 2009). Similarly, the Gümüşköy Ag-only epithermal deposit is the largest silver deposit of Turkey, northeast of the Simav district (123 Moz Ag; Yiğit, 2009), and consists of Ag-rich veins and dissemination along NW-trending structures within the early Miocene Tavşanlı felsic volcanic units and Mesozoic carbonate basement (Arık, 2002). Despite minor Cu-Pb-Zn veins reported on the footwall and hanging-wall of the Simav fault within the Menderes Massif basement (e.g., İnkaya prospect; Özen and Arık, 2015), the absence of time constraints hinders genetic correlations with neighboring low-sulfidation epithermal veins and syn-tectonic intrusions, or Pre-Cenozoic orogenic events.

The Pınarbaşı porphyry Mo-Cu prospect occurs at the eastern termination of the Simav district and differs from the contemporaneous easterly hydrothermal systems (Figure 4.3A-B; Table 4.1). The Pınarbaşı prospect consists of quartz-sulfide vein stockworks with potassic alteration overprinted by phyllic alteration affecting early Miocene monzonitic and porphyric granitic stocks (Figures 4.4C-E and 5A; Delibaş et al., 2017). Mineralized intrusive

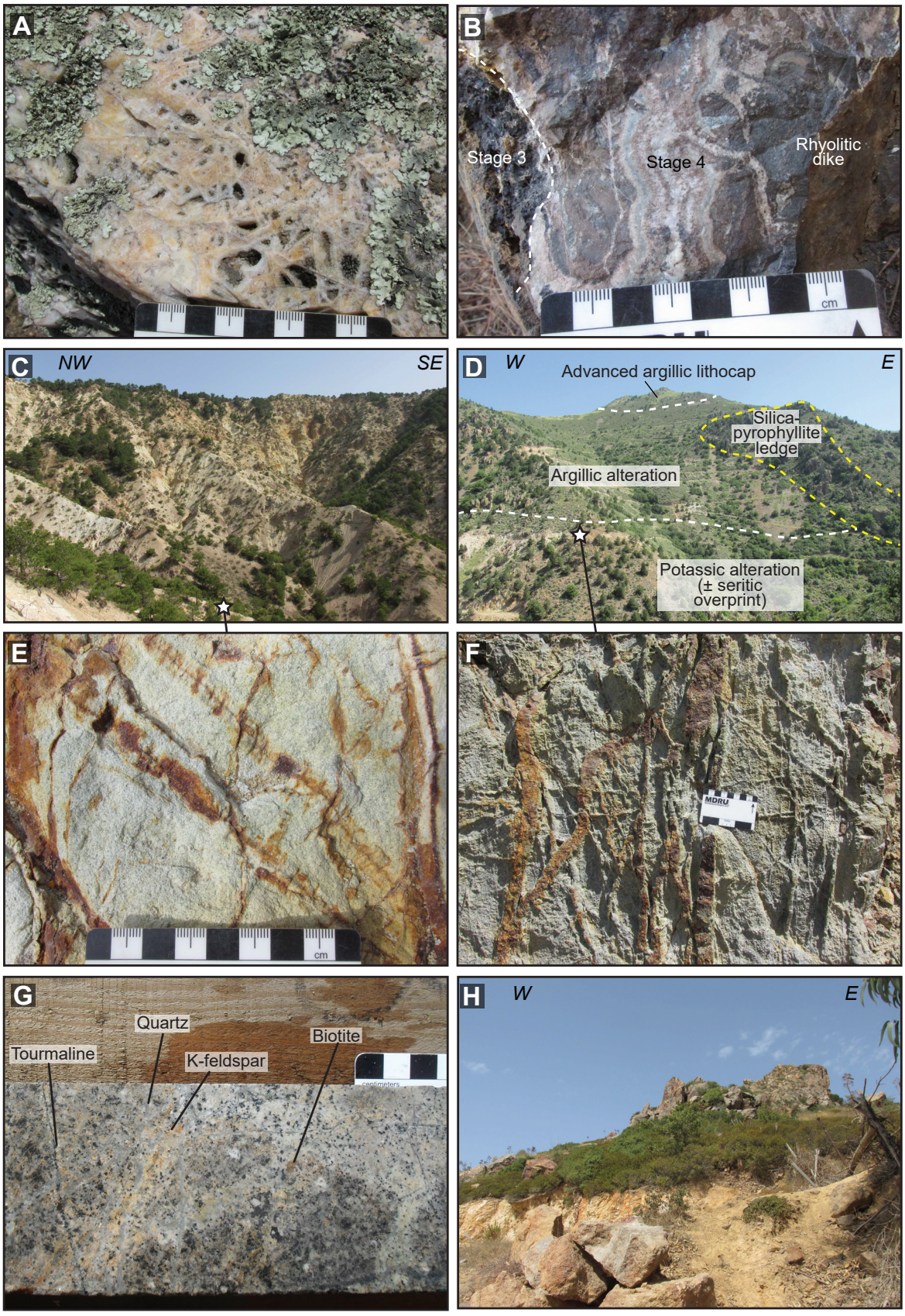
A
B
Stage 3
Stage 4
Rhyolitic dike
cm
C
NW
SE
D
W
E
Advanced argillic lithocap
Silica-pyrophyllite ledge
Argillic alteration
Potassic alteration (± seritic overprint)
E
cm
F
MDRU
G
Quartz
Tourmaline
K-feldspar
Biotite
H
W
E

Figure 4.4 Macro-photographs of mineralized porphyry and epithermal occurrences in western Anatolia. A. Silica replacement after bladed calcite at the Kepez low-sulfidation epithermal Au-Ag deposit, Simav district; B. Quartz-rhodochrosite ± rhodonite-pyroxmangite-pyrite-galena crustiform-colloform textured vein (vein stage 4) cutting Mn-oxidized quartz- rhodochrosite -rhodonite-calcite vein (vein stage 3) and rhyolite dike from the Efemçukuru low- to intermediate-sulfidation epithermal Au deposit, İzmir district; C. Northeast-looking panoramic view of the Pınarbaşı porphyry Mo-Cu prospect, Simav district; D. North-looking panoramic view of the Afyon-Sandıklı porphyry Au-Cu prospect illustrating the short distance between the high-temperature potassic alteration zone and the overlying advanced argillic lithocap; E. Close-up photograph of the argillic- and phyllic-altered monzonitic stock at the Pınarbaşı porphyry Mo-Cu prospect, Simav district; F. Close-up photograph of the dense quartz -sulfide vein stockwork and potassic alteration within the monzonitic stock at the Afyon-Sandıklı porphyry Au-Cu prospect; G. Core photograph of the mineralized potassic alteration (Intrusive phase 1) at the Kışladağ porphyry Au deposit, Uşak district; H. Silica cap overlying an argillic-altered andesitic unit at the Karatoprak high-sulfidation epithermal occurrence, Bodrum district.

rocks crop out in the northeastern Menderes Massif along the northwestern margin of the NE-trending Erdogmus-Yenigediz graben, cut by the southerly Simav fault. Delibaş et al. (2017) reported that the NE- and E-trending normal faults of the Erdogmus-Yenigediz graben cut the vein stockwork and control the distribution of quartz-molybdenite-chalcopyrite-sphalerite-fahlore-galena veins, as well as molybdenite-hematite-bearing silicified zones. Distal Sb-Au-Ag-Pb-Zn-rich low-sulfidation epithermal-style silicified zones in the limestone basement are juxtaposed to the Pınarbaşı intrusion, and upon the advanced argillic overprint on high-temperature porphyry-style alteration (Delibaş et al., 2017). In addition, the Erdogmus-Yenigediz graben hosts numerous hydrothermal Sb- (Hg-Au-Ag) occurrences such as Cebrail and Göynük (Yiğit, 2009).

4.3.3 İzmir low- to intermediate-sulfidation epithermal Au district

West of the Menderes Massif, the İzmir district is defined by the structurally-controlled, low- to intermediate-sulfidation epithermal-style Au veins, including the Efemçukuru deposit and Arapdağ occurrence (Figure 4.3C; Table 4.1). The Efemçukuru veins are hosted within the carbonate-rich phyllites of the Mesozoic to Paleocene Bornova Flysch sequence and the rhyolite dykes of the middle Miocene Cumaovası volcanic suite (Oyman et al., 2003; Boucher, 2016). The Efemçukuru gold deposit (3.4 Moz Au; Eldorado Gold Corp., 2017) formed within the NE-trending Seferihisar horst in the south-easternmost part of the İzmir-Balıkesir Transfer Zone. The orebody consists of the NW- to NNW-trending Kestanebeleni and Kokarpınar

quartz-rhodochrosite veins that are controlled by steeply-dipping NW- to NNW-trending faults (Boucher, 2016). Boucher (2016) defined six successive stages of veining: 1) calc-silicate anastomosing veins, 2) quartz-rhodochrosite brecciating and banded veins, 3) banded quartz-rhodochrosite ± pyrite, 4) quartz-pyrite-galena-sphalerite, 5) base metal-rich sulfides, and 6) late quartz-carbonate (Figure 4.4B). Gold mineralization is dominantly associated with vein stages 3-4 ± 5 and followed by base metal mineralization at stages 4-5 (Boucher, 2016). Northeast of Efemçukuru, the Arapdağ Au-Ag occurrence consists of NW- to WNW-trending mineralized tension quartz veins, vein stockwork and dissemination within middle Miocene silicified dacitic lavas (Sayılı and Gonca, 1999).

4.3.4 Uşak porphyry Au district

The Kışladağ porphyry Au deposit and Sayacık porphyry prospect define the Uşak district on the eastern flank of the Menderes Massif, which is the most endowed gold district of Turkey (21.5 Moz; Table 4.1). Both porphyry systems are within the middle Miocene Beydağ stratovolcano and Menderes metamorphic basement rocks along the NE-trending Uşak-Güre graben (Figure 4.3D). The Kışladağ deposit is a gold-only porphyry deposit and consists of mineralized monzonitic porphyry stocks that are coeval with the Beydağ pyroclastic and lava units (Baker et al., 2016). Gold mineralization is dominantly concentrated within the potassic (biotite-K-feldspar ± actinolite) alteration core, surrounded and partially overlapped by the tourmaline-white mica (± pyrite-albite-quartz) alteration assemblage (Baker et al., 2016; Figures 4.4G and 4.5B-C). The porphyry orebody is post-dated by non-mineralized argillic and advanced argillic alteration assemblages that affect topographically higher rocks on the east side of the deposit (Baker et al., 2016). Southwest of Kışladağ, the Sayacık prospect has similar geological features to Kışladağ, which includes gold-rich quartz vein stockworks within a monzonitic porphyry dyke overlain by the argillic-altered andesitic flows of the Beydağ stratovolcano (Bickford et al., 2016).

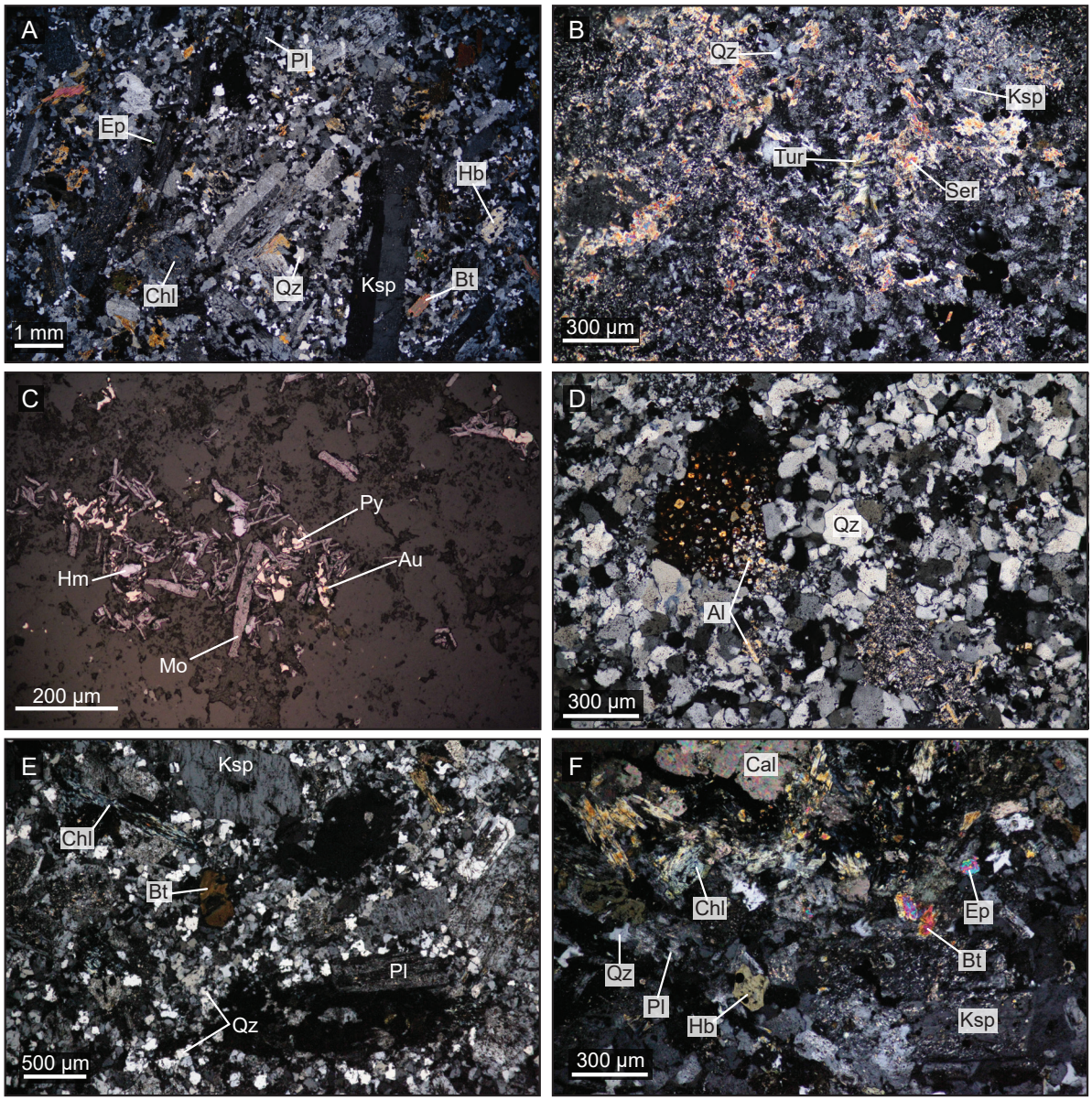

Figure 4.5 Optical micro-photographs of mineralized porphyry and epithermal occurrences in western Anatolia. A. Cross polarized light (x 5): post-mineralization monzonite at the Pınarbaşı porphyry Mo-Cu prospect; B. Cross polarized light (x 10): potassic and tourmaline-white mica (sericite) alteration assemblages at the Kışladağ porphyry Au deposit, Uşak district; C. Plane polarized and reflected light (x 20): sulfide mineralization within the monzonitic stock at the Kışladağ porphyry Au deposit, Uşak district; D. Cross polarized light (x 2): monzonite host rock at the Afyon-Sandıklı porphyry Au-Cu prospect; E. Cross polarized light (x 10): lithocap at the Afyon-Sandıklı porphyry Au-Cu prospect; F. Cross polarized light (x 10): skarn alteration of the Kadıkalesi monzonite, Bodrum district. Al = alunite; Au = gold; Bt = biotite; Cal = calcite; Chl = chlorite; Ep = epidote; Hb = hornblende; Hm = hematite; Ksp = K-feldspar; Mo = molybdenite; Pl = plagioclase; Py = pyrite; Qz = quartz; Ser = sericite (white mica); Tur = tourmaline.

4.3.5 Afyon-Sandıklı porphyry Au-Cu prospect

The Afyon-Sandıklı porphyry Au-Cu prospect in eastern western Anatolia along the Kırka-Afyon-İsparta trend, is similar to the Kışladağ and Sayacık porphyry systems (Figure 4.3D; Table 4.1). Porphyry mineralization at Afyon-Sandıklı is hosted within the late Miocene, alkaline Afyon volcanic complex (14-8 Ma) that includes monzonitic porphyry stocks, trachyte and latite lavas emplaced on the Taurus platform (Figure 4.5E). The Afyon-Sandıklı prospect is characterized by quartz-sulfide vein stockwork with potassic alteration overprinted by white mica and minor tourmaline alteration (Figure 4.4F). Mineralization comprises chalcocite, bornite, chalcopyrite, pyrite, molybdenite and tetrahedrite (Sönmez and Kuşcu, 2016). The porphyry system is overlain by a barren, high-sulfidation epithermal lithocap that is surrounded by widespread argillic alteration (Figures 4.4D and 5D).

4.3.6 Bodrum high-sulfidation epithermal and skarn district

Southwest of the Menderes Massif, the Bodrum volcanic complex (12-9 Ma) is composed of monzonitic stocks, basaltic andesitic to dacitic lavas and domes, block-and-ash flows, and caldera-filled andesitic ignimbrite that were deposited on the Mesozoic marbles of the Taurus platform along the E-trending Gokova graben (Figure 4.3E; Table 4.1; Robert et al., 1992; Kurt and Arslan, 2001; Ulusoy et al., 2004). The andesitic units around the caldera in the southern Bodrum volcanic complex were affected by high-sulfidation-style argillic and advanced argillic alteration assemblages including resistant vuggy silica lithocaps such as those on the hills above Karatoprak (Figure 4.4H). Supergene Fe-oxihydroxide alteration indicates the presence of hypogene sulfide minerals, notably pyrite. Skarn alteration and associated Pb-Zn-Cu mineralization occur at the contact between the monzonitic intrusions and marble such as Kadıkalesi and Girelbelen (Figure 4.5F). Hydrothermal epidote, chlorite, hematite, quartz and actinolite alteration is typical.

4.3.7 Konya high-sulfidation epithermal Au-Ag-(Cu) district

The several high-sulfidation epithermal Au prospects such as İnlice, Doğanbey, Oğlakcı, Gavur Gölü and Karaören that define the Konya district are hosted by the late Miocene Konya volcanic complex at the termination of the NW-trending Akşehir normal fault in the Taurus platform (Figure 4.6A; Table 4.1). The İnlice high-sulfidation epithermal Au deposit (0.26 Moz) is hosted within the Miocene Erenkilit volcanic complex, 40 km southwest of Konya. The İnlice orebodies consist of two NW-trending, 70°-SW-dipping silica ledges controlled by a NW-trending dextral strike-slip normal fault system that cut the porphyritic biotite andesite lava/dome (Figure 4.7A; Hall et al., 2007). A NNE-trending fault separates the two mineralized ledges and may have previously facilitated the mineralized fluids. The silica ledges are characterized by vuggy silica alteration filled by hypogene alunite (Figure 4.8A), and cross-cut by low-temperature and low-pH granular, chalcedonic and massive silica veinlets. In addition, three types of mineralized breccia occur at İnlice: 1) polymict phreatic breccia, 2) monomict cement-supported pyrite-enargite hydrothermal breccia and 3) monomict clast-supported silica-pyrite (?) hydrothermal breccia (Figure 4.7C). Gold mineralization is associated with alunite-filled vuggy silica, chalcedony with high Ag:Au ratios (Hall et al., 2007), and breccias. Advanced argillic, argillic and chloritization alteration assemblages distally occur around the orebodies.

The Doğanbey prospect is northwest of the Erenkilit complex, 55 km west of Konya, and is composed of a main (north) and south zones that are separated by an E-trending valley. Two-pyroxene andesitic to dacitic flows/domes host rocks, which are overlain by unaltered rhyodacitic to rhyolitic lavas, are affected by an opal to chalcedony horizon and underlying structurally-controlled silica-alunite ledges and breccias (Figures 4.7G and 8B). Kaolinite and illite overprint alteration occurs between the ledges. Mineralization is characterized by disseminated pyrite (< 5 %), quartz and pyrite veinlets and minor hydrothermal silica-pyrite breccias. At depth, those quartz veinlets have dark grey rims and translucent core, and yield weak Au and Mo anomalies that could be in association with potassic alteration subsequently

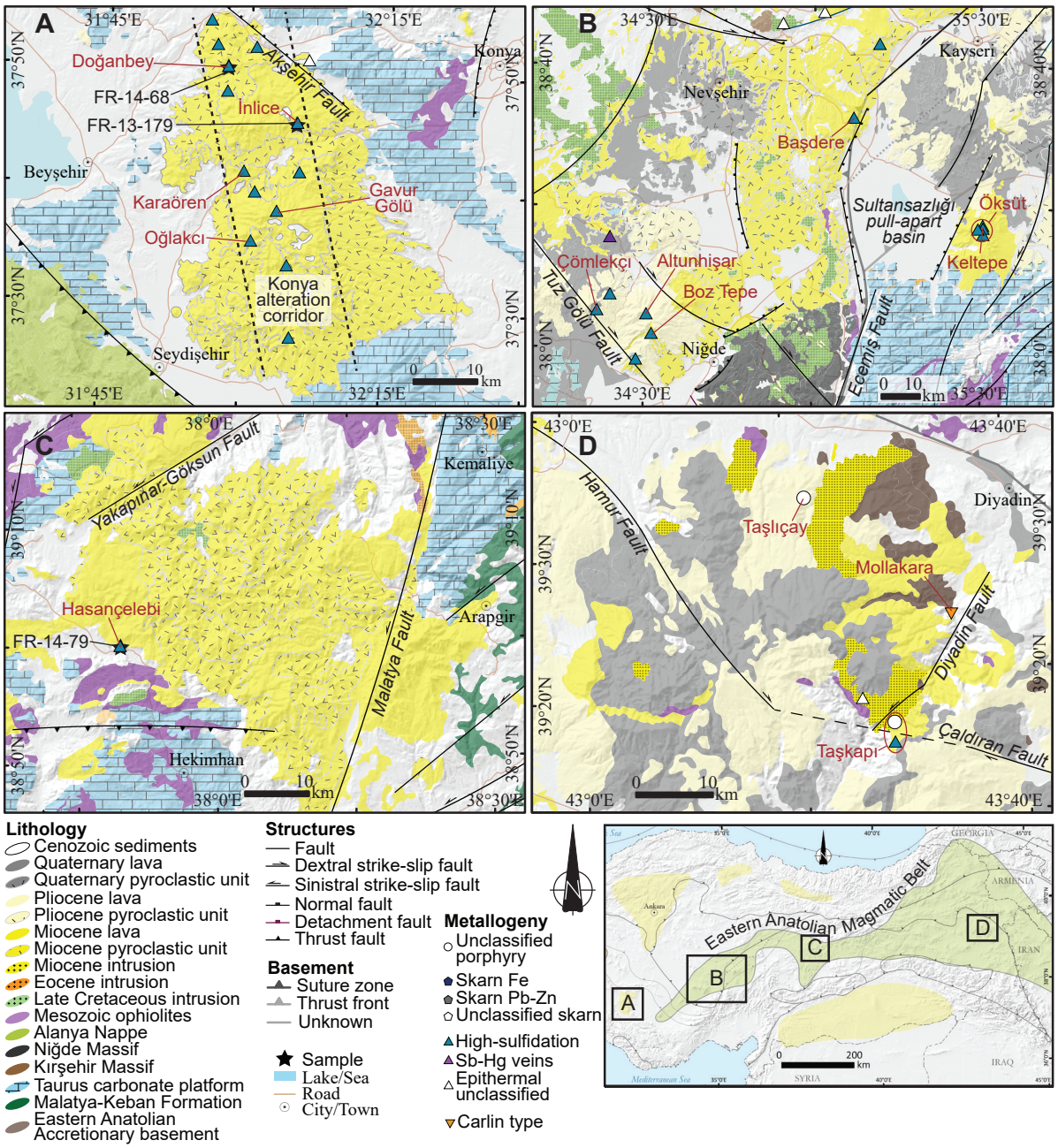

Figure 4.6 Geological maps (modified from MTA, 2002) of the Konya district (A – 1:300,000 scale), Niğde and Kayseri districts (B – 1:500,000 scale), Hasançelebi area (C – 1:300,000) and Ağrı district (D – 1:250,000 scale) showing the distribution of porphyry, epithermal, Carlin-style and skarn occurrences, prospects and deposits, and analyzed samples in central and eastern Anatolia. Lambert Conic projection, European Datum 1950. Base map: SRTM 90 m digital elevation models (Jarvis et al., 2008).

overprinted by advanced argillic alteration (Hall et al., 2007).

The prospects and occurrences of the Konya district including Oğlakcı, Gavur Gölü and Karaören are characterized by typical high-sulfidation epithermal features, namely structurally-controlled silica-alunite ledges, advanced to argillic alteration, hydrothermal and phreatic breccias, and andesitic host rocks, similar to İnlice and Doğanbey. However, those high-sulfidation epithermal systems are commonly covered by barren andesitic to rhyolitic lavas to pyroclastic deposits, and lack outcropping causative intrusions and associated porphyry mineralization.

4.3.8 Niğde high-sulfidation epithermal district

The Niğde district, northeast of the Konya district, is composed of several high-sulfidation epithermal alteration occurrences such as at Altunhişar, Boz Tepe and Çömlekçı (Figure 4.6B). Those occurrences are in the Pliocene Melendiz stratovolcano along the Tuz Gölü dextral strike-slip fault, southeast of the Hasandağ stratovolcano. This district has limited exposures of hydrothermally-altered clinopyroxene andesitic lavas because of the widespread, overlying barren Pliocene to Quaternary basaltic to andesitic lava flows (Figures 4.7E-F). The economic potential of this district is unknown. However, those high-sulfidation epithermal occurrences have similar features to those in the Konya district and include structurally-controlled silica ledges, argillic and advanced argillic alteration assemblages, Fe-oxihydroxide dissemination, fracture-filled veinlets, minor breccias, and absence of intrusive rocks and high-temperature alteration assemblages.

4.3.9 Kayseri high-sulfidation epithermal Au district

Similar to the Konya and Niğde districts, high-sulfidation epithermal mineralization of the Kayseri district such as at Öksüt and Başdere occurs within andesitic lavas and domes of the late Miocene Develidağ and Tekkedağ volcanic complexes, respectively, on both sides of the Sultansazlığı pull-apart basin (Figure 4.6B; Table 4.1). Hydrothermally-altered clinopyroxene ± hornblende-orthopyroxene andesitic lavas and domes and breccias are partially covered by

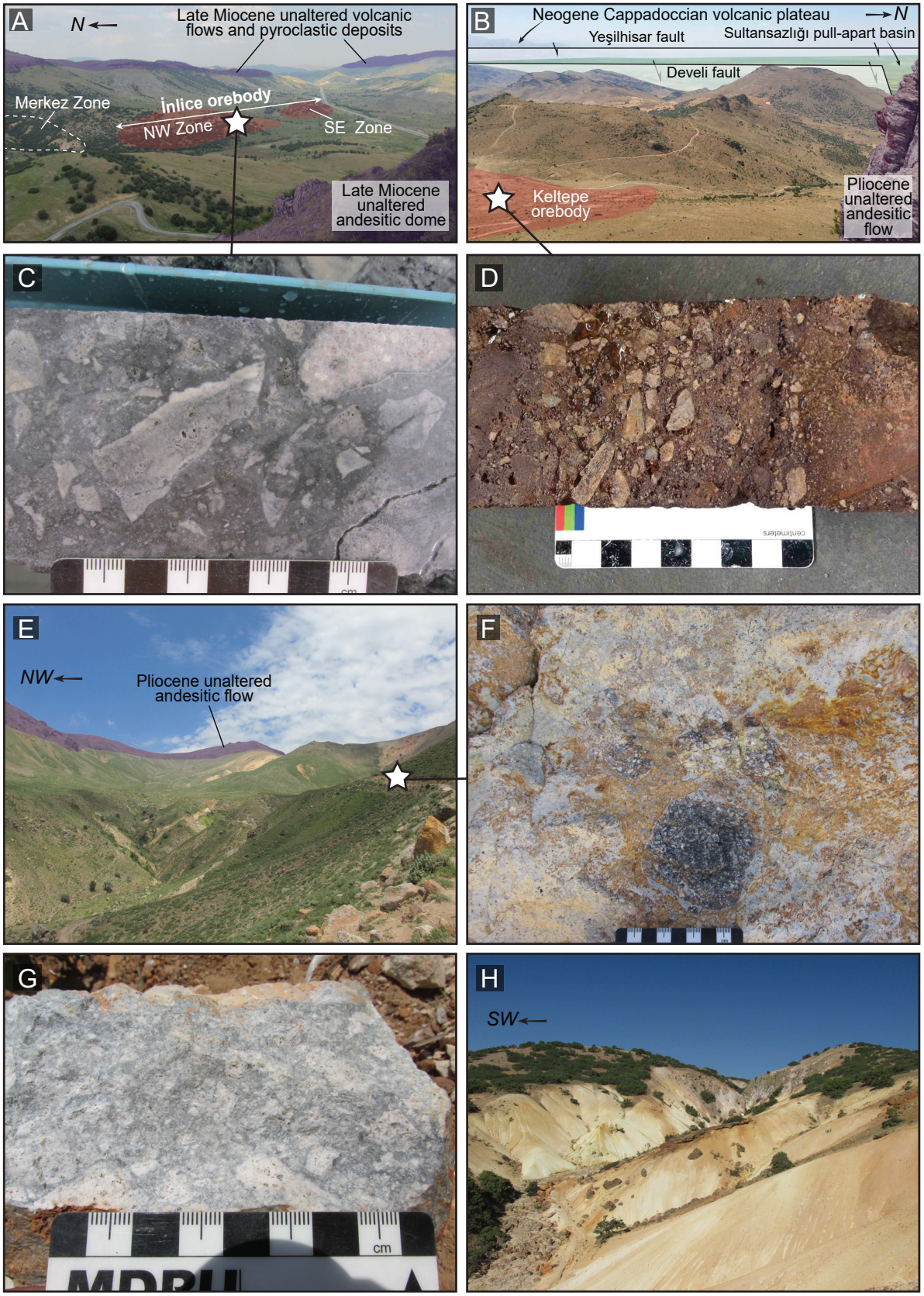
A
N
Late Miocene unaltered volcanic flows and pyroclastic deposits
Merkez Zone
inlice orebody
NW Zone
SE Zone
Late Miocene unaltered andesitic dome
B
Neogene Cappadoccian volcanic plateau
N
Yeşilhisar fault
Sultansazlığı pull-apart basin
Develi fault
Keltepe orebody
Pliocene unaltered andesitic flow
C
D
E
NW
Pliocene unaltered andesitic flow
F
G
cm
H
SW

Figure 4.7 Macro-photographs of mineralized porphyry occurrences in central Anatolia. A. East-looking panoramic view of the Inlice high-sulfidation epithermal Au deposit, Konya district; B. West-looking panoramic view of the Keltepe ore body at the Öksüt high-sulfidation epithermal Au deposit, Kayseri district; C. Polymict, Au-bearing, silica-pyrite, phreatic breccia, İnlice high sulfidation epithermal Au deposit, Konya district; D. Silica-altered clasts, Fe-oxide diatreme breccia, Öksüt high-sulfidation epithermal Au deposit, Kayseri district; E. Northeast-looking panoramic view of the argillic-altered Altunhişar high-sulfidation epithermal occurrence, Niğde district; F. Argillic-altered andesitic unit from the Boz Tepe high-sulfidation epithermal occurrence, Niğde district; G. Silica-alunite advanced argillic alteration affecting a volcanic breccia at the Doğanbey high-sulfidation epithermal Au prospect, Konya district; H. Northeast-looking photograph of the Başdere high-sulfidation epithermal occurrence, Kayseri district.

unaltered Pliocene volcanic flows. The Öksüt gold deposit (1.32 Moz Au) is mainly divided into Keltepe and Güneytepe orebodies that form of a NW-trending mineralized silica ledge (Figure 4.7B). Mineralized bodies are composed of multiphase, polymict, quartz-Fe-oxide and quartz-alunite breccias as part a sub-volcanic vent or diatreme, and overprinted by vuggy quartz and quartz-alunite, quartz-kaolinite, patchy silica and opal/chalcedony alteration (Figures 4.7D and 4.8C; Reid et al., 2015). The silica ledge is surrounded by an alteration halo characterized by advanced argillic, argillic and outward chlorite-smectite assemblages. Gold mineralization and related alteration are controlled by NW-trending normal faults and offset by late NE-trending strike-slip structures (Cihan, 2016). Hypogene mineralization consists of free gold, pyrite, enargite and luzonite (Lashko, 2013; Reid et al., 2015). The breccia and vuggy silica zones are subject to strong oxidation and supergene processes that favored gold enrichment and the formation of supergene copper mineralization (i.e., chalcocite, covellite and malachite); copper was leached out from the deeper part of the hydrothermal system (Reid et al., 2015), although no intrusive units and high-temperature alteration assemblages were intercepted.

Başdere is a high-sulfidation epithermal occurrence in the late Miocene clinopyroxene-bearing andesite lavas of the Tekkedağ volcano on the western margin of the Sultansazlığı pull-apart basin. This epithermal occurrence has vuggy to granular silica containing up to 1 % pyrite and quartz-kaolinite alteration assemblage. This one kilometer-long alteration corridor is controlled by a swarm of inferred NW-trending faults, similar to the Öksüt deposit (Figure 4.7H).

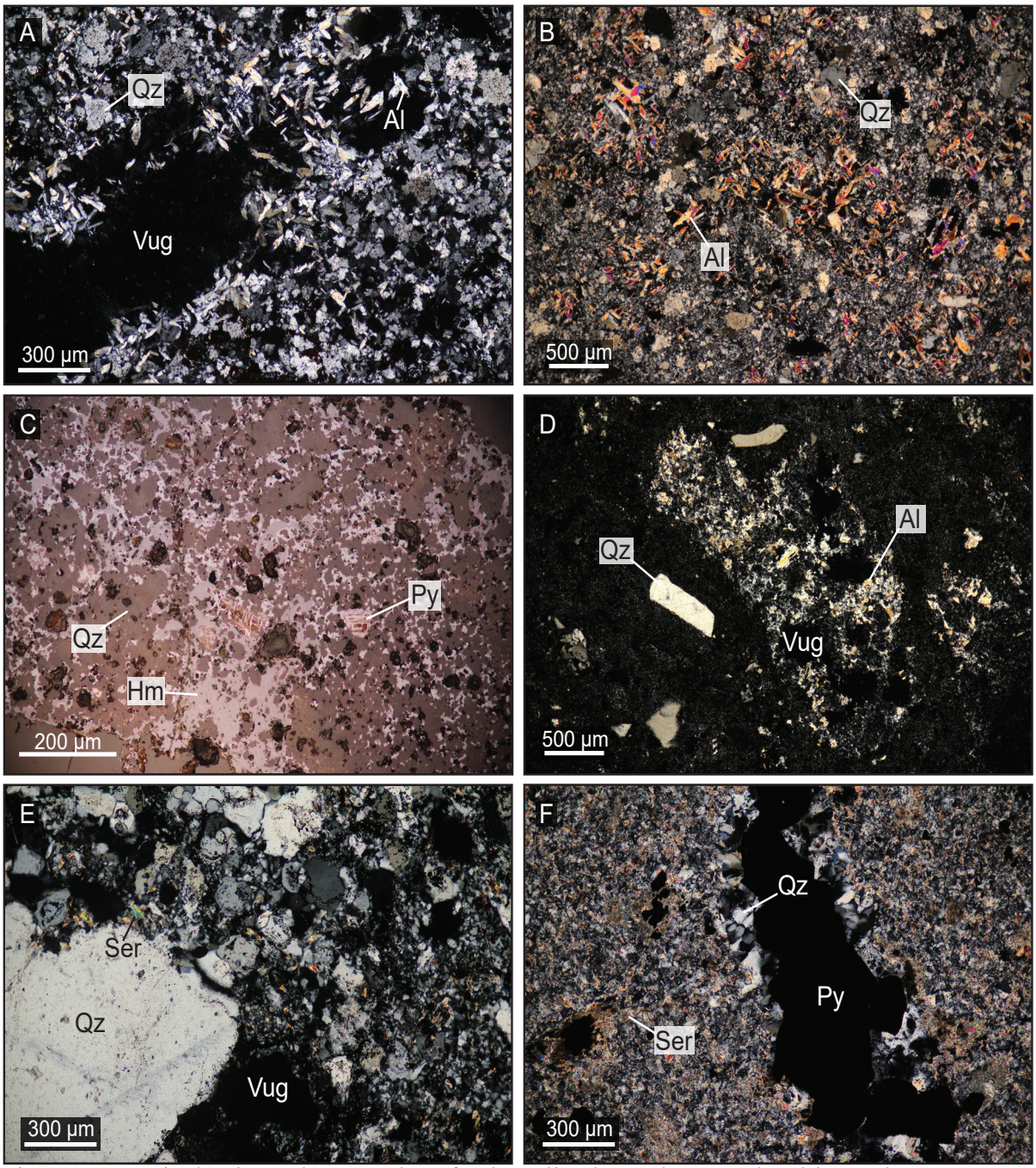

Figure 4.8 Optical micro-photographs of mineralized porphyry and epithermal occurrences in central and eastern Anatolia. A. Cross polarized light (x 10): vuggy silica alteration from the İnlice high-sulfidation epithermal Au deposit, Konya district; B. Cross polarized light (x 5): advanced argillic alteration assemblage from the Doğanbey high sulfidation epithermal Au prospect, Konya district; C. Plan polarized and reflected light (x 20): mineralized, Fe-oxide diatreme breccia with silica-altered clasts, Öksüt high-sulfidation epithermal Au deposit, Kayseri district; D. Cross polarized light (x 5): vuggy silica alteration at the Hasançelebi high-sulfidation epithermal Au-Ag prospect; E. Cross polarized light (x 10): decalcification and silica replacement alteration at the Carlin-style Mollakara Au-Ag deposit, Ağrı district; F. Cross polarized light (x 10): phyllic-altered granodiorite in the porphyry zone of the Taşkapı porphyry-epithermal prospect, Ağrı district. Al = alunite; Hm = hematite; Py = pyrite; Qz = quartz; Ser = sericite (white mica).

4.3.10 Hasançelebi high-sulfidation epithermal Au-Ag prospect

The Hasançelebi high-sulfidation epithermal Au-Ag prospect consists of a swarm of N-dipping (60°) silica ledges and breccias in the Oligocene to middle Miocene volcanic sandstones of the Yamadağ volcanic succession (> 21-12 Ma) in eastern Anatolia (Figures 4.6C and 9A; Table 4.1). Mineralized breccia types mainly include chaotic, cement-supported, polymict, silica-Fe-oxide phreatomagmatic breccia showing angular to sub-angular juvenile clasts, and monomict, pyrite ± enargite hydrothermal breccia; traces of alunite and silica pseudo-breccias are also present. In addition, the resistant ledges are composed of vuggy to massive silica alteration surrounded by advanced argillic to argillic alteration assemblages (Figures 4.8C, 4.8E and 4.9C). The mineralized epithermal system is covered by unaltered clinopyroxene-bearing andesitic flows and intruded by a mafic dome.

4.3.11 Tunceli porphyry Cu-Au-Mo district

The Tunceli district in eastern Anatolia contains the Oligocene Cevizlidere Cu-Au-Mo porphyry deposit and Sin and Mamliş prospects (Figure 4.1; Table 4.1). The Cevizlidere deposit is the largest porphyry Cu deposit in Anatolia (1.6 Moz Au and 3.7 Blbs Cu; Table 4.2) and hosted within NW-trending elongated porphyric dioritic to granodioritic stocks that intruded the Paleozoic limestones of the Keban Unit (İmer et al., 2014). Those mineralized stocks are controlled by the Ovacık pull-apart basin along the NE-trending sinistral fault (İmer et al., 2014). Dioritic and granodioritic stocks are affected by potassic and phyllic alteration associated with quartz-magnetite-chalcopyrite-pyrite ± molybdenite ± bornite veinlets and disseminations of chalcopyrite and bornite (İmer et al., 2014). Kociumbas and Page (2009) also report carbonate alteration and base metal skarn mineralization at the intrusion-limestone contacts.

4.3.12 Ağrı porphyry, high-sulfidation epithermal and Carlin-style Au-(Cu-Ag?) district

Limited mineral exploration has been focused on the Ağrı magmatic complex, south of the İzmir-Ankara-Erzincan suture zone and along the Iranian border (Figure 4.6D; Table

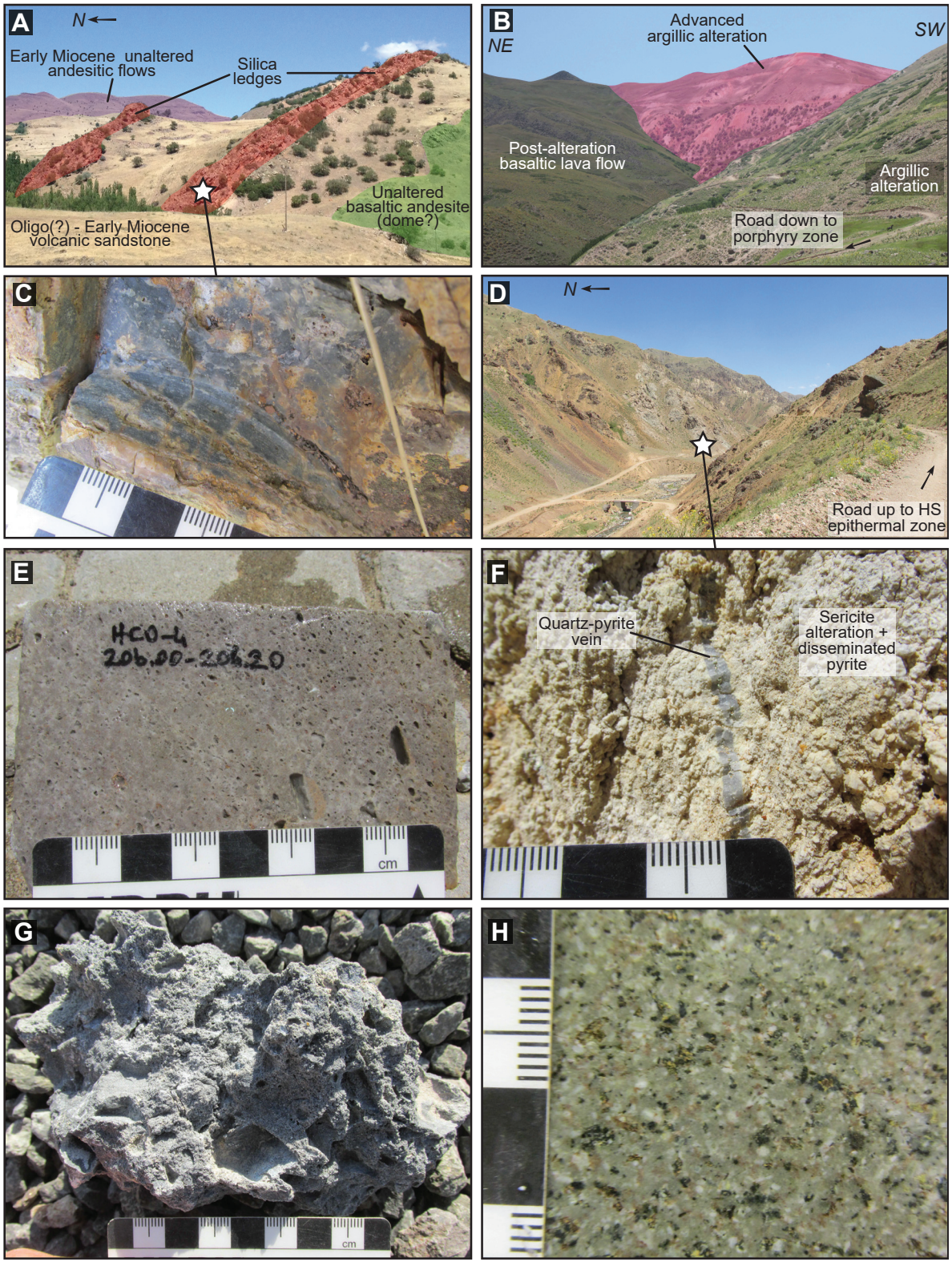

Figure 4.9 Macro-photographs of mineralized hydrothermal occurrences in eastern Anatolia. A. East-looking view of the Hasançelebi high-sulfidation epithermal Au-Ag prospect; B. Southwest-looking view of the high-sulfidation epithermal zone of the Taşkapı porphyry-epithermal prospect, Ağrı district; C. Close-up photograph of massive silica alteration in a silica

ledge at the Hasançelebi high-sulfidation epithermal Au-Ag prospect; D. East-looking view of phyllic-altered porphyry zone of the Taşkapı porphyry-epithermal prospect, Ağrı district; E. Mineralized vuggy silica alteration at the Hasançelebi high-sulfidation epithermal Au-Ag prospect; F. Close-up photograph of the phyllic alteration zone within the Taşkapı granodiorite, Ağrı district; G. Decalcification alteration at the Carlin-style Mollakara Au-Ag deposit, Ağrı district; H. Propylitic-altered granite at the Taşlıçay porphyry prospect, Ağrı district.

4.1). This complex is composed of early Miocene monzonitic to granitic plutons covered by Neogene extrusive basaltic to rhyolitic rocks. Although there is no genetic relationship with the nearby plutons of the Ağrı magmatic complex, the Carlin-style Mollakara Au-Ag deposit is the first reported gold deposit in this part of Turkey (4.5 Moz Au; Table 4.2). The Mollakara hydrothermal alteration system is within Paleozoic dolomitic marble and affects the overlying Miocene volcanic units (Çolakoğlu et al., 2011). Alteration is characterized by decalcification, brecciation, jasperoid and silicification. N- to N10-trending high-angle normal faults, defining a horst structure, control the mineralization (Çolakoğlu et al., 2011; Figures 4.8E and 4.9G).

The Ağrı district also includes several porphyry and high-sulfidation epithermal occurrences within and around the early Miocene plutons of the Ağrı magmatic complex. For instance, the Taşkapı prospect consists of a phyllic-altered monzonitic pluton cut by quartz-pyrite vein stockwork (Figures 4.8F, 4.9D and 4.9F), and an overlying high-sulfidation epithermal-style lithocap, which is accompanied by breccias, argillic and advanced argillic alteration zones (Figure 4.9B). The Taşlıçay monzonitic pluton, ca. 30 km north of Taşkapı, is also affected by a widespread propylitic alteration suggesting the presence of another and distinct hydrothermal system (Figure 4.9H).

4.4 Methodology of gold mineralization dating

Magmatism and associated porphyry and epithermal Au (-Cu) mineralization events peaked several times during the late Cenozoic. Although the magmatic episodes were previously constrained throughout Anatolia (e.g., Dilek and Altunkaynak, 2009; Ersoy and Palmer, 2013; Chapter 2) and despite recent geochronological studies carried out some deposits and prospects, mainly in western Anatolia (Yılmaz et al., 2013; İmer et al., 2014; Baker et al., 2016; Boucher, 2016; Delibaş et al., 2017), the timing of gold mineralization along the Anatolian Trend is

undetermined. Temporal constraints on gold mineralization are provided by Re-Os model ages on molybdenite mineralization, $^{40}Ar/^{39}Ar$ plateau or isochron ages on hydrothermal alunite alteration associated with the mineralization event and/or by dating the crystallization age of the igneous host rock or post-alteration units by the U-Pb technique. Seven new geochronological constraints are reported herein that include three U-Pb zircon dates from the Bodrum district (FR-15-31), and the Pınarbaşı (FR-15-18) and Afyon-Sandıklı porphyry prospects in western Anatolia (FR-14-49); one Re-Os model age on molybdenite mineralization at the Afyon-Sandıklı porphyry prospect (FR-14-165); and three $^{40}Ar/^{39}Ar$ alunite age data from the İnlice deposit (FR-13-179), Doğanbey (FR-14-68; Konya district) and Hasançelebi high-sulfidation epithermal prospects (FR-14-79) in central and eastern Anatolia, respectively. These newly-acquired age data are interpreted complementary to the previously-published U-Pb, Re-Os and $^{40}Ar/^{39}Ar$ age data from other late Cenozoic porphyry-epithermal systems and mineralized igneous rocks along the Anatolian Trend (Aydoğan et al., 2008; Yılmaz et al., 2013; İmer et al., 2014; Baker et al., 2016; Bickford et al., 2016; Boucher, 2016; Delibaş et al., 2017; Chapter 2).

U-Pb dating of igneous zircons by laser ablation (LA)-ICP-MS method was conducted at the Pacific Center for Isotopic and Geochemical Research (PCIGR), The University of British Columbia, Canada, whereas $^{40}Ar/^{39}Ar$ and Re-Os dating were performed at the Université of Genève and University of Alberta, respectively. The detailed procedure for LA-ICP-MS U-Pb, $^{40}Ar/^{39}Ar$ and Re-Os dating techniques, and the data compilation methodology, are provided in Chapter 2 and in the appendix E (Baker et al., 2016), respectively; the results are provided in Table 4.3; the isotopic analyses are in the appendix C (Tables C.1 and C.2).

4.5 Age dating results

An unaltered monzonitic intrusion at the Pınarbaşı Au (-Mo) porphyry prospect in western Anatolia has a $^{206}Pb/^{238}U$ weighted average age of 17.86 ± 0.18 Ma from the analysis of 21 concordant zircon grains (FR-15-18; Figures 4.10A-B). This intrusion post-dates and constrains the sulfide mineralization previously dated at 18.3 and 18.2 ± 0.1 Ma (Re-Os technique on molybdenite; Delibaş et al., 2017). Molybdenite mineralization from the Afyon-

Sandıklı Au-Cu porphyry prospect in western Anatolia yields a Re-Os model age of 11.63 ± 0.05 Ma (FR-14-165). The Afyon-Sandıklı quartz-sulfide vein stockwork cross-cuts a porphyric monzonitic intrusion that yields a $^{206}Pb/^{238}U$ weighted average age of 11.64 ± 0.20 Ma based on results from 18 zircon grains (FR-14-49; Figures 4.10C-D). This age is consistent with the regional $^{40}Ar/^{39}Ar$ ages in the Afyon volcanic complex (14-8 Ma; Besang et al., 1977; Akal et al., 2013). The skarn-altered monzonite in the Bodrum district yields a U-Pb crystallization age of 9.76 ± 0.06 Ma determined from 19 zircon grains (FR-15-31; Figures 4.10E-F). This date is within the range of previously-published $^{40}Ar/^{39}Ar$ ages from the Bodrum volcanic suite (13-7 Ma; Robert et al., 1992; Fahmi et al., 1997).

The age of high-sulfidation epithermal advanced argillic alteration in central and eastern Anatolia is determined by $^{40}Ar/^{39}Ar$ dating of hydrothermal and hypogene alunite. The hydrothermal alunite crystals from the high-sulfidation epithermal İnlice deposit and Hasançelebi prospect yield disturbed $^{40}Ar/^{39}Ar$ dating results of 8.16 ± 0.25 (FR-13-179; Figure 4.11A) and 20.44 ± 0.86 Ma (FR-14-79; Figure 4.11B), respectively. The age of the alunite alteration at Doğanbey is constrained by an inverse isochron age of 10.61 ± 0.80 Ma (FR-14-68; Figures 4.C-D). These $^{40}Ar/^{39}Ar$ alunite dating analyses suffered from Ar loss due to the

Table 4.3 Summary of LA-ICP-MS U-Pb, $^{40}Ar/^{39}Ar$ and Re-Os dating results from selected gold deposits and prospects along the late Cenozoic Anatolian Trend.

Intrusive unit (Zircon, LA-ICP-MS U-Pb)

Sample	*Lat (°N)*	*Long (°E)*	*District*	*Prospect*	*Mineralization style*	*Lithology host*	*Concordia age (Ma)*	*MSWD*	n
FR-15-18	39.0165	29.3229	-	Pınarbaşı	Porphyry	Monzonite	17.86 ± 0.18	1.6	21
FR-14-49	38.5013	30.3382	-	Afyon-Sandıklı	Porphyry	Monzonite	11.64 ± 0.20	0.98	18
FR-15-31	37.0310	27.2580	Bodrum	Kadıkalesı	Skarn	Monzonite	9.76 ± 0.06	0.82	19

Ore (Molybdenite, Re-Os)

Sample	*Lat (°N)*	*Long (°E)*	*District*	*Prospect*	*Mineralization style*	*Lithology host*	*Re ppm*	*^{187}Re ppm*	*^{187}Os ppb*	*Model age (Ma)*
FR-14-165	38.5021	30.3393	-	Afyon-Sandıklı	Porphyry	Monzonite	539.3 ± 1.4	339.0 ± 0.9	65.68 ± 0.13	11.63 ± 0.05

Advanced argillic alteration (Alunite, $^{40}Ar/^{39}Ar$)

Sample	*Lat (°N)*	*Long (°E)*	*District*	*Deposit/ Prospect*	*Mineralization style*	*Lithology host*	*Plateau age (Ma)*	*Total fusion age (Ma)*	*Inverse isochron (Ma)*
FR-13-179	37.7559	32.0878	Konya	İnlice	HS epithermal	Biotite andesite	8.16 ± 0.25[1]	8.01 ± 0.26	8.55 ± 0.64
FR-14-68	37.8374	31.9551	Konya	Doğanbey	HS epithermal	Two-pyroxene andesite	9.69 ± 0.10	9.41 ± 0.09	10.61 ± 0.80[1]
FR-14-79	38.9992	37.8464	-	Hasançelebi	HS epithermal	Clinopyroxene andesite	20.44 ± 0.86[1]	20.26 ± 0.31	14.86 ± 5.39

[1] *Preferred age*

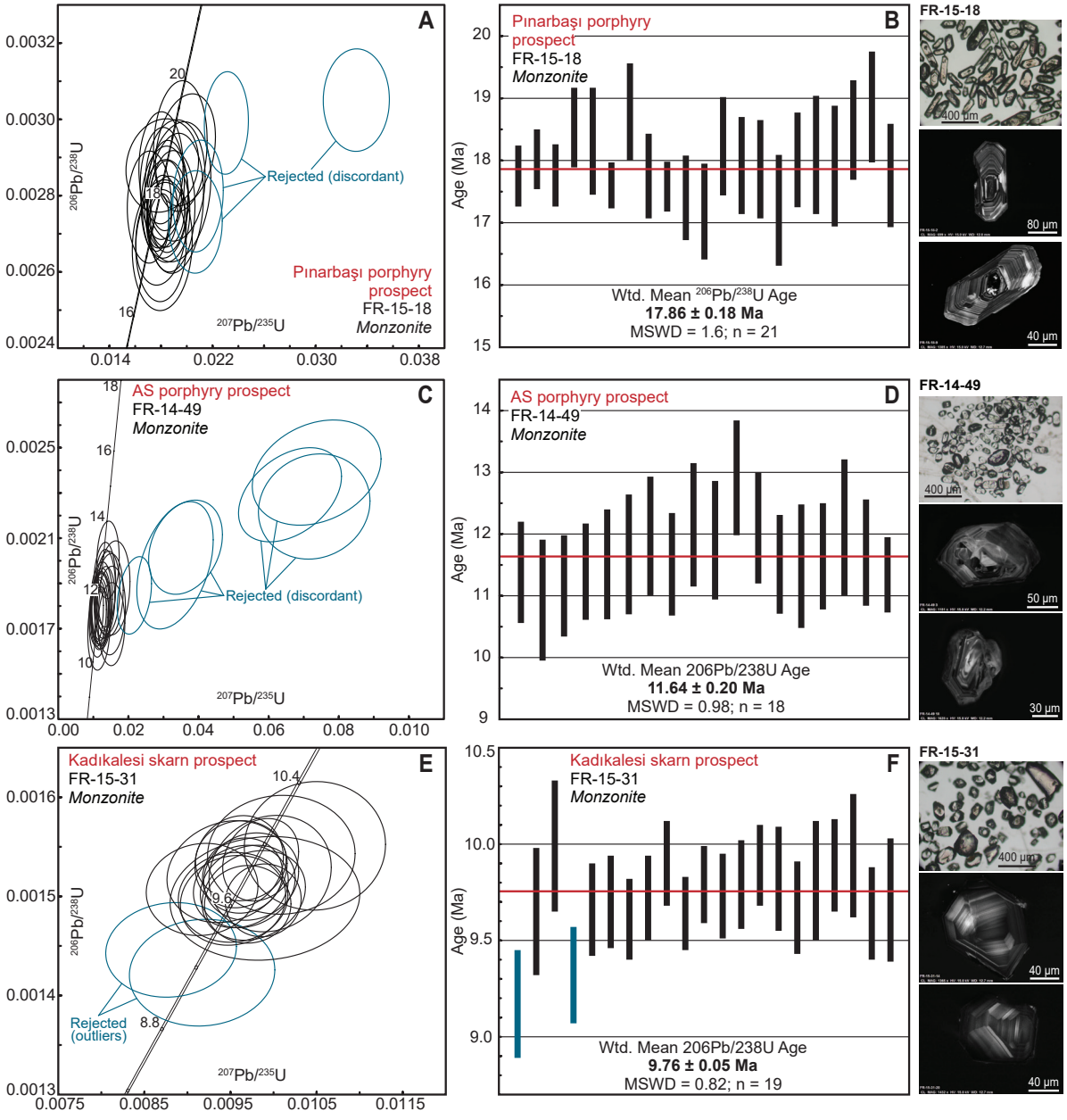

Figure 4.10 Concordia and weighted average $^{206}U/^{238}U$ age plots for igneous zircons from the late Cenozoic post-mineralization monzonite at the Pınarbaşı porphyry Mo-Cu prospect (A-B), monzonitic host rock at the Afyon-Sandıklı porphyry Au-Cu (C-D) and Kadıkalesi skarn prospects (E-F). Discordant and outlier analyses are in blue; analyses used for calculation of the weighted average $^{206}Pb/^{238}U$ age for each sample are in black. All errors are reported at 2σ level. MSWD: mean square of weighted deviates. The images (right) under optical microscope and cathodoluminescence for each sample display the internal structure of representative igneous zircon grains.

small size of analyzed alunite grains (< 100 μm) and did not yield any reliable age plateau. Nonetheless, the age data are consistent with the U-Pb crystallization ages of the magmatic host rock in Chapter 2 at 8.67 ± 0.13 and 10.21 ± 0.13 Ma at İnlice and Doğanbey, respectively. The post-alteration andesitic lava flow that overlies the high-sulfidation epithermal alteration at the Hasançelebi Au-Ag prospect has a crystallization age of 21.32 ± 0.29 Ma (Chapter 2) that slightly overlaps the $^{40}Ar/^{39}Ar$ result presented herein.

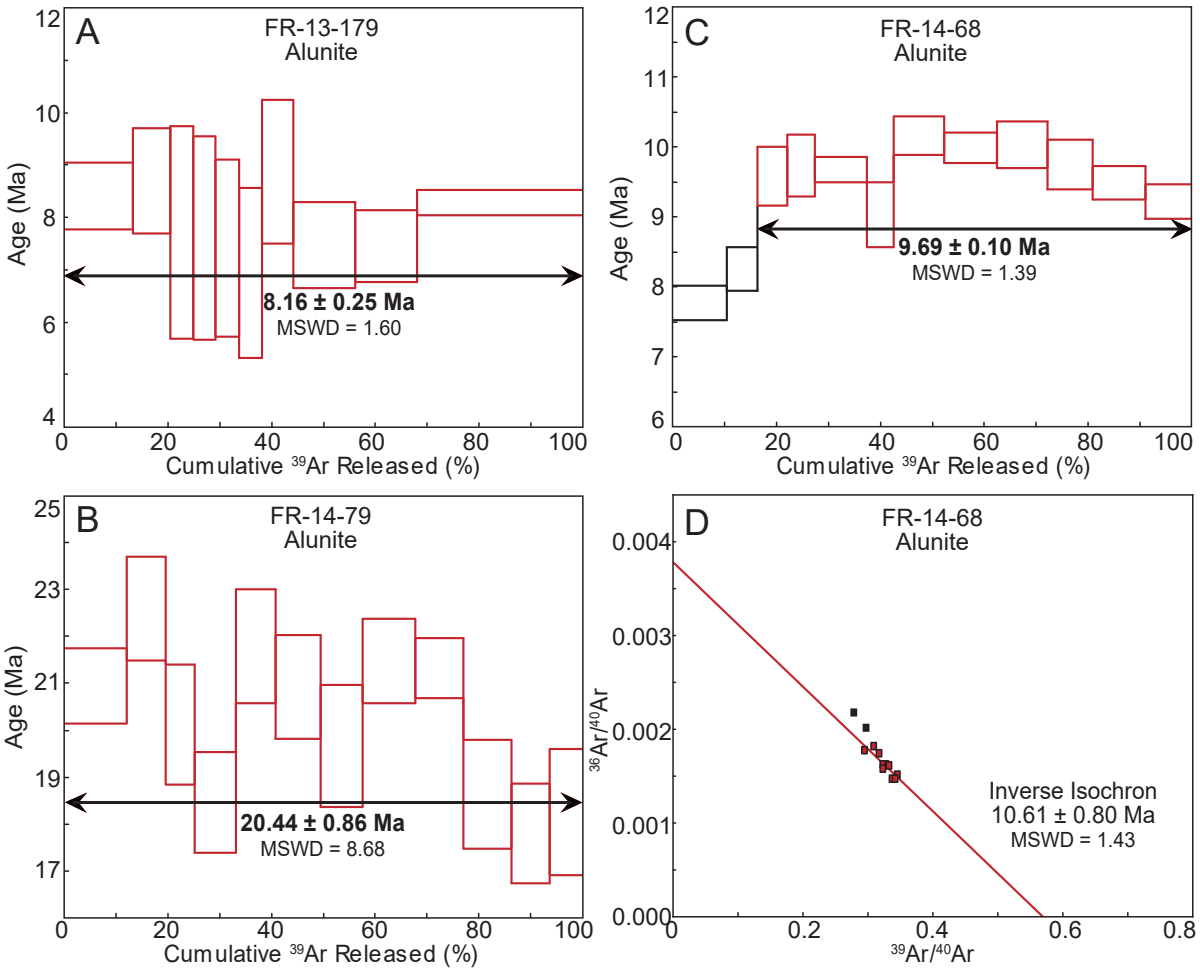

Figure 4.11 $^{40}Ar/^{39}Ar$ age plateaus and inverse isochron for analyzed hypogene alunite from the İnlice (A), Hasançelebi (B) and Doğanbey (C-D) high-sulfidation epithermal Au (-Ag) prospects and deposits. Excluded analyses are in black. All errors are reported at 2σ level. MSWD: mean square of weighted deviates.

4.6 Discussion

4.6.1 Style and distribution of gold-bearing ore systems

4.6.1.1 Spatial distribution of precious and base metal mineralization in western Anatolia

Although the formation of low- and intermediate-sulfidation epithermal vein systems is coeval with porphyry mineralization in western Anatolia, both styles of mineralizing systems are spatially distinct and do not share genetic relationships. Late Cenozoic low- and intermediate-sulfidation epithermal mineralization in western Anatolia such as in the İzmir and Simav districts, occurs preferentially along the northern and western edges of the Menderes Massif. The early Miocene volcanism that hosts this type of epithermal mineralization is characterized by dacitic to rhyolitic ignimbrites, lava-domes and volcaniclastic products emplaced at the initiation of Menderes Massif exhumation (e.g., Erkül et al., 2005b). This exhumation of the Menderes Massif was also accompanied by the formation of syn-tectonic granitic intrusions that produced sub-economic Fe-Pb-Zn skarn mineralization at their contacts with the calcareous basement rocks. In contrast, porphyry prospects and deposits including Kışladağ, Pınarbaşı, Sayacık and Afyon-Sandıklı are on the northeastern and eastern margins of the Menderes Massif. This porphyry mineralization has limited molybdenum and copper endowment hosted within the monzonitic intrusions.

4.6.1.2 Boron-rich hydrothermal alteration in western Anatolia

Middle to late Miocene hydrothermal alteration systems in western Anatolia are characterized by abundant boron-bearing alteration phases including tourmaline at the Kışladağ (Baker et al., 2016) and Afyon-Sandıklı porphyry systems (Sönmez and Kuşcu, 2016; this Chapter), and rare axinite at the Efemçukuru low- to intermediate-sulfidation epithermal deposit (Oyman et al., 2003; Boucher, 2016). In addition, western Anatolia hosts world-class Neogene borate deposits including Bigadiç, Kerstelek and Emet formed in lacustrine-evaporitic volcano-sedimentary basins (Helvacı, 2015). Although boron is an incompatible element that preferentially concentrates in the fractioning melts, the anomalous excess of boron alteration phases in hydrothermal systems requires boron-rich magma source. Such a magma enrichment

reflects the substantial contribution of the Anatolian metasedimentary basement, and/or pelagic sediment-derived fluids into the subduction zone in which boron fractionates and easily transfers from the subducted slab to arc magma source. (Ryan and Langmuir, 1993; Leeman et al., 1994; Leeman and Sisson, 1996). Sediment input during the mantle metasomatism is confirmed by petrological investigations conducted in western Anatolia (e.g., Ersoy and Palmer, 2013). Alternatively, boron could also have been scavenged by ascending magma and hydrothermal fluids from deeper boron-rich evaporates through the metasedimentary basement and along the Neogene volcano-sedimentary basins in western Anatolia (Helvacı, 2015).

4.6.1.3 Orogenic and epithermal gold mineralization in western Anatolia

Gold-bearing quartz vein mineralization occurs within the core of the various metamorphic massifs throughout Anatolia, in particular in the Menderes Massif, and is thought to be the result of pre-Cenozoic orogenic systems (Yiğit, 2006; Gessner et al., 2017). The absence of genetic and temporal constraints on gold mineralization and the presence of active geothermal systems raise the controversy about the origin of those hydrothermal gold vein systems in western Anatolia, namely orogenic or epithermal style (Yiğit, 2006). A commonly held view suggests that pre-Cenozoic gold mineralization could have been remobilized from the lower crust during the Cenozoic geothermal phase and Barrovian-type metamorphism during the core complex formation (Yiğit, 2006, 2009). Field observations in the center of the Menderes Massif provided in this study confirm the orogenic affinity of those gold-rich quartz veins that cross cut the basement schistosity and show ductile deformation. Thus, this cross-cutting relationship thereby excludes a Cenozoic remobilization that would have preferentially focused those veins along Cenozoic-aged rock schistosity and brittle structures such as in the northern Menderes Massif in the Simav district. In addition, the abundance of Sb (-Hg) mineralization nearby those gold-bearing veins in the Menderes Massif (e.g., Cebrail and Göynük deposits and prospects) may also suggest an orogenic affinity and a formation at the end of the metamorphic event and at shallow depths (Groves et al., 1998). However, the observations presented herein suggest that this shallow mineralization is not related to

the pre-Cenozoic orogenic systems but is a late overprint that results from the Cenozoic geothermal activity in the Menderes Massif. The shallow Sb-Hg-rich part of the Pre-Cenozoic orogenic gold-rich quartz vein systems was likely eroded during the Cenozoic exhumation of metamorphic host units.

4.6.1.4 High-sulfidation epithermal mineralization in central Anatolia

Most high-sulfidation epithermal occurrences on the Anatolide-Tauride Block are in three districts, namely Konya, Niğde and Kayseri in central Anatolia. Reported gold resources culminate at only about 1.6 Moz distributed between the Öksüt and İnlice deposits. Porphyry mineralization is absent, although weak signs of overprinted high-temperature alteration assemblages are locally observed (e.g., Hall et al., 2007). Most late Miocene to Pliocene volcanism in central Anatolia such as the Konya volcanic complex, Melendiz, Tekkedağ and Develidağ stratovolcanoes, hosts numerous mineralized alteration systems that are post-dated by the barren and voluminous basaltic to andesitic lava flows and pyroclastic products from the Pliocene to Quaternary Hasandağ and Erciyes stratovolcanoes. In contrast, Andean-style high-sulfidation epithermal deposits are mostly coeval with volumetrically restricted or absent volcanism; stratovolcanoes are typically unmineralized (Bissig et al., 2015).

4.6.1.5 Potential for epithermal- and porphyry-style mineralization in eastern Anatolia

The abundance and density of mineral occurrences decreases eastwards to eastern Anatolia where volcanism is the most voluminous. The isolated Hasançelebi high-sulfidation epithermal Au-Ag prospect in the western part of eastern Anatolia is similar to its counterparts of central Anatolia and is also partially overlain by barren andesitic lava flows within the Yamadağ volcanic complex. Porphyry-style mineralization occurs within most of the late Cenozoic intrusive units mapped in the eastern part of eastern Anatolia such as in the Tunceli and Ağrı districts where high-sulfidation epithermal mineralization is not preserved, except at the Taşkapı prospect. Despite the limited number of porphyry and epithermal occurrences, the potential for both precious and base metal resources in this region is high as highlighted by the distal syn- to post-Miocene (?) Carlin-type Mollakara Au-Ag (4.5 Moz Au) and Cevizlidere Cu-

Au-Mo porphyry deposits (1.6 Moz; 3.7 Blbs Cu). In addition, the abundance of hot springs, in particular in the Ağrı district (Çolakoğlu et al., 2011; Pasvanoğlu, 2013), suggests the potential for low-sulfidation epithermal vein systems in eastern Anatolia.

4.6.2 Regional structural control on gold mineralization

The Anatolian Trend is affected by contrasting tectonic regimes dominated by continental extension in the west and compression in the east. The widespread distribution of late Cenozoic magmatism and associated hydrothermal mineralization is controlled by the numerous high-permeability extensional sites along strike-slip faults and intersections in central and eastern Anatolia, and detachment faults, strike-slip corridors and grabens in western Anatolia.

4.6.2.1 Western Anatolia

Miocene magmatism in western Anatolia was emplaced in a northerly-trending extensional to transtensional continental rifting or back-arc setting during a major period of crustal thinning that was dominated by the exhumation of the Menderes metamorphic core complex (e.g., Hetzel et al., 1995; Seyitoğlu, 1997; Bozkurt and Oberhänsli, 2001; Ersoy et al., 2010; Prelević et al., 2010). Epithermal, porphyry and structurally-controlled base-metal deposits formed during the tectonic denudation in the Menderes Massif region in the Neogene (Gessner et al., 2017; Menant et al., 2018; Roche, 2018). This crustal extensional phase produced a high geothermal gradient and dense brittle faulting network in the metamorphic basement that facilitated the crustal emplacement of fertile magmas and hydrothermal fluids along detachment faults and WNW- to NE-trending graben and faults, and at graben and fault intersections (Figure 4.12; Gessner et al., 2017; Menant et al., 2018; Roche, 2018). Although the role of regional detachment faults as control on gold mineralization has been proposed in western Anatolia (e.g., Menant et al., 2018; Roche, 2018), field observations presented herein suggest that most of gold mineralization is along high-angle normal and strike-slip structures, away from those low-angle detachment faults. For instance, the NNE-trending sinistral İzmir-Balıkesir Transfer Zone, the ENE-trending Sındırgı structural corridor and WNW-trending faults (i.e., Simav normal fault) in northwest Anatolia are favorable for the formation of low-

and intermediate-sulfidation epithermal Au-Ag vein systems (< 4 Moz Au) in NW- to NNW-trending dilational sites as observed at Kızıltepe, Kepez, Tavşan, Efemçukuru and Arapdağ (Sayılı and Gonca, 1999; Şener et al., 2009; Boucher, 2016). Similarly, the emplacement of the NW-trending Pınarbaşı intrusion and associated porphyry mineralization is controlled by the Erdogmus-Yenigediz graben along the WNW-trending Simav fault (Delibaş et al., 2017). Shallow Sb-Hg mineralization (e.g., Gediz and Halıköy) occurs along high-angle normal faults developed since the late Miocene (Ring et al., 2003). The emplacement of epithermal vein within volcanic complexes is strongly influenced by local, syn-volcanic structures and porosity of host lithologies that enhance the hydrothermal fluid diffusion and lower the metal content such as in the Simav district. Conversely, basement-hosted vein systems preferentially formed within less porous rocks that force hydrothermal fluids to flow along major structures thereby leading to the increase in metal content (e.g., Efemçukuru deposit).

4.6.2.2 Central Anatolia

The spatial distribution of central Anatolian volcanic edifices and thus associated epithermal mineralization is controlled by the conjugate, NW-trending, dextral Tuz Gölü and NE-trending, sinistral Ecemiş faults, ENE-trending structures (Pasquare et al., 1988), and normal faults (e.g., Akşehir fault). Those structures formed in response to the transtensional and transpressional regime that resulted from the regional N-trending compression (Dhont et al., 1998; Koçyiğit and Beyhan, 1998; Toprak, 1998; Koçyiğit and Erol, 2001).

The Konya volcanic complex that hosts numerous high-sulfidation epithermal occurrences was emplaced at the tip of the Akşehir normal fault. The distribution of epithermal occurrences are aligned along the NNW-trending Konya alteration corridor (Figure 4.6A). The presence of such a corridor coupled with the NNW-trending elongation of the Konya volcanic complex suggests the presence of a regional, deep and covered structure that controlled the emplacement of volcanic edifices and hydrothermal mineralization.

The numerous high-sulfidation epithermal occurrences of the Niğde district are hosted within the Melendiz stratovolcano that is part of the SW-trending Sivas-Cappadocia-Hasandağ-

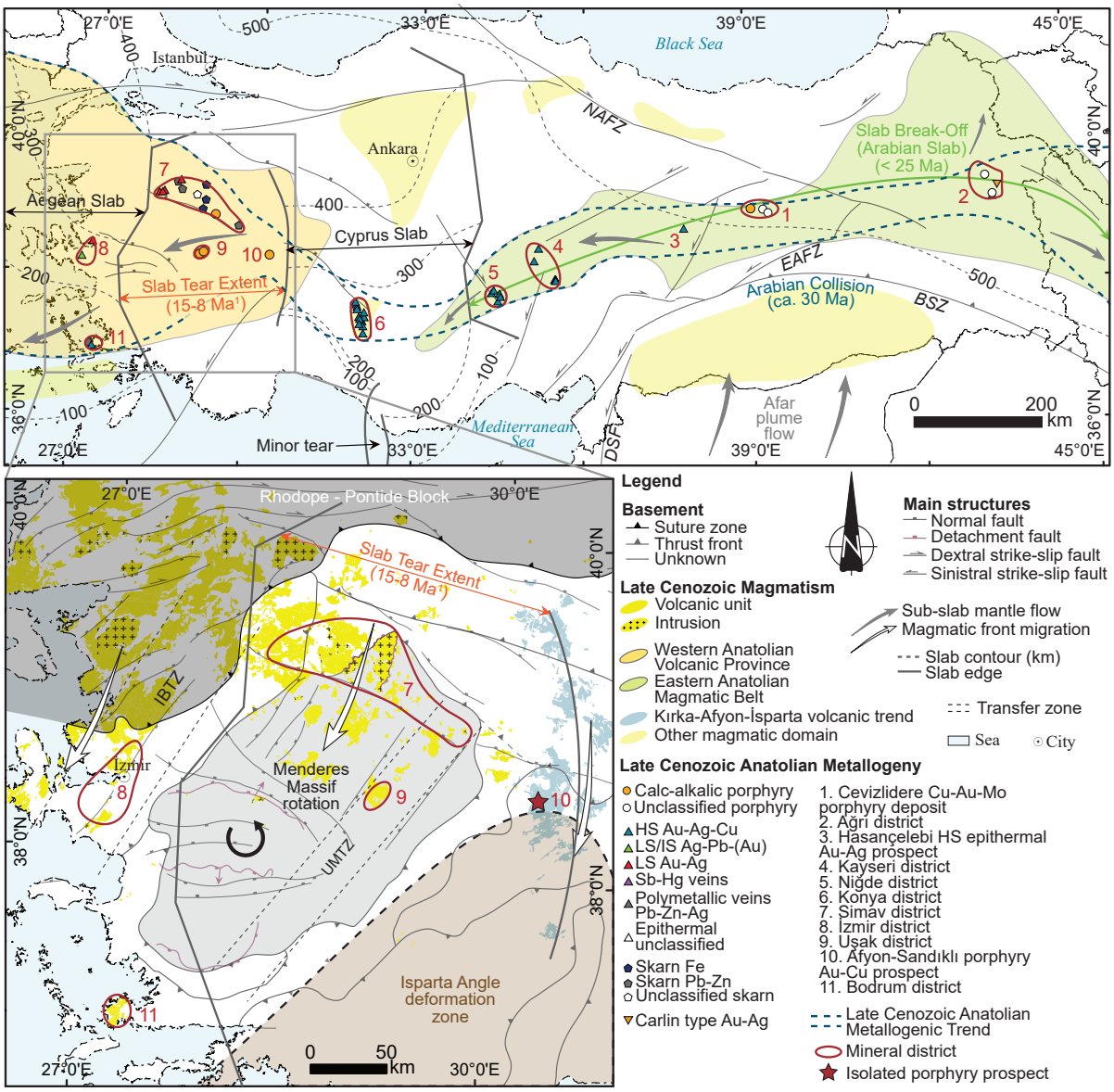

Figure 4.12 Top: simplified tectono-magmatic map of Turkey illustrating the distribution of the late Cenozoic magmatic domains, key mineral deposits and prospects, mineral districts and the late Cenozoic Anatolian Metallogenic Trend defined in this Chapter. The slab contours (in km; Biryol et al., 2011) show the segmentation of the Southern Neotethyan slab and the resulting mantle flow directions (grey arrows). Bottom: simplified tectono-magmatic map of western Anatolia displaying the distribution of mineral deposits, prospects and districts, late Cenozoic magmatic complexes, magmatic front migration (white arrow), major structures, deformation zones and extent of the tear-related slab window defined by Biryol et al. (2011).

Karaman volcanic axis which is offset by the NW-trending dextral strike-slip Tuz Gölü fault (Figure 4.6B). The Melendiz stratovolcano is at the intersection of this volcanic axis and the Tuz Gölü fault, which has been active since the late Eocene as a strike-slip structure (Cemen et al., 1999).

The high-sulfidation epithermal occurrences in the Kayseri district were emplaced in late Miocene volcanic edifices along the NE-trending sinistral strike-slip Ecemiş fault (Figure 4.6C). Sinistral motion along the Ecemiş fault during Pliocene initiated formation of the transtensional Sultansazlığı pull-apart basin that was subsequently filled by Pliocene to Quaternary sediments and volcanic and volcaniclastic products from the Erciyes stratovolcano (Koçyiğit and Erol, 2001). This pull-apart basin separated the mineralized late Miocene volcanic units that are now exposed on its both sides (Toprak, 1998). For instance, the Öksüt high-sulfidation epithermal gold deposit is located within the late Miocene Develidağ stratovolcano on the eastern flank of the Sultansazlığı basin whereas the Başdere high-sulfidation epithermal occurrence within the late Miocene Tekkedağ volcanic units on the western flank of this transtensional basin.

4.6.2.3 Eastern Anatolia

The emplacement of eastern Anatolian mineralizing magmas into the upper crust was controlled by the formation of extensional site at fault intersections and along the many major strike-slip fault zones that traverse the region such as the North Anatolian, Malatya and Ovacık fault zones (Koçyiğit et al., 2001; Westaway et al., 2008; Kaymakçı et al., 2010). The Yamadağ volcanic complex that hosts the Hasançelebi high-sulfidation epithermal Au-Ag prospect was emplaced between the NNE- to NE-trending sinistral Yakapınar-Göksun and Malatya faults during the early to middle Miocene NW-trending extension (Kaymakçı et al., 2006). Both faults also control the distribution of the mineralized Late Cretaceous plutons in the region of Divriği and the Eocene Bizmişen and Çaltı plutons (e.g., Kuşcu et al., 2013). The Cevizlidere porphyry Cu-Au-Mo deposit was emplaced in a pull-apart basin along the Ovacık sinistral strike-slip fault (İmer et al., 2014). Whereas the mineralized Eocene plutons in central and eastern Anatolia are in fault splays (Kuşcu et al., 2010), Oligocene to Miocene mineralized

magmatic units are emplaced either along the fault segments or pull-apart basins. The magma and mineralization emplacement coincides with NW-directed extension that prevailed in eastern Anatolia between 25 and 11 Ma (Kaymakçı et al., 2010). The mineralized plutons in the Ağrı district are exposed near the inferred intersection between the NW-trending dextral Hamur, WNW-trending dextral Çaldıran and NNE-trending sinistral strike-slip faults (Figure 4.6D).

4.6.3 Paleodepth of porphyry ore emplacement

Field observations presented herein show that high-sulfidation epithermal-style alteration is prevalent throughout the late Cenozoic Anatolian Trend, as opposed to porphyry mineralization, but the lithocap endowment strongly varies along this Trend. For instance, silica lithocaps and ledges in western Anatolia are barren in contrast to those in central Anatolia and at the Hasançelebi high-sulfidation epithermal prospect in eastern Anatolia. Those barren lithocaps and ledges in western Anatolia formed tens to a few hundred meters above co-genetic, shallowly-emplaced, gold-rich porphyry stocks into the volcanic rocks such as at Kışladağ and Afyon-Sandıklı (Baker et al., 2016; this Chapter). Ideal erosion conditions in the middle Miocene exposed the shallow gold-rich porphyry ore bodies and preserved the overlying barren lithocaps in western Anatolia. In contrast, the lithocap at the early Miocene Pınarbaşı porphyry prospect is eroded (Delibaş et al., 2017); there is no observed outcropping porphyry alteration in the late Miocene Bodrum district, despite the presence of a lithocap and advanced argillic alteration assemblage at the Karatoprak prospect.

The compressed nature of alteration systems from high-temperature potassic to low-temperature advanced argillic alteration assemblages, inferred to be co-genetic, is present in eastern Anatolia such as at Taşkapı in the Ağrı district. In addition, the Cevizlidere Cu-Au-Mo porphyry deposit in the central part of eastern Anatolia formed at shallow level in the apparent absence of epithermal alteration and mineralization, certainly eroded (İmer et al., 2014). Conversely, shallow-level high-temperature alteration assemblages are apparently absent in central Anatolia and at Hasançelebi where most of silica-alunite lithocaps, ledges and breccias

are mineralized, perhaps except at the Doğanbey prospect in the Konya district (Hall et al., 2007).

The comparison between western and central Anatolian hydrothermal gold systems suggests an analogy with the El Indio and Maricunga gold belts in the Andes. The El Indio belt is characterized by mineralized high-sulfidation epithermal lithocaps in absence of shallow porphyry mineralization, similar to central Anatolia, whereas the gold endowment of the Maricunga belt is provided by shallowly-emplaced porphyry gold systems (Muntean and Einaudi, 2000; Bissig et al., 2015) such as those in western Anatolia (e.g., Kışladağ deposit; Baker et al., 2016), and probably in eastern Anatolia (e.g., Cevizlidere deposit and Taşkapı prospect). The abundance of banded quartz veinlets that include dark grey bands of micrometer-sized magnetite grains and trapped vapor in the Maricunga deposits is the evidence of shallow emplacement (Muntean and Einaudi, 2000). Those banded quartz veins are present at Kışladağ in association with tourmaline (Baker et al., 2016), and also at the Doğanbey high-sulfidation prospect in the Konya district (Hall et al., 2007). The field observations in Anatolia reported herein are in accordance with previous empirical (Cox and Singer, 1988; Sillitoe, 1997) and microthermometric studies (Murakami et al., 2010) that correlated metal endowment of lithocaps and relative emplacement depth of porphyry ore (Figure 4.13). The shallow emplacement of porphyry ore (< 3 km) has a tendency to favor Au and Cu co-precipitation giving rise to barren overlying lithocaps whereas deeply-emplaced porphyry systems (> 3 km) will preferentially precipitate Cu and Mo at depth and release gold-rich hydrothermal fluids that will reach and precipitate in the epithermal environment (Murakami et al., 2010).

The shallow emplacement of porphyry ore bodies in western Anatolia is controlled by the alkaline monzonitic nature of causative magmatism that can reach shallower depth (Schmincke, 2004; p. 125), as well as a regional extensional regime and crustal thinning (ca. 30 km; Zhu et al., 2006; Tezel et al., 2013). This contrasts with the calc-alkaline andesitic composition of mineralized volcanics rocks and probably causative deeply-emplaced plutons (> 3 km), transtensional to transpressional tectonic regime and thicker crust in central Anatolia

(ca. 40 km; Gök et al., 2007; Çakır and Erduran, 2011). Therefore, magma alkalinity and tectonic regime control the crustal emplacement of fertile magma in Anatolia. In addition, the composition of the local wall-rock, namely carbonate and ophiolite units in central and eastern Anatolia, may have also played a role in the magma emplacement and mineral precipitation as showed at the Eocene Çöpler intermediate-sulfidation epithermal deposit and associated

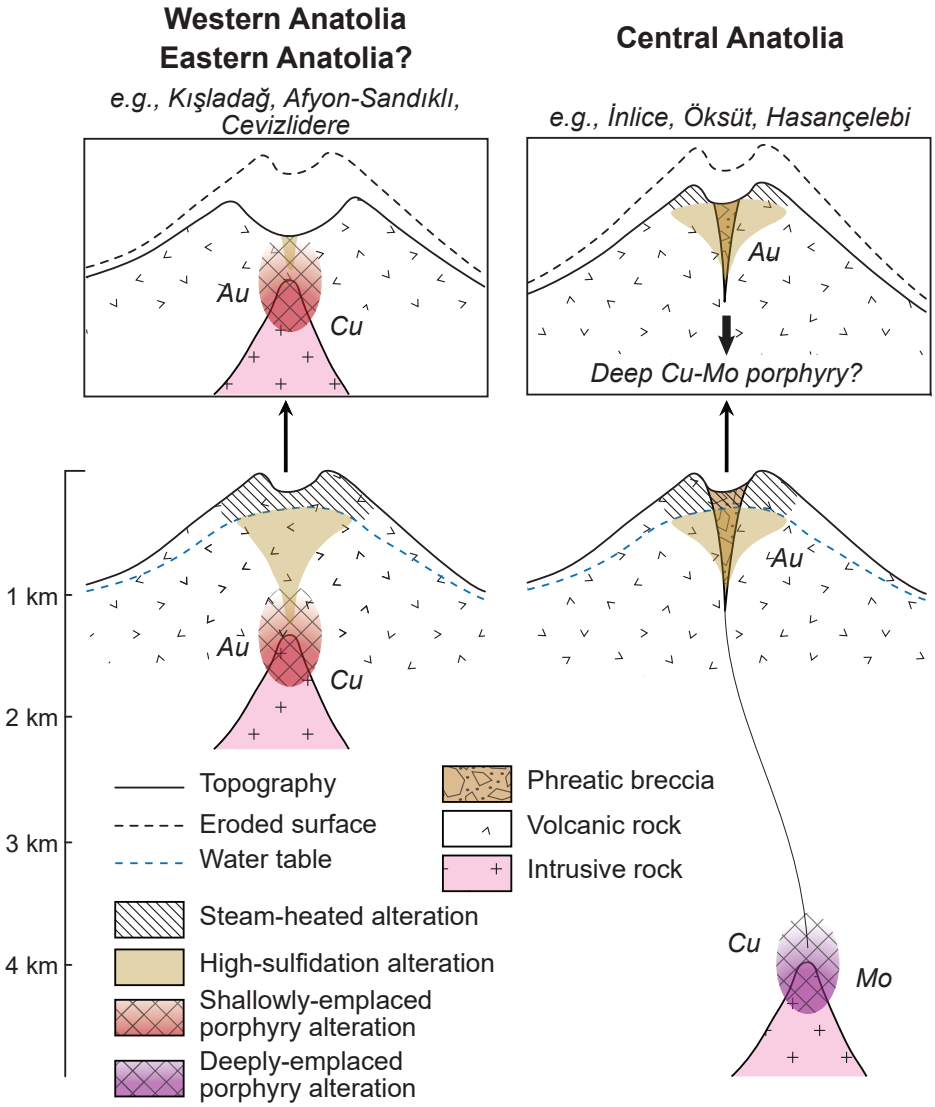

Figure 4.13 Schematic geometry and relative metal endowment of Anatolia porphyry and epithermal environments (upper part) and simplified relationship between emplacement depth of the causative intrusion and mineralization style in a volcanic environment (lower part; after Bissig et al., 2015; inspired from Murakami et al., 2010). Left: shallow-emplaced porphyry stock (< 3 km) leading to the Cu and Au co-precipitation in the porphyry zone only (western Anatolia and at Cevizlidere in the eastern part of eastern Anatolia); Right: deeply-emplaced intrusion controlling the high-temperature co-precipitation of Cu and Mo in the porphyry zone and transportation of Au-bearing bisulfide complexes to the shallower epithermal zone (central Anatolia and Hasançelebi in the western part of eastern Anatolia).

porphyry system in eastern Anatolia (İmer et al., 2013, 2016). Beyond crustal controls on the spatial distribution of metals, metal endowment in the magma is primarily controlled by the composition of magmatic sources and processes in the lithosphere that are out of scope of this Chapter.

4.6.4 Timing and duration of gold mineralization events

4.6.4.1 Western Anatolia

Hydrothermal mineralization formed between ca. 21 and 9 Ma in western Anatolia (Figure 4.14). Skarn-style Fe-Pb-Zn mineralization occurred at ca. 21-20 Ma around the syn-tectonic Alaçam and Eğrigöz plutons (Ring and Collins, 2005; Hasözbek et al., 2011), and between 19.4 ± 0.9 and 17.8 ± 0.7 Ma at Baklan (Aydoğan et al., 2008). Low- and intermediate-sulfidation epithermal Au (-Ag) mineralization is restricted to western Anatolia and peaked at 18.3 ± 0.2 Ma at the Kızıltepe deposit in the Simav district (Yılmaz et al., 2013; Figure 4.14). In addition, steam-heated hydrothermal alunite and kaolinite alteration also occurred in the Simav district between 20.6 and 17.3 Ma (Ece et al., 2013). In the İzmir district, low- and intermediate-sulfidation epithermal mineralization is constrained by the dating of post-mineralization volcanism (14.7 ± 0.5 Ma; Sayılı and Gonca, 1999) at the northerly Arapdağ prospect and pre-veining rhyolitic dykes dated at 13.17 ± 0.25 Ma at the southerly Efemçukuru gold deposit (Boucher, 2016). Thus, low- and intermediate-sulfidation epithermal mineralization peaked between 19 and 13 Ma in western Anatolia.

Detailed geochronology on the porphyry prospects and deposits in western Anatolia reveals that porphyry-style mineralization occurred between 18 and 11 Ma but each of them resulted from the relatively short duration of the hydrothermal event (< 1 m.y.) generated by a limited number of intrusive phases (≤ 4; Baker et al., 2016; this Chapter). The Afyon-Sandıklı Au (-Cu) mineralization, dated at 11.63 ± 0.05 Ma by Re-Os, is bracketed by the pre- to syn-alteration monzonitic stock and post-alteration monzonitic dike dated at 11.64 ± 0.20 (this Chapter) and 10.97 ± 0.09 Ma by U-Pb zircon dates, respectively (Sönmez and Kuşcu, 2016). Thus, the Afyon-Sandıklı mineralization event formed over a duration between 0.38 and 0.96

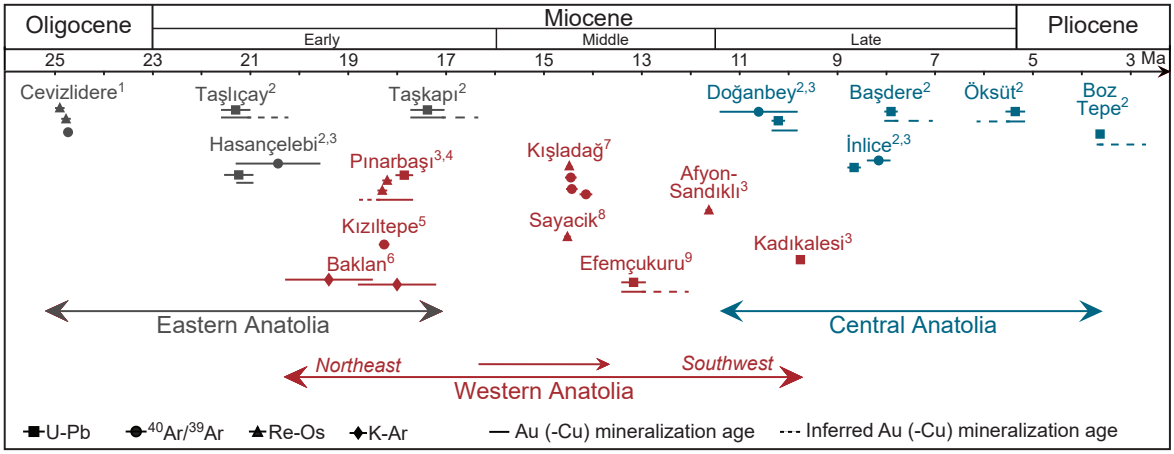

Figure 4.14 Time scale illustrating the timing of gold mineralization in western (red), central (blue) and eastern Anatolia (grey), with the exception of the Baklan skarn Pb-Zn occurrence. Error bars are reported at 2σ level. Gold mineralization is inferred to occur during the deposition of sulfides, dated by Re-Os technique, and hypogene alunite, dated by $^{40}Ar/^{39}Ar$ technique, in porphyry and high-sulfidation epithermal systems, respectively. The dating of pre- or post-mineralization igneous units by U-Pb and K-Ar methods also provides constraints on the timing of gold mineralization illustrated by horizontal full (high confidence) and dashed bars (low confidence). The early Miocene skarn Fe-Pb-Zn occurrences at the Eğrigöz and Alaçam plutons (ca. 21-20 Ma) are not displayed because of the high number of available dates in the literature, as opposed to the Baklan pluton. References: [1]İmer et al., 2014; [2]Chapter 2; [3]this Chapter; [4]Delibaş et al., 2017; [5]Yılmaz et al., 2013; [6]Aydoğan et al., 2008; [7]Baker et al., 2016; [8]Bickford et al., 2016; [9]Boucher, 2016.

m.y. Re-Os model ages on porphyry mineralization in the Uşak district are 14.49 ± 0.06 and 14.51 ± 0.06 Ma at the Kışladağ gold deposit and Sayacık prospect, respectively (Baker et al., 2016; Bickford et al., 2016). The deposition of gold mineralization at the Kışladağ deposit occurred within < 0.4 m.y. (14.76 ± 0.01-14.36 ± 0.02 Ma; Baker et al., 2016). However, the duration of the Pınarbaşı Mo-Cu mineralization event is only constrained by the timing of sulfide mineralization (18.3 to 18.2 ± 0.1 Ma by Re-Os; Delibaş et al., 2017) and the post-alteration monzonite (17.86 ± 0.18 Ma by U-Pb; this Chapter) yielding a minimum duration of the hydrothermal event between 0.1 and 0.7 m.y.

The youngest mineralizing event in western Anatolia may be in the Bodrum district where the age of the Kadıkalesi skarn alteration is constrained by the U-Pb dating of the monzonitic host (9.76 ± 0.06 Ma). However, the age of the high-sulfidation epithermal alteration at Karatoprak is unknown but assumed to be similar to the surrounding volcanic and intrusive rocks dated between 13 and 7 Ma; (Robert et al., 1992; Fahmi et al., 1997).

4.6.4.2 Central Anatolia

The timing of epithermal gold and silver mineralization at the Konya district is uncertain because the $^{40}Ar/^{39}Ar$ alunite ages are disturbed and do not define plateau. In addition, there are no time constraints on brecciation events and direct evidence of gold and alunite co-precipitation at the Doğanbey prospect and İnlice deposit. Nonetheless, the age data presented herein suggest that the Doğanbey precious metal mineralization likely formed between 10.34 and 9.81 Ma constrained by the andesite host rock that crystallized at 10.21 ± 0.13 Ma (U-Pb on zircon; Chapter 2) and hydrothermal alunite alteration dated at 10.61 ± 0.80 Ma ($^{40}Ar/^{39}Ar$ technique; this Chapter). Similarly, the İnlice precious metal mineralization is assumed to be constrained by the timing of the hydrothermal alunite alteration dated at 8.16 ± 0.25 Ma ($^{40}Ar/^{39}Ar$). Thus, gold mineralization at the Konya district occurred between approximately 10 and 8 Ma (Figure 4.14).

The timing of hydrothermal alteration and associated gold mineralization at the Kayseri district (8-5 Ma) is bracketed by the andesitic host rock of the Başdere high-sulfidation epithermal occurrence and the post-alteration andesite at the Öksüt gold deposit dated at 7.92 ± 0.14 and 5.36 ± 0.20 Ma, respectively, in Chapter 2. However, time constraints on high-sulfidation epithermal alteration in the Niğde district (ca. 3 Ma) are only provided by the U-Pb crystallization age of the andesitic host rock at Boz Tepe (3.62 ± 0.06 Ma; Chapter 2).

4.6.4.3 Eastern Anatolia

Although the Hasançelebi high-sulfidation epithermal Au-Ag prospect is similar to its counterparts in central Anatolia, it occurred much earlier in the early Miocene. Hasançelebi precious metal mineralization is constrained by the precipitation of hydrothermal alunite dated at 20.44 ± 0.86 Ma by $^{40}Ar/^{39}Ar$ and the post-alteration andesitic lava flow emplaced at 21.23 ± 0.33 Ma (U-Pb on zircon; Chapter 2). Thus, precious metal mineralization at Hasançelebi likely formed around 21 Ma (between > 21.30 and 20.90 Ma; Figure 4.14).

Porphyry mineralization formed from 25 to 17 Ma. The age of porphyry mineralization at the Cevizlidere deposit is 24.90 to 24.78 ± 0.10 Ma from Re-Os model ages on molybdenite

(İmer et al., 2014) whereas porphyry mineralization in the Ağrı district (ca. 21-17 Ma) is constrained by the U-Pb crystallization age of the intrusive host rock including 21.32 ± 0.29 and 17.38 ± 0.36 Ma at the Taşkapı and Taşlıçay prospects, respectively (Chapter 2). İmer et al. (2014) postulated a short-lived hydrothermal and magmatic activity at Cevizlidere (ca. 0.5 m.y.), which is similar to the porphyry systems in western Anatolia (see above).

The longevity of hydrothermal activity and causative magmatism in Anatolian porphyry-epithermal deposits and prospects is consistent with that in the other multiphase porphyry deposits along the Western Tethyan Orogenic Belt that range from < 0.1 to > 4.0 m.y. such as Medet, Bulgaria (ca. 1.4 m.y.; Peytcheva et al., 2009), Miduk, Iran (ca. 1.7 m.y.; McInnes et al., 2005), and Reko Diq in Pakistan (ca. 1 m.y.; Razique et al., 2014), and also worldwide porphyry deposits (e.g., Arribas et al., 1995; McInnes et al., 2005; Chiaradia et al., 2009). Uncertainties on the longevity of porphyry systems result from either the number of successive magmatic pulses that incrementally contribute to the total metal budget of the deposit (Sillitoe, 2010), erroneous estimate of the emplacement age of the causative intrusion and methodological problems in dating methods (Sillitoe and Mortensen, 2010; Chiaradia et al., 2014). Nonetheless, theoretical modeling reveals that life spans required for consolidation of individual porphyry intrusions (< 40 k.y.; Cathles et al., 1997), porphyry ore deposition (< 100 k.y.; McInnes et al., 2005) and the formation of potassic alteration (< 2 k.y.; Cathles and Shannon, 2007) are significantly shorter than those measured by isotopic dating techniques.

4.6.5 Temporal and spatial migration of gold mineralization and mantle dynamics

The timing of late Cenozoic Anatolian hydrothermal mineralization events defined in this study varies through space (Figure 4.14): 1) 25-17 Ma in eastern Anatolia; 2) 21-9 Ma in western Anatolia; 3) 10-3 Ma in central Anatolia. Precious and base metal mineralization is contemporaneous with widespread magmatism and the formation of stratovolcanoes throughout Anatolia as suggested by field observations and confirmed by U-Pb, $^{40}Ar/^{39}Ar$ and Re-Os dating at the porphyry and epithermal districts (Chapter 2; this Chapter). Gold-rich porphyry and epithermal mineralization experienced the same temporal and spatial migrations as their

magmatic hosts (Figure 4.12). For instance, mineralization ages become younger westwards along the Eastern Anatolian Magmatic Belt, reflecting the migration of the magmatic front from eastern to central Anatolia as interpreted in Chapter 2. The contrasting distribution between Oligocene to early Miocene porphyry mineralization in eastern Anatolia and the late Miocene to Pliocene high-sulfidation epithermal mineralization in central Anatolia is the result of differential erosion levels along the vertical hydrothermal porphyry-high-sulfidation epithermal profile after the onset of the Arabian continental collision. Conversely, the western Anatolian magmatic front migrated southwards during the Cenozoic (Dilek and Altunkaynak, 2009) giving way to younger hydrothermal mineralization southwestwards from ca. 21 to 9 Ma.

Mineralized porphyry intrusions are typically the final episode of a given magmatic cycle in the Andes (Haschke et al., 2002; Bissig et al., 2003; Richards, 2003). In contrast, post-subduction porphyry deposits may form at the early stages of tectonic perturbations (e.g., Pettke et al., 2010). In Anatolia, the three major magmatic episodes since the Mesozoic include Late Cretaceous arc to back-arc, Eocene post-collisional to back-arc, and late Cenozoic back-arc and post-subduction episodes, each of which were accompanied by the formation of porphyry and epithermal precious and base metal mineralization (Yiğit, 2009; İmer et al., 2013; Kuşcu et al., 2013; this Chapter). The final magmatic episodes in the late Cenozoic were terminated by the initiation of barren volcanism since 8, 3 and 17 Ma in western, central and eastern Anatolia, respectively. Pliocene to Quaternary barren volcanism is more alkaline, less hydrous and/or composed of sub-slab asthenosphere-derived melts with or without a subduction component (e.g., Keskin, 2003; Şen et al., 2004; Ersoy and Palmer, 2013) implying that the conditions to generate fertile magma are no longer sustained.

Late Cenozoic Anatolian magmatism was generated in back-arc and a broad range of post-subduction tectonic scenarios including slab roll-back, tearing and break-off, and lithospheric mantle removal (e.g., Keskin, 2003, 2007; Şengör et al., 2008; Dilek and Altunkaynak, 2009, 2010; Prelević et al., 2012; Ersoy and Palmer, 2013; Jolivet et al., 2013; Jolivet et al., 2015;

Prelević et al., 2015; Delph et al., 2017; Göğüş et al., 2017; McNab et al., 2017; Reid et al., 2017; Chapter 2). The upwelling asthenospheric mantle and anomalous heating to the base of the lithosphere play a crucial role for the formation of post-subduction magmatism (e.g., Davies and von Blanckenburg, 1995) and associated porphyry and epithermal systems (e.g., Wang et al., 2006; Richards, 2009, 2015; Moritz et al., 2016b), in particular in the context of slab tearing and break-off (De Boorder et al., 1998; Cloos et al., 2005; Vos et al., 2007; Shafiei et al., 2009; Logan and Mihalynuk, 2014; Hou et al., 2015).

4.6.5.1 Slab roll-back-, back-arc- and slab tear-related gold mineralization in western Anatolia

In western Anatolia, the impingement of hot asthenosphere to the base of the overriding lithosphere coupled with the southwestward retreat of the Hellenic trench and Aegean back-arc development caused the surface uplift, crustal thinning, regional change in magma chemistry towards mantle-derived compositions, and formation of low-angle detachment faults and high-angle WSW- and NE-trending structures and grabens (Figure 4.12; e.g., Jolivet and Faccenna, 2000; Dilek and Altunkaynak, 2009; van Hinsbergen, 2010; Jolivet et al., 2013). The acceleration of the Aegean roll-back rate relative to the Cyprus slab segment beneath central Anatolia initiated the S-trending sub-vertical tear between both slab segments from 15 to 8 Ma (Figure 4.15; Jolivet et al., 2015). The controversial and alternative Neogene shallow subduction scenario supported by seismic data of earthquake hypocenters distribution (Doglioni et al., 2002; Agostini et al., 2008; Agostini et al., 2010) does not account for the widespread production and southwestward migration of surface magmatism, crustal block rotation and the lithospheric mantle magma source, as commonly reported in the Aegean-western Anatolia region. Instead, this shallow subduction scenario may have occurred from the Late Cretaceous to Eocene (Prelević et al., 2012) to fertilize the Anatolian lithospheric mantle but not in the Neogene.

Although the location of gold mineralization on the overriding crust is spatially coincident with the underlying tear-related slab window in the mantle as imaged today by

seismic tomography in western Anatolia (De Boorder et al., 1998), gold mineralization formation initiated at ca. 19 Ma, thus prior to the tear-related slab window opening but during the initial episode of regional back-arc extension in the early to middle Miocene (Ring et al., 2003; Gessner et al., 2013). Low- and intermediate-sulfidation epithermal gold vein mineralization formed either prior to the slab tear event such as at the Simav district between

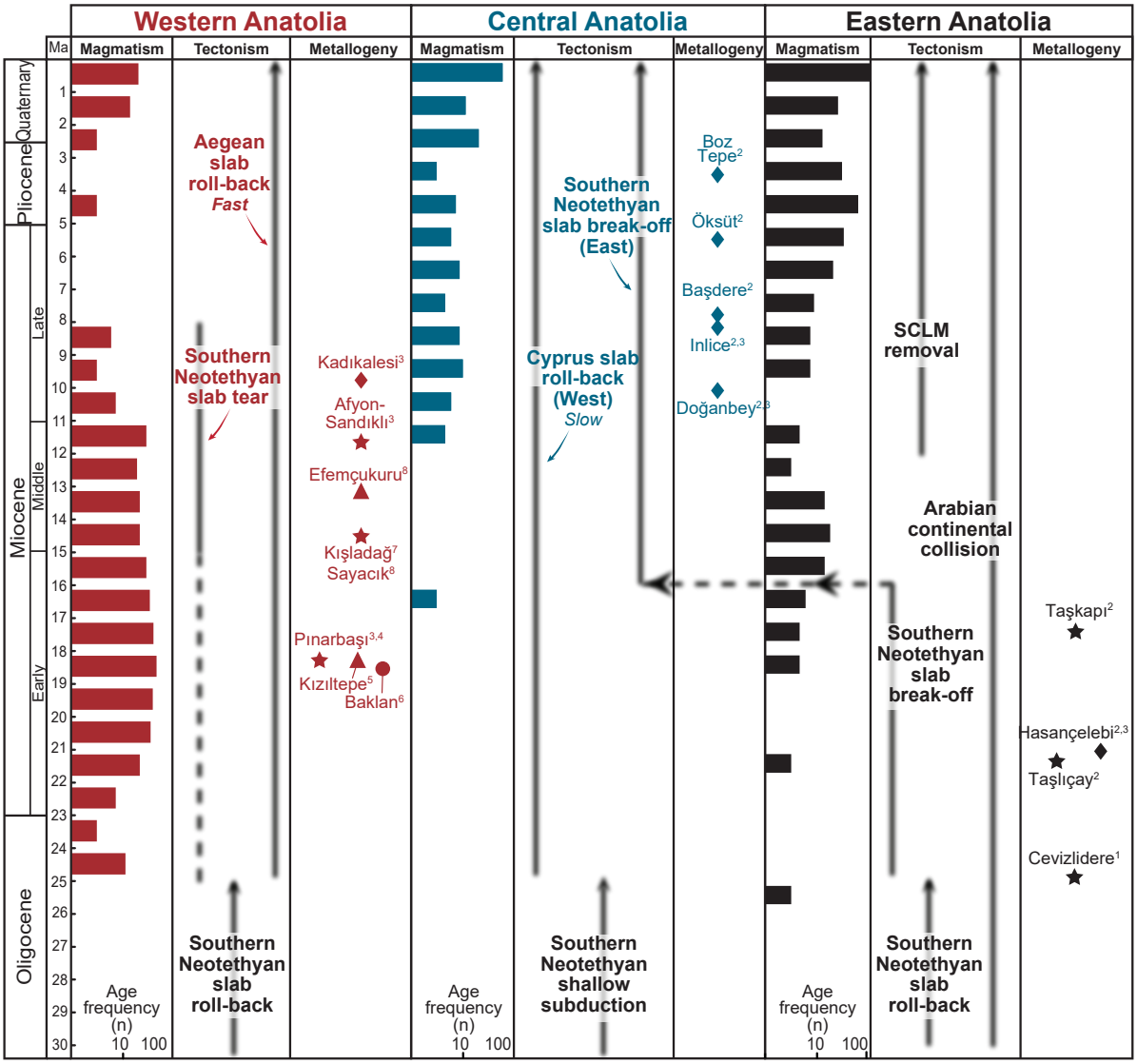

Figure 4.15 Geological time scale illustrating the succession and association of post-subduction tectonic, magmatic and metallogenic events in western (red), central (blue) and eastern Anatolia (grey) since the Oligocene. The timing of tectonic events are from Jolivet et al. (2015) and Chapter 2. Timing and references of porphyry (star), high-sulfidation (diamond) and low- and intermediate-sulfidation epithermal (triangle) and skarn (circle) mineralization events are provided in Figure 4.14. The age histogram of plutonic and volcanic units results from the compilation of U-Pb, $^{40}Ar/^{39}Ar$ and K-Ar isotopic dates from the literature in western Anatolia (n = 312; this Chapter) and central and eastern Anatolia (n = 428; Chapter 2).

19 and 18 Ma, or beyond the extent of the slab tear window such as at the İzmir district at ca. > 14-13 Ma. Although this epithermal mineralization shows no to moderate contributions from a magmatic source (Yılmaz et al., 2013; Boucher, 2016), those low-temperature (< 300°C) gold-bearing vein systems were influenced by the emplacement and southwestward migration of regional intermediate to felsic volcanism during continental rifting along the İzmir-Balıkesir Transfer Zone. The southwestward migration of epithermal gold mineralization formation from the northerly Ovacık and Kızıltepe deposits (ca. 19-18 Ma) to Arapdağ (ca. > 14 Ma) to the southerly Efemçukuru deposit (ca. 13 Ma) is a direct consequence of the Aegean slab roll-back and back-arc development. The formation of these epithermal deposits resulted from the increasing thermal gradient and enhanced crustal fluid flow during crustal extension and rifting, and exhumation and rotation of the Menderes metamorphic core complex (Gessner et al., 2017).

In contrast, western Anatolian porphyry mineralization peaked at 18 Ma at the Pınarbaşı prospect, and occurred mainly during the slab tear development between 15 and 11 Ma in the Uşak district and at the Afyon-Sandıklı prospect. Those porphyry deposits and prospects were emplaced near the boundary between the Aegean and Cyprus slabs, east of the Menderes Massif, where the tear-related slab window opened. Igneous host rocks along the S-trending Kırka-Afyon-İsparta volcanic trend and the Uşak-Muğla Transfer Zone were directly affected by toroidal flow of asthenosphere. Evidences are provided by the temporal increase and westward decrease of the asthenospheric component in the magma (Dilek and Altunkaynak, 2010; Karaoğlu and Helvacı, 2014; Prelević et al., 2015). Flow of asthenospheric propagated southwestwards to the southwestern edge of the Menderes Massif causing fertile magmatism at the Bodrum district in the late Miocene (this Chapter), and subsequently contributing to the Quaternary Aegean volcanic arc (Klaver et al., 2016).

The Aegean slab roll-back and back-arc, the formation of the slab tear, the resulting toroidal flow of asthenosphere and the concomitant crustal exhumation account for the current distribution of gold deposits around the Menderes Massif core. These processes can account for

the spatial segregation between the slab tear-related, easterly and southerly, intrusion-related systems, and the back-arc-related, northerly and westerly, low- and intermediate-sulfidation epithermal veins. The activation of regional detachment faults and the rapid exhumation of the Menderes metamorphic core complex during the Miocene significantly eroded the potential middle Miocene mineralized magmatic complexes and pre-Oligocene orogenic vein systems that may have been emplaced in the center of the Menderes Massif between the İzmir and Uşak districts. Consequently, this region is dominated by the remnant of orogenic and epithermal gold-bearing veins and the numerous small placer gold occurrences such as along the historically significant Pactolus (Gediz) River, which provided wealth to Croesus (560-546 BC), King of Lydia.

4.6.5.2 Slab steepening- and break-off-related gold mineralization in central and eastern Anatolia

The arrival of the buoyant Arabian platform in the Oligocene (ca. 30 Ma) to the southern margin of eastern Anatolia terminated the northward subduction of the Southern Neotethyan oceanic slab and initiated slab steepening (30-25 Ma) followed by break-off at ca. 25 Ma (Figure 4.15; see Chapter 2, and references therein for discussion). Slab steepening gave rise to a brief magmatic pulse (Chapter 2) that was accompanied by the formation of the Cevizlidere porphyry Cu-Au-Mo deposit at ca. 25 Ma (İmer et al., 2014). Subsequently, the slab break-off event was responsible for the westward propagation of the magmatic front starting at 21 Ma (Chapter 2) and crustal uplift (Schildgen et al., 2014; McNab et al., 2017) from eastern to central Anatolia along the Eastern Anatolian Magmatic Belt under a localized extensional tectonic regime (Kaymakçı et al., 2010). The formation of slab break-off-related magmatic complex in the upper crust was accompanied by the production of Au (-Cu) high-sulfidation epithermal and porphyry mineralization, such as at the easterly Ağrı district, Hasançelebi high-sulfidation epithermal prospect and westerly Niğde and Kayseri districts. However, the sustained heat flow beneath eastern and central Anatolia during the slab window opening eroded the lithospheric mantle (Keskin, 2007; Delph et al., 2017; McNab et al., 2017;

Chapter 2) and produced voluminous barren volcanism that partially or entirely covered the mineralized slab break-off-related magmatism. Barren volcanism is characterized by greater interactions between lithospheric and asthenospheric components such as the Hasandağ and Erciyes stratovolcanoes in central Anatolia and the Erzurum-Kars volcanic plateau in eastern Anatolia (e.g., Keskin, 2003; Kürkçüoğlu et al., 2004; Keskin, 2007; Şengör et al., 2008; Özdemir and Güleç, 2013; Kürkçüoğlu et al., 2015; Neill et al., 2015).

As suggested in Chapter 2, late Miocene volcanism in the Konya district results from the southward retreat of the Cyprus slab since the early Miocene based on magmatic age migrations along the S-trending alignment of Galatia-Sulutas-Konya magmatic complexes and recent tomographic studies that show the sharp edge and coherence of the underlying Cyprus slab (Figure 4.12; e.g., Biryol et al., 2011). An alternative scenario suggests that the southward delamination of the Cyprus slab since the early Miocene accounts for the absence or attenuated lithospheric mantle beneath central Anatolia, based on tomographic studies (Bartol and Govers, 2014; Delph et al., 2017). Thus, the formation of the high-sulfidation epithermal prospects in the Konya district are not affected by slab rupture but results from the Cyprus slab roll-back or delamination event in the Miocene as opposed to their counterparts in the easterly Niğde and Kayseri districts and the westerly Afyon-Sandıklı porphyry Au (-Cu) prospect (Figure 4.1).

In summary, the late Cenozoic segmentation of the Southern Neotethyan oceanic slab allowed flow of asthenosphere to invade the Anatolian mantle domain and remobilize fertile lithospheric and crustal material required for the production of gold-rich magmas in a post-subduction setting (e.g., Richards, 2009; Hronsky et al., 2012).

4.6.6 Comparison with the neighboring late Cenozoic gold provinces along the Western Tethyan Orogenic Belt

Although this Chapter focuses on the late Cenozoic mineralization of the Anatolian Metallogenic Trend, the tectono-magmatic scenarios depicted above laterally extend westwards to Greece (e.g., Jolivet et al., 2013) and southeastwards to the Lesser Caucasus and Iran (Hafkenscheid et al., 2006). The Anatolian Trend laterally connects to the major neighboring

metallogenic provinces in Greece (Melfos and Voudouris, 2017), northwest Turkey (Yiğit, 2012; Sánchez et al., 2016), Lesser Caucasus (Moritz et al., 2016a) and northeast Iran (Richards and Sholeh, 2016).

4.6.6.1 Greece and northwest Turkey

Occurrences of precious and base metal mineralization in Greece consist of porphyry, high- and intermediate-sulfidation epithermal, carbonate-replacement and reduced-intrusion Mo-W mineralization styles (Siron et al., 2016; Melfos and Voudouris, 2017). Reduced-intrusion Mo-W mineralization is absent in Anatolia; low-sulfidation epithermal vein systems are apparently absent in Greece. In addition, the porphyry and epithermal deposits in Greece are endowed in Te, PGE and Re (Economou-Eliopoulos and Eliopoulos, 2000; Voudouris et al., 2007) that is attributed to the high magmatic oxidation state, limited contribution of meteoric fluids (Economou-Eliopoulos and Eliopoulos, 2000) and metasomatic agents in the mantle source (e.g., Sun et al., 2003; Cook et al., 2009). Such metal grade has not been reported along the Anatolide-Tauride Block except perhaps for Te enrichment in the Biga district (Smith et al., 2014). In contrast, the styles of late Cenozoic intrusion-related mineralization in the Biga district (ca. 9 Moz gold) on the Rhodope-Pontide Block are similar to those on the Anatolide-Tauride Block, and dominantly include porphyry, skarn and high-, intermediate- and low-sulfidation epithermal systems (Yiğit, 2012).

Regional back-arc extension is responsible for the formation of many grabens, half-grabens and detachment faults that control the distribution and emplacement of calc-alkaline to shoshonitic igneous units and associated mineralization (e.g., Yiğit, 2012; Sánchez et al., 2016; Gessner et al., 2017; Melfos and Voudouris, 2017). Precious and base metal mineralization formation peaked in the Oligocene (33-25 Ma), early Miocene (22-19 Ma), middle to late Miocene (14-7 Ma) and Pliocene-Pleistocene (3-1.5 Ma) in Greece (Melfos and Voudouris, 2017). Whereas the first mineralization peak coincides with a major mineralization event in the Biga district of northwest Turkey, the second and third events are simultaneous with the major mineralization peak in western Anatolia (21-9 Ma). Despite this simultaneity of mineralization

episodes, magmatism and associated mineralization in Greece resulted from mantle wedge suction during the Aegean slab roll-back episode apparently without any contribution from the slab tear-derived toroidal flow of asthenosphere.

4.6.6.2 Lesser Caucasus and Iran

Neogene syn- to post-collisional porphyry- and epithermal-style deposits in the Lesser Caucasus dominantly produced copper and molybdenum mineralization during the Oligocene (34-31 Ma) and early Miocene (ca. 26-21 Ma) along translithospheric faults in the Zangezur-Ordubad region on the South Armenian Block (Moritz et al., 2016a). Although this province is well-endowed in precious and base metals, gold mineralization mostly formed prior to the Neogene and is rare or absent during the Neogene, perhaps with the exception of the Zod/Sotk low-sulfidation epithermal deposit (Moritz et al., 2017).

Similarly, Neogene precious and base metal mineralization in Iran is dominated by porphyry Cu-Mo deposits and a few epithermal gold systems that formed in a collisional setting (Richards and Sholeh, 2016). Interestingly, the prevailing exposition of porphyry mineralization and intrusions without volcanic equivalents (e.g., the Urumieh-Dokhtar Belt; Shafiei et al., 2009), coupled with the poor preservation of epithermal systems imply deeper erosion levels than in Anatolia. The rare Neogene epithermal gold systems preferentially formed in northwest Iran in the middle to late Miocene (Richards and Sholeh, 2016) and include the Sari Gunay diatreme-hosted gold deposit (Richards et al., 2006). This region also hosts many porphyry Cu-Mo deposits in the Arasbaran Belt such as Sungun, Masjed Daghi and Haft Chesmeh (27-17 Ma), similar to those along the Oligocene to Miocene Urumieh-Dokhtar and Kerman Belts of southwest Iran. The porphyry systems of the Arasbaran Belt have similar mineralization to those the Zangezur-Ordubad region in southern Armenia (Aghazadeh et al., 2015; Moritz et al., 2016a) and are contemporaneous with the porphyry systems in Anatolian Ağrı district about 250 km west.

Those Neogene porphyry deposits in northwest Iran and southern Armenia are thought to be emplaced in the early stages of the Arabian continental collision in response to crustal

thickening and possible delamination (Aghazadeh et al., 2015; Jamali and Mehrabi, 2015; Moritz et al., 2016b). However, large-scale kinematic reconstructions and tomographic studies proposed that the onset of the Arabian continental collision in the Oligocene initiated the break-off of the Southern Neotethyan oceanic slab at ca. 30 Ma in northwest Zagros (Hafkenscheid et al., 2006; Mouthereau et al., 2012). Thus, this slab break-off tectonic event could have been responsible for the formation of those Oligocene to early Miocene porphyry Cu-Mo deposits in southern Armenia and northwest Iran. This sub-horizontal slab rupture subsequently propagated westwards along the Eastern Anatolian Magmatic Belt (Chapter 2) and possibly southeastwards in Iran (Hafkenscheid et al., 2006; Omrani et al., 2008). The lateral connection and transition between the late Cenozoic Anatolian Trend in Turkey, the Arasbaran and possibly the Urumieh-Dokhtar Belts in Iran, and the Zangezur-Ordubad region in Armenian deserve further investigations.

4.7 Conclusion

The late Cenozoic Anatolian Metallogenic Trend defined in this study is composed of nine porphyry and epithermal districts and isolated prospects that contain significant gold (33 Moz) and minor copper (3.7 Blbs) resources. These districts, deposits, prospects and occurrences are distributed along three Trend segments in western, central and eastern Anatolia. Field observations revealed that mineralization in western Anatolia was preferentially deposited around the exhumed core of the Menderes Massif, and is dominated by low- and intermediate-sulfidation epithermal Au-Ag systems in the north and west, and porphyry and skarn mineralization in the east and south. In contrast, central Anatolia is dominated by high-sulfidation epithermal Au systems whereas eastern Anatolia contains porphyry, high-sulfidation epithermal and Carlin-style precious and base metal mineralization. Those hydrothermal systems and associated igneous host rocks were emplaced at extensional sites along grabens, strike-slip corridors, fault intersections and pull-apart basins in a context of crustal extension in western Anatolia and transtension to transpression in central and eastern Anatolia.

Geochronological results presented herein, and interpreted with age data from Chapter

2, suggest that precious and base metal porphyry, skarn and epithermal mineralization formed at: 1) 25-17 Ma in eastern Anatolia; 2) 21-9 Ma in western Anatolia; 3) 10-3 Ma in central Anatolia. The timing of mineralization coincides with post-subduction segmentation and roll-back events of the Arabian, Cyprus and Aegean segments of the Southern Neotethyan oceanic slab in the late Cenozoic. The steepening of Arabian slab segment at the onset of the Arabian continental collision in the Oligocene resulted in a brief pulse of magmatism and porphyry mineralization in the Tunceli district. Subsequently, the Arabian slab broke off and the resulting sub-horizontal rupture propagated westwards to central Anatolia from the early to middle Miocene, followed by the slab window opening until the present times (Biryol et al., 2011; Schildgen et al., 2014; Chapter 2). This event was accompanied by the westward migration of the magmatic front and associated porphyry and high-sulfidation epithermal mineralization from the easterly Ağrı district, Hasançelebi high-sulfidation epithermal prospect to the westerly Kayseri and Niğde districts. The southward roll-back of the Cyprus slab gave way to the formation of the Konya district in central Anatolia. The combined roll-back and tearing of the Aegean slab resulted in the southwestward migration of the magmatic front and associated mineralization in western Anatolia. Thus, this study suggests that the post-subduction slab segmentation events and resulting thermal events at 25 and 15 Ma produced the bulk of Anatolian gold mineralization. The break-off- and tear-related slab window opening and long-lived asthenosphere upwelling are yet responsible for the increasing production of barren volcanism through time that partially covers mineralized magmatic complexes.

Chapter 5: Petrogenetic controls on post-subduction magma fertility in the late Cenozoic Anatolian Metallogenic Trend, Turkey

5.1 Introduction

Porphyry deposits and associated epithermal mineralization form in arc subduction, post-subduction and post-collisional tectonic settings (e.g., Sillitoe, 1972; Richards, 2003, 2009; Sillitoe, 2010). However, different tectonic settings indicate that there are contrasting first-order controls on the production of fertile magma, i.e., capable of forming precious and base metal magmatic-hydrothermal ore deposits. In arc magmas, the bulk of metals are sourced from the metasomatized asthenospheric mantle, and to lesser extent by the oceanic crust and sediments via dehydration fluids or melting (e.g., Richards, 2011). In contrast, metal sources in post-subduction and post-collisional settings are controversial and include 1) the fertilization of the subcontinental lithospheric mantle (SCLM; Pettke et al., 2010; Mair et al., 2011) by asthenosphere-derived low-degree partial melts (Hronsky et al., 2012; Griffin et al., 2013); 2) subduction-modified cumulates in the lower crust as artifacts of previous cycles of arc magmatism (Chiaradia et al., 2009; Richards, 2009); and/or 3) juvenile lower crust after arc magma underplating (Hou et al., 2009; Shafiei et al., 2009). The infiltration of hot asthenosphere into the mantle wedge is typical in post-subduction tectonic settings as a result of slab tearing (subvertical rupture) or break-off (subhorizontal rupture). High thermal gradient may remobilize metasomatized and metal-rich regions from the lithospheric mantle and/or lower crust to generate fertile magmas (Lips, 2002; Wang et al., 2006; Hou et al., 2009; Richards, 2009, 2011; Logan and Mihalynuk, 2014). The influx of barren and drier, asthenosphere-derived melts may dilute the hydrous, metal-rich magmas (e.g., Hronsky et al., 2012) and cause a drastic reduction of magma fertility over time.

The Western Tethyan Orogenic Belt formed from the amalgamation of many Gondwana-derived crustal blocks that were accreted to the southern active margin of Laurasia during the successive Mesozoic to Cenozoic accretionary and collisional tectonic events (Şengör and

Yılmaz, 1981; Şengör et al., 1984; Stampfli and Borel, 2004). This complex tectono-magmatic belt was favorable for the generation of fertile magmas and associated magmatic-hydrothermal ore deposits in response to its subduction, slab tearing, roll-back and break-off, and lithospheric mantle delamination tectonic settings (Janković, 1997; Lips, 2002; Yiğit, 2006, 2009, 2012; İmer et al., 2013; Kuşcu et al., 2013; Bertrand et al., 2014; Richards, 2015; Moritz et al., 2016b; Menant et al., 2018; Chapter 4). Substantial gold resources (ca. 112 Moz; Baker, 2017) in the Carpathian, Balkan, Aegean and Anatolian regions such as Rosia Montana, Skouries, Kışladağ, and Efemçukuru (Lips, 2002; Neubauer et al., 2005; Manske et al., 2006; Yiğit, 2009; Baker et al., 2016; Boucher, 2016; Siron et al., 2016; Menant et al., 2018), and copper in the Lesser Caucasus and Zagros areas (> 60 Bt; Shafiei et al., 2009; Richards et al., 2012; Moritz et al., 2016a; Moritz et al., 2016b; Richards and Sholeh, 2016) formed in these tectonic settings during the Cenozoic. Most of the gold-rich porphyry and epithermal deposits formed during trench retreat and slab segmentation events after the onset of the Arabia-Eurasia continental collision from the Oligocene to Pliocene (Menant et al., 2018; Chapter 4). However, the genetic relationship between post-subduction tectonic events, asthenospheric upwelling and magma fertility has not been well-established, despite recent efforts in western Anatolia (Menant et al., 2018).

Fertility of Anatolian magmatism evolved through time and space during the late Cenozoic in response to post-subduction slab rupture and roll-back tectonic events and resulting asthenospheric upwelling. Evidence is provided by new geochemical and Sr-Nd-Pb isotopic geochemical data that are focused on the major late Cenozoic porphyry, skarn and high-sulfidation epithermal occurrences, prospects and deposits from western Anatolia, associated with the geochemical results from mineralized igneous units in central and eastern Anatolia (Chapter 3). Those results are interpreted with previously-published, deposit-focused geochemical data throughout Anatolia (İmer et al., 2014; Baker et al., 2016; Delibaş et al., 2017).

5.2 Late Cenozoic tectonic, magmatic and metallogenic framework of the Anatolide-Tauride Block

5.2.1 Tectonic and geodynamic evolution

The Western Tethyan Orogenic Belt resulted from the indentation of Gondwana-derived crustal fragments including the Rhodope-Pontide Block, Anatolide-Tauride Block (Figure 5.1), Bitlis-Pütürge Massifs and Central Anatolian Crystalline Complex in Turkey into the southern active margin of Laurasia since the Paleozoic (Şengör and Yılmaz, 1981; Şengör et al., 1984; Stampfli, 2000; Stampfli and Borel, 2004). The collision of the Gondwana-derived crustal fragments to Laurasia closed the numerous branches of the Paleotethys and Neotethys oceans along a series of northward-dipping subduction zones (Şengör and Yılmaz, 1981; Robertson and Dixon, 1984; Şengör et al., 1984; Okay and Tüysüz, 1999; Okay et al., 2006; van Hinsbergen et al., 2016). The Southern Neotethys Ocean, south of the Anatolide-Tauride Block, was the last remaining oceanic basin that closed along the current Bitlis suture zone at the onset of the Arabia-Eurasia continental collision in either the Eocene (Rolland et al., 2012), Oligocene (Jolivet and Faccenna, 2000; Agard et al., 2005; Allen and Armstrong, 2008; Barrier and Vrielynck, 2008; McQuarrie and van Hinsbergen, 2013; Karaoğlan et al., 2016), or Miocene (Şengör and Yılmaz, 1981; Dewey et al., 1986; Yılmaz, 1993; Yiğitbaş and Yilmaz, 1996; Robertson et al., 2007; Şengör et al., 2008; Hüsing et al., 2009; Okay et al., 2010; Robertson et al., 2016).

The Anatolide-Tauride Block is a continental lithosphere-derived platform that underwent major internal deformation during the closure of the surrounding Neotethyan oceanic basins since the Late Cretaceous (Robertson et al., 2013; van Hinsbergen et al., 2016). This Block consists of north-verging, thrusted and folded slices of Paleozoic to Mesozoic carbonate and clastic passive margin sequences (e.g., Taurus platform), Mesozoic ophiolites (e.g., İzmir-Ankara-Erzincan suture zone and Lycian Nappes; Collins and Robertson, 1997; Sarıfakıoğlu et al., 2017) and exhumed Neoproterozoic to Paleozoic crystalline massifs (Şengör and Yılmaz, 1981; Okay and Tüysüz, 1999; Görür and Tüysüz, 2001; Moix et al., 2008;

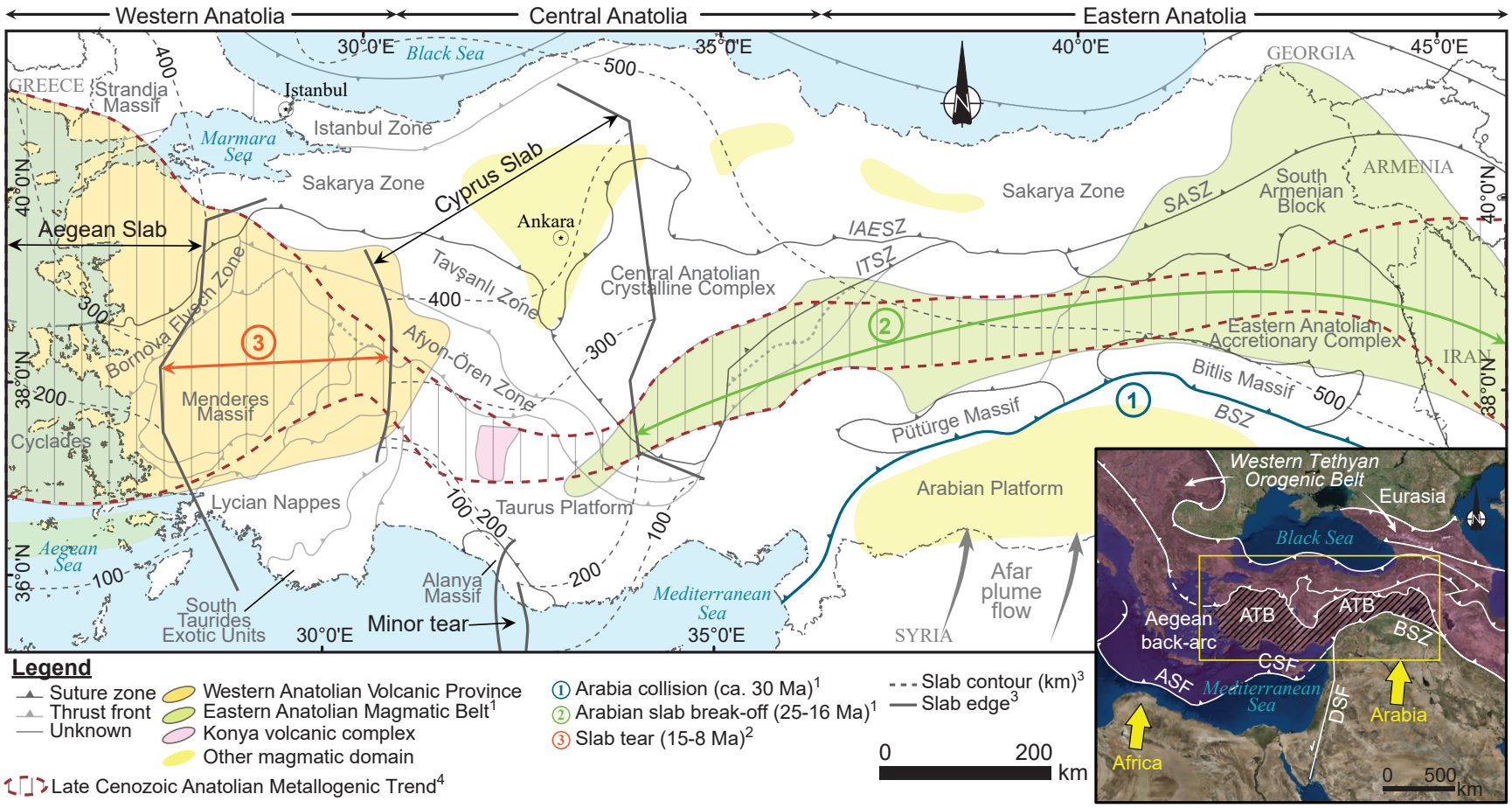

Figure 5.1 Simplified tectono-magmatic map of Turkey showing the location of the basement boundaries, late Cenozoic magmatic belts, provinces and other domain, and the Anatolian Metallogenic Trend. The map also displays the succession of major tectonic events since the Oligocene that includes the Arabian continental collision (1), Arabian slab break-off and westward propagation to central Anatolia (2), and the Aegean slab tear (3) as the result of the differential roll-back rates between the Aegean and Cyprus slabs (see Chapter 2 for more details). Background on the location map is from Google Earth. BSZ = Bitlis Suture Zone; IAESZ = İzmir-Ankara-Erzincan Suture Zone; ITSZ = Inner Tauride Suture Zone; SASZ = Sevan-Akera Suture Zone. References: [1]Chapter 2; [2]Jolivet et al., 2015; [3]Biryol et al., 2011; [4]Chapter 3.

Lefebvre et al., 2013; Topuz et al., 2017). Some fragments of the subducted passive margin were diachronously exhumed and metamorphosed at high pressure and low temperature conditions during the Late Cretaceous and Eocene (e.g., Tavşanlı Zone, Afyon-Ören Zone and Cyclades; Sherlock et al., 1999; Pourteau et al., 2013; Plunder et al., 2015). In contrast, the crystalline massifs recorded multiphase high-grade metamorphism from the Neoproterozoic to Oligocene (e.g., Menderes Massif, Bitlis-Pütürge and Central Anatolian Crystalline Complex; Dilek and Whitney, 2000; Whitney et al., 2001; Whitney and Bozkurt, 2002; Régnier et al., 2007; Ustaömer et al., 2009; Oberhänsli et al., 2010).

The indentation of the Arabia plate into eastern Anatolia contributed to the fragmentation of the Southern Neotethyan oceanic slab into three segments: Aegean, Cyprus and Arabian (Figure 5.1; Faccenna et al., 2006; Biryol et al., 2011; Schildgen et al., 2014; Chapter 2). Upon closure of the Southern Neotethyan Ocean in eastern Anatolia in the Oligocene, the subducted oceanic slab continued to subduct along the retreating Hellenic and Cyprus trenches beneath western and central Anatolia during the Cenozoic (Le Pichon and Angelier, 1981; Jolivet and Faccenna, 2000; Jolivet et al., 2013). Onset of the Arabian continental collision initiated the break-off of the Southern Neotethyan slab and its westward propagation up to the Cyprus slab since the late Oligocene (Faccenna et al., 2006; Biryol et al., 2011; Schildgen et al., 2014; Chapter 2). The slab rupture in the east contributed to increase pull load on the still-attached Aegean and Cyprus slabs (Faccenna et al., 2006) according to the tomographic images that show the deep lateral continuity of the Southern Neotethyan slab in the mantle connecting the Aegean, Cyprus and Arabian slab segments (Piromallo and Morelli, 2003; Biryol et al., 2011). Slab break-off and increasing pull load in the west modified mantle flow patterns (Le Pichon and Kreemer, 2010) and led to the westward extrusion of the Anatolian microplate along the North and East Anatolian Fault Zones (Şengör, 1985; Jolivet and Faccenna, 2000; Faccenna et al., 2006; Özeren and Holt, 2010). In western Anatolia, the roll back of the Aegean slab initiated in the Eocene and formed the Aegean extensional back-arc basin (Le Pichon and Angelier, 1981; Jolivet et al., 2013). However, the increasing pull load in the middle Miocene contributed

to the acceleration of the Aegean slab roll-back relative to the Cyprus slab (Chapter 2) and caused the formation of a S-trending, sub-vertical slab tear between 15 and 8 Ma (Figure 5.1; van Hinsbergen, 2010; Biryol et al., 2011; Jolivet et al., 2015; Prelević et al., 2015).

The slab break-off in the Arabian domain and slab tearing in the Aegean domain are the causative tectonic events that are responsible for the opening of slab windows (Piromallo and Morelli, 2003; Biryol et al., 2011) and the resulting infiltration of hot sub-slab asthenosphere to beneath western, central and eastern Anatolia (e.g., Keskin, 2003, 2007; Şengör et al., 2008; Dilek and Altunkaynak, 2009; Faccenna et al., 2013; Sternai et al., 2014; Prelević et al., 2015; Menant et al., 2016; Chapter 2). This infiltration of hot asthenosphere to the base of the lithosphere caused local to regional extensional to transtensional stress regime in the crust (Kaymakçı et al., 2010), exhumation and rotation of crystalline massifs, crustal doming, thermal erosion of the lithosphere and/or the production of widespread calc-alkaline to alkaline magmatism (e.g., Keskin, 2003, 2007; Dilek and Altunkaynak, 2009; van Hinsbergen, 2010; Prelević et al., 2012; Jolivet et al., 2013; Jolivet et al., 2015; Prelević et al., 2015; Reid et al., 2017; Chapter 3). The subcontinental lithospheric mantle (SCLM) is attenuated throughout Anatolia due to long-lived asthenospheric heating (e.g., Gök et al., 2003; Keskin, 2003, 2007; Şengör et al., 2008; Gans et al., 2009; Mutlu and Karabulut, 2011; Prelević et al., 2012; Bartol and Govers, 2014; Kind et al., 2015; Delph et al., 2017; Göğüş et al., 2017). However, the interpretation of seismic tomographic data can be controversial at shallow depth (< 100 km) and in the presence of melt in the lithosphere (Foulger et al., 2015; Garzanti et al., 2017).

The easterly Arabian continental collision, the westerly Aegean back-arc opening and the tectonic extrusion of the Anatolian microplate since the Oligocene resulted in contrasting crustal stress regimes. The Aegean back-arc domain in western Anatolia was dominated by N-trending crustal extension manifested by the exhumation of metamorphic core complexes such as the Menderes Massif along regional E-trending, shallowly-dipping, north- and south-verging detachment faults (e.g., Simav, Kuzey and Güney), these were subsequently reactivated by steeply-dipping normal faults bounding the present grabens (e.g. Gediz and Büyük; Bozkurt

and Park, 1994; Lips et al., 2001). The asymmetric exhumation and anticlockwise rotation of the Menderes Massif was accommodated by two lateral NE-trending shear zones, namely the westerly İzmir-Balıkesir and the easterly Uşak-Muğla Transfer Zones (e.g., Uzel and Sözbilir, 2008; Karaoğlu and Helvacı, 2014). In contrast, the Arabian domain in eastern Anatolia underwent N-trending compression. The resulting production of a dense network of conjugate, NE- to NW-trending strike-slip faults and many pull-apart basins in eastern and central Anatolia (see Bozkurt (2001) and Koçyiğit et al. (2001) for review) accommodated the westward extrusion of the Anatolian microplate (McClusky et al., 2000; Faccenna et al., 2006).

5.2.2 Late Cenozoic Anatolian magmatism

Late Cenozoic magmatism in Anatolia is divided into the Western Anatolian Volcanic Province, Eastern Anatolian Magmatic Belt and the transitional Konya volcanic complex (Figure 5.1). Magma intruded the pre-Cenozoic crystalline, ophiolitic and passive margin basement, and was preferentially emplaced in extensional sites in pull-apart basins and along graben and detachment faults.

The late Cenozoic magmatic suites of Western Anatolian Volcanic Province are along the NE-trending İzmir-Balıkesir and Uşak-Muğla Transfer Zones, on the northern part of Menderes Massif, and along the N-trending Kırka-Afyon-İsparta trend (Figure 5.2; Dilek and Altunkaynak, 2009; Ersoy and Palmer, 2013; Karaoğlu and Helvacı, 2014). Both Transfer Zones were the locus of magmatic activity that migrated southwards from the early to middle Miocene (Erkül et al., 2005; Karaoğlu et al., 2010; Erkül and Erkül, 2012; Ersoy et al., 2014). Magmatic activity was also synchronous with the exhumation of the Menderes Massif along regional E-trending detachments faults. The syn-tectonic early Miocene Eğrigöz and middle Miocene Salihli and Turgutlu plutons and associated volcanic products emplaced on the footwall of the northerly Menderes detachment faults and also controlled by NE-trending grabens such as the Selendi, Gördes and Uşak-Güre basins (Ring and Collins, 2005; Glodny and Hetzel, 2007; Ersoy et al., 2010; Karaoğlu et al., 2010; Erkül and Erkül, 2012; Ersoy et al., 2012a). East of the Menderes Massif, the northerly early Miocene, calc-alkaline to alkaline

Kırka (21-17 Ma) to middle Miocene, alkaline, Afyon (14-8 Ma) and southerly, Plio-Quaternary, ultrapotassic İsparta-Gölcük magmatic rocks (4 Ma to Present) define the S-trending Kırka-Afyon-İsparta trend (Figure 5.2A; Alıcı et al., 1998; Kumral et al., 2006; Dilek and Altunkaynak, 2010; Prelević et al., 2012; Platevoet et al., 2014; Prelević et al., 2015). The final volcanic event in western Anatolia produced the Na-alkaline basalts of the Quaternary Kula volcanic suite in the center of the Menderes Massif (Alıcı et al., 2002).

The Konya volcanic complex was emplaced at the termination of the Akşehir normal fault in the Central Taurides between the Western Anatolian Volcanic Province and Eastern Anatolian Magmatic Belt. In this region, volcanic activity migrated southwards from the northerly, early Miocene Galatian volcanic province on the Rhodope-Pontide Block (21-17 Ma) to the middle Miocene Sulutas lavas and lamprophyres (16-12 Ma) to the southerly Konya andesitic volcanic complex (12-3 Ma; Chapter 2). The oldest volcanic products in the central Anatolia are the late Miocene andesitic to dacitic rocks of the Develidağ stratovolcano, Tekkedağ volcano and İncesu and Cappadocian ignimbrites (Temel et al., 1998b; Le Pennec et al., 2005; Koralay, 2010; Kürkçüoğlu, 2010). Volcanic activity continued in the Pliocene and Quaternary without interruption and contributed to the edification of the Melendiz, Hasandağ and Erciyes stratovolcanoes and NE-striking trend of monogenic volcanoes at Acigöl, Karapınar and Karaman (Pasquare et al., 1988; Aydar and Gourgaud, 1998; Deniel et al., 1998; Toprak, 1998; Şen et al., 2003; Schmitt et al., 2011; Aydin et al., 2014; Reid et al., 2017; Dogan-Kulahci et al., 2018). The southwestward propagation of magmatic activity in central Anatolia formed the SW-trending axis of Sivas-Cappadocia-Hasandağ-Karaman volcanic complexes between the Ecemiş and Tuz Gölü strike-slip faults in the western part of the Eastern Anatolian Magmatic Belt (Chapter 2).

Late Cenozoic magmatic complexes in the eastern part of the Eastern Anatolian Magmatic Belt include the localized, calc-alkaline to alkaline, dioritic porphyry stocks in Cevizlidere (26-25 Ma; İmer et al., 2014), monzonitic to granitic intrusions of the Ağrı complex (21-17 Ma; Chapter 2), monzonitic Sarıçimen pluton (12-11 Ma; Çolakoğlu and Arehart, 2010),

and the andesitic to dacitic lavas and pyroclastic units of the Yamadağ (21-12 Ma) and Kepez (15-13 Ma) suites (Kürüm et al., 2008; Ekici et al., 2009; Ekici, 2016; Chapter 2). Those Oligocene to middle Miocene igneous units were covered by the widespread Erzurum-Kars volcanic plateau (12 Ma to Present; e.g., Pearce et al., 1990; Keskin et al., 1998; Keskin, 2003, 2007; Şengör et al., 2008).

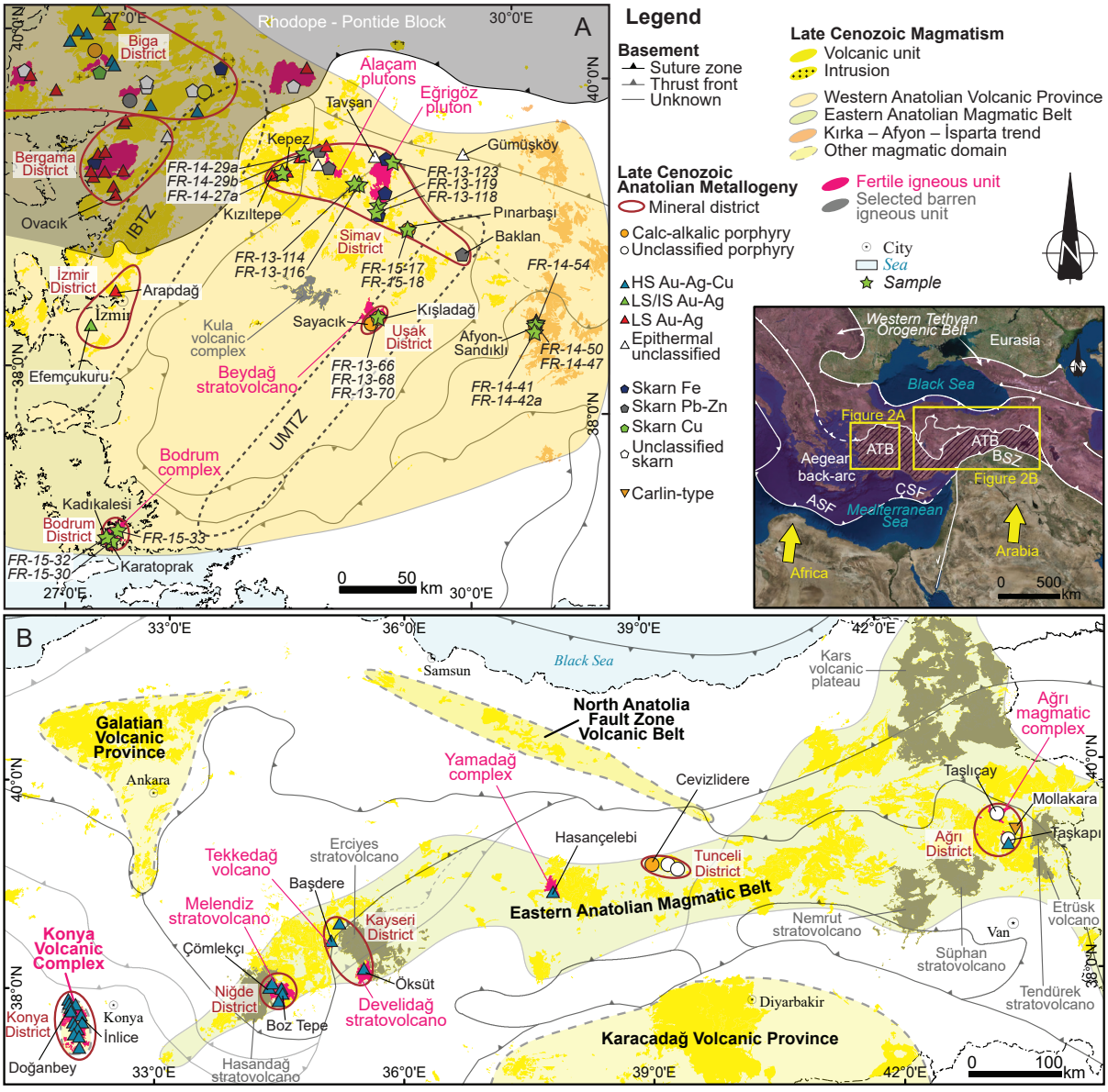

Figure 5.2 Maps of western (A) and central and eastern Anatolia (B) displaying the basement boundaries, late Cenozoic igneous units (modified from MTA, 2002), belts and provinces, and major intrusion-related occurrences, prospects, deposits and districts (Chapter 4). The fertile igneous units hosting and causing hydrothermal mineralization are in pink whereas representative barren igneous suites are in grey. Some fertile plutons are too small and not visible on those maps such as at the Afyon-Sandıklı, Pınarbaşı, Baklan and Cevizlidere prospects and deposits. The green stars show the location of samples for element and isotopic analyses in western Anatolia. IBTZ = İzmir-Balıkesir Transfer Zone; UMTZ = Uşak-Muğla Transfer Zone.

The slab tear- and break-off-related infiltrations of hot asthenosphere beneath Anatolia are responsible for widespread magmatism since the late Cenozoic (26 Ma to Present). The formation of the Western Anatolian Volcanic Province is the magmatic response to the development of the back-arc basin in the Aegean and western Anatolian region related to the fast roll-back of Aegean slab and its subsequent tearing (Figure 5.1; Innocenti et al., 2005; Dilek and Altunkaynak, 2009, 2010; Prelević et al., 2012; Ersoy and Palmer, 2013). In contrast, late Cenozoic magmatism along the Eastern Anatolia Magmatic Belt was produced in response to 1) the steepening (30-25 Ma); 2) break-off initiation and westward propagation of the Arabian slab from eastern (25-16.5 Ma) to central Anatolia at the onset of the Arabian continental collision; and 3) subsequent lithospheric mantle removal (12 Ma to Present; Figure 5.1; Keskin, 2003, 2007; Şengör et al., 2008; İmer et al., 2014; Ekici, 2016; Chapter 2). The westward extent of the slab break-off and window reached the eastern edge of the Cyprus slab (Biryol et al., 2011). The resulting westward toroidal mantle flow fields attained the central Anatolian region producing widespread calc-alkaline volcanism since the late Miocene (Chapter 2). The long-lived asthenospheric heating during the break-off-related slab window opening resulted in lithospheric mantle removal by delamination (Keskin, 2003, 2007; Şengör et al., 2008; Bartol and Govers, 2014; Topuz et al., 2017) or convective dripping (Kaislaniemi et al., 2014; Neill et al., 2015; Göğüş et al., 2017; Chapter 3).

5.2.3 Late Cenozoic Anatolian precious and base metal metallogeny

Late Cenozoic Anatolian igneous complexes host many gold-rich porphyry and epithermal deposits, prospects and occurrences (Yiğit, 2006, 2009; Gessner et al., 2017; Menant et al., 2018) that define the late Cenozoic Anatolian Metallogenic Trend (33 Moz Au and 3.7 Blbs Cu; compilation in Chapter 4). Although some porphyry and epithermal prospects are spatially isolated (e.g., Afyon-Sandıklı and Hasançelebi), most of those mineral systems occur in nine clusters in western, central and eastern Anatolia (Chapter 4).

5.2.3.1 Western Anatolia

Porphyry-, skarn- and epithermal-style precious and base metal mineralization formed between 21 and 9 Ma in western Anatolia at the Simav, İzmir, Uşak and Bodrum districts as well as at the isolated Afyon-Sandıklı porphyry Au-Cu prospect (Figure 5.2A; Chapter 4). The loci of mineralized magmatic complexes migrated southwestwards during the Miocene in Anatolia as a result of the Aegean slab roll-back (Chapter 4), although this migration initiated in the Late Cretaceous in the northerly Balkans (Menant et al., 2018). Regional extension, exhumation of metamorphic core complexes and associated crustal heating, and related ductile and brittle structures control the formation and distribution of metal deposits in the upper crust (Gessner et al., 2017; Menant et al., 2018).

The Simav district consists of economic to sub-economic, NW-trending, low-sulfidation epithermal Au-Ag deposits and prospects such as the Kızıltepe deposit (0.26 Moz Au resources and reserves; Ariana Resources, 2017), porphyry Mo-Au prospect (i.e., Pınarbaşı), and Pb-Zn-Fe skarn occurrences. Precious and base metal mineralization at Simav is hosted within the early Miocene, medium- to high-K calc-alkaline, dacitic to rhyolitic volcanic and pyroclastic units in the Bigadiç, Sındırgı and Simav areas (Şener et al., 2009; Yılmaz et al., 2013), monzonitic Pınarbaşı stock (Delibaş et al., 2017), and granitic Alaçam, Eğrigöz and Koyunoba plutons (Uğurcan and Oyman, 2016). Magmatism and associated hydrothermal mineralization is in the hanging-wall of the ESE-trending, N-dipping, high-angle Simav normal fault and the footwall of Simav, low-angle, detachment fault during the first phase of the Menderes metamorphic core complex exhumation in the early Miocene (e.g., Işik and Tekeli, 2001; Isik et al., 2004; Dilek and Altunkaynak, 2009; Hasözbek et al., 2010). Similar low- to intermediate-sulfidation epithermal gold veins are in the İzmir district along the İzmir-Balıkesir Transfer Zone, west of the Menderes Massif. Mineralized veins, such as Arapdağ and Efemçukuru (3.4 Moz Au resources, reserves and past production; Sayılı and Gonca, 1999; Boucher, 2016; Eldorado Gold Corp., 2017) cut middle Miocene andesitic to rhyolitic volcanic units.

The other porphyry prospects and deposits of western Anatolia are in the Uşak district along the NE-trending Uşak-Güre graben such as the Kışladağ gold deposit (21.5 Moz Au resources, reserves and past production; Baker et al., 2016; Chapter 4) and Sayacik prospect, and the easterly Afyon-Sandıklı Au-Cu prospect along the Kırka-Afyon-İsparta trend. Porphyry mineralization in the Uşak district was dated at ca 14.5 Ma and is hosted within high-K calc-alkaline monzonitic intrusions (Baker et al., 2016; Bickford et al., 2016) whereas the Afyon-Sandıklı porphyry prospect was emplaced within alkaline monzonitic intrusions at 11.6 Ma (Chapter 4). The Bodrum district consists of skarn, polymetallic vein and high-sulfidation epithermal occurrences dated at ca. 9 Ma that are hosted within the late Miocene alkaline, trachyandesitic to monzonitic units of the Bodrum volcanic complex in the southwestern part of the Menders Massif (Chapter 4).

5.2.3.2 Central Anatolia

The central Anatolian region is dominated by high-sulfidation epithermal Au-Ag mineralization and alteration that formed between 10 and 3 Ma at the Konya, Niğde and Kayseri districts (< 2 Moz Au reserves and resources; Figure 5.2B; Chapter 4). The distribution of those three districts is structurally-controlled by the Akşehir normal (Konya district), Tuz Gölü dextral strike-slip (Niğde district), and Ecemiş sinistral strike-slip faults (Kayseri district). Those numerous high-sulfidation epithermal occurrences are characterized by multi-phase hydrothermal, phreatic and/or phreatomagmatic breccias such as at İnlice and Öksüt in the Konya and Kayseri districts, respectively (Hall et al., 2007; Reid et al., 2015), mineralized vuggy silica ledges, and advanced argillic and argillic alteration assemblages (Chapter 4). Porphyry-style alteration is either absent or weak such as at the Doğanbey prospect in the Konya district (Hall et al., 2007).

5.2.3.3 Eastern Anatolia

Despite the limited number of mineral occurrences in eastern Anatolia, recent discoveries highlight the high potential for gold and copper mineralization such as the Carlin-style Mollakara Au deposits in the Ağrı district (4.5 Moz Au; all resources and reserves; Koza Gold,

2015), and the Cevizlidere porphyry Cu-Au deposits in the Tunceli district (3.7 Blbs Cu and 1.6 Moz Au inferred resources; Figure 5.2B; Kociumbas and Page, 2009). Gold and copper mineralization in eastern Anatolia formed between 25 and 17 Ma (Chapter 4). The Cevizlidere deposit and satellite prospects (e.g., Sin and Mamliş) are hosted within dioritic to granodioritic stocks dated at ca. 26-25 Ma and emplaced within a pull-apart basin along the NE-trending Ovacık sinistral strike-slip fault (İmer et al., 2014). The monzonitic to granitic intrusions of the Ağrı district were affected by porphyry-style alteration and mineralization such as at Taşkapı and Taşlıçay between 21 and 17 Ma (Chapter 4). Distal alteration zones such as the Carlin-style Mollakara gold deposit and the high-sulfidation epithermal zone at Taşkapı may be coeval with the intrusion-related porphyry prospects in the Ağrı district based on field observations (Chapter 4). The Hasançelebi high-sulfidation epithermal Au-Ag prospect in the western part of eastern Anatolia is within the early Miocene Yamadağ volcanic complex. This prospect is similar to its high-sulfidation epithermal counterparts in central Anatolia and includes mineralized hydrothermal to phreatomagmatic breccias and vuggy to massive silica ledges that formed at ca. 21 Ma (Chapter 4).

5.3 Data acquisition and assessment

A suite of 21 igneous rock samples from the Simav, Uşak and Bodrum districts and the Afyon-Sandıklı porphyry prospect in western Anatolia were selected for lithogeochemical analyses in order to characterize the geochemical signature of mineralized igneous suites relative to the barren units. Sampling was focused on the least-altered part of Oligocene to Pliocene igneous units that host or post-date porphyry-, skarn- and epithermal-style alteration and precious and base metal mineralization. All of the samples were evaluated by hand lens and petrographically to assess their degree of hydrothermal alteration (e.g., sericite, chlorite, clays, silica, alkali feldspar, biotite and epidote) and weathering (Fe-oxide, Fe-oxihydroxide and clays). The fresh to weakly altered/weathered samples were selected, and subsequently cleaned of weathering surfaces, enclaves, xenoliths, factures and veins. Sample location and descriptions are provided in the appendix D (Table D.1). Major, minor and trace element

concentrations were obtained by X-ray fluorescence and inductively coupled plasma-mass spectrometry (ICP-MS) analyses (Table 5.1) by Bureau Veritas Labs in Vancouver, Canada. FeO concentrations were determined by titration. Sample FR-14-28, which yielded a total volatile content (LOI) greater than 5 wt %, was rejected. Major oxides for samples with LOI between 1 and 5 wt % were normalized to a 100 wt % volatile-free basis. In addition, samples evaluated for both Fe_2O_3 and FeO contents having Fe^{3+}/Fe^{2+} ratios > 8 and LOI > 2 wt % were considered to be weathered or altered (FR-14-82; FR-14-73 (Chapter 3); FR-15-30), and are not further considered.

The newly-acquired lithogeochemical data were interpreted in association with lithogeochemical data from the Kayseri, Konya, Ağrı and Niğde districts and Hasançelebi high-sulfidation epithermal prospect in central and eastern Anatolia (Chapter 3) and previously-published geochemical data from other mineralized igneous units (Baklan, Cevizlidere, Kışladağ and Pınarbaşı) along the late Cenozoic Anatolian Metallogenic Trend (Aydoğan et al., 2008; İmer et al., 2014; Baker et al., 2016; Delibaş et al., 2017). In addition, the Chemical Index of Alteration diagram (CIA; Nesbitt and Young, 1982) provides insight into weathering processes that could have affected the primary geochemical composition of the samples

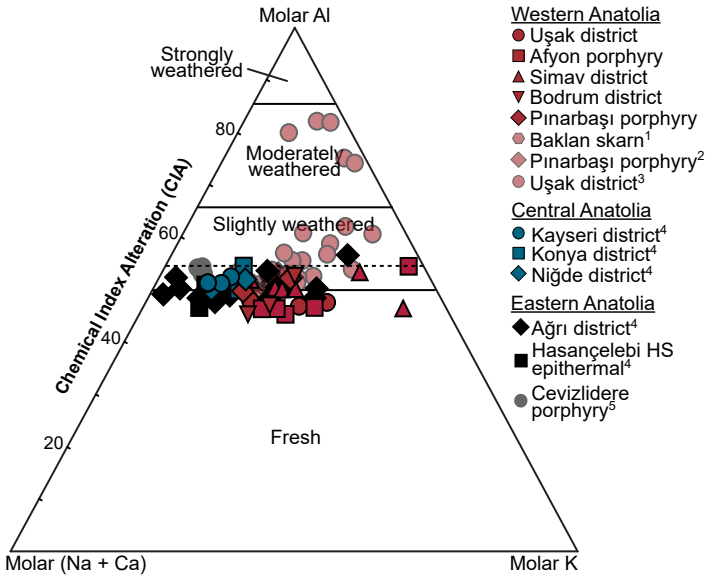

Figure 5.3 Alteration index (Al_2O_3-CaO+Na_2O-K_2O) ternary diagram to quantify the degree of weathering of analyzed rock samples (Nesbitt and Young, 1982); References: [1]Aydoğan et al., 2008; [2]Delibaş et al., 2017; [3]Baker et al., 2016; [4]Chapter 3; [5]İmer et al., 2014.

Table 5.1 Major and trace element analyses of igneous rocks hosting precious or base metals along the late Cenozoic Anatolian Metallogenic Trend.

Sample #	FR-14-41	FR-14-42a	FR-14-47	FR-14-50	FR-14-54	FR-15-30	FR-15-32	FR-15-33	FR-13-114	FR-13-116	FR-13-118
District	Afyon	Afyon	Afyon	Afyon	Afyon	Bodrum	Bodrum	Bodrum	Simav	Simav	Simav
Locality	Dutağaç	Dutağaç	Karacaören	Karacaören	Karacaören	Turgutreis	Turgutreis	Dağbelen	Karakoca	Kayalıdere	Söğüt
Lat (°N)	38.4599	38.4608	38.5010	38.5019	38.5122	37.0160	37.0368	37.0838	39.2654	39.2592	39.1073
Long (°E)	30.3403	30.3425	30.3288	30.3387	30.3490	27.2891	27.2542	27.3351	28.9299	28.8935	29.0765
Occurrence/Deposit			Afyon-Sandıklı	Afyon-Sandıklı	Afyon-Sandıklı	Karatoprak	Kadıkalesi				
Rock type	Trachyte	Trachyte	Monzonite	Monzonite	Megacrystic monzonite	Andesite	Monzodiorite	Monzodiorite	Granite	Granite	Granite
Age (Ma)[b]	11	11	11.6	11.6	11	10	10	10	21	21	21
SiO_2	60.2	63.0	65.2	65.4	62.4	60.6	59.5	57.9	72.3	72.8	69.6
TiO_2	1.04	0.76	0.61	0.83	0.70	0.73	0.59	0.53	0.23	0.22	0.47
Al_2O_3	16.8	15.33	15.03	14.29	15.29	18.44	16.82	16.07	14.89	14.51	15.19
$Fe_2O_{3\ (t)}$	4.13	4.54	3.34	3.68	4.63	4.51	4.89	4.63	2.11	2.03	2.98
FeO			1.28		0.84	0.33	2.65				
CaO	4.77	3.64	2.05	0.05	3.39	2.36	4.39	5.80	1.40	1.46	2.4
MgO	2.32	2.22	1.49	4.21	1.82	0.64	2.05	1.74	0.48	0.49	0.86
Na_2O	3.76	3.53	3.38	0.45	3.69	3.65	3.58	3.27	3.97	3.8	3.6
K_2O	4.85	4.96	6.19	7.15	5.52	5.22	4.96	4.25	4.69	4.51	4.34
MnO	0.06	0.08	0.06	0.04	0.11	0.03	0.10	0.13	0.06	0.06	0.04
P_2O_5	0.73	0.52	0.30	0.27	0.50	0.13	0.29	0.25	0.09	0.08	0.13
Cr_2O_3	0.006	0.005	0.007	0.015	0.004	0.003	0.001	0.004	<0.001	<0.001	0.001
SO_3	<0.002	<0.002	<0.002	<0.002	<0.002	0.006	0.01	0.191	<0.002	0.006	<0.002
V_2O_5	0.025	0.017	0.013	0.017	0.015	0.018	0.014	0.019	0.002	0.003	0.01
LOI	0.82	0.67	1.44	2.65	0.97	2.65	1.69	4.37	0.52	0.84	0.71
TOTAL	99.97	99.65	99.53	99.47	99.57	99.29	99.21	99.44	100.88		100.61
Mg#	58.6	55.2	52.9	74.2	49.7	26.3	51.3	48.6	36.4	37.8	42.1
Ba	1655	1563	1663	2004	2013	1316	1132	1391	1009	842	1236
Be	5	5	6	1	4	6	5	4	6	5	<1
Co	11.8	12.5	7.3	7.3	17.8	6.2	11.4	9.7	1.7	2.1	4.7
Cs	4.1	13.0	12.1	17.6	9.1	8.8	14.2	8.5	3.9	5.9	7.4
Ga	19	17.5	18.3	15.4	17.0	20.5	19.2	18.0	15.2	14.4	14.8
Hf	10.5	9.2	10	14.5	8.5	9.3	10.9	5.7	4.8	4.3	5.2
Nb	39.9	33.5	39.7	44.4	37.1	38.3	41.1	17.8	15.0	15.7	11.8
Rb	153	168.3	286.9	348.3	176.9	211.9	246.1	160	154.9	166.5	147.5
Sn	3	2	3	15	3	3	5	2	2	4	4
Sr	1378.3	1290	1180.9	656.2	1713.1	967.4	877.9	818.3	190.3	164.9	322.2
Ta	2.6	2.3	3.3	2.7	2.8	2.5	3.5	1.4	1.3	1.4	1.2
Th	36.6	30.9	67.9	52.1	43.5	68.5	104.8	39.0	21.8	19.1	21.9
U	14.3	13.8	19.5	22.0	17.6	25.7	33.2	12.2	6.2	6.1	5.3
V	151	98	78	84	85	106	83	99	<8	<8	37
W	4.2	3.8	8.6	4.9	0.9	8.3	11.6	8.3	<0.5	<0.5	3.9
Zr	430.9	356.7	375.2	540.2	339.1	359.6	441.9	223.8	181.3	156.2	192.4
Y	30.6	21.8	18.4	14.4	22.4	44.5	24.2	22.0	20.5	20.9	20.1
La	107.0	98.0	86.1	97.2	124.8	107.5	103.4	68.6	46.8	41.2	46.7
Ce	191.9	167.2	139.7	171.9	204.8	198.9	180.7	121.5	85.1	74.2	86.3
Pr	21.17	18.03	14.83	18.58	23.03	22.28	17.99	12.65	8.28	7.41	8.51
Nd	79.5	64.6	51.4	70.0	82.4	81.7	58.8	43.4	29.6	27.2	29.5
Sm	12.29	9.92	7.94	11.92	12.34	13.85	8.94	7.29	4.99	4.44	5.08
Eu	3.04	2.52	1.97	3.12	2.99	3.36	1.73	1.75	0.83	0.69	0.98
Gd	9.42	7.42	5.61	8.08	8.32	11.27	6.26	5.95	4.36	4.08	4.05
Tb	1.26	0.90	0.73	1.09	0.99	1.48	0.80	0.76	0.67	0.63	0.62
Dy	6.33	4.46	3.88	5.28	4.57	8.05	4.63	4.07	3.41	3.59	3.42
Ho	1.22	0.82	0.65	0.80	0.73	1.45	0.84	0.72	0.65	0.74	0.72
Er	3.25	2.29	1.96	1.90	2.13	4.38	2.41	2.09	1.87	2.10	2.05
Tm	0.48	0.32	0.3	0.25	0.32	0.62	0.39	0.31	0.3	0.34	0.32
Yb	3.24	2.26	1.96	1.62	2.08	3.94	2.55	2.15	2.15	2.08	2.26
Lu	0.47	0.3	0.28	0.21	0.31	0.59	0.41	0.31	0.33	0.33	0.33
Mo	1.8	1.0	1.2	102.5	0.3	2.0	6.9	2.2	0.5	0.8	1.2
Cu	12.9	14.9	52.3	145.6	23.3	24.1	20.2	13.9	0.7	0.7	5.0
Pb	15.5	8.8	147.6	151.4	6.6	7.0	20.3	25.5	3.6	4.5	23.5
Zn	69	42	43	156	72	44	38	44	26	24	27
Ni	10.8	19.6	11.6	23.9	28.6	5.8	6.2	6	3.2	2.5	3.8
As	1.6	0.8	14.5	6.7	1.9	4.1	5.8	5.3	<0.5	0.9	1.4
Cd	<0.1	<0.1	0.1	<0.1	<0.1	<0.1	<0.1	<0.1	<0.1	<0.1	<0.1
Sb	1.5	0.3	0.7	0.1	0.3	0.6	0.4	0.2	<0.1	<0.1	<0.1
Bi	0.2	0.2	0.6	0.4	<0.1	<0.1	0.3	0.2	<0.1	0.1	0.3
Ag	<0.1	<0.1	0.1	0.9	<0.1	<0.1	<0.1	<0.1	<0.1	<0.1	<0.1
Au	<0.5	<0.5	7	151.5	0.9	<0.5	<0.5	<0.5	1	<0.5	2.3
Hg	0.02	0.05	<0.01	<0.01	<0.01	<0.01	<0.01	<0.01	<0.01	<0.01	<0.01
Tl	<0.1	0.2	0.2	3.6	0.3	0.2	0.2	0.1	0.3	0.3	0.4
Se	<0.5	<0.5	<0.5	<0.5	<0.5	<0.5	<0.5	<0.5	<0.5	<0.5	<0.5
Sc	7.1	5.5	3.9	9.1	4.0	7.7	2.7	6.8	3.9	3.7	3.5
Te	<0.2	<0.2	<0.2	<0.2	<0.2	<1	<1	<1	<1	<1	<1

Table 5.1 (Continued) Major and trace element analyses of igneous rocks hosting precious or base metals along the late Cenozoic Anatolian Metallogenic Trend.

Sample #	FR-13-119	FR-13-123	FR-14-27a	FR-14-28[a]	FR-14-29a	FR-15-17	FR-15-18	FR-13-66	FR-13-68	FR-13-70
District	Simav	Simav	Simav	Simav	Simav	Simav	Simav	Uşak	Uşak	Uşak
Locality	Söğüt	Küreci	Sındırgı	Sındırgı	Alaçam	Pınarbaşı	Pınarbaşı	Kışladag	Kışladag	Kışladag
Lat (°N)	39.1489	39.4089	39.2893	39.3659	39.4200	39.0184	39.0165	38.4821	38.4821	38.4821
Long (°E)	29.0895	29.1667	28.3286	28.4445	28.4881	29.3212	29.3229	29.1488	29.1488	29.1488
Occurrence/ Deposit			Kızıltepe	Kızıltepe		Pınarbaşı	Pınarbaşı	Kışladag	Kışladag	Kışladag
Rock type	Granitic dike	Granite	Trachydacite	Dacite	Granodiorite	Monzonite	Quartz-monzonite	Monzonite	Monzonite	Monzonite
Age (Ma)[b]	21	21	20	20	20	17	17.86	14.76	14.36	14.76
SiO_2	76.0	69.7	66.2	64.1	67.1	60.8	68.0	61.8	61.5	61.4
TiO_2	0.18	0.47	0.47	0.49	0.47	0.56	0.36	0.53	0.56	0.78
Al_2O_3	12.04	15.26	14.88	14.73	15.62	17.04	15.51	14.63	15.72	14.83
$Fe_2O_{3\ (t)}$	1.28	3.28	3.38	3.91	3.87	5.17	3.05	5.48	6.23	5.09
FeO						2.19	1.09		3.43	3.49
CaO	0.27	2.62	0.75	3.32	3.55	4.63	1.79	2.82	4.31	2.13
MgO	0.41	1.09	1.90	1.65	1.50	1.73	0.93	3.86	2.35	4.00
Na_2O	1.18	3.60	1.66	1.48	3.37	3.85	3.56	3.01	3.71	2.5
K_2O	7.52	4.07	6.13	4.27	3.08	3.44	4.32	5.43	3.79	6.32
MnO	0.03	0.07	0.05	0.07	0.08	0.09	0.03	0.08	0.16	0.2
P_2O_5	0.04	0.15	0.14	0.14	0.13	0.29	0.10	0.26	0.27	0.46
Cr_2O_3	<0.001	<0.001	0.002	<0.001	0.001	<0.001	<0.001	0.009	0.005	0.016
SO_3	0.008	<0.002	<0.002	0.007	<0.002	0.016	0.004	0.221	0.029	0.138
V_2O_5	<0.002	0.01	0.009	0.01	0.011	0.019	0.009	0.014	0.019	0.016
LOI	1.21	0.54	3.68	5.32	0.61	1.41	1.46	2.27	1.74	2.13
TOTAL	100.34	101.04	99.47	99.69	99.51	99.4	99.4	100.67	100.67	100.81
Mg#	44.6	45.5	58.6		49.4	45.7	43.4	63.9	48.7	66.4
Ba	556	1068	1408	931	713	2063	1666	481	1146	1753
Be	<1	5	1	<1	4	3	4	3	2	<1
Co	1.7	5.0	5.3	5.4	6.9	7.0	3.5	8.1	11.1	17
Cs	5.3	5.6	6.4	14.2	6.5	11.9	6.8	25.6	2.9	13.4
Ga	10.7	15.0	14.9	15.2	16.8	19	17.9	17.9	15.5	13.7
Hf	3.3	5.3	5.2	4.7	4.6	5.6	5.0	6.6	4.9	8.1
Nb	14.1	13.4	12.1	10.4	10.4	14.8	14.3	17	12.7	20.4
Rb	302.1	145.2	199.3	156.6	120.2	92.9	122.7	243.7	117.0	241
Sn	3	3	3	6	5	4	3	6	4	9
Sr	57.2	293.2	258.3	112.3	315.5	777.2	379.8	353.8	862.6	694
Ta	1.6	1.3	1.2	0.8	1.1	0.9	1.3	1.0	0.8	1.2
Th	27.2	18.2	19.3	11.3	15.5	27.7	30.1	22.8	23.6	23.1
U	9.8	5.9	5.3	3.9	5.3	5.6	8.8	7.7	5.2	9.5
V	<8	35	73	59	69	105	51	55	72	65
W	2.8	0.6	1.7	1.0	0.6	0.5	<0.5	4.5	3.3	7.7
Zr	98.2	210.7	189.8	168.9	155.7	237.6	180.9	262	194.7	316
Y	20.4	24.7	23.5	18.8	19.2	34.1	20.4	15.2	17.9	26.7
La	20.4	42.8	41.7	28.2	38.7	66.5	51.4	75.0	62.4	69.9
Ce	44.9	74.6	69.3	51.3	74.4	108.6	89.4	138.1	115.3	134.4
Pr	4.47	7.77	7.52	5.68	8.04	12.61	8.73	13.43	11.9	14.03
Nd	15.2	27.5	27.2	20.8	29.0	43.9	28.8	47.8	42.3	51.4
Sm	3.26	5.17	4.70	4.05	4.86	7.92	5.01	7.34	6.9	8.47
Eu	0.42	0.96	0.99	0.67	0.95	1.87	1.12	1.30	1.61	2.13
Gd	3.04	4.64	4.37	3.73	4.34	7.57	4.16	4.88	4.98	6.45
Tb	0.55	0.70	0.71	0.59	0.63	1.13	0.62	0.60	0.66	0.85
Dy	3.21	3.97	4.07	3.25	3.62	6.80	3.78	2.90	3.29	4.23
Ho	0.74	0.87	0.84	0.66	0.71	1.37	0.70	0.56	0.63	0.86
Er	2.36	2.53	2.39	1.91	2.14	3.88	2.17	1.51	1.87	2.39
Tm	0.39	0.38	0.37	0.32	0.32	0.61	0.34	0.22	0.28	0.34
Yb	2.70	2.65	2.56	2.11	2.25	4.09	2.36	1.46	1.76	2.17
Lu	0.41	0.43	0.37	0.31	0.34	0.65	0.38	0.23	0.26	0.32
Mo	1.7	0.8	0.2	0.3	0.5	0.5	0.7	28.3	3.9	7.7
Cu	0.7	1.3	5.3	5.5	3.2	116	24.7	569.5	106.9	658.4
Pb	109.2	4.5	17.6	29.5	6.5	22.1	27.8	107.7	22.0	41.3
Zn	33	29	47	55	53	97	35	107	63	2634
Ni	1.7	3.2	3.9	3.6	2.8	2.7	2.0	13.4	8.2	29.7
As	1.7	1.0	2.0	7.6	0.9	0.5	<0.5	20.5	25.6	125.2
Cd	<0.1	<0.1	<0.1	0.1	<0.1	0.4	<0.1	0.5	0.2	6.4
Sb	0.3	<0.1	0.2	0.1	<0.1	0.2	<0.1	0.8	1	0.8
Bi	0.3	<0.1	0.1	0.3	0.1	<0.1	1.5	1.1	0.6	1.7
Ag	0.1	<0.1	<0.1	0.2	<0.1	<0.1	<0.1	0.2	<0.1	0.8
Au	1.3	1.1	<0.5	2.2	<0.5	<0.5	0.8	578.7	137.3	437.5
Hg	<0.01	<0.01	<0.01	<0.01	<0.01	<0.01	<0.01	<0.01	<0.01	<0.01
Tl	0.2	0.4	<0.1	<0.1	0.5	0.1	<0.1	0.9	<0.1	0.8
Se	<0.5	<0.5	<0.5	<0.5	<0.5	<0.5	<0.5	<0.5	<0.5	<0.5
Sc	2.7	2.6	4.3	5.2	5.2	2.6	2.4	5.9	2.6	5.8
Te	<1	<1	<0.2	<0.2	<0.2	<1	<1	<1	<1	<1

[a]LOI > 5 wt %; [b]Age data from Chapter 4; Kışladağ dates are in the appendix E (Baker et al., 2016).

provided in this study (Chapter 3; this Chapter) and compiled from literature. Figure 5.3 shows that most of the rock samples have CIA values between 45 and 55 indicating that those rocks are fresh to slightly weathered. Samples with CIA values greater than 55 were considered weathered, and rejected from further consideration.

A suite of four rock samples previously analyzed for whole-rock elemental geochemistry was selected for Sr-Nd-Pb isotopic analyses in order to characterize the isotopic signature of mineralized igneous suites relative to the barren units and constrain magmatic sources and processes (Tables 5.2-5.3). The selected samples are from the Kışladağ porphyry gold deposit in the Uşak district (FR-13-68), Afyon-Sandıklı porphyry prospect (FR-14-50) and a skarn-altered monzonitic intrusion (FR-15-32) and argillic-altered andesitic lava in the Bodrum district (FR-15-30). The results were interpreted in association with radiogenic isotope data from the Kayseri, Konya, Ağrı and Niğde districts and Hasançelebi high-sulfidation epithermal prospect in central and eastern Anatolia (Chapter 3). Rb-Sr and Sm-Nd isotope systematics were obtained on whole-rock pulps whereas Pb isotope data were measured from hand-picked feldspar separates. All of the isotope analyses were carried out at the Pacific Centre for Isotopic and Geochemical Research at The University of British Columbia; Pb and Nd isotopic ratios were analyzed by the Nu Plasma 214 multi-collector ICP-MS; Sr isotopic ratios were obtained by the Triton TIMS; Rb, Sr, Sm and Nd concentrations were determined by the Thermo Finnigan Element2 high resolution ICP-MS. The detailed protocol for Sr-Nd-Pb isotopic analyses (Weis et al., 2006; Fourny et al., 2016) is explained in Chapter 3.

Table 5.2 Radiogenic Sr and Nd isotope data from late Cenozoic igneous units in western Anatolia.

Samples[a]	District	Deposit/ Prospect	Age[b] (Ma)	Rb (ppm)	Sr (ppm)	$^{87}Sr/^{86}Sr$	±2σ	$(^{87}Sr/^{86}Sr)_i$	Sm (ppm)	Nd (ppm)	$^{143}Nd/^{144}Nd$	±2σ	$(^{143}Nd/^{144}Nd)_i$	ε_{Nd}	$(\varepsilon_{Nd})_i$	τ_{DM}[c]	τ_{DM}[d]
FR-15-30	Bodrum	Karatoprak	9	208.11	922.62	0.705909	0.000005	0.70572	13.53	80.52	0.512539	0.000006	0.51253	-1.7	-1.8	0.84	1.00
FR-15-32	Bodrum	Kadıkalesi	9.8	189.57	753.52	0.706430	0.000007	0.70622	8.56	57.11	0.512546	0.000008	0.51254	-1.6	-1.7	0.76	0.99
FR-14-50	-	Afyon-Sandıklı	11	304.65	598.61	0.705996	0.000010	0.70558	12.71	71.02	0.512572	0.000006	0.51256	-1.0	-1.2	0.85	0.95
FR-13-68[b]	Uşak	Kışladağ	14.36	80.89	769.32	0.706327	0.000008	0.70624	6.97	41.99	0.512516	0.000006	0.51251	-2.0	-2.2	0.87	1.04

[a] Sample description, coordinates and trace element concentrations can be found in the appendix D

[b] Refer to Chapter 4 for age data

[c] Single-stage DM model age

[d] Two-stage DM model age (Liew and Hofmann, 1988)

Table 5.3 Radiogenic Pb isotope data from late Cenozoic igneous units in western Anatolia.

Samples[a]	District	Deposit/ Prospect	Age[b] (Ma)	$^{206}Pb/^{204}Pb$	±2σ	$^{207}Pb/^{204}Pb$	±2σ	$^{208}Pb/^{204}Pb$	±2σ
FR-15-30	Bodrum	Karatoprak	9	18.9149	0.0012	15.6763	0.0009	38.9296	0.0027
FR-15-32	Bodrum	Kadıkalesi	9.8	18.9375	0.0020	15.6879	0.0019	38.9880	0.0050
FR-14-50	-	Afyon-Sandıklı	11	18.9470	0.0009	15.6842	0.0008	38.9138	0.0022
FR-13-68[b]	Uşak	Kışladağ	14.36	19.0214	0.0012	15.6995	0.0011	39.0919	0.0028

[a] Sample description and coordinates are in the appendix D

[b] Refer to Chapter 4 for age data

5.4 Results

The mineralized Miocene igneous rocks in western Anatolia are dominantly plutonic and intermediate to felsic in composition with SiO_2 from 54 to 77 wt % and a median of 61.8 ± 5.5 wt % SiO_2 (1σ). Plutonic rocks and their volcanic equivalents are classified according to the total alkali versus silica (TAS) diagram of Middlemost (1994) and Le Maitre et al. (2002), respectively (Figure 5.4A-B). The mineralized igneous rocks at the Afyon -Sandıklı porphyry prospect and Bodrum district are alkaline trachyandesite and trachyte, similar to the Ağrı district in eastern Anatolia, whereas the Simav volcanic rocks are subalkaline between trachydacite and rhyolite. The plutons in the Simav district are granodiorite and granite (Figure 5.5A-B); the Cevizlidere stocks in the Tunceli district are diorite to granodiorite (İmer et al., 2014). The intrusive units from the Uşak and Bodrum districts, and Afyon-Sandıklı and Pınarbaşı porphyry prospects are monzonite to quartz-monzonite with minor monzodiorite (Figure 5.5C-F) like some intrusive rocks in the Ağrı district.

The late Cenozoic igneous units that host porphyry and epithermal alteration in western Anatolia have a high-K calc-alkaline to shoshonitic affinity with a K_2O/Na_2O ratio > 1 whereas those in central and eastern Anatolia are medium- to high-K calc-alkaline and characterized by a K_2O/Na_2O ratio < 1 (Figures 5.4C-D). Volcanic rocks in central Anatolia are transitional from medium-K to high-K calc-alkaline whereas the intrusive rocks in eastern Anatolia are transitional to sodic and dominantly medium-K to high-K calc-alkaline. Mineralized igneous rocks in western Anatolia are dominantly potassic to highly potassic ranging from high-K calc-alkaline to shoshonitic affinity. Although some mineralized host rocks in the Uşak and Bodrum districts and at the Afyon-Sandıklı porphyry prospect are alkaline, their hydrothermal alteration

is typical of calc-alkalic porphyry systems that is characterized by ubiquitous phyllic, argillic and advanced argillic alteration assemblages, and absence of calc-sodic alteration assemblage (Chapter 4), which is more typical of alkalic porphyry systems (Lang et al., 1995).

The trace element signature of late Cenozoic igneous host rocks to porphyry and epithermal mineralization have similar patterns between the three Anatolian magmatic domains based on the primitive mantle-normalized spider diagram (Figure 5.6). Those similarities

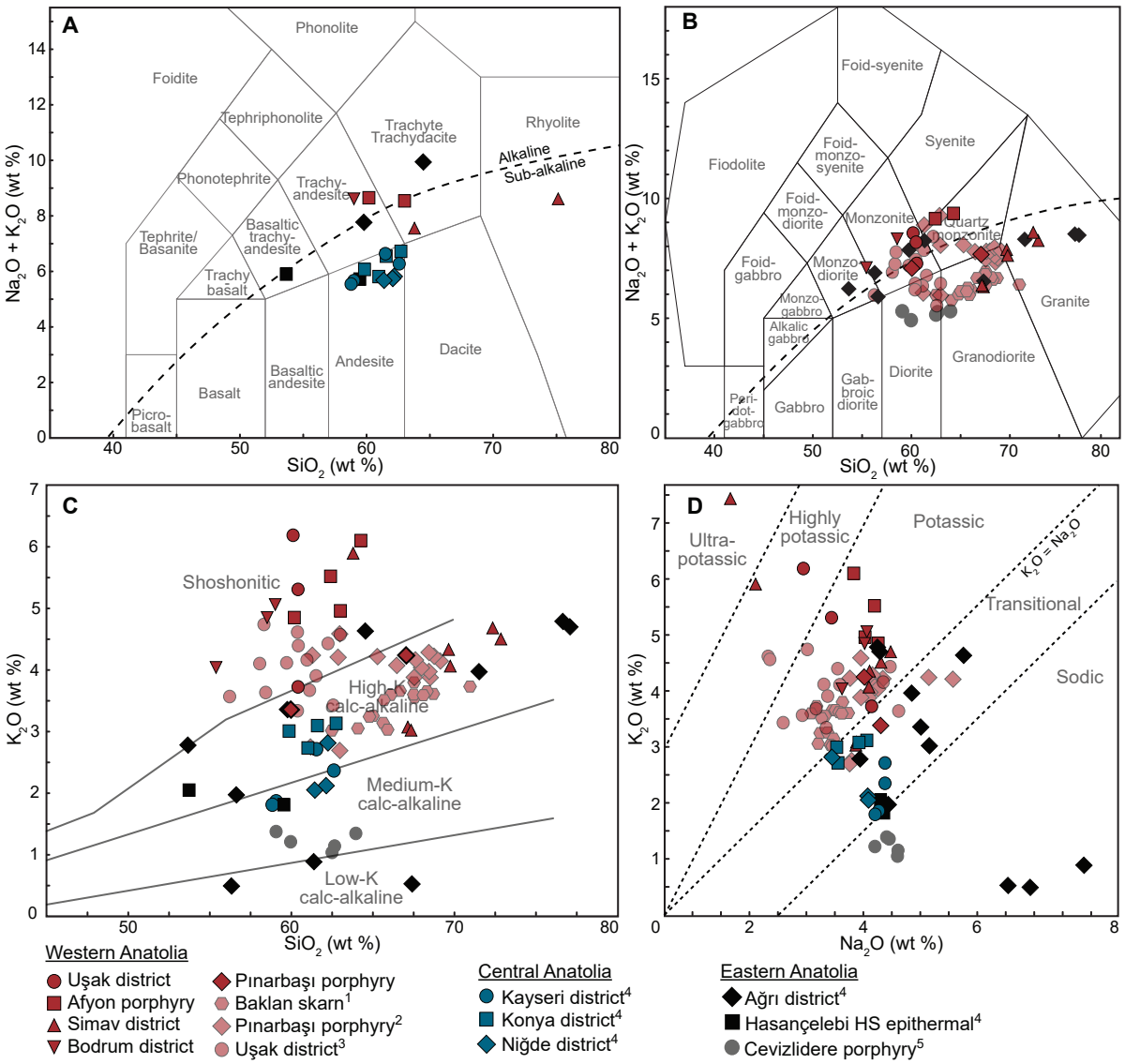

Figure 5.4 Total alkali versus silica (TAS) diagram for fertile volcanic (A; Le Maitre et al., 2002) and plutonic rocks (B; Middlemost, 1994); K_2O versus SiO_2 (C; Peccerillo and Taylor, 1976); K_2O versus Na_2O diagrams (D; Le Maitre et al., 2002); References: [1]Aydoğan et al., 2008; [2]Delibaş et al., 2017; [3]Baker et al., 2016; [4]Chapter 3; [5]İmer et al., 2014.

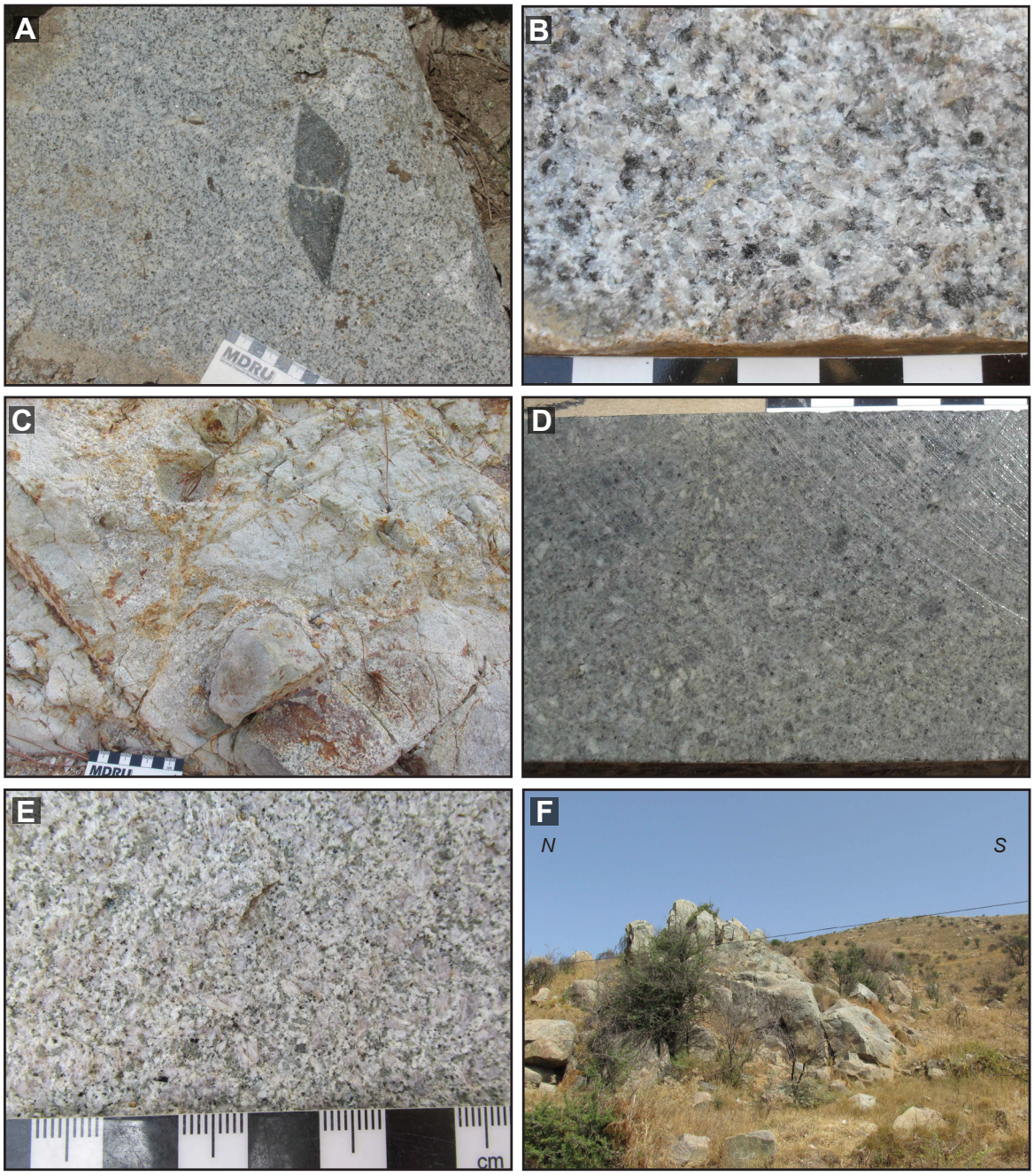

Figure 5.5 Macro-photographs of the Alaçam granodiorite (A), Simav granite (B), Pınarbaşı monzonite (C), Kışladağ monzonite (INT-3; D), Afyon-Sandıklı monzonite (E) and Bodrum monzonite (F) from western Anatolia.

include negative anomalies in Nb, Ta and Ti that are consistent with subduction-related signature. However, igneous rocks in western Anatolia are more enriched in large ion lithophile elements (LILE; i.e., Cs, Rb, Ba and K) and some igneous rocks near Simav have troughs in Sr, and Ba to lesser degree. In central Anatolia, the mineralized volcanic units have a narrow range of trace element compositions as opposed to the igneous units in eastern Anatolia.

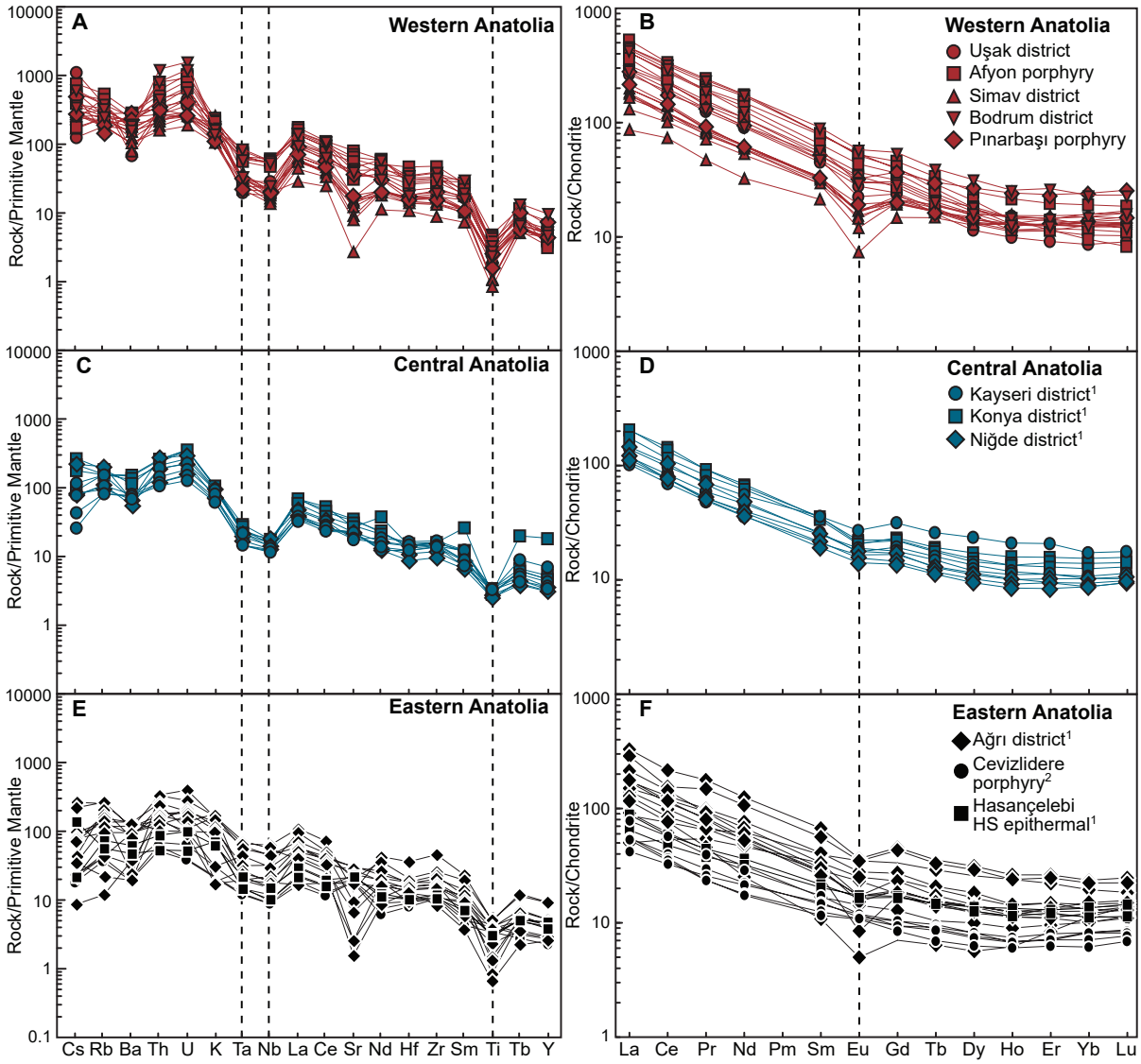

Figure 5.6 Primitive mantle-normalized trace element (McDonough et al., 1992) and chondrite-normalized rare earth element diagrams (Sun and McDonough, 1989) of fertile rock samples from western (A-B), central (C-D) and eastern Anatolia (E-F). References: [1]Chapter 3; [2]İmer et al., 2014.

On the chondrite-normalized rare earth element diagram (Figure 5.6), all samples are characterized by a similar listric-shaped pattern with the absence of heavy rare earth element depletion (HREE) that reflects hornblende ± clinopyroxene and absence of garnet fractionation. The weak negative Eu anomalies for some felsic rocks at the Simav and Ağrı districts is an effect of plagioclase fractionation.

The middle to late Miocene mineralized igneous units in western Anatolia yield initial $^{87}Sr/^{87}Sr$ isotope ratios of 0.70624 at the Kışladağ porphyry Au deposit of the Uşak district, 0.70558 at the Afyon-Sandıklı porphyry Au-Cu prospect and 0.70572 and 0.70622 at the Bodrum district (Figure 5.7; Table 5.2). The initial $^{143}Nd/^{144}Nd$ isotope ratios of the Kışladağ and Afyon-Sandıklı porphyry systems, and Bodrum district are 0.51251, 0.51256, and from 0.51253 to 0.51254, respectively (Figure 5.7; Table 5.2). The initial $^{87}Sr/^{87}Sr$ and $^{143}Nd/^{144}Nd$ isotope ratios of the Kışladağ sample are slightly lower and greater, respectively, than the previously-published data from the volcanic equivalents along the Uşak-Güre basin (Karaoğlu and Helvacı, 2014). The result from the Afyon-Sandıklı porphyry prospect is consistent with previously-published isotopic data from the Afyon volcanic complex (Prelević et al., 2012; Prelević et al., 2015). Those middle to late Miocene-aged mineralized igneous rocks in western Anatolia are clustered between the early Miocene igneous rocks affected by a strong crustal component and the post-mineralization, Pliocene to Quaternary, mantle-derived volcanic units of the Kula complex. Results from mineralized igneous rocks in western Anatolia cluster, together with the fertile rocks from central and eastern Anatolia (Chapter 3), near the bulk silicate earth composition on the initial $^{87}Sr/^{87}Sr$ versus $^{143}Nd/^{144}Nd$ diagram. Those results strongly contrast with the younger barren volcanic rocks in western, central and eastern Anatolia that show a broader range with more depleted isotopic values. Radiogenic Sr and Nd isotope compositions highlight the crustal affinity of mineralized igneous rocks in Anatolia that are characterized by initial $^{87}Sr/^{87}Sr$ and $^{143}Nd/^{144}Nd$ isotopic ratios, and ε_{Nd} ranging from 0.70404 to 0.70639, 0.51251 to 0.51268, and -2.2 to +1.0 respectively (Figure 5.7). Those isotopic ranges are consistent with the global isotopic signature of continental arcs and epithermal

mineralization host rocks that have initial ε_{Nd} and $^{87}Sr/^{86}Sr$ values that cluster between -3 and +1 and 0.7045 and 0.7060, respectively (du Bray, 2017).

The Kışladağ porphyry deposit has $^{206}Pb/^{204}Pb$, $^{207}Pb/^{204}Pb$ and $^{208}Pb/^{204}Pb$ ratios of 19.0214, 15.6995 and 39.0919, respectively (Figure 5.8; Table 5.3). Those ratios are higher than those from the Afyon-Sandıklı porphyry prospect (18.9470, 15.6842 and 38.9138, respectively) and Bodrum districts (18.9149 to 18.9375, 15.6763 to 15.6879, and 38.9296 to 38.9880, respectively). The results presented herein are consistent with previously published Pb isotope data from the non-altered units at the Uşak-Güre and Afyon volcanic complexes as well as the Pb ratios from the mineralized igneous units in central and eastern Anatolia. Anatolian mineralized igneous rocks have elevated Pb isotopic ratios that confirm the upper

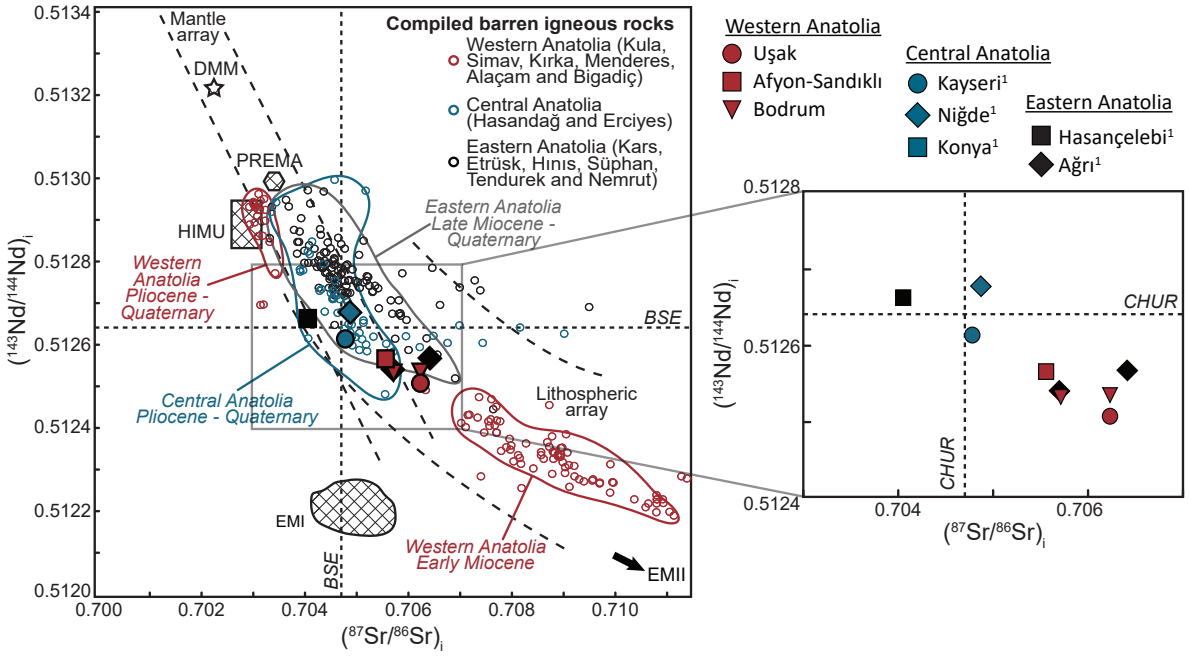

Figure 5.7 Initial $^{87}Sr/^{86}Sr$ versus $^{143}Nd/^{144}Nd$ diagram displaying the isotopic signature of fertile (large symbols) and barren (small open circles) late Cenozoic igneous units in Anatolia. BSE = bulk silicate Earth (Bouvier et al., 2008); EMI, EMII, HIMU, PREMA, DMM reservoirs from Zindler and Hart (1986). Data source for barren igneous rocks: western Anatolia (Alıcı et al., 2002; Innocenti et al., 2005; Dilek and Altunkaynak, 2009; Agostini et al., 2010; Dilek and Altunkaynak, 2010; Hasözbek et al., 2011; Altunkaynak et al., 2012; Chakrabarti et al., 2012; Çoban et al., 2012; Erkül and Erkül, 2012; Ersoy et al., 2012a; Ersoy et al., 2012b; Erkül et al., 2013; Aldanmaz et al., 2015; Yücel-Öztürk, 2016), central Anatolia (Notsu et al., 1995; Deniel et al., 1998; Kürkçüoğlu et al., 1998; Şen et al., 2004; Siebel et al., 2011; Reid et al., 2017) and eastern Anatolia (Pearce et al., 1990; Notsu et al., 1995; Buket and Temel, 1998; Keskin et al., 1998; Keskin et al., 2006; Özdemir, 2011; Çubukçu et al., 2012; Özdemir and Güleç, 2013; Lebedev et al., 2016; Oyan et al., 2016; Kaygusuz et al., 2018). Reference: [1]Chapter 3.

crustal and subduction components (Figure 5.8). The radiogenic Sr-Nd-Pb isotope signature of Anatolian mineralized igneous rocks strongly contrasts with the younger and barren Pliocene to Quaternary volcanic suites throughout Anatolia that are dominated by a mantle component, which is depleted, and characterized by higher initial $^{143}Nd/^{144}Nd$ and lower initial $^{87}Sr/^{86}Sr$, $^{206}Pb/^{204}Pb$, $^{207}Pb/^{204}Pb$ and $^{208}Pb/^{204}Pb$ isotopic ratios.

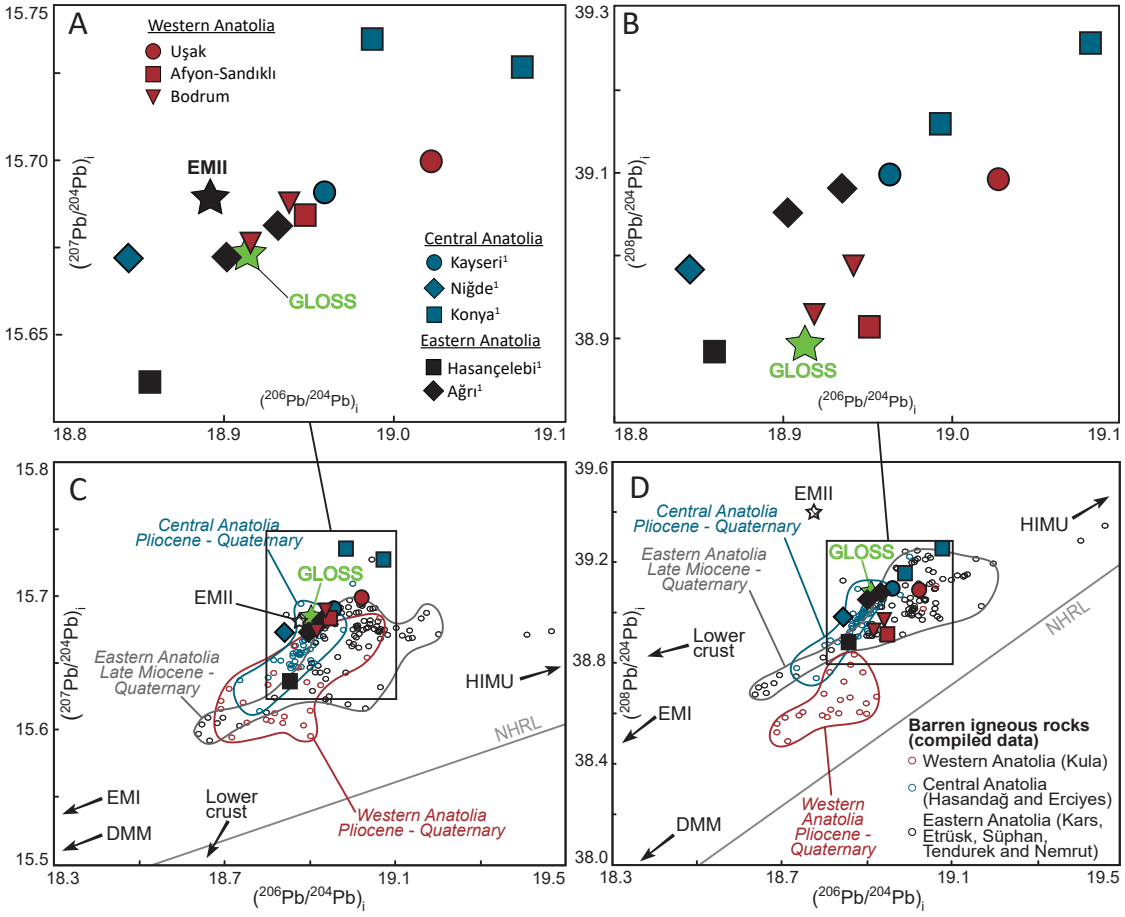

Figure 5.8 A. $(^{206}Pb/^{204}Pb)_i$ versus $(^{207}Pb/^{204}Pb)_i$; B. $(^{206}Pb/^{204}Pb)_i$ versus $(^{208}Pb/^{204}Pb)_i$ diagrams displaying the isotopic signature of fertile (large symbols) and barren (small open circles) late Cenozoic igneous units in Anatolia. GLOSS = global subducting sediment composition (Plank and Langmuir, 1998); NHRL = Northern Hemisphere reference line (Hart, 1984); EMI, EMII, HIMU, DMM reservoirs from Zindler and Hart (1986). Orogene, upper and lower crust evolution curves are from Zartman and Doe (1981). Data source for barren igneous rocks: western Anatolia (Notsu et al., 1995; Alıcı et al., 2002; Innocenti et al., 2005; Dilek and Altunkaynak, 2010; Chakrabarti et al., 2012; Aldanmaz et al., 2015), central Anatolia (Notsu et al., 1995; Deniel et al., 1998; Kürkçüoğlu et al., 1998; Şen et al., 2004; Siebel et al., 2011; Reid et al., 2017) and eastern Anatolia (Pearce et al., 1990; Notsu et al., 1995; Keskin et al., 1998; Keskin et al., 2006; Özdemir, 2011; Özdemir and Güleç, 2013; Lebedev et al., 2016; Oyan et al., 2016). Refence: [1]Chapter 3.

5.5 Discussion

5.5.1 Fertility of late Cenozoic Anatolian magmatism

Ideal magmatic conditions for the formation of porphyry systems require high oxidation states (> FMQ +1.3-2; e.g., Sillitoe, 1979; Ishihara, 1981; Mungall, 2002; Richards and Kerrich, 2007; Lee et al., 2012), and high water (≥ 4 wt %; Burnham, 1979) and sulfur contents (> 1000 ppm; Chambefort et al., 2008). Such conditions favor hornblende fractionation and suppress the early plagioclase fractionation which yields an adakitic magma signature (i.e., $SiO_2 \geq 56$ wt %; $Al_2O_3 \geq 15$ wt %; $Na_2O \geq 3$ wt %; Sr/Y ≥ 20; La/Yb ≥ 20; Y ≤ 10 ppm; Yb ≤ 1ppm; Richards and Kerrich, 2007; Castillo, 2012). Worldwide porphyry systems are typically associated with high Sr/Y and La/Yb magmas that accumulated and matured at the base of the crust in the MASH zone (melting, assimilation, storage and homogenization; Hildreth and Moorbath, 1988; Annen et al., 2005) in arc settings (Richards and Kerrich, 2007; Richards, 2011; Chiaradia et al., 2012; Richards et al., 2012; Bissig et al., 2017). When the production of arc magma ceases, cumulates of hydrous material in the former MASH zone can be remobilized during post-subduction or post-collisional events to yield similar fertile magmas and associated porphyry systems (Richards, 2009), and elemental and isotopic geochemical signatures (Richards, 2015). Additionally, the genesis of adakitic magma may result from many processes including slab melting (Defant and Drummond, 1990; Martin et al., 2005), lower crust melting (Petford and Gallagher, 2001; Zellmer et al., 2012) and fractional crystallization of amphibole ± garnet (Macpherson et al., 2006; Rodriguez et al., 2007; Alonso-Perez et al., 2009), possibly accompanied by crustal contamination (Chiaradia et al., 2009).

5.5.1.1 Magma volatile content and oxidation state

Late Cenozoic mineralized igneous rocks throughout Anatolia are hydrous and oxidized. Evidence includes hydrous mafic, titanite and iron oxide phenocrysts, high Ba/Ta and Fe^{3+}/Fe^{2+} and low $(Dy/Yb)_N$ ratios. The intrusive rocks that host porphyry and skarn mineralization in western Anatolia contain hornblende and biotite phenocrysts (2-11 %) that reflect their hydrous character, and pyroxene crystals (< 7 %) such as at Pınarbaşı, Kışladağ, Afyon and Bodrum

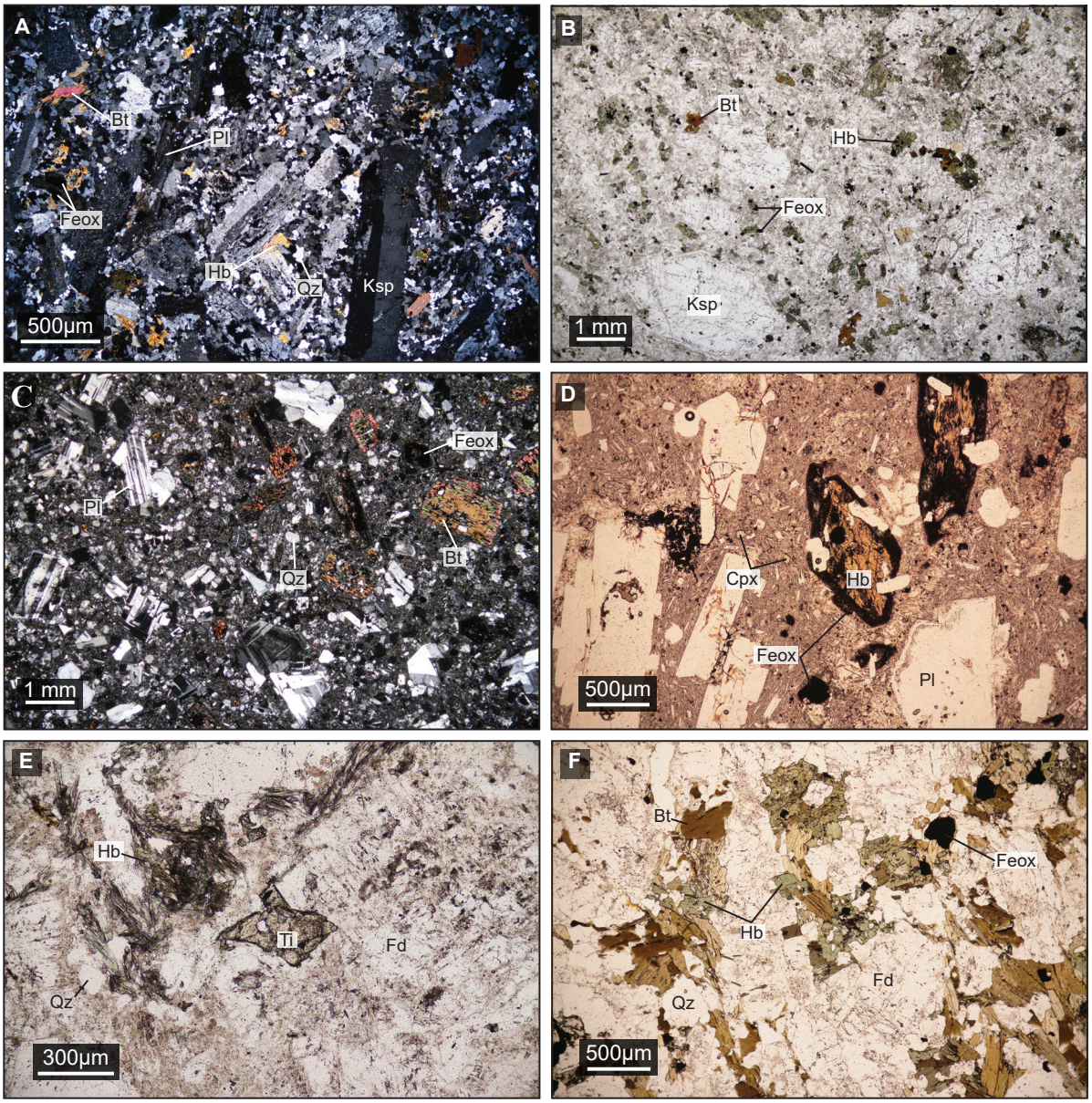

Figure 5.9 Optical microphotographs of representative rock texture and mineralogy from Anatolian fertile igneous rocks and highlighting the distribution of mafic phenocrysts (see Table D.1 for sample descriptions): A. Megacrystic monzonite, Afyon-Sandıklı porphyry Au-Cu prospect (FR-14-47; cross polarized light); B. Monzonite, Bodrum district (FR-15-32; plane polarized light); C. Biotite andesite, Konya district (FR-13-181; cross polarized light); D. Clinopyroxene andesite with Fe-oxide rims around hornblende crystals, Hasançelebi high-sulfidation epithermal Au-Ag prospect (FR-14-82; plane polarized light); E. Granite, Ağrı district (FR-14-143; plane polarized light); F. Monzodiorite, Ağrı district (FR-14-132; plane polarized light). Bt = biotite; Cpx = clinopyroxene; Fd = feldspar; Feox = iron oxide (magnetite and/or hematite); Hb = hornblende; Ksp = alkali feldspar; Pl = plagioclase; Qz = quartz; Ti = titanite.

(Figures 5.9A-B). In central Anatolia, the mafic mineralogy of hydrothermally-altered lavas is dominated by pyroxene (3-7 %) and minor biotite and hornblende phenocrysts (≤ 5 %; Figure 5.9C; Chapter 3), similar to their barren counterparts (e.g., Deniel et al., 1998). In contrast, the altered intrusive units in eastern Anatolia dominantly contain up to 20 % hydrous mafic phenocrysts (e.g., biotite and hornblende; Figures 5.9E-F) whereas the mafic mineralogy of the overlying and barren volcanic units are composed of both hornblende and pyroxene crystals (3-20 %; Keskin et al., 1998; Özdemir et al., 2006; Ekici et al., 2009; Özdemir, 2011; Chapter 3). Post-alteration igneous units can contain > 5 % pyroxene phenocrysts with or without hornblende such as at the Afyon-Sandıklı and Öksüt prospects, or regionally in eastern Anatolia; hornblende-rich (> 5 %) igneous rocks are typically mineralized throughout Anatolia. However,

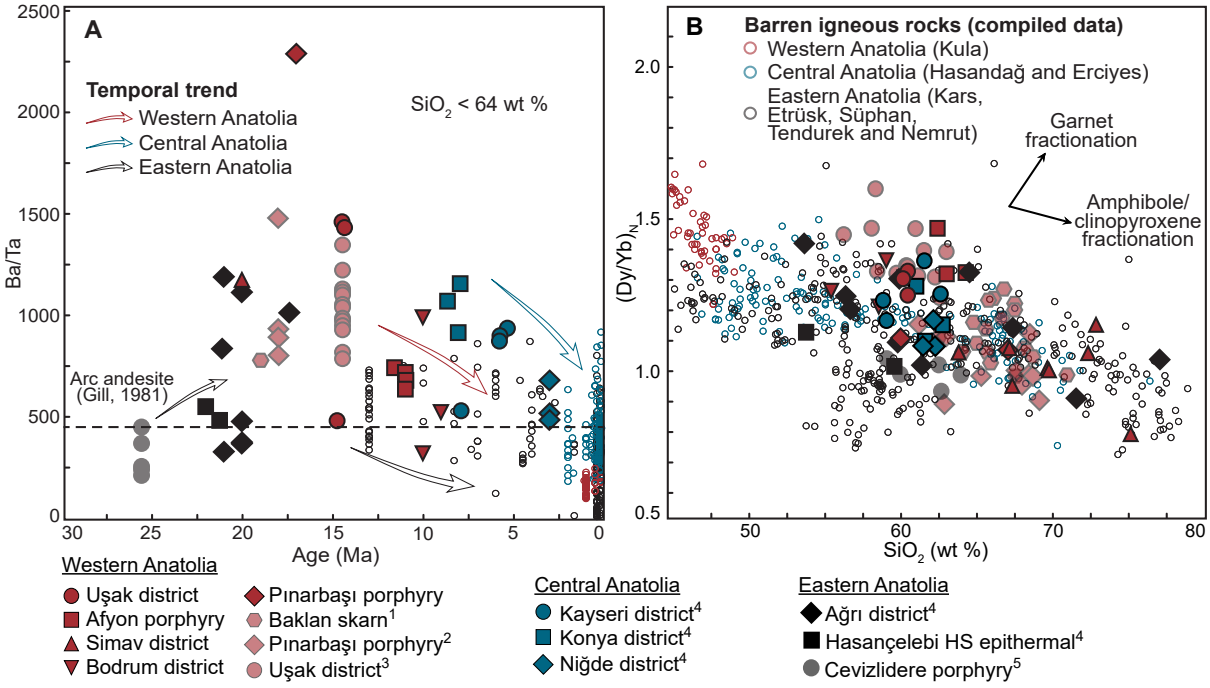

Figure 5.10 A. Ba/Ta versus age (Ma); the dashed line represents the composition of an arc-type andesite defined by Gill (1981) at Ba/Ta = 428; arrows represent temporal increase/decrease; only the mafic and intermediate igneous rocks are plotted (SiO_2 < 64 wt %) to minimize the effect of crustal contamination and fractionation; B. $(Dy/Yb)_N$ versus SiO_2 (Davidson et al., 2007). Data source for barren igneous rocks (small open circles): Pearce et al., 1990; Aydar et al., 1995; Notsu et al., 1995; Aydar and Gourgaud, 1998; Deniel et al., 1998; Kürkçüoğlu et al., 1998; Aydar and Gourgaud, 2002; Aydin, 2008 Keskin et al., 1998; Alıcı et al., 2002; Şen et al., 2003; Şen et al., 2004; Tokçaer et al., 2005; Keskin et al., 2006; Dogan et al., 2008; Güçtekin and Köprübaşı, 2009; Dilek and Altunkaynak, 2010; Ustunisik and Kilinc, 2011; Çubukçu et al., 2012; Dogan et al., 2013; Grützner et al., 2013; Aydin et al., 2014; Dogan, 2016; Lebedev et al., 2016 Aldanmaz, 2002; Özdemir et al., 2006; Özdemir, 2011; Aldanmaz et al., 2015; Peretyazhko et al., 2015; Oyan et al., 2016; Reid et al., 2017. References: [1]Aydoğan et al., 2008; [2]Delibaş et al., 2017; [3]Baker et al., 2016; [4]Chapter 3; [5]İmer et al., 2014.

the relative proportions of pyroxene and hydrous mafic minerals is not consistent along the Anatolian Trend. Hornblende, biotite and pyroxene crystals coexist without significant modal abundance variations between mineralized and barren igneous units. In addition, hornblende phenocrysts can be rimmed by clinopyroxene and Fe-Ti oxides in the Anatolian volcanic units (Figure 5.9D) due to volatile loss during magma ascent (Rutherford and Hill, 1993) such as at Kula (Alıcı et al., 2002), Konya (Temel et al., 1998a), Yamadağ (Ekici et al., 2009) and Hasandağ (Deniel et al., 1998).

Trace element ratios support the metasomatized character of late Cenozoic mineralized Anatolian igneous units. Those units, with the exception of the intrusive rocks from Cevizlidere in the Tunceli district, dominantly have high Ba/Ta ratios, which is an indicator of subduction-related metasomatism (Hickey et al., 1986), similar to arc-type andesite (Ba/Ta > 428; Gill, 1981) (Figure 5.10A). This ratio can also be high for the felsic rocks (SiO_2 > 64 wt %), which are not displayed on Figure 5.10A, because of crustal contamination and crystal fractionation. Conversely, the younger and barren igneous units have lower Ba/Ta and are thus less, or not, metasomatized. The drop of the Ba/Ta ratio between the early mineralized and late barren igneous units represents the loss of volatile content in the melting source through time (Hickey et al., 1986; Hildreth and Moorbath, 1988; Chapter 3). In eastern Anatolia, the increasing Ba/Ta ratio from the Oligocene to early Miocene likely reflects the additional contributions from the asthenospheric wedge and SCLM in volatiles prior to the slab break-off event. In addition, the negative correlation between $(Dy/Yb)_N$ and SiO_2 confirms the hornblende ± clinopyroxene fractionation and absence of garnet residue in the magma source (Figure 5.10B; Davidson et al., 2007) as interpreted above from the listric-shaped REE patterns for all the mineralized Anatolian igneous rocks (Figure 5.6).

The oxidized magmatic state of late Cenozoic Anatolian mineralized igneous rocks is confirmed by high Fe^{3+}/Fe^{2+} ratios (Figures 5.11A-B) and the ubiquitous presence of magnetite phenocrysts, and accessory titanite within some mineralized plutons in the Ağrı district (Figure 5.9). The Fe^{3+}/Fe^{2+} ratio of rocks decreases through time from 3.6-4.5 at ca. 8 Ma to 1.3-1.4 at

ca. 3 Ma in central Anatolia, and from 2.3 at ca. 21 Ma to 0.6 in the Ağrı district of eastern Anatolia (Figure 5.11C). In contrast, this Fe^{3+}/Fe^{2+} ratio decreases westwards from 1.46-4.4 at the easterly Afyon-Sandıklı porphyry Au (-Cu) prospect to 0.7 at the westerly Bodrum district (Figure 5.11D). However, the Fe^{3+}/Fe^{2+} ratios of mineralized igneous rocks are not significantly higher than barren volcanic units from mostly in western and eastern Anatolia (e.g., Kula, Süphan and Nemrut volcanic edifices). Nonetheless, an apparent temporal decrease of the magma oxidation state is observed in central Anatolia.

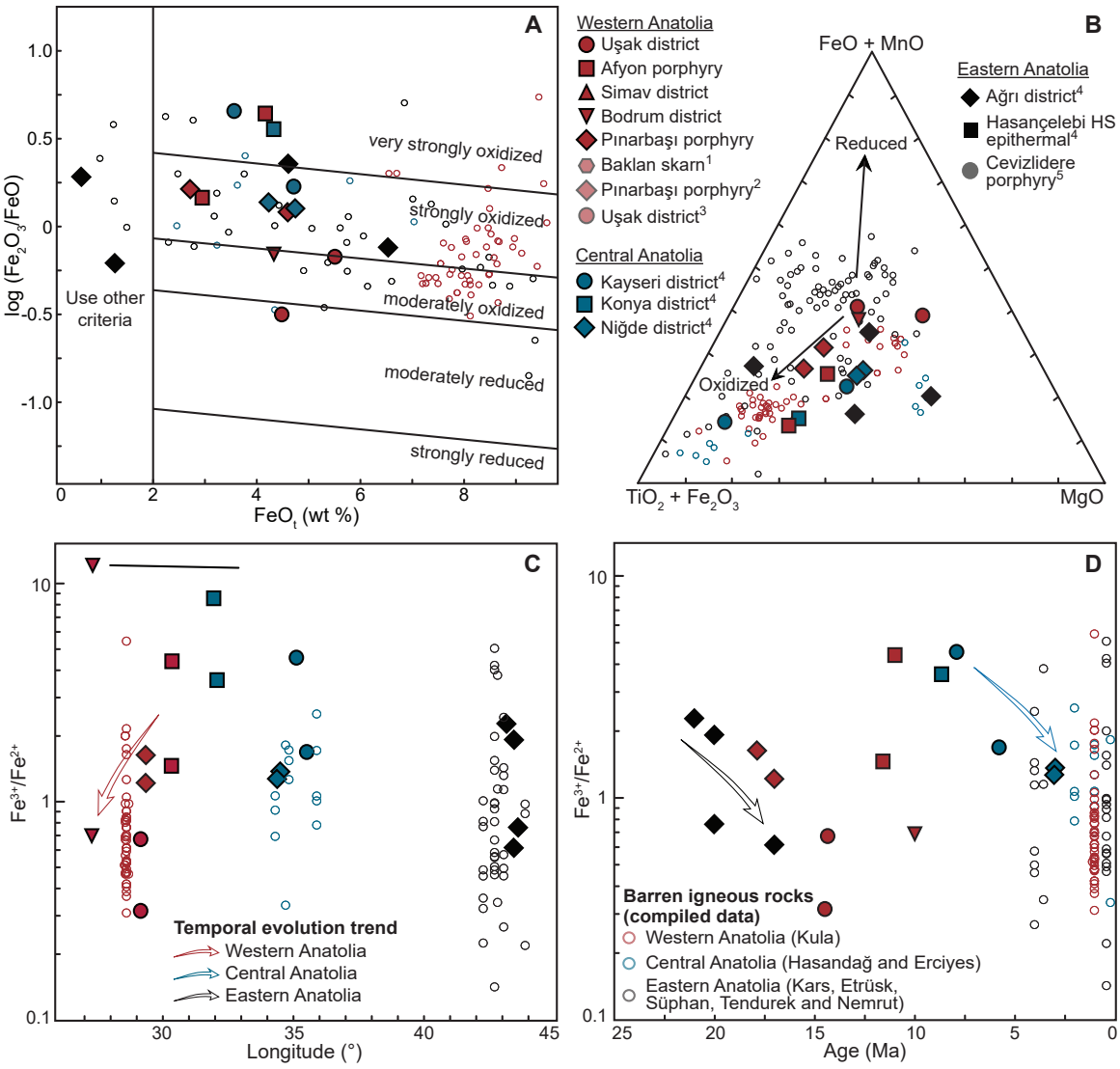

Figure 5.11 A. Total FeO content (FeO_t) versus log (Fe_2O_3/FeO) diagram (modified from Blevin, 2004) illustrating the redox affinity of fertile and barren Anatolian magmatism. Blevin (2004) recommends to use petrographic and magnetic criteria for rocks yielding a FeO_t content lower than 2 wt %; B. FeO + MnO-Fe_2O_3 + TiO_2-MgO ternary diagram (modified from Chappell and White, 1992); C. Fe^{3+}/Fe^{2+} versus longitude; D. Fe^{3+}/Fe^{2+} versus age. References: [1]Aydoğan et al., 2008; [2]Delibaş et al., 2017; [3]Baker et al., 2016; [4]Chapter 3; [5]İmer et al., 2014.

5.5.1.2 Early hornblende ± clinopyroxene fractionation

The late Cenozoic Anatolian igneous rocks that host porphyry, skarn and high-sulfidation epithermal mineralization are characterized by contrasting Sr/Y and La/Yb ratios, despite similar oxidation (Fe^{3+}/Fe^{2+}) and degree of metasomatism (Ba/Ta). In western Anatolia, mineralized igneous rocks younger than 15 Ma have Sr/Y ratios of ≥ 20 as opposed to their early Miocene counterparts (Figure 5.12A). This high Sr/Y ratio (≥ 20) implies hornblende crystallization under hydrous magmatic conditions that was accompanied by limited early plagioclase fractionation (Defant and Drummond, 1990; Richards et al., 2012). Those hydrous conditions are supported by the presence of hornblende and biotite phenocrysts, low $(Dy/Yb)_N$ and, to a lesser extent, elevated Ba/Ta ratios (see above). However, the relatively high Y content (≥ 15 ppm) excludes the possibility of garnet fractionation. In contrast, the mineralized igneous rocks in central and eastern Anatolia have Sr/Y ratios that are < 45 and indicate a weak adakitic-like signature, except a few non-adakitic rocks in the Ağrı district, whereas their barren counterparts are dominantly non-adakitic, particularly in central Anatolia (Figure 5.12B). The negative correlation of Sr/Y ratio with SiO_2 indicates plagioclase fractionation for both fertile and barren igneous suites in central and eastern Anatolia and for the early Miocene rocks in western Anatolia (Figures 5.12C-D). Conversely, the middle to late Miocene igneous rocks in western Anatolia have a positive correlation of Sr/Y ratios with SiO_2, which is controlled by the hornblende fractionation.

The La/Yb ratio versus Yb and SiO_2 diagrams show the same geochemical pattern in the corresponding rock groups as the Sr/Y ratio versus Y and SiO_2 diagrams, except that the mineralized igneous rocks in central and eastern Anatolia lack an adakite signature (5 < La/Yb < 25; Figure 5.13). Only the middle to late Miocene igneous rocks from western Anatolia yield high La/Yb ratios (> 25) as opposed to their early Miocene counterparts in western Anatolia (10 < La/Yb < 25), which reflect the fractionation of garnet, hornblende and titanite (Macpherson et al., 2006; Richards and Kerrich, 2007; Castillo, 2012). However, garnet fractionation in the melting source is ruled out again because of the high Yb content (≥ 1.5 ppm). The La/Yb ratio

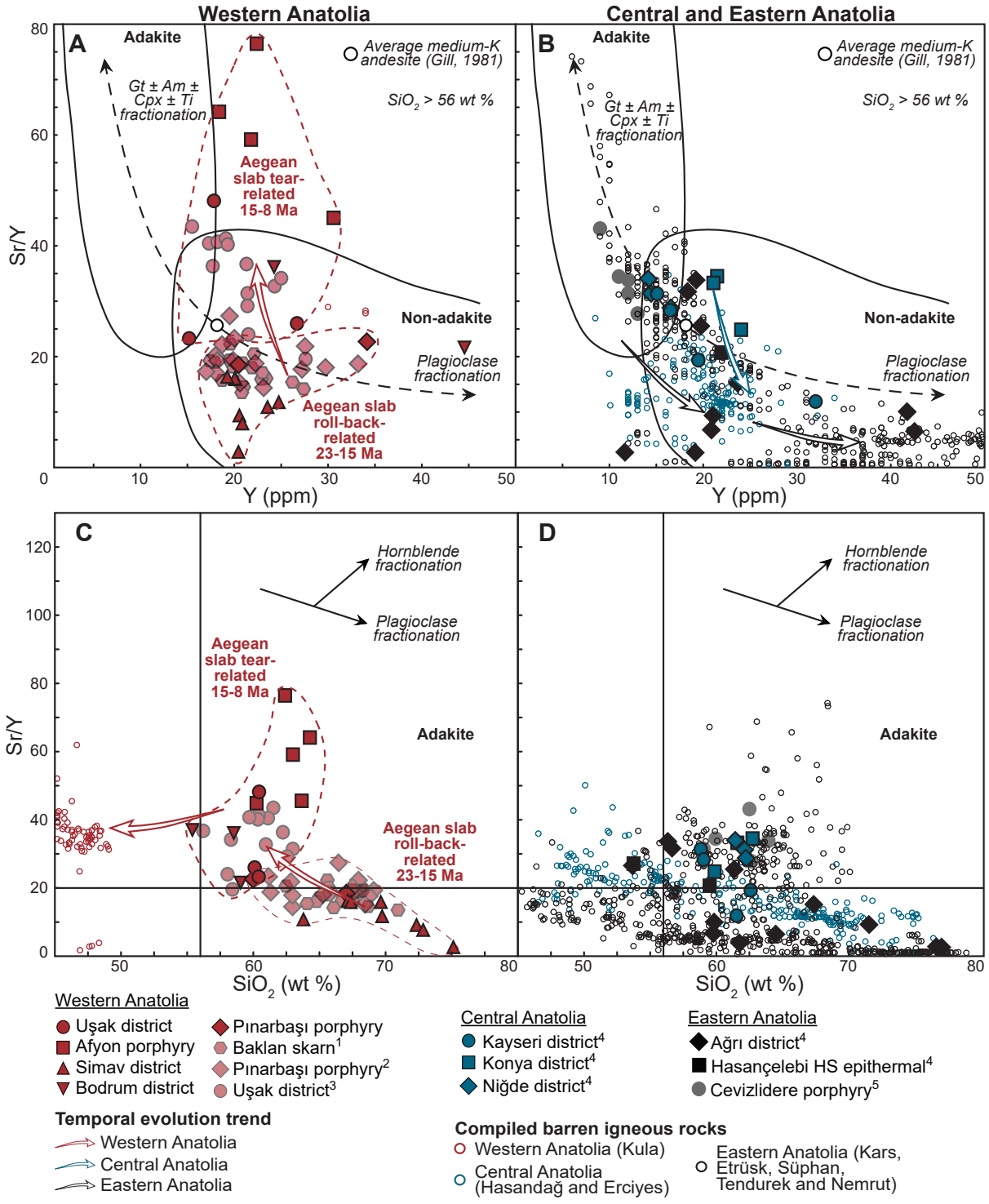

Figure 5.12 Sr/Y versus Y diagrams for western (A) and central and eastern Anatolia (B; fields and trends from Defant and Drummond (1990) and Richards and Kerrich (2007)); mafic igneous rocks are excluded ($SiO_2 \leq 56$ wt %); Sr/Y versus SiO_2 diagrams for western (C) and central and eastern Anatolia (D; Richards and Kerrich, 2007). Average andesite composition by Gill (1981); References: [1]Aydoğan et al., 2008; [2]Delibaş et al., 2017; [3]Baker et al., 2016; [4]Chapter 3; [5]İmer et al., 2014.

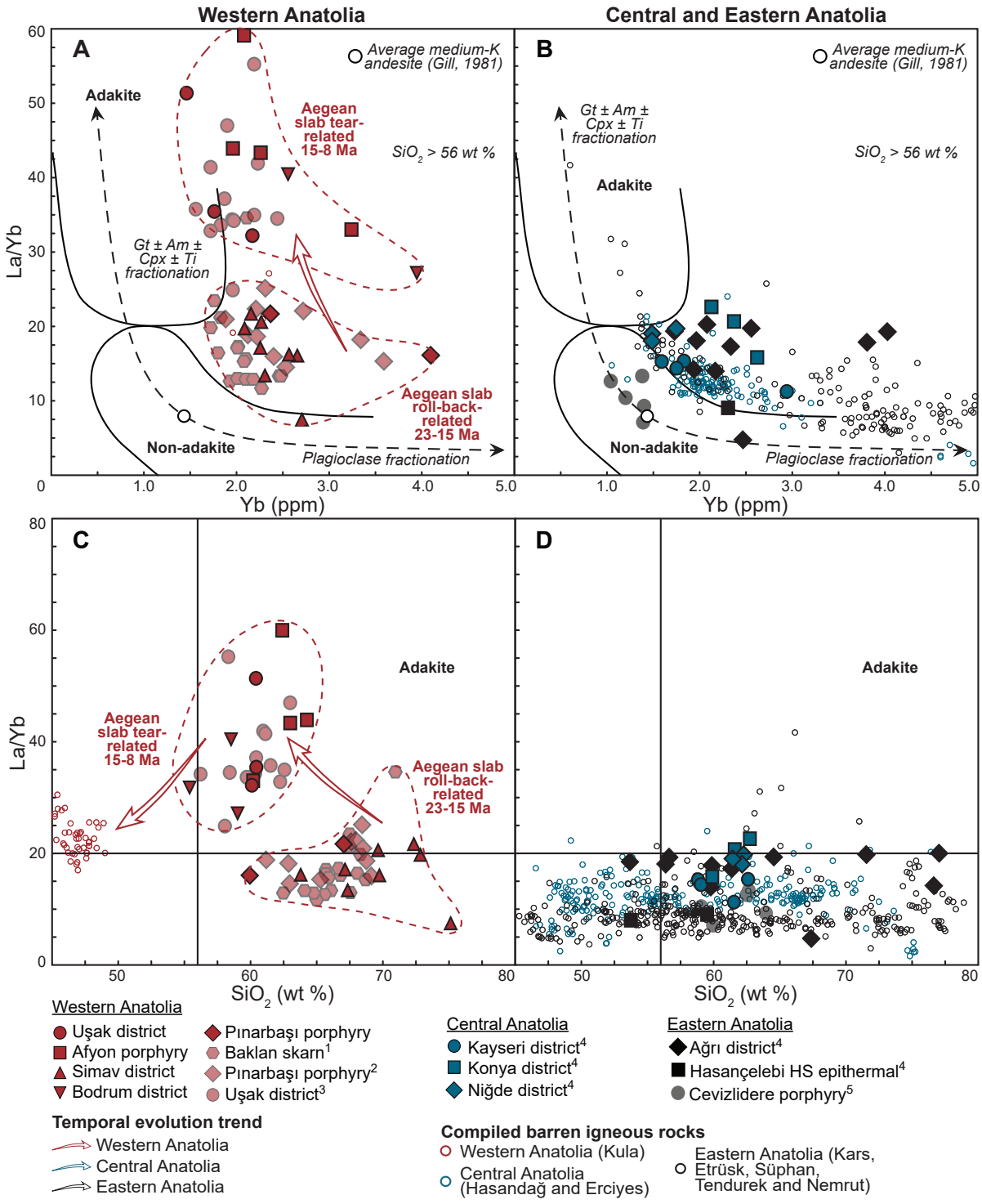

Figure 5.13 La/Yb versus Yb diagrams for western (A) and central and eastern Anatolia (B; fields and trends from Castillo et al. (1999) and Richards and Kerrich (2007); mafic igneous rocks are excluded ($SiO_2 \leq 56$ wt %); La/Yb versus SiO_2 diagrams for western (C) and central and eastern Anatolia (D; Richards and Kerrich, 2007). Average andesite composition by Gill (1981); References: [1]Aydoğan et al., 2008; [2]Delibaş et al., 2017; [3]Baker et al., 2016; [4]Chapter 3; [5]İmer et al., 2014.

fails to discriminate mineralized from barren rocks, in particular in central and eastern Anatolia.

To summarize, the middle to late Miocene adakitic-like igneous units in western Anatolia have the best geochemical indicators for magma fertility along the late Cenozoic Anatolian Metallogenic Trend. Conversely, the late Cenozoic igneous rocks in central and eastern Anatolia, and the early Miocene units in western Anatolia have less favorable geochemical features of magma fertility, despite the presence of outcropping hydrothermally-altered rocks in those regions. The lack of garnet fractionation indicators in the melting source suggests that melting likely occurred at depths below the spinel stability field throughout Anatolia (also see discussion in Chapter 3) without melt contributions from the subducting slab.

5.5.1.3 Magma alkalinity

The increase in magma alkalinity ($K_2O + Na_2O$) with time is typically observed in post-subduction tectonic settings (e.g., Liégeois et al., 1998; Maury et al., 2000; Coulon et al., 2002; Oyhantçabal et al., 2007). However, magma alkalinity does not vary significantly in central Anatolia (McNab et al., 2017), but slightly increases eastwards from central to eastern Anatolia where the crust is thicker (Chapter 3). Although the post-subduction mafic, alkaline igneous units along the Western Tethyan Orogenic Belt appear to be barren (Richards, 2015), the results presented herein do not show a significant alkalinity contrast between mineralized and barren igneous rocks, in particular in both western and central Anatolia (Figure 5.14A). The young and barren volcanic units in western and eastern Anatolia are characterized by a broader Na_2O range (1 to 9 wt %) than the early and mineralized igneous units ($2.4 < Na_2O < 7.4$ wt %; Figure 5.14B). The Na-rich lavas such as in Kula and Tendürek in western and eastern Anatolia result from OIB-like melts with limited contribution from the lithospheric mantle (Alıcı et al., 2002; Lebedev et al., 2016). In addition, the middle to late Miocene mineralized igneous units in western Anatolia are alkaline, in contrast to those in central Anatolia; barren rocks can also be either calc-alkaline or alkaline such as in the Pliocene and Quaternary in central and eastern Anatolia. Thus, magma alkalinity is not a robust fertility criterion. Yet, the igneous rocks with

Na_2O contents > 5 wt % are likely to be barren according to Figure 5.14B.

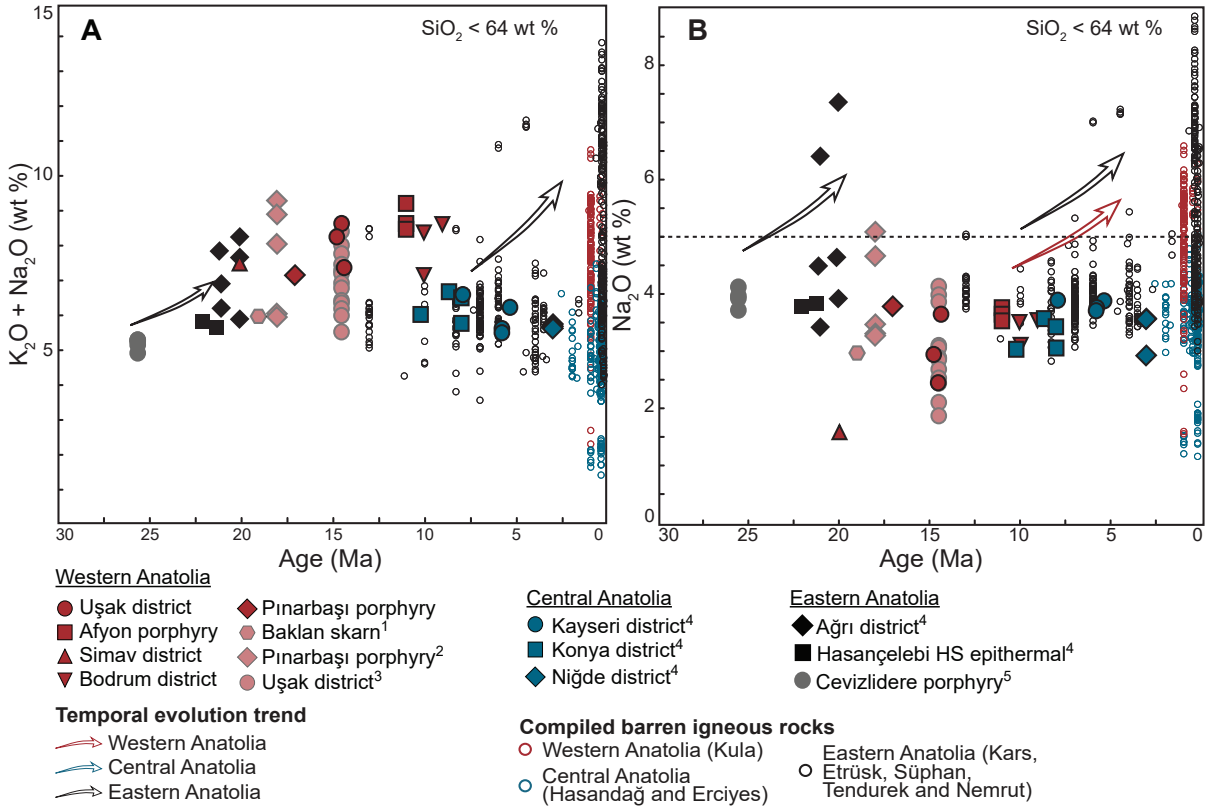

Figure 5.14 A. Alkalinity ($K_2O + Na_2O$) versus age; B. Na_2O versus age. The horizontal dashed line is the approximate maximum threshold for fertility ($Na_2O \leq 5$ wt %). Refer to Figures 5.3 and 5.10 for the references and symbols; only the mafic and intermediate igneous rocks are plotted ($SiO_2 < 64$ wt %) to minimize the effect of crustal contamination and fractionation; References: [1]Aydoğan et al., 2008; [2]Delibaş et al., 2017; [3]Baker et al., 2016; [4]Chapter 3; [5]İmer et al., 2014.

5.5.2 Slab segmentation, mantle dynamics and magma petrogenesis

5.5.2.1 Temporal evolution of magma fertility

The late Cenozoic mineralized igneous suites of Anatolia represent a small portion (ca. 8 %) of the total area covered by late Cenozoic magmatic complexes (Figure 5.2). Mineralized igneous units preferentially formed at the beginning of post-subduction tectono-magmatic events, and during back-arc development, from 21 to 9, 10 to 3, and 25 to 17 Ma in western, central and eastern Anatolia, respectively (Chapter 4). In western Anatolia, fertile magmatism produced the mineralized intermediate igneous suites in Afyon, Uşak and Bodrum areas in the middle to late Miocene (15-9 Ma). This period of fertile magmatism is bracketed by the early Miocene, back-arc-related, mineralized felsic igneous units of the Simav district (21-17 Ma)

that appear to geochemically be less fertile according to low Sr/Y and La/Yb ratios (Figure 5.15A-B), and the Pliocene to Quaternary, barren, OIB-like, mafic lavas of the Kula complex. Oligocene to Miocene mineralized igneous rocks in central and eastern Anatolia are characterized by indicators of low magma fertility, such as low Sr/Y and La/Yb ratios, for porphyry mineralization, despite the presence of numerous high-sulfidation epithermal- and porphyry-style occurrences (Chapter 4). The contrast between the field observations and the geochemical signatures of igneous host rocks confirms that both high Sr/Y and La/Yb magmas are not a prerequisite for the formation of porphyry systems (Richards and Kerrich, 2007; Chiaradia et al., 2012). Most of the Pliocene to Quaternary volcanic rocks are barren and show a geochemical evolution towards less, or not, metasomatized (lower Ba/Ta ratio) and slightly less oxidizing magmatic conditions that are increasingly less favorable for the formation of porphyry and associated epithermal mineralization.

Nonetheless, among all of the magma fertility criteria for porphyry mineralization, the Ba/Ta (Figure 5.10A) and Sr/Y ratios (Figure 5.15A), SiO_2 (Figure 5.4C) and Na_2O contents (Figure 5.14B), and initial ε_{Nd} values (Figure 5.15C) effectively discriminate between fertile and barren igneous rocks in Anatolia. In contrast, the La/Yb ratio only discriminates in western Anatolia (Figure 5.15B), whereas magma alkalinity ($K_2O + Na_2O$; Figure 5.14A) and oxidation state (Fe^{3+}/Fe^{2+}; Figure 5.11C-D) lack obvious contrasting signatures between mineralized and unmineralized igneous units in Anatolia. The initial ε_{Nd} values clearly indicate that the fertile igneous rocks have a lithospheric component (initial $\varepsilon_{Nd} \leq 1$) whereas barren igneous units result from mantle (asthenosphere)-dominant melts (initial $\varepsilon_{Nd} > 1$; Figure 5.15C). Given that the fertile igneous rocks were emplaced at the beginning of the regional magmatic cycle (Chapter 4), the transition from lithosphere- to asthenosphere-dominant magmas reflects the increasing interaction of lithosphere- with asthenosphere-derived melts, regardless of crustal thinning (west) or thickening scenario (central-east). Thus, the asthenospheric upwelling through the Arabian slab break-off at ca. 25 Ma (Chapter 2) and Aegean slab tear at ca. 15 Ma (Jolivet et al., 2015) initiated the production of fertile magmas by remobilizing the

metasomatized, metal-bearing SCLM domains. Subsequently, the fertile magmas were diluted and replaced by barren, drier and slightly less oxidized asthenospheric melts due to the exhaustion of metasomatic components.

In addition, the apparent increase in magma fertility from the early to middle Miocene in western Anatolia is accompanied by higher $(Sm/Yb)_N$ ratios that represent the greater involvement of hornblende fractionation, probably influenced by greater residence time in the lower or mid-crust (this Chapter), and possibly deep melts (Figure 5.15D; Prelević et al., 2012). Increasing $(Sm/Yb)_N$ ratios through time result from sub-slab mantle infiltration during the Aegean slab tear between 15 and 8 Ma (Jolivet et al., 2015). The prolonged asthenospheric heating and crustal thinning gradually led to the shallow melting source as represented by decreasing $(Sm/Yb)_N$ ratios since the middle Miocene. In central and eastern Anatolia, melting occurred at shallow depths with limited fractionation of hornblende to account for the low and relatively constant $(Sm/Yb)_N$ ratios. The tectonic scenarios along the Anatolian Trend contrast with the Andean and Iranian orogenic processes where crustal thickening and deeper melting sources to the garnet stability field were involved and ultimately led to more favorable conditions for magma maturation and fertility for large Cu-rich porphyry systems (e.g., Kay and Mpodozis, 2001; Richards, 2003; Chiaradia et al., 2009; Shafiei et al., 2009).

5.5.2.2 Metal and magma source(s)

Metal sources in post-subduction settings include the SCLM fertilization by asthenosphere-derived low-degree partial melts (Pettke et al., 2010; Mair et al., 2011; Hronsky et al., 2012; Griffin et al., 2013), subduction-modified cumulates in the lower crust as artifacts of previous cycles of arc magmatism (Chiaradia et al., 2009; Richards, 2009) and/or juvenile lower crust after arc magma underplating (Hou et al., 2009; Shafiei et al., 2009). Trapped Au-rich residual sulfides from previous subduction cycles may be available for subsequent remobilization during post-subduction or post-collisional tectonic and thermal events (Solomon, 1990; Richards, 2009) under oxidized conditions (Jugo, 2009) such as slab tear or break-off events (Lips, 2002; Wang et al., 2006; Vos et al., 2007; Hou et al., 2009; Logan and Mihalynuk,

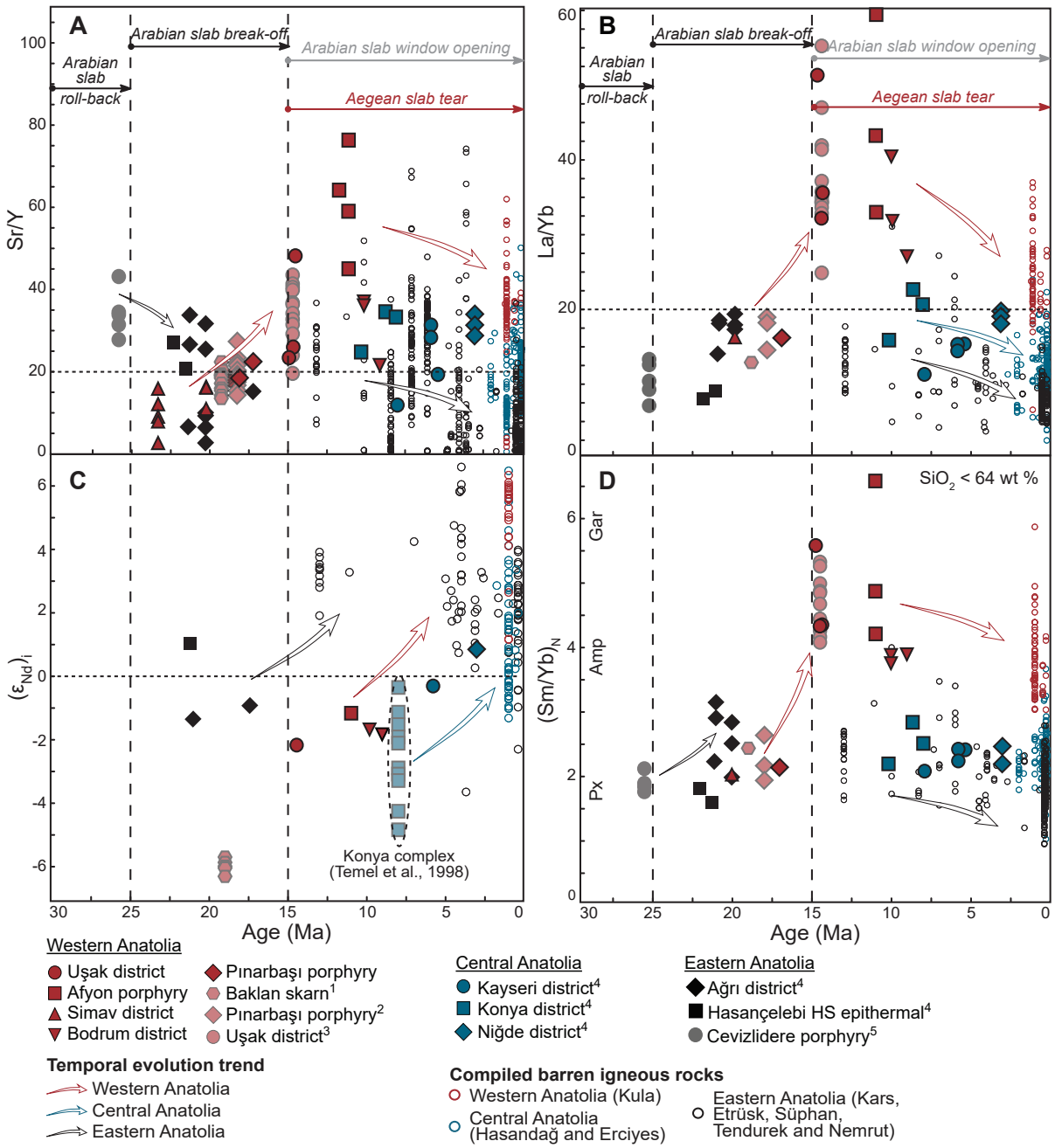

Figure 5.15 Age versus Sr/Y (A), La/Yb (B), $(\varepsilon_{Nd})_i$ (C) and $(Sm/Yb)_N$ (D; base diagram from Kay and Mpodozis (2001); Px = pyroxene; Amp = amphibole; Gar = garnet); timing of tectonic episodes are from Chapter 2 and Jolivet et al. (2015); Refer to Figures 5.3 and 5.10 for the references and symbols; only the mafic and intermediate igneous rocks are plotted (SiO_2 < 64 wt %) in the diagram 5.15D to minimize the effect of crustal contamination and fractionation; References: [1]Aydoğan et al., 2008; [2]Delibaş et al., 2017; [3]Baker et al., 2016; [4]Chapter 3; [5]İmer et al., 2014.

2014). Thus, the formation of porphyry deposits in post-subduction settings depends on the effectiveness of remobilization and the composition of remobilized material.

The previously metasomatized SCLM was the major source of Neogene magma throughout Anatolia and melted during back-arc, slab roll-back, tear (western Anatolia; Prelević et al., 2012; Ersoy and Palmer, 2013) and break-off events (central and eastern Anatolia; Chapter 3). Metasomatism of the Anatolian SCLM likely occurred during the Late Cretaceous to Eocene period based of Lu-Hf residence time calculation (Reid et al., 2017), possibly through a shallow subduction episode (Prelević et al., 2010, 2012), and perhaps during the Neoproterozoic based on regional Nd model ages (Pe-Piper and Piper, 2001; Chapter 3). Magma contributions from the lower crust were suggested in western (Ersoy et al., 2012a; Karaoğlu and Helvacı, 2014) and eastern Anatolia (Keskin et al., 2006; Oyan, 2018) but not in central Anatolia (McNab et al., 2017). However, the geochemical results on fertility of igneous rocks presented herein indicate the lack of garnet fractionation in the melting process, the low Sr content, except in the middle to late Miocene in western Anatolia, and highly variable initial $^{87}Sr/^{86}Sr$ ratios. Taken together, those results suggest a minor role of the lower crust and subducting slab melting on magma generation as opposed to the spinel-facies SCLM and upper crustal contamination. Nonetheless, middle to late Miocene magmas in western Anatolia may have stalled in the lower and/or mid-crust to accumulate hydrous magmas at depth and evolve through hornblende and pyroxene fractionation (high Sr/Y and La/Yb ratios) in the absence of garnet residue to become more fertile.

The high Au:Cu ratio of porphyry systems in western Anatolia is explained by the alkaline affinity of their causative igneous rocks, previously metasomatized SCLM magma source (Müller and Groves, 1993; Jensen and Barton, 2000; Müller, 2002; Hronsky et al., 2012), possible contribution from remelted Au-rich sulfide residues (Richards, 2009; Menant et al., 2018), crustal thinning in back-arc and slab tear settings (De Boorder et al., 1998; Menant et al., 2018), and their shallow emplacement depth (Murakami et al., 2010; Chapter 4).

The compressional regime, calc-alkaline magma affinity and greater crustal thickness

in central and eastern Anatolia would have enhanced the potential for Cu-rich porphyry systems like in the Lesser Caucasus (Moritz et al., 2016b) and northwest Iran (Hezarkhani, 2006; Aghazadeh et al., 2015). However, the geochemical signature of the igneous rocks in central and eastern Anatolia suggests that these rocks are less favorable for porphyry mineralization, despite the presence of porphyry occurrences in the Ağrı and Tunceli districts. The contrast between the metasomatized and oxidized character of those mineralized magmas (high Ba/Ta and Fe^{3+}/Fe^{2+} ratios) and their lack of evidence for significant early hornblende fractionation (low to moderate Sr/Y and La/Yb ratios) in central and eastern Anatolia likely results from the relative short residence time in the lower or mid-crust. In addition, the majority of porphyry deposits in eastern Anatolia formed in the Late Cretaceous and Eocene (Kuşcu et al., 2013) implying that there was less-fertile material to remobilize from the SCLM and/or lower crust during the late Cenozoic. Nonetheless, the prevailing high-sulfidation epithermal occurrences in central and eastern Anatolia suggest that some mineralized porphyry orebodies may be present but are not yet exposed.

5.5.2.3 Progressive loss of the SCLM and migration of melting loci

The post-slab break-off, long-lived, asthenospheric heating to the SCLM base coupled with the dehydration of the broken-off slab triggered SCLM instability and its removal by convective dripping in the late Miocene under central and eastern Anatolia (Figure 5.16; Chapter 3). The geochemical evolution of western Anatolian igneous units also indicates significant lithosphere-asthenosphere interactions that led to the conversion of the lower parts of the SCLM into asthenosphere by heating and dripping between 20 and 12 Ma (Prelević et al., 2012). The SCLM thinning event was triggered by asthenosphere upwelling during slab roll-back and tearing tectonic events (Alıcı et al., 2002; Prelević et al., 2012). The current thin SCLM beneath Anatolia is confirmed by tomographic imaging (Angus et al., 2006; Gök et al., 2007; Çakır and Erduran, 2011; Kind et al., 2015; Komut, 2015; Delph et al., 2017; Oruç et al., 2017). Thus, SCLM-asthenosphere interactions mixed the highly and poorly hydrated (contrasting Ba/Ta ratios), lithospheric- and asthenospheric-derived (contrasting initial εNd

values), metal-enriched and metal-depleted materials at the lithosphere-asthenosphere boundary. This interaction led to the production of weakly fertile to barren magmas at shallow depths in the spinel-facies stability field (low $(Sm/Yb)_N$ ratio; Chapter 3). The SCLM thinning or removal through time results in a decrease of magma fertility and metal endowment. (e.g., Hronsky et al., 2012; Gessner et al., 2017).

The late Cenozoic fertile magmatism in Anatolia is limited in volume, formed relatively early during the regional magmatic cycle, and was widely distributed throughout the belt, as opposed to widespread barren magmatism (Figure 5.2). Many mineralized igneous complexes were subsequently (partially) covered by barren lavas and pyroclastic deposits throughout the

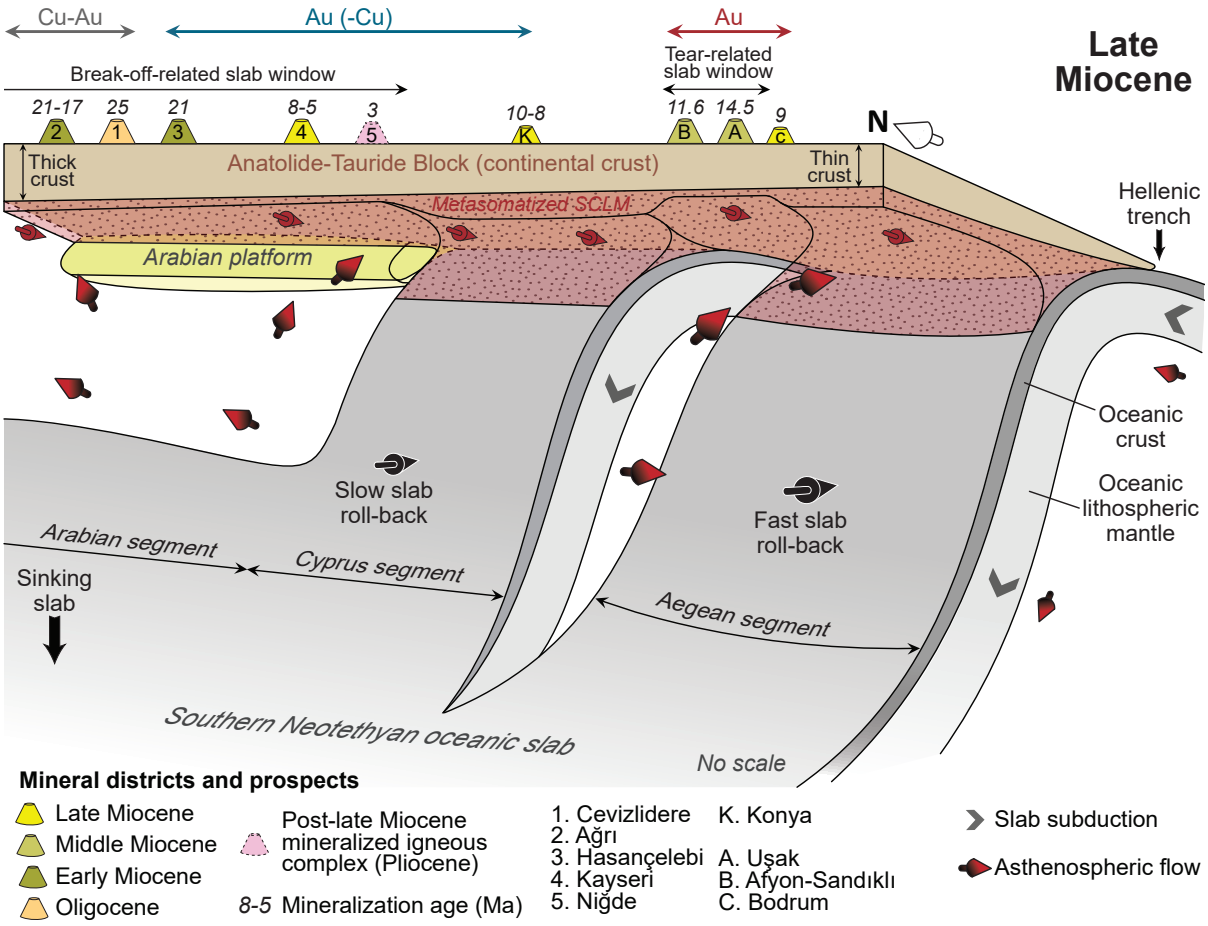

Figure 5.16 3D cartoon of the segmentation of the Southern Neotethyan oceanic slab in the late Miocene due to the easterly slab break-off and westerly slab tear events (inspired from Menant et al., 2018 and Chapter 2, and based on tomographic interpretations (Biryol et al., 2011) in Figure 5.1). The opening of slab windows induced toroidal (west) and poloidal (east) asthenospheric flow fields that gradually eroded the metasomatized subcontinental lithospheric mantle (SCLM) beneath the Anatolide-Tauride Block.

Anatolian Metallogenic Trend as confirmed by field observations in Chapter 4. Porphyry deposits are scarce and likely covered in central and eastern Anatolia and conversely, some were likely removed by extreme crustal extension and uplift in western Anatolia. In addition, the significant crustal extension in western Anatolia, the frontal continental collision in the east and the absence of orogen-oblique transtensional fault systems in Anatolia could also explain the limited exposure of fertile magmatism in this region. In contrast, the dominant porphyry copper provinces along the Western Tethyan Orogenic Belt formed along orogen-parallel translithospheric structures that facilitated the ascent and emplacement of fertile magma in the upper crust (Tosdal and Richards, 2001) as observed in the Balkans (Gallhofer et al., 2015; Menant et al., 2018), Lesser Caucasus (Moritz et al., 2016b) and Iran (Allen et al., 2004; Safari et al., 2015; Fonseca et al., 2016).

Segmentation of the Southern Neotethyan oceanic slab after the onset of the Arabian continental collision in the Oligocene caused the spatial and temporal migration of the magmatic front and thereby hindered the long-term focusing of heat source, magma production, accumulation and maturation. Instead, the increasing rate of the Aegean slab roll-back in western Anatolia and slab window opening in central and eastern Anatolia promoted the spreading of the partial melting zone beneath Anatolia (e.g., Kaislaniemi et al., 2014; Menant et al., 2018). Although SCLM instability is typically required to produce gold deposits in post-subduction and post-collisional settings (Bierlein et al., 2009; Richards, 2009; Hronsky et al., 2012; Griffin et al., 2013; Richards, 2015), the upwelling of hot and dry asthenosphere not only triggers the metallogenic peak but also progressively reduces the production of fertile magma such as in Anatolia during the late Cenozoic.

5.6 Conclusion

Widespread late Cenozoic magmatism along the Anatolian Metallogenic Trend hosts many gold-rich porphyry- and epithermal-style systems that preferentially formed with intermediate hypabyssal and extrusive rocks that range in composition from andesite to trachyte and their plutonic equivalents. The new geochemical analyses from mineralized igneous rocks

in western Anatolia (this Chapter) and central and eastern Anatolia (Chapter 3) suggest that the SiO_2 (61.8 ± 5.5 wt %) and Na_2O (2.4 to 7.4 wt %) contents, Sr/Y (> 20) and Ba/Ta ratios (> 428) and initial ε_{Nd} values (≤ 1) are the geochemical criteria that best indicate magma fertility of the late Cenozoic post-subduction igneous suites along the Anatolian Metallogenic Trend. Conversely, magma alkalinity ($K_2O + Na_2O$ and K_2O/Na_2O ratio), La/Yb ratio and oxidation state (Fe^{3+}/Fe^{2+}) do not effectively distinguish mineralized from unmineralized igneous units in Anatolia.

The geochemical indicators for magma fertility evolve through time along the late Cenozoic Anatolian Metallogenic Trend. In western Anatolia, magma fertility is optimal in the middle to late Miocene igneous rocks (15-9 Ma), after the less-fertile early Miocene, weakly mineralized, syn-tectonic magmatism (21-18 Ma) and before the Pliocene to Quaternary, OIB-like, barren mafic lavas of the Kula complex. In eastern and central Anatolia, magma is fertile at the beginning of the regional magmatic cycles at 26 and 12 Ma, respectively. However, geochemical indicators for magma fertility in eastern and central Anatolia are weak compared to the middle to late Miocene igneous rocks in western Anatolia, and gradually evolve towards less hydrous, less oxidized, shallowly-produced and mantle-dominant magmas.

The geochemical character of Anatolian fertile magmas is due to hornblende ± clinopyroxene and plagioclase fractionation in the absence of garnet residue to account for low $(Sm/Yb)_N$ and $(Dy/Yb)_N$ ratios, and Sr contents. Although magmatic contributions from the lower crust were suggested for western and eastern Anatolia (Ersoy et al., 2012a; Oyan, 2018), the metasomatized Anatolian SCLM is herein shown to be the major source of fertile magmas. The thinning of the SCLM during post-subduction tectonic events is controlled by the asthenospheric upwelling that progressively converts the SCLM to asthenosphere by heating.

The spatial migration of slab rupture, slab window opening and mantle flow hinders the maturation, long-lived heating and stabilization of the magma production loci. The progressive loss of SCLM, volatile contents and migration of the melting source regions, and possible short crustal residence time ultimately lead to the reduction of magma fertility through time. Fertile

magmatism produced small and sparse magmatic complexes and associated porphyry and epithermal systems such as along the Anatolian Trend. Thus, the segmentation of the Southern Neotethyan oceanic slab triggered asthenosphere upwelling that initiated the formation of porphyry and epithermal deposits along the Anatolian Trend, and subsequently contributed to the annihilation of the fertile magma production.

Chapter 6: Conclusions

Results and contributions from the research work presented in this dissertation reveal that late Cenozoic magmatism and associated magmatic-hydrothermal precious and base metal mineralization throughout Anatolia resulted from post-subduction slab rupture events, including tearing and break-off. Field, petrographic, geochronological and geochemical data acquired and compiled during this PhD research work provide new insights into the geodynamic evolution of the Eastern Mediterranean region, and post-subduction tectonics, magmatism and metallogeny, exemplified by the Anatolian case study.

6.1 Part 1: Temporal, spatial and geochemical evolution of late Cenozoic magmatism along the Eastern Anatolian Magmatic Belt

The determination of late Cenozoic metallogenic processes in Anatolia required the definition of a robust tectono-magmatic framework, in particular in central and eastern Anatolia where many models have been proposed and disputed (e.g., Keskin, 2007; Şengör et al., 2008; Bartol and Govers, 2014; Govers and Fichtner, 2016; Delph et al., 2017). The extensive compilation, integration and interpretation of previously-published geochronological and geochemical data from late Cenozoic igneous rocks done in this study allowed to define the timing and geochemical characteristics of 26 igneous complexes in central and eastern Anatolia. The compiled databases were complemented and strengthened by a few new U-Pb zircon dates, and lithogeochemical and radiogenic Sr-Nd-Pb isotope data from the less-studied Konya, Karaman, Melendiz, Tekkedağ, Develidağ, Yamadağ and Ağrı igneous complexes.

6.1.1 Definition of the Eastern Anatolian Magmatic Belt

The temporal and spatial constraints on late Cenozoic magmatism in central and eastern Anatolia (Chapter 2) highlight the westward migration (48 mm/year) of the magmatic front from eastern (21-15 Ma) to central Anatolia (12 Ma-Present). The narrow E- to NE-trending alignment of igneous complexes is defined in this dissertation as the Eastern Anatolian Magmatic Belt that links the central and eastern Anatolian magmatic domains, which were

studied independently in the literature. The newly-defined Eastern Anatolian Magmatic Belt is interpreted to form in response to sub-horizontal rupture propagation of the subducting Southern Neotethyan oceanic slab and resulting asthenospheric flow since ca. 25 Ma after the onset of the Arabia-Eurasia continental collision at ca. 30 Ma, in accordance with large-scale tomography and numerical modeling studies (e.g., Biryol et al., 2011; Menant et al., 2016). The brief late Oligocene magmatic pulse (26-25 Ma) resulted from slab steepening event (30-25 Ma) subsequent to initiation of the Arabia-Eurasia continental collision, and was delayed a few millions years during slab weakening and break-off. Magmatism was active a few million years after the slab rupture initiation and began earlier than previously documented, specifically in the early Miocene (21 Ma) in eastern Anatolia. Slab break-off-related magmatism was subsequently covered by the volcanic products of the Erzurum-Kars plateau since ca. 13-11 Ma in eastern Anatolia, previously interpreted as a result of the lithospheric mantle removal (Keskin, 2003, 2007; Şengör et al., 2008).

6.1.2 Slab break-off-related magmatism

Interpretations in Chapter 2 suggest that the late Cenozoic magmas in the Yamadağ, Ağrı and Sivas areas in eastern Anatolia emplaced in the upper crust between 21 and 15 Ma, during the slab break-off event (25-16.5 Ma). Those slab break-off-related igneous complexes share similar magmatic features (Chapter 3) including 1) a temporal increase in the depth of melting, degree of enrichment and asthenospheric component; 2) general consistency in magma alkalinity; 3) a decreasing subduction signature through time. Magma was generated by the melting of the previously-metasomatized Anatolian SCLM and asthenosphere by decompression, which was largely controlled by the slab rupture propagation and break-off, and ingress of Arabian and African subslab asthenosphere.

Although early to middle Miocene eastern Anatolian magmatism formed in response to the sub-horizontal slab rupture propagation, middle Miocene to Present magmatism in central Anatolia, with the exception of the Konya and Sulutas volcanic complexes, resulted from slab window opening and the lateral sub-slab mantle flow from eastern Anatolia. This mantle flow

initiated when the sub-horizontal slab rupture reached the northwestern edge of the Arabian continental lithosphere in the middle Miocene. Therefore, slab break-off-related magmatism in central Anatolia is the less mature equivalent (i.e., more metasomatized, less alkaline and less-pronounced asthenospheric component) than that in eastern Anatolia. The magmatic activity was accompanied by slab break-off-related crustal uplift that started at ca. 23 Ma in eastern Anatolia (Karaoğlan et al., 2016), and propagated westwards to reach central Anatolia at ca. 15-7 Ma (Cosentino et al., 2012; Schildgen et al., 2014; Karaoğlan et al., 2016; McNab et al., 2017).

6.1.3 SCLM removal-related magmatism

The presence of water and the sustained advection of asthenospheric heat destabilized the thickened Anatolian SCLM root, leading to its removal by small-scale sublithospheric convection and the second major magmatic event since ca. 13-11 Ma in eastern Anatolia (Kaislaniemi et al., 2014; Neill et al., 2015; Chapter 2). The compilation and integration of previously-published age data (Chapter 2) indicate that this young magmatic phase, which produced the middle Miocene to Pliocene Kars-Erzurum volcanic plateau and Pliocene to Quaternary stratovolcanoes in eastern Anatolia, is distinct in time from the earlier slab break-off-related magmatic event; both phases are separated by a brief hiatus between ca. 15 and 13 Ma. In addition, the interpretation of compiled geochemical analyses and integration of previous petrological models in Chapter 3 suggest that this SCLM removal-related magmatism was characterized by 1) increasing contributions from the crust; 2) drier mantle source conditions, even though subduction signature was still recorded in some Quaternary stratovolcanoes (e.g., Ararat); 3) coexistence of highly alkaline, silica-undersaturated (e.g., the Tendürek stratovolcano) and calc-alkaline, silica-saturated magmatism (e.g., the Ararat stratovolcano); 4) decreasing depth of mantle sources.

To summarize, results in Part 1 indicate that late Cenozoic magmatism in central and eastern Anatolia formed in two distinct phases that exhibit different timing and geochemical signatures but overlap in space, in particular in eastern Anatolia. Spatial migration of slab

break-off-related magmatism and temporal shift in magma composition are controlled by the slab dynamics beneath Anatolia, long-lived asthenospheric heating, which began earlier in eastern Anatolia, and lithospheric thickness.

6.1.4 Implications for the geodynamic evolution of the Eastern Mediterranean region

One of the key features in Chapter 2 is that slab break-off was initiated in eastern Anatolia (ca. 25 Ma) before development of the slab tear in western Anatolia (15 Ma; van Hinsbergen, 2010; Jolivet et al., 2015). The westward propagation of the sub-horizontal slab rupture stopped at the northwesternmost edge of the Arabia plate at ca. 19.5-16.5 Ma. It is suggested in Chapter 2 that this slab break-off event contributed to the acceleration of the Aegean slab roll-back and North Anatolian fault zone development in the middle-late Miocene because of the lateral continuity of the Southern Neotethyan slab in the mantle and additional slab pull force (Faccenna et al., 2006). Thus, this slab break-off in eastern and central Anatolia may also have contributed to the slab tear initiation between the Aegean and Cyprus slabs (15-8 Ma; van Hinsbergen, 2010; Jolivet et al., 2015), the initiation of the Cyprus slab roll-back since the early Miocene (Biryol et al., 2011; Koç et al., 2012), SCLM removal in eastern Anatolia in the late Miocene (e.g., Neill et al., 2015; Topuz et al., 2017), and the production of the widespread late Cenozoic magmatism in central and eastern Anatolia (Chapters 2 and 3).

This study emphasizes that the geochemical signature of post-subduction, syn-collisional magmatism, as recorded by primitive basalts, constantly evolves through time and space, and recorded shifts in mantle source domains. Anatolia is thereby a natural laboratory to investigate the complex geochemical evolution of post-subduction magmatism, controlled by the three-dimensional subducted slab dynamics, asthenosphere upwelling and change in lithosphere thickness.

6.2 Part 2: Late Cenozoic Anatolian gold metallogeny

The complex tectono-magmatic evolution of the Anatolide-Tauride Orogenic Belt during the late Cenozoic was responsible for the production of fertile magmas that formed

gold-rich porphyry and epithermal mineralization throughout Anatolia. The second part of this dissertation characterizes those gold-rich mineral deposits, constrains the timing of gold mineralization, and determines the petrogenetic controls on fertile magmatism. This study is based on the acquisition of new geochronological and geochemical data from mineralized systems in western (Kepez, Eğrigöz, Pınarbaşı, Kışladağ, Afyon-Sandıklı, Kadıkalesi and Karatoprak), central (Inlice, Doğanbey, Boz Tepe, Çömlekçı, Başdere, Öksüt) and eastern Anatolia (Hasançelebi, Taşkapı and Taşlıçay). Additional data from the Pınarbaşı (Delibaş et al., 2017), Baklan (Aydoğan et al., 2008), Kışladağ (Baker et al., 2016) in western Anatolia and Cevizlidere mineralized systems in eastern Anatolia (İmer et al., 2014) are integrated to the new geochronological and geochemical data sets.

6.2.1 Characterization of late Cenozoic Anatolian mineral districts

The E-trending alignment of the late Cenozoic porphyry, epithermal and skarn occurrences, prospects and deposits in Anatolia is defined in Chapter 4 as the late Cenozoic Anatolian Metallogenic Trend. Those occurrences, prospects and deposits are clustered into nine porphyry and epithermal districts that share similar features based on field observations (e.g., rock type, age, style of mineralization and structural control; Chapter 4). In total, those nine mineral districts contain significant gold (33 Moz) and minor copper (3.7 Blbs) reserves and resources (compilation in Chapter 4). However, those mineral districts, deposits, prospects and occurrences are not randomly distributed along the Anatolian Metallogenic Trend. Mineralization in western Anatolia was preferentially deposited or preserved around the exhumed core of the Menderes Massif, and mainly consists of low- and intermediate-sulfidation epithermal Au-Ag systems in the north and west, and porphyry and skarn mineralization in the east and south. In contrast, central Anatolia is dominated by high-sulfidation epithermal Au prospects and deposits whereas eastern Anatolia contains porphyry, high-sulfidation and Carlin-style precious and base metal mineralization. Those hydrothermal systems and associated igneous host rocks emplaced at extensional sites along grabens, strike-slip corridors, fault intersections and pull-apart basins in a context of crustal extension in western Anatolia and

compression in central and eastern Anatolia.

6.2.2 Timing of late Cenozoic Anatolian gold mineralization and tectonic implications

New geochronological data constrain the timing of late Cenozoic gold-rich, porphyry, epithermal and skarn mineralization that occurred at: 1) 25-17 Ma in eastern Anatolia; 2) 21-9 Ma in western Anatolia; 3) 10-3 Ma in central Anatolia. The timing of gold mineralization coincides with post-subduction segmentation and roll-back events of the Arabian, Cyprus and Aegean segments of the Southern Neotethyan oceanic slab in the late Cenozoic based on the tectonic reconstructions in Chapters 2 and 3, and new temporal and spatial constraints on gold mineralization (Chapter 4).

Porphyry mineralization (e.g., Cevizlidere) in the Tunceli district in eastern Anatolia resulted from a brief pulse of magmatism during the steepening of Arabian slab segment at the onset of the Arabia-Eurasia continental collision in the Oligocene. The Arabian slab break-off initiation at ca. 25 Ma, its westward propagation and slab window opening since the early Miocene, described in Chapters 2 and 3, were accompanied by the westward migration of the magmatic front and associated porphyry and high-sulfidation epithermal mineralization from the Ağrı district, Hasançelebi high-sulfidation epithermal prospect in eastern Anatolia to the Kayseri and Niğde districts in central Anatolia. In contrast, the high-sulfidation epithermal occurrences of the Konya district in the western part of central Anatolia formed during the southward roll-back of the Cyprus slab.

In western Anatolia, the combined roll-back and tearing (15 Ma) of the Aegean slab resulted in the southwestward migration of the magmatic front and associated mineralization. However, middle to late Miocene-aged porphyry and high-sulfidation mineralization formed during and above opening slab tear-related window in western Anatolia as opposed to the early to middle Miocene-aged low to intermediate-sulfidation epithermal gold mineralization. Thus, the post-subduction slab segmentation events and resulting thermal events at 25 and 15 Ma contributed to produce the bulk of Anatolian gold mineralization in the late Cenozoic.

6.2.3 Post-subduction magma fertility in Anatolia

New lithogeochemical and Sr-Nd-Pb isotope data (Chapter 5) from mineralized igneous units along late Cenozoic magmatism along the Anatolian Metallogenic Trend provide new insights into the genetic relationship between asthenospheric upwelling during slab rupture events and the production of gold-rich porphyry and epithermal deposits and prospects. Those gold-rich magmatic-hydrothermal systems preferentially formed with intermediate hypabyssal and extrusive rocks that range in composition from andesite to trachyte and their plutonic equivalents. The SiO_2 (61.8 ± 5.5 wt %) and Na_2O (2.4 to 7.4 wt %) contents, Sr/Y (> 20) and Ba/Ta ratios (> 428) and initial ε_{Nd} values (≤ 1) are the geochemical criteria that best indicate magma fertility of the late Cenozoic post-subduction igneous suites along the Anatolian Metallogenic Trend. Conversely, magma alkalinity ($K_2O + Na_2O$ and K_2O/Na_2O ratio), La/Yb ratio and oxidation state (Fe^{3+}/Fe^{2+}) do not effectively distinguish mineralized from unmineralized igneous units in Anatolia.

As depicted in Chapter 5, geochemical indicators for magma fertility evolve through time along the late Cenozoic Anatolian Metallogenic Trend. In western Anatolia, magma fertility is optimal in the middle to late Miocene igneous rocks (15-9 Ma), after the less-fertile early Miocene, weakly mineralized, syn-tectonic magmatism (21-18 Ma) and before the Pliocene to Quaternary, OIB-like, barren mafic lavas of the Kula complex. In eastern and central Anatolia, magma is fertile at the beginning of the regional magmatic cycles at 26 and 12 Ma, respectively. However, geochemical indicators for magma fertility in eastern and central Anatolia are weak compared to the middle to late Miocene igneous rocks in western Anatolia, and gradually evolve towards less metasomatized, less oxidized, shallowly-produced and mantle-dominant magmas.

Hornblende ± clinopyroxene and plagioclase fractionation affected the geochemical character of Anatolian fertile magmas in the absence of garnet residues to account for low $(Sm/Yb)_N$ and $(Dy/Yb)_N$ ratios and Sr contents (Chapter 5). The metasomatized Anatolian SCLM is herein shown to be the major source of fertile magmas, even though some contributions

from the lower crust are possible. The thinning of the SCLM during post-subduction tectonic events is controlled by the asthenospheric upwelling that progressively erodes the SCLM to asthenosphere by dripping.

6.2.4 Implications for post-subduction gold metallogeny

The spatial migration of slab rupture, slab window opening and mantle flow hinders the maturation, long-lived heating and stabilization of the magma production loci. The progressive loss of SCLM, volatile contents and migration of the melting source regions, and possible short crustal residence time ultimately lead to the reduction of magma fertility through time. Fertile magmatism produced small and sparse magmatic complexes and associated porphyry and epithermal systems such as along the Anatolian Trend. Thus, the segmentation of the Southern Neotethyan oceanic slab triggered asthenosphere upwelling that initiated the formation of porphyry and epithermal deposits along the Anatolian Trend, and subsequently contributed to the annihilation of the fertile magma production.

6.3 Final remarks

The study of post-subduction metallogeny requires the investigation of the three-dimensional slab dynamics through time-space constraints on geological, deformation, tectonic and magmatic events that are interpreted with numerical modeling and tomographic models. Previous metallogenic models dominantly relied on two-dimensional interactions between subduction dynamics and ore genesis, and thus failed to depict along-strike variations of slab dynamics such as in slab segmentation scenarios. The fate of the subducted oceanic slab, such as the Southern Neotethyan slab in the Eastern Mediterranean region, at the termination of the subduction commonly involves variably-oriented ruptures that induce passive asthenospheric upwelling. The timing of slab rupture initiation, the spatial evolution of rupture propagation, resultant mantle flow beneath the overriding crust and the remobilization of the fertile SCLM are the first-order controls on the timing and spatial distribution of post-subduction fertile magmatism and associated mineralization.

The geochemical signature of post-subduction Anatolian magmas is complex due to the interplay between crustal, lithospheric and asthenospheric components that evolve through time and space. I interpret a general trend towards less fertile and more mantle-dominant that reflects a gradual loss of volatiles and a greater input of hot asthenosphere. However, the geochemical signature of post-subduction magmatism is not specific to a particular tectonic scenario including slab roll-back, tear, break-off or window, and SCLM removal by delamination or dripping. Geochronology, spatial distribution of magmatic complexes, crustal deformation studies, numerical and analogue modeling and tomographic models provide robust constraints on the evolution of slab geometry and mantle dynamics. Thus, geochemical data can be used to support a specific tectonic model and more importantly, investigate the magmatic processes and sources that caused magmatism in the upper crust.

The late Cenozoic Anatolian Metallogenic Trend is prospective for porphyry- and epithermal-style gold mineralization but the tectono-magmatic events along this Trend may not be favorable for the formation of a world-class gold province and copper deposits. Magmatism tends to become more and more barren through time. Therefore, mineral exploration should focus on the oldest late Cenozoic volcanic edifices and suites, especially in central and eastern Anatolia, including the Konya, Melendiz, Tekkedağ, Develidağ and Yamadağ volcanic complexes and the outcropping Oligocene to early Miocene intrusive units in the Tunceli and Ağrı districts. Many mineralized occurrences formed at the beginning of the regional thermal event, and are characterized by a specific combination of geochemical indicators (intermediate composition, high Sr/Y and Ba/Ta ratios, and negative initial ε_{Nd}). Field investigations revealed that the late Cenozoic Anatolian mineralized systems are typically exposed at the bottom of the regional volcanic stratigraphy, notably at the bottom of valleys or hill flanks that are partially capped by barren volcanic and volcaniclastic units, along major normal and strike-slip faults. Mineralization can also be partially covered by barren volcanic products, particularly in central and eastern Anatolia. The distribution of fertile igneous units are now well-identified and should help conduct further investigations on the newly-defined mineral districts with an emphasis on

local volcanic stratigraphy, structures, alteration patterns, mineral paragenesis and detailed geochronology and geochemistry.

References

Abgarmi, B., Delph, J.R., Ozacar, A.A., Beck, S.L., Zandt, G., Sandvol, E., Turkelli, N. and Biryol, C.B., 2017, Structure of the crust and African slab beneath the central Anatolian plateau from receiver functions: New insights on isostatic compensation and slab dynamics: Geosphere, v. 13, p. 1774-1787.

Adiyaman, Ö., Chorowicz, J., Arnaud, O.N., Gündogdu, M.N. and Gourgaud, A., 2001, Late Cenozoic tectonics and volcanism along the North Anatolian Fault: new structural and geochemical data: Tectonophysics, v. 338, p. 135-165.

Agard, P., Omrani, J., Jolivet, L. and Mouthereau, F., 2005, Convergence history across Zagros (Iran): constraints from collisional and earlier deformation: International Journal of Earth Sciences, v. 94, p. 401-419.

Aghazadeh, M., Hou, Z., Badrzadeh, Z. and Zhou, L., 2015, Temporal–spatial distribution and tectonic setting of porphyry copper deposits in Iran: constraints from zircon U–Pb and molybdenite Re–Os geochronology: Ore Geology Reviews, v. 70, p. 385-406.

Agostini, S., Ryan, J., Tonarini, S. and Innocenti, F., 2008, Drying and dying of a subducted slab: Coupled Li and B isotope variations in Western Anatolia Cenozoic Volcanism: Earth and Planetary Science Letters, v. 272, p. 139-147.

Agostini, S., Doglioni, C., Innocenti, F., Piero, M. and Tonarini, S., 2010, On the Geodynamics of the Aegean rift: Tectonophysics, v. 488, p. 7-21.

Ahmadzadeh, G., Jahangiri, A., Lentz, D. and Mojtahedi, M., 2010, Petrogenesis of Plio-Quaternary post-collisional ultrapotassic volcanism in NW of Marand, NW Iran: Journal of Asian Earth Sciences, v. 39, p. 37-50.

Akal, C., Helvacı, C., Prelević, D. and van den Bogaard, P., 2013, High-K volcanism in the Afyon region, western Turkey: from Si-oversaturated to Si-undersaturated volcanism: International Journal of Earth Sciences, v. 102, p. 435-453.

Aktaş, G. and Robertson, A., 1984, The Maden complex, SE Turkey: evolution of a Neotethyan active margin: Geological Society, London, Special Publications, v. 17, p. 375-402.

Akurgal, E., 1962, The early period and the golden age of Ionia: American Journal of Archaeology, v. 66, p. 369-379.

Al-Lazki, A.I., Seber, D., Sandvol, E., Turkelli, N., Mohamad, R. and Barazangi, M., 2003, Tomographic Pn velocity and anisotropy structure beneath the Anatolian plateau (eastern Turkey) and the surrounding regions: Geophysical Research Letters, v. 30, p. 1-4.

Alacer Gold, 2016, Alacer Gold annouces a new reserve for its Gediktepe project providing future growth: (http://www.alacergold.com/docs/default-source/press-releases/2016-09-13-gediktepe-pfs-final-(with-jorc-table).pdf?sfvrsn=6).

Aldanmaz, E., 2002, Mantle source characteristics of alkali basalts and basanites in an extensional intracontinental plate setting, western Anatolia, Turkey: implications for multi-stage melting: International Geology Review, v. 44, p. 440-457.

Aldanmaz, E., Pearce, J.A., Thirlwall, M. and Mitchell, J., 2000, Petrogenetic evolution of late

Cenozoic, post-collision volcanism in western Anatolia, Turkey: Journal of Volcanology and Geothermal Research, v. 102, p. 67-95.

Aldanmaz, E., Pickard, M., Meisel, T., Altunkaynak, Ş., Sayıt, K., Şen, P., Hanan, B.B. and Furman, T., 2015, Source components and magmatic processes in the genesis of Miocene to Quaternary lavas in western Turkey: constraints from HSE distribution and Hf–Pb–Os isotopes: Contributions to Mineralogy and Petrology, v. 170, p. 23.

Alıcı, P., Temel, A. and Gourgaud, A., 2002, Pb–Nd–Sr isotope and trace element geochemistry of Quaternary extension-related alkaline volcanism: a case study of Kula region (western Anatolia, Turkey): Journal of Volcanology and Geothermal Research, v. 115, p. 487-510.

Alıcı, P., Temel, A., Gourgaud, A., Kieffer, G. and Gündoğdu, M., 1998, Petrology and geochemistry of potassic rocks in the Gölcük area (Isparta, SW Turkey): genesis of enriched alkaline magmas: Journal of Volcanology and Geothermal Research, v. 85, p. 423-446.

Allen, M., Jackson, J. and Walker, R., 2004, Late Cenozoic reorganization of the Arabia-Eurasia collision and the comparison of short-term and long-term deformation rates: Tectonics, v. 23, p. 1-17.

Allen, M.B. and Armstrong, H.A., 2008, Arabia–Eurasia collision and the forcing of mid-Cenozoic global cooling: Palaeogeography, Palaeoclimatology, Palaeoecology, v. 265, p. 52-58.

Alonso-Perez, R., Müntener, O. and Ulmer, P., 2009, Igneous garnet and amphibole fractionation in the roots of island arcs: experimental constraints on andesitic liquids: Contributions to Mineralogy and Petrology, v. 157, p. 541.

Alpaslan, M., 2007, Early to middle Miocene intra-continental basaltic volcanism in the northern part of the Arabian plate, SE Anatolia, Turkey: geochemistry and petrogenesis: Geological Magazine, v. 144, p. 867-882.

Alpaslan, M. and Terzioğlu, N., 1996, Comparative geochemical features of the Upper Miocene and Pliocene volcanics around Arguvan (NW Malatya): Geological Bulletin of Turkey, v. 39, p. 75-86.

Alpaslan, M., Frei, R., Boztug, D., Kurt, M.A. and Temel, A., 2004, Geochemical and Pb-Sr-Nd isotopic constraints indicating an enriched-mantle source for Late Cretaceous to early Tertiary volcanism, Central Anatolia, Turkey: International Geology Review, v. 46, p. 1022-1041.

Alpaslan, M., Ekici, T., Otlu, N., Boztug, D. and Temel, A.d.n., 2005, Magmatic processes and mixing origin of andesite: Miocene Karamağara volcanics, Central Anatolia, Turkey: Geological Journal, v. 40, p. 193-214.

Altunkaynak, Ş., 2007, Collision-driven slab breakoff magmatism in northwestern Anatolia, Turkey: The Journal of geology, v. 115, p. 63-82.

Altunkaynak, Ş., Dilek, Y., Genç, C.Ş., Sunal, G., Gertisser, R., Furnes, H., Foland, K.A. and Yang, J., 2012, Spatial, temporal and geochemical evolution of Oligo–Miocene granitoid magmatism in western Anatolia, Turkey: Gondwana Research, v. 21, p. 961-986.

Angus, D., Wilson, D.C., Sandvol, E. and Ni, J., 2006, Lithospheric structure of the Arabian and Eurasian collision zone in eastern Turkey from S-wave receiver functions: Geophysical Journal International, v. 166, p. 1335-1346.

Annen, C., Blundy, J. and Sparks, R., 2005, The genesis of intermediate and silicic magmas in deep crustal hot zones: Journal of Petrology, v. 47, p. 505-539.

Arculus, R., 1994, Aspects of magma genesis in arcs: Lithos, v. 33, p. 189-208.

Arger, J., Mitchell, J. and Westaway, R.W., 2000, Neogene and Quaternary volcanism of southeastern Turkey: Geological Society, London, Special Publications, v. 173, p. 459-487.

Ariana Resources, P., 2017, Major increase in Kiziltepe resource: (https://arianaresources.com/2017/1093-ariana-resources-plc-major-increase-in-kiziltepe-resource-2017-05-03-070009).

Arık, F., 2002, Gümüşköy (Kütahya, Turkey) gümüş yataginin jeokimyasal modellemesi: Selçuk Üniv. Fen. Bilim. Enst. PhD Thesis.

Armijo, R., Meyer, B., Hubert, A. and Barka, A., 1999, Westward propagation of the North Anatolian fault into the northern Aegean: Timing and kinematics: Geology, v. 27, p. 267-270.

Armstrong, T., Brown, F., Duggan, A., Hallewell, M., Harding, W., Hayes, T., Holmes, G., Kuchling, K., Monaghan, B., Orava, D., Hendrik, J.H. and Puritch, E., 2012, Feasibility Study of the Yenipazar Project, Turkey: 271 p.

Arribas, A.J., Hedenquist, J.W., Itaya, T., Okada, T., Concepción, R.A. and Garcia Jr, J.S., 1995, Contemporaneous formation of adjacent porphyry and epithermal Cu-Au deposits over 300 ka in northern Luzon, Philippines: Geology, v. 23, p. 337-340.

Asan, K. and Ertürk, A., 2013, First Evidence of Lamprophyric Magmatism from the Konya Region, Turkey: a Genetic Link to High-K Volcanism: Acta Geologica Sinica, v. 87, p. 1617-1629.

Ates, A., Kearey, P. and Tufan, S., 1999, New gravity and magnetic anomaly maps of Turkey: Geophysical Journal International, v. 136, p. 499-502.

Aydar, E. and Gourgaud, A., 1998, The geology of Mount Hasan stratovolcano, central Anatolia, Turkey: Journal of volcanology and geothermal research, v. 85, p. 129-152.

Aydar, E. and Gourgaud, A., 2002, Garnet-bearing basalts: an example from Mt. Hasan, central Anatolia, Turkey: Mineralogy and Petrology, v. 75, p. 185-201.

Aydar, E., Gourgaud, A., Deniel, C., Lyberis, N. and Gundogdu, N., 1995, Le volcanisme quaternaire d'Anatolie centrale (Turquie): association de magmatismes calco-alcalin et alcalin en domaine de convergence: Canadian Journal of Earth Sciences, v. 32, p. 1058-1069.

Aydar, E., Schmitt, A.K., Çubukçu, H.E., Akin, L., Ersoy, O., Sen, E., Duncan, R.A. and Atici, G., 2012, Correlation of ignimbrites in the central Anatolian volcanic province using zircon and plagioclase ages and zircon compositions: Journal of Volcanology and Geothermal Research, v. 213, p. 83-97.

Aydin, F., 2008, Contrasting complexities in the evolution of calc-alkaline and alkaline melts of the Nigde volcanic rocks, Turkey: textural, mineral chemical and geochemical evidence: European Journal of Mineralogy, v. 20, p. 101-118.

Aydin, F., Schmitt, A.K., Siebel, W., Sönmez, M., Ersoy, Y., Lermi, A., Dirik, K. and Duncan, R., 2014, Quaternary bimodal volcanism in the Niğde Volcanic Complex (Cappadocia, central Anatolia, Turkey): age, petrogenesis and geodynamic implications: Contributions to Mineralogy and Petrology, v. 168, p. 1078.

Aydoğan, M.S., Coban, H., Bozcu, M. and Akıncı, Ö., 2008, Geochemical and mantle-like isotopic (Nd, Sr) composition of the Baklan Granite from the Muratdağı Region (Banaz, Uşak), western Turkey: Implications for input of juvenile magmas in the source domains of western Anatolia Eocene–Miocene granites: Journal of Asian Earth Sciences, v. 33, p. 155-176.

Baker, T., 2017, Diversity of gold deposits in the Cenozoic West Tethyan magmatic belt, SE Europe: implications for exploration: Proceedings of the 14th SGA Biennial Meeting, Québec City, Canada, p. 19-22.

Baker, T., Bickford, D., Juras, S., Lewis, P., Oztas, Y., Ross, K., Tukac, A., Rabayrol, F., Miskovic, A., Friedman, R., Creaser, R.A. and Spikings, R., 2016, The geology of the Kisladag porphyry gold deposit, Turkey: Society of Economic Geologists Special Publication 19, v. p. 57-83.

Bakırcı, T., Yoshizawa, K. and Özer, M.F., 2012, Three-dimensional S-wave structure of the upper mantle beneath Turkey from surface wave tomography: Geophysical Journal International, v. 190, p. 1058-1076.

Bao, X., Eaton, D.W. and Gu, Y.J., 2016, Rayleigh wave azimuthally anisotropic phase velocity maps beneath western Canada: Journal of Geophysical Research: Solid Earth, v. 121, p. 1821-1834.

Barazangi, M., Sandvol, E. and Seber, D., 2006, Structure and tectonic evolution of the Anatolian plateau in eastern Turkey: Geological Society of America Special Papers, v. 409, p. 463.

Barrier, E. and Vrielynck, B., 2008, Palaeotectonic maps of the Middle East: scale 1:18,500,000.

Bartol, J. and Govers, R., 2014, A single cause for uplift of the Central and Eastern Anatolian plateau?: Tectonophysics, v. 637, p. 116-136.

Benn, K., Odonne, F. and de Saint Blanquat, M., 1998, Pluton emplacement during transpression in brittle crust: new views from analogue experiments: Geology, v. 26, p. 1079-1082.

Bertrand, G., Guillou-Frottier, L. and Loiselet, C., 2014, Distribution of porphyry copper deposits along the western Tethyan and Andean subduction zones: Insights from a paleotectonic approach: Ore Geology Reviews, v. 60, p. 174-190.

Bertrand, H., Chazot, G., Blichert-Toft, J. and Thoral, S., 2003, Implications of widespread high-μ volcanism on the Arabian Plate for Afar mantle plume and lithosphere composition: Chemical Geology, v. 198, p. 47-61.

Besang, C., Eckhardt, F., Harre, W., Kreuzer, H. and Müller, P., 1977, Radiometrische altersbestimmungen an neogenen eruptivgesteinen der Türkei: Geologisches Jahrbuch, v. 25, p. 3-36.

Bickford, D., Tukac, A., Oztas, Y. and Baker, T., 2016, Exploration overview of the Sayacık and Kışladağ gold porphyries, Western Anatolia Volcanic Province, Turkey: SEG Conference: Tethyan Tectonics and Metallogeny, Çeşme, Turkey, Oral presentation.

Bierlein, F.P., Groves, D.I. and Cawood, P.A., 2009, Metallogeny of accretionary orogens—the connection between lithospheric processes and metal endowment: Ore Geology Reviews, v. 36, p. 282-292.

Bigazzi, G., Yegingil, Z., Ercan, T., Oddone, M. and Özdogan, M., 1997, Age determination of obsidian bearing volcanics in Eastern Anatolia using the fission track dating method: Geological Bulletin of Turkey, v. 40, p. 57-72.

Bilir, E., 2015, Geochemical and geochronological characterization of the Early-Middle Eocene magmatism and related epithermal systems of the Eastern Pontides, Turkey: Unpublished M.Sc thesis, Muğla, Turkey, Muğla Sitki Koçman University, 138 p.

Bird, P., 1978, Initiation of intracontinental subduction in the Himalaya: Journal of Geophysical Research: Solid Earth, v. 83, p. 4975-4987.

Bird, P., 1979, Continental delamination and the Colorado Plateau: Journal of Geophysical Research: Solid Earth, v. 84, p. 7561-7571.

Biryol, C.B., Beck, S.L., Zandt, G. and Özacar, A.A., 2011, Segmented African lithosphere beneath the Anatolian region inferred from teleseismic P-wave tomography: Geophysical Journal International, v. 184, p. 1037-1057.

Bissig, T., Clark, A.H., Lee, J.K. and von Quadt, A., 2003, Petrogenetic and metallogenetic responses to Miocene slab flattening: new constraints from the El Indio-Pascua Au–Ag–Cu belt, Chile/Argentina: Mineralium Deposita, v. 38, p. 844-862.

Bissig, T., Clark, A.H., Rainbow, A. and Montgomery, A., 2015, Physiographic and tectonic settings of high-sulfidation epithermal gold–silver deposits of the Andes and their controls on mineralizing processes: Ore Geology Reviews, v. 65, p. 327-364.

Bissig, T., Leal-Mejía, H., Stevens, R.B. and Hart, C.J., 2017, High Sr/Y Magma Petrogenesis and the Link to Porphyry Mineralization as Revealed by Garnet-Bearing I-Type Granodiorite Porphyries of the Middle Cauca Au-Cu Belt, Colombia: Economic Geology, v. 112, p. 551-568.

Black, L.P., Kamo, S.L., Allen, C.M., Davis, D.W., Aleinikoff, J.N., Valley, J.W., Mundil, R., Campbell, I.H., Korsch, R.J. and Williams, I.S., 2004, Improved 206 Pb/238 U microprobe geochronology by the monitoring of a trace-element-related matrix effect; SHRIMP, ID–TIMS, ELA–ICP–MS and oxygen isotope documentation for a series of zircon standards: Chemical Geology, v. 205, p. 115-140.

Black, R. and Liegeois, J.-P., 1993, Cratons, mobile belts, alkaline rocks and continental lithospheric mantle: the Pan-African testimony: Journal of the Geological Society, v. 150, p. 89-98.

Blevin, P.L., 2004, Redox and Compositional Parameters for Interpreting the Granitoid Metallogeny of Eastern Australia: Implications for Gold-rich Ore Systems: Resource Geology, v. 54, p. 241-252.

Blundell, D.J., 2002, The timing and location of major ore deposits in an evolving orogen: the geodynamic context: Geological Society, London, Special Publications, v. 204, p. 1-12.

Bonin, B., 1990, From orogenic to anorogenic settings: evolution of granitoid suites after a major orogenesis: Geological Journal, v. 25, p. 261-270.

Boucher, K., 2016, The structural and fluid evolution of the Efemçukuru epithermal gold deposit, western Turkey: Unpublished M.Sc thesis, The University of British Columbia, 466 p.

Bouvier, A., Vervoort, J.D. and Patchett, P.J., 2008, The Lu–Hf and Sm–Nd isotopic composition of CHUR: constraints from unequilibrated chondrites and implications for the bulk composition of terrestrial planets: Earth and Planetary Science Letters, v. 273, p. 48-57.

Bozkurt, E., 2001, Neotectonics of Turkey–a synthesis: Geodinamica acta, v. 14, p. 3-30.

Bozkurt, E., 2003, Origin of NE-trending basins in western Turkey: Geodinamica Acta, v. 16, p. 61-81.

Bozkurt, E. and Park, L.R., 1994, Southern Menderes Massif: an incipient metamorphic core complex in western Anatolia, Turkey: Journal of the Geological Society, v. 151, p. 213-216.

Bozkurt, E. and Oberhänsli, R., 2001, Menderes Massif (Western Turkey): structural, metamorphic and magmatic evolution–a synthesis: International Journal of Earth Sciences, v. 89, p. 679-708.

Boztuğ, D., 2000, S-I-A-type intrusive associations: geodynamic significance of synchronism between metamorphism and magmatism in Central Anatolia, Turkey: Geological Society, London, Special Publications, v. 173, p. 441-458.

Boztuğ, D., Jonckheere, R., Heizler, M., Ratschbacher, L., Harlavan, Y. and Tichomirova, M., 2009, Timing of post-obduction granitoids from intrusion through cooling to exhumation in central Anatolia, Turkey: Tectonophysics, v. 473, p. 223-233.

Bradshaw, T. and Smith, E.I., 1994, Polygenetic Quaternary volcanism at Crater Flat, Nevada: Journal of Volcanology and Geothermal Research, v. 63, p. 165-182.

Brunetti, P., 2016, Magmatic-hydrothermal evolution and post-ore modifications of the Halilaga porphyry Cu-Au deposit, NW Turkey: Unpublished M.Sc thesis, The University of British Columbia, 289 p.

Bucha, V. and Mellaart, J., 1967, Archaeomagnetic intensity measurements on some neolithic samples from Catal Hüyük (Anatolia): Archaeometry, v. 10, p. 23-25.

Buiter, S.J.H., 2000, Surface deformation resulting from subduction and slab detachment: Unpublished PhD thesis, Utrecht, Utrecht University, 130 p.

Buket, E. and Temel, A., 1998, Major-element, trace-element, and Sr–Nd isotopic geochemistry and genesis of Varto (Muş) volcanic rocks, Eastern Turkey: Journal of Volcanology and Geothermal Research, v. 85, p. 405-422.

Burnham, C.W., 1979, Magmas and hydrothermal fluids: Geochemistry of Hydrothermal Ore Deposits., v. p. 71-136.

Çakır, Ö. and Erduran, M., 2011, On the P and S receiver functions used for inverting the one-dimensional upper mantle shear-wave velocities: Surveys in geophysics, v. 32, p. 71-98.

Cambel, H. and Braidwood, R.J., 1970, An early farming village in Turkey: Scientific American, v. 222, p. 50-57.

Candan, O., 1997, Blueschist relics in the Mesozoic series of the Menderes Massif and correlation with Samos Island, Cyclades: Schweiz Mineralogische und Petrographische Mitteilungen, v. 77, p. 95-99.

Candan, O., Çetinkaplan, M., Oberhänsli, R., Rimmelé, G. and Akal, C., 2005, Alpine high-P/low-T metamorphism of the Afyon Zone and implications for the metamorphic evolution of Western Anatolia, Turkey: Lithos, v. 84, p. 102-124.

Candan, O., Dora, O., Oberhänsli, R., Çetinkaplan, M., Partzsch, J., Warkus, F. and Dürr, S., 2001, Pan-African high-pressure metamorphism in the Precambrian basement of the Menderes Massif, western Anatolia, Turkey: International Journal of Earth Sciences, v. 89, p. 793-811.

Candela, P. and Piccoli, P., 2005, Magmatic processes in the development of porphyry-type ore systems: Economic Geology 100th Anniversary Volume, v. p. 25-37.

Cassard, D., Lips, A.L., Leistel, J.-M., Itard, Y., Debeglia-Marchand, N., Guillou-Frottier, L., Spakman, W., Stein, G. and Husson, Y., 2004, Understanding and assessing European mineral resources–a new approach using GIS Central Europe: Swiss Bulletin of Mineralogy and Petrology, v. 84, p. 3-24.

Castillo, P.R., 2012, Adakite petrogenesis: Lithos, v. 134, p. 304-316.

Castillo, P.R., Janney, P.E. and Solidum, R.U., 1999, Petrology and geochemistry of Camiguin Island, southern Philippines: insights to the source of adakites and other lavas in a complex arc setting: Contributions to Mineralogy and Petrology, v. 134, p. 33-51.

Cathles, L. and Shannon, R., 2007, How potassium silicate alteration suggests the formation of porphyry ore deposits begins with the nearly explosive but barren expulsion of large volumes of magmatic water: Earth and Planetary Science Letters, v. 262, p. 92-108.

Cathles, L.M., Erendi, A. and Barrie, T., 1997, How long can a hydrothermal system be sustained by a single intrusive event?: Economic Geology, v. 92, p. 766-771.

Cemen, I., Göncüoglu, M.C. and Dirik, K., 1999, Structural evolution of the Tuzgölü basin in Central Anatolia, Turkey: The Journal of Geology, v. 107, p. 693-706.

Cesare, B., Rubatto, D. and Gómez-Pugnaire, M.T., 2009, Do extrusion ages reflect magma generation processes at depth? An example from the Neogene Volcanic Province of SE Spain: Contributions to Mineralogy and Petrology, v. 157, p. 267-279.

Ceyhan, N., 2003, Lead Isotope geochemistry of Pb-Zn deposits from Eastern Taurides, Turkey: Unpublished thesis, METU, 105 p.

Chakrabarti, R., Basu, A.R. and Ghatak, A., 2012, Chemical geodynamics of western Anatolia: International Geology Review, v. 54, p. 227-248.

Chambefort, I., Dilles, J.H. and Kent, A.J., 2008, Anhydrite-bearing andesite and dacite as a source for sulfur in magmatic-hydrothermal mineral deposits: Geology, v. 36, p. 719-722.

Chappell, B. and White, A., 1992, I-and S-type granites in the Lachlan Fold Belt: Earth and

Environmental Science Transactions of the Royal Society of Edinburgh, v. 83, p. 1-26.

Chiaradia, M., 2014, Copper enrichment in arc magmas controlled by overriding plate thickness: Nature Geoscience, v. 7, p. 43-46.

Chiaradia, M., Merino, D. and Spikings, R., 2009, Rapid transition to long-lived deep crustal magmatic maturation and the formation of giant porphyry-related mineralization (Yanacocha, Peru): Earth and Planetary Science Letters, v. 288, p. 505-515.

Chiaradia, M., Schaltegger, U. and Spikings, R., 2014, Time Scales of Mineral Systems—Advances in Understanding Over the Past Decade: Society of Economic Geologists Special Publication, v. 18, p. 37-58.

Chiaradia, M., Ulianov, A., Kouzmanov, K. and Beate, B., 2012, Why large porphyry Cu deposits like high Sr/Y magmas?: Scientific reports, v. 2, p. 685.

Çiçek, M. and Oyman, T., 2016, Origin and evolution of hydrothermal fluids in epithermal Pb-Zn-Cu±Au±Ag deposits at Koru and Tesbihdere mining districts, Çanakkale, Biga Peninsula, NW Turkey: Ore Geology Reviews, v. 78, p. 176-195.

Ciobanu, C.L., Cook, N.J. and Stein, H., 2002, Regional setting and geochronology of the Late Cretaceous Banatitic magmatic and metallogenetic belt: Mineralium Deposita, v. 37, p. 541-567.

Clark, M. and Robertson, A., 2002, The role of the Early Tertiary Ulukisla Basin, southern Turkey, in suturing of the Mesozoic Tethys ocean: Journal of the Geological Society, v. 159, p. 673-690.

Clemens, J. and Mawer, C., 1992, Granitic magma transport by fracture propagation: Tectonophysics, v. 204, p. 339-360.

Cloos, M., Sapiie, B., Quarles van Ufford, A., Weiland, R.J., Warren, P.Q. and McMahon, T.P., 2005, Collisional delamination in New Guinea: The geotectonics of subducting slab breakoff: In M. Cloos, B. Sapiie, A.Q. van Ufford, R.J. Weiland, P.Q. Warren and T.P. McMahon (eds.), Collisional Delamination in New Guinea: The Geotectonics of Subducting Slab Breakoff: Geological Society of America, p. 1-55.

Çoban, H. and Flower, M.F., 2006, Mineral phase compositions in silica-undersaturated 'leucite'lamproites from the Bucak area, Isparta, SW Turkey: Lithos, v. 89, p. 275-299.

Çoban, H., Karacık, Z. and Ece, Ö.I., 2012, Source contamination and tectonomagmatic signals of overlapping Early to Middle Miocene orogenic magmas associated with shallow continental subduction and asthenospheric mantle flows in Western Anatolia: A record from Simav (Kütahya) region: Lithos, v. 140, p. 119-141.

Çolakoğlu, A.R. and Arehart, G.B., 2010, The petrogenesis of Sarıçimen (Çaldıran-Van) quartz monzodiorite: Implication for initiation of magmatism (Late Medial Miocene) in the east Anatolian collision zone, Turkey: Lithos, v. 119, p. 607-620.

Çolakoğlu, A.R., Oruç, M., Arehart, G.B. and Poulson, S., 2011, Geology and isotope geochemistry (C–O–S) of the Diyadin gold deposit, Eastern Turkey: A newly-discovered Carlin-like deposit: Ore Geology Reviews, v. 40, p. 27-40.

Collins, A.S. and Robertson, A.H., 1997, Lycian melange, southwestern Turkey: an emplaced Late Cretaceous accretionary complex: Geology, v. 25, p. 255-258.

Conticelli, S., Guarnieri, L., Farinelli, A., Mattei, M., Avanzinelli, R., Bianchini, G., Boari, E., Tommasini, S., Tiepolo, M. and Prelević, D., 2009, Trace elements and Sr–Nd–Pb isotopes of K-rich, shoshonitic, and calc-alkaline magmatism of the Western Mediterranean Region: genesis of ultrapotassic to calc-alkaline magmatic associations in a post-collisional geodynamic setting: Lithos, v. 107, p. 68-92.

Cook, N.J., Ciobanu, C.L., Spry, P.G. and Voudouris, P., 2009, Understanding gold-(silver)-telluride-(selenide) mineral deposits: Episodes, v. 32, p. 249-263.

Cosentino, D., Schildgen, T.F., Cipollari, P., Faranda, C., Gliozzi, E., Hudáčková, N., Lucifora, S. and Strecker, M.R., 2012, Late Miocene surface uplift of the southern margin of the Central Anatolian Plateau, Central Taurides, Turkey: Geological Society of America Bulletin, v. 124, p. 133-145.

Coulon, C., Megartsi, M.h., Fourcade, S., Maury, R.C., Bellon, H., Louni-Hacini, A., Cotten, J., Coutelle, A. and Hermitte, D., 2002, Post-collisional transition from calc-alkaline to alkaline volcanism during the Neogene in Oranie (Algeria): magmatic expression of a slab breakoff: Lithos, v. 62, p. 87-110.

Cox, D.P. and Singer, D.A., 1988, Distribution of gold in porphyry copper deposits: 23 p.

Çubukçu, H., Ulusoy, İ., Aydar, E., Ersoy, O., Şen, E., Gourgaud, A. and Guillou, H., 2012, Mt. Nemrut volcano (Eastern Turkey): temporal petrological evolution: Journal of Volcanology and Geothermal Research, v. 209, p. 33-60.

Dalrymple, G.B. and Lanphere, M.A., 1974, $^{40}Ar/^{39}Ar$ age spectra of some undisturbed terrestrial samples: Geochimica et cosmochimica acta, v. 38, p. 715-738.

Davidson, J., Turner, S., Handley, H., Macpherson, C. and Dosseto, A., 2007, Amphibole "sponge" in arc crust?: Geology, v. 35, p. 787-790.

Davies, J.H. and von Blanckenburg, F., 1995, Slab breakoff: a model of lithosphere detachment and its test in the magmatism and deformation of collisional orogens: Earth and Planetary Science Letters, v. 129, p. 85-102.

Davis, J. and Hawkesworth, C., 1993, The petrogenesis of 30–20 Ma basic and intermediate volcanics from the Mogollon-Datil Volcanic Field, New Mexico, USA: Contributions to Mineralogy and Petrology, v. 115, p. 165-183.

De Boorder, H., Spakman, W., White, S. and Wortel, M., 1998, Late Cenozoic mineralization, orogenic collapse and slab detachment in the European Alpine Belt: Earth and Planetary Science Letters, v. 164, p. 569-575.

Defant, M.J. and Drummond, M.S., 1990, Derivation of some modern arc magmas by melting of young subducted lithosphere: Nature, v. 347, p. 662.

Delibaş, O. and Genç, Y., 2012, Re-Os molybdenite ages of granitoid-hosted Mo–Cu occurrences from central Anatolia (Turkey): Ore Geology Reviews, v. 44, p. 39-48.

Delibaş, O., Moritz, R., Chiaradia, M., Selby, D., Ulianov, A. and Revan, M.K., 2017, Post-collisional magmatism and ore-forming systems in the Menderes massif: new constraints from the Miocene porphyry Mo–Cu Pınarbaşı system, Gediz–Kütahya, western Turkey: Mineralium Deposita, v. 52, p. 1157-1178.

Delibaş, O., Moritz, R., Ulianov, A., Chiaradia, M., Saraç, C., Revan, K.M. and Göç, D., 2016,

Cretaceous subduction-related magmatism and associated porphyry-type Cu–Mo prospects in the Eastern Pontides, Turkey: new constraints from geochronology and geochemistry: Lithos, v. 248, p. 119-137.

Delph, J.R., Abgarmi, B., Ward, K.M., Beck, S.L., Ozacar, A.A., Zandt, G., Sandvol, E., Turkelli, N. and Kalafat, D., 2017, The effects of subduction termination on the continental lithosphere: Linking volcanism, deformation, surface uplift, and slab tearing in central Anatolia: Geosphere, v. 13, p. 1-18.

Demir, T., Seyrek, A., Guillou, H., Scaillet, S., Westaway, R. and Bridgland, D., 2009, Preservation by basalt of a staircase of latest Pliocene terraces of the River Murat in eastern Turkey: evidence for rapid uplift of the eastern Anatolian Plateau: Global and Planetary Change, v. 68, p. 254-269.

Deniel, C., Aydar, E. and Gourgaud, A., 1998, The Hasan Dagi stratovolcano (Central Anatolia, Turkey): evolution from calc-alkaline to alkaline magmatism in a collision zone: Journal of Volcanology and Geothermal Research, v. 87, p. 275-302.

DePaolo, D.J., 1981, Trace element and isotopic effects of combined wallrock assimilation and fractional crystallization: Earth and Planetary Science Letters, v. 53, p. 189-202.

Dewey, J., Hempton, M., Kidd, W., Saroğlu, F. and Şengör, A., 1986, Shortening of continental lithosphere: the neotectonics of Eastern Anatolia—a young collision zone: Geological Society, London, Special Publications, v. 19, p. 1-36.

Dhont, D., Chorowicz, J., Yürür, T., Froger, J.-L., Köse, O. and Gündogdu, N., 1998, Emplacement of volcanic vents and geodynamics of Central Anatolia, Turkey: Journal of Volcanology and Geothermal Research, v. 85, p. 33-54.

Dickinson, W.R., 1975, Potash-depth (K-h) relations in continental margin and intra-oceanic magmatic arcs: Geology, v. 3, p. 53-56.

Dilek, Y. and Whitney, D., 2000, Cenozoic crustal evolution in Central Anatolia: extension, magrnatism and landscape development: Proceedings of the Third International Conference on the Geology of the Eastern Mediterranean: Geological Survey Department. Nicosia, Cyprus, p. 183-192.

Dilek, Y. and Altunkaynak, Ş., 2009, Geochemical and temporal evolution of Cenozoic magmatism in western Turkey: mantle response to collision, slab break-off, and lithospheric tearing in an orogenic belt: Geological Society, London, Special Publications, v. 311, p. 213-233.

Dilek, Y. and Altunkaynak, Ş., 2010, Geochemistry of Neogene–Quaternary alkaline volcanism in western Anatolia, Turkey, and implications for the Aegean mantle: International Geology Review, v. 52, p. 631-655.

Dilek, Y., Imamverdiyev, N. and Altunkaynak, Ş., 2010, Geochemistry and tectonics of Cenozoic volcanism in the Lesser Caucasus (Azerbaijan) and the peri-Arabian region: collision-induced mantle dynamics and its magmatic fingerprint: International Geology Review, v. 52, p. 536-578.

Dixon, C. and Pereira, J., 1974, Plate tectonics and mineralization in the Tethyan region: Mineralium Deposita, v. 9, p. 185-198.

Dogan-Kulahci, G.D., Temel, A., Gourgaud, A., Varol, E., Guillou, H. and Deniel, C., 2018,

Contemporaneous alkaline and calc-alkaline series in Central Anatolia (Turkey): Spatio-temporal evolution of a post-collisional Quaternary basaltic volcanism: Journal of Volcanology and Geothermal Research, v. 356, p 56-74.

Dogan, A.U., Dogan, M., Kilinc, A. and Locke, D., 2008, An isobaric–isenthalpic magma mixing model for the Hasan Dagi volcano, Central Anatolia, Turkey: Bulletin of Volcanology, v. 70, p. 797-804.

Dogan, A.U., Dogan, M., Peate, D.W. and Dogruel, Z., 2011, Textural and mineralogical diversity of compositionally homogeneous dacites from the summit of Mt. Erciyes, Central Anatolia, Turkey: Lithos, v. 127, p. 387-400.

Dogan, A.U., Peate, D.W., Dogan, M., Yesilyurt-Yenice, F.I. and Unsal, O., 2013, Petrogenesis of mafic–silicic lavas at Mt. Erciyes, central Anatolia, Turkey: Journal of Volcanology and Geothermal Research, v. 256, p. 16-28.

Dogan, G.D.K., 2016, Chronological, magmatological and geochemical study of post-collisional basaltic volcanism in Central Anatolia and its spatio-temporal evolution: Unpublished PhD thesis, Clermont-Ferrand, France, Universite Blaise Pascal - Clermont-Ferrand II, 230 p.

Doglioni, C., Agostini, S., Crespi, M., Innocenti, F., Piero, M., Riguzzi, F. and Savasci, Y., 2002, On the extension in western Anatolia and the Aegean Sea: Journal of the Virtual Explorer, v. 8, p. 1-16.

du Bray, E.A., 2017, Geochemical characteristics of igneous rocks associated with epithermal mineral deposits—A review: Ore Geology Reviews, v. 80, p. 767-783.

Ece, Ö.I., Ekinci, B., Schroeder, P.A., Crowe, D. and Esenli, F., 2013, Origin of the Düvertepe kaolin–alunite deposits in Simav Graben, Turkey: Timing and styles of hydrothermal mineralization: Journal of Volcanology and Geothermal Research, v. 255, p. 57-78.

Economou-Eliopoulos, M. and Eliopoulos, D.G., 2000, Palladium, platinum and gold concentration in porphyry copper systems of Greece and their genetic significance: Ore Geology Reviews, v. 16, p. 59-70.

Einaudi, M., Meinert, L.D. and Newberry, R.J., 1981, Skarn deposits: economic Geology 75th Anniversary Volume, v. p. 317-391.

Ekici, T., 2016, Collision-related slab break-off volcanism in the Eastern Anatolia, Kepez volcanic complex (Turkey): Geodinamica Acta, v. 28, p. 223-239.

Ekici, T., Alpaslan, M., Parlak, O. and Temel, A., 2007, Geochemistry of the Pliocene basalts erupted along the Malatya-Ovacik fault zone (MOFZ), eastern Anatolia, Turkey: Implications for source characteristics and partial melting processes: Chemie der Erde-Geochemistry, v. 67, p. 201-212.

Ekici, T., Alpaslan, M., Parlak, O. and Ucurum, A., 2009, Geochemistry of the Middle Miocene Collision-Related Yamadağı (Eastern Anatolia) Calc-Alkaline Volcanics, Turkey: Turkish Journal of Earth Sciences, v. 18, p. 511-528.

Ekici, T., Macpherson, C.G., Otlu, N. and Fontignie, D., 2014, Foreland magmatism during the Arabia–Eurasia collision: Pliocene–Quaternary activity of the Karacadağ Volcanic Complex, SW Turkey: Journal of Petrology, v. 55, p. 1753-1777.

Eldorado Gold Corp., 2017, Resources and reserves: (https://www.eldoradogold.com/assets/resources-and-reserves/default.aspx).

Elkins-Tanton, L.T., 2007, Continental magmatism, volatile recycling, and a heterogeneous mantle caused by lithospheric gravitational instabilities: Journal of Geophysical Research: Solid Earth, v. 112, p. 1-13.

Ellam, R., 1992, Lithospheric thickness as a control on basalt geochemistry: Geology, v. 20, p. 153-156.

Erkül, F., Helvacı, C. and Sözbilir, H., 2005a, Stratigraphy and geochronology of the Early Miocene volcanic units in the Bigadiç borate basin, Western Turkey: Turkish Journal of Earth Sciences, v. 14, p. 227-253.

Erkül, F., Helvacı, C. and Sözbilir, H., 2005b, Evidence for two episodes of volcanism in the Bigadiç borate basin and tectonic implications for western Turkey: Geological Journal, v. 40, p. 545-570.

Erkül, F., Erkül, S.T., Ersoy, Y., Uysal, İ. and Klötzli, U., 2013, Petrology, mineral chemistry and Sr–Nd–Pb isotopic compositions of granitoids in the central Menderes metamorphic core complex: constraints on the evolution of Aegean lithosphere slab: Lithos, v. 180, p. 74-91.

Erkül, S.T., 2012, Petrogenetic evolution of the Early Miocene Alaçamdağ volcano-plutonic complex, northwestern Turkey: implications for the geodynamic framework of the Aegean region: International Journal of Earth Sciences, v. 101, p. 197-219.

Erkül, S.T. and Erkül, F., 2012, Magma interaction processes in syn-extensional granitoids: the Tertiary Menderes Metamorphic Core Complex, western Turkey: Lithos, v. 142, p. 16-33.

Ershov, A. and Nikishin, A., 2004, Recent geodynamics of the Caucasus-Arabia-East Africa region: Geotectonics, v. 38, p. 123-136.

Ersoy, E., Çemen, İ., Helvacı, C. and Billor, Z., 2014a, Tectono-stratigraphy of the Neogene basins in Western Turkey: Implications for tectonic evolution of the Aegean Extended Region: Tectonophysics, v. 635, p. 33-58.

Ersoy, E.Y. and Palmer, M.R., 2013, Eocene-Quaternary magmatic activity in the Aegean: Implications for mantle metasomatism and magma genesis in an evolving orogeny: Lithos, v. 180, p. 5-24.

Ersoy, Y.E., Helvacı, C. and Sözbilir, H., 2010, Tectono-stratigraphic evolution of the NE–SW-trending superimposed Selendi basin: Implications for late Cenozoic crustal extension in Western Anatolia, Turkey: Tectonophysics, v. 488, p. 210-232.

Ersoy, Y.E., Helvacı, C. and Palmer, M.R., 2012a, Petrogenesis of the Neogene volcanic units in the NE–SW-trending basins in western Anatolia, Turkey: Contributions to Mineralogy and Petrology, v. 163, p. 379-401.

Ersoy, Y.E., Palmer, M.R., Uysal, İ. and Gündoğan, İ., 2014b, Geochemistry and petrology of the Early Miocene lamproites and related volcanic rocks in the Thrace Basin, NW Anatolia: Journal of Volcanology and Geothermal Research, v. 283, p. 143-158.

Ersoy, Y.E., Helvacı, C., Uysal, İ., Karaoğlu, Ö., Palmer, M.R. and Dindi, F., 2012b, Petrogenesis

of the Miocene volcanism along the İzmir-Balıkesir Transfer Zone in western Anatolia, Turkey: Implications for origin and evolution of potassic volcanism in post-collisional areas: Journal of Volcanology and Geothermal Research, v. 241, p. 21-38.

Eyuboğlu, Y., Santosh, M., Yi, K., Tuysuz, N., Korkmaz, S., Akaryali, E., Dudas, F.O. and Bektas, O., 2014, The Eastern Black Sea-type Volcanogenic Massive Sulfide Deposits: Geochemistry, zircon U–Pb geochronology and an overview of the geodynamics of ore genesis: Ore Geology Reviews, v. 59, p. 29-54.

Faccenna, C., Becker, T.W., Jolivet, L. and Keskin, M., 2013, Mantle convection in the Middle East: Reconciling Afar upwelling, Arabia indentation and Aegean trench rollback: Earth and Planetary Science Letters, v. 375, p. 254-269.

Faccenna, C., Bellier, O., Martinod, J., Piromallo, C. and Regard, V., 2006, Slab detachment beneath eastern Anatolia: A possible cause for the formation of the North Anatolian fault: Earth and Planetary Science Letters, v. 242, p. 85-97.

Faccenna, C., Becker, T.W., Auer, L., Billi, A., Boschi, L., Brun, J.P., Capitanio, F.A., Funiciello, F., Horvàth, F. and Jolivet, L., 2014, Mantle dynamics in the Mediterranean: Reviews of Geophysics, v. 52, p. 283-332.

Fahmi, N., Rossy, M., Rebetez, M., Chambaudet, A. and El Kheir, A.A., 1997, Fission track dating and thermal history of some volcanic and plutonic complex rocks from Turkey and France: Radiation measurements, v. 28, p. 559-564.

Fayon, A.K., Whitney, D.L., Teyssier, C., Garver, J.I. and Dilek, Y., 2001, Effects of plate convergence obliquity on timing and mechanisms of exhumation of a mid-crustal terrain, the Central Anatolian Crystalline Complex: Earth and Planetary Science Letters, v. 192, p. 191-205.

Ferrari, L., 2004, Slab detachment control on mafic volcanic pulse and mantle heterogeneity in central Mexico: Geology, v. 32, p. 77-80.

Fichtner, A., Saygin, E., Taymaz, T., Cupillard, P., Capdeville, Y. and Trampert, J., 2013, The deep structure of the North Anatolian fault zone: Earth and Planetary Science Letters, v. 373, p. 109-117.

Floyd, P.A., Göncüoğlu, M.C., Winchester, J.A. and Yaliniz, M.K., 2000, Geochemical character and tectonic environment of Neotethyan ophiolitic fragments and metabasites in the Central Anatolian Crystalline Complex, Turkey: Geological Society, London, Special Publications, v. 173, p. 183-202.

Foley, S., 1992, Vein-plus-wall-rock melting mechanisms in the lithosphere and the origin of potassic alkaline magmas: Lithos, v. 28, p. 435-453.

Fonseca, A., Miškovic, A., Siddorn, J., Monoury, S. and Rahimi, M., 2016, Regional integrated structural and alteration analysis of magnetic and infrared remote sensing data from the Kerman belt, Iran: Society of Economic Geologists Special Publication, v. 19, p. 237-258.

Foulger, G.R., Panza, G.F., Artemieva, I., Bastow, I.D., Cammarano, F., Doglioni, C., Evans, J.R., Hamilton, W.B., Lustrino, M. and Thybo, H., 2015, What lies deep in the mantle below: EOS, Transactions of the Geophysical Union, v. 96, p. 1-6.

Fourny, A., Weis, D. and Scoates, J.S., 2016, Comprehensive Pb-Sr-Nd-Hf isotopic, trace

element, and mineralogical characterization of mafic to ultramafic rock reference materials: Geochemistry, Geophysics, Geosystems, v. 17, p. 739-773.

Franklin, J.M., Gibson, H., Jonasson, I. and Galley, A., 2005, Volcanogenic massive sulfide deposits: Economic Geology 100th Anniversary Volume, v. 98, p. 523-560.

Freeburn, R., Bouilhol, P., Maunder, B., Magni, V. and van Hunen, J., 2017, Numerical models of the magmatic processes induced by slab breakoff: Earth and Planetary Science Letters, v. 478, p. 203-213.

Frizon de Lamotte, D., Raulin, C., Mouchot, N., Wrobel-Daveau, J.C., Blanpied, C. and Ringenbach, J.C., 2011, The southernmost margin of the Tethys realm during the Mesozoic and Cenozoic: Initial geometry and timing of the inversion processes: Tectonics, v. 30, p. 1-22.

Fyfe, W., 1992, Magma underplating of continental crust: Journal of Volcanology and Geothermal Research, v. 50, p. 33-40.

Galer, S. and Abouchami, W., 1998, Practical application of lead triple spiking for correction of instrumental mass discrimination: Mineral. Mag. A, v. 62, p. 491-492.

Gallhofer, D., Quadt, A.v., Peytcheva, I., Schmid, S.M. and Heinrich, C.A., 2015, Tectonic, magmatic, and metallogenic evolution of the Late Cretaceous arc in the Carpathian-Balkan orogen: Tectonics, v. 34, p. 1813-1836.

Gans, C.R., Beck, S.L., Zandt, G., Biryol, C.B. and Ozacar, A.A., 2009, Detecting the limit of slab break-off in central Turkey: new high-resolution Pn tomography results: Geophysical Journal International, v. 179, p. 1566-1572.

Garzanti, E., Radeff, G. and Malusà, M.G., 2017, Slab breakoff: A critical appraisal of a geological theory as applied in space and time: Earth-Science Reviews, v. 177, p. 303-319.

Gasparon, M., Rosenbaum, G., Wijbrans, J. and Manetti, P., 2009, The transition from subduction arc to slab tearing: Evidence from Capraia Island, northern Tyrrhenian Sea: Journal of Geodynamics, v. 47, p. 30-38.

Gasquet, D., Levresse, G., Cheilletz, A., Azizi-Samir, M.R. and Mouttaqi, A., 2005, Contribution to a geodynamic reconstruction of the Anti-Atlas (Morocco) during Pan-African times with the emphasis on inversion tectonics and metallogenic activity at the Precambrian–Cambrian transition: Precambrian Research, v. 140, p. 157-182.

Gazel, E., Plank, T., Forsyth, D.W., Bendersky, C., Lee, C.T.A. and Hauri, E.H., 2012, Lithosphere versus asthenosphere mantle sources at the Big Pine Volcanic Field, California: Geochemistry, Geophysics, Geosystems, v. 13, p. 1-25.

Gencalioğlu-Kuşcu, G., 2011, Geochemical characterization of a Quaternary monogenetic volcano in Erciyes Volcanic Complex: Cora Maar (Central Anatolian Volcanic Province, Turkey): International Journal of Earth Sciences, v. 100, p. 1967-1985.

Gencalioğlu-Kuşcu, G. and Geneli, F., 2010, Review of post-collisional volcanism in the Central Anatolian Volcanic Province (Turkey), with special reference to the Tepekoy Volcanic Complex: International Journal of Earth Sciences, v. 99, p. 593-621.

Gerstenberger, H. and Haase, G., 1997, A highly effective emitter substance for mass

spectrometric Pb isotope ratio determinations: Chemical geology, v. 136, p. 309-312.

Gerya, T.V., Yuen, D.A. and Maresch, W.V., 2004, Thermomechanical modelling of slab detachment: Earth and Planetary Science Letters, v. 226, p. 101-116.

Gessner, K., Markwitz, V. and Güngör, T., 2017, Crustal fluid flow in hot continental extension: tectonic framework of geothermal areas and mineral deposits in western Anatolia: Geological Society, London, Special Publications, v. 453, p. 1-23.

Gessner, K., Gallardo, L.A., Markwitz, V., Ring, U. and Thomson, S.N., 2013, What caused the denudation of the Menderes Massif: review of crustal evolution, lithosphere structure, and dynamic topography in southwest Turkey: Gondwana Research, v. 24, p. 243-274.

Ghasemi, A. and Talbot, C.J., 2006, A new tectonic scenario for the Sanandaj–Sirjan Zone (Iran): Journal of Asian Earth Sciences, v. 26, p. 683-693.

Gill, J.B., 1981, Orogenic andesites and plate tectonics: Springer Science & Business Media, 390 p.

Glodny, J. and Hetzel, R., 2007, Precise U–Pb ages of syn-extensional Miocene intrusions in the central Menderes Massif, western Turkey: Geological Magazine, v. 144, p. 235-246.

Göğüş, O.H., Pysklywec, R.N., Şengör, A. and Gün, E., 2017, Drip tectonics and the enigmatic uplift of the Central Anatolian Plateau: Nature communications, v. 8, p. 1538.

Gök, R., Pasyanos, M.E. and Zor, E., 2007, Lithospheric structure of the continent—continent collision zone: eastern Turkey: Geophysical Journal International, v. 169, p. 1079-1088.

Gök, R., Sandvol, E., Türkelli, N., Seber, D. and Barazangi, M., 2003, Sn attenuation in the Anatolian and Iranian plateau and surrounding regions: Geophysical Research Letters, v. 30, p. 1-4.

Göncüoğlu, M.C., 1986, Geochronological data from the southern part (Niğde area) of the Central Anatolian Massif: Mineral Research and Technical Institute of Turkey (MTA) Bulletin, v. 105, p. 83-96.

Görür, N. and Tüysüz, O., 2001, Cretaceous to Miocene palaeogeographic evolution of Turkey: implications for hydrocarbon potential: Journal of Petroleum Geology, v. 24, p. 119-146.

Görür, N., Oktay, F., Seymen, I. and Şengör, A., 1984, Palaeotectonic evolution of the Tuzgölü basin complex, Central Turkey: sedimentary record of a Neo-Tethyan closure: Geological Society, London, Special Publications, v. 17, p. 467-482.

Govers, R. and Wortel, M., 2005, Lithosphere tearing at STEP faults: response to edges of subduction zones: Earth and Planetary Science Letters, v. 236, p. 505-523.

Govers, R. and Fichtner, A., 2016, Signature of slab fragmentation beneath Anatolia from full-waveform tomography: Earth and Planetary Science Letters, v. 450, p. 10-19.

Griffin, W., Begg, G. and O'reilly, S.Y., 2013, Continental-root control on the genesis of magmatic ore deposits: Nature Geoscience, v. 6, p. 905-910.

Groves, D.I., Goldfarb, R.J., Gebre-Mariam, M., Hagemann, S. and Robert, F., 1998, Orogenic

gold deposits: a proposed classification in the context of their crustal distribution and relationship to other gold deposit types: Ore geology reviews, v. 13, p. 7-27.

Grützner, T., Prelević, D. and Akal, C., 2013, Geochemistry and origin of ultramafic enclaves and their basanitic host rock from Kula Volcano, Turkey: Lithos, v. 180, p. 58-73.

Güçtekin, A. and Köprübaşı, N., 2009, Geochemical characteristics of mafic and intermediate volcanic rocks from the Hasandağ and Erciyes volcanoes (Central Anatolia, Turkey): Turkish Journal of Earth Sciences, v. 18, p. 1-27.

Guezou, J.-C., Temiz, H., Poisson, A. and Gürsoy, H., 1996, Tectonics of the Sivas basin: The Neogene record of the Anatolian accretion along the inner Tauric suture: International Geology Review, v. 38, p. 901-925.

Gustafson, L., 1978, Some major factors of porphyry copper genesis: Economic Geology, v. 73, p. 600-607.

Hafkenscheid, E., Wortel, M. and Spakman, W., 2006, Subduction history of the Tethyan region derived from seismic tomography and tectonic reconstructions: Journal of Geophysical Research: Solid Earth, v. 111, p. 1-26.

Hall, D.J., Foster, R.P., Yildiz, B. and Redwood, S.D., 2007, The Inlice High-sulphidation Epithermal Gold Discovery: Defining a Potential New Gold Belt in Turkey: Proceedings of the Ninth Biennial SGA Meeting, Dublin, p. 113-116.

Hart, S.R., 1984, A large-scale isotope anomaly in the Southern Hemisphere mantle: Nature, v. 309, p. 753.

Haschke, M., Scheuber, E., Günther, A. and Reutter, K.J., 2002, Evolutionary cycles during the Andean orogeny: repeated slab breakoff and flat subduction?: Terra Nova, v. 14, p. 49-55.

Hasözbek, A., Akay, E., Erdoğan, B., Satır, M. and Siebel, W., 2010, Early Miocene granite formation by detachment tectonics or not? A case study from the northern Menderes Massif (Western Turkey): Journal of Geodynamics, v. 50, p. 67-80.

Hasözbek, A., Satır, M., Erdoğan, B., Akay, E. and Siebel, W., 2011, Early Miocene post-collisional magmatism in NW Turkey: geochemical and geochronological constraints: International Geology Review, v. 53, p. 1098-1119.

Hattori, K.H. and Keith, J.D., 2001, Contribution of mafic melt to porphyry copper mineralization: evidence from Mount Pinatubo, Philippines, and Bingham Canyon, Utah, USA: Mineralium Deposita, v. 36, p. 799-806.

Hedenquist, J.W. and Lowenstern, J.B., 1994, The role of magmas in the formation of hydrothermal ore deposits: Nature, v. 370, p. 519-527.

Hellstrom, J., Paton, C., Woodhead, J. and Hergt, J., 2008, Iolite: software for spatially resolved LA-(quad and MC) ICPMS analysis: Mineralogical Association of Canada short course series, v. 40, p. 343-348.

Helvacı, C., 2015, Geological features of Neogene basins hosting borate deposits: an overview of deposits and future forecast, Turkey: Bulletin of the Mineral Research and Exploration, v. p. 169-215.

Hemming, S., McLennan, S. and Hanson, G., 1994, Lead isotopes as a provenance tool for quartz: Examples from plutons and quartzite, northeastern Minnesota, USA: Geochimica et cosmochimica acta, v. 58, p. 4455-4464.

Hernlund, J.W., Tackley, P.J. and Stevenson, D.J., 2008, Buoyant melting instabilities beneath extending lithosphere: 1. Numerical models: Journal of Geophysical Research: Solid Earth, v. 113, p. 1-17.

Herzberg, C., Fyfe, W. and Carr, M., 1983, Density constraints on the formation of the continental Moho and crust: Contributions to Mineralogy and Petrology, v. 84, p. 1-5.

Hetzel, R., Passchier, C.W., Ring, U. and Dora, Ö.O., 1995, Bivergent extension in orogenic belts: the Menderes massif (southwestern Turkey): Geology, v. 23, p. 455-458.

Hezarkhani, A., 2006a, Hydrothermal evolution of the Sar-Cheshmeh porphyry Cu–Mo deposit, Iran: evidence from fluid inclusions: Journal of Asian Earth Sciences, v. 28, p. 409-422.

Hezarkhani, A., 2006b, Petrology of the intrusive rocks within the Sungun porphyry copper deposit, Azerbaijan, Iran: Journal of Asian Earth Sciences, v. 27, p. 326-340.

Hickey, R.L., Frey, F.A., Gerlach, D.C. and Lopez-Escobar, L., 1986, Multiple sources for basaltic arc rocks from the southern volcanic zone of the Andes (34–41 S): trace element and isotopic evidence for contributions from subducted oceanic crust, mantle, and continental crust: Journal of Geophysical Research: Solid Earth, v. 91, p. 5963-5983.

Higgins, M., 2014, New Kinematic and Geochronologic Evidence for the Quaternary Evolution of the Central Anatolian Fault Zone: Unpublished MASc thesis, Toronto, Ontario, University of Toronto, 108 p.

Hildreth, W. and Moorbath, S., 1988, Crustal contributions to arc magmatism in the Andes of central Chile: Contributions to mineralogy and petrology, v. 98, p. 455-489.

Hirose, K. and Kawamoto, T., 1995, Hydrous partial melting of lherzolite at 1 GPa: the effect of H2O on the genesis of basaltic magmas: Earth and Planetary Science Letters, v. 133, p. 463-473.

Hole, M., Rogers, G., Saunders, A. and Storey, M., 1991, Relation between alkalic volcanism and slab-window formation: Geology, v. 19, p. 657-660.

Hollings, P., Cooke, D. and Clark, A., 2005, Regional geochemistry of Tertiary igneous rocks in central Chile: Implications for the geodynamic environment of giant porphyry copper and epithermal gold mineralization: Economic Geology 100th Anniversary Volume, v. 98, p. 887-904.

Hou, Z., Yang, Z., Qu, X., Meng, X., Li, Z., Beaudoin, G., Rui, Z., Gao, Y. and Zaw, K., 2009, The Miocene Gangdese porphyry copper belt generated during post-collisional extension in the Tibetan Orogen: Ore geology reviews, v. 36, p. 25-51.

Hou, Z., Yang, Z., Lu, Y., Kemp, A., Zheng, Y., Li, Q., Tang, J., Yang, Z. and Duan, L., 2015, A genetic linkage between subduction- and collision-related porphyry Cu deposits in continental collision zones: Geology, v. 43, p. 247-250.

Houseman, G., 1996, From mountains to basin: Nature, v. 379, p. 771-772.

Houseman, G.A. and Molnar, P., 1997, Gravitational (Rayleigh–Taylor) instability of a layer with non-linear viscosity and convective thinning of continental lithosphere: Geophysical Journal International, v. 128, p. 125-150.

Houseman, G.A., McKenzie, D.P. and Molnar, P., 1981, Convective instability of a thickened boundary layer and its relevance for the thermal evolution of continental convergent belts: Journal of Geophysical Research: Solid Earth, v. 86, p. 6115-6132.

Hronsky, J.M., Groves, D.I., Loucks, R.R. and Begg, G.C., 2012, A unified model for gold mineralisation in accretionary orogens and implications for regional-scale exploration targeting methods: Mineralium Deposita, v. 47, p. 339-358.

Hu, X., Garzanti, E., Wang, J., Huang, W., An, W. and Webb, A., 2016, The timing of India-Asia collision onset–Facts, theories, controversies: Earth-Science Reviews, v. 160, p. 264-299.

Huang, Z., Wang, L., Zhao, D., Xu, M., Mi, N., Yu, D., Li, H. and Li, C., 2010, Upper mantle structure and dynamics beneath Southeast China: Physics of the Earth and Planetary Interiors, v. 182, p. 161-169.

Hubert-Ferrari, A., King, G., Van Der Woerd, J., Villa, I., Altunel, E. and Armijo, R., 2009, Long-term evolution of the North Anatolian Fault: new constraints from its eastern termination: Geological Society, London, Special Publications, v. 311, p. 133-154.

Hüsing, S.K., Zachariasse, W.-J., van Hinsbergen, D.J., Krijgsman, W., Inceöz, M., Harzhauser, M., Mandic, O. and Kroh, A., 2009, Oligocene–Miocene basin evolution in SE Anatolia, Turkey: constraints on the closure of the eastern Tethys gateway: Geological Society, London, Special Publications, v. 311, p. 107-132.

İmer, A., Richards, J.P. and Creaser, R.A., 2013, Age and tectonomagmatic setting of the Eocene Çöpler–Kabataş magmatic complex and porphyry-epithermal Au deposit, East Central Anatolia, Turkey: Mineralium Deposita, v. 48, p. 557-583.

İmer, A., Richards, J.P. and Muehlenbachs, K., 2016, Hydrothermal Evolution of the Çöpler Porphyry-Epithermal Au Deposit, Erzincan Province, Central Eastern Turkey: Economic Geology, v. 111, p. 1619-1658.

İmer, A., Richards, J.P., Creaser, R.A. and Spell, T.L., 2014, The late Oligocene Cevizlidere Cu-Au-Mo deposit, Tunceli Province, eastern Turkey: Mineralium Deposita, v. p. 1-19.

Innocenti, F., Mazzuoli, R., Pasquare, G., Di Brozolo, F.R. and Villari, L., 1976, Evolution of the volcanism in the area of interaction between the Arabian, Anatolian and Iranian plates (Lake Van, Eastern Turkey): Journal of Volcanology and Geothermal Research, v. 1, p. 103-112.

Innocenti, F., Mazzuoli, R., Pasquare, G., Serri, G. and Villari, L., 1980, Geology of the volcanic area north of Lake Van (Turkey): Geologische Rundschau, v. 69, p. 292-323.

Innocenti, F., Mazzuoli, R., Pasquare, G., Di Brozolo, F.R. and Villari, L., 1982, Tertiary and quaternary volcanism of the Erzurum-Kars area (Eastern Turkey): geochronological data and geodynamic evolution: Journal of Volcanology and Geothermal Research, v. 13, p. 223-240.

Innocenti, F., Agostini, S., Di Vincenzo, G., Doglioni, C., Manetti, P., Savaşçin, M. and Tonarini, S., 2005, Neogene and Quaternary volcanism in Western Anatolia: magma sources and

geodynamic evolution: Marine Geology, v. 221, p. 397-421.

Irvine, T. and Baragar, W., 1971, A guide to the chemical classification of the common volcanic rocks: Canadian Journal of Earth Sciences, v. 8, p. 523-548.

Isacks, B., Oliver, J. and Sykes, L.R., 1968, Seismology and the new global tectonics: Journal of Geophysical Research, v. 73, p. 5855-5899.

Ishihara, S., 1981, The granitoid series and mineralization: Economic Geology 75th Anniversary Volume, v. p. 458-484.

Isik, V., Tekeli, O. and Seyitoğlu, G., 2004, The 40Ar/39Ar age of extensional ductile deformation and granitoid intrusion in the northern Menderes core complex: implications for the initiation of extensional tectonics in western Turkey: Journal of Asian Earth Sciences, v. 23, p. 555-566.

Işik, V. and Tekeli, O., 2001, Late orogenic crustal extension in the northern Menderes massif (western Turkey): evidence for metamorphic core complex formation: International Journal of Earth Sciences, v. 89, p. 757-765.

Jaffey, A., Flynn, K., Glendenin, L., Bentley, W.t. and Essling, A., 1971, Precision measurement of half-lives and specific activities of U 235 and U 238: Physical Review C, v. 4, p. 1889.

Jaffey, N., Robertson, A. and Pringle, M., 2004, Latest Miocene and Pleistocene ages of faulting, determined by $^{40}Ar/^{39}Ar$ single-crystal dating of airfall tuff and silicic extrusives of the Erciyes Basin, central Turkey: evidence for intraplate deformation related to the tectonic escape of Anatolia: Terra Nova, v. 16, p. 45-53.

Jamali, H. and Mehrabi, B., 2015, Relationships between arc maturity and Cu–Mo–Au porphyry and related epithermal mineralization at the Cenozoic Arasbaran magmatic belt: Ore Geology Reviews, v. 65, p. 487-501.

Janković, S., 1977, The copper deposits and geotectonic setting of the Thethyan Eurasian Metallogenic Belt: Mineralium Deposita, v. 12, p. 37-47.

Janković, S., 1997, The Carpatho-Balkanides and adjacent area: a sector of the Tethyan Eurasian metallogenic belt: Mineralium Deposita, v. 32, p. 426-433.

Jarvis, A., Reuter, H.I., Nelson, A. and Guevara, E., 2008, Hole-filled SRTM for the globe Version 4: available from the CGIAR-CSI SRTM 90m Database (http://srtm.csi.cgiar.org), v. p.

Jensen, E.P. and Barton, M.D., 2000, Gold deposits related to alkaline magmatism: SEG Reviews - Gold in 2000, v. 13, p. 279-314.

Jiang, Y.-H., Jiang, S.-Y., Ling, H.-F. and Dai, B.-Z., 2006, Low-degree melting of a metasomatized lithospheric mantle for the origin of Cenozoic Yulong monzogranite-porphyry, east Tibet: geochemical and Sr–Nd–Pb–Hf isotopic constraints: Earth and Planetary Science Letters, v. 241, p. 617-633.

Jolivet, L. and Faccenna, C., 2000, Mediterranean extension and the Africa-Eurasia collision: Tectonics, v. 19, p. 1095-1106.

Jolivet, L., Faccenna, C., Huet, B., Labrousse, L., Le Pourhiet, L., Lacombe, O., Lecomte, E.,

Burov, E., Denele, Y. and Brun, J.-P., 2013, Aegean tectonics: Strain localisation, slab tearing and trench retreat: Tectonophysics, v. 597, p. 1-33.

Jolivet, L., Menant, A., Sternai, P., Rabillard, A., Arbaret, L., Augier, R., Laurent, V., Beaudoin, A., Grasemann, B. and Huet, B., 2015, The geological signature of a slab tear below the Aegean: Tectonophysics, v. 659, p. 166-182.

Jugo, P.J., 2009, Sulfur content at sulfide saturation in oxidized magmas: Geology, v. 37, p. 415-418.

Kadıoğlu, Y.K., Dilek, Y. and Foland, K.A., 2006, Slab break-off and syncollisional origin of the Late Cretaceous magmatism in the Central Anatolian crystalline complex, Turkey: Geological Society of America Special Papers, v. 409, p. 381-415.

Kaislaniemi, L., Van Hunen, J., Allen, M. and Neill, I., 2014, Sublithospheric small-scale convection—A mechanism for collision zone magmatism: Geology, v. 42, p. 291-294.

Karakaya, N., 1991, Altınekin (Konya) civarının jeolojisi ve mineralojik petrografik incelemesi: Unpublished thesis, Selçuk Üniversitesi Fen Bilimleri Enstitüsü.

Karaoğlan, F., 2016, Tracking the uplift of the Bolkar Mountains (south-central Turkey): evidence from apatite fission track thermochronology: Turkish Journal of Earth Sciences, v. 25, p. 64-80.

Karaoğlan, F., Parlak, O., Hejl, E., Neubauer, F. and Klötzli, U., 2016, The temporal evolution of the active margin along the Southeast Anatolian Orogenic Belt (SE Turkey): Evidence from U–Pb, Ar–Ar and fission track chronology: Gondwana Research, v. 33, p. 190-208.

Karaoğlu, Ö. and Helvacı, C., 2014, Isotopic evidence for a transition from subduction to slab-tear related volcanism in western Anatolia, Turkey: Lithos, v. 192, p. 226-239.

Karaoğlu, Ö., Helvacı, C. and Ersoy, Y., 2010, Petrogenesis and $^{40}Ar/^{39}Ar$ geochronology of the volcanic rocks of the Uşak-Güre basin, western Türkiye: Lithos, v. 119, p. 193-210.

Karsli, O., Chen, B., Uysal, I., Aydin, F., Wijbrans, J.R. and Kandemir, R., 2008, Elemental and Sr–Nd–Pb isotopic geochemistry of the most recent Quaternary volcanism in the Erzincan Basin, Eastern Turkey: framework for the evaluation of basalt–lower crust interaction: Lithos, v. 106, p. 55-70.

Karsli, O., Dokuz, A., Kaliwoda, M., Uysal, I., Aydin, F., Kandemir, R. and Fehr, K.-T., 2014, Geochemical fingerprints of Late Triassic calc-alkaline lamprophyres from the Eastern Pontides, NE Turkey: A key to understanding lamprophyre formation in a subduction-related environment: Lithos, v. 196, p. 181-197.

Kaviani, A., Paul, A., Bourova, E., Hatzfeld, D., Pedersen, H. and Mokhtari, M., 2007, A strong seismic velocity contrast in the shallow mantle across the Zagros collision zone (Iran): Geophysical Journal International, v. 171, p. 399-410.

Kay, R.W. and Kay, S.M., 1993, Delamination and delamination magmatism: Tectonophysics, v. 219, p. 177-189.

Kay, S.M. and Mpodozis, C., 2001, Central Andean ore deposits linked to evolving shallow subduction systems and thickening crust: GSA Today, v. 11, p. 4-9.

Kay, S.M., Coira, B. and Viramonte, J., 1994, Young mafic back arc volcanic rocks as indicators of continental lithospheric delamination beneath the Argentine Puna plateau, central Andes: Journal of Geophysical Research: Solid Earth, v. 99, p. 24323-24339.

Kay, S.M., Godoy, E. and Kurtz, A., 2005, Episodic arc migration, crustal thickening, subduction erosion, and magmatism in the south-central Andes: Geological Society of America Bulletin, v. 117, p. 67-88.

Kaygusuz, A., Aslan, Z., Aydınçakır, E., Yücel, C., Gücer, M.A. and Şen, C., 2018, Geochemical and Sr-Nd-Pb isotope characteristics of the Miocene to Pliocene volcanic rocks from the Kandilli (Erzurum) area, Eastern Anatolia (Turkey): Implications for magma evolution in extension-related origin: Lithos, v. 296, p. 332-351.

Kaymakçı, N., İncezöz, M. and Ertepınar, P., 2006, 3D-Architecture and Neogene Evolution of the Malatya Basin: Inferences for the Kinematics of the Malatya and Ovacık Fault Zones: Turkish Journal of Earth Sciences, v. 15, p. 123-154.

Kaymakçı, N., Inceöz, M., Ertepınar, P. and Koç, A., 2010, Late Cretaceous to recent kinematics of SE Anatolia (Turkey): Geological Society, London, Special Publications, v. 340, p. 409-435.

Kelemen, P., Hanghøj, K. and Greene, A., 2014, One view of the geochemistry of subduction-related magmatic arcs, with an emphasis on primitive andesite and lower crust: Treatise on Geochemistry 2nd Edition, v. p. 749-805.

Keller, J., 1974, Quaternary maar volcanism near Karapinar in Central Anatolia: Bulletin Volcanologique, v. 38, p. 378-396.

Keller, J., Burgath, K., Jung, D. and Wolff, F., 1977, Geologie und Petrologie des neogenen Kalkalkali-Vulkanismus von Konya (Erenler Dag-Alaca Dag-Massiv, Zentral-Anatolien): Geologisches Jahrbuch, v. 25, p. 37-117.

Keller, J., Jung, D., Eckhardt, F. and Kreuzer, H., 1992, Radiometric ages and chemical characterization of the Galatean andesite massif, Pontus, Turkey: Acta Vulcanologica, v. 2, p. 267-276.

Kepezhinskas, P., Defant, M.J. and Drummond, M.S., 1996, Progressive enrichment of island arc mantle by melt-peridotite interaction inferred from Kamchatka xenoliths: Geochimica et Cosmochimica Acta, v. 60, p. 1217-1229.

Keskin, M., 2003, Magma generation by slab steepening and breakoff beneath a subduction-accretion complex: An alternative model for collision-related volcanism in Eastern Anatolia, Turkey: Geophysical Research Letters, v. 30, p. 1-4.

Keskin, M., 2007, Eastern Anatolia: a hotspot in a collision zone without a mantle plume: Geological Society of America Special Papers, v. 430, p. 693-722.

Keskin, M., Pearce, J.A. and Mitchell, J., 1998, Volcano-stratigraphy and geochemistry of collision-related volcanism on the Erzurum–Kars Plateau, northeastern Turkey: Journal of Volcanology and Geothermal Research, v. 85, p. 355-404.

Keskin, M., Genç, Ş.C. and Tüysüz, O., 2008, Petrology and geochemistry of post-collisional Middle Eocene volcanic units in North-Central Turkey: evidence for magma generation by slab breakoff following the closure of the Northern Neotethys Ocean: Lithos, v. 104, p. 267-305.

Keskin, M., Pearce, J.A., Kempton, P.D. and Greenwood, P., 2006, Magma-crust interactions and magma plumbing in a postcollisional setting: geochemical evidence from the Erzurum-Kars volcanic plateau, eastern Turkey: Special Papers-Geological Society of America, v. 409, p. 475.

Keskin, M., Chugaev, A., Lebedev, V., Sharkov, E., Oyan, V. and Kavak, O., 2012, The geochronology and origin of mantle sources for late cenozoic intraplate volcanism in the frontal part of the Arabian plate in the Karacadağ neovolcanic area of Turkey. Part 2. The results of geochemical and isotope (Sr-Nd-Pb) studies: Volcanology and Seismology, v. 6, p. 361.

Kesler, S.E., 1973, Copper, molybdenum and gold abundances in porphyry copper deposits: Economic Geology, v. 68, p. 106-112.

Ketin, I., 1966, Tectonic units of Anatolia (Asia Minor): Mineral Research and Exploration Institute of Turkey, v. 66, p. 22-34.

Kheirkhah, M., Allen, M. and Emami, M., 2009, Quaternary syn-collision magmatism from the Iran/Turkey borderlands: Journal of Volcanology and Geothermal Research, v. 182, p. 1-12.

Kind, R., Eken, T., Tilmann, F., Sodoudi, F., Taymaz, T., Bulut, F., Yuan, X., Can, B. and Schneider, F., 2015, Thickness of the lithosphere beneath Turkey and surroundings from S receiver functions: Solid Earth, v. 6, p. 971-984.

Kirchenbaur, M., Münker, C., Schuth, S., Garbe-Schönberg, D. and Marchev, P., 2011, Tectonomagmatic constraints on the sources of Eastern Mediterranean K-rich lavas: Journal of Petrology, v. 53, p. 27-65.

Kissel, C., Laj, C., Poisson, A. and Görür, N., 2003, Paleomagnetic reconstruction of the Cenozoic evolution of the Eastern Mediterranean: Tectonophysics, v. 362, p. 199-217.

Klaver, M., Davies, G.R. and Vroon, P.Z., 2016, Subslab mantle of African provenance infiltrating the Aegean mantle wedge: Geology, v. 44, p. 367-370.

Klaver, M., Djuly, T., de Graaf, S., Sakes, A., Wijbrans, J., Davies, G. and Vroon, P., 2015, Temporal and spatial variations in provenance of Eastern Mediterranean Sea sediments: Implications for Aegean and Aeolian arc volcanism: Geochimica et Cosmochimica Acta, v. 153, p. 149-168.

Klemme, S. and O'Neill, H.S., 2000, The near-solidus transition from garnet lherzolite to spinel lherzolite: Contributions to Mineralogy and Petrology, v. 138, p. 237-248.

Koç, A., Kaymakci, N., Van Hinsbergen, D.J. and Vissers, R.L., 2016, A Miocene onset of the modern extensional regime in the Isparta Angle: constraints from the Yalvaç Basin (southwest Turkey): International Journal of Earth Sciences, v. 105, p. 369-398.

Koç, A., Kaymakci, N., van Hinsbergen, D.J., Kuiper, K.F. and Vissers, R.L., 2012, Tectono-Sedimentary evolution and geochronology of the Middle Miocene Altınapa Basin, and implications for the Late Cenozoic uplift history of the Taurides, southern Turkey: Tectonophysics, v. 532, p. 134-155.

Kociumbas, M. and Page, R., 2009, The Cevizlidere porphyry deposit, Tunceli Province: 114 p.

Koçyiğit, A. and Beyhan, A., 1998, A new intracontinental transcurrent structure: the Central Anatolian Fault Zone, Turkey: Tectonophysics, v. 284, p. 317-336.

Koçyiğit, A. and Erol, O., 2001, A tectonic escape structure: Erciyes pull-apart basin, Kayseri, central Anatolia, Turkey: Geodinamica Acta, v. 14, p. 133-145.

Koçyiğit, A., Yilmaz, A., Adamia, S. and Kuloshvili, S., 2001, Neotectonics of East Anatolian Plateau (Turkey) and Lesser Caucasus: implication for transition from thrusting to strike-slip faulting: Geodinamica Acta, v. 14, p. 177-195.

Koçyiğit, A., Winchester, J.A., Bozkurt, E.n. and Holland, G., 2003, Saraçköy Volcanic Suite: implications for the subductional phase of arc evolution in the Galatean Arc Complex, Ankara, Turkey: Geological Journal, v. 38, p. 1-14.

Komut, T., 2015, High surface topography related to upper mantle flow beneath Eastern Anatolia: Geophysical Journal International, v. 203, p. 1263-1273.

Koppers, A.A., 2002, ArArCALC—software for $^{40}Ar/^{39}Ar$ age calculations: Computers & Geosciences, v. 28, p. 605-619.

Koralay, T., 2010, Petrographic and geochemical characteristics of upper Miocene Tekkedag volcanics (Central Anatolia—Turkey): Chemie der Erde-Geochemistry, v. 70, p. 335-351.

Koralay, T., Kadioglu, Y.K. and Davis, P., 2011, Weak compositional zonation in a silicic magmatic system: Incesu ignimbrite, Central Anatolian Volcanic Province (Kayseri–Turkey): Journal of Asian Earth Sciences, v. 40, p. 371-393.

Korkmaz, G.G., Asan, K., Kurt, H. and Morgan, G., 2017, $^{40}Ar/^{39}Ar$ geochronology, elemental and Sr-Nd-Pb isotope geochemistry of the Neogene bimodal volcanism in the Yükselen area, NW Konya (Central Anatolia, Turkey): Journal of African Earth Sciences, v. 129, p. 427-444.

Koza Gold, 2015, Operational Report & Financials: 60 p.

Kumral, M., Abdelnasser, A. and Budakoglu, M., 2016, Geochemistry of Hydrothermal Alteration Associated with Cenozoic Intrusion-Hosted Cu-Pb-Zn Mineralization at Tavşanlı Area, Kütahya, NW Turkey: Minerals, v. 6, p. 13.

Kumral, M., Coban, H., Gedikoglu, A. and Kilinc, A., 2006, Petrology and geochemistry of augite trachytes and porphyritic trachytes from the Gölcük volcanic region, Isparta, SW Turkey: a case study: Journal of Asian Earth Sciences, v. 27, p. 707-716.

Kürkçüoğlu, B., 2010, Geochemistry and petrogenesis of basaltic rocks from the Develidağ volcanic complex, Central Anatolia, Turkey: Journal of Asian Earth Sciences, v. 37, p. 42-51.

Kürkçüoğlu, B., Sen, E., Aydar, E., Gourgaud, A. and Gündogdu, N., 1998, Geochemical approach to magmatic evolution of Mt. Erciyes stratovolcano Central Anatolia, Turkey: Journal of Volcanology and Geothermal Research, v. 85, p. 473-494.

Kürkçüoğlu, B., Sen, E., Temel, A., Aydar, E. and Gourgaud, A., 2004, Interaction of asthenospheric and lithospheric mantle: the genesis of calc-alkaline volcanism at Erciyes Volcano, Central Anatolia, Turkey: International Geology Review, v. 46, p. 243-258.

Kürkçüoğlu, B., Pickard, M., Şen, P., Hanan, B.B., Sayit, K., Plummer, C., Sen, E., Yurur, T. and Furman, T., 2015, Geochemistry of mafic lavas from Sivas, Turkey and the evolution of Anatolian lithosphere: Lithos, v. 232, p. 229-241.

Kurt, H. and Arslan, M., 2001, Bodrum (GB Anadolu) volkanik kayaçlarının jeokimyasal ve petrolojik özellikleri: fraksiyonel kristalleşme, magma karışımı ve asimilasyona ilişkin bulgular: Yerbilimleri Dergisi, v. 5, p. 15-32.

Kurt, H., Özkan, A. and Koçak, K., 2003, Orta Anadolu da Konya'nın batısındaki dalma batma ile ilişkili volkanik kayaçların jeolojisi, petrografisi ve jeokimyası: Türkiye Jeoloji Bülteni, v. 46, p. 39-51.

Kurt, H., Asan, K. and Ruffet, G., 2008, The relationship between collision-related calcalkaline, and within-plate alkaline volcanism in the Karacadağ area (Konya-Türkiye, central Anatolia): Chemie der Erde-Geochemistry, v. 68, p. 155-176.

Kürüm, S. and Tanyıldızı, Ö., 2017, Geochemical and Sr-Nd isotopic characteristics of Upper Cretaceous (calc-alkaline) and Miocene (alkaline) volcanic rocks: Elazığ, Eastern Taurides, Turkey: Journal of African Earth Sciences, v. 134, p. 332-344.

Kürüm, S., Önal, A., Boztuğ, D., Spell, T. and Arslan, M., 2008, $^{40}Ar/^{39}Ar$ age and geochemistry of the post-collisional Miocene Yamadağ volcanics in the Arapkir area (Malatya Province), eastern Anatolia, Turkey: Journal of Asian Earth Sciences, v. 33, p. 229-251.

Kuşcu, İ. and Erler, A., 1998, Mineralizations in the Central Anatolian Crystalline Complex: metallogeny of a collision related setting: Int Geol Rev, v. 40, p. 552-565.

Kuşcu, İ., Gencalioğlu-Kuşcu, G., Tosdal, R.M., Ulrich, T.D. and Friedman, R., 2010, Magmatism in the southeastern Anatolian orogenic belt: transition from arc to post-collisional setting in an evolving orogen: Geological Society, London, Special Publications, v. 340, p. 437-460.

Kuşcu, İ., Tosdal, R.M., Gencalioğlu-Kuşcu, G., Friedman, R. and Ullrich, T.D., 2013, Late Cretaceous to Middle Eocene magmatism and metallogeny of a portion of the Southeastern Anatolian orogenic belt, East-Central Turkey: Economic Geology, v. 108, p. 641-666.

Kuzucuoglu, C., Pastre, J.-F., Black, S., Ercan, T., Fontugne, M., Guillou, H., Hatte, C., Karabiyikoglu, M., Orth, P. and Türkecan, A., 1998, Identification and dating of tephra layers from Quaternary sedimentary sequences of Inner Anatolia, Turkey: Journal of Volcanology and Geothermal Research, v. 85, p. 153-172.

Lashko, E., 2013, The Ortaçam North high-sulphidation epithermal gold deposit: A description of the breccias and associated mineralisation: Unpublished M.Sc thesis, University of Southampton, 140 p.

Le Pennec, J.-L., Temel, A., Froger, J.-L., Sen, S., Gourgaud, A. and Bourdier, J.-L., 2005, Stratigraphy and age of the Cappadocia ignimbrites, Turkey: reconciling field constraints with paleontologic, radiochronologic, geochemical and paleomagnetic data: Journal of Volcanology and Geothermal Research, v. 141, p. 45-64.

Le Pichon, X. and Angelier, J., 1979, The Hellenic arc and trench system: a key to the neotectonic evolution of the eastern Mediterranean area: Tectonophysics, v. 60, p. 1-42.

Le Pichon, X. and Angelier, J., 1981, The Aegean Sea: Phil. Trans. R. Soc. Lond. A, v. 300, p.

357-372.

Le Pichon, X. and Kreemer, C., 2010, The Miocene-to-present kinematic evolution of the Eastern Mediterranean and Middle East and its implications for dynamics: Annual Review of Earth and Planetary Sciences, v. 38, p. 323-351.

Lebedev, V., Sharkov, E., Keskin, M. and Oyan, V., 2010, Erratum: Geochronology of Late Cenozoic volcanism in the area of Lake Van, Turkey: An example of developmental dynamics for magmatic processes [Doklady earth sciences, 433 (2), pp. 1031–1037]: Doklady Earth Sciences, p. 1548-1554.

Lebedev, V., Sharkov, E., Ünal, E. and Keskin, M., 2016, Late Pleistocene Tendürek Volcano (Eastern Anatolia, Turkey): I. Geochronology and petrographic characteristics of igneous rocks: Petrology, v. 24, p. 127-152.

Lee, C.-T.A., Luffi, P., Chin, E.J., Bouchet, R., Dasgupta, R., Morton, D.M., Le Roux, V., Yin, Q.-z. and Jin, D., 2012, Copper systematics in arc magmas and implications for crust-mantle differentiation: Science, v. 336, p. 64-68.

Leeman, W. and Sisson, V., 1996, Geochemistry of boron and its implications for crustal and mantle processes: Reviews in Mineralogy and Geochemistry, v. 33, p. 645-707.

Leeman, W.P., 1983, The influence of crustal structure on compositions of subduction-related magmas: Journal of Volcanology and Geothermal Research, v. 18, p. 561-588.

Leeman, W.P., Carr, M.J. and Morris, J.D., 1994, Boron geochemistry of the Central American volcanic arc: constraints on the genesis of subduction-related magmas: Geochimica et Cosmochimica Acta, v. 58, p. 149-168.

Lefebvre, C., Barnhoorn, A., van Hinsbergen, D.J., Kaymakci, N. and Vissers, R.L., 2011, Late Cretaceous extensional denudation along a marble detachment fault zone in the Kırşehir massif near Kaman, central Turkey: Journal of Structural Geology, v. 33, p. 1220-1236.

Lefebvre, C., Meijers, M.J., Kaymakci, N., Peynircioğlu, A., Langereis, C.G. and Van Hinsbergen, D.J., 2013, Reconstructing the geometry of central Anatolia during the late Cretaceous: Large-scale Cenozoic rotations and deformation between the Pontides and Taurides: Earth and Planetary Science Letters, v. 366, p. 83-98.

Lei, J. and Zhao, D., 2007, Teleseismic evidence for a break-off subducting slab under Eastern Turkey: Earth and Planetary Science Letters, v. 257, p. 14-28.

Lenoir, X., Garrido, C.J., Bodinier, J.-l., Dautria, J.-M. and Gervilla, F., 2001, The recrystallization front of the Ronda peridotite: evidence for melting and thermal erosion of subcontinental lithospheric mantle beneath the Alboran Basin: Journal of Petrology, v. 42, p. 141-158.

Leo, G.W., Marvin, R. and Mehnert, H., 1974, Geologic framework of the Kuluncak-Sofular area, east-central Turkey, and K-Ar ages of igneous rocks: Geological Society of America Bulletin, v. 85, p. 1785-1788.

Leo, G.W., Onder, E., Kilic, M. and Avci, M., 1978, Geology and mineral resources of the Kuluncak-Sofular area (Malatya K-39a1 and K-39a2 quadrangles), Turkey: G.S. Bulletin, 66 p.

Lepetit, P., Viereck, L., Piper, J.D., Sudo, M., Gürel, A., Çopuroğlu, I., Gruber, M., Mayer, B., Koch, M. and Tatar, O., 2014, $^{40}Ar/^{39}Ar$ dating of ignimbrites and plinian air-fall layers from Cappadocia, Central Turkey: Implications to chronostratigraphic and Eastern Mediterranean palaeoenvironmental record: Chemie der Erde-Geochemistry, v. 74, p. 471-488.

Leroux, G.M., 2016, Stratigraphic and petrographic characterization of HS epithermal Au-Ag mineralization at the TV Tower district, Biga Peninsula, NW Turkey: Unpublished M.Sc thesis, Vancouver, Canada, The University of British Columbia, 198 p.

Levander, A., Schmandt, B., Miller, M., Liu, K., Karlstrom, K., Crow, R., Lee, C.-T. and Humphreys, E., 2011, Continuing Colorado plateau uplift by delamination-style convective lithospheric downwelling: Nature, v. 472, p. 461.

Levin, V., Shapiro, N., Park, J. and Ritzwoller, M., 2002, Seismic evidence for catastrophic slab loss beneath Kamchatka: Nature, v. 418, p. 763.

Li, Z.-H., Xu, Z., Gerya, T. and Burg, J.-P., 2013, Collision of continental corner from 3-D numerical modeling: Earth and Planetary Science Letters, v. 380, p. 98-111.

Liégeois, J.-P., Navez, J., Hertogen, J. and Black, R., 1998, Contrasting origin of post-collisional high-K calc-alkaline and shoshonitic versus alkaline and peralkaline granitoids. The use of sliding normalization: Lithos, v. 45, p. 1-28.

Liew, T. and Hofmann, A., 1988, Precambrian crustal components, plutonic associations, plate environment of the Hercynian Fold Belt of central Europe: indications from a Nd and Sr isotopic study: Contributions to Mineralogy and Petrology, v. 98, p. 129-138.

Lips, A.L., 2002, Correlating magmatic-hydrothermal ore deposit formation over time with geodynamic processes in SE Europe: Geological Society, London, Special Publications, v. 204, p. 69-79.

Lips, A.L., Cassard, D., Sözbilir, H., Yilmaz, H. and Wijbrans, J., 2001, Multistage exhumation of the Menderes massif, western Anatolia (Turkey): International Journal of Earth Sciences, v. 89, p. 781-792.

Lister, G.S., Banga, G. and Feenstra, A., 1984, Metamorphic core complexes of Cordilleran type in the Cyclades, Aegean Sea, Greece: Geology, v. 12, p. 221-225.

Livingston, D.E., Mauger, R.L. and Damon, P.E., 1968, Geochronology of the emplacement, enrichment, and preservation of Arizona porphyry copper deposits: Economic Geology, v. 63, p. 30-36.

Logan, J.M. and Mihalynuk, M.G., 2014, Tectonic controls on early Mesozoic paired alkaline porphyry deposit belts (Cu-Au±Ag-Pt-Pd-Mo) within the Canadian Cordillera: Economic Geology, v. 109, p. 827-858.

Lowell, J.D. and Guilbert, J.M., 1970, Lateral and vertical alteration-mineralization zoning in porphyry ore deposits: Economic Geology, v. 65, p. 373-408.

Ludwig, K., 2012, User's manual for Isoplot version 3.75–4.15: a geochronological toolkit for Microsoft: Excel Berkley Geochronological Center Special Publication, v. 4, p. 1-76.

Lustrino, M., Keskin, M., Mattioli, M., Lebedev, V.A., Chugaev, A., Sharkov, E. and Kavak, O., 2010, Early activity of the largest Cenozoic shield volcano in the circum-Mediterranean

area: Mt. Karacadağ, SE Turkey: European Journal of Mineralogy, v. 22, p. 343-362.

Macpherson, C.G., Dreher, S.T. and Thirlwall, M.F., 2006, Adakites without slab melting: high pressure differentiation of island arc magma, Mindanao, the Philippines: Earth and Planetary Science Letters, v. 243, p. 581-593.

Madanipour, S., Ehlers, T.A., Yassaghi, A. and Enkelmann, E., 2017, Accelerated middle Miocene exhumation of the Talesh Mountains constrained by U-Th/He thermochronometry: evidence for the Arabia-Eurasia collision in the NW Iranian Plateau: Tectonics, v. 36, p.

Maggi, A. and Priestley, K., 2005, Surface waveform tomography of the Turkish–Iranian plateau: Geophysical Journal International, v. 160, p. 1068-1080.

Magni, V., Allen, M.B., Van Hunen, J. and Bouihol, P., 2017, Continental underplating after slab break-off: Earth and Planetary Science Letters, v. 474, p. 59-67.

Mair, J.L., Farmer, G.L., Groves, D.I., Hart, C.J. and Goldfarb, R.J., 2011, Petrogenesis of postcollisional magmatism at Scheelite Dome, Yukon, Canada: Evidence for a lithospheric mantle source for magmas associated with intrusion-related gold systems: Economic Geology, v. 106, p. 451-480.

Manske, S.L., Hedenquist, J.W., O'Connor, G., Tamas, C., Cauuet, B., Leary, S. and Minut, A., 2006, Rosia Montana, Romania: Europe's largest gold deposit: Society of Economic Geologists Newsletter, v. 64, p. 9-15.

Markey, R., Stein, H. and Morgan, J., 1998, Highly precise Re–Os dating for molybdenite using alkaline fusion and NTIMS: Talanta, v. 45, p. 935-946.

Markey, R., Stein, H.J., Hannah, J.L., Zimmerman, A., Selby, D. and Creaser, R.A., 2007, Standardizing Re–Os geochronology: a new molybdenite reference material (Henderson, USA) and the stoichiometry of Os salts: Chemical Geology, v. 244, p. 74-87.

Martin, H., Smithies, R., Rapp, R., Moyen, J.-F. and Champion, D., 2005, An overview of adakite, tonalite–trondhjemite–granodiorite (TTG), and sanukitoid: relationships and some implications for crustal evolution: Lithos, v. 79, p. 1-24.

Mattinson, J.M., 2005, Zircon U–Pb chemical abrasion ("CA-TIMS") method: combined annealing and multi-step partial dissolution analysis for improved precision and accuracy of zircon ages: Chemical Geology, v. 220, p. 47-66.

Maury, R.C., Fourcade, S., Coulon, C., Bellon, H., Coutelle, A., Ouabadi, A., Semroud, B., Megartsi, M.h., Cotten, J. and Belanteur, O., 2000, Post-collisional Neogene magmatism of the Mediterranean Maghreb margin: a consequence of slab breakoff: Comptes Rendus de l'Académie des Sciences-Series IIA-Earth and Planetary Science, v. 331, p. 159-173.

McClusky, S., Reilinger, R., Mahmoud, S., Ben Sari, D. and Tealeb, A., 2003, GPS constraints on Africa (Nubia) and Arabia plate motions: Geophysical Journal International, v. 155, p. 126-138.

McClusky, S., Balassanian, S., Barka, A., Demir, C., Ergintav, S., Georgiev, I., Gurkan, O., Hamburger, M., Hurst, K. and Kahle, H., 2000, Global Positioning System constraints on plate kinematics and dynamics in the eastern Mediterranean and Caucasus: Journal of Geophysical Research: Solid Earth, v. 105, p. 5695-5719.

McDonough, W., Sun, S.-S., Ringwood, A., Jagoutz, E. and Hofmann, A., 1992, Potassium, rubidium, and cesium in the Earth and Moon and the evolution of the mantle of the Earth: Geochimica et Cosmochimica Acta, v. 56, p. 1001-1012.

McInnes, B.I., Evans, N.J., Fu, F.Q. and Garwin, S., 2005, Application of thermochronology to hydrothermal ore deposits: Reviews in Mineralogy and geochemistry, v. 58, p. 467-498.

McInnes, B.I., McBride, J.S., Evans, N.J., Lambert, D.D. and Andrew, A.S., 1999, Osmium isotope constraints on ore metal recycling in subduction zones: Science, v. 286, p. 512-516.

McKenzie, D., 1972, Active tectonics of the Mediterranean region: Geophysical Journal International, v. 30, p. 109-185.

McNab, F., Ball, P., Hoggard, M. and White, N., 2017, Neogene Uplift and Magmatism of Anatolia: Insights From Drainage Analysis and Basaltic Geochemistry: Geochemistry, Geophysics, Geosystems, v. 19, p. 175-213.

McQuarrie, N. and van Hinsbergen, D.J., 2013, Retrodeforming the Arabia-Eurasia collision zone: Age of collision versus magnitude of continental subduction: Geology, v. 41, p. 315-318.

McQuarrie, N., Stock, J., Verdel, C. and Wernicke, B., 2003, Cenozoic evolution of Neotethys and implications for the causes of plate motions: Geophysical research letters, v. 30, p. 1-4.

Meijers, M.J., Kaymakci, N., Van Hinsbergen, D.J., Langereis, C.G., Stephenson, R.A. and Hippolyte, J.C., 2010, Late Cretaceous to Paleocene oroclinal bending in the central Pontides (Turkey): Tectonics, v. 29, p. 1-21.

Meinert, L.D., 2005, World skarn deposits: Economic Geology 100th Anniversary Volume, p. 299-336.

Melfos, V. and Voudouris, P., 2017, Cenozoic metallogeny of Greece and potential for precious, critical and rare metals exploration: Ore Geology Reviews, v. 89, p. 1030-1057.

Menant, A., Sternai, P., Jolivet, L., Guillou-Frottier, L. and Gerya, T., 2016, 3D numerical modeling of mantle flow, crustal dynamics and magma genesis associated with slab roll-back and tearing: The eastern Mediterranean case: Earth and Planetary Science Letters, v. 442, p. 93-107.

Menant, A., Jolivet, L., Tuduri, J., Loiselet, C., Bertrand, G. and Guillou-Frottier, L., 2018, 3D subduction dynamics: A first-order parameter of the transition from copper-to gold-rich deposits in the eastern Mediterranean region: Ore Geology Reviews, v. 94, p. 118-135.

Middlemost, E.A., 1994, Naming materials in the magma/igneous rock system: Earth-Science Reviews, v. 37, p. 215-224.

Miyashiro, A., 1974, Volcanic rock series in island arcs and active continental margins: American Journal of Science, v. 274, p. 321-355.

Moix, P., Beccaletto, L., Kozur, H.W., Hochard, C., Rosselet, F. and Stampfli, G.M., 2008, A new classification of the Turkish terranes and sutures and its implication for the paleotectonic history of the region: Tectonophysics, v. 451, p. 7-39.

Monnereau, M., Rabinowicz, M. and Arquis, E., 1993, Mechanical erosion and reheating of the lithosphere: a numerical model for hotspot swells: Journal of Geophysical Research: Solid Earth, v. 98, p. 809-823.

Moore, W.J., Lanphere, M.A. and Obradovich, J.D., 1968, Chronology of intrusion, volcanism, and ore deposition at Bingham, Utah: Economic Geology, v. 63, p. 612-621.

Morency, C., Doin, M.-P. and Dumoulin, C., 2002, Convective destabilization of a thickened continental lithosphere: Earth and Planetary Science Letters, v. 202, p. 303-320.

Moritz, R., Melkonyan, R., Selby, D., Popkhadze, N., Gugushvili, V., Tayan, R. and Ramazanov, V., 2016a, Metallogeny of the Lesser Caucasus: from arc construction to post-collision evolution: Society of Economic Geologists Special Publication, v. 19, p. 157-192.

Moritz, R., Rezeau, H., Ovtcharova, M., Tayan, R., Melkonyan, R., Hovakimyan, S., Ramazanov, V., Selby, D., Ulianov, A. and Chiaradia, M., 2016b, Long-lived, stationary magmatism and pulsed porphyry systems during Tethyan subduction to post-collision evolution in the southernmost Lesser Caucasus, Armenia and Nakhitchevan: Gondwana Research, v. 37, p. 465-503.

Moritz, R., Rezeau, H., Mederer, J., Gialli, S., Hemon, P., Lavoie, J., Calder, M., Hovakimyan, S., Melkonyan, R., Tayan, R., Popkhadze, N., Gugushvili, V. and Ramazanov, V., 2017, Gold deposits of the Lesser Caucasus: products of successive Mesozoic and Cenozoic geodynamic settings: Proceedings of the 14th SGA Biennial eeting, Québec City, Canada, p. 67-70.

Mortensen, J., Ghosh, D. and Ferri, F., 1995, U-Pb geochronology of intrusive rocks associated with copper-gold porphyry deposits in the Canadian Cordillera: Canadian Institute of Mining and Metallurgy, v. 46, p. 142-158.

Mouthereau, F., Lacombe, O. and Vergés, J., 2012, Building the Zagros collisional orogen: timing, strain distribution and the dynamics of Arabia/Eurasia plate convergence: Tectonophysics, v. 532, p. 27-60.

MTA, 2002, Geological map of Turkey: Ankara, Turkey, scale 1:500,000.

Mullen, E.K. and Weis, D., 2013, Sr-Nd-Hf-Pb isotope and trace element evidence for the origin of alkalic basalts in the Garibaldi Belt, northern Cascade arc: Geochemistry, Geophysics, Geosystems, v. 14, p. 3126-3155.

Müller, D., 2002, Gold-copper mineralization in alkaline rocks: Mineralium Deposita, v. 37, p. 1-3.

Müller, D. and Groves, D.I., 1993, Direct and indirect associations between potassic igneous rocks, shoshonites and gold-copper deposits: Ore Geology Reviews, v. 8, p. 383-406.

Mundil, R., Ludwig, K.R., Metcalfe, I. and Renne, P.R., 2004, Age and timing of the Permian mass extinctions: U/Pb dating of closed-system zircons: Science, v. 305, p. 1760-1763.

Mungall, J.E., 2002, Roasting the mantle: Slab melting and the genesis of major Au and Au-rich Cu deposits: Geology, v. 30, p. 915-918.

Münker, C., 2000, The isotope and trace element budget of the Cambrian Devil River arc system, New Zealand: identification of four source components: Journal of Petrology, v. 41, p. 759-788.

Muntean, J.L. and Einaudi, M.T., 2000, Porphyry gold deposits of the Refugio district, Maricunga belt, northern Chile: Economic Geology, v. 95, p. 1445-1472.

Murakami, H., Watanabe, Y. and Stein, H., 2005, Re-Os ages for molybdenite from the Tepeoba breccia-centered Cu-Mo-Au deposit, western Turkey: Brecciation-triggered mineralization: Mineral Deposit Research: Meeting the Global Challenge, p. 805-808.

Murakami, H., Seo, J.H. and Heinrich, C.A., 2010, The relation between Cu/Au ratio and formation depth of porphyry-style Cu–Au±Mo deposits: Mineralium Deposita, v. 45, p. 11-21.

Mutlu, A.K. and Karabulut, H., 2011, Anisotropic Pn tomography of Turkey and adjacent regions: Geophysical Journal International, v. 187, p. 1743-1758.

Mutlu, H., Sariiz, K. and Kadir, S., 2005, Geochemistry and origin of the Şaphane alunite deposit, Western Anatolia, Turkey: Ore Geology Reviews, v. 26, p. 39-50.

Neill, I., Meliksetian, K., Allen, M.B., Navasardyan, G. and Kuiper, K., 2015, Petrogenesis of mafic collision zone magmatism: The Armenian sector of the Turkish–Iranian Plateau: Chemical Geology, v. 403, p. 24-41.

Nesbitt, H. and Young, G., 1982, Early Proterozoic climates and plate motions inferred from major element chemistry of lutites: Nature, v. 299, p. 715.

Netzeband, G., Gohl, K., Hübscher, C., Ben-Avraham, Z., Dehghani, G., Gajewski, D. and Liersch, P., 2006, The Levantine Basin—crustal structure and origin: Tectonophysics, v. 418, p. 167-188.

Neubauer, F., Lips, A., Kouzmanov, K., Lexa, J. and Ivaˇşcanu, P., 2005, 1: Subduction, slab detachment and mineralization: The Neogene in the Apuseni Mountains and Carpathians: Ore Geology Reviews, v. 27, p. 13-44.

Notsu, K., Fujitani, T., Ui, T., Matsuda, J. and Ercan, T., 1995, Geochemical features of collision-related volcanic rocks in central and eastern Anatolia, Turkey: Journal of Volcanology and Geothermal Research, v. 64, p. 171-191.

Nurlu, N., Parlak, O., Robertson, A. and von Quadt, A., 2016, Implications of Late Cretaceous U–Pb zircon ages of granitic intrusions cutting ophiolitic and volcanogenic rocks for the assembly of the Tauride allochthon in SE Anatolia (Helete area, Kahramanmaraş Region, SE Turkey): International Journal of Earth Sciences, v. 105, p. 283-314.

O'Brien, P.J., 2001, Subduction followed by collision: Alpine and Himalayan examples: Physics of the Earth and Planetary Interiors, v. 127, p. 277-291.

Oberhänsli, R., Candan, O., Bousquet, R., Rimmele, G., Okay, A. and Goff, J., 2010, Alpine high pressure evolution of the eastern Bitlis complex, SE Turkey: Geological Society, London, Special Publications, v. 340, p. 461-483.

Okay, A.İ., 1984, Distribution and characteristics of the north-west Turkish blueschists: Geological Society, London, Special Publications, v. 17, p. 455-466.

Okay, A.İ. and Tüysüz, O., 1999, Tethyan sutures of northern Turkey: Geological Society, London, Special Publications, v. 156, p. 475-515.

Okay, A.İ., Harris, N.B. and Kelley, S.P., 1998, Exhumation of blueschists along a Tethyan

suture in northwest Turkey: Tectonophysics, v. 285, p. 275-299.

Okay, A.İ., Satir, M. and Siebel, W., 2006, Pre-Alpide Palaeozoic and Mesozoic orogenic events in the Eastern Mediterranean region: Geological Society, London, Memoirs, v. 32, p. 389-405.

Okay, A.İ., Zattin, M. and Cavazza, W., 2010, Apatite fission-track data for the Miocene Arabia-Eurasia collision: Geology, v. 38, p. 35-38.

Okay, A.İ., Satır, M., Maluski, H., Siyako, M., Monie, P., Metzger, R. and Akyüz, S., 1996, Paleo-and Neo-Tethyan events in northwestern Turkey: geologic and geochronologic constraints: World And Regional Geology, p. 420-441.

Omrani, J., Agard, P., Whitechurch, H., Benoit, M., Prouteau, G. and Jolivet, L., 2008, Arc-magmatism and subduction history beneath the Zagros Mountains, Iran: a new report of adakites and geodynamic consequences: Lithos, v. 106, p. 380-398.

Onal, A., Boztuğ, D., Arslan, M., Spell, T.L. and Kueruem, S., 2008, Petrology and $^{40}Ar/^{39}Ar$ Age of the Bimodal Orduzu Volcanics (Malatya) from the Western end of the Eastern Anatolian Neogene Volcanism, Turkey: Turkish Journal of Earth Sciences, v. 17, p. 85-109.

Oruç, B., Gomez-Ortiz, D. and Petit, C., 2017, Lithospheric flexural strength and effective elastic thicknesses of the Eastern Anatolia (Turkey) and surrounding region: Journal of Asian Earth Sciences, v. 150, p. 1-13.

Oyan, V., 2018, Ar-Ar dating and petrogenesis of the Early Miocene Taşkapı-Mecitli (Erciş-Van) granitoid, Eastern Anatolia Collisional Zone, Turkey: Journal of Asian Earth Sciences, v. 158, p. 210-226.

Oyan, V., Keskin, M., Lebedev, V.A., Chugaev, A.V. and Sharkov, E.V., 2016, Magmatic evolution of the Early Pliocene Etrüsk stratovolcano, Eastern Anatolian Collision Zone, Turkey: Lithos, v. 256, p. 88-108.

Oygür, V. and Erler, A., 2000, Metallogeny of the Simav graben (Inner Western Anatolia, Turkey): Geological Bulletin of Turkey, v. 43, p. 7-19.

Oyhantçabal, P., Siegesmund, S., Wemmer, K., Frei, R. and Layer, P., 2007, Post-collisional transition from calc-alkaline to alkaline magmatism during transcurrent deformation in the southernmost Dom Feliciano Belt (Braziliano–Pan-African, Uruguay): Lithos, v. 98, p. 141-159.

Oyman, T., Minareci, F. and Pişkin, Ö., 2003, Efemcukuru B-rich epithermal gold deposit (Izmir, Turkey): Ore Geology Reviews, v. 23, p. 35-53.

Özdemir, Y., 2011, Volcanostratigraphy and Petrogenesis of Süphan Stratovolcano: Unpublished thesis, Ankara, METU, 301 p.

Özdemir, Y. and Güleç, N., 2013, Geological and geochemical evolution of the Quaternary Süphan stratovolcano, eastern Anatolia, Turkey: evidence for the Lithosphere–Asthenosphere interaction in post-collisional volcanism: Journal of Petrology, v. 55, p. 37-62.

Özdemir, Y., Karaoğlu, Ö., Tolluoğlu, A.Ü. and Güleç, N., 2006, Volcanostratigraphy and petrogenesis of the Nemrut stratovolcano (East Anatolian High Plateau): the most

recent post-collisional volcanism in Turkey: Chemical Geology, v. 226, p. 189-211.

Özen, Y. and Arık, F., 2015, S, O and Pb isotopic evidence on the origin of the İnkaya (Simav-Kütahya) Cu–Pb–Zn–(Ag) Prospect, NW Turkey: Ore Geology Reviews, v. 70, p. 262-280.

Özeren, M.S. and Holt, W.E., 2010, The dynamics of the eastern Mediterranean and eastern Turkey: Geophysical Journal International, v. 183, p. 1165-1184.

Pang, K.N., Chung, S.L., Zarrinkoub, M.H., Lin, Y.C., Lee, H.Y., Lo, C.H. and Khatib, M.M., 2013, Iranian ultrapotassic volcanism at~ 11 Ma signifies the initiation of post-collisional magmatism in the Arabia–Eurasia collision zone: Terra Nova, v. 25, p. 405-413.

Paquette, J.-L. and Le Pennec, J.-L., 2012, 3.8 Ga zircons sampled by Neogene ignimbrite eruptions in Central Anatolia: Geology, v. 40, p. 239-242.

Parkinson, I.J. and Arculus, R.J., 1999, The redox state of subduction zones: insights from arc-peridotites: Chemical Geology, v. 160, p. 409-423.

Parlak, O., 2006, Geodynamic significance of granitoid magmatism in the southeast Anatolian Orogen: geochemical and geochronogical evidence from Göksun–Afşin (Kahramanmaraş, Turkey) Region: International Journal of Earth Sciences, v. 95, p. 609-627.

Parlak, O., Delaloye, M., Demirkol, C. and Ünlügenç, U.C., 2001, Geochemistry of Pliocene/Pleistocene basalts along the Central Anatolian fault zone (CAFZ), Turkey: Geodinamica Acta, v. 14, p. 159-167.

Parlak, O., Rızaoğlu, T., Bağcı, U., Karaoğlan, F. and Höck, V., 2009, Tectonic significance of the geochemistry and petrology of ophiolites in southeast Anatolia, Turkey: Tectonophysics, v. 473, p. 173-187.

Pasquare, G., Poli, S., Vezzoli, L. and Zanchi, A., 1988, Continental arc volcanism and tectonic setting in Central Anatolia, Turkey: Tectonophysics, v. 146, p. 217-230.

Pasvanoğlu, S., 2013, Hydrogeochemistry of thermal and mineralized waters in the Diyadin (Ağri) area, Eastern Turkey: Applied geochemistry, v. 38, p. 70-81.

Paterson, S.R. and Tobisch, O.T., 1992, Rates of processes in magmatic arcs: implications for the timing and nature of pluton emplacement and wall rock deformation: Journal of Structural Geology, v. 14, p. 291-300.

Pe-Piper, G. and Piper, D.J., 2001, Late Cenozoic, post-collisional Aegean igneous rocks: Nd, Pb and Sr isotopic constraints on petrogenetic and tectonic models: Geological Magazine, v. 138, p. 653-668.

Peach, C., Mathez, E. and Keays, R., 1990, Sulfide melt-silicate melt distribution coefficients for noble metals and other chalcophile elements as deduced from MORB: Implications for partial melting: Geochimica et Cosmochimica Acta, v. 54, p. 3379-3389.

Pearce, J., Bender, J., De Long, S., Kidd, W., Low, P., Güner, Y., Saroglu, F., Yilmaz, Y., Moorbath, S. and Mitchell, J., 1990, Genesis of collision volcanism in Eastern Anatolia, Turkey: Journal of Volcanology and Geothermal Research, v. 44, p. 189-229.

Pearce, J.A., 1983, Role of the sub-continental lithosphere in magma genesis at active continental margins: In C.J. Hawkesworth and M.J. Norry (eds.), Continental basalts and mantle xenoliths: Nantwich, Cheshire, Shiva Publications, p. 230-249.

Peccerillo, A. and Taylor, S.R., 1976, Geochemistry of Eocene calc-alkaline volcanic rocks from the Kastamonu area, northern Turkey: Contributions to mineralogy and petrology, v. 58, p. 63-81.

Peretyazhko, I., Savina, E., Karmanov, N. and Shcherbakov, Y.D., 2015, Genesis of mugearites and benmoreites of Nemrut Volcano, eastern Turkey: Magma mixing and fractional crystallization of trachybasaltic melt: Petrology, v. 23, p. 376-403.

Petford, N. and Gallagher, K., 2001, Partial melting of mafic (amphibolitic) lower crust by periodic influx of basaltic magma: Earth and Planetary Science Letters, v. 193, p. 483-499.

Pettke, T., Oberli, F. and Heinrich, C.A., 2010, The magma and metal source of giant porphyry-type ore deposits, based on lead isotope microanalysis of individual fluid inclusions: Earth and Planetary Science Letters, v. 296, p. 267-277.

Peytcheva, I., Von Quadt, A., Georgiev, N., Ivanov, Z., Heinrich, C. and Frank, M., 2008, Combining trace-element compositions, U–Pb geochronology and Hf isotopes in zircons to unravel complex calcalkaline magma chambers in the Upper Cretaceous Srednogorie zone (Bulgaria): Lithos, v. 104, p. 405-427.

Peytcheva, I., von Quadt, A., Neubauer, F., Frank, M., Nedialkov, R., Heinrich, C. and Strashimirov, S., 2009, U–Pb dating, Hf-isotope characteristics and trace-REE-patterns of zircons from Medet porphyry copper deposit, Bulgaria: implications for timing, duration and sources of ore-bearing magmatism: Mineralogy and Petrology, v. 96, p. 19-41.

Pik, R., Deniel, C., Coulon, C., Yirgu, G. and Marty, B., 1999, Isotopic and trace element signatures of Ethiopian flood basalts: evidence for plume–lithosphere interactions: Geochimica et Cosmochimica Acta, v. 63, p. 2263-2279.

Pilet, S., Baker, M.B. and Stolper, E.M., 2008, Metasomatized lithosphere and the origin of alkaline lavas: Science, v. 320, p. 916-919.

Piromallo, C. and Morelli, A., 2003, P wave tomography of the mantle under the Alpine-Mediterranean area: Journal of Geophysical Research: Solid Earth, v. 108, p. 1-23.

Plank, T. and Langmuir, C.H., 1988, An evaluation of the global variations in the major element chemistry of arc basalts: Earth and Planetary Science Letters, v. 90, p. 349-370.

Plank, T. and Langmuir, C.H., 1998, The chemical composition of subducting sediment and its consequences for the crust and mantle: Chemical geology, v. 145, p. 325-394.

Platevoet, B., Elitok, Ö., Guillou, H., Bardintzeff, J.-M., Yagmurlu, F., Nomade, S., Poisson, A., Deniel, C. and Özgür, N., 2014, Petrology of Quaternary volcanic rocks and related plutonic xenoliths from Gölcük volcano, Isparta Angle, Turkey: Origin and evolution of the high-K alkaline series: Journal of Asian Earth Sciences, v. 92, p. 53-76.

Platt, J. and England, P., 1994, Convective removal of lithosphere beneath mountain belts; thermal and mechanical consequences: American Journal of Science, v. 294, p. 307-336.

Platzman, E., Tapirdamaz, C. and Sanver, M., 1998, Neogene anticlockwise rotation of central Anatolia (Turkey): preliminary palaeomagnetic and geochronological results: Tectonophysics, v. 299, p. 175-189.

Plunder, A., Agard, P., Chopin, C., Pourteau, A. and Okay, A.I., 2015, Accretion, underplating and exhumation along a subduction interface: From subduction initiation to continental subduction (Tavşanlı zone, W. Turkey): Lithos, v. 226, p. 233-254.

Pourteau, A., Candan, O. and Oberhänsli, R., 2010, High-pressure metasediments in central Turkey: Constraints on the Neotethyan closure history: Tectonics, v. 29, p. 1-18.

Pourteau, A., Sudo, M., Candan, O., Lanari, P., Vidal, O. and Oberhänsli, R., 2013, Neotethys closure history of Anatolia: insights from 40Ar–39Ar geochronology and P–T estimation in high-pressure metasedimentary rocks: Journal of Metamorphic Geology, v. 31, p. 585-606.

Prelević, D., Akal, C., Romer, R. and Foley, S., 2010, Lamproites as indicators of accretion and/or shallow subduction in the assembly of south-western Anatolia, Turkey: Terra Nova, v. 22, p. 443-452.

Prelević, D., Akal, C., Romer, R.L., Mertz-Kraus, R. and Helvacı, C., 2015, Magmatic response to slab tearing: constraints from the Afyon Alkaline Volcanic Complex, Western Turkey: Journal of Petrology, v. 56, p. 527-562.

Prelević, D., Akal, C., Foley, S., Romer, R., Stracke, A. and Van Den Bogaard, P., 2012, Ultrapotassic mafic rocks as geochemical proxies for post-collisional dynamics of orogenic lithospheric mantle: the case of southwestern Anatolia, Turkey: Journal of Petrology, v. 53, p. 1019-1055.

Razique, A., Tosdal, R.M. and Creaser, R.A., 2014, Temporal Evolution of the Western Porphyry Cu-Au Systems at Reko Diq, Balochistan, Western Pakistan: Economic Geology, v. 109, p. 2003-2021.

Régnier, J.-l., Mezger, J.E. and Passchier, C.W., 2007, Metamorphism of Precambrian–Palaeozoic schists of the Menderes core series and contact relationships with Proterozoic orthogneisses of the western Çine Massif, Anatolide belt, western Turkey: Geological Magazine, v. 144, p. 67-104.

Reid, G.D., Woodhouse, P., Stallman, M., Cihan, M., Landry, P., Hilkewich, T., Raponi, T.R., D'Souza, K. and Sharpe, C., 2015, Technical NI 43-101 report on the Oksut gold project, Turkey: C.G. Inc., 271 p.

Reid, M.R., Schleiffarth, W.K., Cosca, M.A., Delph, J.R., Blichert-Toft, J. and Cooper, K.M., 2017, Shallow melting of MORB-like mantle under hot continental lithosphere, Central Anatolia: Geochemistry, Geophysics, Geosystems, v. 18, p. 1866-1888.

Reilinger, R., McClusky, S., Vernant, P., Lawrence, S., Ergintav, S., Cakmak, R., Ozener, H., Kadirov, F., Guliev, I. and Stepanyan, R., 2006, GPS constraints on continental deformation in the Africa-Arabia-Eurasia continental collision zone and implications for the dynamics of plate interactions: Journal of Geophysical Research: Solid Earth, v. 111, p. 1-26.

Renne, P.R., Swisher, C.C., Deino, A.L., Karner, D.B., Owens, T.L. and DePaolo, D.J., 1998, Intercalibration of standards, absolute ages and uncertainties in 40Ar/39Ar dating: Chemical Geology, v. 145, p. 117-152.

Richards, J.P., 2003, Tectono-magmatic precursors for porphyry Cu-(Mo-Au) deposit formation: Economic Geology, v. 98, p. 1515-1533.

Richards, J.P., 2009, Postsubduction porphyry Cu-Au and epithermal Au deposits: Products of remelting of subduction-modified lithosphere: Geology, v. 37, p. 247-250.

Richards, J.P., 2011a, High Sr/Y arc magmas and porphyry Cu±Mo±Au deposits: just add water: Economic Geology, v. 106, p. 1075-1081.

Richards, J.P., 2011b, Magmatic to hydrothermal metal fluxes in convergent and collided margins: Ore Geology Reviews, v. 40, p. 1-26.

Richards, J.P., 2015, Tectonic, magmatic, and metallogenic evolution of the Tethyan orogen: From subduction to collision: Ore Geology Reviews, v. 70, p. 323-345.

Richards, J.P. and Kerrich, R., 2007, Special paper: adakite-like rocks: their diverse origins and questionable role in metallogenesis: Economic geology, v. 102, p. 537-576.

Richards, J.P. and Sholeh, A., 2016, The Tethyan Tectonic History and Cu-Au Metallogeny of Iran: In (J.P. Richards ed.), Tectonics and Metallogeny of the Tethyan Orogenic Belt, Society of Economic Geologists Special Publication: p. 193-212.

Richards, J.P., Chappell, B.W. and McCulloch, M.T., 1990, Intraplate-type magmatism in a continent-island-arc collision zone: Porgera intrusive complex, Papua New Guinea: Geology, v. 18, p. 958-961.

Richards, J.P., Wilkinson, D. and Ullrich, T., 2006, Geology of the Sari Gunay epithermal gold deposit, northwest Iran: Economic Geology, v. 101, p. 1455-1496.

Richards, J.P., Spell, T., Rameh, E., Razique, A. and Fletcher, T., 2012, High Sr/Y magmas reflect arc maturity, high magmatic water content, and porphyry Cu±Mo±Au potential: examples from the Tethyan arcs of Central and Eastern Iran and Western Pakistan: Economic Geology, v. 107, p. 295-332.

Richards, S. and Holm, R., 2013, Tectonic preconditioning and the formation of giant porphyry deposits: Society of Economic Geologists Special Publication, v. 17, p. 265-275.

Rimmele, G., Parra, T., Goffe, B., Oberhänsli, R., Jolivet, L. and Candan, O., 2005, Exhumation paths of high-pressure–low-temperature metamorphic rocks from the Lycian Nappes and the Menderes Massif (SW Turkey): a multi-equilibrium approach: Journal of Petrology, v. 46, p. 641-669.

Rimmelé, G., Jolivet, L., Oberhänsli, R. and Goffé, B., 2003, Deformation history of the high-pressure Lycian Nappes and implications for tectonic evolution of SW Turkey: Tectonics, v. 22, p. 1-21.

Rimmelé, G., Oberhänsli, R., Candan, O., Goffé, B. and Jolivet, L., 2006, The wide distribution of HP-LT rocks in the Lycian Belt (Western Turkey): implications for accretionary wedge geometry: Geological Society, London, Special Publications, v. 260, p. 447-466.

Ring, U. and Collins, A.S., 2005, U–Pb SIMS dating of synkinematic granites: timing of core-complex formation in the northern Anatolide belt of western Turkey: Journal of the Geological Society, v. 162, p. 289-298.

Ring, U., Gessner, K., Güngör, T. and Passchier, C., 1999, The Menderes Massif of western

Turkey and the Cycladic Massif in the Aegean—do they really correlate?: Journal of the Geological Society, v. 156, p. 3-6.

Ring, U., Johnson, C., Hetzel, R. and Gessner, K., 2003, Tectonic denudation of a Late Cretaceous–Tertiary collisional belt: regionally symmetric cooling patterns and their relation to extensional faults in the Anatolide belt of western Turkey: Geological Magazine, v. 140, p. 421-441.

Ringwood, A., 1977, Petrogenesis in island arc systems: Island arcs, deep sea trenches and back-arc basins, v. p. 311-324.

Rızaoğlu, T., Parlak, O., Höck, V., Koller, F., Hames, W.E. and Billor, Z., 2009, Andean-type active margin formation in the eastern Taurides: Geochemical and geochronogical evidence from the Baskil granitoid (Elazığ, SE Turkey): Tectonophysics, v. 473, p. 188-207.

Robert, U., Foden, J. and Varne, R., 1992, The Dodecanese Province, SE Aegean: a model for tectonic control on potassic magmatism: Lithos, v. 28, p. 241-260.

Robertson, A.H.F., 2000, Mesozoic-Tertiary tectonic-sedimentary evolution of a south Tethyan oceanic basin and its margins in southern Turkey: Geological Society, London, Special Publications, v. 173, p. 97-138.

Robertson, A.H.F. and Dixon, J.E., 1984, Introduction: aspects of the geological evolution of the Eastern Mediterranean: Geological Society, London, Special Publications, v. 17, p. 1-74.

Robertson, A.H.F., Parlak, O. and Ustaömer, T., 2013, Late Palaeozoic–Early Cenozoic tectonic development of Southern Turkey and the easternmost Mediterranean region: evidence from the inter-relations of continental and oceanic units: Geological Society, London, Special Publications, v. 372, p. 9-48.

Robertson, A.H.F., Parlak, O., Rizaoğlu, T., Ünlügenç, Ü., İnan, N., Tasli, K. and Ustaömer, T., 2007, Tectonic evolution of the South Tethyan ocean: evidence from the Eastern Taurus Mountains (Elazig region, SE Turkey): Geological Society, London, Special Publications, v. 272, p. 231-270.

Robertson, A.H.F., Boulton, S.J., Taslı, K., Yıldırım, N., İnan, N., Yıldız, A. and Parlak, O., 2016, Late Cretaceous–Miocene sedimentary development of the Arabian continental margin in SE Turkey (Adıyaman region): Implications for regional palaeogeography and the closure history of Southern Neotethys: Journal of Asian Earth Sciences, v. 115, p. 571-616.

Roche, V., 2018, Du manteau au système géothermal de haute température : dynamique de subduction et anomalies thermiques en Méditerranée orientale: Unpublished PhD thesis, Université d'Orléans, 464 p.

Rodriguez, C., Sellés, D., Dungan, M., Langmuir, C. and Leeman, W., 2007, Adakitic dacites formed by intracrustal crystal fractionation of water-rich parent magmas at Nevado de Longaví volcano (36.2 S; Andean Southern Volcanic Zone, Central Chile): Journal of Petrology, v. 48, p. 2033-2061.

Rolland, Y., Perincek, D., Kaymakci, N., Sosson, M., Barrier, E. and Avagyan, A., 2012, Evidence for 80–75Ma subduction jump during Anatolide–Tauride–Armenian block accretion and 48Ma Arabia–Eurasia collision in Lesser Caucasus–East Anatolia:

Journal of Geodynamics, v. 56, p. 76-85.

Rosenbaum, G., Gasparon, M., Lucente, F.P., Peccerillo, A. and Miller, M.S., 2008, Kinematics of slab tear faults during subduction segmentation and implications for Italian magmatism: Tectonics, v. 27, p. 1-16.

Ross, P.-S. and Bédard, J.H., 2009, Magmatic affinity of modern and ancient subalkaline volcanic rocks determined from trace-element discriminant diagrams: Canadian Journal of Earth Sciences, v. 46, p. 823-839.

Rudnick, R. and Gao, S., 2014, Composition of the continental crust: Treatise on Geochemistry 2nd Edition, p. 1-51.

Rutherford, M.J. and Hill, P.M., 1993, Magma ascent rates from amphibole breakdown: an experimental study applied to the 1980–1986 Mount St. Helens eruptions: Journal of Geophysical Research: Solid Earth, v. 98, p. 19667-19685.

Ryan, J.G. and Langmuir, C.H., 1993, The systematics of boron abundances in young volcanic rocks: Geochimica et Cosmochimica Acta, v. 57, p. 1489-1498.

Safari, H.O., Bagas, L. and Bafti, B.S., 2015, Structural controls on the localization of Cu deposits in the Kerman Cu metallogenic province of Iran using geoinformatic techniques: Ore Geology Reviews, v. 67, p. 43-56.

Sánchez, M.G., McClay, K.R., King, A.R. and Wijbrams, J.R., 2016, Cenozoic crustal extension and its relationship to porphyry Cu-Au-(Mo) and epithermal Au-(Ag) mineralization in the Biga peninsula, northwestern Turkey: Tectonics and metallogeny of the Tethyan orogenic belt, Soc Econ Geol Spec Pub, v. 19, p. 113-156.

Sandstorm Gold Royalties, 2018, Hot Maden Reserves: (https://sandstormgold.com/our-royalties/hod-maden/).

Sarbas, B. and Nohl, U., 2008, The GEOROC database as part of a growing geoinformatics network: Geoinformatics.

Sarıfakıoğlu, E., Dilek, Y. and Sevin, M., 2017, New synthesis of the Izmir-Ankara-Erzincan suture zone and the Ankara mélange in northern Anatolia based on new geochemical and geochronological constraints: Tectonic evolution, collision, and seismicity of Southwest Asia: In honor of Manuel Berberian's forty-five years of research contributions: Geological Society of America Special Paper, v. 525, p. 1-64.

Satır, M. and Friedrichsen, H., 1986, The origin and evolution of the Menderes Massif, W-Turkey: a rubidium/strontium and oxygen isotope study: Geologische Rundschau, v. 75, p. 703-714.

Sayılı, İ. and Gonca, Ş., 1999, İzmir–Karşıyaka Altıntepe ve Çilektepe sektörlerinin jeolojisi, petrografisi ve diğer metal cevherleşmeleri: MTA Derg, v. 121, p. 199-215.

Schildgen, T.F., Yıldırım, C., Cosentino, D. and Strecker, M., 2014, Linking slab break-off, Hellenic trench retreat, and uplift of the Central and Eastern Anatolian plateaus: Earth-Science Reviews, v. 128, p. 147-168.

Schildgen, T.F., Cosentino, D., Bookhagen, B., Niedermann, S., Yıldırım, C., Echtler, H., Wittmann, H. and Strecker, M.R., 2012, Multi-phased uplift of the southern margin of the Central Anatolian plateau, Turkey: A record of tectonic and upper mantle processes:

Earth and Planetary Science Letters, v. 317, p. 85-95.

Schmincke, H.-U., 2004, Volcanism: Springer Science & Business Media, 324 p.

Schmitt, A.K., Danišík, M., Evans, N.J., Siebel, W., Kiemele, E., Aydin, F. and Harvey, J.C., 2011, Acigöl rhyolite field, Central Anatolia (part 1): high-resolution dating of eruption episodes and zircon growth rates: Contributions to Mineralogy and Petrology, v. 162, p. 1215-1231.

Schmitz, M.D. and Schoene, B., 2007, Derivation of isotope ratios, errors, and error correlations for U-Pb geochronology using 205Pb-235U-(233U)-spiked isotope dilution thermal ionization mass spectrometric data: Geochemistry, Geophysics, Geosystems, v. 8, p. 1-20.

Schwartz, M.A., 2008, The importance of stupidity in scientific research: Journal of Cell Science, v. 121, p. 1771-1771.

Scoates, J.S. and Friedman, R.M., 2008, Precise age of the platiniferous Merensky Reef, Bushveld Complex, South Africa, by the U-Pb zircon chemical abrasion ID-TIMS technique: Economic Geology, v. 103, p. 465-471.

Seghedi, I., Helvacı, C. and Pécskay, Z., 2015, Composite volcanoes in the south-eastern part of İzmir–Balıkesir transfer zone, Western Anatolia, Turkey: Journal of Volcanology and Geothermal Research, v. 291, p. 72-85.

Selby, D. and Creaser, R.A., 2004, Macroscale NTIMS and microscale LA-MC-ICP-MS Re-Os isotopic analysis of molybdenite: Testing spatial restrictions for reliable Re-Os age determinations, and implications for the decoupling of Re and Os within molybdenite: Geochimica et Cosmochimica Acta, v. 68, p. 3897-3908.

Selçuk, A.S., Erturaç, M.K. and Nomade, S., 2016, Geology of the Çaldıran Fault, Eastern Turkey: Age, slip rate and implications on the characteristic slip behaviour: Tectonophysics, v. 680, p. 155-173.

Şen, E., Kürkcüoğlu, B., Aydar, E., Gourgaud, A. and Vincent, P.M., 2003, Volcanological evolution of Mount Erciyes stratovolcano and origin of the Valibaba Tepe ignimbrite (Central Anatolia, Turkey): Journal of Volcanology and Geothermal Research, v. 125, p. 225-246.

Şen, P.A., Temel, A. and Gourgaud, A., 2004, Petrogenetic modelling of Quaternary post-collisional volcanism: a case study of central and eastern Anatolia: Geological Magazine, v. 141, p. 81-98.

Şener, A.K., Arar, M., Wedin, F. and Goodman, S., 2009, Contrasting styles of epithermal gold mineralisation at the Kiziltepe and Tavsan deposits, Western Turkey: Smart science for exploration and mining, proceedings of the 10th Biennial meeting of The Society for Geology Applied to Mineral Deposits, Townsville, Australia, 17th, p. 848-850.

Sengör, A.C. and Natal'In, B.A., 1996, Turkic-type orogeny and its role in the making of the continental crust: Annual Review of Earth and Planetary Sciences, v. 24, p. 263-337.

Şengör, A.M.C., 1985, Strike-slip faulting and related basin formation in zones of tectonic escape: Turkey as a case study: In K.T. Biddle and N. Christie-Blick (eds.), Strike-Slip Faulting and Basin Formation: Special Publication - Society of Economic Paleontologists and Mineralogists, p. 227-264.

Şengör, A.M.C. and Kidd, W.S.F., 1979, Post-collisional tectonics of the Turkish-Iranian plateau and a comparison with Tibet: Tectonophysics, v. 55, p. 361-376.

Şengör, A.M.C. and Yılmaz, Y., 1981, Tethyan evolution of Turkey: a plate tectonic approach: Tectonophysics, v. 75, p. 181-241.

Şengör, A.M.C., Yılmaz, Y. and Sungurlu, O., 1984, Tectonics of the Mediterranean Cimmerides: nature and evolution of the western termination of Palaeo-Tethys: Geological Society, London, Special Publications, v. 17, p. 77-112.

Şengör, A.M.C., Özeren, S., Genç, T. and Zor, E., 2003, East Anatolian high plateau as a mantle-supported, north-south shortened domal structure: Geophysical Research Letters, v. 30, p. 1-4.

Şengör, A.M.C., Özeren, M.S., Keskin, M., Sakınç, M., Özbakır, A.D. and Kayan, I., 2008, Eastern Turkish high plateau as a small Turkic-type orogen: Implications for post-collisional crust-forming processes in Turkic-type orogens: Earth-Science Reviews, v. 90, p. 1-48.

Seyitoğlu, G., 1997, Late Cenozoic tectono-sedimentary development of the Selendi and Uşak-Güre basins: a contribution to the discussion on the development of east–west and north trending basins in western Turkey: Geological Magazine, v. 134, p. 163-175.

Seyrek, A., Westaway, R., Pringle, M., Yurtmen, S., Demir, T. and Rowbotham, G., 2008, Timing of the Quaternary Elazığ volcanism, eastern Turkey, and its significance for constraining landscape evolution and surface uplift: Turkish Journal of Earth Sciences, v. 17, p. 497-541.

Shafiei, B., Haschke, M. and Shahabpour, J., 2009, Recycling of orogenic arc crust triggers porphyry Cu mineralization in Kerman Cenozoic arc rocks, southeastern Iran: Mineralium Deposita, v. 44, p. 265-283.

Sherlock, S., Kelley, S., Inger, S., Harris, N. and Okay, A., 1999, $^{40}Ar/^{39}Ar$ and Rb-Sr geochronology of high-pressure metamorphism and exhumation history of the Tavsanli Zone, NW Turkey: Contributions to Mineralogy and Petrology, v. 137, p. 46-58.

Siebel, W., Schmitt, A.K., Kiemele, E., Danišík, M. and Aydin, F., 2011, Acigöl rhyolite field, central Anatolia (part II): geochemical and isotopic (Sr–Nd–Pb, δ 18 O) constraints on volcanism involving two high-silica rhyolite suites: Contributions to Mineralogy and Petrology, v. 162, p. 1233-1247.

Sillitoe, R.H., 1972, Relation of metal provinces in western America to subduction of oceanic lithosphere: Geological Society of America Bulletin, v. 83, p. 813-818.

Sillitoe, R.H., 1979, Some thoughts on gold-rich porphyry copper deposits: Mineralium Deposita, v. 14, p. 161-174.

Sillitoe, R.H., 1997, Characteristics and controls of the largest porphyry copper-gold and epithermal gold deposits in the circum-Pacific region: Australian Journal of Earth Sciences, v. 44, p. 373-388.

Sillitoe, R.H., 1998, Major regional factors favouring large size, high hypogene grade, elevated gold content and supergene oxidation and enrichment of porphyry copper deposits: Porphyry and Hydrothermal Copper and Gold Deposits—a global perspective: Perth, v. p. 49-60.

Sillitoe, R.H., 2010, Porphyry copper systems: Economic Geology, v. 105, p. 3-41.

Sillitoe, R.H. and Bonham, H.F., 1990, Sediment-hosted gold deposits: Distal products of magmatic-hydrothermal systems: Geology, v. 18, p. 157-161.

Sillitoe, R.H. and Mortensen, J.K., 2010, Longevity of porphyry copper formation at Quellaveco, Peru: Economic Geology, v. 105, p. 1157-1162.

Simmons, S.F., White, N.C. and John, D.A., 2005, Geological characteristics of epithermal precious and base metal deposits: Economic Geology 100th Anniversary Volume, p. 485-522.

Sinclair, H., 1997, Flysch to molasse transition in peripheral foreland basins: The role of the passive margin versus slab breakoff: Geology, v. 25, p. 1123-1126.

Singer, D.A., Berger, V.I. and Moring, B.C., 2008, Porphyry copper deposits of the world: database and tonnage models: U.S.G. Survey, 45 p.

Siron, C.R., Thompson, J.F., Baker, T., Friedman, R., Tsitsanis, P., Russell, S., Randall, S. and Mortensen, J., 2016, Magmatic and metallogenic framework of Au-Cu porphyry and polymetallic carbonate-hosted replacement deposits of the Kassandra mining district, Northern Greece: Society of Economic Geologists, Special Publication, v. 19, p. 29-55.

Sláma, J., Košler, J., Condon, D.J., Crowley, J.L., Gerdes, A., Hanchar, J.M., Horstwood, M.S., Morris, G.A., Nasdala, L. and Norberg, N., 2008, Plešovice zircon—a new natural reference material for U–Pb and Hf isotopic microanalysis: Chemical Geology, v. 249, p. 1-35.

Smith, M.T., Lepore, W.A., Incekaraoğlu, T., Shabestari, P., Boran, H. and Raabe, K., 2014, Küçükdağ: A new, high-sulfidation epithermal Au-Ag-Cu deposit at the TV Tower property in western Turkey: Economic Geology, v. 109, p. 1501-1511.

Smith, M.T., Lepore, W.A., Incekaraoglu, T., Boran, H., Barrios, A., Leroux, G., Ross, K., Büyüksolak, A., Sevimli, A. and Raabe, K., 2016, High-sulfidation epithermal Au and porphyry Cu-Au mineralization at the Karaayi target, Biga peninsula, northwestern Turkey: Society of Economic Geologists Special Publication 19, v. p. 85-112.

Solomon, M., 1990, Subduction, arc reversal, and the origin of porphyry copper-gold deposits in island arcs: Geology, v. 18, p. 630-633.

Sönmez, Ş.U. and Kuşcu, I., 2016, Spatial and temporal alteration model of Afyon-Sandikli (AS) alkaline porphyry Cu-Au deposit: SEG Conference: Tethyan Tectonics and Metallogeny, Çeşme, Turkey, Poster.

Sosson, M., Rolland, Y., Müller, C., Danelian, T., Melkonyan, R., Kekelia, S., Adamia, S., Babazadeh, V., Kangarli, T. and Avagyan, A., 2010, Subductions, obduction and collision in the Lesser Caucasus (Armenia, Azerbaijan, Georgia), new insights: Geological Society, London, Special Publications, v. 340, p. 329-352.

Spakman, W., Wortel, M. and Vlaar, N., 1988, The Hellenic subduction zone: a tomographic image and its geodynamic implications: Geophysical research letters, v. 15, p. 60-63.

Sperner, B., Lorenz, F., Bonjer, K., Hettel, S., Müller, B. and Wenzel, F., 2001, Slab break-off–abrupt cut or gradual detachment? New insights from the Vrancea Region (SE Carpathians, Romania): Terra Nova, v. 13, p. 172-179.

Stampfli, G.M., 2000, Tethyan oceans: Geological Society of London, Special Publications, v. 173, p. 1-23.

Stampfli, G.M. and Borel, G.D., 2004, The TRANSMED transects in space and time: constraints on the paleotectonic evolution of the Mediterranean domain: In W. Cavazza, F. Roure, W. Spakman, G.M. Stampfli and P.A. Ziegler (eds.), The TRANSMED Atlas. The Mediterranean region from crust to mantle: Berlin, Springer, p. 53-80.

Steiger, R.H. and Jäger, E., 1977, Subcommission on geochronology: convention on the use of decay constants in geo-and cosmochronology: Earth and Planetary Science Letters, v. 36, p. 359-362.

Sternai, P., Jolivet, L., Menant, A. and Gerya, T., 2014, Driving the upper plate surface deformation by slab rollback and mantle flow: Earth and Planetary Science Letters, v. 405, p. 110-118.

Sue, C., Thouvenot, F., Fréchet, J. and Tricart, P., 1999, Widespread extension in the core of the western Alps revealed by earthquake analysis: Journal of Geophysical Research: Solid Earth, v. 104, p. 25611-25622.

Sumita, M. and Schmincke, H.-U., 2013, Impact of volcanism on the evolution of Lake Van II: temporal evolution of explosive volcanism of Nemrut Volcano (eastern Anatolia) during the past ca. 0.4 Ma: Journal of Volcanology and Geothermal Research, v. 253, p. 15-34.

Sun, S.-S. and McDonough, W.-s., 1989, Chemical and isotopic systematics of oceanic basalts: implications for mantle composition and processes: Geological Society, London, Special Publications, v. 42, p. 313-345.

Sun, W., Bennett, V.C., Eggins, S.M., Kamenetsky, V.S. and Arculus, R.J., 2003, Enhanced mantle-to-crust rhenium transfer in undegassed arc magmas: Nature, v. 422, p. 294.

Tack, L., Liégeois, J.-P., Deblond, A. and Duchesne, J.-C., 1994, Kibaran A-type granitoids and mafic rocks generated by two mantle sources in a late orogenic setting (Burundi): Precambrian Research, v. 68, p. 323-356.

Tafti, R., Mortensen, J.K., Lang, J.R., Rebagliati, M. and Oliver, J.L., 2009, Jurassic U-Pb and Re-Os ages for the newly discovered Xietongmen Cu-Au porphyry district, Tibet, PRC: Implications for metallogenic epochs in the southern Gangdese belt: Economic Geology, v. 104, p. 127-136.

Takahashi, E. and Kushiro, I., 1983, Melting of a dry peridotite at high pressures and basalt magma genesis: American Mineralogist, v. 68, p. 859-879.

Tanaka, T., Togashi, S., Kamioka, H., Amakawa, H., Kagami, H., Hamamoto, T., Yuhara, M., Orihashi, Y., Yoneda, S. and Shimizu, H., 2000, JNdi-1: a neodymium isotopic reference in consistency with LaJolla neodymium: Chemical Geology, v. 168, p. 279-281.

Tankut, A., Wilson, M. and Yihunie, T., 1998, Geochemistry and tectonic setting of Tertiary volcanism in the Güvem area, Anatolia, Turkey: Journal of Volcanology and Geothermal Research, v. 85, p. 285-301.

Tatar, O., Yurtmen, S., Temiz, H., Guersoy, H., Kocbulut, F., Mesci, B.L. and Guezou, J.C., 2007, Intracontinental Quaternary Volcanism in the Niksar Pull-Apart Basin, North Anatolian Fault Zone, Turkey: Turkish Journal of Earth Sciences, v. 16, p. 417-440.

Tatsumi, Y., Hamilton, D. and Nesbitt, R., 1986, Chemical characteristics of fluid phase released from a subducted lithosphere and origin of arc magmas: evidence from high-pressure experiments and natural rocks: Journal of Volcanology and Geothermal Research, v. 29, p. 293-309.

Tatsumi, Y., Sakuyama, M., Fukuyama, H. and Kushiro, I., 1983, Generation of arc basalt magmas and thermal structure of the mantle wedge in subduction zones: Journal of Geophysical Research: Solid Earth, v. 88, p. 5815-5825.

Temel, A., Gündoğdu, M.N. and Gourgaud, A., 1998a, Petrological and geochemical characteristics of Cenozoic high-K calc-alkaline volcanism in Konya, Central Anatolia, Turkey: Journal of Volcanology and Geothermal Research, v. 85, p. 327-354.

Temel, A., Gündoğdu, M., Gourgaud, A. and Le Pennec, J.-L., 1998b, Ignimbrites of Cappadocia (central Anatolia, Turkey): petrology and geochemistry: Journal of Volcanology and Geothermal Research, v. 85, p. 447-471.

Temizel, I., Arslan, M., Yücel, C., Abdioğlu, E. and Ruffet, G., 2016, Geochronology and geochemistry of Eocene-aged volcanic rocks around the Bafra (Samsun, N Turkey) area: Constraints for the interaction of lithospheric mantle and crustal melts: Lithos, v. 258, p. 92-114.

Teng, L.S., Lee, C., Tsai, Y. and Hsiao, L.-Y., 2000, Slab breakoff as a mechanism for flipping of subduction polarity in Taiwan: Geology, v. 28, p. 155-158.

Tezel, T., Shibutani, T. and Kaypak, B., 2013, Crustal thickness of Turkey determined by receiver function: Journal of Asian Earth Sciences, v. 75, p. 36-45.

Thirlwall, M., 2000, Inter-laboratory and other errors in Pb isotope analyses investigated using a 207 Pb–204 Pb double spike: Chemical Geology, v. 163, p. 299-322.

Thorkelson, D.J., Madsen, J.K. and Sluggett, C.L., 2011, Mantle flow through the Northern Cordilleran slab window revealed by volcanic geochemistry: Geology, v. 39, p. 267-270.

Thorpe, R. and Francis, P., 1979, Variations in Andean andesite compositions and their petrogenetic significance: Tectonophysics, v. 57, p. 53-70.

Titley, S., 1975, Geological characteristics and environment of some porphyry copper occurrences in the southwestern Pacific: Economic Geology, v. 70, p. 499-514.

Tokçaer, M., Agostini, S. and Savaşçin, M.Y., 2005, Geotectonic setting and origin of the youngest Kula volcanics (western Anatolia), with a new emplacement model: Turkish Journal of Earth Sciences, v. 14, p. 143-166.

Toksoy-Köksal, F., Gerdes, A., Göncüoglu, M., Möller, A., Frei, D. and Köksal, S., 2009, U-Pb age and isotope data from the S-and I-type syn-collisional granites in Ekecikdag area, central Anatolia: Goldschmidt Conference, Davos, Switzerland, Poster.

Ton, W.A. and Wortel, M., 1997, Slab detachment in continental collision zones: an analysis of controlling parameters: Geophysical Research Letters, v. 24, p. 2095-2098.

Toprak, V., 1998, Vent distribution and its relation to regional tectonics, Cappadocian Volcanics, Turkey: Journal of Volcanology and Geothermal Research, v. 85, p. 55-67.

Toprak, V. and Göncüoğlu, M.C., 1993, Tectonic control on the development of the Neogene-Quaternary Central Anatolian Volcanic Province, Turkey: Geological Journal, v. 28, p. 357-369.

Topuz, G., Candan, O., Zack, T. and Yılmaz, A., 2017, East Anatolian plateau constructed over a continental basement: No evidence for the East Anatolian accretionary complex: Geology, v. 45, p. 791-794.

Tosdal, R.M. and Richards, J.P., 2001, Magmatic and structural controls on the development of porphyry Cu±Mo±Au deposits: Reviews in Economic Geology, v. 14, p. 157-181.

Uğurcan, O.G. and Oyman, T., 2016, Iron mineralization and associated skarn development around southern contact of the Eğrigöz pluton (northern Menderes Massif-Turkey): Journal of African Earth Sciences, v. 123, p. 309-337.

Ulusoy, I., Cubukcu, E., Aydar, E., Labazuy, P., Gourgaud, A. and Vincent, P., 2004, Volcanic and deformation history of the Bodrum resurgent caldera system (southwestern Turkey): Journal of Volcanology and Geothermal Research, v. 136, p. 71-96.

Ustaömer, P.A., Ustaömer, T., Collins, A.S. and Robertson, A.H., 2009, Cadomian (Ediacaran–Cambrian) arc magmatism in the Bitlis Massif, SE Turkey: magmatism along the developing northern margin of Gondwana: Tectonophysics, v. 473, p. 99-112.

Ustaömer, P.A., Ustaömer, T., Gerdes, A., Robertson, A.H. and Collins, A.S., 2012, Evidence of Precambrian sedimentation/magmatism and Cambrian metamorphism in the Bitlis Massif, SE Turkey utilising whole-rock geochemistry and U–Pb LA-ICP-MS zircon dating: Gondwana Research, v. 21, p. 1001-1018.

Ustunisik, G. and Kilinc, A., 2011, The role of fractional crystallization, magma recharge, and magma mixing in the differentiation of the Small Hasandag volcano, Central Anatolia, Turkey: Lithos, v. 125, p. 984-993.

Uzel, B. and Sözbilir, H., 2008, A first record of a strike-slip basin in western Anatolia and its tectonic implication: the Cumaovası Basin: Turkish Journal of Earth Sciences, v. 17, p. 559-591.

Uzel, B., Langereis, C.G., Kaymakci, N., Sözbilir, H., Özkaymak, Ç. and Özkaptan, M., 2015, Paleomagnetic evidence for an inverse rotation history of Western Anatolia during the exhumation of Menderes core complex: Earth and Planetary Science Letters, v. 414, p. 108-125.

van Coller, Z., Şener, A.K., Mert, B. and Senoz, S., 2016, Structural controls on the Kiziltepe Au-Ag low-sulfidation epithermal vein system, western Turkey: SEG Conference: Tethyan Tectonics and Metallogeny, Çeşme, Turkey, Oral presentation.

van de Zedde, D. and Wortel, M., 2001, Shallow slab detachment as a transient source of heat at midlithospheric depths: Tectonics, v. 20, p. 868-882.

van der Voo, R., Spakman, W. and Bijwaard, H., 1999, Tethyan subducted slabs under India: Earth and Planetary Science Letters, v. 171, p. 7-20.

van Hinsbergen, D.J., 2010, A key extensional metamorphic complex reviewed and restored: the Menderes Massif of western Turkey: Earth-Science Reviews, v. 102, p. 60-76.

van Hinsbergen, D.J. and Schmid, S.M., 2012, Map view restoration of Aegean–West Anatolian

accretion and extension since the Eocene: Tectonics, v. 31, p. 1-40.

van Hinsbergen, D.J., Kaymakci, N., Spakman, W. and Torsvik, T.H., 2010, Reconciling the geological history of western Turkey with plate circuits and mantle tomography: Earth and Planetary Science Letters, v. 297, p. 674-686.

van Hinsbergen, D.J., Maffione, M., Plunder, A., Kaymakcı, N., Ganerød, M., Hendriks, B.W., Corfu, F., Gürer, D., Gelder, G.I. and Peters, K., 2016, Tectonic evolution and paleogeography of the Kırşehir Block and the Central Anatolian Ophiolites, Turkey: Tectonics, v. 35, p. 983-1014.

van Hunen, J. and Allen, M.B., 2011, Continental collision and slab break-off: a comparison of 3-D numerical models with observations: Earth and Planetary Science Letters, v. 302, p. 27-37.

van Hunen, J. and Miller, M.S., 2015, Collisional processes and links to episodic changes in subduction zones: Elements, v. 11, p. 119-124.

Varol, E., Temel, A., Yürür, T., Gourgaud, A. and Bellon, H., 2014, Petrogenesis of the Neogene bimodal magmatism of the Galatean volcanic province, Central Anatolia, Turkey: Journal of Volcanology and Geothermal Research, v. 280, p. 14-29.

Vigneresse, J.L., 2004, A new paradigm for granite generation: Transactions of the Royal Society of Edinburgh: Earth Sciences, v. 95, p. 11-22.

von Quadt, A., Moritz, R., Peytcheva, I. and Heinrich, C.A., 2005, 3: Geochronology and geodynamics of Late Cretaceous magmatism and Cu–Au mineralization in the Panagyurishte region of the Apuseni–Banat–Timok–Srednogorie belt, Bulgaria: Ore Geology Reviews, v. 27, p. 95-126.

Vos, I.M., Bierlein, F.P. and Heithersay, P.S., 2007, A crucial role for slab break-off in the generation of major mineral deposits: insights from central and eastern Australia: Mineralium Deposita, v. 42, p. 515-522.

Voudouris, P., Papavassiliou, C., Alfieris, D. and Falalakis, G., 2007, Gold-silver tellurides and bismuth sulfosalts in the high-intermediate sulfidation Perama Hill deposit, western Thrace (NE Greece): Geol Survey Finland Guide, v. 53, p. 77-84.

Wagner, G.A. and Öztunalı, Ö., 2000, Prehistoric copper sources in Turkey: Der Anschnitt Beiheft, v. 13, p. 31-67.

Walker, G.P., 1989, Gravitational (density) controls on volcanism, magma chambers and intrusions: Australian Journal of Earth Sciences, v. 36, p. 149-165.

Wang, K., Plank, T., Walker, J.D. and Smith, E., 2002, A mantle melting profile across the Basin and Range, SW USA: Journal of Geophysical Research: Solid Earth, v. 107, p. 1-21.

Wang, Q., Wyman, D.A., Xu, J.-F., Zhao, Z.-H., Jian, P., Xiong, X.-L., Bao, Z.-W., Li, C.-F. and Bai, Z.-H., 2006, Petrogenesis of Cretaceous adakitic and shoshonitic igneous rocks in the Luzong area, Anhui Province (eastern China): implications for geodynamics and Cu–Au mineralization: Lithos, v. 89, p. 424-446.

Wdowinski, S., Ben-Avraham, Z., Arvidsson, R. and Ekström, G., 2006, Seismotectonics of the Cyprian arc: Geophysical Journal International, v. 164, p. 176-181.

Weis, D., Kieffer, B., Maerschalk, C., Barling, J., de Jong, J., Williams, G.A., Hanano, D., Pretorius, W., Mattielli, N. and Scoates, J.S., 2006, High-precision isotopic characterization of USGS reference materials by TIMS and MC-ICP-MS: Geochemistry, Geophysics, Geosystems, v. 7, p. 1-30.

Westaway, R., 2003, Kinematics of the Middle East and eastern Mediterranean updated: Turkish Journal of Earth Sciences, v. 12, p. 5-46.

Westaway, R., Demir, T. and Seyrek, A., 2008, Geometry of the Turkey-Arabia and Africa-Arabia plate boundaries in the latest Miocene to Mid-Pliocene: the role of the Malatya-Ovacık Fault Zone in eastern Turkey: eEarth, v. 3, p. 27-35.

Whalen, J.B., McNicoll, V.J., van Staal, C.R., Lissenberg, C.J., Longstaffe, F.J., Jenner, G.A. and van Breeman, O., 2006, Spatial, temporal and geochemical characteristics of Silurian collision-zone magmatism, Newfoundland Appalachians: An example of a rapidly evolving magmatic system related to slab break-off: Lithos, v. 89, p. 377-404.

Whitney, D., Teyssier, C., Dilek, Y. and Fayon, A., 2001, Metamorphism of the Central Anatolian Crystalline Complex, Turkey: influence of orogen-normal collision vs. wrench-dominated tectonics on P–T–t paths: Journal of Metamorphic Geology, v. 19, p. 411-432.

Whitney, D.L. and Dilek, Y., 1997, Core complex development in central Anatolia, Turkey: Geology, v. 25, p. 1023-1026.

Whitney, D.L. and Bozkurt, E., 2002, Metamorphic history of the southern Menderes massif, western Turkey: Geological Society of America Bulletin, v. 114, p. 829-838.

Whitney, D.L., Teyssier, C. and Heizler, M.T., 2007, Gneiss domes, metamorphic core complexes, and wrench zones: Thermal and structural evolution of the Niğde Massif, central Anatolia: Tectonics, v. 26, p. 1-27.

Whitney, D.L., Teyssier, C., Fayon, A.K., Hamilton, M.A. and Heizler, M., 2003, Tectonic controls on metamorphism, partial melting, and intrusion: timing and duration of regional metamorphism and magmatism in the Niğde Massif, Turkey: Tectonophysics, v. 376, p. 37-60.

Wilson, M., Tankut, A. and Guleç, N., 1997, Tertiary volcanism of the Galatia province, north-west Central Anatolia, Turkey: Lithos, v. 42, p. 105-121.

Winter, J.D., 2001, An introduction to igneous and metamorphic petrology: U.S.R.P. Hall, 796 p.

Workman, R.K. and Hart, S.R., 2005, Major and trace element composition of the depleted MORB mantle (DMM): Earth and Planetary Science Letters, v. 231, p. 53-72.

Wortel, M. and Spakman, W., 2000, Subduction and slab detachment in the Mediterranean-Carpathian region: Science, v. 290, p. 1910-1917.

Yalçın, H., Gündoğdu, M.N., Gourgaud, A., Vidal, P. and Uçurum, A., 1998, Geochemical characteristics of Yamadağı volcanics in central east Anatolia: an example from collision-zone volcanism: Journal of Volcanology and Geothermal Research, v. 85, p. 303-326.

Yaliniz, K. and Göncüoglu, M.C., 1998, General geological characteristics and distribution of

the Central Anatolian Ophiolites: Yerbilimleri, v. 20, p. 19-30.

Yiğit, Ö., 2006, Gold in Turkey—a missing link in Tethyan metallogeny: Ore Geology Reviews, v. 28, p. 147-179.

Yiğit, Ö., 2009, Mineral deposits of Turkey in relation to Tethyan metallogeny: implications for future mineral exploration: Economic Geology, v. 104, p. 19-51.

Yiğit, Ö., 2012, A prospective sector in the Tethyan Metallogenic Belt: Geology and geochronology of mineral deposits in the Biga Peninsula, NW Turkey: Ore Geology Reviews, v. 46, p. 118-148.

Yiğitbaş, E. and Yilmaz, Y., 1996, New evidence and solution to the Maden complex controversy of the Southeast Anatolian orogenic belt (Turkey): Geologische Rundschau, v. 85, p. 250-263.

Yılmaz, A., Yılmaz, H., Kaya, C. and Boztug, D., 2010, The nature of the crustal structure of the Eastern Anatolian Plateau, Turkey: Geodinamica Acta, v. 23, p. 167-183.

Yilmaz, H., Alpaslan, M. and Temel, A., 2007, Two-stage felsic volcanism in the western part of the southeastern Anatolian orogen: petrologic and geodynamic implications: International Geology Review, v. 49, p. 120-141.

Yilmaz, H., Oyman, T., Sonmez, F.N., Arehart, G.B. and Billor, Z., 2010, Intermediate sulfidation epithermal gold-base metal deposits in Tertiary subaerial volcanic rocks, Sahinli/Tespih Dere (Lapseki/Western Turkey): Ore Geology Reviews, v. 37, p. 236-258.

Yılmaz, H., Sönmez, F.N., Erhan, A., Şener, A.K. and Tufan, S.T., 2013, Low-sulfidation epithermal Au-Ag mineralization in the Sındırgı District, Balıkesir Province, Turkey: Turkish Journal of Earth Sciences, v. 22, p. 485-522.

Yılmaz, H., 2002, Ovacik gold deposit: an example of quartz-adularia–type gold mineralization in Turkey: Economic Geology, v. 97, p. 1829-1839.

Yılmaz, K., 2010, Origin of anorogenic ‘lamproite-like’potassic lavas from the Denizli region in Western Anatolia Extensional Province, Turkey: Mineralogy and Petrology, v. 99, p. 219-239.

Yilmaz, S., Boztui, D. and Öztürk, A., 1993, Geological setting, petrographic and geochemical characteristics of the Cretaceous and Tertiary igneous rocks in the Hekimhan-Hasançelebi area, north-west Malatya, Turkey: Geological Journal, v. 28, p. 383-398.

Yılmaz, Y., 1990, Comparison of young volcanic associations of western and eastern Anatolia formed under a compressional regime: a review: Journal of Volcanology and Geothermal Research, v. 44, p. 69-87.

Yılmaz, Y., 1993, New evidence and model on the evolution of the southeast Anatolian orogen: Geological Society of America Bulletin, v. 105, p. 251-271.

Yılmaz, Y., Şaroğlu, F. and Güner, Y., 1987, Initiation of the neomagmatism in East Anatolia: Tectonophysics, v. 134, p. 177-199.

Yılmaz, Y., Yiğitbaş, E. and Genç, Ş., 1993, Ophiolitic and metamorphic assemblages of southeast Anatolia and their significance in the geological evolution of the orogenic

belt: Tectonics, v. 12, p. 1280-1297.

Yılmaz, Y., Güner, Y. and Şaroğlu, F., 1998, Geology of the quaternary volcanic centres of the east Anatolia: Journal of volcanology and geothermal research, v. 85, p. 173-210.

Yılmazer, E., Güleç, N., Kuşcu, İ. and Lentz, D.R., 2014, Geology, geochemistry, and geochronology of Fe-oxide Cu (±Au) mineralization associated with Şamlı pluton, western Turkey: Ore Geology Reviews, v. 57, p. 191-215.

Young, W.J., 1972, The fabulous gold of the Pactolus valley: Boston Museum Bulletin, v. 70, p. 4-13.

Yücel-Öztürk, Y., 2016, O, Sr and Nd isotopic constraints on Cenozoic granitoids of Northwestern Anatolia, Turkey: Enrichment by subduction zone fluids: Journal of African Earth Sciences, v. 117, p. 12-28.

Yuen, D.A. and Fleitout, L., 1985, Thinning of the lithosphere by small-scale convective destabilization: Nature, v. 313, p. 125.

Yurtmen, S. and Rowbotham, G., 2002, Geochemistry, mineralogy and petrogenesis of the northeast Niğde volcanics, central Anatolia, Turkey: Geological Journal, v. 37, p. 189-215.

Zellmer, G., Iizuka, Y., Miyoshi, M., Tamura, Y. and Tatsumi, Y., 2012, Lower crustal H2O controls on the formation of adakitic melts: Geology, v. 40, p. 487-490.

Zhu, D.-C., Wang, Q., Zhao, Z.-D., Chung, S.-L., Cawood, P.A., Niu, Y., Liu, S.-A., Wu, F.-Y. and Mo, X.-X., 2015, Magmatic record of India-Asia collision: Scientific Reports, v. 5, p. 14289.

Zhu, L., Mitchell, B.J., Akyol, N., Cemen, I. and Kekovali, K., 2006, Crustal thickness variations in the Aegean region and implications for the extension of continental crust: Journal of Geophysical Research: Solid Earth, v. 111, p. 1-10.

Zimmerman, A., Stein, H.J., Hannah, J.L., Koželj, D., Bogdanov, K. and Berza, T., 2008, Tectonic configuration of the Apuseni–Banat—Timok–Srednogorie belt, Balkans-South Carpathians, constrained by high precision Re–Os molybdenite ages: Mineralium Deposita, v. 43, p. 1-21.

Zindler, A. and Hart, S., 1986, Chemical geodynamics: Annual review of earth and planetary sciences, v. 14, p. 493-571.

Zor, E., 2008, Tomographic evidence of slab detachment beneath eastern Turkey and the Caucasus: Geophysical Journal International, v. 175, p. 1273-1282.

Zor, E., Sandvol, E., Gürbüz, C., Türkelli, N., Seber, D. and Barazangi, M., 2003, The crustal structure of the East Anatolian plateau (Turkey) from receiver functions: Geophysical Research Letters, v. 30, p. 1-4.

Appendix A

A.1 Age data compilation

Table A.1 Geochronological data compilation, central and eastern Anatolia.

Magmatic Complex	Age Range (Ma)	References
Central Anatolia		
Acigöl volcano	0.206 ± 0.040 - Present	(46)
Cappadocia-İncesu ignimbrites	10.7 ± 0.3 – Present	(1), (2), (3), (4), (5), (30)
Develidağ stratovolcano	5.36 ± 0.20	(6)
Erciyes stratovolcano	3.57 ± 1.17 – Present	(1), (7), (8), (9), (10)
Hasandağ stratovolcano	1.5 ± 0.5 – Present	(1), (2), (7), (8), (45)
Karaman vents	2.19 ± 0.41 – 1.79 ± 0.09	(2)
Karapınar vents	4.76 ± 0.27 – Present	(1), (2), (45)
Melendiz stratovolcano	4.9 ± 0.2 – 2.40 ± 0.15	(2), (6)
Tekkedağ volcano	7.92 ± 0.14	(6)
Eastern Anatolia		
Ağrı magmatic complex	21.32 ± 0.29 – 17.38 ± 0.36	(6)
Aladağ volcanic suite	14.9 ± 0.3 – 13.4 ± 0.3	(11)
Ararat volcano	1.51 ± 0.38 – Present	(1), (9)
Cevizlidere stock	25.54 ± 0.40 – 25.29 ± 0.34	(12)
Elazığ volcanic suite	1.87 ± 0.07 to 1.47 ±0.09	(16)
Erzincan volcanic suite	1.06 ± 0.18 – Present	(1), (2), (7), (8), (40)
Erzurum volcanic plateau	13.1 ± 0.6 – Present	(9), (16), (17), (18), (19), (20), (21)
Etrüsk volcano	5.74 ± 0.16 – 3.60 ± 0.15	(11), (13), (14), (15)
Kars volcanic plateau	11.1 ± 1.0 – 1.3 ± 0.6	(18), (21), (22)
Kepez volcanic suite	16.19 ± 0.10 – 13.58 ± 0.17	(23), (24)
Nemrut volcano	1.18 ± 0.46 – Present	(1), (9), (25)
Sarıçimen pluton	12.6 ± 0.3 – 11.9 ± 0.4	(26)
Süphan volcano	5.8 ± 0.3 – Present	(1), (9), (13), (25), (27), (28), (29)
Tendürek volcano	0.71 ± 0.06 – Present	(1), (27), (31)
Yamadağ volcanic complex	21.23 ± 0.33 – 8.9 ± 0.7	(2), (6), (13), (32), (33), (34), (35)
Other volcanic domains		
Konya volcanic complex	ca. 10.21 ± 0.13 – 6.49 ± 0.31*	(2), (6), (36)
Galatian magmatic province	22.52 ± 0.52 – 17.6 ± 0.5	(37), (38), (39)
Sivas volcanic suite	15.0 ± 0.5 – 1.3 ± 0.1	(2), (41)
Sulutas volcanic suite	16.45 ± 0.76 – 11.61 ± 0.04	(42), (43), (44)

(1) Notsu et al. (1995); (2) Platzman et al. (1998); (3) Aydar et al. (2012); (4) Lepetit et al. (2014); (5) Higgins (2014); (6) This study; (7) Aydin et al. (2014); (8) Kuzucuoglu et al. (1998); (9) Pearce et al. (1990); (10) Dogan (2016); (11) Lebedev et al. (2010); (12) İmer

et al. (2014); (13) Innocenti et al. (1980); (14) Oyan et al. (2016); (15) Selçuk et al. (2016); (16) Arger et al. (2000); (17) Seyrek et al. (2008); (18) Bigazzi et al. (1997); (19) Demir et al. (2009); (20) Hubert-Ferrari et al. (2009); (21) Innocenti et al. (1982); (22) Keskin et al. (1998); (23) Onal et al. (2008); (24) Ekici (2016); (25) Sumita and Schmincke (2013); (26) Çolakoğlu and Arehart (2010); (27) Innocenti et al. (1976); (28) Özdemir and Güleç (2013); (29) Özdemir (2011); (30) Paquette and Le Pennec (2012); (31) Lebedev et al. (2016); (32) Ekici et al. (2009); (33) Kürüm et al. (2008); (34) Leo et al. (1974); (35) Leo et al. (1978); (36) Keller et al. (1977); (37) Wilson et al. (1997); (38) Kurt et al. (2008); (39) Varol et al. (2014); (40) Karsli et al. (2008); (41) Jaffey et al. (2004); (42) Koç et al. (2012); (43) Korkmaz et al. (2017); (44) Asan and Ertürk (2013); (45) Reid et al. (2017); (46) Schmitt et al. (2011).

*Time range of the Konya volcanic complex is based on published and verified age data. The original time range (i.e. ca. 12 – 3.2 Ma; Keller et al., 1977) was obtained from unchecked geochronological data, utilized by Temel et al. (1998).

A.2 LA-ICP-MS U-Pb dating analyses

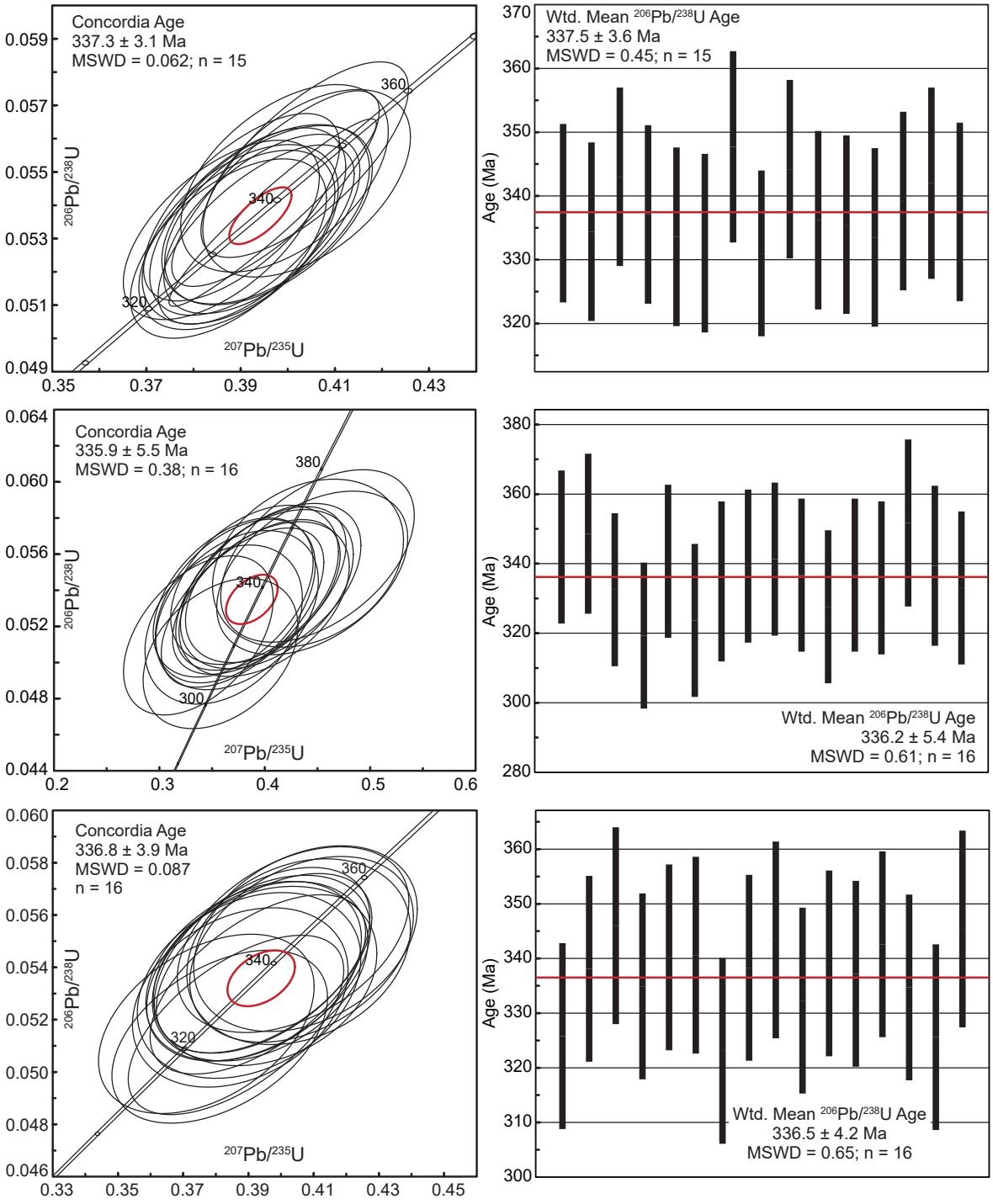

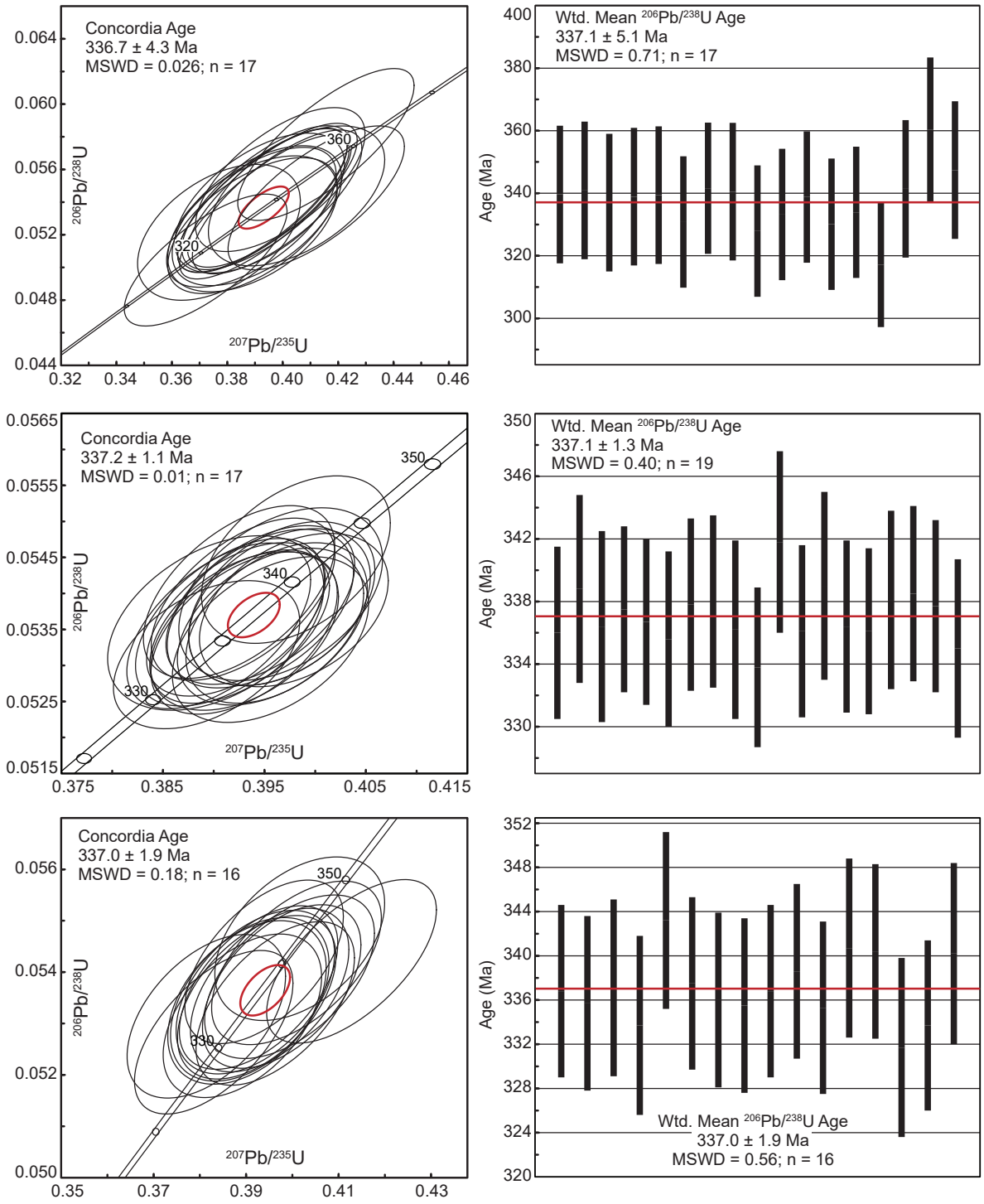

Figure A.1 Concordia plots and $^{206}Pb/^{238}U$ weighted mean histograms of Plešovice zircon standards.

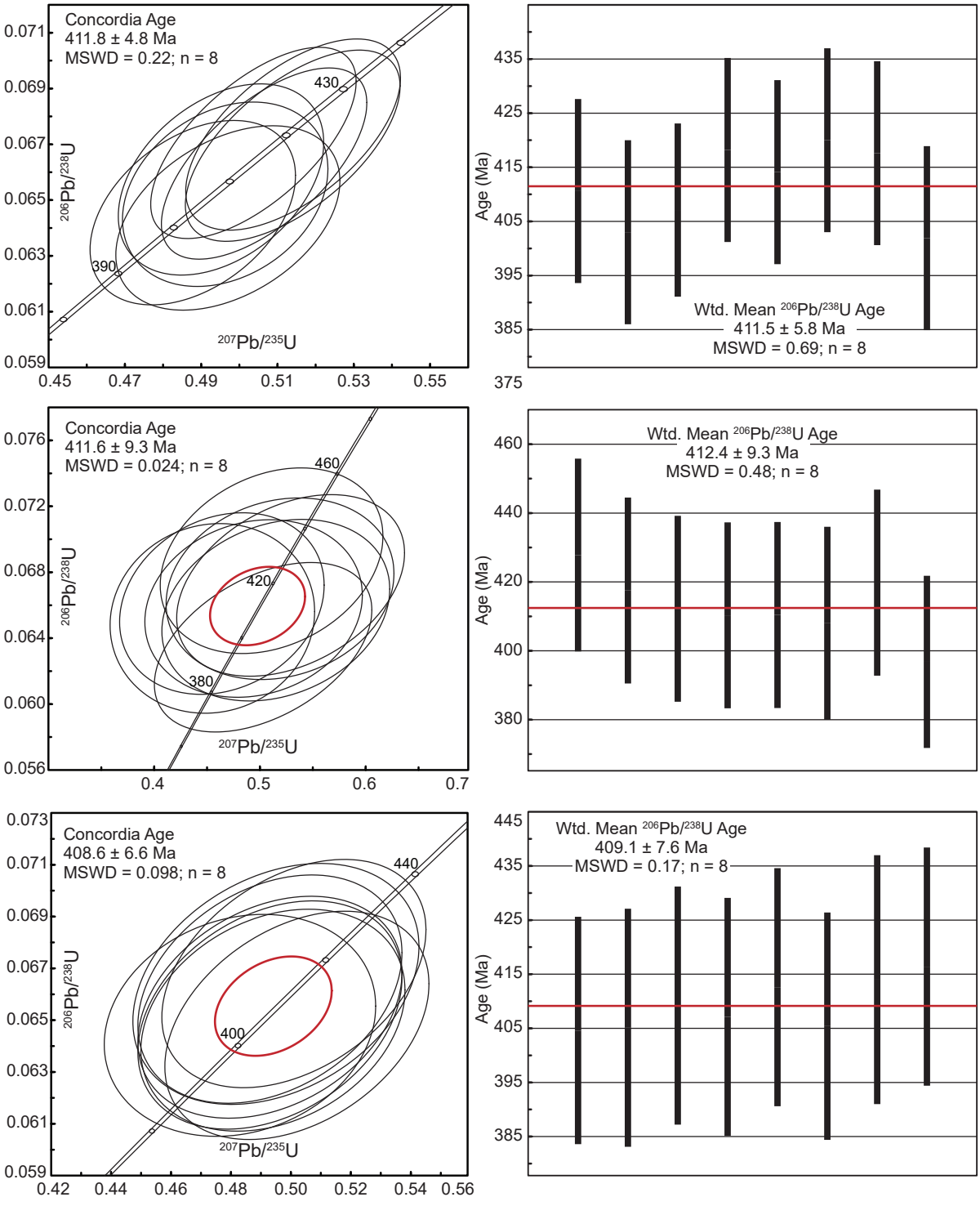
Concordia Age
411.8 ± 4.8 Ma
MSWD = 0.22; n = 8
430
390
$^{206}Pb/^{238}U$
$^{207}Pb/^{235}U$
0.071
0.069
0.067
0.065
0.063
0.061
0.059
0.45
0.47
0.49
0.51
0.53
0.55
Age (Ma)
435
425
415
405
395
385
375
Wtd. Mean $^{206}Pb/^{238}U$ Age
411.5 ± 5.8 Ma
MSWD = 0.69; n = 8
Concordia Age
411.6 ± 9.3 Ma
MSWD = 0.024; n = 8
460
420
380
$^{206}Pb/^{238}U$
$^{207}Pb/^{235}U$
0.076
0.072
0.068
0.064
0.060
0.056
0.4
0.5
0.6
0.7
Wtd. Mean $^{206}Pb/^{238}U$ Age
412.4 ± 9.3 Ma
MSWD = 0.48; n = 8
Age (Ma)
460
440
420
400
380
Concordia Age
408.6 ± 6.6 Ma
MSWD = 0.098; n = 8
440
400
$^{206}Pb/^{238}U$
$^{207}Pb/^{235}U$
0.073
0.071
0.069
0.067
0.065
0.063
0.061
0.059
0.42
0.44
0.46
0.48
0.50
0.52
0.54
0.56
Wtd. Mean $^{206}Pb/^{238}U$ Age
409.1 ± 7.6 Ma
MSWD = 0.17; n = 8
Age (Ma)
445
435
425
415
405
395
385

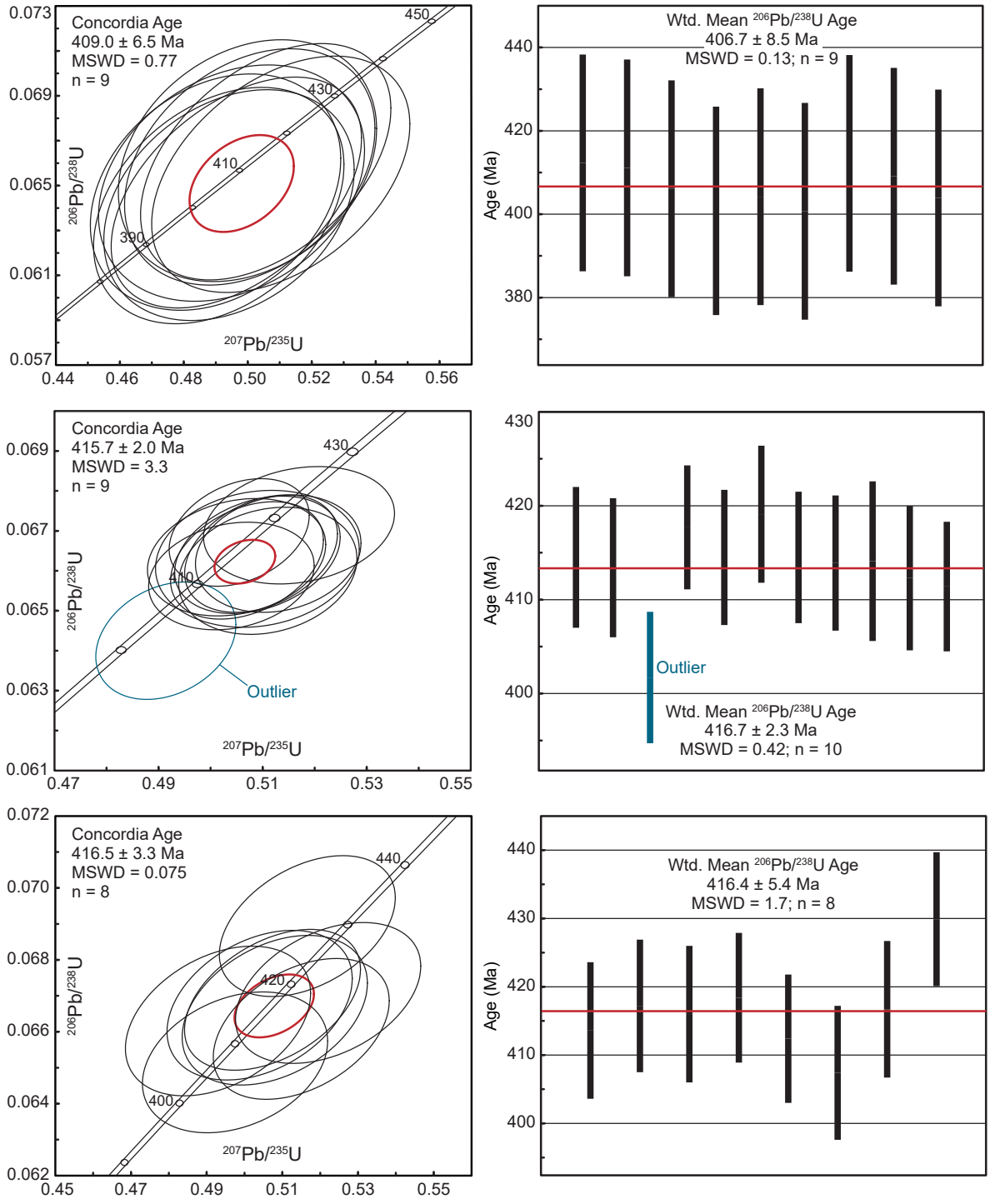

Figure A.2 Concordia plots and $^{206}Pb/^{238}U$ weighted mean histograms of Temora2 zircon standards.

Table A.2 LA-ICP-MS U-Pb isotopic analyses.

Zircon grain analysis	Ion count rate (cps)								Isotope ratios						Calculated ages (Ma)			
	^{202}Hg	^{204}Pb	^{206}Pb	^{207}Pb	^{208}Pb	^{232}Th	^{235}U	^{238}U	$^{207}Pb/^{235}U$	$\pm 2\sigma^a$	$^{206}Pb/^{238}U$	$\pm 2\sigma^a$	$^{207}Pb/^{206}Pb$	$\pm 2\sigma^a$	$^{207}Pb/^{235}U$	$\pm 2\sigma^a$	$^{206}Pb/^{238}U$	$\pm 2\sigma^a$
FR-14-73																		
FR_14_73_0	-36	-43	4230	186	756	311800	7970	1331000	0.010090	0.000790	0.001572	0.000081	0.0463	0.0034	10.19	0.79	10.13	0.52
FR_14_73_1	13	-1	3003	137	380	167900	5840	970000	0.009900	0.000700	0.001545	0.000074	0.0480	0.0028	10.03	0.71	9.95	0.48
FR_14_73_2	-27	-21	3730	174	771	330000	7360	1213000	0.009780	0.000780	0.001544	0.000076	0.0483	0.0036	9.87	0.78	9.94	0.49
FR_14_73_3	41	32	1270	66	177	78600	2370	395000	0.011600	0.001800	0.001641	0.000110	0.0569	0.0092	11.70	1.80	10.57	0.71
FR_14_73_4	52	4	1861	85.8	363	160500	3500	578000	0.009920	0.001000	0.001575	0.000080	0.0472	0.0047	10.07	1.00	10.15	0.51
FR_14_73_5	-19	-6	3430	154	548	259000	6620	1104000	0.010010	0.000820	0.001600	0.000075	0.0447	0.0032	10.09	0.83	10.31	0.48
FR_14_73_6	7	-31	2092	105	287	113600	4055	643300	0.011700	0.001300	0.001662	0.000098	0.0574	0.0072	11.80	1.40	10.70	0.63
FR_14_73_7	-68	-50	1980	97.7	306	141800	3890	655000	0.010370	0.000900	0.001569	0.000076	0.0530	0.0045	10.45	0.90	10.11	0.49
FR_14_73_8	-52	-52	5440	270	933	453000	10240	1762000	0.011140	0.001100	0.001610	0.000080	0.0510	0.0046	11.23	1.10	10.37	0.52
FR_14_73_9	-25	-25	2055	99.3	414	178300	4140	699000	0.011000	0.001200	0.001565	0.000085	0.0544	0.0058	11.00	1.20	10.08	0.55
FR_14_73_10[b]	6	-20	2250	124	356	149600	4600	750000	0.012000	0.001200	0.001573	0.000086	0.0566	0.0059	12.10	1.20	10.13	0.55
FR_14_73_11	39	13	2003	93	388	175400	4080	687000	0.010200	0.001400	0.001558	0.000088	0.0490	0.0068	10.30	1.40	10.04	0.57
FR_14_73_12	44	-37	2920	139	340	156100	5780	974000	0.010330	0.000850	0.001581	0.000075	0.0483	0.0036	10.41	0.85	10.19	0.48
FR_14_73_13	33	19	3130	142	536	241800	6340	1046000	0.009970	0.000860	0.001577	0.000082	0.0465	0.0038	10.06	0.87	10.16	0.53
FR_14_73_14	171	-38	6600	297	1030	473000	13460	2227000	0.010100	0.001200	0.001620	0.000110	0.0467	0.0056	10.20	1.20	10.43	0.71
FR_14_73_15	12	-42	1867	93	341	126500	3730	619000	0.011000	0.001300	0.001574	0.000095	0.0498	0.0053	11.00	1.30	10.14	0.61
FR_14_73_16	128	-17	6120	280	1470	663000	12000	1952000	0.010750	0.001000	0.001634	0.000080	0.0481	0.0042	10.85	1.00	10.53	0.51
FR-14-142																		
FR_14_142_0	89	-25	616	22.7	133	37120	774	125500	0.015300	0.002800	0.002690	0.000220	0.0610	0.0120	15.2	2.7	17.32	1.4
FR_14_142_1	36	-26	676	32.5	92	27230	850	142500	0.016600	0.002600	0.002610	0.000210	0.0540	0.0089	16.5	2.6	16.82	1.4
FR_14_142_2	66	-25	1010	39.3	142	43100	1173	196100	0.016800	0.002700	0.002760	0.000230	0.0476	0.0077	16.8	2.7	17.76	1.4
FR_14_142_3	17	-28	1271	56	175	51900	1562	254700	0.016600	0.002500	0.002710	0.000210	0.0474	0.0072	16.6	2.5	17.42	1.3
FR_14_142_4[c]	72	-19	72700	4080	9780	81700	3630	598000	0.544000	0.036000	0.068600	0.004600	0.0582	0.0017	440	24.0	428.3	28
FR_14_142_5	-10	-29	1636	74.5	318	82900	1927	316300	0.017400	0.001800	0.002820	0.000200	0.0463	0.0043	17.5	1.8	18.15	1.3
FR_14_142_6	-46	-41	1058	53.8	204	48100	1277	217700	0.018000	0.002600	0.002670	0.000210	0.0519	0.0071	18.2	2.6	17.21	1.3
FR_14_142_7	-31	-47	1039	49.3	235	58600	1286	216200	0.018000	0.002300	0.002650	0.000200	0.0543	0.0070	18.0	2.3	17.07	1.3
FR_14_142_8	54	-21	1168	61.1	233	57200	1346	226700	0.019600	0.002500	0.002810	0.000220	0.0539	0.0067	19.7	2.5	18.21	1.4
FR_14_142_9	38	-1	618	35.1	122	31500	778	129400	0.018200	0.003500	0.002640	0.000230	0.0630	0.0130	18.0	3.4	16.96	1.5
FR_14_142_10	-57	-15	875	40.1	165	37400	1024	171800	0.017700	0.002300	0.002750	0.000210	0.0601	0.0089	17.6	2.3	17.69	1.4
FR_14_142_11	-93	-2	891	46.2	228	48700	1032	175900	0.020800	0.004200	0.002700	0.000250	0.0760	0.0180	20.7	4.2	17.40	1.6
FR_14_142_12	-95	-18	1009	47.7	250	66500	1214	209700	0.018200	0.002800	0.002550	0.000220	0.0517	0.0080	18.2	2.8	16.43	1.4
FR_14_142_13	-83	-13	973	51.1	180	43600	1174	196900	0.019100	0.003300	0.002700	0.000230	0.0552	0.0095	19.4	3.3	17.40	1.5
FR_14_142_14	11	8	719	33.6	168	44800	852	145800	0.017900	0.002600	0.002650	0.000210	0.0465	0.0072	17.8	2.6	17.05	1.4
FR_14_142_15[b]	38	13	1006	64.2	239	45500	1138	185000	0.027200	0.004100	0.002930	0.000240	0.0720	0.0110	27.0	4.0	18.80	1.6
FR_14_142_16	19	5	1068	48.2	178	50300	1278	210100	0.017900	0.002300	0.002740	0.000200	0.0491	0.0061	17.9	2.3	17.67	1.3

Table A.2 (Continued) LA-ICP-MS U-Pb isotopic analyses.

Zircon grain analysis	Ion count rate (cps)								Isotope ratios						Calculated ages (Ma)			
	^{202}Hg	^{204}Pb	^{206}Pb	^{207}Pb	^{208}Pb	^{232}Th	^{235}U	^{238}U	$^{207}Pb/^{235}U$	$\pm 2\sigma$[a]	$^{206}Pb/^{238}U$	$\pm 2\sigma$[a]	$^{207}Pb/^{206}Pb$	$\pm 2\sigma$[a]	$^{207}Pb/^{235}U \pm 2\sigma$[a]		$^{206}Pb/^{238}U \pm 2\sigma$[a]	
FR-14-129																		
FR_14_129_0	22	-51	1042	44	192	48900	745	149100	0.019600	0.002600	0.003220	0.000170	0.0473	0.0066	19.5	2.6	20.74	1.1
FR_14_129_1	92	-17	1399	62.4	289	71200	994	196200	0.021400	0.003000	0.003380	0.000200	0.0484	0.0086	21.4	3.0	21.80	1.3
FR_14_129_2	7	-41	1416	59	237	53100	1021	201100	0.019400	0.002000	0.003280	0.000140	0.0481	0.0056	19.6	2.0	21.12	0.92
FR_14_129_3	33	-28	1243	53	273	59200	898	170300	0.021200	0.002900	0.003460	0.000180	0.0473	0.0070	21.2	2.9	22.30	1.2
FR_14_129_4	84	-49	1399	59.8	305	72600	986	185800	0.022700	0.003600	0.003430	0.000210	0.0472	0.0078	22.6	3.5	22.10	1.3
FR_14_129_5	-20	-18	1540	63.5	342	88900	1164	222700	0.021400	0.002700	0.003340	0.000180	0.0466	0.0066	21.4	2.7	21.50	1.1
FR_14_129_6	16	-3	1830	83	518	106100	1378	262000	0.023700	0.003400	0.003250	0.000200	0.0511	0.0076	23.7	3.3	20.90	1.3
FR_14_129_7	7	-14	1207	50.9	244	59300	921	178600	0.020000	0.002300	0.003320	0.000150	0.0434	0.0054	20.0	2.3	21.34	0.95
FR_14_129_8	-83	-41	2396	102.1	606	148000	1795	370000	0.020000	0.001400	0.003217	0.000120	0.0456	0.0035	20.1	1.4	20.70	0.75
FR_14_129_9	-100	-16	1365	67.7	322	78100	1072	205200	0.023800	0.003100	0.003240	0.000180	0.0512	0.0071	23.7	3.1	21.00	1.2
FR_14_129_10	-33	-16	1079	47.9	257	66400	860	173400	0.021800	0.002400	0.003250	0.000150	0.0538	0.0065	21.7	2.4	20.89	0.99
FR 14 129 11[b]	-53	-22	2610	139	758	163000	1990	388000	0.026500	0.002600	0.003400	0.000170	0.0585	0.0060	26.4	2.6	21.94	1.1
FR_14_129_12	-21	-2	1161	46	180	47900	855	166600	0.021000	0.003100	0.003610	0.000190	0.0444	0.0069	20.9	3.0	23.30	1.2
FR_14_129_13	-56	-38	612	27	58	19530	503	95500	0.022300	0.005000	0.003240	0.000270	0.0600	0.0160	22.0	4.9	20.90	1.7
FR_14_129_14	-68	16	1193	58.6	216	49400	941	176000	0.023800	0.003400	0.003350	0.000200	0.0541	0.0080	23.7	3.3	21.50	1.3
FR_14_129_15	-16	2	560	25.4	104	25900	462	93300	0.021200	0.004400	0.003240	0.000240	0.0530	0.0120	21.0	4.3	20.90	1.5
FR 14 129 16[d]	20	0	4300	254	1465	314000	3320	626000	0.030100	0.002100	0.003640	0.000140	0.0625	0.0048	30.0	2.0	23.45	0.89
FR-14-124																		
FR_14_124_1	792	158	868	52	261	24900	594	83100	0.017700	0.002900	0.003020	0.000160	0.0448	0.0084	17.8	2.9	19.40	1
FR_14_124_2	749	158	3180	175	1136	115000	2155	301000	0.021200	0.002000	0.003081	0.000110	0.0518	0.0045	21.2	1.9	19.83	0.69
FR_14_124_3	835	177	1991	106.4	642	64800	1396	185000	0.019900	0.001900	0.003150	0.000120	0.0490	0.0046	19.9	1.9	20.25	0.76
FR_14_124_4	779	182	1066	57	524	52900	731	102000	0.017500	0.002300	0.003110	0.000140	0.0471	0.0069	17.5	2.3	20.03	0.92
FR_14_124_5	855	173	881	53.5	345	32320	593	82400	0.020300	0.002800	0.003130	0.000160	0.0499	0.0080	20.2	2.7	20.12	1.1
FR_14_124_6	817	177	365	33.2	93	6410	232	31000	0.017600	0.007400	0.003070	0.000290	0.0730	0.0480	15.8	7.2	19.80	1.9
FR 14 124 7[b]	808	184	4040	245	2110	199000	2700	373000	0.026600	0.002500	0.003267	0.000110	0.0615	0.0053	26.5	2.4	21.03	0.73
FR_14_124_8	774	184	1671	90.6	506	53900	1194	166000	0.019700	0.002100	0.003010	0.000120	0.0488	0.0052	19.7	2.1	19.40	0.8
FR_14_124_9	808	187	995	65.1	253	21530	697	96000	0.022600	0.003000	0.003150	0.000160	0.0554	0.0077	22.5	2.9	20.28	1
FR 14 124 10[b]	826	171	630	59.5	317	27580	428	58300	0.033600	0.004700	0.003170	0.000190	0.0940	0.0160	32.8	4.6	20.40	1.2
FR_14_124_11	825	181	2229	117.9	762	80100	1633	220000	0.020400	0.001900	0.003087	0.000110	0.0487	0.0045	20.4	1.9	19.87	0.7
FR_14_124_12	811	179	1730	98	393	38050	1222	167000	0.022100	0.002200	0.003160	0.000130	0.0522	0.0053	22	2.2	20.36	0.84
FR_14_124_13	798	159	2385	132	859	89800	1678	232000	0.021600	0.001900	0.003150	0.000120	0.0526	0.0045	21.6	1.9	20.30	0.77
FR_14_124_14	829	176	6530	312	2263	236000	4800	644000	0.019510	0.001300	0.003129	0.000097	0.0458	0.0027	19.59	1.3	20.14	0.62
FR_14_124_15	825	183	1634	94.8	622	65900	1190	163000	0.021600	0.002200	0.003080	0.000130	0.0540	0.0056	21.5	2.1	19.85	0.81
FR_14_124_16	740	189	1975	103.1	635	66500	1486	204000	0.019100	0.001900	0.003010	0.000120	0.0476	0.0048	19.1	1.9	19.35	0.8
FR_14_124_17	781	179	1940	105.8	531	57200	1388	192000	0.021800	0.002400	0.003140	0.000140	0.0503	0.0058	21.7	2.3	20.21	0.89
FR 14 124 18[c]	757	167	25120	1409	2122	13480	1112	153000	0.385000	0.022000	0.052300	0.001800	0.0559	0.0024	328.4	16	328.40	11
FR_14_124_19	785	164	1310	80	470	48900	990	139000	0.022800	0.005500	0.002940	0.000240	0.0720	0.0220	23.3	5.6	18.90	1.6
FR_14_124_20	764	179	926	52.2	393	36900	726	96700	0.017700	0.002700	0.003000	0.000170	0.0508	0.0084	17.6	2.6	19.30	1.1
FR_14_124_21	822	181	1940	108	773	76400	1533	206000	0.019500	0.002500	0.003070	0.000160	0.0499	0.0060	19.5	2.5	19.73	1
FR_14_124_22	794	189	2034	104.7	837	91000	1551	217000	0.018800	0.001800	0.002958	0.000110	0.0488	0.0046	18.8	1.8	19.04	0.73

Table A.2 (Continued) LA-ICP-MS U-Pb isotopic analyses.

Zircon grain analysis	Ion count rate (cps)								Isotope ratios						Calculated ages (Ma)			
	^{202}Hg	^{204}Pb	^{206}Pb	^{207}Pb	^{208}Pb	^{232}Th	^{235}U	^{238}U	$^{207}Pb/^{235}U$	$\pm 2\sigma^a$	$^{206}Pb/^{238}U$	$\pm 2\sigma^a$	$^{207}Pb/^{206}Pb$	$\pm 2\sigma^a$	$^{207}Pb/^{235}U \pm 2\sigma^a$		$^{206}Pb/^{238}U \pm 2\sigma^a$	
FR-13-181																		
FR13-181-c1r1	25	1.8	1507	74.4	345	520000	6320	904000	0.008660	0.000890	0.001293	0.000050	0.0054	0.0052	8.75	0.83	8.33	0.26
FR13-181-c1r2	6	9.1	271	13.3	60	91200	1146	149100	0.009000	0.003000	0.001400	0.000130	0.0250	0.0250	9.00	3.0	9.02	0.79
FR13-181-c1r3	17	7.1	1089	51.7	181	226000	4420	622000	0.008440	0.000960	0.001360	0.000066	0.0060	0.0058	8.52	0.91	8.76	0.38
FR13-181-c1r5	20	5.1	952	41.9	170	215000	3870	540000	0.007900	0.001100	0.001376	0.000069	0.0063	0.0061	8.00	1.1	8.86	0.39
FR13-181-c1r13	34	3.3	1010	46.3	432	661000	4470	617000	0.007900	0.001200	0.001271	0.000096	0.0096	0.0095	8.00	1.2	8.19	0.59
FR13-181-c1r14	-3	8.7	791	39.9	252	398000	3370	461000	0.009200	0.001200	0.001342	0.000073	0.0074	0.0073	9.30	1.2	8.65	0.42
FR13-181-c1r15	20	5.8	1538	77.2	300	453000	6250	887000	0.009210	0.000890	0.001345	0.000057	0.0048	0.0046	9.30	0.82	8.66	0.31
FR13-181-c2r1	17	3	1461	66.2	300	449000	5960	832000	0.008230	0.000860	0.001357	0.000056	0.0048	0.0047	8.32	0.80	8.74	0.30
FR13-181-c2r2	16	1.9	1157	50.7	249	321000	4650	657000	0.008400	0.001100	0.001364	0.000064	0.0070	0.0069	8.50	1.0	8.78	0.36
FR13-181-c2r3	18	-0.4	150	9.5	35.1	53900	625	84200	0.011100	0.004000	0.001390	0.000160	0.0380	0.0380	11.6	4.1	8.96	0.99
FR13-181-c2r4[b]	17	7	480	28.9	74	103600	1906	262700	0.011600	0.002000	0.001435	0.000086	0.0110	0.0110	11.6	1.9	9.24	0.51
FR13-181-c2r9	15	-2.2	1221	63.6	212	320000	4850	683000	0.010000	0.001100	0.001382	0.000068	0.0060	0.0058	10.1	1.0	8.90	0.39
FR13-181-c2r10	25	-3.2	903	41.9	182	258800	3830	539000	0.008100	0.001100	0.001295	0.000063	0.0065	0.0064	8.20	1.1	8.34	0.36
FR13-181-c2r11	18	4.8	296	11.3	56	86900	1155	158800	0.007400	0.002200	0.001440	0.000120	0.0140	0.0140	7.40	2.2	9.29	0.74
FR13-181-c2r12	15	-5	1800	84.2	347	512000	7290	1.05E+06	0.008310	0.000890	0.001349	0.000059	0.0054	0.0052	8.40	0.84	8.69	0.32
FR13-181-c2r13	20	-0.6	461	23.1	106	146600	2037	278500	0.008700	0.001500	0.001299	0.000086	0.0100	0.0100	8.80	1.5	8.37	0.52
FR13-181-c2r14	10	-5.8	1154	59.1	202	283000	4600	643000	0.009700	0.001100	0.001393	0.000058	0.0059	0.0058	9.70	1.0	8.98	0.31
FR-14-82																		
FR_14_82_0	65	-17	1048	51.6	191	53200	934	175800	0.023400	0.003900	0.003310	0.000240	0.0615	0.0098	23.7	3.9	21.30	1.5
FR_14_82_1	15	6	509	25.8	122	34700	505	94600	0.022900	0.005200	0.003150	0.000310	0.0860	0.0210	23.2	5.2	20.20	2.0
FR_14_82_2	-32	-25	1559	69.2	424	120700	1469	280300	0.019300	0.002200	0.003240	0.000200	0.0463	0.0047	19.3	2.2	20.89	1.3
FR_14_82_3	-13	-16	1480	72.9	368	112000	1420	259000	0.020700	0.002400	0.003140	0.000200	0.0532	0.0058	20.6	2.4	20.22	1.3
FR_14_82_4	-62	-34	583	22.5	149	43800	532	103200	0.017700	0.003400	0.003260	0.000230	0.0560	0.0120	17.5	3.4	21.00	1.5
FR_14_82_5	28	-21	334	17.6	68	16320	325	60900	0.025900	0.007000	0.003230	0.000350	0.0750	0.0220	25.4	6.8	20.80	2.2
FR_14_82_6	-4	-6	515	24.7	83	27210	466	90000	0.021800	0.004900	0.003340	0.000310	0.0610	0.0160	21.5	4.8	21.50	2.0
FR_14_82_7	29	-34	2580	115	554	163200	2401	466000	0.020300	0.002300	0.003300	0.000210	0.0463	0.0045	20.4	2.3	21.23	1.3
FR_14_82_8	48	-1	589	32	157	40920	574	108300	0.022500	0.004000	0.003220	0.000240	0.0840	0.0210	22.2	3.9	20.70	1.5
FR_14_82_9	-17	-9	412	17.1	83	25030	367	74400	0.020400	0.005300	0.003250	0.000350	0.1030	0.0370	20.1	5.2	20.90	2.3
FR_14_82_10	44	-18	2490	126	913	254000	2250	440000	0.025100	0.003000	0.003420	0.000220	0.0522	0.0055	25.1	3.0	22.03	1.4
FR_14_82_11	29	-5	688	27.3	147	39600	647	129400	0.018800	0.003200	0.003240	0.000250	0.0513	0.0095	18.7	3.2	20.80	1.6
FR_14_82_12	-1	-22	427	17.6	71	24460	407	81600	0.021700	0.004700	0.003300	0.000310	0.0820	0.0260	21.4	4.6	21.20	2.0
FR_14_82_13	3	-21	1117	47.8	303	82200	1044	202500	0.021400	0.002700	0.003420	0.000220	0.0503	0.0059	21.4	2.7	22.02	1.4
FR_14_82_14	2	13	804	30.2	186	55900	733	150700	0.018900	0.003200	0.003290	0.000240	0.0464	0.0085	18.8	3.2	21.10	1.5
FR_14_82_15	17	-29	2210	103	700	209000	2030	391000	0.021800	0.002600	0.003430	0.000220	0.0503	0.0058	21.7	2.6	22.07	1.4
FR_14_82_16	20	9	477	22.1	105	36580	473	92200	0.019700	0.004200	0.003290	0.000260	0.0650	0.0170	19.4	4.1	21.20	1.7
FR 14 82 17[b]	23	-24	483	11.4	137	37100	489	93600	0.012400	0.003900	0.003250	0.000270	0.0540	0.0230	12.3	3.8	20.90	1.7
FR_14_82_18	1	-32	890	41.5	226	64000	836	169000	0.017500	0.003700	0.003150	0.000250	0.0610	0.0180	17.4	3.7	20.30	1.6
FR_14_82_19	56	-15	13170	620	3540	973000	12480	2460000	0.022760	0.001700	0.003443	0.000190	0.0472	0.0017	22.8	1.7	22.15	1.2
FR_14_82_20	-7	-13	910	46.4	217	64100	820	172000	0.023600	0.003400	0.003370	0.000230	0.0561	0.0081	23.5	3.3	21.70	1.5
FR_14_82_21	2	-33	613	23.2	130	40100	579	119600	0.020000	0.004600	0.003260	0.000270	0.0590	0.0160	19.7	4.6	21.00	1.7
FR_14_82_22	38	21	588	25.4	139	44200	580	111200	0.019400	0.003700	0.003320	0.000260	0.0510	0.0110	19.5	3.7	21.40	1.7

Table A.2 (Continued) LA-ICP-MS U-Pb isotopic analyses.

Zircon grain analysis	Ion count rate (cps)								Isotope ratios						Calculated ages (Ma)			
	^{202}Hg	^{204}Pb	^{206}Pb	^{207}Pb	^{208}Pb	^{232}Th	^{235}U	^{238}U	$^{207}Pb/^{235}U$	$\pm 2\sigma$[a]	$^{206}Pb/^{238}U$	$\pm 2\sigma$[a]	$^{207}Pb/^{206}Pb$	$\pm 2\sigma$[a]	$^{207}Pb/^{235}U$	$\pm 2\sigma$[a]	$^{206}Pb/^{238}U$	$\pm 2\sigma$[a]
FR-15-36																		
FR_15_36_0	-12	-25	454	15.9	81	163300	2737	429500	0.003110	0.000920	0.000594	0.000041	0.0470	0.0150	3.14	0.93	3.82	0.27
FR_15_36_1	33	4	397	20.3	82	151900	2504	412600	0.004400	0.001000	0.000582	0.000047	0.1090	0.0320	4.40	1.10	3.75	0.30
FR_15_36_2	36	-7	612	23.8	154	292700	4041	629000	0.003090	0.000800	0.000569	0.000043	0.0540	0.0160	3.12	0.81	3.67	0.27
FR_15_36_3	33	-28	394	20.6	121	174300	2664	422200	0.003850	0.000770	0.000538	0.000037	0.0740	0.0180	3.88	0.78	3.47	0.24
FR_15_36_4	44	10	291	16.1	64	104700	1909	301100	0.004040	0.000990	0.000571	0.000042	0.0880	0.0490	4.10	1.00	3.68	0.27
FR_15_36_5	33	-21	492	22.6	130	206000	3260	523000	0.003130	0.000870	0.000563	0.000036	0.0710	0.0200	3.16	0.88	3.63	0.23
FR_15_36_6	-31	-26	452	18.1	124	206500	2970	472400	0.003360	0.000650	0.000580	0.000035	0.0860	0.0220	3.33	0.65	3.74	0.23
FR_15_36_7	12	-24	489	20.4	144	206100	3046	480000	0.003520	0.000910	0.000603	0.000047	0.0470	0.0150	3.55	0.92	3.89	0.31
FR_15_36_8	-141	-71	345	15.1	77	126000	2049	336000	0.003060	0.000900	0.000579	0.000045	0.1040	0.0310	3.08	0.91	3.73	0.29
FR_15_36_9	-41	-15	356	21.2	120	168600	2578	415000	0.004200	0.001400	0.000532	0.000053	0.1010	0.0400	4.20	1.40	3.43	0.34
FR_15_36_10	-15	-32	307	13	41	102800	2119	335200	0.003100	0.001100	0.000548	0.000053	0.0740	0.0500	3.10	1.10	3.53	0.34
FR_15_36_11	114	-2	251	13.8	67	87600	1789	288000	0.003700	0.001300	0.000543	0.000058	0.0580	0.0780	3.70	1.30	3.50	0.38
FR_15_36_12	132	1	339	19.3	91	119400	2270	356000	0.004200	0.001100	0.000561	0.000049	0.1120	0.0340	4.20	1.10	3.61	0.32
FR_15_36_13	2	-19	438	19.8	97	156100	2896	451600	0.003440	0.000640	0.000568	0.000037	0.0540	0.0330	3.47	0.65	3.66	0.24
FR_15_36_14	8	-31	351	16.8	81	130500	2302	366000	0.004080	0.000980	0.000537	0.000040	0.0740	0.0410	4.10	0.98	3.46	0.26
FR_15_36_15	29	-20	513	24	119	168800	2880	451000	0.004200	0.001100	0.000621	0.000052	0.1030	0.0360	4.20	1.10	4.00	0.34
FR_15_36_16	4	-34	315	16.1	69	115400	2086	338700	0.003560	0.000910	0.000541	0.000039	0.0920	0.0260	3.58	0.91	3.48	0.25
FR_15_36_17	-45	-19	323	14.4	71	123500	2235	346800	0.003120	0.000810	0.000545	0.000039	0.1100	0.0290	3.14	0.82	3.51	0.25
FR_15_36_18	82	-7	340	14.8	133	161500	2337	364000	0.003400	0.001100	0.000542	0.000050	0.0970	0.0470	3.40	1.10	3.49	0.32
FR_15_36_19	-18	-51	373	17.1	76	133900	2591	420000	0.003300	0.001000	0.000529	0.000047	0.0750	0.0310	3.40	1.00	3.41	0.30
FR-15-40																		
FR_15_40_0	46	19	1494	73.9	495	373400	4640	720000	0.008680	0.001000	0.001258	0.000064	0.0517	0.0064	8.8	1.0	8.11	0.4
FR_15_40_1	9	-10	499	24.6	146	98200	1520	241400	0.008400	0.001300	0.001274	0.000079	0.0790	0.0180	8.4	1.3	8.21	0.5
FR_15_40_2	-31	-29	976	50.2	299	232700	3140	498000	0.008700	0.001200	0.001223	0.000067	0.0554	0.0087	8.7	1.2	7.88	0.4
FR_15_40_3	-35	16	505	22.1	125	109100	1718	267100	0.007500	0.001400	0.001133	0.000073	0.0840	0.0190	7.6	1.4	7.30	0.5
FR 15 40 4[b]	10	-9	1001	36.8	250	197100	3076	473000	0.006370	0.000910	0.001263	0.000057	0.0412	0.0062	6.4	0.9	8.14	0.4
FR 15 40 5[c]	63	5	3E+05	43800	27900	59700	2079	316900	11.660000	0.410000	0.473900	0.011000	0.1767	0.0024	2577	33	2502	50
FR 15 40 6[c]	-45	-23	10540	527	1481	99690	3280	505000	0.086600	0.004700	0.012540	0.000350	0.0496	0.0021	84.3	4.3	80.3	2.2
FR 15 40 7[c]	-10	-11	56900	3340	8420	91300	3970	598000	0.469000	0.023000	0.056000	0.002200	0.0593	0.0018	393	15	351	13
FR_15_40_8	19	-2	698	27.8	214	154700	2159	341400	0.006900	0.001200	0.001247	0.000067	0.0451	0.0088	6.9	1.2	8.03	0.4
FR_15_40_9	-16	16	508	21.4	108	75200	1483	234000	0.007600	0.001600	0.001291	0.000097	0.0530	0.0130	7.8	1.7	8.32	0.6
FR 15 40 10[d]	-24	8	940	36.2	138	98600	2679	406000	0.007500	0.001700	0.001370	0.000100	0.0420	0.0100	7.6	1.7	8.82	0.7
FR 15 40 11[b]	-35	-5	431	16.7	96	71600	1423	219900	0.005400	0.001300	0.001173	0.000079	0.0690	0.0210	5.5	1.3	7.56	0.5
FR_15_40_12	-54	-23	1154	51.6	329	277000	3570	561000	0.008000	0.001300	0.001230	0.000082	0.0512	0.0090	8.0	1.3	7.92	0.5
FR_15_40_13	-62	-32	477	22.1	110	86300	1526	242700	0.007700	0.001500	0.001235	0.000089	0.0780	0.0210	7.7	1.5	7.95	0.6
FR_15_40_14	-56	-20	306	18.9	66	57400	1017	161300	0.009600	0.004600	0.001180	0.000170	0.0930	0.0380	9.6	4.6	7.60	1.1
FR_14_40_0	9	-14	334	14.6	113	76400	927	165000	0.008500	0.002100	0.001222	0.000110	0.1230	0.0340	8.5	2.1	7.87	0.7
FR_14_40_1a	-31	-19	201	9.7	47	39600	594	108000	0.006000	0.002000	0.001150	0.000120	0.1890	0.0540	6.0	2.0	7.41	0.8
FR_14_40_2a	18	-24	155	4.1	35.7	30750	434	75700	0.005700	0.002700	0.001260	0.000160	0.3340	0.0880	5.6	2.7	8.12	1.0
FR_14_40_3a	-9	-24	1224	47.9	89	64200	3319	601000	0.007100	0.001400	0.001224	0.000091	0.0435	0.0050	7.2	1.4	7.88	0.6
FR 14 40 4a[d]	-27	-19	299	14.1	87	66800	898	165000	0.007100	0.001800	0.001070	0.000100	0.0500	0.1400	7.1	1.8	6.89	0.7
FR_14_40_5a	1	-12	364	21.9	60	42600	1022	179000	0.010900	0.003700	0.001270	0.000180	0.1550	0.0730	11.4	3.8	8.20	1.1
FR_14_40_6a	-14	-15	265	13	83	60190	764	138600	0.007600	0.002100	0.001211	0.000120	0.1960	0.0570	7.6	2.1	7.80	0.8
FR_14_40_7a	5	-27	310	11.4	87	65020	846	151100	0.006200	0.001800	0.001213	0.000110	0.1070	0.0390	6.2	1.8	7.81	0.7
FR_14_40_8a	-45	-36	413	18.4	85	77200	1116	207600	0.009700	0.002500	0.001250	0.000130	0.1140	0.0450	9.8	2.5	8.07	0.8
FR 14 40 9a[d]	-65	-34	99	3.7	10.6	16580	302	58100	0.005200	0.002700	0.001020	0.000140	0.7900	0.1300	5.1	2.7	6.56	0.9
FR_14_40_10a	-11	-21	162	10.6	32.5	30800	491	88500	0.009000	0.002900	0.001160	0.000130	-0.6900	0.4900	8.8	2.9	7.47	0.9
FR_14_40_11a	45	-8	331	16.3	104	70500	914	159500	0.009000	0.002300	0.001300	0.000130	0.1310	0.0480	9.0	2.3	8.37	0.8
FR 14 40 12a[c]	-13	-19	34460	1586	3690	269700	9700	1687000	0.087800	0.015000	0.012720	0.000870	0.0475	0.0014	85.4	14	81.7	5.6

Table A.2 (Continued) LA-ICP-MS U-Pb isotopic analyses.

Zircon grain analysis	Ion count rate (cps)								Isotope ratios						Calculated ages (Ma)			
	^{202}Hg	^{204}Pb	^{206}Pb	^{207}Pb	^{208}Pb	^{232}Th	^{235}U	^{238}U	$^{207}Pb/^{235}U$	$\pm 2\sigma$[a]	$^{206}Pb/^{238}U$	$\pm 2\sigma$[a]	$^{207}Pb/^{206}Pb$	$\pm 2\sigma$[a]	$^{207}Pb/^{235}U \pm 2\sigma$[a]		$^{206}Pb/^{238}U \pm 2\sigma$[a]	
FR-13-254																		
FR13-254c1r1	35	8.6	152	10.3	40	84500	956	122300	0.007900	0.003500	0.000830	0.000110	0.1240	0.0690	7.9	3.5	5.3	0.7
FR13-254c1r2	30	8	118	1.9	28.9	73600	700	93900	0.001900	0.003100	0.000900	0.000150	0.0440	0.0700	1.9	3.1	5.8	1.0
FR13-254c1r3	37	1.5	140	3.7	18	75300	730	110000	0.004400	0.003700	0.000950	0.000150	0.0580	0.0650	4.3	3.8	6.1	1.0
FR13-254c1r5	27	-1	111	4.7	28	61200	641	86900	0.003600	0.004500	0.000940	0.000180	0.0860	0.0890	3.4	4.5	6.1	1.2
FR13-254c1r7	33	4.4	103	5.6	21	62000	652	87600	0.006300	0.004000	0.000810	0.000160	0.1040	0.0800	6.2	4.0	5.2	1.0
FR13-254c1r10	57	2.6	125	5.3	32	85100	915	125500	0.005100	0.003000	0.000740	0.000140	0.0520	0.0750	5.0	3.0	4.8	0.9
FR13-254c1r13	29	3	125	3.9	30	64900	769	98600	0.004700	0.004100	0.000880	0.000160	0.0100	0.1100	4.6	4.1	5.7	1.0
FR13-254c1r14	50	7	142	6.3	54	108600	880	118000	0.004400	0.002800	0.000830	0.000120	0.0140	0.0570	4.4	2.8	5.3	0.8
FR13-254c1r15	44	12	233	13.6	90	199000	1590	220000	0.006300	0.002200	0.000753	0.000083	0.0620	0.0260	6.3	2.2	4.9	0.5
FR13-254c2r2	32	13.3	194	7.4	48	142000	1240	168000	0.004100	0.002100	0.000807	0.000098	0.0280	0.0240	4.1	2.1	5.2	0.6
FR13-254c2r3	31	15	136	6.6	33	73100	854	119100	0.005500	0.004700	0.000860	0.000200	0.0200	0.0940	5.4	4.7	5.5	1.3
FR13-254c2r5	13	18	113	5.6	29	80600	760	103000	0.005600	0.003600	0.000860	0.000150	0.0730	0.0590	5.5	3.7	5.5	1.0
FR13-254c2r7	56	23.3	171	6.1	47	131000	1088	147000	0.003200	0.002700	0.000850	0.000100	0.0270	0.0300	3.2	2.7	5.5	0.7
FR13-254c2r8	55	19.3	113	4.6	19	78000	761	105500	0.004700	0.003100	0.000800	0.000130	0.0410	0.0650	4.7	3.1	5.2	0.9
FR13-254c2r10	41	7.4	233	6.4	80	176000	1350	183000	0.003700	0.002400	0.000900	0.000110	0.0330	0.0250	3.7	2.4	5.8	0.7
FR13-254c2r6	51	8.5	97	7.4	22	49200	568	79500	0.011100	0.006900	0.000880	0.000230	0.0700	0.1200	11	6.8	5.7	1.5

[a]Propagated error

[b]Discordant grain analysis.

[c]Xenocryst grain.

[d]Outlier analysis.

Appendix B

This section provides more details about the data compilation and geochemical affinity of central and eastern Anatolian igneous complexes (Table B.1), analyzed rock samples (Table B.2), analytical quality control (Figure B.1; Tables B.3 to B.9), and additional geochemical diagrams related to Chapter 3 (Figure B.2 to B.4).

B.1 Geochemical data compilation, sorting and interpretation

The published whole-rock geochemical data from late Cenozoic igneous units in central and eastern Anatolia were compiled and carefully filtered to generate a working database of 2270 analyses (Table B.1).

Table B.1 Late Cenozoic igneous complexes of central and eastern Anatolia.

Igneous Complex	Location	Surface (km^2)[a]	Main lithologies	Minor lithologies	Magmatic affinity[b]	Period	Age (Ma)[c]	References
Central Anatolia								
Develidağ	Develi	277	Andesite, basaltic andesite, basalt	Trachybasalt	MK	Late Miocene	5.36 ± 0.20	1, 3
Erciyes	Kayseri	2,484	Dacite, basaltic andesite, andesite	Basalt, rhyolite, basaltic trachyandesite, trachybasalt	MK	Pliocene to Quaternary	3.57 ± 1.17 - Present	4-14
Hasandağ	Aksaray	1,721	Basalt, andesite, rhyolite, dacite, basaltic andesite	Trachybasalt, basaltic trachyandesite, tephrite, trachyte	M-HK to SHO	Late Miocene to Quaternary	1.5 ± 0.5 - Present	5, 8, 10, 12, 14-23
Incesu-Cappodicia	Nevsehir	3,921	Dacite, trachyte, rhyolite	Andesite, trachyandesite, basaltic andesite	M-HK to SHO	Late Miocene - Pliocene	10.7 ± 0.3 - Present	24-28
Karapınar	Karapınar	420	Basalt, basaltic andesite		MK	Pliocene to Quaternary	5.98 ± 0.25 - Present	8, 12, 14, 26
Karaman	Karaman	115	Andesite		HK	Pliocene to Quaternary	2.19 ± 0.41 - 1.79 ± 0.09	26
Melendiz	Niğde	1,291	Andesite	Trachybasalt, dacite, rhyolite, trachyte	M-HK to SHO	Pliocene	4.9 ± 0.2 - 2.40 ± 0.15	1, 18, 26, 29
Tekkedağ	Yeşihlisar	128	Andesite		M-HK	Late Miocene	7.92 ± 0.14	1, 30
Eastern Anatolia								
Ağrı	Diyadin	170	Monzodiorite, monzonite, granite	Alkalic gabbro, granodiorite	HK to LK to SHO	Early to middle Miocene	21.32 ± 0.29 – 17.38 ± 0.36	1
Ararat	Doğubeyazıt	1,036	Basaltic andesite, andesite	Dacite, trachybasalt, tephrite, rhyolite	MK	Quaternary	1.51 ± 0.38 - Present	12, 32-34
Cevizlidere	Ovacık	3	Diorite	Granodiorite	MK	Oligocene	25.49 ± 0.10 to 25.10 ± 0.14	35
Elazığ	Elazığ	97	Basanite/tephrite, trachybasalt		HK to SHO	Quaternary	1.87 ± 0.07 to 1.47 ± 0.09	2, 81
Erzincan	Erzincan	42	Rhyolite	Dacite, andesite, trachyandesite	HK	Quaternary	1.06 ± 0.18 – Present	45
Erzurum	Erzurum, Hınıs	19,028	Trachybasalt, basaltic trachyandesite, trachyandesite, rhyolite	Basalt, basaltic andesite, andesite, dacite, tephrite	HK	Late Miocene to Quaternary	13.1 ± 0.6 - Present	32, 38-44, 80

Table B.1 (Continued) Late Cenozoic igneous complexes of central and eastern Anatolia.

Igneous Complex	Location	Surface (km^2)[a]	Main lithologies	Minor lithologies	Magmatic affinity[b]	Period	Age (Ma)[c]	References
Eastern Anatolia (continued)								
Etrüsk	Erciş	324	Trachyte, trachyandesite	Basalt	HK to SHO	Pliocene to Quaternary	5.74 ± 0.16 – 3.60 ± 0.15	36-37
Kars	Kars	14,577	Basalt, andesite, rhyolite, dacite, basaltic andesite, basaltic trachyandesite	Trachyandesite, trachyte, trachybasalt	M-HK to SHO	Late Miocene to Quaternary	11.1 ± 1.0 - 1.3 ± 0.6	32, 38, 41, 46-47
Kepez	Malatya	505	Basaltic trachyandesite, andesite, dacite, rhyolite	Trachyte, trachyandesite, trachybasalt, basalt	M-HK to SHO	Middle Miocene	16.19 ± 0.10 – 13.58 ± 0.17	48-50
Nemrut	Tatvan	2,024	Trachyte, rhyolite, basalt, basaltic trachyandesite, trachyandesite	Trachybasalt	HK to SHO	Quaternary	1.18 ± 0.46 - Present	12, 32, 34, 51-54
Sarıçimen	Çaldıran	2	Monzodiorite, monzonite		HK	Middle Miocene	12.6 ± 0.3 – 11.9 ± 0.4	31
Şüphan	Adilcevaz	1,633	Basaltic trachyandesite, trachyandesite, rhyolite	Dacite, trachyte	HK to SHO	Quaternary	5.8 ± 0.3 - Present	12, 32, 34, 51, 55
Tendurek	Doğubeyazıt	720	Trachyandesite, trachyte, phonolite, tephrite, trachybasalt	Basaltic trachyandesite, tephrite, tephriphonolite	HK to SHO	Quaternary	0.71 ± 0.06 – Present	12, 14, 32, 34, 57
Yamadağ	Arapgir	2,524	Basalt, basaltic andesite, andesite, dacite	Trachybasalt, basaltic trachyandesite, trachyandesite, trachyte, tephrite	MK to SHO	Early to late Miocene	21.23 ± 0.33 to 8.90 ± 0.70	1, 26, 58-68
Yıgıtdağ	Van	314	Basalt, basaltic trachyandesite, trachyandesite		HK to SHO	Quaternary	-	69
Other igneous complexes								
Konya	Konya	509	Andesite, dacite	Basalt, lamproite	HK	Late Miocene	10.21 ± 0.13 – 6.49 ± 0.31	1, 70-74
Sivas	Şarkışla	876	Basalt, basanite, picrobasalt	Andesite, basaltic trachyandesite, basaltic andesite	HK	Middle Miocene to Quaternary	15.0 ± 0.5 – 1.3 ± 0.1	26, 75-78
Sulutas	Konya	4	Basalt, dacite		HK	Early to middle Miocene	16.45 ± 0.76 – 11.61 ± 0.04	79

[a]Area calculated from surface polygons of the 1:500,000-scale MTA geological map of Turkey (2002)

[b]Refer to geochemical fields in Peccerillo & Taylor (1976): SHO = shoshonitic; HK = high-K calc-alkaline; MK = medium-K calc-alkaline; LK = low-K calc-alkaline.

[c]Age intervals from Chapter 2 (Table A.2)

References: (1) This Chapter; (2) Kürüm and Tanyıldızı (2017); (3) Kürkçüoğlu (2010); (4) Aydar and Gourgaud (1998); (5) Aydar et al. (1995); (6) Dogan et al. (2011); (7) Dogan et al. (2013); (8) Dogan (2016); (9) Gencalioğlu-Kuşcu (2011); (10) Güçtekin and Köprübaşı (2009); (11) Kürkçüoğlu et al. (1998); (12) Notsu et al. (1995); (13) Şen et al. (2003); (14) Şen et al. (2004); (15) Deniel et al. (1998); (17) Aydar and Gourgaud (2002); (18) Aydin (2008); (19) Aydin et al. (2014); (20) Dogan et al. (2008); (21) Siebel et al. (2011); (22) Ustunisik and Kilinc (2011); (23) Yurtmen and Rowbotham (2002); (24) Koralay et al. (2011); (25) Temel et al. (1998b); (26) Platzman et al. (1998); (27) Aydar et al. (2012); (28) Lepetit et al. (2014); (29) Gencalioğlu-Kuşcu and Geneli (2010); (30) Koralay (2010); (31) Çolakoğlu and Arehart (2010); (32) Pearce et al. (1990); (33) Kheirkhah et al. (2009); (34) Yılmaz et al. (1998); (35) İmer et al. (2014); (36) Oyan et al. (2016); (37) Lebedev et al. (2010); (38) Bigazzi et al. (1997); (39) Demir et al. (2009); (40) Hubert-Ferrari et al. (2009); (41) Innocenti et al. (1982); (42) Buket and Temel (1998); (44) Yılmaz et al. (1987); (45) Karsli et al. (2008); (46) Keskin et al. (1998); (47) Keskin et al. (2006); (48) Yilmaz et al. (2007); (49) Onal et al. (2008); (50) Ekici (2016); (51) Sumita and Schmincke (2013); (52) Çubukçu et al. (2012); (53) Özdemir et al. (2006); (54) Peretyazhko et al. (2015); (55) Innocenti et al. (1980); (56) Özdemir and Güleç (2013); (57) Lebedev et al. (2016); (58) Arger et al. (2000); (59) Leo et al. (1974); (60) Leo et al. (1978); (61) Ekici et al. (2007); (62) Ekici et al. (2009); (64) Kürüm et al. (2008); (65) Alpaslan and Terzioğlu (1996); (66) Alpaslan et al. (2004); (67) Yalçın et al. (1998); (68) Yilmaz et al. (1993); (69) Kheirkhah et al. (2009); (70) Asan and Ertürk (2013); (71) Kurt et al. (2003); (72) Temel et al. (1998a); (73) Keller et al. (1977); (74) Koç et al. (2012); (75) Kürkçüoğlu et al. (2015); (76) Alpaslan et al. (2005); (77) Parlak et al. (2001); (78) Jaffey et al. (2004); (79) Korkmaz et al. (2017); (80) Kaygusuz et al. (2018); (81) Arger et al., 2000.

B.2 Lithogeochemical analysis QA-QC

The 57 lithogeochemical analyses presented in this thesis were part of a larger dataset that included blind reference material (n = 12) and duplicate sample analyses (n = 9) for quality control. The degree of alteration and weathering were assessed petrographically prior to the rock selection (Table B.2) to exclude samples that were affected by iron oxidation and hydrothermal sericite, potassic (biotite, alkali feldspar), chlorite, clay, silica and epidote alteration. The analyzed MDRU reference materials were BAS-1, P-1 and WP-1; the internally-certified analytical values of those reference materials were obtained by median calculation of historical analyses carried out at MDRU (BAS-1 = 50; P-1 = 57; WP-1 = 76; Tables B3 to B5) through various analytical techniques. If the element value was below the detection limit (< DL), the half of the detection limit (DL) was used for calculation. Outlier values for each element were discarded if lower or greater than 2.5*SD (standard deviation). The warning (2*SD) and failure limits (3*SD) are provided for the elements having accepted values only. If the number of valid data is lower than 10, then the reference value is statistically unreliable and thus the data is

Table B.2 Petrographic descriptions of rock samples analyzed for major and trace element and/or Sr-Nd-Pb isotope geochemistry (central and eastern Anatolia)..

Sample	Igneous Complex	Location	Lat (°N)	Long (°E)	Lithology	Texture	Mineralogy[a]	Alteration
Central Anatolia								
FR-13-181	Konya	Inlice	37.7509	32.0754	Biotite andesite	hypocrystalline, porphyritic, felty	pl, bt, opx, feox, qz, hb	
FR-14-59	Konya	Mihaliç tepe	37.3935	33.1380	Biotite andesite	hypocrystalline, porphyritic, felty	pl, bt, hb, feox, cpx	
FR-14-73	Konya	Doğanbey	37.8230	31.9460	Two-pyroxene andesite	hypocrystalline, porphyritic, felty	pl, bt, cpx, bt, opx, hb	
FR-15-40	Tekkedağ	Başdere	38.5481	35.1129	Clinopyroxene andesite	hypocrystalline, porphyritic, felty	pl, cpx, feox, bt, hb	
FR-13-234	Develidağ	Öksüt	38.2836	35.5079	Two-pyroxene andesite?	hypocrystalline, porphyritic, felty	pl, hb/px?, feox, bt	clay-sil (mod)
FR-13-237	Develidağ	Öksüt	38.2836	35.5079	Two-pyroxene andesite	hypocrystalline, porphyritic, felty	pl, cpx, opx, feox	
FR-13-254	Develidağ	Öksüt	38.2891	35.5121	Two-pyroxene andesite	hypocrystalline, porphyritic, trachytic	pl, cpx, feox, opx	
FR-14-75	Melendiz	Çömlekçı	38.0849	34.3484	Clinopyroxene andesite	hypocrystalline, porphyritic, trachytic	pl, cpx, mt, bt, qz	
Eastern Anatolia								
FR-14-82	Yamadağ	Hasançelebi	39.0081	37.8231	Clinopyroxene andesite	hypocrystalline, porphyritic, felty	pl, cpx, feox, bt, hb, qz	
FR-14-110	Erzurum	Hınıs	39.3262	41.6741	Trachyandesite	hypocrystalline, trachytic	pl, cpx, ol, feox	
FR-14-117	Erzurum	İdrisli	39.7019	41.4207	Two-pyroxene andesite	hypocrystalline, porphyritic, felty, amygdaloidal	pl, cpx, opx, feox	
FR-14-125	Ağrı	Diyadin	39.5451	43.4229	Granite	allotriomorphic, seriate	ksp, qz, pl, bt, mt	
FR-14-127	Ağrı	Diyadin	39.4706	43.3682	Trachyandesite	hypocrystalline, porphyritic, felty, subpoikilitic (pl)	pl, feox, opx, cpx	
FR-14-129	Ağrı	Diyadin	39.5990	43.2638	Monzonite	hypidiomorphic, porphyric	pl, ksp, qz, opx, feox	propylitic (strong)[b]
FR-14-132	Ağrı	Diyadin	39.5187	43.1419	Monzodiorite	hypidiomorphic, seriate	pl, qz, ksp, bt, hb, mt, cpx, tour	
FR-14-133	Ağrı	Diyadin	39.4602	43.5840	Trachyte	hypocrystalline, felty, porphiritic	pl, cpx, feox, opx	
FR-14-134	Ağrı	Diyadin	39.4265	43.5079	Monzonite	hypidiomorphic	pl, qz, ksp, feox, ti	chl-ser-cal (mod)
FR-14-140	Ağrı	Taşkapı	39.2764	43.4510	Monzonite	allotriomorphic, equigranular	ksp, qz, pl, feox, bt, ti	chl-ser-FeOH (mod)
FR-14-143	Ağrı	Taşkapı	39.3234	43.4080	Granite	allotriomorphic, seriate	ksp, pl, qz, hb, mt, ti	ser, propylitic (weak)[b]
AM-12-TR-006	Ağrı	Taşlıçay	43.5690	39.3955	Monzodiorite	hypidiomorphic, seriate, strong fabric	pl, qz, hb, bt, ti, mt	
AM-12-TR-009	Kars	Kars	42.2866	39.9536	Dacite	hypocrystalline, porphyritic, felty, amygdaloidal	pl, hb, bt, feox	
AM-12-TR-010	Kars	Kars	42.4633	40.1198	Two-pyroxene andesite	hypocrystalline, porphyritic, felty	pl, feox, cpx, opx	
AM-12-TR-013	Kars	Kars	42.6889	40.1715	Two-pyroxene andesite	hypocrystalline, felty	pl, feox, cpx, opx	

Abbreviations: bt = biotite; cal = calcite; chl = chlorite; cpx = clinopyroxene; feox = Fe-oxide; FeOH = Fe-oxihydroxide; hb = hornblende; ksp = alkali feldspar; mod = moderate; mt = magnetite; ol = olivine; opx = orthopyroxene; qz = quartz; pl = plagioclase; px = pyroxene; ser = sericite; sil = silica; ti = titanite; tour = tourmaline.

[a] mineral order from the most to the least abundant

[b] propylitic alteration assemblage includes hydrothermal epidote, chlorite and calcite

“insufficient”. If less than 50 % of data are valid, the % RSD (median/SD) is > 10 %, or the accepted value is < 10 * DL, the reference “indicative value” is indicated in the comments.

The mean percentile difference (MPD = [original-duplicate]/mean) was calculated to compare original and duplicate samples. The accepted threshold was ± 20 %; the MPD values of all the elements for each pair of samples were < 20 %. In addition, the empirical analysis of geochemical errors was performed using the Error Envelope Program 2.2 made by D.J. Thorkelson (2012). This program allowed to compare the results of analyzed duplicate samples and calculate the precision of each element. Similar data were plotted along the 1:1 regression line; an error envelope surrounded the data. The linear equation of this envelope was: $y = mx + b$ where b was the absolute error (detection limit) and m the relative error, which was manually adjusted to fit the data (Figure B.4; Table B.7).

The tables B.8 and B.9 report the quality control results for Sr-Nd-Pb isotopic analyses including measurement of sample replicates, duplicates and standard materials.

Table B.3 Reference values for BAS-1 standard.

BAS-1											
Element	Unit	DL	Number of data	**Accepted value**	**2SD**	%RSD	+2SD[1]	-2SD[1]	+3SD[2]	-3SD[2]	Comments
SiO_2	%	0.1	49	**52.7**	**0.7**	0.69%	53.4	52.0	53.8	51.6	
Al_2O_3	%	0.01	47	**15.30**	**0.34**	1.12%	15.64	14.96	15.81	14.79	
TiO_2	%	0.01	50	**1.31**	**0.09**	3.34%	1.40	1.22	1.44	1.18	
$Fe_2O_{3\,(t)}$	%	0.01	49	**10.82**	**0.37**	1.71%	11.19	10.45	11.38	10.26	
FeO	%	0.01	13	**8.73**	**0.19**	1%					Indicative value
CaO	%	0.01	50	**8.09**	**0.29**	1.81%	8.38	7.80	8.53	7.65	
MgO	%	0.01	50	**7.20**	**0.29**	2.04%	7.49	6.90	7.63	6.76	
Na_2O	%	0.01	50	**3.23**	**0.26**	3.96%	3.49	2.97	3.61	2.85	
K_2O	%	0.01	47	**0.53**	**0.05**	4.68%	0.58	0.48	0.60	0.46	
Cr_2O_3	%	0.001	30	**0.030**	**0.002**	3.07%	0.032	0.028	0.033	0.027	
MnO	%	0.01	49	**0.14**	**0.01**	4.08%	0.15	0.13	0.16	0.12	
P_2O_5	%	0.01	49	**0.22**	**0.03**	6.86%	0.25	0.19	0.27	0.17	
V_2O_5	%	0.002	8	**0.028**	**0.002**	4%					Insufficient data
SO_3	%	0.002	12	**0.006**	**0.063**	523%					Insufficient data
BaO	%	0.01	21	**0.02**	**0.00**	0.00%					Indicative value
LOI	%	0.01	45	**-0.02**	**0.28**	-694%					Indicative value
Ag	ppm	0.1	33								<DL
As	ppm	0.5	14	**3.2**	**6.3**	100%					Indicative value
Au	ppb	0.5	12	**10.5**	**29.1**	139%					Indicative value
Ba	ppm	1	49	**177**	**21**	6%	197	156	207	146	
Bi	ppm	0.1	15								<DL
Cd	ppm	0.1	14								<DL
Ce	ppm	0.1	49	**20.0**	**2.1**	5%	22.1	17.9	23.2	16.8	
Cl	ppm	1	4	**246**	**8**	2%					Insufficient data
Co	ppm	0.2	50	**45.0**	**5.8**	6%	50.8	39.2	53.8	36.2	
Cr	ppm	0.1	33	**220.0**	**23.3**	5%	243.3	196.7	254.9	185.1	
Cs	ppm	0.1	46	**0.1**	**0.1**	74%					Indicative value
Cu	ppm	0.1	47	**59.0**	**10.2**	9%	69.2	48.8	74.3	43.7	
Dy	ppm	0.05	50	**2.96**	**0.38**	6%	3.33	2.58	3.52	2.39	
Er	ppm	0.03	49	**1.50**	**0.19**	6%	1.69	1.31	1.78	1.22	
Eu	ppm	0.02	50	**1.20**	**0.18**	7%	1.37	1.02	1.46	0.93	
Ga	ppm	0.5	48	**18.7**	**2.4**	6%	21.1	16.3	22.3	15.1	
Gd	ppm	0.05	49	**3.33**	**0.42**	6%	3.75	2.91	3.97	2.69	
Hf	ppm	0.1	48	**2.2**	**0.5**	10%					Indicative value
Hg	ppm	0.01	13	**0.07**	**0.02**	15%					Indicative value
Ho	ppm	0.02	48	**0.60**	**0.07**	6%	0.67	0.52	0.70	0.49	
La	ppm	0.1	49	**8.9**	**1.2**	7%	10.1	7.7	10.8	7.0	
Lu	ppm	0.01	44	**0.20**	**0.02**	5%	0.22	0.18	0.23	0.17	
Mo	ppm	0.1	27	**2.0**	**1.9**	47%					Indicative value
Nb	ppm	0.1	49	**7.0**	**1.4**	10%					Indicative value
Nd	ppm	0.3	49	**12.5**	**1.4**	5%	13.9	11.1	14.5	10.5	
Ni	ppm	0.1	50	**170.0**	**26.1**	8%	196.1	143.9	209.2	130.8	
Pb	ppm	0.1	42	**2.5**	**7.5**	150%					Indicative value
Pr	ppm	0.02	49	**2.72**	**0.40**	7%	3.12	2.32	3.31	2.13	
Rb	ppm	0.1	49	**6.3**	**1.1**	9%	7.4	5.2	8.0	4.6	
S	ppm	1	4	**422**	**59**	7%					Insufficient data
Sb	ppm	0.1	14	**0.1**	**0.3**	133%					Insufficient data
Sc	ppm	0.1	10	**9.8**	**15.4**	79%					Indicative value
Se	ppm	0.5	12	**0.3**	**1.0**	194%					Insufficient data
Sm	ppm	0.05	49	**3.20**	**0.59**	9%	3.79	2.61	4.08	2.32	
Sn	ppm	1	38								<DL
Sr	ppm	0.5	50	**459.0**	**54.2**	6%	513.2	404.8	540.3	377.7	
Ta	ppm	0.1	49	**0.4**	**0.2**	24%					Indicative value
Tb	ppm	0.01	50	**0.52**	**0.07**	7%	0.59	0.45	0.63	0.41	
Te	ppm	1	11								<DL
Th	ppm	0.2	49	**0.8**	**0.5**	31%					Indicative value
Tm	ppm	0.01	17	**0.21**	**0.03**	6%					Indicative value
U	ppm	0.1	47	**0.3**	**0.1**	19%					Indicative value
V	ppm	8	49	**157**	**28**	9%	185	129	199	115	
W	ppm	0.5	46	**1.0**	**1.8**	90%					Indicative value
Y	ppm	0.1	48	**15.1**	**1.9**	6%	16.9	13.2	17.9	12.2	
Yb	ppm	0.05	50	**1.30**	**0.16**	6%	1.46	1.14	1.54	1.06	
Zn	ppm	1	49	**100**	**37**	19%					Indicative value
Zr	ppm	0.1	47	**83.3**	**9.0**	5%	92.3	74.3	96.8	69.8	

[1] Warning limits; 2 failure limits; < DL = lower than detection limit

Methods: Fusion XRF whole-rock + ICP-MS trace elements; Lithium borate fusion ICP-MS whole-rock; Aqua regia Base metals

Table B.4 Reference values for P-1 standard.

P-1											
Element	Unit	DL	Number of data	**Accepted value**	**2SD**	%RSD	+2SD[1]	-2SD[1]	+3SD[2]	-3SD[2]	Comments
SiO_2	%	0.1	57	**70.3**	**1.0**	0.71%	71.3	69.3	71.8	68.8	
Al_2O_3	%	0.01	57	**14.34**	**0.46**	1.60%	14.80	13.88	15.03	13.65	
TiO_2	%	0.01	55	**0.38**	**0.04**	5.35%	0.42	0.34	0.44	0.32	
$Fe_2O_{3(t)}$	%	0.01	57	**3.78**	**0.14**	1.87%	3.92	3.64	3.99	3.57	
FeO	%	0.01	21	**2.21**	**0.36**	8%					Indicative value
CaO	%	0.01	56	**3.40**	**0.11**	1.57%	3.51	3.29	3.56	3.24	
MgO	%	0.01	55	**1.04**	**0.09**	4.22%	1.13	0.95	1.17	0.91	
Na_2O	%	0.01	52	**3.81**	**0.24**	3.11%	4.04	3.57	4.16	3.45	
K_2O	%	0.01	57	**2.09**	**0.12**	2.82%	2.21	1.97	2.27	1.91	
Cr_2O_3	%	0.001	36	**0.020**	**0.008**	20.58%					Indicative value
MnO	%	0.01	57	**0.08**	**0.02**	10.73%					Indicative value
P_2O_5	%	0.01	56	**0.08**	**0.02**	9.51%					Indicative value
V2O5	%	0.002	14	**0.011**	**0.003**	12%					Indicative value
SO3	%	0.002	16	**0.001**	**0.009**	454%					Insufficient data
BaO	%	0.01	13	**0.09**	**0.01**	5.79%					Indicative value
LOI	%	0.01	53	**0.44**	**0.11**	12.46%					Indicative value
Ag	ppm	0.1	28								<DL
As	ppm	0.5	16	**0.3**	**0.3**	66%					Insufficient data
Au	ppb	0.5	16	**0.4**	**4.3**	503%					Insufficient data
Ba	ppm	1	47	**781**	**91**	6%					
Bi	ppm	0.1	15								<DL
Cd	ppm	0.1	15								<DL
Ce	ppm	0.1	44	**25.5**	**4.0**	8%	29.5	21.5	31.5	19.5	
Cl	ppm	1	3	**9**	**1**	5%					Insufficient data
Co	ppm	0.2	49	**7.0**	**1.5**	11%					Indicative value
Cr	ppm	0.1	17	**150.0**	**20.0**	7%					Indicative value
Cs	ppm	0.1	43	**1.1**	**0.2**	10%					Indicative value
Cu	ppm	0.1	47	**9.0**	**9.8**	54%					Indicative value
Dy	ppm	0.05	43	**3.00**	**0.52**	9%	3.52	2.48	3.78	2.22	
Er	ppm	0.03	42	**2.02**	**0.28**	7%	2.30	1.74	2.43	1.61	
Eu	ppm	0.02	41	**0.72**	**0.14**	9%	0.86	0.58	0.92	0.52	
Ga	ppm	0.5	48	**14.0**	**2.4**	9%	16.4	11.6	17.7	10.3	
Gd	ppm	0.05	42	**2.80**	**0.42**	7%	3.22	2.38	3.43	2.17	
Hf	ppm	0.1	43	**3.9**	**1.0**	13%					Indicative value
Hg	ppm	0.01	15								<DL
Ho	ppm	0.02	42	**0.67**	**0.14**	11%					Indicative value
La	ppm	0.1	43	**13.0**	**2.4**	9%	15.4	10.6	16.6	9.4	
Lu	ppm	0.01	42	**0.38**	**0.07**	9%	0.45	0.31	0.48	0.28	
Mo	ppm	0.1	24	**0.5**	**0.9**	96%					Indicative value
Nb	ppm	0.1	50	**3.0**	**1.4**	24%					Indicative value
Nd	ppm	0.3	44	**12.0**	**1.8**	8%	13.8	10.2	14.7	9.3	
Ni	ppm	0.1	47	**3.4**	**3.6**	53%					Indicative value
Pb	ppm	0.1	47	**6.7**	**8.0**	59%					Indicative value
Pr	ppm	0.02	44	**2.99**	**0.48**	8%	3.46	2.51	3.70	2.27	
Rb	ppm	0.1	52	**46.1**	**6.4**	7%	52.5	39.7	55.7	36.5	
Sb	ppm	0.1	17								<DL
Sc	ppm	0.1	13	**2.7**	**0.7**	13%					Indicative value
Se	ppm	0.5	0								<DL
Sm	ppm	0.05	44	**2.59**	**0.70**	13%					Indicative value
Sn	ppm	1	24	**2**	**1**	29%					Indicative value
Sr	ppm	0.5	52	**224.4**	**29.9**	7%	254.3	194.5	269.2	179.6	
Ta	ppm	0.1	39	**0.3**	**0.1**	23%					Indicative value
Tb	ppm	0.01	44	**0.50**	**0.09**	9%	0.59	0.41	0.64	0.36	
Te	ppm	1	9	**0.1**	**0**	166%					Insufficient data
Th	ppm	0.2	39	**4.0**	**1.6**	20%					Indicative value
Tm	ppm	0.01	43	**0.31**	**0.08**	13%					Indicative value
U	ppm	0.1	44	**1.4**	**0.4**	16%					Indicative value
V	ppm	8	48	**62**	**15**	13%					Indicative value
W	ppm	0.5	41	**1.0**	**3.7**	184%					Indicative value
Y	ppm	0.1	52	**19.1**	**2.9**	8%	22.0	16.2	23.4	14.8	
Yb	ppm	0.05	43	**2.22**	**0.35**	8%	2.57	1.87	2.75	1.69	
Zn	ppm	1	47	**40**	**16**	20%					Indicative value
Zr	ppm	0.1	50	**127.1**	**16.0**	6%	143.0	111.1	151.0	103.1	

[1] Warning limits; 2 Failure limits; < DL = lower than detection limit

Methods: Fusion XRF whole-rock + ICP-MS trace elements; Aqua regia base metals

Table B.5 Reference values for WP-1 standard.

WP-1											
Element	Unit	DL	Number of data	**Accepted value**	**2SD**	%RSD	+2SD[1]	-2SD[1]	+3SD[2]	-3SD[2]	Comments
SiO_2	%	0.1	76	**64.5**	**0.8**	0.59%	65.3	63.7	65.6	63.4	
Al_2O_3	%	0.01	75	**16.61**	**0.18**	0.55%	16.79	16.43	16.88	16.34	
TiO_2	%	0.01	77	**0.50**	**0.02**	1.96%	0.52	0.48	0.53	0.47	
$Fe_2O_{3\,(t)}$	%	0.01	76	**4.37**	**0.11**	1.31%	4.48	4.26	4.54	4.20	
FeO	%	0.01	6	**2.21**	**0.26**	6%					Insufficient data
CaO	%	0.01	78	**4.96**	**0.11**	1.12%	5.07	4.85	5.13	4.79	
MgO	%	0.01	76	**2.65**	**0.06**	1.14%	2.71	2.59	2.74	2.56	
Na_2O	%	0.01	77	**4.33**	**0.18**	2.05%	4.51	4.15	4.60	4.06	
K_2O	%	0.01	77	**1.62**	**0.03**	0.88%	1.65	1.59	1.66	1.58	
Cr_2O_3	%	0.001	71	**0.010**	**0.003**	16.16%					Indicative value
MnO	%	0.01	71	**0.08**	**0.00**	0.00%					Indicative value
P_2O_5	%	0.01	76	**0.17**	**0.01**	3.60%	0.18	0.16	0.19	0.15	
V2O5	%	0.002	33	**0.016**	**0.002**	7%					Indicative value
SO3	%	0.002									<DL
BaO	%	0.01	6	**0.07**	**0.01**	9.89%					Insufficient data
LOI	%	0.01	53	**0.14**	**0.19**	67.85%					Indicative value
Ag	ppm	0.1									<DL
As	ppm	0.5									<DL
Au	ppb	0.5									<DL
Ba	ppm	1	78	**616**	**61**	5%	676	555	707	524	
Bi	ppm	0.1									<DL
Cd	ppm	0.1									<DL
Ce	ppm	0.1	71	**27.6**	**2.6**	5%	30.2	25.0	31.6	23.6	
Cl	ppm	1	0								<DL
Co	ppm	0.2	75	**11.6**	**7.9**	34%					Indicative value
Cr	ppm	0.1	27	**19.6**	**44.3**	113%					Indicative value
Cs	ppm	0.1	70	**0.4**	**0.1**	16%					Indicative value
Cu	ppm	0.1	71	**11.9**	**4.1**	17%					Indicative value
Dy	ppm	0.05	70	**2.26**	**0.22**	5%	2.48	2.04	2.59	1.93	
Er	ppm	0.03	70	**1.28**	**0.12**	5%	1.40	1.16	1.46	1.10	
Eu	ppm	0.02	70	**0.83**	**0.09**	5%	0.92	0.74	0.96	0.70	
Ga	ppm	0.5	72	**17.4**	**1.9**	5%	19.3	15.5	20.2	14.6	
Gd	ppm	0.05	71	**2.66**	**0.26**	5%	2.92	2.40	3.05	2.27	
Hf	ppm	0.1	69	**3.2**	**0.3**	4%	3.5	2.9	3.6	2.8	
Hg	ppm	0.01									<DL
Ho	ppm	0.02	72	**0.44**	**0.06**	7%	0.50	0.38	0.53	0.35	
La	ppm	0.1	70	**13.3**	**1.2**	4%	14.5	12.1	15.0	11.6	
Lu	ppm	0.01	70	**0.20**	**0.03**	7%	0.23	0.17	0.24	0.16	
Mn	ppm	1	21	**129**	**17**	7%					Indicative value
Mo	ppm	0.1	69	**0.52**	**0.2**	20%					Indicative value
Nb	ppm	0.1	76	**3.3**	**1.0**	15%					Indicative value
Nd	ppm	0.3	70	**14.3**	**1.3**	5%	15.6	12.9	16.3	12.2	
Ni	ppm	0.1	63	**8.0**	**1.1**	7%	9.1	6.9	9.6	6.4	
Pb	ppm	0.1	67	**2.9**	**0.9**	15%					Indicative value
Pd	ppb	1									<DL
Pr	ppm	0.02	71	**3.49**	**0.26**	4%	3.75	3.23	3.87	3.11	
Rb	ppm	0.1	75	**21.5**	**2.2**	5%	23.7	19.3	24.7	18.3	
Sb	ppm	0.1									<DL
Sc	ppm	0.1	53	**9.0**	**8.2**	45%					Indicative value
Se	ppm	0.5									<DL
Sm	ppm	0.05	70	**2.85**	**0.32**	6%	3.17	2.53	3.34	2.36	
Sn	ppm	1									<DL
Sr	ppm	0.5	77	**737.0**	**77.6**	5%	814.6	659.4	853.4	620.6	
Ta	ppm	0.1	71	**0.2**	**0.1**	21%					Indicative value
Tb	ppm	0.01	70	**0.40**	**0.04**	5%	0.44	0.36	0.46	0.34	
Te	ppm	1									<DL
Th	ppm	0.2	70	**2.0**	**0.3**	7%	2.3	1.7	2.4	1.6	
Tm	ppm	0.01	72	**0.19**	**0.03**	7%	0.22	0.16	0.23	0.15	
U	ppm	0.1	71	**0.8**	**0.1**	9%					Indicative value
V	ppm	8	73	**86**	**13**	8%	99	73	106	66	
W	ppm	0.5									<DL
Y	ppm	0.1	77	**12.5**	**1.7**	7%	14.2	10.8	15.0	10.0	
Yb	ppm	0.05	72	**1.28**	**0.19**	8%	1.47	1.09	1.57	0.99	
Zn	ppm	1	66	**24**	**8**	16%					Indicative value
Zr	ppm	0.1	76	**121.0**	**11.7**	5%	132.6	109.3	138.4	103.5	

[1] Warning limits; [2] failure limits; < DL = lower than detection limit

Methods: Fusion XRF whole-rock +ICP-MS trace elements; Fusion ICP-MS whole-rock + Aqua Regia ICP-MS Ultratrace

Table B.6 Summary of analyzed reference material and comparison with reference values.

			BAS-1									
Sample #	Unit	DL	FR-14-75b	FR-14-122b	FR-13-181s	Accepted value	2SD	%RSD	+2SD	-2SD	+3SD	-3SD
SiO_2	%	*0.1*	52.7	52.7	53.1	**52.7**	**0.7**	0.7%	53.4	52.0	53.8	51.6
Al_2O_3	%	*0.01*	15.35	15.41	15.38	**15.30**	**0.34**	1.12%	15.64	14.96	15.81	14.79
TiO_2	%	*0.01*	1.30	1.30	1.30	**1.31**	**0.09**	3.34%	1.40	1.22	1.44	1.18
$Fe_2O_{3\,(t)}$	%	*0.01*	10.90	10.85	10.92	**10.82**	**0.37**	1.71%	11.19	10.45	11.38	10.26
CaO	%	*0.01*	8.07	8.05	8.09	**8.09**	**0.29**	1.81%	8.38	7.80	8.53	7.65
MgO	%	*0.01*	7.35	7.33	7.30	**7.20**	**0.29**	2.04%	7.49	6.90	7.63	6.76
Na_2O	%	*0.01*	3.27	3.31	3.32	**3.23**	**0.26**	3.96%	3.49	2.97	3.61	2.85
K_2O	%	*0.01*	0.52	0.53	0.53	**0.53**	**0.05**	4.68%	0.58	0.48	0.60	0.46
Cr_2O_3	%	*0.001*	0.028	0.031	0.031	**0.030**	**0.002**	3.07%	0.032	0.028	0.033	0.027
MnO	%	*0.01*	0.14	0.14	0.14	**0.14**	**0.01**	4.08%	0.15	0.13	0.16	0.12
P_2O_5	%	*0.01*	0.21	0.22	0.22	**0.22**	**0.03**	6.86%	0.25	0.19	0.27	0.17
V2O5	%	*0.002*	0.030	0.028	0.027	**0.028**	**0.002**	3.571%				
SO3	%	*0.002*	0.001	0.001	0.011	**0.006**	**0.063**	523%				
LOI	%	*-5.11*	-0.02	-0.02	-0.02	**-0.02**	**0.28**	-694%				
Total	%	*0.01*	100.01	100.02	100.49							
Ag	ppm	*0.1*	0.05	0.1	0.05							
As	ppm	*0.5*	3.2	3.7	2.5	**3.2**	**6.3**	100%				
Au	ppb	*0.5*	10.5	10.1	9.7	**10.5**	**29.1**	139%				
Ba	ppm	*1*	175	176	193	**177**	**21**	6%	197	156	207	146
Be	ppm	*1*	0.5	0.5	0.5							
Bi	ppm	*0.1*	0.05	0.05	0.05							
Cd	ppm	*0.1*	0.05	0.05	0.05							
Ce	ppm	*0.1*	18.6	17.4	20.4	**20.0**	**2.1**	5.3%	22.1	17.9	23.2	16.8
Co	ppm	*0.2*	43.0	44.2	43.9	**45.0**	**5.8**	6.5%	50.8	39.2	53.8	36.2
Cs	ppm	*0.1*	0.1	0.1	0.05	**0.1**	**0.1**	74%				
Cu	ppm	*0.1*	60.0	60.7	53.1	**59.0**	**10.2**	8.65%	69.2	48.8	74.3	43.7
Dy	ppm	*0.05*	2.71	2.62	2.96	**2.96**	**0.38**	6.37%	3.33	2.58	3.52	2.39
Er	ppm	*0.03*	1.41	1.44	1.49	**1.50**	**0.19**	6.25%	1.69	1.31	1.78	1.22
Eu	ppm	*0.02*	1.20	1.16	1.15	**1.20**	**0.18**	7.43%	1.37	1.02	1.46	0.93
Ga	ppm	*0.5*	14.3	17.1	15.0	**18.7**	**2.4**	6.4%	21.1	16.3	22.3	15.1
Gd	ppm	*0.05*	2.99	3.36	3.50	**3.33**	**0.42**	6.37%	3.75	2.91	3.97	2.69
Hf	ppm	*0.1*	2.2	2.3	2.0	**2.2**	**0.5**	10%				
Hg	ppm	*0.01*	0.07	0.09	0.06	**0.07**	**0.02**	15.2%				
Ho	ppm	*0.02*	0.53	0.53	0.54	**0.60**	**0.07**	6.01%	0.67	0.52	0.70	0.49
La	ppm	*0.1*	8.7	7.8	9.6	**8.9**	**1.2**	7.0%	10.1	7.7	10.8	7.0
Lu	ppm	*0.01*	0.19	0.18	0.19	**0.20**	**0.02**	4.69%	0.22	0.18	0.23	0.17
Mo	ppm	*0.1*	1.7	1.6	1.7	**2.0**	**1.9**	47%				
Nb	ppm	*0.1*	6.2	6.2	5.9	**7.0**	**1.4**	10%				
Nd	ppm	*0.3*	11.3	11.8	12.3	**12.5**	**1.4**	5.4%	13.9	11.1	14.5	10.5
Ni	ppm	*0.1*	168.8	168.5	151.9	**170.0**	**26.1**	7.69%	196.1	143.9	209.2	130.8
Pb	ppm	*0.1*	1.3	1.3	0.8	**2.5**	**7.5**	150%				
Pr	ppm	*0.02*	2.47	2.53	2.62	**2.72**	**0.40**	7.29%	3.12	2.32	3.31	2.13
Rb	ppm	*0.1*	6.0	5.8	5.5	**6.3**	**1.1**	9%	7.4	5.2	8.0	4.6
Sb	ppm	*0.1*	0.1	0.1	0.05	**0.1**	**0.3**	133%				
Sc	ppm	*0.1*	2.5	2.2	2.0	**9.8**	**15.4**	79%				
Se	ppm	*0.5*	0.25	0	0.250	**0.3**	**1.0**	194%				
Sm	ppm	*0.05*	2.61	3.07	3.08	**3.20**	**0.59**	9%	3.79	2.61	4.08	2.32
Sn	ppm	*1*	1.0	0.5	0.5							
Sr	ppm	*0.5*	497.8	450.8	503.9	**459.0**	**54.2**	6%	513.2	404.8	540.3	377.7
Ta	ppm	*0.1*	0.5	0.5	0.3	**0.4**	**0.2**	24%				
Tb	ppm	*0.01*	0.50	0.47	0.55	**0.52**	**0.07**	7%	0.59	0.45	0.63	0.41
Te	ppm	*1*	0.1	0.1	0.5							
Th	ppm	*0.2*	0.6	0.5	0.9	**0.8**	**0.5**	31%				
Tm	ppm	*0.01*	0.20	0.19	0.20	**0.21**	**0.03**	6.28%				
U	ppm	*0.1*	0.1	0.2	0.2	**0.3**	**0.1**	19%				
V	ppm	*8*	153	159	136	**157**	**28**	8.9%	185	129	199	115
W	ppm	*0.5*	0.3	0.3	0.3	**1.0**	**1.8**	90%				
Y	ppm	*0.1*	13.7	13.7	14.1	**15.1**	**1.9**	6%	16.9	13.2	17.9	12.2
Yb	ppm	*0.05*	1.20	1.23	1.29	**1.30**	**0.16**	6.22%	1.46	1.14	1.54	1.06
Zn	ppm	*1*	70	72	58	**100**	**37**	19%				
Zr	ppm	*0.1*	81.2	81.8	80.5	**83.3**	**9.0**	5.4%	92.3	74.3	96.8	69.8

Orange = within the warning zone; Red = within the failure zone

Table B.6 (Continued) Summary of analyzed reference material and comparison with reference values.

			P-1										
Sample #	Unit	DL	FR-13-118s	FR-14-108b	FR-14-132b	FR-13-329s	Accepted value	2SD	%RSD	+2SD	-2SD	+3SD	-3SD
SiO_2	%	0.1	71.2	70.4	70.2	71.0	**70.3**	**1.0**	0.7%	71.3	69.3	71.8	68.8
Al_2O_3	%	0.01	14.52	14.30	14.30	14.42	**14.34**	**0.46**	1.6%	14.80	13.88	15.03	13.65
TiO_2	%	0.01	0.39	0.39	0.39	0.36	**0.38**	**0.04**	5.4%	0.42	0.34	0.44	0.32
Fe_2O_3 (t)	%	0.01	3.75	3.72	3.75	3.78	**3.78**	**0.14**	1.9%	3.92	3.64	3.99	3.57
CaO	%	0.01	3.40	3.37	3.38	3.40	**3.40**	**0.11**	1.6%	3.51	3.29	3.56	3.24
MgO	%	0.01	1.03	1.05	1.05	1.04	**1.04**	**0.09**	4.2%	1.13	0.95	1.17	0.91
Na_2O	%	0.01	3.91	3.89	3.86	3.90	**3.81**	**0.24**	3.1%	4.04	3.57	4.16	3.45
K_2O	%	0.01	2.15	2.07	2.09	2.12	**2.09**	**0.12**	2.8%	2.21	1.97	2.27	1.91
Cr_2O_3	%	0.001	0.019	0.020	0.020	0.020	**0.020**	**0.008**	20.6%				
MnO	%	0.01	0.08	0.08	0.08	0.08	**0.08**	**0.02**	10.7%				
P_2O_5	%	0.01	0.07	0.07	0.07	0.07	**0.08**	**0.02**	9.5%				
V2O5	%	0.002	0.010	0.011	0.010	0.011	**0.011**	**0.003**	12%				
SO3	%	0.002	0.001	0.001	0.001	0.001	**0.001**	**0.009**	454%				
LOI	%	-5.11	0.46	0.45	0.45	0.44	**0.44**	**0.11**	12.5%				
Total	%	0.01	101.14	99.98	99.76	100.77							
Ag	ppm	0.1	0.05	0.05	0.05	0.05							
As	ppm	0.5	0.3	0.6	0.3	0.3	**0.3**	**0.3**	66%				
Au	ppb	0.5	1.0	0.3	1.0	0.3	**0.4**	**4.3**	503%				
Ba	ppm	1	807	749	744	790	**781**	**91**	6%	872	690	917	645
Be	ppm	1	0.5	0.5	2.0	0.5							
Bi	ppm	0.1	0.05	0.05	0.05	0.05							
Cd	ppm	0.1	0.1	0.05	0.05	0.05							
Ce	ppm	0.1	25.0	22.6	21.0	26.0	**25.5**	**4.0**	8%	29.5	21.5	31.5	19.5
Co	ppm	0.2	6.5	7.4	6.0	6.9	**7.0**	**1.5**	11%				
Cs	ppm	0.1	1.2	1.0	1.0	1.1	**1.1**	**0.2**	10%				
Cu	ppm	0.1	7.50	11.2	9.4	9.2	**9.0**	**9.8**	54%				
Dy	ppm	0.05	2.83	2.70	2.74	2.86	**3.00**	**0.52**	9%	3.52	2.48	3.78	2.22
Er	ppm	0.03	2.01	1.87	1.91	1.88	**2.02**	**0.28**	7%	2.30	1.74	2.43	1.61
Eu	ppm	0.02	0.72	0.72	0.63	0.73	**0.72**	**0.14**	9%	0.86	0.58	0.92	0.52
Ga	ppm	0.5	11.6	12.4	11.6	12.6	**14.0**	**2.4**	9%	16.4	11.6	17.7	10.3
Gd	ppm	0.05	2.82	2.52	2.48	2.84	**2.80**	**0.42**	7%	3.22	2.38	3.43	2.17
Hf	ppm	0.1	3.6	3.2	3.3	3.6	**3.9**	**1.0**	13%				
Hg	ppm	0.01	0.010	0.005	0.005	0.005							
Ho	ppm	0.02	0.71	0.61	0.64	0.64	**0.67**	**0.14**	11%				
La	ppm	0.1	12.5	12.1	10.6	13.9	**13.0**	**2.4**	9%	15.4	10.6	16.6	9.4
Lu	ppm	0.01	0.36	0.34	0.32	0.35	**0.38**	**0.07**	9%	0.45	0.31	0.48	0.28
Mo	ppm	0.1	0.7	0.6	0.4	0.4	**0.5**	**0.9**	96%				
Nb	ppm	0.1	2.6	2.6	2.6	2.7	**3.0**	**1.4**	24%				
Nd	ppm	0.3	11.3	11.1	9.8	11.7	**12.0**	**1.8**	8%	13.8	10.2	14.7	9.3
Ni	ppm	0.1	3.3	4.3	3.6	3.4	**3.4**	**3.6**	53%				
Pb	ppm	0.1	2.2	2.8	3.6	2.4	**6.7**	**8.0**	59%				
Pr	ppm	0.02	2.70	2.73	2.66	2.96	**2.99**	**0.48**	8%	3.46	2.51	3.70	2.27
Rb	ppm	0.1	43.1	44.3	44.0	45.9	**46.1**	**6.4**	7%	52.5	39.7	55.7	36.5
Sb	ppm	0.1	0.10	0.10	0.10	0.05							
Sc	ppm	0.1	2.7	3.1	3.4	2.7	**2.7**	**0.7**	13%				
Se	ppm	0.5	0.25	0.25	0.25	0.25							
Sm	ppm	0.05	2.52	2.52	2.34	2.51	**2.59**	**0.70**	13%				
Sn	ppm	1	1	2	2	2	**2**	**1**	29%				
Sr	ppm	0.5	247.2	240.2	207.7	244.7	**224.4**	**29.9**	7%	254.3	194.5	269.2	179.6
Ta	ppm	0.1	0.3	0.3	0.2	0.2	**0.3**	**0.1**	23%				
Tb	ppm	0.01	0.46	0.45	0.43	0.45	**0.50**	**0.09**	9%	0.59	0.41	0.64	0.36
Te	ppm	1	0.5	0.1	0.1	0.5	**0.1**	**0.3**	166%				
Th	ppm	0.2	4.0	3.6	3.7	4.6	**4.0**	**1.6**	20%				
Tm	ppm	0.01	0.33	0.30	0.31	0.32	**0.31**	**0.08**	13%				
U	ppm	0.1	1.4	1.2	1.3	1.4	**1.4**	**0.4**	16%				
V	ppm	8	34	60	54	56	**62**	**15**	13%				
W	ppm	0.5	1.2	0.3	0.5	0.3	**1.0**	**3.7**	184%				
Y	ppm	0.1	18.9	17.5	16.7	18.6	**19.1**	**2.9**	8%	22.0	16.2	23.4	14.8
Yb	ppm	0.05	2.24	2.08	2.06	2.18	**2.22**	**0.35**	8%	2.57	1.87	2.75	1.69
Zn	ppm	1	35	36	40	36	**40**	**16**	20%				
Zr	ppm	0.1	123.7	128.6	127.1	134.3	**127.1**	**16.0**	6%	143.0	111.1	151.0	103.1

Orange = within the warning zone; Red = within the failure zone

Table B.6 (Continued) Summary of analyzed reference material and comparison with reference values.

			WP-1											
Sample #	Unit	DL	FR-14-42b	FR-14-148b	FR-13-29s	FR-13-313s	FR-13-133b	Accepted value	2SD	%RSD	+2SD	-2SD	+3SD	-3SD
SiO_2	%	*0.1*	65.1	65.1	65.3	65.0	64.4	**64.5**	**0.8**	0.6%	65.3	63.7	65.6	63.4
Al_2O_3	%	*0.01*	16.69	16.71	16.77	16.69	16.46	**16.61**	**0.18**	0.5%	16.79	16.43	16.88	16.34
TiO_2	%	*0.01*	0.50	0.51	0.50	0.51	0.48	**0.50**	**0.02**	2.0%	0.52	0.48	0.53	0.47
Fe_2O_3 (t)	%	*0.01*	4.41	4.41	4.38	4.33	4.38	**4.37**	**0.11**	1.3%	4.48	4.26	4.54	4.20
CaO	%	*0.01*	4.96	4.94	4.92	4.92	4.89	**4.96**	**0.11**	1.1%	5.07	4.85	5.13	4.79
MgO	%	*0.01*	2.68	2.68	2.61	2.65	2.61	**2.65**	**0.06**	1.1%	2.71	2.59	2.74	2.56
Na_2O	%	*0.01*	4.38	4.40	4.36	4.39	4.35	**4.33**	**0.18**	2.1%	4.51	4.15	4.60	4.06
K_2O	%	*0.01*	1.62	1.63	1.62	1.62	1.60	**1.62**	**0.03**	0.9%	1.65	1.59	1.66	1.58
Cr_2O_3	%	*0.001*	0.010	0.010	0.007	0.010	0.011	**0.010**	**0.003**	16.2%				
MnO	%	*0.01*	0.08	0.08	0.08	0.08	0.08	**0.08**	**0.00**	0.0%				
P_2O_5	%	*0.01*	0.17	0.17	0.18	0.18	0.17	**0.17**	**0.01**	3.6%	0.18	0.16	0.19	0.15
V2O5	%	*0.002*	0.017	0.016	0.015	0.016	0.016	**0.016**	**0.002**	7%				
SO3	%	*0.002*	0.001	0.001	0.001	0.001	0.002							
LOI	%	*-5.11*	0.15	0.12	0.14	0.11	0.16	**0.14**	**0.19**	67.8%				
Total	%	*0.01*	100.93	100.90	101.11	100.66	99.78							
Ag	ppm	*0.1*	0.05	0.05	0.1	0.1	0.1							
As	ppm	*0.5*	0.25	0.25	0.25	0.25	0.25							
Au	ppb	*0.5*	0.25	0.25	1.5	0.25	0.05							
Ba	ppm	*1*	612	610	605	657	634	**616**	**61**	5%	676	555	707	524
Bi	ppm	*0.1*	0.05	0.05	0.05	0.05	0.05							
Cd	ppm	*0.1*	0.05	0.05	0.05	0.05	0.05							
Ce	ppm	*0.1*	26.1	25.6	29.6	29.0	27.2	**27.6**	**2.6**	5%	30.2	25.0	31.6	23.6
Co	ppm	*0.2*	12.8	12.5	12.3	12.5	12.8	**11.6**	**7.9**	34%				
Cs	ppm	*0.1*	0.3	0.4	0.5	0.4	0.3	**0.4**	**0.1**	16%				
Cu	ppm	*0.1*	13.2	12.2	11.9	11.0	11.1	**11.9**	**4.1**	17%				
Dy	ppm	*0.05*	2.08	2.26	2.35	2.31	2.30	**2.26**	**0.22**	5%	2.48	2.04	2.59	1.93
Er	ppm	*0.03*	1.32	1.23	1.23	1.32	1.28	**1.28**	**0.12**	5%	1.40	1.16	1.46	1.10
Eu	ppm	*0.02*	0.76	0.80	0.79	0.84	0.88	**0.83**	**0.09**	5%	0.92	0.74	0.96	0.70
Ga	ppm	*0.5*	16.5	16.4	15.8	17.9	17.0	**17.4**	**1.9**	5%	19.3	15.5	20.2	14.6
Gd	ppm	*0.05*	2.51	2.60	2.55	2.72	2.88	**2.66**	**0.26**	5%	2.92	2.40	3.05	2.27
Hf	ppm	*0.1*	3.1	2.9	3.0	3.2	3.2	**3.2**	**0.3**	4%	3.5	2.9	3.6	2.8
Hg	ppm	*0.01*	0.01	0.01	0.01	0.01	0.01							
Ho	ppm	*0.02*	0.44	0.40	0.46	0.44	0.42	**0.44**	**0.06**	7%	0.50	0.38	0.53	0.35
La	ppm	*0.1*	14.3	12.1	14.6	14.3	13.6	**13.3**	**1.2**	4%	14.5	12.1	15.0	11.6
Lu	ppm	*0.01*	0.22	0.19	0.20	0.21	0.22	**0.20**	**0.03**	7%	0.23	0.17	0.24	0.16
Mo	ppm	*0.1*	0.6	0.5	0.6	0.5	0.5	**0.52**	**0.2**	20%				
Nb	ppm	*0.1*	3.5	2.6	2.8	3.2	3.1	**3.3**	**1.0**	15%				
Nd	ppm	*0.3*	13.1	13.9	13.9	13.9	14.6	**14.3**	**1.3**	5%	15.6	12.9	16.3	12.2
Ni	ppm	*0.1*	8.9	8.3	8.4	7.8	7.5	**8.0**	**1.1**	7%	9.1	6.9	9.6	6.4
Pb	ppm	*0.1*	3.2	3.3	2.6	2.6	2.9	**2.9**	**0.9**	15%				
Pr	ppm	*0.02*	3.16	3.31	3.37	3.47	3.55	**3.49**	**0.26**	4%	3.75	3.23	3.87	3.11
Rb	ppm	*0.1*	21.4	21.4	20.3	21.5	22.4	**21.5**	**2.2**	5%	23.7	19.3	24.7	18.3
Sb	ppm	*0.1*	0.1	0.1	0.05	0.05	0.05							
Sc	ppm	*0.1*	1.3	1.2	0.3	0.3	1.3	**9.0**	**8.2**	45%				
Se	ppm	*0.5*	0.25	0.25	1.0	1.1	0.25							
Sm	ppm	*0.05*	2.68	2.93	2.63	2.91	2.89	**2.85**	**0.32**	6%	3.17	2.53	3.34	2.36
Sn	ppm	*1*	1	1	1	1	1							
Sr	ppm	*0.5*	800.3	711.8	768.5	765.4	768.7	**737.0**	**77.6**	5%	814.6	659.4	853.4	620.6
Ta	ppm	*0.1*	0.2	0.1	0.2	0.3	0.3	**0.2**	**0.1**	21%				
Tb	ppm	*0.01*	0.37	0.38	0.40	0.39	0.39	**0.40**	**0.04**	5%	0.44	0.36	0.46	0.34
Te	ppm	*1*	0.1	0.1	0.5	0.5	0.5							
Th	ppm	*0.2*	1.5	1.8	1.9	2.0	1.9	**2.0**	**0.3**	7%	2.3	1.7	2.4	1.6
Tm	ppm	*0.01*	0.17	0.18	0.20	0.20	0.19	**0.19**	**0.03**	7%	0.22	0.16	0.23	0.15
U	ppm	*0.1*	0.7	0.7	0.7	0.8	0.7	**0.8**	**0.1**	9%				
V	ppm	*8*	87	78	62	96	87	**86**	**13**	8%	99	73	106	66
V2O5	%	*0.002*	0.017	0.016	0.015	0.016	0.016	**0.016**	**0.002**	7%				
W	ppm	*0.5*	0.25	0.50	0.25	0.25	0.80							
Y	ppm	*0.1*	12.2	11.5	12.6	12.5	12.2	**12.5**	**1.7**	7%	14.2	10.8	15.0	10.0
Yb	ppm	*0.05*	1.30	1.23	1.14	1.32	1.28	**1.28**	**0.19**	8%	1.47	1.09	1.57	0.99
Zn	ppm	*1*	28	26	24	24	24	**24**	**8**	16%				
Zr	ppm	*0.1*	120.9	120.7	117.2	124.5	126.1	**121.0**	**11.7**	5%	132.6	109.3	138.4	103.5

Orange = within the warning zone; Red = within the failure zone

Table B.7 Comparison between original and duplicate samples (see text for explanation about MPD (mean percentile difference) and precision calculation.

Element	Analyte	FR-14-29a	Duplicate	MPD	FR-13-116	Duplicate	MPD	FR-13-254	Duplicate	MPD	FR-14-80a	Duplicate	MPD
SiO2	wt %	67.1	67.3	0.07%	72.8	72.8	0.00%	62.6	62.2	0.16%	55.8	55.9	0.04%
TiO2	wt %	0.47	0.49	1.04%	0.22	0.22	0.00%	0.73	0.74	0.34%	0.71	0.70	0.35%
Al2O3	wt %	15.62	15.66	0.064%	14.51	14.46	0.09%	16.54	16.44	0.152%	16.24	16.37	0.20%
Fe2O3 (t)	wt %	3.87	3.90	0.19%	2.03	2.06	0.37%	5.4	5.36	0.19%	6.47	6.50	0.12%
CaO	wt %	3.55	3.61	0.42%	1.46	1.48	0.34%	4.83	4.73	0.52%	6.97	7.08	0.39%
MgO	wt %	1.5	1.5	0.0%	0.49	0.50	0.51%	3.12	3.14	0.16%	2.54	2.47	0.70%
Na2O	wt %	3.37	3.36	0.07%	3.8	3.8	0.00%	3.88	3.86	0.13%	3.94	3.93	0.06%
K2O	wt %	3.08	3.03	0.41%	4.51	4.52	0.06%	2.35	2.33	0.21%	2.14	2.16	0.23%
MnO	wt %	0.08	0.08	0.00%	0.06	0.06	0.00%	0.08	0.08	0.00%	0.15	0.15	0.00%
P2O5	wt %	0.13	0.12	2.00%	0.08	0.08	0.00%	0.17	0.17	0.00%	0.18	0.18	0.00%
Cr2O3	wt %	0.001	0.001	0.000%	<0.001	<0.001		0.009	0.008		0.01	0.01	
LOI	wt %	0.61	0.66	1.97%	0.84	0.86	0.59%	0.96	0.98	0.52%	3.72	3.82	0.66%
SO3	wt %	<0.002	<0.002		0.006	<0.002		<0.002	<0.002		0.005	0.01	
SUM	wt %	99.51	99.81	0.075%	101.00	101.02	0.00%	100.86	100.21	0.16%	99.03	99.4	0.09%
Ba	ppm	713	728	0.52%	842	846	0.12%	562	576	0.62%	332	332	0.00%
Be	ppm	4	3	7%	5	8	12%	<1	2		<1	3	
Co	ppm	6.9	6.6	1.1%	2.1	1.9	2.50%	15.8	16.1	0.47%	16.6	16.0	0.92%
Cs	ppm	6.5	6.2	1.2%	5.9	6.4	2.03%	1.8	1.9	1.35%	3.2	3.0	1.61%
Ga	ppm	16.8	16.1	1.06%	14.4	15	1.02%	14.7	14.9	0.34%	15.9	15.0	1.46%
Hf	ppm	4.6	4.3	1.7%	4.3	4.6	1.69%	4.4	4.2	1.16%	3.2	3.1	0.79%
Nb	ppm	10.4	9.9	1.2%	15.7	15.8	0.16%	9	9	0.00%	7.2	7.6	1.35%
Rb	ppm	120.2	115.6	0.975%	166.5	170.2	0.55%	68.3	68.3	0.00%	36.0	36.3	0.21%
Sn	ppm	5	4	6%	4	3	7.14%	<1	<1		<1	<1	
Sr	ppm	315.5	322.9	0.580%	164.9	169	0.61%	377.3	382.6	0.35%	477.9	485.0	0.37%
Ta	ppm	1.1	0.9	5.0%	1.4	1.3	1.85%	0.6	0.7	3.85%	0.6	0.4	10%
Th	ppm	15.5	13.3	3.82%	19.1	23.5	5.16%	12.2	12.3	0.20%	4.5	4.6	0.55%
U	ppm	5.3	3.9	7.6%	6.1	5.4	3.04%	3.9	3.9	0.00%	1.1	1.2	2.17%
V	ppm	69	70	0.4%	<8	<8		81	78		165	164	
W	ppm	0.6	<0.5		<0.5	0.9		1.6	1.1		<0.5	<0.5	
Zr	ppm	155.7	148.5	1.183%	156.2	168.5	1.89%	162.9	164.1	0.18%	118.4	114.6	0.82%
Y	ppm	19.2	20.0	1.02%	20.9	23.3	2.71%	19.5	18.8	0.91%	17.5	17.0	0.72%
La	ppm	38.7	31.0	5.52%	41.2	49.7	4.68%	28.1	28.3	0.18%	15.4	15.2	0.33%
Ce	ppm	74.4	61.8	4.63%	74.2	89.7	4.73%	51.2	51.6	0.19%	29.3	29.3	0.00%
Pr	ppm	8.04	6.77	4.29%	7.41	9.08	5.06%	5.61	5.80	0.83%	3.60	3.56	0.28%
Nd	ppm	29.0	24.4	4.31%	27.2	30.7	3.02%	21.7	21.5	0.23%	15.0	14.1	1.55%
Sm	ppm	4.86	4.49	1.98%	4.44	5.45	5.11%	3.98	4.01	0.19%	3.12	3.28	1.25%
Eu	ppm	0.95	0.88	1.91%	0.69	0.79	3.38%	1.02	1.05	0.72%	1.01	1.03	0.49%
Gd	ppm	4.34	3.99	2.10%	4.08	4.66	3.32%	3.97	4.00	0.19%	3.52	3.42	0.72%
Tb	ppm	0.63	0.62	0.40%	0.63	0.72	3.33%	0.6	0.6	0.00%	0.55	0.54	0.46%
Dy	ppm	3.62	3.28	2.46%	3.59	4.04	2.95%	3.43	3.45	0.15%	3.21	3.43	1.66%
Ho	ppm	0.71	0.75	1.37%	0.74	0.79	1.63%	0.67	0.71	1.45%	0.65	0.65	0.00%
Er	ppm	2.14	2.10	0.47%	2.1	2.21	1.28%	1.85	1.91	0.80%	2.02	1.98	0.50%
Tm	ppm	0.32	0.32	0.00%	0.34	0.35	0.72%	0.29	0.29	0.00%	0.27	0.28	0.91%
Yb	ppm	2.25	2.30	0.55%	2.08	2.32	2.73%	1.83	1.74	1.26%	1.90	1.85	0.67%
Lu	ppm	0.34	0.36	1.43%	0.33	0.34	0.75%	0.29	0.28	0.88%	0.29	0.27	1.79%
Mo	ppm	0.5	0.3	13%	0.8	0.7	3.33%	2.1	2.1	0.00%	1.2	1.1	2.17%
Cu	ppm	3.2	4.0	5.6%	0.7	0.8	3.33%	23.4	21.4	2.23%	14.8	14.3	0.86%
Pb	ppm	6.5	6.4	0.4%	4.5	4.2	1.72%	5.1	5.0	0.50%	2.0	1.9	1.28%
Zn	ppm	53	53	0.0%	24	23	1.06%	27	27	0.00%	52	52	0.00%
Ni	ppm	2.8	3.6	6.3%	2.5	1.8	8.14%	10.0	9.5	1.28%	9.5	9.2	0.80%
As	ppm	0.9	1.6	14%	0.9	0.8	2.94%	1.4	1.4	0.00%	1.1	1.4	6.00%
Cd	ppm	<0.1	<0.1		<0.1	<0.1		<0.1	<0.1		<0.1	<0.1	
Sb	ppm	<0.1	<0.1		<0.1	<0.1		0.2	<0.1		<0.1	<0.1	
Bi	ppm	0.1	0.2	17%	0.1	0.1	0.0%	<0.1	<0.1		<0.1	<0.1	
Ag	ppm	<0.1	<0.1		<0.1	<0.1		<0.1	<0.1		<0.1	<0.1	
Au	ppb	<0.5	<0.5		<0.5	<0.5		<0.5	<0.5		<0.5	<0.5	
Hg	ppm	<0.01	<0.01		<0.01	<0.01		<0.01	<0.01		<0.01	<0.01	
Se	ppm	<0.5	<0.5		<0.5	<0.5		<0.5	<0.5		<0.5	<0.5	
Sc	ppm	5.2	5.1	0.5%	3.7	3.7	0.0%	2.6	2.2	4.2%	13.7	13.7	0.00%
Te	ppm	<0.2	<0.2		<1	<1		<1	<1		<1	<1	

Table B.7 (Continued) Comparison between original and duplicate samples (see text for explanation about MPD (mean percentile difference) and precision calculation.

Element	FR-13-273a	Duplicate	MPD	FR-13-328b	Duplicate	MPD	FR-13-17	Duplicate	MPD	FR-14-111a	Duplicate	MPD
SiO2	69.2	68.2	0.36%	70.7	70.2	0.18%	69.5	69.6	0.04%	48.7	49.1	0.20%
TiO2	16.79	16.67	0.18%	16.53	16.2	0.50%	15.85	15.97	0.19%	21.3	20.92	0.45%
Al2O3	1.35	1.78	6.87%	0.52	0.51	0.49%	1.71	1.70	0.15%	5.7	5.97	1.157%
Fe2O3 (t)	5.3	5.46	0.74%	0.49	0.48	0.52%	2.04	2.01	0.37%	14.06	14.17	0.19%
CaO	1.26	1.45	3.51%	0.08	0.07	3.33%	0.76	0.76	0.00%	6.78	7.15	1.33%
MgO	5.63	5.49	0.63%	4.7	4.64	0.32%	4.14	4.17	0.18%	1.83	1.82	0.14%
Na2O	0.18	0.18	0.00%	7.01	6.83	0.65%	5.18	5.19	0.05%	0.06	0.06	0.00%
K2O	0.04	0.04	0.00%	0.02	0.02	0.00%	0.04	0.04	0.00%	0.09	0.09	0.00%
MnO	0.44	0.46	1.11%	0.31	0.29	1.67%	0.22	0.21	1.16%	0.51	0.55	1.89%
P2O5	0.13	0.13	0.00%	0.03	0.03	0.00%	0.08	0.09	2.94%	0.03	0.03	0.00%
Cr2O3	<0.001	<0.001		<0.001	<0.001		0.001	0.002		0.056	0.067	4.47%
LOI	0.41	0.46	2.87%	0.61	0.59	0.83%	0.63	0.65	0.78%	1.05	1.11	1.39%
SO3	<0.002	<0.002		<0.002	<0.002		0.012	0.007		<0.002	<0.002	
SUM	100.83	100.39	0.11%	101.11	100	0.28%	100.45	100.65	0.05%	100.22	101.08	0.21%
Ba	211	222	1.27%	461	439	1.22%	922	908	0.38%	16	15	1.61%
Be	2	4		9	8		4	5		<1	<1	
Co	3.8	4.3	3.09%	0.5	0.3	12.5%	3.1	3.7	4.41%	27	28.7	1.53%
Cs	<0.1	<0.1		0.9	0.8	2.94%	9.9	10.1	0.50%	<0.1	<0.1	
Ga	12.3	14.4	3.93%	22.6	22	0.67%	18.6	18.5	0.13%	12.3	11.5	1.68%
Hf	3.7	3.4	2.11%	9.1	9.5	1.08%	5.5	5.6	0.45%	0.7	0.5	8.33%
Nb	12.3	15	4.95%	48.3	47.2	0.58%	13.9	13.7	0.36%	0.2	0.2	0.00%
Rb	1.6	2.3	8.97%	114.8	111.8	0.66%	194.9	193.2	0.22%	1	0.8	5.56%
Sn	<1	1		3	3		2	2		<1	<1	
Sr	459.2	452.8	0.35%	120.4	118	0.50%	860.5	861	0.01%	156.7	158.6	0.30%
Ta	1.1	1.1	0.00%	3.3	3.3	0.00%	1.2	1.2	0.00%	<0.1	<0.1	
Th	13.9	10.9	6.05%	29.8	30.2	0.33%	31.4	31.5	0.08%	<0.2	<0.2	
U	2.5	1.9	6.82%	6.3	6.8	1.91%	11.2	10.4	1.85%	<0.1	<0.1	
V	32	83		11	11		<8	<8		156	158	
W	1.1	0.8		<0.5	<0.5		<0.5	<0.5		<0.5	<0.5	
Zr	140.2	137.6	0.47%	440.2	466.4	1.44%	184.1	178.3	0.80%	23.7	23.4	0.32%
Y	16	16.7	1.07%	11.1	10.9	0.45%	10	9.9	0.25%	9.6	10.1	1.27%
La	63.4	57.5	2.44%	21.1	22.7	1.83%	42.4	45.8	1.93%	1.3	1.6	5.17%
Ce	93.7	84.2	2.67%	60.7	60	0.29%	77.2	81.6	1.39%	4	3.9	0.63%
Pr	7.54	7.05	1.68%	5.68	5.97	1.24%	7.63	7.87	0.77%	0.56	0.62	2.54%
Nd	22.4	21.5	1.03%	17.4	19.9	3.35%	25.2	26.1	0.88%	3.2	3.3	0.77%
Sm	3.2	3.45	1.88%	2.96	3.22	2.10%	4.02	4.14	0.74%	1.04	1.12	1.85%
Eu	0.86	0.89	0.86%	0.33	0.35	1.47%	1.04	1.08	0.94%	0.49	0.47	1.04%
Gd	2.97	3.18	1.71%	2.38	2.39	0.10%	3.05	3.03	0.16%	1.5	1.43	1.19%
Tb	0.47	0.45	1.09%	0.36	0.36	0.00%	0.39	0.39	0.00%	0.27	0.27	0.00%
Dy	2.5	2.93	3.96%	2.05	2.14	1.07%	1.97	1.98	0.13%	1.76	1.71	0.72%
Ho	0.51	0.56	2.34%	0.38	0.39	0.65%	0.34	0.34	0.00%	0.36	0.39	2.00%
Er	1.65	1.68	0.45%	1.29	1.19	2.02%	0.89	0.94	1.37%	1.1	1.17	1.54%
Tm	0.26	0.27	0.94%	0.21	0.22	1.16%	0.15	0.14	1.72%	0.16	0.17	1.52%
Yb	1.76	1.83	0.97%	1.44	1.52	1.35%	0.96	0.87	2.46%	1.05	0.91	3.57%
Lu	0.28	0.31	2.54%	0.24	0.24	0.00%	0.14	0.13	1.85%	0.16	0.16	0.00%
Mo	0.2	<0.1		<0.1	0.1		0.3	0.2	10.0%	<0.1	<0.1	
Cu	0.9	1	3%	0.6	0.6	0.00%	0.7	0.7	0.00%	36.9	35.2	1.18%
Pb	1	1.1	2%	1.1	1.1	0.00%	10	10.7	1.69%	0.4	0.6	10%
Zn	2	3	10%	3	3	0.00%	27	28	0.91%	2	2	0.00%
Ni	0.3	0.9	25%	1.6	1.5	1.61%	9.9	11.1	2.86%	22.5	23.2	0.77%
As	0.5	<0.5		2.1	1.9	2.50%	0.6	<0.5		<0.5	<0.5	
Cd	<0.1	<0.1		<0.1	<0.1		<0.1	<0.1		<0.1	<0.1	
Sb	<0.1	<0.1		<0.1	<0.1		<0.1	<0.1		<0.1	<0.1	
Bi	<0.1	<0.1		<0.1	<0.1		0.1	0.1		<0.1	<0.1	
Ag	<0.1	<0.1		<0.1	<0.1		<0.1	<0.1		<0.1	<0.1	
Au	<0.5	<0.5		<0.5	<0.5		<0.5	<0.5		<0.5	<0.5	
Hg	<0.01	<0.01		<0.01	<0.01		<0.01	<0.01		<0.01	<0.01	
Se	<0.5	<0.5		<0.5	<0.5		<0.5	<0.5		<0.5	<0.5	
Sc	0.8	0.9	2.9%	0.5	0.4	5.6%	1.7	180.0%	1.43%	1.8	1.9	1.4%
Te	<1	<1		<1	<1		<1	<1		<0.2	<0.2	

Table B.7 (Continued) Comparison between original and duplicate samples (see text for explanation about MPD (mean percentile difference) and precision calculation.

Element	FR-13-149a	Duplicate	MPD	Absolute error (wt % or ppm)	Relative error (wt % or ppm)	Precision (wt % or ppm)
SiO2	66.5	67.1	0.22%	0.1	1.5	1.07
TiO2	15.94	16	0.09%	0.01	2	0.21
Al2O3	4.21	4.14	0.42%	0.01	3.5	0.31
Fe2O3 (t)	4.07	4.11	0.24%	0.01	3.5	0.13
CaO	1.62	1.59	0.47%	0.01	4	0.13
MgO	3.86	3.87	0.06%	0.01	2.5	0.09
Na2O	2.52	2.53	0.10%	0.01	2	0.08
K2O	0.1	0.09	2.63%	0.01	1.5	0.03
MnO	0.43	0.42	0.59%	0.01	3.5	0.02
P2O5	0.13	0.14	1.85%	0.01	1	0.01
Cr2O3	0.002	<0.001				
LOI	0.57	0.57	0.00%			
SO3	<0.002	<0.002				
SUM	100.02	100.68	0.16%			
Ba	570	571	0.04%	1	3.5	19
Be	3	<1				
Co	8.9	8	2.66%	0.2	5	0.67
Cs	1.4	1.3	1.85%	0.1	4	0.23
Ga	14.1	13.8	0.54%	0.5	3	0.97
Hf	3.1	3.2	0.79%	0.1	3	0.23
Nb	8.1	8.3	0.61%	0.1	3	0.52
Rb	66.3	64.4	0.73%	0.1	2.5	2.24
Sn	1	<1				
Sr	309.8	301.5	0.68%	0.5	2	7.7
Ta	0.7	0.7	0.00%	0.1	4	0.14
Th	15	14.1	1.55%	0.2	14	2.4
U	2.2	2.1	1.16%	0.1	17	0.83
V	71	67	1.45%	8	1	8.66
W	<0.5	<0.5				
Zr	109.8	114.2	0.98%	0.1	5	8.38
Y	14.7	14	1.22%	0.1	7	1.18
La	26	26.2	0.19%	0.1	14	4.42
Ce	42.8	43.7	0.52%	0.1	12	6.87
Pr	4.44	4.46	0.11%	0.02	12.5	0.75
Nd	15.8	15.8	0.00%	0.3	10	2.27
Sm	2.81	2.73	0.72%	0.05	4.5	0.20
Eu	0.75	0.74	0.34%	0.02	7	0.08
Gd	2.78	2.63	1.39%	0.05	8	0.3
Tb	0.38	0.38	0.00%	0.01	8	0.05
Dy	2.33	2.18	1.66%	0.05	9	0.29
Ho	0.54	0.47	3.47%	0.02	6	0.05
Er	1.45	1.42	0.52%	0.03	3.5	0.09
Tm	0.23	0.22	1.11%	0.01	1	0.01
Yb	1.72	1.69	0.44%	0.05	5	0.13
Lu	0.26	0.26	0.00%	0.01	3.5	0.02
Mo	<0.1	<0.1				
Cu	4	3.5	3.33%	0.1	14	1.34
Pb	2	1.9	1.28%	0.1	4	0.24
Zn	33	33	0.00%	1	1	1.25
Ni	2	1.7	4.05%	0.1	15	1.12
As	<0.5	<0.5				
Cd	<0.1	<0.1				
Sb	<0.1	<0.1				
Bi	<0.1	<0.1				
Ag	<0.1	<0.1				
Au	<0.5	<0.5				
Hg	<0.01	<0.01				
Se	<0.5	<0.5				
Sc	1.9	1.9	0.0%			
Te	<0.2	<0.2				

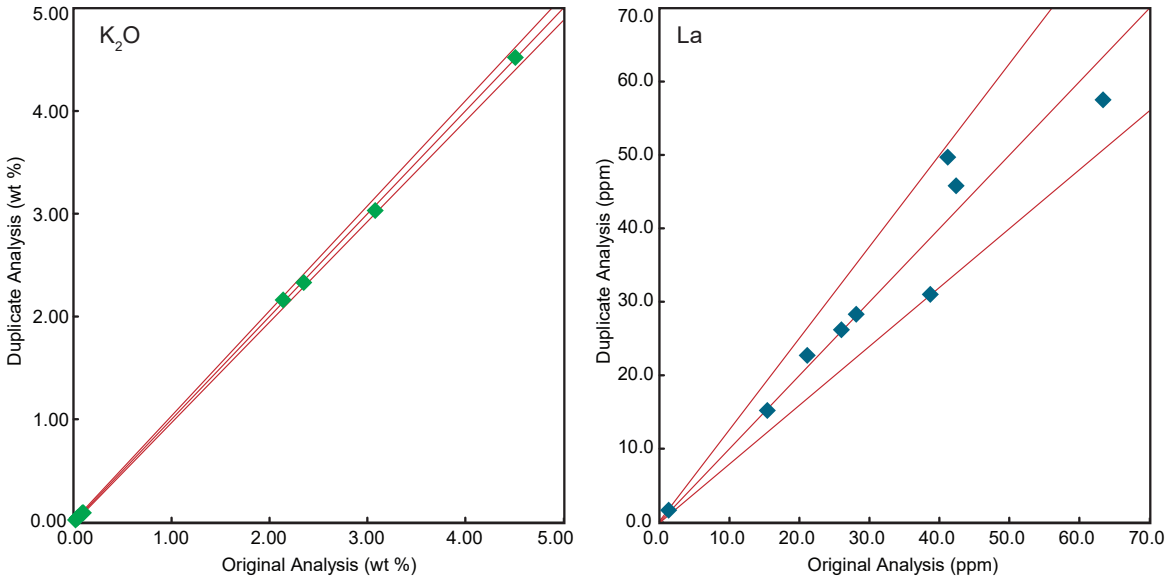

Figure B.1 Examples of iterative error calculation for duplicate samples (left: K_2O; right: La). The samples are included within the error envelope (y = mx + b) obtained from the addition of the absolute (b) and relative (m) errors.

Table B.8 Rb-Sr and Sm-Nd elemental concentration QA-QC.

ppm in original samples	Nd	Sm	Rb	Sr	Remarks
AGV-1 GeoRem	**31.70**	**5.72**	**66.60**	**660.00**	**published**
AGV-1-1	32.74	5.91	66.68	673.74	
AGV-1-2	32.39	5.88	66.49	670.72	
AGV-1-3	32.33	5.84	66.38	672.93	
AGV-1-4	32.20	5.84	66.08	669.62	
AGV-1-5	32.05	5.88	65.67	668.02	
%RSD rep runs	0.79	0.49	0.60	0.35	
AGV-2 GeoRem	**30.50**	**5.49**	**66.30**	**661.00**	**published**
AGV-2-FR-Sav	28.16	5.07	60.65	604.31	
AGV-2-FR	29.68	5.44	58.04	647.45	
G-3 Cotta	**54.00**	**7.40**	**156.00**	**440.00**	**published**
G-3 Park et al, 2012	**55.00**	**7.40**	**171.00**	**463.00**	**published**
G-3 FR1	52.22	7.00	159.76	457.87	
G-3 FR2	52.83	6.86	163.34	449.09	
JB-3 NOAA Tech Mem ORCA 94	**15.60**	**4.27**	**15.10**	**403.00**	**published**
Makishima and Nakamura, 2006	**15.90**	**4.17**	**14.00**	**414.00**	**published**
JB-3 FR1	14.69	4.07	13.25	399.52	
JB-3 FR2	15.05	4.19	13.66	405.57	
FR-13-68	41.99	6.97	80.89	769.32	
FR-13-149	15.33	2.89	36.78	318.44	
FR-13-149b	14.91	2.70	58.62	290.40	
FR-13-149b-rep	14.88	2.73	57.75	288.81	
%RSD rep runs	0.13	0.75	1.06	0.39	
FR-15-34	17.22	3.23	64.18	419.54	
FR-15-34-rep	17.33	3.23	64.26	437.82	
%RSD rep runs	0.43	0.03	0.09	3.01	
FR-15-34b	17.42	3.27	64.80	419.80	
FR-15-34b-rep	17.57	3.24	64.94	418.66	
%RSD rep runs	0.57	0.69	0.16	0.19	

Table B.9 Radiogenic Pb isotope analyses QA-QC.

	Ln-Ln correction	208Pb/204Pb	±2σ	207Pb/204Pb	±2σ	206Pb/204Pb	±2σ
Replicates (repeat analysis of the same chemically prepared solution by MC-ICP-MS)							
FR/DSN/R12	FR-15-34	38.9850	0.0058	15.6722	0.0016	18.8431	0.0020
FR/DSN/R12*	FR-15-34 replicate	38.9834	0.0019	15.6712	0.0007	18.8423	0.0008
Diff/ppm		**41**		**60**		**41**	
FR/DSN/R18	FR-14-94	38.8776	0.0034	15.6456	0.0012	18.8298	0.0014
FR/DSN/R18b	FR-14-94 replicate	38.8809	0.0051	15.6465	0.0017	18.8318	0.0020
Diff/ppm		**-85**		**-57**		**-102**	
Duplicates (analysis of a separate solution prepared by the same chemical process by MC-ICP-MS)							
FR/DSN/R12	FR-15-34	38.9850	0.0058	15.6722	0.0016	18.8431	0.0020
FR/DSN/R24	FR-15-34b	38.9855	0.0031	15.6722	0.0012	18.8429	0.0015
Diff/ppm		**-12**		**0**		**9**	
Reference Material							
FR/DSN/AGV-2		38.5452	0.0033	15.6175	0.0012	18.8706	0.0014
FR/DSN/AGV-2		38.5472	0.0035	15.6185	0.0013	18.8725	0.0014
Diff/ppm		**-51**		**-64**		**-101**	
	AGV-2 Lab Average	**38.5494**		**15.6190**		**18.8723**	
	2SD	**0.0111**		**0.0037**		**0.0051**	
	ppm	**287**		**238**		**270**	
	n = 39						

Average isotopic values of standard NBS981		**208Pb/204Pb**	**±2σ**	**207Pb/204Pb**	**±2σ**	**206Pb204/Pb**	**±2σ**
16-Mar-17 n=11	**Insturment NP214**	36.7214	0.0029	15.4994	0.0012	16.9432	0.0011
17-Mar-17 n=9	**Instrument NP214**	36.7209	0.0025	15.4991	0.0010	16.9429	0.0010
NBS981 values used for SSB normalization (Galer and Abouchami, 1998)		**36.7219**		**15.4963**		**16.9405**	

B.3 Geochemical features of the late Cenozoic igneous complexes in central and eastern Anatolia

Non-critical geochemical diagrams mentioned in Chapter 3 include 1) AFM and Th/Yb versus Zr/Y diagrams that illustrate the calc-alkaline affinity of the late Cenozoic igneous complexes in central and eastern Anatolia and absence of tholeiitic rocks (Figures B.2A-B); 2) total alkali versus silica rock classification for plutonic rocks (Middlemost, 1994; Figure B.2C).

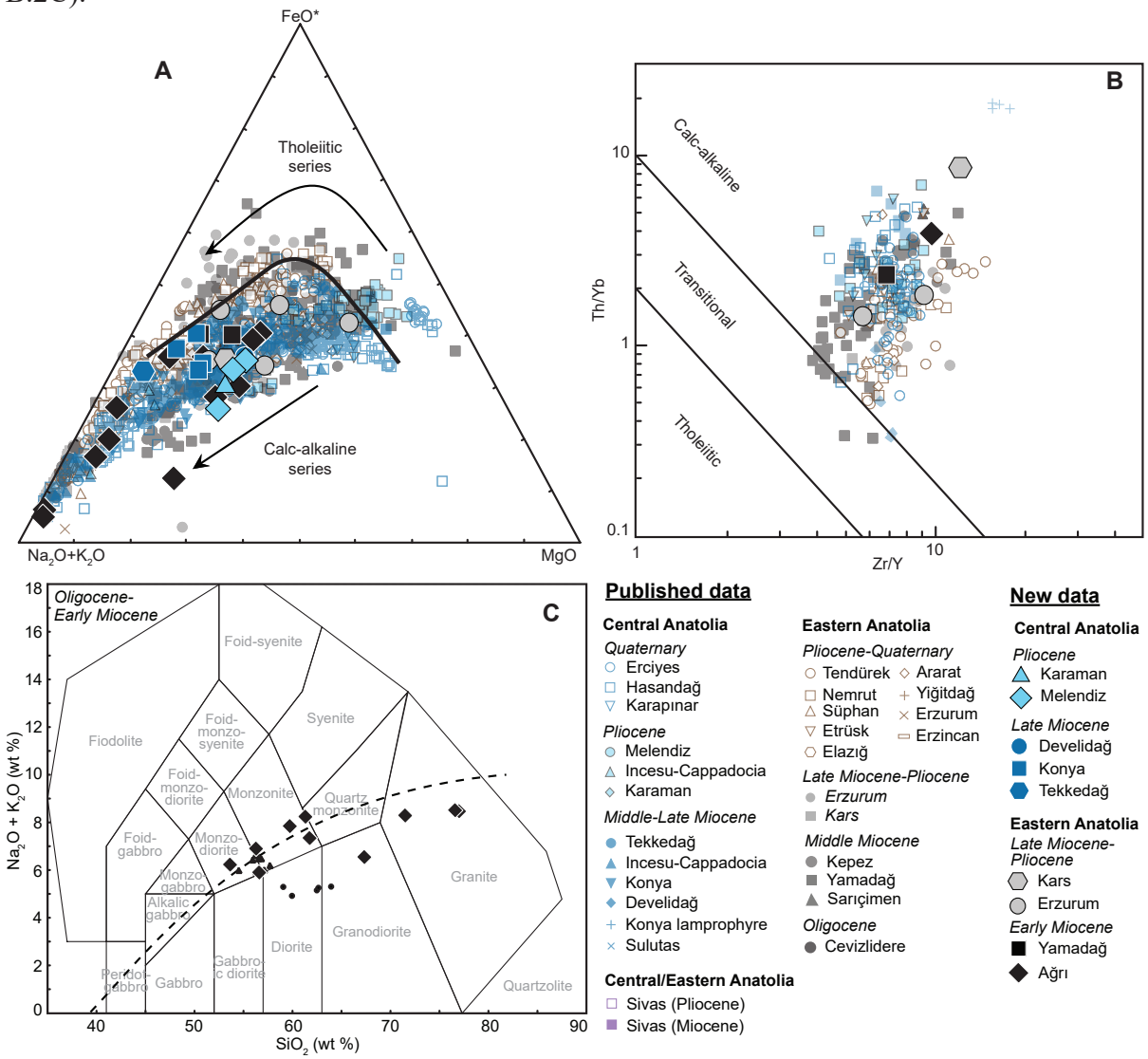

Figure B.2 AFM (A; Irvine and Baragar, 1971) and Th/Yb versus Zr/Y diagrams (B; Ross and Bedard, 2009) showing the calc-alkaline affinity of the late Cenozoic igneous suites in central and eastern Anatolia. The Total Alkali versus Silica diagram (C) for plutonic rocks (Middlemost, 1994) provides rock names for the Oligocene to early Miocene plutonic rocks in eastern Anatolia; these rock samples were plotted in the Total Alkali versus Silica diagram for volcanic rocks in Chapter 3 (Figure 3.7).

The calculation of Nd model ages from rock samples throughout the Eastern Anatolian Magmatic Belt revealed the Neoproterozoic-aged Anatolian lithosphere (τ_{DM} comprised between 0.35 and 0.9 Ga; Figure B.3).

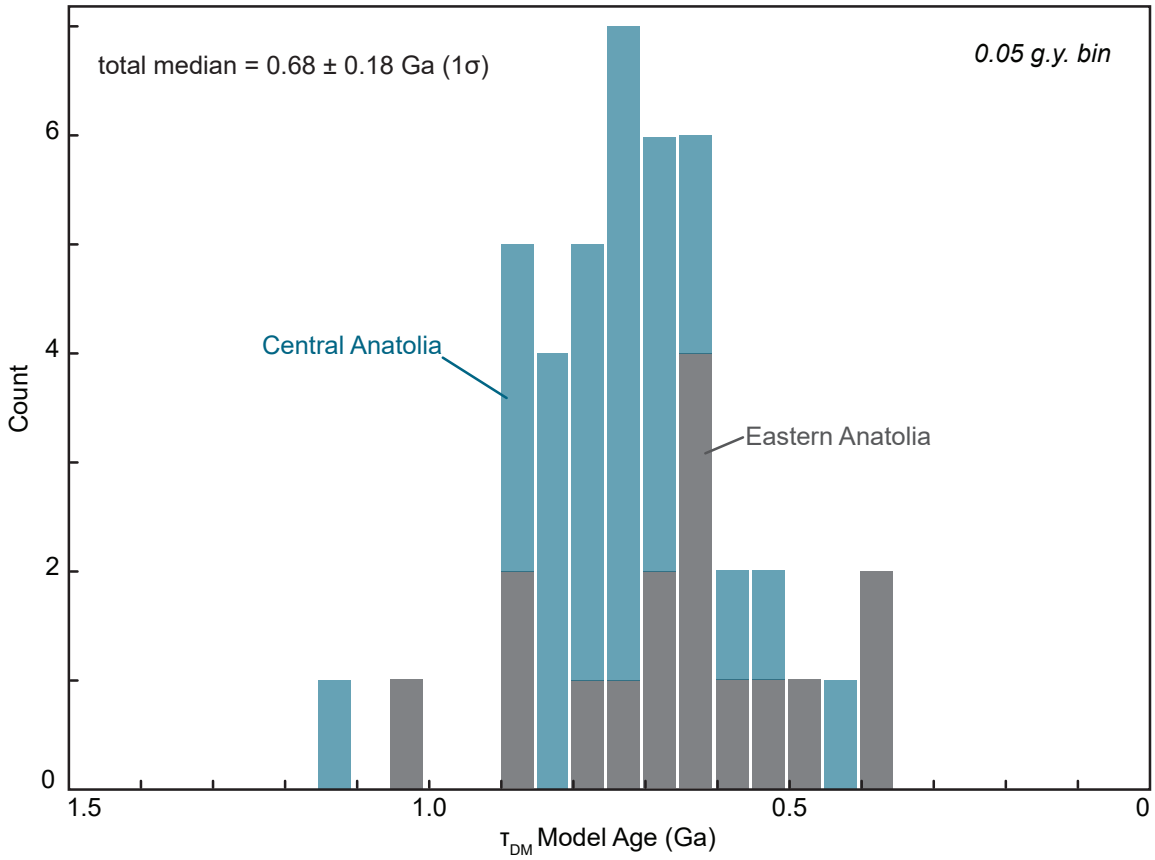

Figure B.3 Nd model age histogram from late Cenozoic igneous rocks along the Eastern Anatolian Magmatic Belt; single-stage model age calculation.

B.4 Primary melt calculation

In this study, primary and primitive melts are all the rocks with an Mg # ≥ 70 and ≥ 62, respectively. Primary melts were used to identify the magma source(s) of central and eastern Anatolian igneous complexes (see Figure 11). Rocks from a same igneous suite may have various Mg # but are expected to result from the same magma source. When the initial $^{87}Sr/^{86}Sr$ and $^{143}Nd/^{144}Nd$ ratios of each suite were plotted against Mg #, each rock suite yields a regression line. The initial $^{87}Sr/^{86}Sr$ and $^{143}Nd/^{144}Nd$ ratios were calculated at Mg # = 70 for the suites having a regression coefficient greater or equal to 0.5 and averaged the isotopic ratios for primitive samples if n ≥ 2. If neither conditions were met for a rock suite, the primary melt composition was not calculated. Graphical and statistical results are provided in Table 3.4 and Figure B.4.

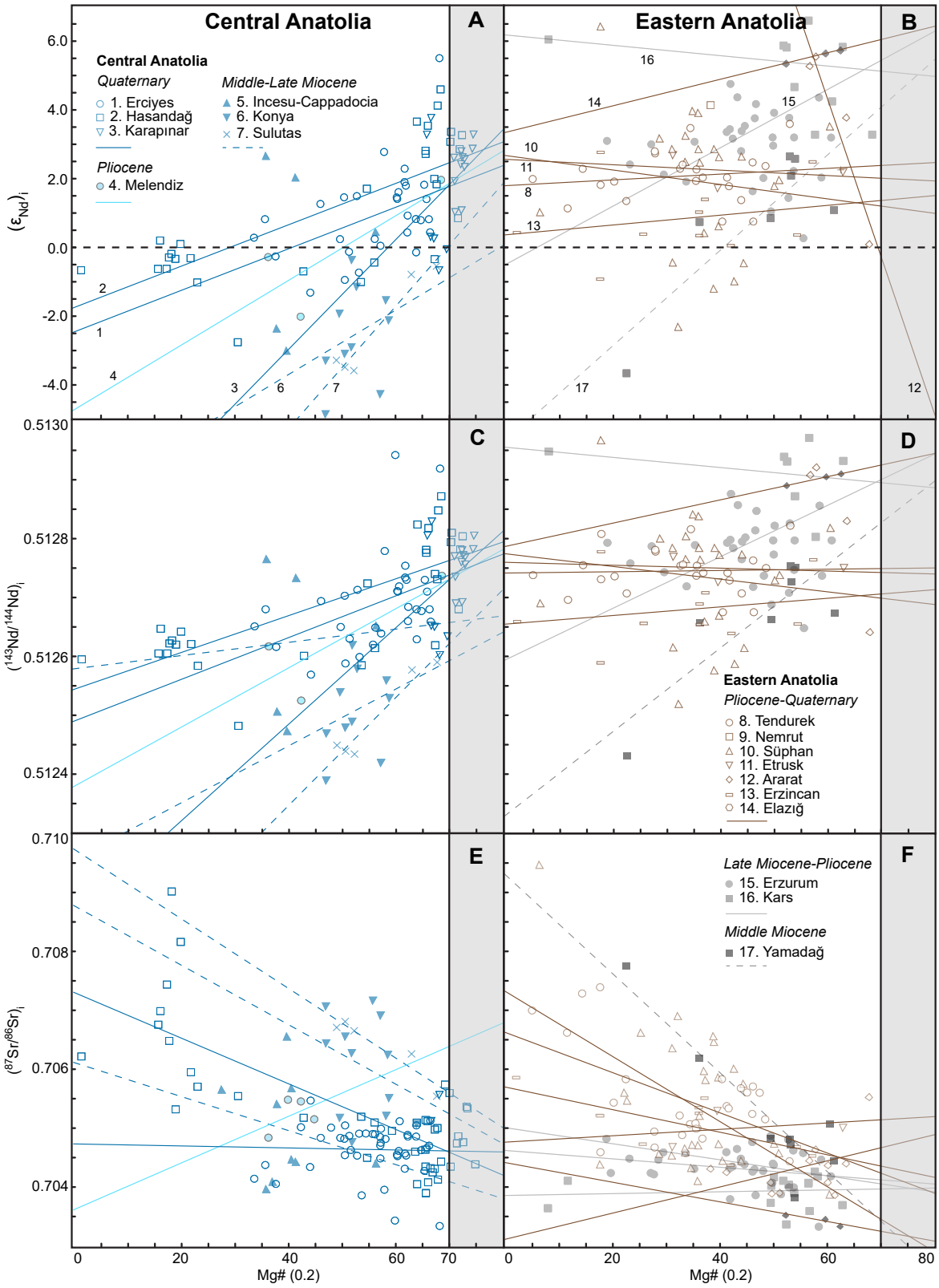

Figure B.4 $(\varepsilon_{Nd})_i$, $(^{143}Nd/^{144}Nd)_i$ and $(^{87}Sr/^{86}Sr)_i$ versus Mg# (assuming $Fe^{3+}/Fe^{2+} = 0.2$) showing the regression lines of isotopic data from the late Cenozoic igneous suites in central and eastern Anatolia. Primary melt calculation were made at Mg # = 70 (see text above for explanation).

Appendix C

This section contains the analytical results obtained for the U-Pb (Table C.1) and $^{40}Ar/^{39}Ar$ age determination (Table C.2) that are presented in Chapter 4.

Table C.1 LA-ICP-MS U-Pb isotopic analyses.

Zircon grain analysis	Ion count rate (cps)								Isotope ratios						Calculated ages (Ma)			
	^{202}Hg	^{204}Pb	^{206}Pb	^{207}Pb	^{208}Pb	^{232}Th	^{235}U	^{238}U	$^{207}Pb/^{235}U$	$\pm 2\sigma$[a]	$^{206}Pb/^{238}U$	$\pm 2\sigma$[a]	$^{207}Pb/^{206}Pb$	$\pm 2\sigma$[a]	$^{207}Pb/^{235}U \pm 2\sigma$[a]		$^{206}Pb/^{238}U \pm 2\sigma$[a]	
FR-15-18																		
FR 15 18 1[b]	1855	400	2317	197	730	124700	2561	381400	0.033200	0.002100	0.003050	0.000110	0.0832	0.0064	33.0	2.1	19.60	0.7
FR_15_18_2	1760	397	9470	464	2370	579000	11100	1700000	0.018500	0.001100	0.002758	0.000076	0.0479	0.0029	18.6	1.1	17.75	0.5
FR_15_18_3	1726	382	4060	205.7	1395	345800	4765	729000	0.018380	0.001000	0.002800	0.000075	0.0491	0.0027	18.5	1.0	18.02	0.5
FR_15_18_4	1745	363	4770	240	950	250800	5790	884000	0.018110	0.000970	0.002758	0.000078	0.0480	0.0029	18.2	1.0	17.76	0.5
FR_15_18_5	1980	378	6960	327	1460	379000	8120	1222000	0.018100	0.002300	0.002879	0.000100	0.0465	0.0062	18	2.3	18.5	1
FR_15_18_6	1750	383	4840	252	964	243000	5860	895000	0.019100	0.001900	0.002840	0.000130	0.0489	0.0057	19.2	1.9	18.31	0.9
FR_15_18_7	1748	344	8470	412	4680	1274000	10450	1576000	0.017920	0.000730	0.002734	0.000058	0.0474	0.0019	18.1	0.7	17.60	0.4
FR 15 18 8[b]	1639	401	5460	318	2071	540000	6250	960000	0.023100	0.001400	0.002990	0.000110	0.0578	0.0040	23.3	1.4	19.23	0.7
FR_15_18_9	1696	346	4080	215	1660	386000	4870	741000	0.019900	0.001900	0.002920	0.000120	0.0495	0.0046	20.0	1.9	18.78	0.8
FR_15_18_10	1660	340	6230	325	1510	423000	7660	1181000	0.018400	0.001500	0.002760	0.000110	0.0493	0.0043	18.8	1.5	17.75	0.7
FR_15_18_11	1430	325	10020	475	5400	1637000	12920	2002000	0.017760	0.000700	0.002730	0.000062	0.0482	0.0019	17.9	0.7	17.58	0.4
FR_15_18_12	1511	313	4130	213	804	224900	5270	814000	0.018000	0.001600	0.002700	0.000110	0.0491	0.0043	18.1	1.6	17.40	0.7
FR 15 18 13[b]	1445	303	6220	354	2220	606000	8100	1237000	0.020700	0.001700	0.002730	0.000110	0.0546	0.0050	20.8	1.7	17.60	0.7
FR_15_18_1a	530	103	1909	97.2	298	100200	2483	428900	0.018000	0.001600	0.002669	0.000120	0.0515	0.0043	18.1	1.5	17.18	0.8
FR_15_18_2a	571	99	2428	115.9	641	210600	3060	519600	0.018100	0.001400	0.002832	0.000120	0.0470	0.0033	18.2	1.4	18.23	0.8
FR 15 18 3a[b]	576	129	1995	108.1	483	158400	2558	426900	0.020900	0.001600	0.002798	0.000120	0.0553	0.0041	21.0	1.6	18.01	0.8
FR_15_18_4a	535	83	4500	219	1109	367500	5600	970000	0.018300	0.001500	0.002783	0.000120	0.0494	0.0039	18.4	1.5	17.92	0.8
FR_15_18_5a	560	101	2208	98.2	648	218300	2833	483800	0.017100	0.001400	0.002770	0.000120	0.0460	0.0035	17.1	1.4	17.86	0.8
FR_15_18_6a	486	104	1184	63.1	217	67200	1547	269100	0.018100	0.001900	0.002670	0.000140	0.0504	0.0053	18.1	1.9	17.20	0.89
FR_15_18_7a	555	104	2529	125.2	746	235800	3234	548500	0.018500	0.001300	0.002798	0.000120	0.0513	0.0035	18.5	1.3	18.01	0.76
FR_15_18_8a	528	104	2184	112	624	205100	2773	479700	0.019300	0.002100	0.002810	0.000150	0.0525	0.0056	19.4	2.1	18.09	0.95
FR_15_18_9a	547	130	2950	148	886	270400	3690	626000	0.019100	0.001800	0.002780	0.000150	0.0516	0.0047	19.2	1.8	17.91	0.97
FR_15_18_10a	519	109	2278	106.6	632	190500	2824	476400	0.018000	0.001400	0.002873	0.000120	0.0476	0.0036	18.1	1.4	18.49	0.8
FR_15_18_11a	565	106	1938	93.5	430	136500	2302	393400	0.019500	0.001700	0.002930	0.000140	0.0522	0.0045	19.7	1.6	18.86	0.89
FR_15_18_12a	565	110	2744	134.1	811	257500	3576	602000	0.018800	0.001500	0.002759	0.000130	0.0503	0.0038	19.2	1.5	17.76	0.83

Table C.1 (Continued) LA-ICP-MS U-Pb isotopic analyses.

Zircon grain analysis	Ion count rate (cps)								Isotope ratios						Calculated ages (Ma)			
	^{202}Hg	^{204}Pb	^{206}Pb	^{207}Pb	^{208}Pb	^{232}Th	^{235}U	^{238}U	$^{207}Pb/^{235}U$	$\pm 2\sigma^a$	$^{206}Pb/^{238}U$	$\pm 2\sigma^a$	$^{207}Pb/^{206}Pb$	$\pm 2\sigma^a$	$^{207}Pb/^{235}U \pm 2\sigma^a$		$^{206}Pb/^{238}U \pm 2\sigma^a$	
FR-15-31																		
FR_15_31_1[c]	1566	306	2847	143.3	786	408800	6994	1095000	0.009170	0.000690	0.001423	0.000044	0.0488	0.0040	9.3	0.7	9.17	0.28
FR_15_31_2	1485	298	2096	111.2	626	324500	4874	755000	0.009900	0.000900	0.001498	0.000051	0.0482	0.0046	10.0	0.9	9.65	0.33
FR_15_31_3	1273	302	7720	402	3220	1702000	18020	2844000	0.010480	0.000670	0.001551	0.000053	0.0490	0.0035	10.6	0.7	9.99	0.34
FR_15_31_4[c]	1428	314	3520	163	1140	612000	8770	1376000	0.008810	0.000620	0.001446	0.000039	0.0443	0.0032	8.9	0.6	9.32	0.25
FR_15_31_5	1450	296	5040	245	1921	1102000	12120	1887000	0.009530	0.000520	0.001499	0.000037	0.0463	0.0026	9.7	0.5	9.66	0.24
FR_15_31_6	1388	266	5240	243	2040	1138000	12320	1930000	0.009170	0.000530	0.001507	0.000038	0.0447	0.0028	9.3	0.5	9.70	0.24
FR_15_31_7	1412	296	9070	438	3840	2098000	23000	3499000	0.009700	0.000410	0.001492	0.000032	0.0471	0.0022	9.9	0.4	9.61	0.21
FR_15_31_8	1356	284	7280	340	3710	2127000	17700	2791000	0.009620	0.000450	0.001510	0.000034	0.0460	0.0022	9.7	0.5	9.72	0.22
FR_15_31_9	1424	306	8710	412	2837	1588000	20750	3215000	0.009850	0.000360	0.001537	0.000034	0.0474	0.0018	10.0	0.4	9.90	0.22
FR_15_31_10	1397	320	11520	553	2771	1500000	28250	4421000	0.009880	0.000360	0.001496	0.000030	0.0478	0.0018	9.98	0.36	9.64	0.19
FR_15_31_11	1420	287	9000	419	4053	2298000	22200	3441000	0.009640	0.000380	0.001521	0.000031	0.0457	0.0018	9.74	0.38	9.79	0.2
FR_15_31_12	1399	298	7380	336	2670	1526000	17740	2789000	0.009700	0.000450	0.001510	0.000034	0.0452	0.0021	9.8	0.45	9.73	0.22
FR_15_31_13	1332	299	8690	413	3130	1767000	21030	3298000	0.009740	0.000450	0.001520	0.000036	0.0464	0.0022	9.84	0.45	9.79	0.23
FR_15_31_14	1359	300	9280	438	3410	1931000	22940	3565000	0.009620	0.000430	0.001536	0.000033	0.0460	0.0022	9.72	0.44	9.89	0.21
FR_15_31_15	1310	296	7100	324	3270	1874000	17370	2775000	0.009460	0.000570	0.001525	0.000042	0.0463	0.0029	9.55	0.57	9.82	0.27
FR_15_31_16	1219	245	10530	511	3430	2001000	26090	4164000	0.009770	0.000490	0.001501	0.000037	0.0483	0.0025	9.87	0.5	9.67	0.24
FR_15_31_17	1273	248	7390	356	3610	2143000	18050	2877000	0.009960	0.000580	0.001523	0.000048	0.0493	0.0031	10.06	0.58	9.81	0.31
FR_15_31_18	1291	281	8730	403	3190	1808000	21560	3408000	0.009600	0.000420	0.001535	0.000038	0.0460	0.0021	9.73	0.42	9.89	0.24
FR_15_31_19	1312	306	4490	222	1209	689000	11090	1739000	0.010090	0.000700	0.001542	0.000049	0.0482	0.0036	10.18	0.7	9.94	0.32
FR_15_31_20	1235	257	7680	357	3530	2083000	19060	3031000	0.009530	0.000500	0.001496	0.000037	0.0450	0.0025	9.63	0.51	9.64	0.24
FR_15_31_21	1273	311	6120	297	2950	1721000	15490	2435000	0.009810	0.000850	0.001508	0.000049	0.0482	0.0045	9.91	0.85	9.71	0.32

Table C.1 (Continued) LA-ICP-MS U-Pb isotopic analyses.

Zircon grain analysis	Ion count rate (cps)								Isotope ratios						Calculated ages (Ma)			
	^{202}Hg	^{204}Pb	^{206}Pb	^{207}Pb	^{208}Pb	^{232}Th	^{235}U	^{238}U	$^{207}Pb/^{235}U$	$\pm 2\sigma^a$	$^{206}Pb/^{238}U$	$\pm 2\sigma^a$	$^{207}Pb/^{206}Pb$	$\pm 2\sigma^a$	$^{207}Pb/^{235}U \pm 2\sigma^a$		$^{206}Pb/^{238}U \pm 2\sigma^a$	
FR-14-49																		
FR_14_49_1	582	115	4450	221	726	344000	8160	1475000	0.011750	0.002100	0.001766	0.000130	0.0492	0.0039	11.85	2.1	11.38	0.82
FR_14_49_2	575	111	2310	124	396	221000	4480	814000	0.011600	0.002600	0.001700	0.000150	0.0505	0.0073	11.7	2.6	10.93	0.98
FR_14_49_3	530	93	2700	130	725	370000	5070	954000	0.011400	0.002100	0.001733	0.000130	0.0477	0.0045	11.49	2.1	11.16	0.82
FR_14_49_4	558	101	2406	117	554	269200	4414	826000	0.011250	0.002000	0.001769	0.000120	0.0468	0.0032	11.33	2	11.39	0.78
FR_14_49_5	517	113	1375	71.4	183	83000	2538	471000	0.012200	0.002400	0.001781	0.000140	0.0512	0.0060	12.2	2.4	11.51	0.89
FR_14_49_6	562	107	2180	118	448	194000	4100	762000	0.012300	0.002600	0.001812	0.000150	0.0527	0.0076	12.4	2.6	11.67	0.97
FR 14 49 7[b]	620	164	4050	510	1330	386000	6830	1237000	0.036300	0.008600	0.002060	0.000170	0.1160	0.0180	36	8.4	13.26	1.1
FR_14_49_8	504	109	1800	98	424	167000	3280	616000	0.014000	0.002900	0.001859	0.000150	0.0527	0.0076	14	2.9	11.97	0.96
FR_14_49_9	527	100	2906	136.9	663	363000	5580	1030000	0.011980	0.002100	0.001788	0.000130	0.0478	0.0034	12.14	2.1	11.51	0.83
FR_14_49_10	554	125	2970	152	509	260000	5580	990000	0.013200	0.002600	0.001886	0.000160	0.0523	0.0064	13.3	2.6	12.15	1
FR 14 49 11[b]	512	112	2137	442	1206	173100	3078	575000	0.066100	0.012000	0.002292	0.000170	0.2090	0.0170	64.4	12	14.76	1.1
FR 14 49 12[b]	510	93	2580	152	133	69600	5360	964000	0.015200	0.003100	0.001720	0.000150	0.0564	0.0074	15.3	3.1	11.08	0.96
FR_14_49_13	548	134	4120	214	980	449000	8430	1460000	0.014600	0.003200	0.001848	0.000150	0.0495	0.0083	14.70	3.20	11.90	0.96
FR_14_49_14	590	123	4740	226	1091	533000	8860	1514000	0.014200	0.002600	0.002004	0.000140	0.0482	0.0040	14.30	2.60	12.91	0.93
FR_14_49_15	536	144	3010	146.7	541	285100	5470	976000	0.013390	0.002400	0.001879	0.000140	0.0497	0.0038	13.58	2.40	12.10	0.90
FR_14_49_16	548	115	2666	129.7	529	265700	4990	900000	0.012300	0.002200	0.001784	0.000130	0.0502	0.0036	12.45	2.20	11.51	0.80
FR 14 49 17[b]	576	190	4030	448	1580	476000	7060	1290000	0.033300	0.008900	0.001980	0.000230	0.1180	0.0240	33.10	8.70	12.70	1.50
FR_14_49_18	581	117	1560	89	468	180000	2930	535000	0.015000	0.003400	0.001780	0.000160	0.0590	0.0100	15.00	3.40	11.48	1.00
FR 14 49 19[b]	589	144	2170	445	1140	140000	3260	591000	0.073000	0.013000	0.002240	0.000190	0.2160	0.0210	71.20	13.00	14.44	1.20
FR 14 49 20[b]	586	154	5760	1220	3590	412000	8630	1494000	0.073700	0.015000	0.002390	0.000190	0.2040	0.0210	72.00	14.00	15.38	1.20
FR_14_49_21	589	108	2204	102.7	355	165400	4380	738000	0.012200	0.002300	0.001808	0.000130	0.0478	0.0044	12.30	2.30	11.64	0.86
FR_14_49_22	542	121	2180	124	450	218000	4280	738000	0.015800	0.003800	0.001880	0.000170	0.0544	0.0098	15.90	3.80	12.11	1.10
FR_14_49_23	599	118	4160	211	1000	500000	8080	1420000	0.013200	0.002400	0.001816	0.000130	0.0497	0.0041	13.20	2.40	11.70	0.86
FR 14 49 24[b]	613	150	4690	406	1380	488000	9080	1563000	0.021700	0.004000	0.001847	0.000140	0.0886	0.0071	21.80	4.00	11.90	0.92
FR_14_49_1a	1535	313	15330	690	591	215000	25500	4200000	0.011660	0.001000	0.001760	0.000095	0.0485	0.0036	11.77	1.00	11.34	0.61

[a]Propagated error; [b]Discordant grain analysis; [c]Outlier analysis

Table C.2 $^{40}Ar/^{39}Ar$ isotopic analyses.

Heating step	40Ar/39Ar	±1s	37Ar/39Ar	±1s	36Ar/39Ar	±1s	$40Ar^*/39Ar_k$	±1s	40Ar(mol)	40Ar* (%)	$39Ar_k$ (%)	Age (Ma)	±2s	K/Ca	±2s
FR-14-79 alunite, J=0.001089±0.0000017															
1	23.30331	0.0628843	0.00103	0.00153	0.04256	0.00070	10.726053	0.205761	1.964E-15	46.03	12.03	20.95	0.80	416.151	1231.147
2	23.10693	0.0959638	0.00155	0.00252	0.03903	0.00097	11.573083	0.285861	1.215E-15	50.08	7.50	22.59	1.11	276.747	898.092
3	22.99850	0.1070048	0.00661	0.00490	0.04298	0.00112	10.296388	0.329409	9.117E-16	44.77	5.66	20.12	1.28	65.077	96.506
4	21.53154	0.0668264	0.01103	0.00246	0.04090	0.00093	9.445735	0.275207	1.196E-15	43.87	7.93	18.46	1.07	38.993	17.391
5	20.80288	0.0573125	0.00597	0.00268	0.03263	0.00105	11.160661	0.311622	1.127E-15	53.65	7.73	21.79	1.21	71.969	64.445
6	21.62870	0.0658781	0.01284	0.00320	0.03694	0.00097	10.712503	0.287091	1.316E-15	49.53	8.69	20.92	1.12	33.493	16.673
7	21.74622	0.0606709	0.01213	0.00231	0.03954	0.00113	10.062753	0.334087	1.221E-15	46.27	8.02	19.66	1.30	35.437	13.475
8	20.31160	0.0543333	0.00187	0.00299	0.03152	0.00078	10.996609	0.231362	1.447E-15	54.14	10.17	21.48	0.90	230.177	737.333
9	20.51342	0.0619721	0.00000	0.00288	0.03248	0.00056	10.915705	0.165229	1.346E-15	53.21	9.37	21.32	0.64	35.585	13.531
10	20.32507	0.0534001	0.00246	0.00205	0.03651	0.00101	9.534145	0.299057	1.320E-15	46.91	9.27	18.63	1.16	174.606	291.369
11	19.47189	0.0670342	0.00000	0.00222	0.03507	0.00093	9.107278	0.273640	1.002E-15	46.77	7.34	17.80	1.06	176.289	294.177
12	19.80956	0.0818825	0.00000	0.00425	0.03543	0.00117	9.337645	0.345677	8.735E-16	47.14	6.29	18.25	1.34	176.289	294.177
Plateau Age 20.44±0.86 Ma			Inverse Isochron Age 14.86±5.39			Total Fusion Age 20.26±0.31 Ma									
FR14-68, alunite J=0.0033610±5.4E-6															
1	3.59447	0.00736	0.01169	0.0003	0.00782	0.00014	1.284143	0.040332	1.41E-15	35.73	10.51	7.77	0.49	36.798	1.76
2	3.36298	0.00708	0.01218	0.0006	0.00676	0.00017	1.364503	0.051451	7.41E-16	40.57	5.9	8.25	0.62	35.308	3.175
3	3.04576	0.00637	0.01169	0.0005	0.00495	0.00024	1.584099	0.069987	6.49E-16	52.01	5.7	9.58	0.84	36.768	2.936
4	3.09484	0.00651	0.01148	0.0006	0.00503	0.00025	1.608541	0.073077	6.06E-16	51.97	5.24	9.73	0.88	37.444	4.047
5	2.89203	0.00587	0.01296	0.0004	0.00437	0.0001	1.599384	0.02969	1.09E-15	55.3	10.09	9.67	0.36	33.183	1.947
6	3.23082	0.00684	0.01459	0.001	0.00588	0.00026	1.492631	0.075971	6.20E-16	46.2	5.13	9.03	0.92	29.476	3.918
7	2.96317	0.00603	0.01238	0.0005	0.00434	0.00015	1.680848	0.045569	1.08E-15	56.72	9.75	10.16	0.55	34.719	2.728
8	3.08734	0.00637	0.01177	0.0005	0.00486	0.00012	1.65238	0.03591	1.17E-15	53.52	10.1	9.99	0.43	36.547	3.046
9	2.92491	0.00594	0.01292	0.0003	0.00429	0.00019	1.658053	0.055566	1.06E-15	56.69	9.67	10.03	0.67	33.274	1.646
10	3.38655	0.00693	0.01290	0.0004	0.00601	0.0002	1.611933	0.059834	1.11E-15	47.6	8.77	9.75	0.72	33.343	2.074
11	3.00061	0.00607	0.01341	0.0004	0.00484	0.00013	1.569165	0.039694	1.14E-15	52.29	10.19	9.49	0.48	32.057	1.848
12	3.14638	0.00637	0.01124	0.0005	0.00549	0.00014	1.524085	0.040437	1.05E-15	48.44	8.95	9.22	0.49	38.259	3.141
Weighted Mean Age 9.69±0.10 Ma			Total Fusion Age 9.41±0.09 Ma			**Inverse Isochron Age 10.61±0.80 Ma**									
FR13-179, alunite J=0.003355±5.4E-6															
1	4.55239	0.00932	0.01947	0.0004	0.0107	0.00018	1.392267	0.052804	1.43E-15	30.58	13.29	8.41	0.64	22.081	0.995
2	3.96232	0.00857	0.02016	0.0009	0.00854	0.00028	1.439834	0.083345	6.74E-16	36.34	7.21	8.69	1	21.325	1.788
3	3.9371	0.00919	0.02121	0.0015	0.009	0.00057	1.277883	0.168237	4.08E-16	32.46	4.39	7.72	2.03	20.274	2.816
4	3.58415	0.00828	0.02620	0.0014	0.00787	0.00054	1.258446	0.16064	3.57E-16	35.11	4.22	7.6	1.94	16.413	1.73
5	3.85122	0.00881	0.01930	0.0012	0.00888	0.00048	1.227426	0.140343	4.21E-16	31.87	4.64	7.41	1.69	22.28	2.651
6	4.53647	0.01289	0.02360	0.0011	0.01147	0.00046	1.147091	0.134767	4.74E-16	25.29	4.44	6.93	1.63	18.218	1.62
7	4.29066	0.01074	0.02022	0.0005	0.00955	0.00039	1.469276	0.11437	6.06E-16	34.24	5.99	8.87	1.38	21.264	1.03
8	5.14332	0.01087	0.02430	0.0005	0.01322	0.00023	1.236634	0.067806	1.45E-15	24.04	11.96	7.47	0.82	17.698	0.728
9	3.81835	0.00820	0.02662	0.0006	0.00875	0.00019	1.233422	0.057207	1.07E-15	32.3	11.93	7.45	0.69	16.154	0.68
10	2.86523	0.00620	0.02494	0.0003	0.00506	0.00007	1.370229	0.019909	2.16E-15	47.82	31.94	8.27	0.24	17.239	0.434
Plateau Age 8.16±0.25 Ma			Total Fusion Age 8.01±0.26 Ma			Inverse Isochron Age 8.55±0.64 Ma									

Appendix D

The table D.1 below summarizes the lithological, textural and mineralogical features of the selected rock samples from western Anatolia presented in Chapter 5. Those samples were petrologically assessment before being submitted for geochemical analyses.

Quality control of lithogeochemical and radiogenic isotope data is described in the Appendix B.

Table D.1 Descriptions of rock samples analyzed for major and trace element and/or Sr-Nd-Pb isotope geochemistry (western Anatolia - Chapter 5).

Sample	District	Igneous Complex	Location	Lat (°N)	Long (°E)	Lithology	Texture	Mineralogy[a]	Alteration
Western Anatolia									
FR-13-114	Simav	Simav intrusion	Eğrigöz	39.2654	28.9299	Granite	allotriomorphic, perthite, poikilitic (ksp)	ksp, qz, pl, bt, feox	
FR-15-18		Pınarbaşı stock	Pınarbaşı	39.0165	29.3229	Quartz monzonite	hypidiomorphic, porphyric	ksp, qz, pl, bt, mt	
FR-14-29	Simav	Simav intrusion	Alaçam	39.4200	28.4881	Granodiorite	hypidiomorphic, poikilitic, local myrmekite	qz, pl, ksp, bt, hb, opx, tour	
FR-14-27a	Simav	Bigadic	Red Rabbit	39.2893	28.3286	Trachydacite	hypocrystalline, porphyritic, flety	pl, qz, ksp, bt, hb?, feox, mu	chl-ser (mod)
FR-13-68	Usak	Uşak-Güre	Kışladağ	38.4818	29.1491	Monzonite	hypocrystalline, porphyric, poikilitic (pl)	pl, ksp, bt, feox, hb, qz, cpx	sil-chl-ser-clay (mod)
FR-14-47		Afyon	Sandıklı	38.5010	30.3288	Quartz monzonite	megacrystic, poikilitic, hypidiomorphic, perthite	ksp, pl, qz, opx, bt, hb, ru	
FR-14-54		Afyon	Sandıklı	38.5122	30.3490	Quartz monzonite	hypidiomorphic, porphyritic	ksp, pl, cpx, bt, feox, qz	
FR-15-32	Bodrum	Bodrum	Turgutreis	37.0368	27.2542	Monzonite	hypidiomorphic, porphyritic	ksp, pl, hb, qz, feox, bt, tour	

Abbreviations: bt = biotite; chl = chlorite; cpx = clinopyroxene; feox = Fe-oxide; hb = hornblende; ksp = alkali feldspar; mod = moderate; mt = magnetite; mu = muscovite; opx = orthopyroxene; qz = quartz; pl = plagioclase; ru = rutileser = sericite; sil = silica; ti = titanite; tour = tourmaline;

[a]mineral order from the most to the least abundant

Appendix E

Some geochronological data were acquired from the Kışladağ porphyry gold mine in Turkey during this PhD research project. I was invited by Timothy Baker (Eldorado Gold) to publish those data and contribute to his paper "The Geology of the Kışladağ Porphyry Gold Deposit, Turkey" published in the Society of Economic Geologists, Special Publication 16 (p. 57-83) in 2016. I was responsible to write two sections about geochronological data presentation and interpretation, and make a table and two figures. The geochronological data include CA-TIMS U-Pb, Re-Os and $^{40}Ar/^{39}Ar$ dates provided by Richard Friedman (PCIGR-UBC), Robert A. Creaser (University of Alberta) and Richard Spikings (University of Geneva), respectively. Timothy Baker, Aleksandar Mišković, Richard Friedman, Robert Creaser and Richard Spikings edited my section in this manuscript.

E.1 Geochronology of the Kışladağ porphyry gold deposit

High-precision U-Pb dating of chemically abraded magmatic zircons by the ID-TIMS technique in Intrusions 2 and 3 was supplemented by $^{40}Ar/^{39}Ar$ geochronology of hydrothermal biotite and alunite, and Re-Os dating of molybdenite in order to constrain the age of mineralization and different hydrothermal events (Figures E.1 and E.2). The ages of the youngest primary zircons from Intrusions 2 and 3 are 14.76 ± 0.01 Ma (FR-13-66) and 14.36 ± 0.02 Ma (FR-13-68), respectively (Tables E.1 and E.2). These ages are consistent with the crosscutting relationships observed in core and outcrop, where the gold mineralization-hosting Intrusion 2 is cut by the poorly mineralized Intrusion 3. Intrusion 2 cuts the Beydağı volcanic package, thus placing a lower age limit on the local volcanism (> 14.76 ± 0.01 Ma). The youngest unaltered andesitic flows at the top of the Beydağı volcanic remnant stratigraphy were dated at 12.15 ± 0.15 Ma ($^{40}Ar/^{39}Ar$ dating on igneous biotite; Karaoğlu et al., 2010).

Gold mineralization is most strongly developed in Intrusions 1 and 2, whereas Intrusion 3 contains sub-economic concentrations. Molybdenite from quartz-sulfide vein stockworks of potassic-altered Intrusion 1 (FR-14-169) yielded a Re-Os model age of 14.49 ± 0.06 Ma (Table

E.1). This is consistent with the geologic field relationships and geochronology of Intrusions 2 and 3 that bracket the main stage of mineralization between 14.76 ± 0.01 and 14.36 ± 0.02 Ma. Secondary biotite from potassic alteration in Intrusions 1 (GC-115-465) and 2 (GC-52-216.4) yielded $^{40}Ar/^{39}Ar$ plateau ages of 14.44 ± 0.12 and 14.42 ± 0.12 Ma, respectively (Figure E.1; Tables E.1 and E.3). These $^{40}Ar/^{39}Ar$ data and Re-Os age highlight a close temporal relationship between sulfide mineralization and the main potassic alteration event, all occurring around 14.5 Ma. Another aliquot of secondary biotite from Intrusion 1 (GC-40-415) was also dated by $^{40}Ar/^{39}Ar$ technique at 14.15 ± 0.14 Ma. This age does not overlap with the age data obtained from the other hydrothermal biotite crystals collected from Intrusions 1 and 2 (14.44 ± 0.12 and 14.42 ± 0.12 Ma), and postdates the poorly mineralized Intrusion 3. However, as described in the "Deposit Geology" section (in Baker et al.'s paper, 2016), Intrusion 3 locally contains a weak potassic alteration, suggesting there are localized high temperature hydrothermal events post main-stage potassic and mineralization events which this biotite age may reflect.

The age of alunite crystals from the advanced argillic alteration zone within the latitic Beydağı volcanic rocks has been determined at 13.84 ± 0.29 Ma by $^{40}Ar/^{39}Ar$ dating, consistent with field observations where it overprints the potassic alteration. Because the alunite plateau age suffers from some gas loss (disturbed plateau age), the timing of the late lower temperature hydrothermal event can only be constrained accurately by the Intrusion 3 (14.36 ± 0.02 Ma) and post-alteration Beydağı andesite (12.15 ± 0.15 Ma; Karaoğlu et al., 2010).

E.2 Age of the Kışladağ magmatic-hydrothermal system

The detailed geochronological results from the Kışladağ deposit constrain the timing and duration of the main gold mineralization stage to < 0.4 m.y (14.76 ± 0.02-14.36 ± 0.02 Ma; Figure E.2) and evolving in the following sequence; (1) Intrusion 1 (> 14.76 ± 0.02 Ma), (2) Intrusion 2 (14.76 ± 0.02 Ma), (3) potassic alteration (14.4 ± 0.1 Ma) coeval with mineralization (14.49 ± 0.06 Ma), (4) Intrusion 3 (14.36 ± 0.02 Ma), (5) post-Intrusion 3 weak potassic alteration (14.15 ± 0.14 Ma), and (6) advanced argillic alteration (14.36 ± 0.02-12.15 ± 0.15 Ma). The succession of magmatic and high- to low-temperature hydrothermal

events are interpreted to represent cooling of the Kışladağ magmatic system and the collapse of the hydrothermal column, whereby the lower temperature argillic and advanced argillic alteration overprints the high-temperature potassic assemblage. The deposition of gold can be constrained by the emplacement of the sulfide mineralization dated at 14.49 ± 0.06 Ma by Re-Os on molybdenite.

Despite the difficulties in comparing the time scales of porphyry deposit formation, the life span of the Kışladağ main mineralization-stage hydrothermal system and gold deposition appear consistent with other worldwide multiphase porphyry deposits that range from < 0.1 to > 4.0 m.y., and along the Western Tethyan Orogenic Belt, such as Medet, Bulgaria (1.4 m.y.; Peytcheva et al., 2009), Miduk, Iran (1.7 m.y.; McInnes et al., 2005), and Reko Diq in Pakistan (1 m.y.; Razique et al., 2014). However, these life spans are orders of magnitude longer than the theoretically modeled times required for consolidation of individual porphyry intrusions (< 40 k.y.; Cathles et al., 1997), porphyry Cu ore formation (< 100 k.y.; McInnes et al., 2005), and major potassic alteration events (< 2,000 y.; Cathles and Shannon, 2007). Long-lived porphyry systems are more prevalent and result from either the repetition of magmatic pulses, each incrementally adding metals to the total budget of the deposit (Sillitoe, 2010), or methodological problems such as the accuracy of the intercalibration among the U-Pb, $^{40}Ar/^{39}Ar$, and Re-Os dating methods, or the erroneous estimate of the emplacement age of the causative intrusion, as discussed by Sillitoe and Mortensen (2010) and Chiaradia et al. (2014). There is no apparent relationship between the size of porphyry deposits and the duration of the intrusive activity (Sillitoe, 2010). However, the duration of magmatic activity is considered to be the main parameter defining the total hydrothermal life spans of porphyry systems dictated by the total time elapsed between the emplacement of the first and last porphyry phases (Sillitoe and Mortensen, 2010). The bulk of gold mineralization may be introduced during an early and discrete stage of these life spans (Sillitoe and Mortensen, 2010): 14.49 ± 0.06 Ma in the case of Kışladağ.

District geochronology along the Uşak-Güre graben has highlighted the southwestward migration of the volcanism within the basin from 17.29 ± 0.13 to 12.15 ± 0.15 Ma (Karaoğlu et al., 2010). The northern Elmadağ volcano is the oldest (17.29 ± 0.13-16.28 ± 0.09 Ma), whereas the İtecektepe and Beydağı volcanic centers are younger (15.04 ± 0.10 and 12.15 ± 0.15 Ma; Karaoğlu et al., 2010). The new radiometric results and field observations obtained from the Kışladağ deposit and the Beydağı volcanic center indicate that magmatism at the Beydağı volcanic center took place in three successive episodes; (1) pre-porphyry effusive latitic magmatism (> 14.760 ± 0.013 Ma), (2) Kışladağ monzonite porphyry intrusive stocks (> 14.76 ± 0.01-14.36 ± 0.02 Ma), and (3) post-alteration andesitic volcanism (12.15 ± 0.15 Ma; Karaoğlu et al., 2010).

Table E.1 Summary of the new geochronological data obtained from the Kışladağ deposit.

Intrusive suite (Zircon, CA-ID-TIMS U-Pb)								
Sample	*Lithology Type*	*Drill Hole*	*From (m)*	*To (m)*	*Concordia age (Ma)*	*MSWD*		
FR-13-66	Intrusion 2	GC-361	804	805	14.76 ± 0.01	0.02		
FR-13-68	Intrusion 3	GC-371	349	350	14.36 ± 0.02	0.78		
Ore (Molybdenite, Re-Os)								
Sample	*Lithology host*	*Easting*	*Northing*	*Re ppm*	*^{187}Re ppm*	*^{187}Os ppb*	*Model age (Ma)*	
FR-14-169	Intrusion 1	687500	4261780	5738 ± 15	3606 ± 9	870.4 ± 0.68	14.49 ± 0.06	
Potassic alteration (Biotite, ^{40}Ar/^{39}Ar)								
Sample	*Lithology host*	*Drill Hole*	*From (m)*	*To (m)*	*Plateau age (Ma)*	*Total fusion age (Ma)*	*Inverse isochron (Ma)*	*^{39}Ar %*
GC-40-415	Intrusion 1	GC-40	415	416	14.15 ± 0.14*	-	14.12 ± 0.15	93.9
GC-52-216.	Intrusion 2	GC-52	216.4	217	14.42 ± 0.12*	-	14.42 ± 0.13	99.9
GC-115-46:	Intrusion 1	GC-115	465	466	14.44 ± 0.12*	-	14.41 ± 0.13	99.9
Advanced argillic alteration (Alunite, ^{40}Ar/^{39}Ar)								
Sample	*Lithology host*	*Drill Hole*	*From (m)*	*To (m)*	*Plateau age (Ma)*	*Total fusion age (Ma)*	*Inverse isochron (Ma)*	*^{39}Ar %*
FR-13-65	Latite lava flow	GC-367A	43.3	44	13.84 ± 0.29*	13.44 ± 0.22	15.22 ± 2.91	52.93
					**Preferred age*			

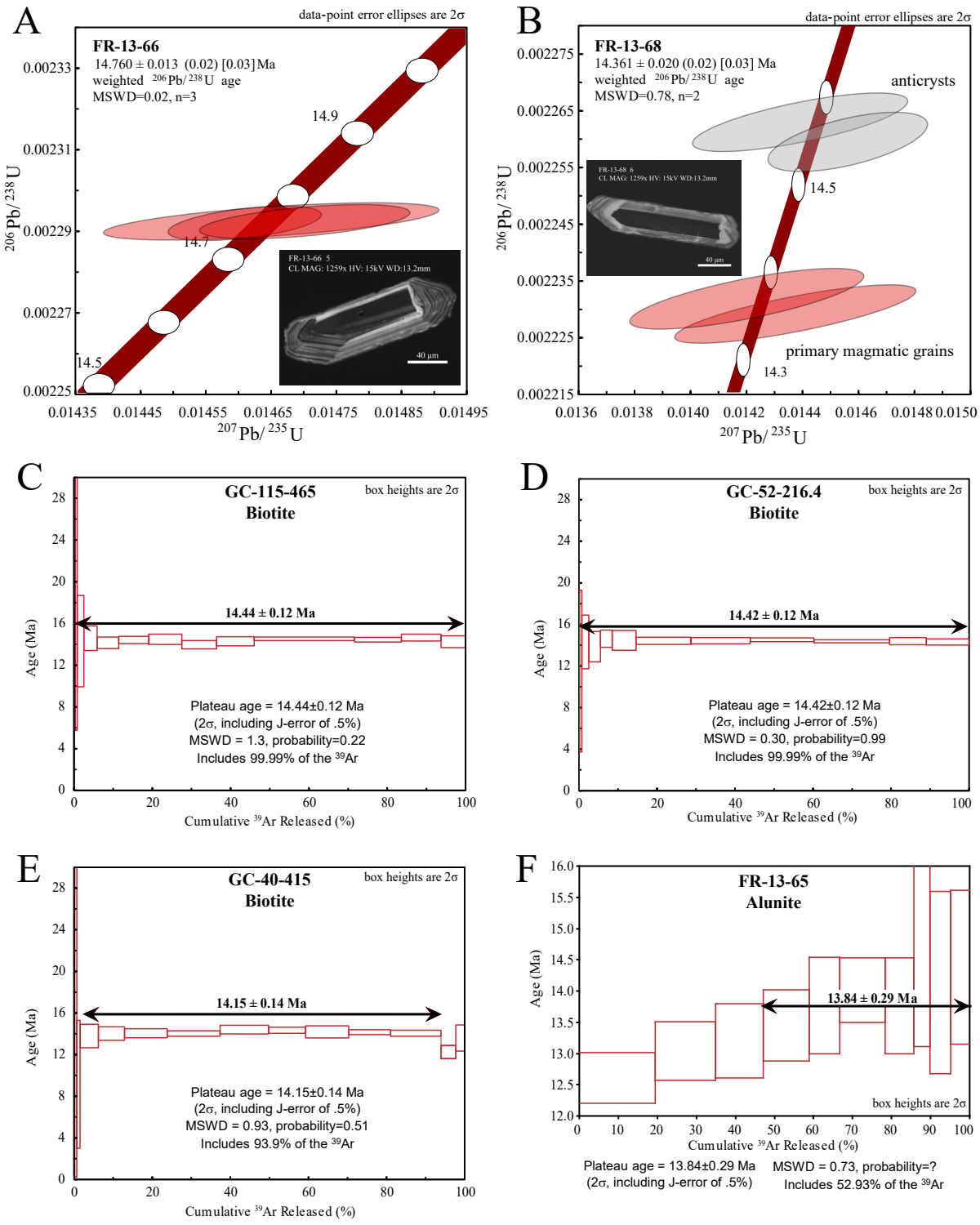

Figure E.1 A. and B. U-Pb Concordia plots for FR-13-66 (Intrusion 2, n = 3) and FR-13-68 (Intrusion 3, n = 2) also showing the two anticrystic grains analyzed. C. D. E. and F. $^{40}Ar/^{39}Ar$ plateau age diagrams for GC-115-465 (hydrothermal biotite, potassic alteration, Intrusion 1), GC-52-216.4 (hydrothermal biotite, potassic alteration, Intrusion 2), GC-40-415 (hydrothermal biotite, potassic alteration, Intrusion 1) and FR-13-65 (hypogene alunite, advanced argillic alteration, latite lava flows).

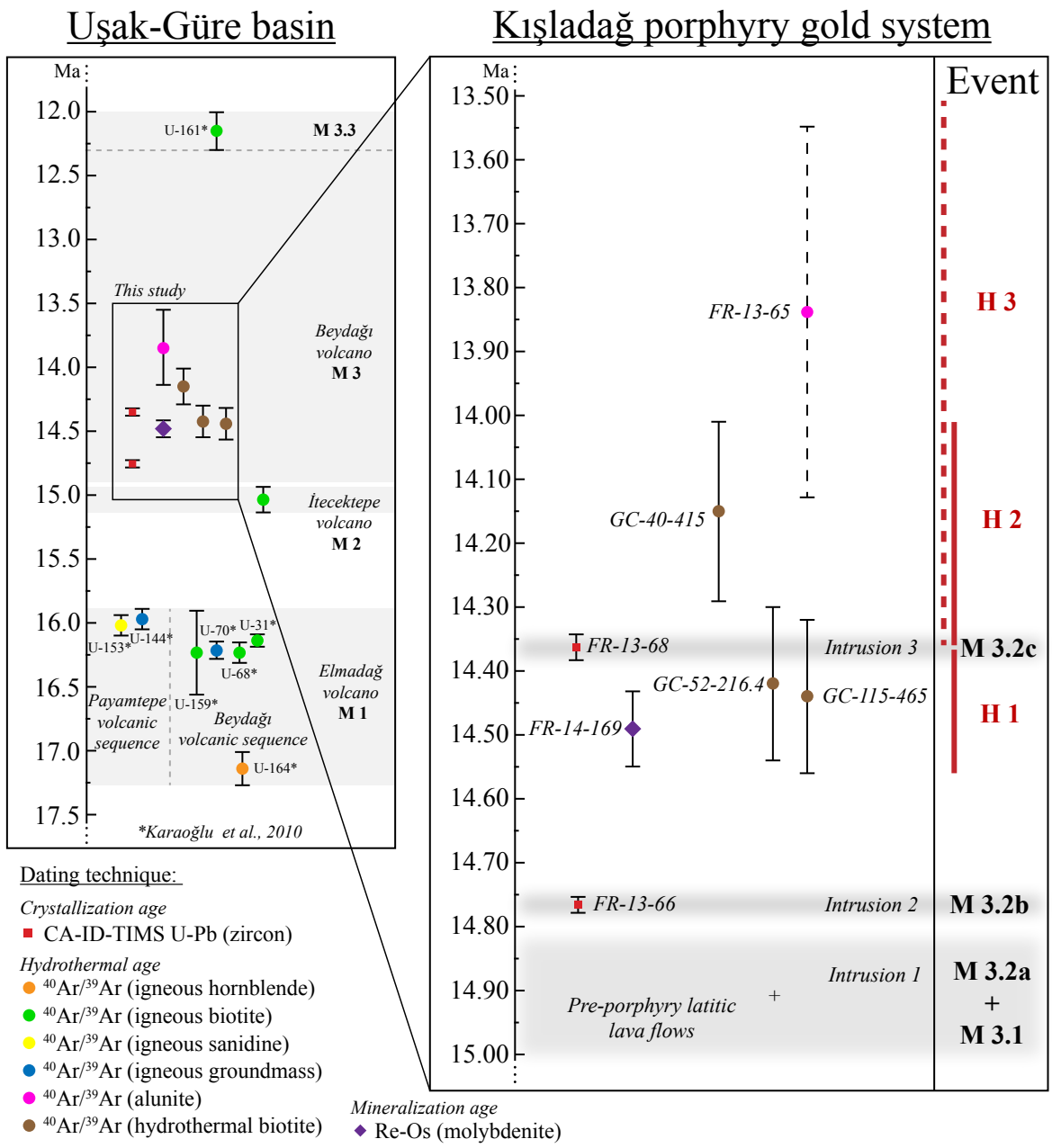

Figure E.2 Timescale diagram illustrating the succession of the magmatic (M) and hydrothermal (H) events in the Uşak - Güre basin (left side) and at the Kışladağ deposit (right side). Magmatism in the Uşak - Güre basin took place in three distinct episodes: (M1) Elmadağ volcano (17.29 ± 0.13-16.28 ± 0.09 Ma); (M2) İtecektepe volcano (15.04 ± 0.10 Ma); and (M3) Beydağı volcano (~15-12.15 ± 0.15 Ma). The latter magmatic phase can be divided into three local magmatic episodes: (M3.1) preporphyry latitic lava flows (> 14.76 ± 0.01 Ma); (M3.2) porphyry intrusive phases including Intrusion 1 (> 14.76 ± 0.01 Ma; M3.2a), Intrusion 2 (14.76 ± 0.01 Ma; M3.2b) and Intrusion 3 (14.36 ± 0.02 Ma; M3.2c). Hydrothermal events likely occurred in at least three distinct pulses at Kışladağ including: (H1) potassic alteration, sulfide precipitation, and gold deposition (14.49 ± 0.06-14.42 ± 0.12 Ma); (H2) weak potassic alteration post-Intrusion 3 (< 14.36 ± 0.02-14.15 ± 0.15 Ma); and (H3) late advanced argillic alteration (< 14.36 ± 0.02-12.15 ± 0.15 Ma).

E.3 CA-ID-TIMS U-Pb dating analytical procedure

U-Pb dating by Chemical Abrasion-Isotope Dilution-Thermal Ionization Mass Spectrometry (CA-ID-TIMS) on magmatic zircon was conducted on the Intrusions 2 (FR-13-66) and 3 (FR-13-68) at the Pacific Center for Isotope Geochemistry Research (PCIGR) (Table E2). CA-ID-TIMS procedures described here are modified from Mundil et al. (2004), Mattinson (2005) and Scoates and Friedman (2008). After rock samples underwent standard mineral separation procedures, zircons were handpicked in alcohol. The clearest, crack- and inclusion-free grains were selected, photographed and then annealed in quartz glass crucibles at 900˚C for 60 hours. Annealed grains were transferred into 3.5 mL PFA screwtop beakers, ultrapure HF (up to 50% strength, 500 mL) and HNO_3 (up to 14 N, 50 mL) were added and caps were closed finger tight. The beakers were placed in 125 mL PTFE liners (up to four per liner) and about 2 mL HF and 0.2 mL HNO_3 of the same strength as acid within beakers containing samples were added to the liners. The liners were then slid into stainless steel Parr™ high pressure dissolution devices, which were sealed and brought up to a maximum of 200˚C for 8-16 hours (typically 175˚C for 12 hours). Beakers were removed from liners and zircon was separated from leachate. Zircons were rinsed with >18 MΩ.cm water and sub-boiled acetone. Then 2 mL of sub-boiled 6N HCl was added and beakers were set on a hotplate at 80˚-130˚C for 30 minutes and again rinsed with water and acetone. Masses were estimated from the dimensions (volumes) of grains. Single grains were transferred into clean 300 mL PFA microcapsules (crucibles), and 50 mL 50% HF and 5 mL 14 N HNO_3 were added. Each was spiked with a $^{233\text{-}235}U\text{-}^{205}Pb$ tracer solution (EARTHTIME ET535), capped and again placed in a Parr liner (8-15 microcapsules per liner). HF and nitric acids in a 10:1 ratio, respectively, were added to the liner, which was then placed in Parr high pressure device and dissolution was achieved at 240˚C for 40 hours. The resulting solutions were dried on a hotplate at 130˚C, 50 mL 6N HCl was added to microcapsules and fluorides were dissolved in high pressure Parr devices for 12 hours at 210˚C. HCl solutions were transferred into clean 7 mL PFA beakers and dried with 2 mL of 0.5 N H_3PO_4. Samples were loaded onto degassed, zone-refined Re

filaments in 2 mL of silicic acid emitter (Gerstenberger and Haase, 1997).

Isotopic ratios were measured a modified single collector VG-54R or 354S (with Sector 54 electronics) thermal ionization mass spectrometer equipped with analogue Daly photomultipliers. Analytical blanks were 0.2 pg for U and up to 1 pg for Pb. U fractionation was determined directly on individual runs using the EARTHTIME ET535 mixed $^{233\text{-}235}U$-^{205}Pb isotopic tracer and Pb isotopic ratios were corrected for fractionation of 0.25 %/amu, based on replicate analyses of NBS-982 reference material and the values recommended by Thirlwall (2000). Data reduction employed the Excel-based program of Schmitz and Schoene (2007). Standard Concordia diagrams were constructed and regression intercepts, weighted averages calculated with Isoplot (Ludwig, 2003). Unless otherwise noted all errors were quoted at the 2 sigma or 95% level of confidence. Isotopic dates were calculated with the decay constants λ_{238} = 1.55125-10 and λ_{235} = 9.8485-10 (Jaffey et al., 1971). EARTHTIME U-Pb synthetic solutions were analysed on an on-going basis to monitor the accuracy of results.

E.4 $^{40}Ar/^{39}Ar$ dating analytical procedure

Hand-picked, unoxidized, hypogene, hydrothermal alunite and biotite separates from the advanced argillic and potassic alteration zones respectively, were rinsed in de-ionized water and 5% HNO_3 in an ultrasonic bath, packed in copper foil and irradiated in the CLICIT facility of the TRIGA reactor at Oregon State University for 12 hours. Samples were degassed by step-heating with a 55W CO_2-IR laser (Photon Machines Inc.) that was rastered over the samples to provide even-heating of the grains, and the extracted gas was gettered (SAES GP50 ST101 and AP10) in a stainless steel UHV line, after passing through a cold trap chilled to ~150 Kelvin. Fish Canyon Tuff sanidine was used as a fluence monitor, with an age of 28.02 ± 0.16 Ma (1σ internal uncertainty; Renne et al., 1998). Argon isotopes were analyzed at the University of Geneva using a multi-collector GV Instruments Argus mass spectrometer equipped with four high-gain (1012 Ω) Faraday detectors, and a single 1011 Ω Faraday detector (^{40}Ar). Time-zero regressions were fitted to data collected from twelve cycles and ages were calculated using the 40K decay constant of Steiger and Jaeger (1977). Age plateaus were determined using the

criteria of Dalrymple and Lanphere (1974), and data reduction utilized ArArCalc (Koppers, 2002). The complete data set, along with additional analytical information is presented in Table E.3.

E.5 Re-Os dating analytical procedure

Re-Os dating on molybdenite (FR-14-169) was performed at the University of Alberta in Edmonton (AB, Canada). A molybdenite mineral separate was produced by metal-free crushing followed by gravity and magnetic concentration methods. Methods used for molybdenite analysis are described in detail by Selby and Creaser (2004) and Markey et al. (2007). The ^{187}Re and ^{187}Os concentrations in molybdenite were determined by isotope dilution mass spectrometry using Carius-tube, solvent extraction, anion chromatography and negative thermal ionization mass spectrometry techniques. A mixed double spike containing known amounts of isotopically enriched ^{185}Re, ^{190}Os, and ^{188}Os analysis was used. Isotopic analysis was made using a ThermoScientific Triton mass spectrometer by Faraday collector. Total procedural blanks for Re and Os were less than < 3 picograms and 2 picograms, respectively, which were insignificant for the Re and Os concentrations in molybdenite. The Chinese molybdenite powder HLP-5 (Markey et al., 1998), was analyzed as a standard. For this control sample over a period of two years (2013-2015), an average Re-Os date of 221.56 ± 0.40 Ma (1SD uncertainty, n=10) was obtained. This Re-Os age date was within uncertainty to that reported by Markey et al. (1998) of 221.0 ± 1.0 Ma.

Table E.2 U-Th-Pb isotopic data - CA-ID-TIMS

Compositional Parameters										Radiogenic Isotope Ratios								Isotopic Ages						
Sample (a)	Wt. mg (h)	U ppm (i)	Pb ppm (i)	Th / U (b)	$^{206}Pb^*$ x10^{-13} mol (c)	mol % $^{206}Pb^*$ (c)	Pb^*/Pb_c (c)	Pb_c (pg) (c)	$^{206}Pb/^{204}Pb$ (d)	$^{208}Pb/^{206}Pb$ (e)	$^{207}Pb/^{206}Pb$ (e)	% err (f)	$^{207}Pb/^{235}U$ (e)	% err (f)	$^{206}Pb/^{238}U$ (e)	% err (f)	corr. coef.	$^{207}Pb/^{206}Pb$ (g)	± (f)	$^{207}Pb/^{235}U$ (g)	± (f)	$^{206}Pb/^{238}U$ (g)	± (f)	Comments
FR-13-66																								
A	0.0036	666	1.7	0.182	0.2325	96.78%	8	0.64	574	0.061	0.047822	1.316	0.015442	1.409	0.002342	0.151	0.648	90.46	31.10	15.56	0.22	15.08	0.02	xenocryst[j]
B	0.0027	919	2.3	0.368	0.2356	97.08%	10	0.58	635	0.119	0.046346	1.354	0.014649	1.447	0.002292	0.164	0.607	15.68	32.45	14.77	0.21	14.76	0.02	
C	0.0027	1016	2.6	0.230	0.2764	97.68%	12	0.54	797	0.080	0.049810	1.111	0.016703	1.196	0.002432	0.160	0.583	186.12	25.79	16.82	0.20	15.66	0.02	xenocryst[j]
D	0.0043	1080	2.6	0.318	0.4409	98.55%	20	0.53	1279	0.103	0.046226	0.602	0.014608	0.664	0.002292	0.151	0.501	9.43	14.45	14.73	0.10	14.76	0.02	
E	0.0040	846	2.1	0.370	0.3214	97.84%	13	0.58	855	0.120	0.046512	0.836	0.014701	0.905	0.002292	0.150	0.526	24.25	20.01	14.82	0.13	14.76	0.02	
FR-13-68																								
A	0.0030	768	2.1	0.561	0.2160	96.23%	8	0.69	491	0.180	0.046118	2.075	0.014389	2.206	0.002263	0.188	0.721	3.78	49.85	14.51	0.32	14.57	0.03	anticryst
B	0.0027	431	1.2	0.601	0.1076	94.75%	6	0.49	353	0.196	0.046765	2.331	0.014372	2.478	0.002229	0.190	0.788	37.26	55.64	14.49	0.36	14.35	0.03	
C	0.0040	377	1.2	0.487	0.1746	96.91%	10	0.46	599	0.184	0.054545	1.076	0.020994	1.165	0.002792	0.142	0.661	393.61	24.09	21.10	0.24	17.97	0.03	xenocryst[j]
D	0.0019	668	1.8	0.641	0.1175	95.32%	6	0.47	395	0.206	0.046138	2.292	0.014196	2.435	0.002232	0.198	0.744	4.81	55.03	14.31	0.35	14.37	0.03	
E	0.0026	527	1.3	0.456	0.1284	96.87%	9	0.34	591	0.148	0.046741	1.510	0.014561	1.614	0.002259	0.190	0.590	36.00	36.05	14.68	0.24	14.55	0.03	anticryst

(a) A, B etc. are labels for fractions composed of single zircon grains or fragments; all fractions annealed and chemically abraded after Mattinson (2005) and Scoates and Friedman (2008).
(b) Model Th/U ratio calculated from radiogenic 208Pb/206Pb ratio and 207Pb/235U age.
(c) Pb* and Pbc represent radiogenic and common Pb, respectively; mol % $^{206}Pb^*$ with respect to radiogenic, blank and initial common Pb.
(d) Measured ratio corrected for spike and fractionation only. Mass discrimination of 0.25%/amu based on analysis of NBS-982; all Daly analyses.
(e) Corrected for fractionation, spike, and common Pb; all common Pb was assumed to be procedural blank: 206Pb/204Pb = 18.50 ± 1.0%; 207Pb/204Pb = 15.50 ± 1.0%; 208Pb/204Pb = 38.40 ± 1.0% (all uncertainties 1-sigma).
(f) Errors are 2-sigma, propagated using the algorithms of Schmitz and Schoene (2007) and Crowley et al. (2007).
(g) Calculations are based on the decay constants of Jaffey et al. (1971). 206Pb/238U and 207Pb/206Pb ages corrected for initial disequilibrium in 230Th/238U using Th/U [magma] = 3.
(h) Nominal fraction weights estimated from photomicrographic grain dimensions, adjusted for partial dissolution during chemical abrasion.
(i) Nominal U and total Pb concentrations subject to uncertainty in photomicrographic estimation of weight and partial dissolution during chemical abrasion.
(j) Xenocryst or grain with inherited core.

Table E.3 $^{40}Ar/^{39}Ar$ dating data – Hypogene alunite (FR-13-65) from the Kışladağ gold mine.

Step-Heating	$^{40}Ar/^{39}Ar$	±1σ	$^{37}Ar/^{39}Ar$	±1σ	$^{36}Ar/^{39}Ar$	±1σ	$^{40}Ar^*/^{39}Ar_k$	±1σ	^{40}Ar(mol)	$^{40}Ar^*$ (%)	$^{39}Ar_k$ (%)	Age (Ma)	±2σ (Ma)	K/Ca	±2σ
FR13-65 alunite, J=0.0033544±5.4E-6															
1	5.18307	0.01042	0.03669	0.00041	0.01047	0.00012	2.090995	0.033718	2.968E-15	40.34	19.43	12.61	0.41	11.720	0.264
2	4.68820	0.00950	0.03814	0.00046	0.00856	0.00013	2.162194	0.038963	2.136E-15	46.12	15.46	13.04	0.47	11.273	0.270
3	4.44169	0.00913	0.03947	0.00047	0.00763	0.00017	2.190227	0.049380	1.595E-15	49.31	12.18	13.21	0.59	10.893	0.260
4	4.12619	0.00838	0.03815	0.00048	0.00642	0.00016	2.231022	0.047562	1.437E-15	54.07	11.82	13.45	0.57	11.272	0.284
5	4.35781	0.00903	0.04058	0.00066	0.00703	0.00022	2.283634	0.064084	1.004E-15	52.40	7.82	13.77	0.77	10.597	0.343
6	3.99418	0.00810	0.04004	0.00053	0.00566	0.00015	2.324670	0.042998	1.370E-15	58.20	11.64	14.01	0.52	10.740	0.286
7	4.04053	0.00847	0.03747	0.00068	0.00595	0.00022	2.283730	0.063936	8.785E-16	56.52	7.38	13.77	0.77	11.474	0.417
8	4.13907	0.00912	0.04262	0.00091	0.00581	0.00043	2.426074	0.125905	4.999E-16	58.61	4.10	14.62	1.51	10.090	0.431
9	4.12256	0.00875	0.03864	0.00067	0.00602	0.00041	2.345457	0.121592	6.450E-16	56.89	5.31	14.14	1.46	11.128	0.386
10	3.98714	0.00878	0.04197	0.00111	0.00543	0.00035	2.385513	0.102719	5.729E-16	59.83	4.87	14.38	1.23	10.246	0.541

Plateau Age 13.84±0.29 Ma (7 steps, 52.93% ^{39}Ar)

Total Fusion Age 13.44±0.22 Ma

Inverse Isochron Age 15.22±2.91 Ma

Mass discrimination 0.9794±0.051.

Data are corrected for blanks, interfering nucleogenic reactions and decay of 37Ar and 39Ar.

Irradiated for 12 hours at Oregon State University, TRIGA, CLICIT, 39Ar/37Ar 6.73E-4, 36Ar/37Ar 2.64E-4, 40Ar/39Ar 1.01E-3, 38Ar/39Ar 1.138E-2.

Steps highlighted with bold text are included in the calculation of the weighted mean age and the plateau age.

Samples heated with a IR-CO2 laset for 30 seconds, with 5 minutes cleaning with a ST101 and AP10 getter in a stainless teel extraction line.

Data collected with an Argus mass spectrometer. Multi collection with 1E11Ω Faraday (40Ar) and 1E12Ω Faradays (39Ar. 38Ar. 37Ar. 36Ar).